Design and Analysis of Biomimetic Medusa Robots

Alexis A. Villanueva

Dissertation submitted to the faculty of the Virginia Polytechnic Institute and State University in partial fulfillment of the requirements for the degree of

Doctor of Philosophy

In

Mechanical Engineering

Shashank Priya
John H. Costello
Pavlos P. Vlachos
Rolf Mueller
Andrew J. Kurdila

March 20, 2013
Blacksburg, Virginia

Keywords: jellyfish, biomimetic, kinematic, robot, shape memory alloy

© Alexis A. Villanueva

Design and Analysis of Biomimetic Medusa Robots

Alexis A. Villanueva

ABSTRACT

The design of unmanned underwater vehicle (UUV) was inspired by the form and functionality of Jellyfish. These natural organisms were chosen as bio-inspiration for a multitude of reasons including: efficiency, good room for payload, and a wide range of sizes and morphology. Shape memory alloy (SMA) actuators were selected as the primary source of actuation for the propulsion of the artificial jellyfish node. These actuators offer high power density which enables a compact system size and silent operation which is preferred for surveillance. SMA wires mimic the form and function of natural muscles; allowing for a wider range of applications than conventional actuators. Commercial SMA wires (100 um in diameter) can exhibit a 4% deformation of the initial actuator length with a blocking stress of over 200 MPa.

The deformation of SMA wire is not enough to mimic the bell contraction of jellyfish. In order to resolve this problem, a beam-shape composite actuator using SMA wires as the active component, termed as BISMAC, was designed to provide large curvature. The BISMAC design was inspired by rowing jellyfish bell contraction. Characterization of maximum deformation in underwater conditions was performed for different actuator configurations to analyze the effect of design parameters that include silicone thickness, flexible steel thickness and distance between SMA and flexible steel. A constant cross-section (CC) BISMAC of 16 cm in length was found to achieve deformation with a radius of curvature of 3.5 cm. Under equilibrium conditions, the CC-BISMAC was found to achieve 80% of maximum deformation consuming 7.9 J per cycle

driven at 16.2 V/0.98 A and frequency of 0.25 Hz. Using the a developed analytical model, an actuator design was fabricated mimicking the maximum deformation profile of the *A. aurita*. The optimized AA-BISMAC achieved a maximum curvature of 0.428 1/cm as compared to 0.438 1/cm for the *A. aurita* with an average squared root error of 0.043 (1/cm), 10.2% of maximum *A. aurita* curvature.

BISMAC actuators are unidirectional flexible actuators capable of exhibiting high curvature. To extend the application range of these actuators, they were modified to achieve bidirectional deformation. The new bidirectional actuators termed as “BiFlex” actuators had the capability to achieve large deformation in two directions. The FlexLegs consist of six segments which can be actuated individually. Two different sets of legs were constructed to determine the effect of size. The small legs measured 35.8 mm in height and 63.2 mm in width and the large legs were 97.4 mm in height and 165.4 mm in width. The small FlexLegs achieved a maximum deformation of 12 % and 4 % in the x- and y-direction respectively using a power of 0.7 W while producing a maximum force of 0.023 N. They were also able to withstand a load of 1.18 N. The large FlexLegs had a maximum deformation of 57 % and 39 % in the x- and y-direction respectively using a power of 3 W while producing a force of 0.045 N. They were able to withstand a load of 0.25 N. The legs were also able to perform several walking algorithms consisting of stepping, crabbing and yawing.

In order to reduce the power consumption and contraction time of SMA wires, a feedback control scheme using wire resistance was developed. The controller required the knowledge of threshold resistance and safe current inputs which were determined experimentally. The overheating effect of SMA wires was analyzed for BioMetal Fiber (BMF) and Flexinol 100 µm diameter wires revealing an increase in resistance as the wires overheated. The controller was

first characterized on a SMA wire with bias spring system for a BMF 100 using $I_{hi} = 0.5$ A and $I_{low} = 0.2$ A, where hi corresponds to peak current for fast actuation and low corresponds to the safe current which prevents overheating and maintains desired deformation. A contraction of 4.59% was achieved in 0.06 s using the controller and the deformation was maintained for 2 s at low current. The BISMAC actuator was operated using the controller with $I_{hi} = 1.1$ A and $I_{low} = 0.65$ A achieving a 67% decrease in contraction time compared to using a constant driving current of $I_{low} = 0.2$ A and a 60% decrease in energy consumption compared to using constant $I_{hi} = 0.5$ A while still exceeding the contraction requirements of the *Aurelia aurita*.

Two fundamental parameters at the composition level were associated with the power consumption of SMA: i) martensite to austentite phase transition temperature and ii) thermal hysteresis. Ideally, one would like to reduce both these quantities and for this purpose an equiatomic Ni-Ti alloy was modified with Cu. Replacing nickel with 10 at% copper reduces the thermal hysteresis by 50% or more. For Ni-Ti alloys with nickel content greater than 50 at%, transition temperature decreases linearly at a rate of 100 ºC/Ni at%. Given these two power reducing factors, an alloy with composition of $Ni_{40+x}Ti_{50-x}Cu_{10}$ was synthesized with x = 0, ±1, ±2, ±3, ±4, ±5. Metal powders were melted in an argon atmosphere using an RF induction furnace to produce ingots. All the synthesized samples were characterized by differential scanning calorimetric (DSC) analysis to reveal martensite to austenite and austenite to martensite transition temperatures during heating and cooling cycles respectively. Scanning electron microscopy (SEM) was conducted to identify the density and microstructure of the fractured samples. The results show the possibility of achieving low power consuming high performance SMAs.

Using the BISMAC actuator and feedback control system, a robotic jellyfish called Robojelly that mimics the morphology and kinematics of the *Aurelia aurita* species was created. A systematic fabrication technique was developed to replicate the essential structural features of *A. aurita*. Robojelly's body was fabricated from RTV silicone having a total mass of 242 g and bell diameter of 16.4 cm. Robojelly was able to generate enough thrust in static water conditions to propel itself and achieve a proficiency of 0.19 s^{-1} while the *A. aurita* achieves a proficiency of around 0.25 s^{-1}. A thrust analysis based on empirical measurements for natural jellyfish was used to compare the performance of the different robotic configurations. The configuration with best performance was a Robojelly with segmented bell and a passive flap structure. Robojelly was found to consume an average power on the order of 17 W with the actuators not having fully reached thermal steady state. A comparative kinematics analysis was conducted between a natural *Aurelia aurita* and Robojelly. The resistance feedback controller was implemented to tailor the deformation profile of BISMAC actuators embedded in Robojelly. Robojelly's performance was quantified in terms of thrust production and power consumption during vertical swimming experiments. A maximum average instantaneous thrust production of 0.006 N was achieved at a driving current (I_{hi}) of 1.5 A with 35% duty cycle. Rapid heating of SMA wires was found to reduce power consumption and increase thrust. The bell kinematic analysis revealed resemblance and differences in bell deformation trajectories of the biomimetic and natural jellyfish. The inflexion point of the *A. aurita* was found to convert an inner bell trajectory into an outer one during contraction which assists the thrust production

A biomimetic robot inspired by *Cyanea capillata*, termed as "Cyro", was developed to meet the functional demands of underwater surveillance in defense and civilian applications. The design of Cyro required kinematics of large *C. capillata* which are elusive creatures. Obtaining

accurate kinematic data of animals is essential for many biological studies and bio-inspired engineering applications. Many animals such as the *C. capillata* however, are either too large or too delicate to transport to controlled environments where accurate kinematic data can easily be obtained. Often, in situ recordings are the only means available but are often subject to multi-axis motion and relative magnification changes with time, which lead to large discrepancies in animal kinematics. In Chapter 5, techniques to compensate for magnification and body rotation of animal footage were developed. A background reference point and animal dimensions were used to account for magnification. A linear fit of body points were used to measure body rotation. These techniques help resolve animal kinematics from in situ video footage. The techniques were applied to a large jellyfish, *Cyanea capillata,* swimming in ocean waters. The bell kinematics were captured by digitizing exumbrella profiles for two full swimming cycles. Magnification was accounted for by tracking a reference point on the ocean floor and by tracking the *C. capillata* exumbrella arclength in order to have a constant scale through the swimming cycles. A linear fit of the top bell portion was used to find the body angle with respect to the camera coordinate system. Bell margin trajectories over two swimming cycles confirm the accuracy of the correction techniques. The corrected profiles were filtered and interpolated to provide a set of time-dependent points along the bell. The ability to use in situ footage with significant multi-axis motion provides an opportunity to analyze previously impractical footage for gaining a better understanding of large or delicate organisms.

The swimming kinematics of the *C. capillata* were analyzed after extracting the required kinematics from the in situ video. A discrete model of the exumbrella was developed and used to analyze the kinematics. The exumbrella discretization was done using three different methods. The first method consists of analyzing the animal anatomy for structural and mechanical

features. The second method consists of analyzing the bell kinematics for areas of highest deformation over time. The third method consists of optimizing node locations that can provide minimal error with comparison to the digitized profiles.

Two kinematic models of the *C. capillata* swimming motion were developed by fitting Fourier series to the discretized segments and angles formed by each segment. The four-segment anatomical kinematic model was used to analyze the bell kinematics of the *C. capillata*. It was found that the bell does not deform uniformly over time with segments lagging behind others. Hysteresis between contraction and relaxation was also present through most of the exumbrella. The bell margin had the largest hysteresis with an outer path during contraction and inner path during relaxation. The subumbrella volume was approximated based on the exumbrella kinematics and was found to increase during contraction.

Cyro was designed to mimic the morphology and swimming mechanism of the natural counterpart. The body of the vehicle consists of a rigid support structure with linear DC motors which actuate eight mechanical arms. The mechanical arms in conjunction with artificial mesoglea create the hydrodynamic force required for propulsion. The full vehicle measures 170 cm in diameter and has a total mass of 76 kg. An analytical model of the mechanical arm kinematics was developed. The analytical and experimental bell kinematics were analyzed and compared to the *C. capillata*. Cyro reached the water surface untethered and autonomously from a depth of 182 cm in five actuation cycles. It achieved an average velocity of 8.47 cm/s while consuming an average power of 70 W. A thrust stand was developed to calculate the thrust directly from a single bell segment yielding an average thrust of 27.9 N for the whole vehicle. Steady state velocity during Cyro's swimming test was not reached but the measured

performance during its last swim cycle resulted in a cost of transport of 10.9 J/kg·m and total efficiency of 3%.

It was observed that a passive flexible margin or flap, drastically increases the performance of the Robojelly. The effects of flap length and geometry on Robojelly were analyzed using PIV. The flap was defined as the bell section which is located between the flexion point and bell margin. The flexion point was established as the location where the bell undergoes a significant change compliance and therefore in slope. The flap was analyzed in terms of its kinematics and hydrodynamic contribution. An outer trajectory is achieved by the flap margin during contraction while an inner trajectory is achieved during relaxation. The flap kinematics was found to be replicable using a passive flexible structure. Flaps of constant cross section and varying lengths were put on the robotic vehicle to conduct a systematic parametric study. Robojelly's swimming performance was tested with and without a flap. This revealed a thrust increase 1340% with the addition of a flap. Velocity field measurements were performed using planar Time Resolved Digital Particle Image Velocimetry (TRDPIV) to analyze the change in vortex structures as a function of flap length. The robot input parameters stayed constant over the different configurations tested thus maintaining a near constant power consumption. Non-dimensional circulation results show a dependence on flap kinematics and geometry. The robot was approximated as a series of pitching panels circularly oriented around its apex. The first circulation peak of the pitching panel approximation revealed a normalized standard deviation of 0.23. A piston apparatus was designed and built to test different flexible margin configurations. This apparatus allow the isolation of the flap parameters and remove the uncertainties coming from the robotic vehicle.

Dedication

To my mother who raised me. I am grateful for your unconditional love and your commitment at raising me to best of your abilities. You founded my morals and gave me the discipline I needed to become the person that I am today and complete this level of education.

To my father who guided me. I am grateful for the knowledge you shared and your constant support. You gave me great opportunities and put me in the direction that I am today.

Acknowledgments

I thank Dr. Priya for advising me and giving a series of unique opportunities during the course of my PhD. His unmatched dedication to our work has made a significant difference to my success and the success of our research. He made sure I had everything necessary to conduct my work and provided motivation and support when needed. I appreciate the time we had together and hope we can continue to collaborate in the future.

The Office of Naval Research for providing constant funding through the years of my PhD. This has allowed me to explore various fields of research with all the tools needed. It also funded my education throughout the completion of this degree.

Past and present CIMSS, CEHMS and BMDL colleagues, you have shared a large amount of technical knowledge which allowed me to become a better researcher. You have expended my horizons with knowledge from cultures around the world and allowed me to grow as a person. Your friendship made this experience that much more enjoyable.

The Jellyfish Autonomous Node and Colonies MURI group, I had a great time collaborating with you and learning about your fields of expertise. I appreciate the time we spent sharing ideas and discussing.

Table of Contents

Chapter 1

Introduction

Chapter 2

Jellyfish Inspired Propulsion Using Shape Memory Alloy Based Artificial Muscles

Chapter 3

BISMAC Actuator Control System and Power Reduction Techniques

Chapter 4

Robojelly Design, Performance and Control

Chapter 5

Cyanea capillata Robojelly

Chapter 6

Biomimetic Autonomous Robot Inspired by the *Cyanea capillata* (Cyro)

Chapter 7

Flexible Margin

Chapter 8

Conclusions

Appendix

List of Figures

List of Tables

Attributions

Several colleagues have contributed to the publications which in are associated to this dissertation. These publications and colleagues are listed in the Publication section of this document. The work presented in this dissertation was mainly produced by myself. Work performed by others was omitted from the dissertation and referenced. Supporting work from senior design teams has been a key contribution to the progress of my work but the majority of the designing and analysis was performed by myself. My advisor, Dr. Shashank Priya, has contributed to text editing of this dissertation.

Chapter 1

Introduction

For the design of bio-inspired or biomimetic robots, it is critical to have a good understanding of key features and function of the natural model. The more knowledge of the natural model is obtained, the more accurately it can be replicated. In some instances, mimicry of nature can lead to a better understanding of the natural features and functions as will be shown in later chapters. This chapter will cover the key features and functions of medusa which are critical to the development of biomimetic robots. A background on relevant actuator technology which can enable the replication of the natural animal will also be given. This is followed by a survey of existing unmanned underwater vehicles (UUVs) pertinent to the objectives of this study. For the purpose of this document, the terms autonomous underwater vehicles (AUV) and unmanned underwater vehicles (UUVS) or unmanned undersea vehicles (UUVs) are used interchangeably. This survey will serve as a comparison benchmark for the technology developed in the present research. Lastly, an overview of jellyfish bio-inspired vehicles developed by other researchers is given.

The terms biomimetic and bio-inspired are often used without a clear differentiation between both. In this document, the two terms are distinguished based on the following: Biomimetic and bio-inspiration differ based on the goal or intent of their application. If the intent is to copy nature as closely as possible then this is considered biomimetic. If the intent is simply to use some principles or observations from nature, then it is considered bio-inspiration.

1.1 Medusa Biology

1.1.1 Background

In the Animalia kingdom, medusae , also called jellyfish, are part of the Cnidaria phylum. Cnidaria refers to animals that have cnida cells which are stinging cells used to capture prey (Arai 1997). Medusae are part of the Medusozoa subphylum. This subphylum can be separated into three classes: Hydrozoa, Scyphozoa and Anthozoa. The Syphosoa class is known as the "true jellyfish". Animals in this class spend most of their lives in the adult stage which is known as the medusa. Scyphosoa will be the main class covered in this research and will be referred to medusa or jellyfish interchangeably (Goldsborough, 1910).

Jellyfish come in over 8,000 species and are found in ocean waters around the world (Cook, 2010). Most jellyfish are found in marine waters but approximately 100 of them are found in fresh water. Jellyfish have been found at depths reaching 7000 m (Kramp, 1959). At approximately 95% water, jellyfish are neutrally buoyant (Lowndes, 1942). They use ocean currents to travel and reach feeding waters (Hays et al., 2008). The oscillating locomotion of jellyfish is twofold. It allows them to displace themselves in water and it allows them to feed. The feeding mechanism varies from one species to another but most rely on water circulation around their body to capture their food.

Their morphology also greatly varies from one species to another. Their size can vary between a few mm to over 2 m in diameter (Russell, 1970; Omori and Kitamura, 2004). Intricate oral structures and tentacles can be found on some species. These are usually for food capturing. The large diversity, extensive distribution and passive nature of jellyfish show high adaptability and efficiency attributes. These are attractive attributes for a UUV. Having an efficient vehicle

capable of traveling long distances for large distances would reduce maintenance, monitoring and refueling of the vehicle. A versatile vehicle able to operate in a large number of environments would extend the range of possible applications of a single vehicle.

1.1.2 Anatomy

Some basic anatomical features of jellyfish must first be identified to understand the functions of a given species and the differences between species. Jellyfish are relatively simple multiorgan organisms. They are known to be the oldest multiorgan animal (Albert, 2010). The main part of the jellyfish is the bell as shown in Fig. 1.1 and 1.2.

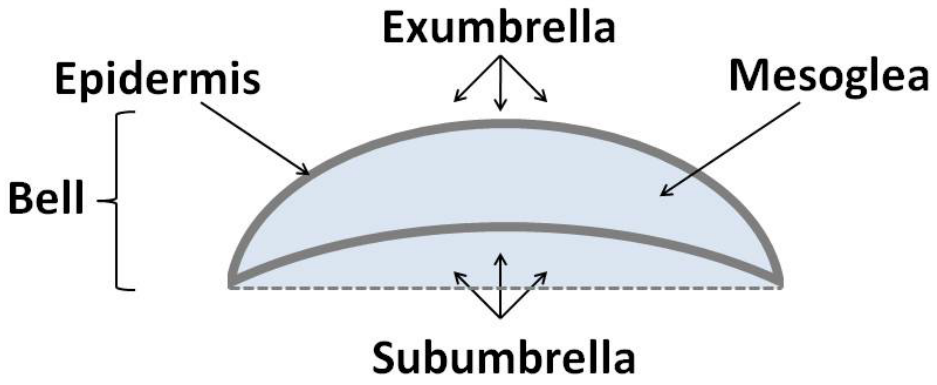

Figure 1.1: Basic anatomical features of a jellyfish (Villanueva et al., 2010a).

The bell produces thrust for swimming and contains the vital organs. The inner part of the bell is called the subumbrella while the outer part is the exumbrella. The outer layer of the bell is the epidermis which is basically a thin skin layer as shown in Fig. 1.1 and 1.2. The mesoglea consists of most of the bell and is bounded by the epidermis.

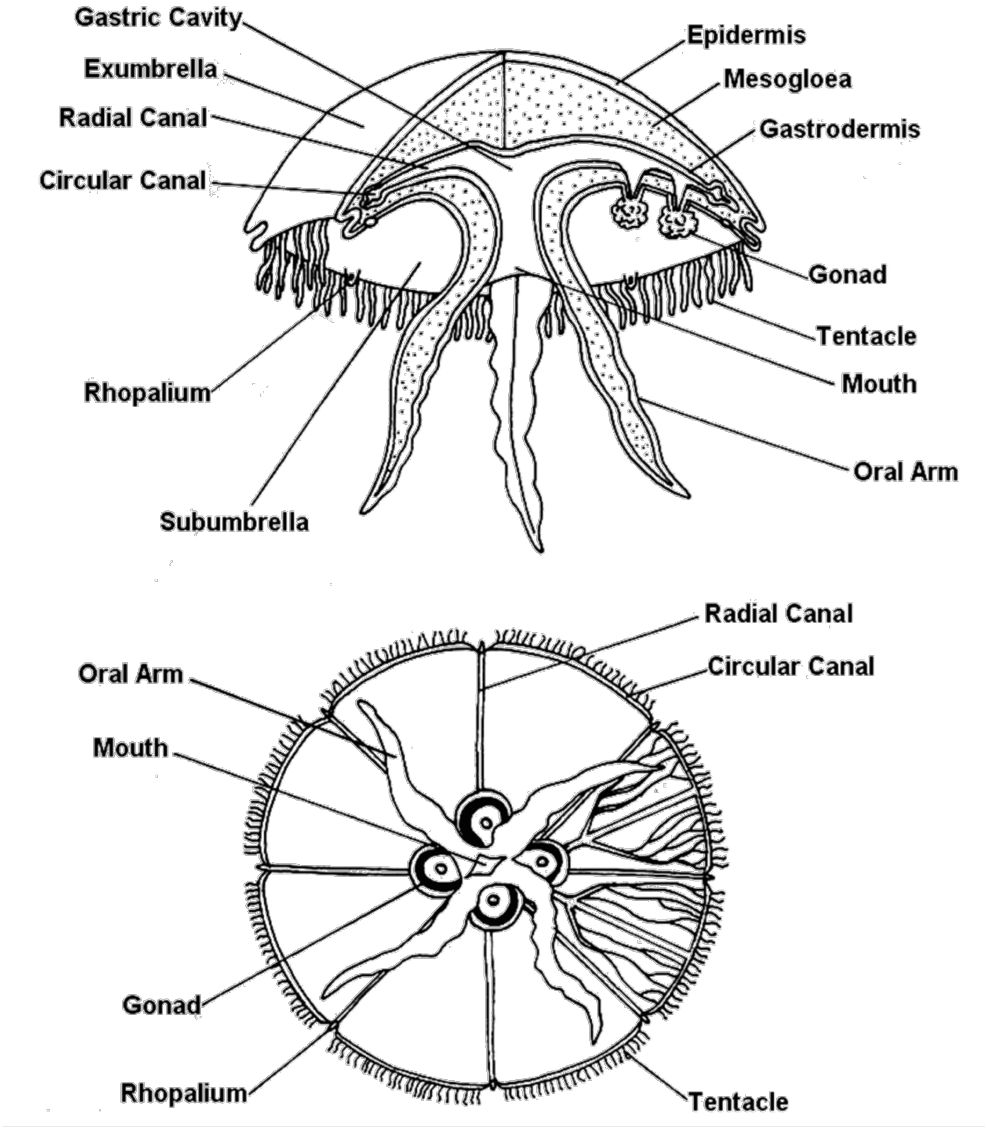

Figure 1.2: Anatomical features of an *Aurelia aurita* (Image with permission from Cronodon)

Tentacles can be found on the bell margin depending on the species. The bell margin refers to the bell's outermost edge. The tentacles are passive in motion and are used to capture prey from water flowing through them. Tentacles are usually have a higher concentration in cnidocytes which are the stinging cells. Oral arms extrude from the subumbrella and are used to transport

captured food in the tentacles to the mouth which is located at the center of the subumbrella. Food is digested in the gonads located at the center of the bell around the apex.

The medusa anatomical description given above is for *Aurelia aurita* which is one of the most basic and also common species of jellyfish. Anatomical features vary greatly amongst species. For example, jellyfish vary in sizes ranging from centimeters to meters. Tentacles can be found in large amount extruding from subumbrella that consists most of the jellyfish's mass. An entire oral structure can also be found in the subumbrella which acts as a complex water filter. Some of these traits will be highlighted in following sections.

1.1.3 Propulsion Mechanism

This section discusses the features found in jellyfish pertaining to their propulsion mechanism. Due to the wide variety of jellyfish, the information presented is not available for all species. In fact, information pertaining to the propulsion mechanism of jellyfish is limited or not available for most species. Studying the species for which the information is available still gives a good general understanding of jellyfish propulsion mechanics.

1.1.3.1 Muscles

Jellyfish swim in an oscillating manner by contracting and relaxing their bell (Krueger et al., 2008). Contraction occurs by contracting muscles located in the subumbrella. This causes water to eject from the subumbrellar cavity and produces thrust (Costello and Colin, 1994). During relaxation, the bell regains its relaxed geometry and refills the subumbrellar cavity. The frequency of actuation varies with species and also with size. In general, actuation frequency will decrease with bell diameter of a given species (McHenry and Jed, 2003).

Satterlie et al. (2005) has laid out a muscle map of the *Cubozoan* which shows how muscles are distributed in its subumbrella. Circular muscles distributed around the bell contract to produce deformation for swimming. Radial muscles are used to bring captured food to the mouth by bending the bell towards the mouth. Muscle structures can be expected to vary with species such as for the *Cyanea capillata* but in general circular muscles are responsible for swimming.

1.1.3.2 Joints

Joints in a jellyfish are an important feature contributing to their propulsion mechanism (Gladfelter, 1972). They are geometrical features found in the mesoglea of jellyfish as shown in Fig. 1.3. The joints help relocate mesoglea upon bell contraction in order to minimize material being put in compression and tension. The stiff mesoglea would be energy costly to compress and stretch. Another advantage of mesoglea relocation is seen in the relaxation mechanism. Upon relocation, bell walls thicken and radial fibers connected across the mesoglea are stretched. These fibers store elastic energy which is released upon bell relaxation causing the bell to passively regain is relaxed position.

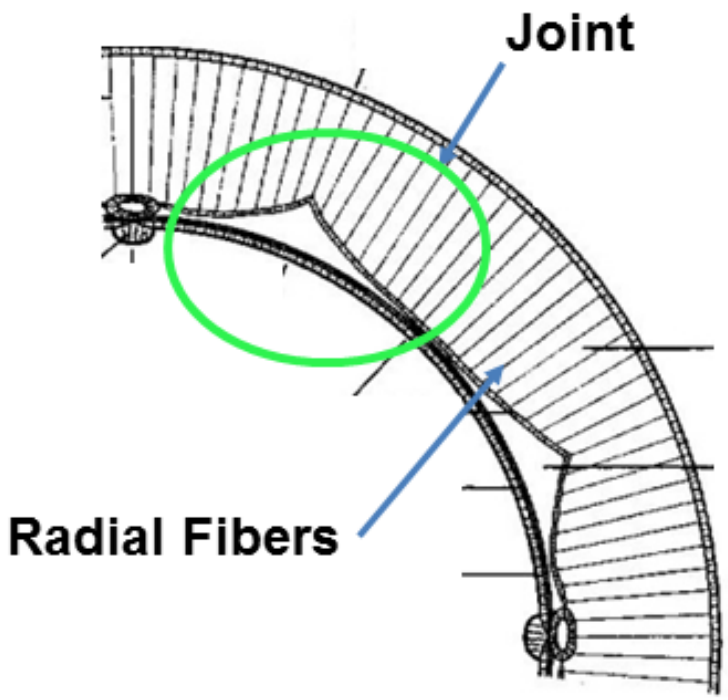

Figure 1.3: Cross sectional view of quarter of a bell of a *Polyorchis montereyensis* depicting the radial joints and radial fibers. Redrawn from Gladfelter (1972).

1.1.3.3 Swimming Modes

Jellyfish swim using two different main types of propulsion called jetting and rowing as shown in Fig. 1.4. Based on this distinction, jellyfish can be divided into two categories: jetters and rowers (Colin and Costello, 2002; Dabiri et al., 2005; Blough et al., 2011).

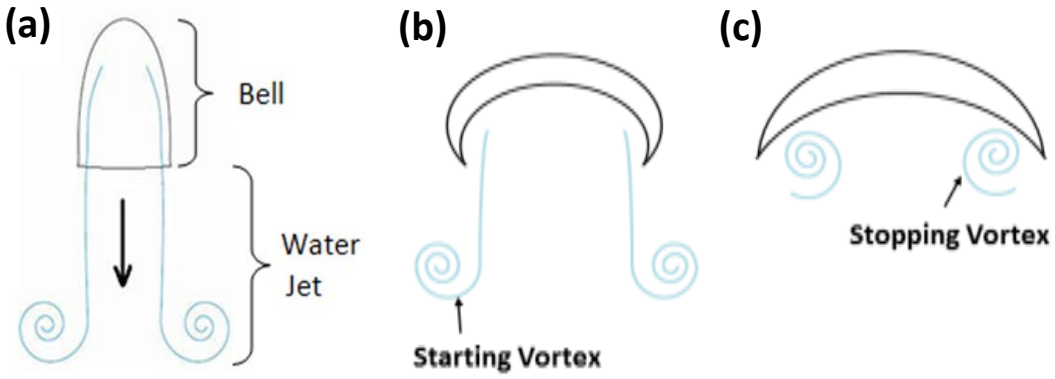

Figure 1.4: Jellyfish propulsion mechanism: (a) jetting propulsion, (b) rowing propulsion with starting vortex during contraction and (c) stopping vortex during relaxation.

Jetting propulsion consist of water being ejected from the bell as it contracts. This creates a toroid vortex which moves away from the body. When relaxing, the bell is refilled with no particular structure (Daniel, 1983). Jetters are known to be more proficient swimmers then rowers while rowers are more efficient (Daniel, 1983; Sahin et al., 2009). The velocity and accelerations reached by these animals is a function of their size. Jellyfish are limited to a one cell layer of muscle for propulsion (Costello et al., 2008). This limits the amount of thrust which can be produced by these animals limiting the size these animals are able to reach (McHenry, 2007, Herschlag and Miller 2011). Jetters usually do not exceed a bell diameter of a few centimeters but some jellyfish can exceed 2 m in diameter (Russell, 1970). The jellyfish capable of reaching these dimensions are rowers and the key to phenomenon lies in their method of propulsion. Rowers have developed a wake structure which allows them to produce more thrust given their limited muscle structure and therefore reach bigger dimensions. Rowers produce a starting vortex during contraction as with jetters, shown in Fig. 1.4. During relaxation, a second toroid vortex is formed under the bell. During contraction, the starting and stopping vortices interact with each other (Dabiri et al., 2005). They both spin in opposite directions causing the

mass of the wake vortex to increase. This causes the jellyfish to build more thrust then it would without the stopping vortex.

1.1.4 Sensors

The *Aurelia aurita* is again chosen to study jellyfish sensor anatomy and function. *A. aurita* have eight rhopalia which are the main sensory organs of the jellyfish. The rhopalia are located along the bell margin at eight evenly spaced locations. This organ consists in part of a light sensor called ocelli. The capability and complexity of this organ varies from one species to another. Some species have ocelli which are closer to eyes. The rhopalia also has a gravity sensor called the statocyst. The statocyst consists of a hollow spherical structure with sensory cells on the walls and a mobile ball called the statolith, shown in Fig. 1.5. The statocyst walls are covered with ciliary hairs which also help with sensing. The statolith moves inside the statocyst as jellyfish moves and the statolith applies pressure on the sensory walls. The sensory walls along with the ciliary hairs tell the jellyfish in what orientation it is and what accelerations it is undergoing.

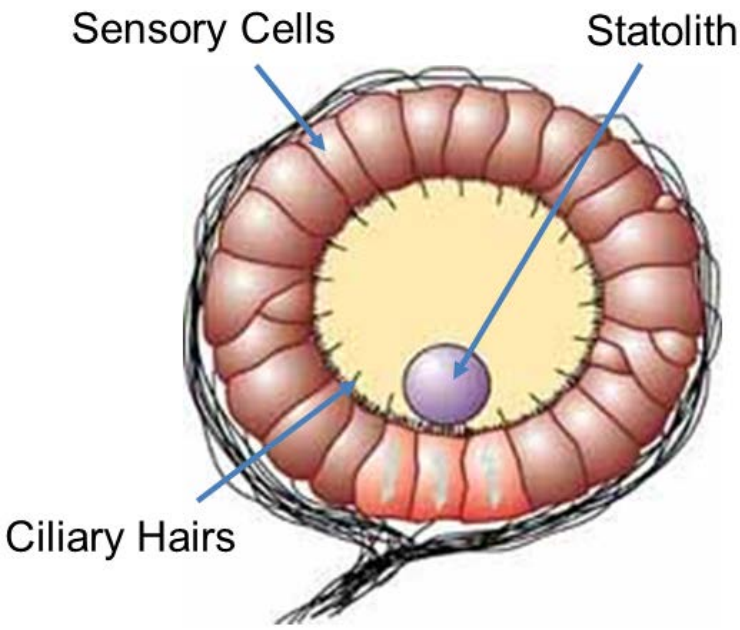

Figure 1.5: Statocyst, redrawn with permission from author (Davis W. J., 1968).

Jellyfish also have chemoreceptors to detect chemicals. These sensors are very sensitive and can detect the scent of nearby organisms. *Aurelia* sp. have chemoreceptors which cover most of their body including the bell and tentacles. The chemoreceptors in the *Aurelia* sp. are thought to be located in the cnidocytes which are also the stinging cells of jellyfish. Also located in the cnidocytes are mechanoreceptors. These are somatosensory which means they are able to sense touch. Both chemoreceptors and mechanoreceptors are hypothesized to function and to be located where mentioned based on behavioral experiments and literature from other species. Jellyfish are also able to sense small pressure waves. Ciliary hairs and the mechanoreceptors in the cnidocytes are thought to be responsible for this sensing ability (Albert, 2010).

1.1.5 Relevant Species Overview

Three main species of jellyfish were selected for their significance to UUV design: the *Aurelia aurita*, *Mastigias papua* and *Cyanea capillata*. These species offer features which can be incorporated inside a vehicle in order to achieve various missions. Though these features are not necessarily unique to those species, they offer a simple morphology which allows for the isolation of important variables.

1.1.5.1 Aurelia aurita

Aurelia aurita also known as Moon Jellyfish are a very common species found in ocean waters around the world. They are part of the Semaeostomea order, Ulmaridae family and *Aurelia* Genus. Their morphology is simple and a large amount of data and analysis are available about this species (Bajcar et al., 2009). *A. aurita* in their adult phase can reach bell diameters of up to 30 cm. They are translucid and have oral arms in their subumbrella (Dawson 2003), as shown Fig. 1.6. *A. aurita* have small tentacles on their bell margin which are used to capture food as they swim. Four oral arms extrude from their subumbrella and are used to bring food captured in their tentacles to their mouth. Four gonads located at the center of the bell digest food.

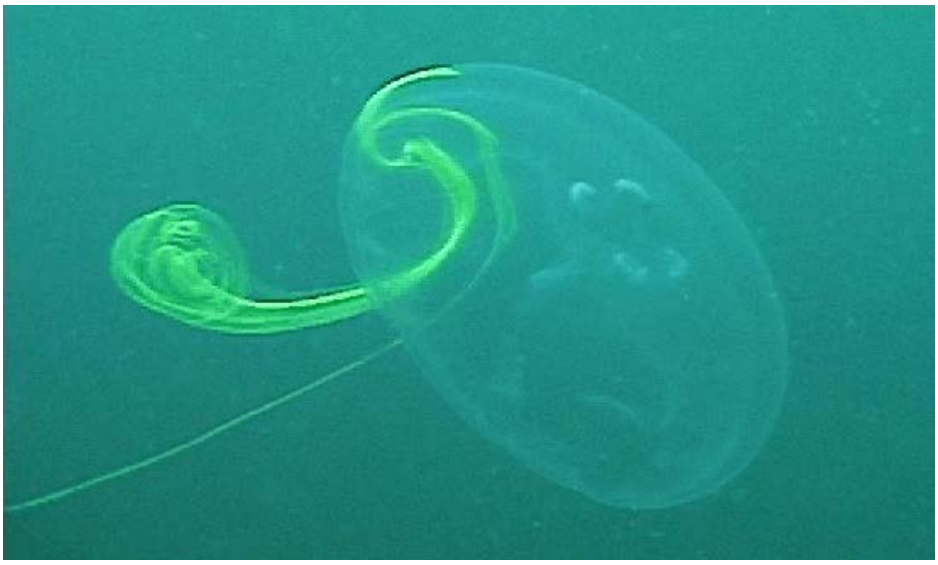

Figure 1.6: Aurelia aurita during a dye test showing the starting and stopping vortex. Image courtesy of Dr. Jack Costello, Providence College.

1.1.5.2 Mastigias

The second type of animal which is of interest to UUV design is the genus of *Mastigias*. This genus is interesting because of the prominent oral structure found under the bell, see Fig. 1.7.

Figure 1.7: Mastigias showing the oral structure. Image courtesy of Dr. Jack Costello, Providence College.

Instead of relying on tentacles for capturing food and oral arms to transport this food, *Mastigias* use an oral structure as a filter to directly capture food from water. The main filtering components are the oral arms which have a much different morphology and function then the *Aurelia aurita*'s. Figure 1.8 shows the oral arms and terminal clubs which are long extrusions extending from the bottom of the oral arms. Their shape and size varies among species and their exact purpose remains unknown. The terminal clubs were found to reduce in size compared to the *Mastigias papua* found in ocean water as they evolved in lakes (Dawson, 2005a).

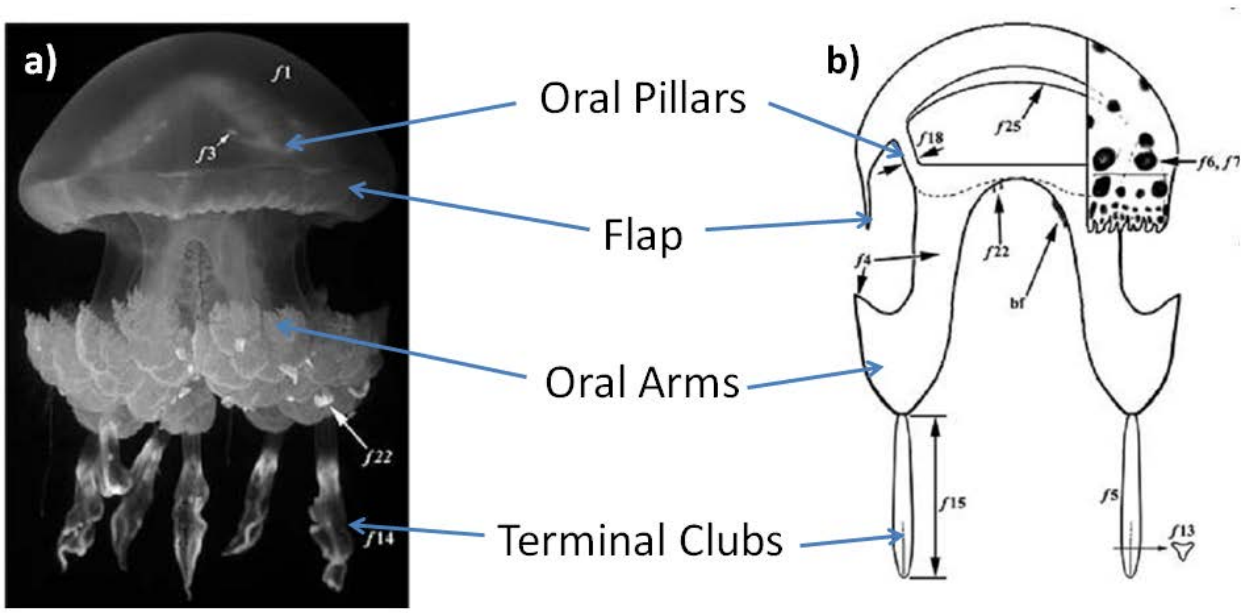

Figure 1.8: The *Mastigias* oral structure showing its different components, redrawn from Dawson (2005b)

From a propulsion standpoint, the oral structure is passive. Yet, this structure is thought to not have a drastic decrease in propulsion efficiency. This raises interests for UUV design especially since oral structures are also found on larger jellyfish such as *Nomura*. Such a structure lends itself to significant extra payload volume. Also, the filtering capability of the structure is attractive for some applications such as chemical filtering for water quality control. In both these cases, a thorough understanding of the hydrodynamics of the animal is important. Though this has not yet been well documented, the morphology and behavior of this animal have been thoroughly explored (Kishinoue, 1895; Uchida, 1926; Dawson 2005a; Dawson, 2005b).

1.1.5.3 Cyanea capillata

The *Cyanea capillata* is another interesting species for the design of UUVs. It is one of the few species to have a segmented bell as shown in Fig. 1.9. Most species such as *Aurelia aurita* and *Mastigias papua* will have a uniform bell. A segmented bell is easier to replicate due to material limitations as will be explained in later chapters.

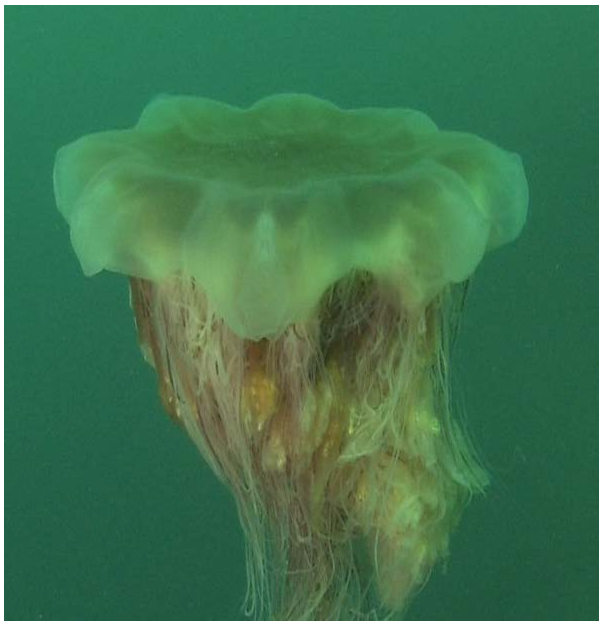

Figure 1.9: *Cyanea capillata* showing the segmented bell.

Cyanea capillata can reach bell diameters greater than 2 m with tentacles exceeding 36 m in length (Russell, 1970). Their very large size makes them worth studying for vehicle design as one may want to have a larger vehicle for some applications. The segmented bell features a different muscle structure then encountered in jellyfish with uniform bell. The *C. capillata* has circular muscles spanning approximetly 25% of the radius. It also has two sets of radial muscles per bell segment that contribute to swimming (Gladfelter, 1973).

1.2 Propulsion Mechanism for Biomimetic Robots

One of the most important aspects of a biomimetic robot is the actuators. The actuators dictate in large part form, function and efficiency. The form of biomimetic robots is often critical as certain features from the natural counterpart are necessary in order to replicate the same physics. A bulky actuating system will cause the form to be different then desired due to the lack of space or excess weight. When trying to prevent these downsides, a designer will often have to sacrifice the functionality or efficiency. For example, reducing the size of an actuator until it fits in the bio-inspired design will also reduce its force and sometimes displacement capability. Also, smaller actuators are usually less efficient. Lastly, if the robot utilizes actuators which or not efficient, even if the designer matches all the properties of the natural counterpart, the robot will be inherently inefficient due to its actuators.

1.2.1 Biological

Jellyfish are relatively flexible animals with no rigid structures supporting their body. Comparatively, other bio-inspired robotic designs deal with animals which have a rigid internal structure. Some example animals with rigid internal structures include dogs, humans, tunas and birds. These rigid structures can act as a point of anchorage and leverage for the actuators. Biomimetic designs for these animals usually rely on some form of links and joints to mimic the form and function of their natural counterparts. Jellyfish mainly consist of a flexible mesoglea which is deformed by large muscle contractions. Jellyfish muscles can contract approximately 50% of their original length based on the kinematics of their bells (Villanueva et al., 2010b).

Common mechanism used to mimic rigid structures cannot be applied directly to mimic the form and function of jellyfish.

1.2.2 Conventional Actuators

Conventional actuators are actuators which have been used for a relatively long period of time and are used in a vast variety of applications. These types of actuators include DC motors, pneumatics and hydraulics. DC electric motors which include servo and stepper are widely used in robotics. These motors offer a good balance between force, speed and control but have a bad form factor for biomimetic design. Pneumatic actuators are often used in industrial applications. These actuators are clean and versatile. Hydraulic actuators are very powerful and are also often used in industrial applications. Both pneumatic and hydraulic actuators consist of a bulky system has been used in biomimetic robotics but the power supply usually has to be put externally to the system.

1.2.3 Smart Material Actuators

With progress in material research, novel actuators are constantly being developed. Some of these actuators are very promising for applications in robotics. These types of actuators are referred to as artificial muscles. Some of the most prominent technology includes smart materials such as shape memory alloy, piezoelectric and electroactive polymers (EAP). Karpelson et al. (2008) shows a comprehensive description of the different types of actuators being research and used as artificial muscles for robotic applications.

This table clearly shows the compromise done when selecting actuators for a bio-inspired design. Though it might be tempting to select an actuator with maximum deflection, force and speed to reach the requirements of the natural counterpart, the efficiency of the robot will eventually become of high importance. If the best performing humanoid can only operate in the battle field for 2 min, it becomes useless. For a jellyfish vehicle, two of the most prominent technologies are shape memory alloy and dielectric elastomers. Shape memory alloy offer high strength, large deformation and a good form factor. The slow actuation is not an issue since the jellyfish of interest (rowers) do not actuate fast. The main downside is efficiency which is very pour for these actuators. Dielectric elastomers which fall in the category of EAPs, offer high deflection and force whit a good contraction speed. They are also very efficient. Their main downside is their form and high voltage. Their form in the sense of the way they actuate is difficult to apply as an alternative to artificial muscle. They usually consist of a flat sheet which is supported by an external structure to maximize function. Also, creating the high voltage needed to operate these actuators can be difficult with a limited amount of space.

Natural muscles offer the best balance of form, functionality, and efficiency which is not matched by any actuators currently available. This makes it difficult to design robotic systems which would require such technology.

1.2.4 Actuation Mechanisms

Coupled with actuators, the actuation mechanism also plays a critical role in the design of bio-inspirited robots. The actuator chosen for a design is often not enough to achieve a given deformation, force or speed. It usually requires some form of mechanism to meet the

performance criteria or simply because the biological system works that way. The most common mechanical system found in robotics consists of links and joints. There are other more novel designs which have potential such as tensigrity structures, and flexible beams. Other important aspects to consider when selecting an actuation mechanism are the efficiency of the structure and the ability of integration in the system. Animals such as birds, dogs, humans, fish often have some form of skin over their internal structure and actuation mechanism. This skin plays an important functional role in terms of aerodynamics, hydrodynamics or protection from the environment. A mechanical system which is inefficient because of energy losses such as friction can severely reduce the efficiency of the robot. Also, when embedding the actuation mechanism inside a skin which is often a must for aerodynamics and hydrodynamics applications, more losses can be seen in the system depending on its ability to properly integrate. Natural actuation mechanism are very efficient, they have a series of conduits and fluids which reduce friction coupled with composite materials which offer low resistance to deformation in one direction and high stiffness in the other.

Links and joint although often used, are limited in their applications. They have difficulty achieving intricate curvatures and are usually bulky. There are also lots friction losses in all the joints. Tensigrity structures are a more novel approach at reducing some of the losses encountered in regular link and joint mechanisms. They utilize a beams put in compression and cables put in tension to create a structure which can easily be deformed. The downside of such a structure is the ability to ingrate inside a body. These types of structures along with links and joints structures, have form cavities within. These need to be filled with a liquid, solid or gas depending on the application. For underwater applications, gases do not work well due to the pressure gradient encountered at increasing depth. Liquids are a possibility but have not been

used in any mechanism which could be found. Solids can also be used but must be flexible enough to allow deformation during actuation and must be able to withstand he high pressure. The common biological material with both these remarkable features is blubber. When dealing with high curvatures, flexible beams can be used. These mechanism resemble the mechanism used in biological specimen and do not have any cavities which must be filled. One of the downside is the internal resistance. Unlike biological specimen, no conduits or fluids are present to reduce friction losses. The flexible beams are small and compact and depending on low losses can be kept, they might be the best actuation mechanism for jellyfish robots.

1.3 Conventional UUVs and Ocean Surveillance Systems

1.3.1 Conventional designs

One of the most popular UUV or AUV (autonomous underwater vehicle) is the Remote Environment Monitoring Units (REMUS) 100 with customers in countries such as Australia, UK, Singapore and the USA. The technology is developed by the Oceanographic Systems Laboratory at the Woods Hole Oceanographic Institute and the vehicles are developed by Hydroid in Pocasset Massachusetts. The REMUS 100 has a conventional design which consists of a torpedo like body with propeller in the back. It consists of a rigid hull design to minimize drag and the vehicle has to be plugged in order to recharge its batteries (WHOI). The REMUS 100 weighs approximately 80 kg and is capable of going at depths of 100 m. It can serve both civilian applications and military applications. This UUV has been widely used by the US Navy, Woods Hole Institute of Oceanography, and other agencies. The vehicle comes standard with a few instruments such as an Acoustic Doppler Current Profiler (ADCP) and light scattering

sensor. It can also be fitted with a series of other instruments depending on the need of a certain application. The REMUS is able to operate for up to 8 hours before needing servicing. The vehicle has shown the ability to cover an area of up to 80 kilometers at a velocity of 3 knots. It can cover slightly more at lower speeds.

The REMUS family also includes other models which have different capabilities. The largest vehicle is the semi-autonomous REMUS 6000. As the name suggests, it is rated for depths down to 6000 m and is able to operate for 13 hours. It is much larger at 817 kg and offers the ability to carry more complex instrumentation.

1.3.2 Novel designs (other than bio-inspired)

One of the most interesting and promising design for UUVs is called the Waveglider. This innovative design manufactured by Liquid Robotics. This vehicle is not necessarily an underwater vehicle but can achieve some of the tasks of underwater vehicles and is therefore considered in this section. The Waveglider consists of two parts: the float and glider. The float is the main part of the vehicle which lays on the surface. The glider is underwater and tethered to the float.

The interaction between the two parts when the system encounters waves causes the vehicle to move forward. The surface part of the vehicle is equipped with solar panels which allows for energy harvesting which powers the different electronics. The propulsion mechanism is all passive and the electronics are powered by energy harvesting which leads to prolonged operations. The main vehicle can be fitted with different sensors and since it is at the surface, it is able to easily communicate to a ground station. The main downside of the Waveglider is the fact

that the main vehicle which contains all the instruments is located at the surface. This greatly limits the sensing capability of the vehicle.

1.4 Jellyfish inspired UUV

1.4.1 Features

There are a few jellyfish inspired vehicles which have been developed. The first vehicle and perhaps the most well-known is the Aquajelly (Festo). This vehicle is inspired by jellyfish but does not truly emulate any of its functions.

Propulsion is achieved by 8 fins circularly distributed around the bell. The fins are actuated by a central electric motor. The fin motion does not emulate any of the two propulsion mechanisms found in jellyfish. The vehicle achieves turning using a mechanism that allows it to shift its center of gravity. The natural jellyfish does not use this strategy for turning as their center of gravity is over their center of buoyancy since the animals are close to 99% water. The vehicle has a charging station at the surface with the vehicles are able to find autonomously. This is a very good concept for UUV is would add autonomy by increasing the operating time. No known data has been published on the efficiency of the vehicle making it difficult to judge it this vehicle has any commercial potential.

Several other jellyfish inspired vehicles using smart materials have been developed. These vehicles were developed either to prove the capability of new actuators or as a proof of concept (Yang et al. 2007, Villanueva et al. 2009). An example is the robot developed by Guo et al. (2003). This robot combines SMA wires to contract the bell and IMPC actuators which are a

form of EAP, to actuate fins. This vehicle achieves a very poor performance since the SMAs are not able to contract enough to achieve a full bell contraction. The IMPC actuators have a slow actuation frequency limiting the performance of the vehicle.

Lastly, the Robojelly is a SMA based jellyfish inspired vehicle (Villanueva et al. 2011). The design as shown in Fig. 1.10, emulates the geometry and function of *A. aurita*. The bell of the vehicle is segmented instead of being uniform like its natural counterpart. This is due to limitation in the silicone material and deformation mechanism used.

Figure 1.10: Robojelly, jellyfish inspired robotic vehicle actuated by shape memory alloy (Villanueva et al., 2011)

The Robojelly has proven the ability to reproduce the kinematics and performance of the *A. aurita*. It has not yet been able to match the hydrodynamic efficiency. Also, the SMA actuators used have a very poor inherent efficiency. This causes the vehicle to a high power consumption which could prevent it from any commercial application. It does provide a good scientific

platform to study different parameters on jellyfish which would other not be possible with a live animal.

The lack in performance or efficiency of these vehicles is mainly attributed to the actuation mechanism used. A few strategies can be used to bridge this gap. The actuators could be made more efficient and more performing. Also, more efficient actuators such as dielectric elastomers could be used. This would require novel actuation mechanism to achieve proper motion but could potentially lead to more efficient vehicles.

1.5 References

Albert D. J. (2010). What's on the mind of a jellyfish? A review of behavioural observations on Aurelia sp. jellyfish. *Neurosci. Biobehav. R.* 35, 474–482

Arai M N (1997). A Functional Biology of Scyphozoa *London: Chapman & Hall* pp 35, 188-193

Bajcar T, Malacic V, Malej A and Sirok B (2009). Kinematic properties of jellyfish Aurelia sp. *Hydrobiologia*,**616** 279-289

Blough T, Colin S P, Costello J H and Marques A C (2011). Ontogenetic Changes in the Bell Morphology and Kinematics and Swimming Behavior of a Rowing Medusae. *Biol Bull.* 220(1):6-14.

Colin S P and Costello J H (2002). Morphology, swimming performance and propulsive mode of six co-occurring hydromedusae *J. Exp. Biol.* 205 427-437,

Cook S (2010). New Zealand Coastal Marine Invertebrates *Christchurch: Canterbury University Press* pp 229-230

Costello J H, Colin S P (1994). Morphology, fluid motion and predation by the scyphomedusa *Aurelia aurita Mar. Biol*. 121 327-334

Cronodon, http://cronodon.com/BioTech/Jellyfish.html

Dabiri J P, Colin S P and Costello J H (2005). Flow patterns generated by oblate medusan jellyfish: field measurements and laboratory analyses *J. Exp. Biol.* 208 1257–1265

Daniel T L (1983). Mechanics and energetics of medusae jet propulsion *Can. J. Zool.* **61** 1406 - 1420

Daniel T L (1985). Cost of locomotion: Unsteady Medusae Swiming. *J. Exp. Biol.* Vol. 119, pp. 149-164

Dawson M. N. (2003). Macro-morphological variation among cryptic species of the moon jellyfish, Aurelia (Cnidaria: Scyphozoa) *Mar. Biol.* 143 369–379, DOI:10.1007/s00227-003-1070-3

Dawson M. N. (2005a). Five new subspecies of Mastigias (Scyphozoa: Rhizostomeae: Mastigiidae) from marine lakes, Palau, Micronesia. *J. Mar. Biol. Ass. U.K.* 85, 679–694

Dawson M. N. (2005b). Morphological variation and systematics in the Scyphozoa: Mastigias (Rhizostomeae, Mastigiidae) – a golden unstandard? *Hydrobiologia* 537, 185–206

Festo, Esslingen, Germany. http://www.festo.com/

Gladfelter W. G. (1972). Structure and function of the locomotory system of Polyorchis montereyensis (Cnidaria, Hydrozoa) *Helgol. Wiss. Meeresunters.* 23 38–79

Gladfelter W. G. (1973). Structure and function of the locomotory system of the Scyphomedusa Cyanea capillata *Mar. Biol.* 14 150–160

Goldsborough A (1910). Medusae of the World. *Carnegie Institute of Washington* Vol. 3

Hays G C, Doyle T K, Houghton J D R, Lilley M K S, Metcalfe J D, Righton D (2008). Diving behavior of jellyfish equipped with electronic tags. *Journal of Plankton Research* 30: 325-331.

Herschlag G, Miller L (2011). Reynolds number limits for jet propulsion, a numerical study of simplified jellyfish. *J Theor Biol*. 285(1):84-95

Karpelson M, Wei G, Wood R (2008). A Review of Actuation and Power Electronics Options for Flapping-Wing Robotics Insects. IEEE ICRA. pp. 779-786

Kishinoue K., (1895). Description of a new Rhizostoma Mastigias physophora nov. spec. Dobutsugaku Zassi, 9, 86-88

Kramp P L (1959). Stephanoscyphus (Scyphozoa) *Galatea Report* **1** 173-185

Krueger P S, Moslemi A A, Nichols J T, Bartol I K and Stewart W J (2008). Vortex Rings in Bio-inspired and Biological Jet Propulsion. *Adv. In Sci. and Tech.* Vol. 58 pp. 237-246

Liquid Robotics Inc., Sunnyvale, California, USA. http://liquidr.com/

Lowndes, A. G. (1942). Percentage of Water in Jelly-Fish. Nature, 150, 234–235.

McHenry M. J. and Jed J. (2003). The ontogenetic scaling of hydrodynamics and swimming performance in jellyfish (Aurelia aurita). *J. Exp. Biol.* 206, 4125-4137

McHenry M. J. (2007). Comparitive Biomechanics: The Jellyfish Paradox Resolved *Current Biology* 17 R632-R633

Oceanographic Systems Laboratory, Woods Hole Institute of Oceanographic (2008) http://www.whoi.edu/page.do?pid=29856

Russell, F. S. (1970). The medusae of the British Isles. II. Pelagic Scyphozoa. Cambridge University Press, Cambridge, UK

Satterlie R. A., Thomas K. S. and Gray G. C. (2005). Muscle Organization of the Cubozoan Jellyfish Tripedalia cystophora Conant 1897 *Biol. Bull.* 209 154-163

Sahin M, Mohseni K and Colin S P (2009). The numerical comparison of flow patterns and propulsive performances for the hydromedusae *Sarsia tubulosa* and *Aequorea victoria J. Exp. Biol.* **212**, 2656-2667

Seibel B A and Drazen J C (2007). The rate of metabolism in marine animals: environmental constraints, ecological demands and energetic opportunities *Phil. Trans. R. Soc. B* 362 2061-2078

Uchida, T. (1926). The Anatomy and Development of a Rhizostome Medusa, Mastigias papua L. Agassiz, with Observations on the Phylogeny of Rhizostomae. J. Fac. Sci. Tokyo Univ. (sect. IV, Zool.), 1, 45-95

Villanueva A, Bresser S, Chung S, Tadesse Y, and Priya S (2009). Jellyfish inspired underwater unmanned vehicle *Proc. SPIE*; 7287, 72871G

Villanueva A, Joshi K, Blottman J. and Priya S (2010a). A Bio-Inspired Shape Memory Alloy (BISMAC) Actuator. *Smart Mat. Struct.* 19, 025013

Villanueva, A. and Priya, S. (2010b). BISMAC control using SMA resistance feedback. *Proc. SPIE* 7642 76421Z

Villanueva A, Smith C, Priya S (2011). Biomimetic Robotic Jellyfish (Robojelly) using Shape Memory Alloy. *Bioinspir. Biomim.* 6, 036004

Yang Y, Ye X and Guo S (2007). A New Type of Jellyfish-Like Microrobot *Proceeding of the 2007 IEEE Intl. Conference on Integration Technology*

Chapter 2

Jellyfish Inspired Propulsion Using Shape Memory Alloy Based Artificial Muscles

Combined with the field of biomimetics smart material actuators have opened the opportunity to construct devices that are not only efficient but also demonstrate multiple functionalities (Blottman and Richards, 2006; Colin and Costello, 2002). At the same time, the understanding of biological systems has provided new impetus for development of actuation technologies as required to recreate motions and behavior which nature has spent centuries optimizing. Our research interest is in creating unmanned undersea vehicles (UUVs) which can operate autonomously for extensive periods of time. These vehicles could be used for long term surveillance in both civilian and defense applications generating their own energy and making on-board decisions as required for survival. Thus, the structure and locomotion mechanism of these vehicles must be highly efficient in order to enhance the lifetime and mobility. Prior research has shown that medusae (jellyfish) can offer many of these desired attributes (Dabiri et al., 2005), specifically a category of jellyfish referred to as rowers. Jellyfish are one of the oldest surviving organisms in the ocean. They have adapted and perfected their motion to yield the great swimming efficiencies over millions of years of evolution. One way to obtain similar propulsive efficiencies as that of jellyfish is to recreate its swimming motion. During propulsion, the medusa's body produces a characteristic deformation which results in a flow of water creating thrust. The composite actuators developed in this study are intended to replicate the swimming motion of rowing medusae and mimic their deformation cycle. Further, in order to better understand the behavior of this actuator and to be able to achieve the desired deformation

curvature, an analytical model was developed which shows the role of key material and structural parameters.

In this chapter, two different types artificial muscles were investigated. The application of these artificial muscles is to mimic the kinematics and dynamics of natural jellyfish while also mimicking their morphology. A literature survey was initially conducted to identify the potential actuation system for this specific application. It was found that shape memory alloys (SMAs) have many advantages and most importantly adequate form factor and high force density for serving the role of artificial muscles in bio-inspired designs. Two different artificial muscles were investigated which are SMA wires applied directly and composite actuator using SMA wires.

The first propulsion mechanism (Jetsum) aimed at replicating the jetting propulsion. Large displacement was achieved using SMA wires and by leveraging the displacement of a bell segment about a hinge. SMA wire contraction was made adequate by maximizing SMA length in the design. One of the biggest drawbacks of such a strategy is the friction encountered by the SMA wires as it contracts against a guiding surface. Guiding surfaces are sometimes necessary to route the SMA wires. The second design presented in Section 2.1 minimizes friction by keeping the wires on one plane and using low friction conduits. This design uses a hollow central hub which houses the actuators and electronics. This requires a special flexible conduit capable of withstanding high heat and seal off water.

The second artificial muscle design presented in this chapter is called Bio-Inspired Shape Memory Alloy Composite (BISMAC). These composite actuators are intended to replicate the

propulsion mechanism of a rowing jellyfish. The deformation profile of rowing jellyfish is more complex than that of a jetter. The bell undergoes large curvature which could not be achieved with the SMA wires applied directly. The BISMAC concept was extended to bidirectional actuators as described in Section 2.3. Being able to deform in two directions opens the possibility for their implementation in a series of new applications. As an example, the bidirectional BISMAC was applied towards the design of a legs.

2.1 Jellyfish Inspired Unmanned Underwater Vehicle

An unmanned underwater vehicle (UUV) was designed from inspiration of the form and functionality of jellyfish. These natural organisms were chosen as bio-inspiration for a multitude of reasons including: efficiency of locomotion, lack of natural predators, adequate form and shape to incorporate payload, and varying range of sizes. The structure consists of a central hub surrounded by bell segments and microcontroller driving system. The locomotion of UUV was achieved by shape memory alloy "Biometal Fiber" actuation which possesses large strain and blocking force with adequate response time. The main criterion in design of UUV was the use of low-profile shape memory alloy actuators which act as artificial muscles. In this manuscript, we discuss the design of two Jellyfish prototypes and present experimental results illustrating their performance and power consumption.

2.1.1 Background

Recently there is growing interest in design and development of unmanned underwater vehicles (UUV) for both deep and shallow water surveillance. The UUV must be autonomously controlled and perform intelligent operation for at least 48 hrs, consume low power for both

motion and station-keeping, use efficient propulsion mechanism to conduct surveillance in larger perimeters, and survive any possible danger. In the future, such vehicles will be able to achieve self-powering capability by utilizing bio-fuel cells or energy harvesting approaches. However, the capability of these power generation schemes is still low and will require fundamental improvements to meet the system demand. The UUVs can also be deployed as autonomous nodes for communication and enhance the surveillance efficiency (Blottman and Richards, 2006). Current systems utilize stationary buoys which have limited radius of surveillance and are usually restricted to coastal regions due to anchoring requirements. Conventional non-stationary vehicles can also be used but require constant maintenance and refueling. In order to find a solution to these shortcomings, we took inspiration from the biology of undersea organisms. In particular, our research was focused on jellyfish which can satisfy most of the criteria mentioned above while having a simple anatomical structure. This research therefore focuses developing an artificial jellyfish.

Jellyfish can be separated into two categories called “Prolate” and “Oblate”. One of the main features differentiating these two categories is their mode of transportation. Prolate medusea use a jetting type of propulsion while oblate medusae use rowing propulsion (Colin and Costello, 2002). An example of a jetter can be seen in Fig. 2.1.1 (a). Jetters are usually smaller, swim faster, and have a higher cycle frequency. They produce larger amounts of thrust per bell size and have a simpler propulsion mechanism than rowers. Figure 2.1.1(b) shows a picture of a jetting jellyfish and an illustration of its propulsion method. The bell of the jellyfish contracts and expels water through the bell margin hence creating thrust. On the other hand, rowers are more energy efficient and attain wider bell diameters. The overall efficiency of rowers allows the

jellyfish to reach much greater dimensions than Prolate medusae (Dabiri et al., 2005). Figure 2.1.1(c) shows a picture of a rowing jellyfish featuring large size and open bell shape.

The advantages of one type of medusa over the other with respect to their form and function are important in order to design an appropriate jellyfish node. The ideal vehicle design would combine characteristics of both Prolates and Oblates such as high propulsive efficiency for long distance traveling, high speeds and accelerations for quick change in trajectories and large vehicle dimensions for payload. Another important feature of medusae is their ability to conserve neutral buoyancy.

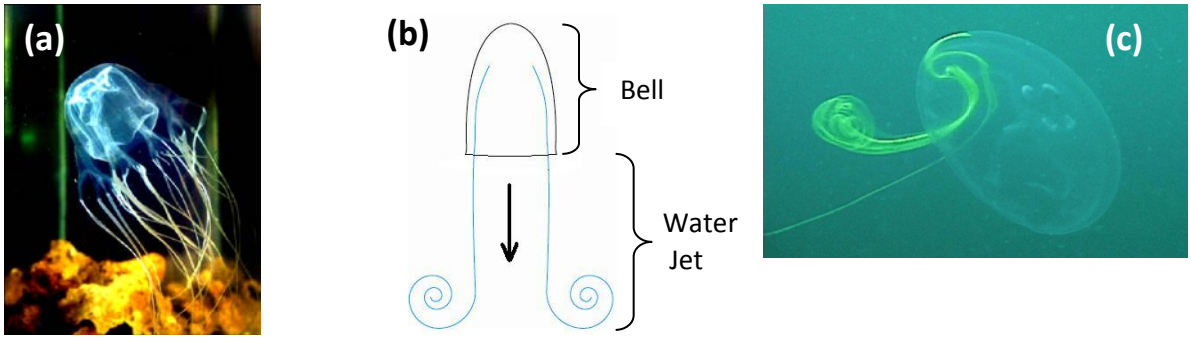

Figure 2.1.1: (a) Box-shaped bell jellyfish with large height-to-diameter ratio and uses a jetting propulsion (ePedia). (b) Representation of the jetting mechanism . (c) Image of an *Aurelia aurita* showing the rowing propulsion mechanism.

Prior jellyfish UUV attempts have focused on creating a robotic vehicle which resembles but not mimic the function and morphology of jellyfish. A prime example is the AquaJelly by Festo (Stoll, 2008). AquaJelly's design utilizes an electric motor coupled with pair of actuators that control eight tentacle-like appendages for creating thrust. While the form of AquaJelly resembles a jellyfish, the robotic locomotion is quite different than that of medusae propulsion. Guo et al. have presented the micro-robot prototype of jellyfish utilizing four SMA actuators to contract a soft bell-like structure for propulsion (Guo et al., 2007; Yang et al., 2007). The proposed system was energy efficient, small in size but did not demonstrate the ability to carry

any payload and function in varying environments. In this study, SMA wires were also chosen as the primary source of actuation. Biometal wires exhibit a 4% deformation of initial actuator length with a blocking stress of over 200 MPa. However, both the stress rate and deformation exhibited by SMA wire is dependent on the magnitude of applied pre-stress. For example, a 100μm Biometal fiber exhibits stress rate of 10 – 80 MPa/sec with an applied pre-stress ranging from 0 – 320 MPa.

2.1.2 Medusa as Bio-Inspiration

Some important medusae anatomical features are shown in Fig. 2.1.2. The bell deformation is of main interest as it is responsible for propulsion. The top and bottom layer of the bell consists of a membrane called epidermis which is separated by mesoglea. The bell's exterior part is referred to as exumbrella and the inner cavity as subumbrella. The medusa's swimming cycle consists of two phases. The first phase is contraction where subumbrellar muscles shorten and contract the bell to expel water and create thrust. These muscles are part of a muscle sheet which is limited to one cell layer thickness creating a constraint on the force available for propulsion. The relaxation phase follows with the bell regaining its original configuration using stored elastic energy. Medusae do not have muscles to recover their initial bell configuration rather they rely on elastic energy stored in their structure during contraction as described by Megill et al. (2005). Fibers in the mesoglea are stretched during bell contraction as the walls thicken allowing them to store elastic energy which is used for bell relaxation. Daniel (1982) has shown the importance of resilience in the structure for efficiency and cost of locomotion and found that efficiency is proportional to the energy imparted to bell during contraction. This mechanism is of great asset for a vehicle since it does not require the use of

actuators for the relaxation phase which can lead to reduction in space requirement for the propulsion mechanism.

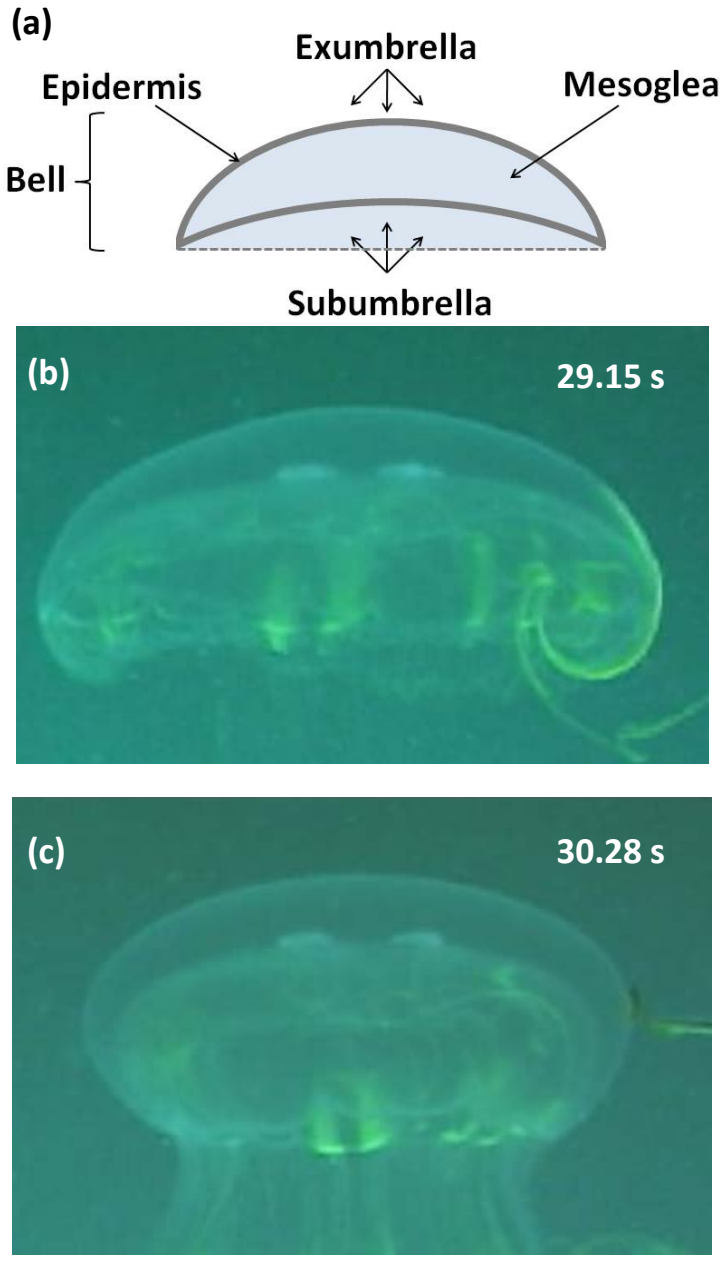

Figure 2.1.2: (a) Basic anatomy of the A. aurita's bell, (b) A. aurita relaxed configuration, (c) A. aurita contracted configuration. Pictures (b) and (c) were provided by Prof. John H. Costello, Biology Department, Providence College, Providence, RI.

Medusae can be separated into two categories “oblate” and “prolate” as pointed out in literature depending upon their fineness ratio which is the ratio of bell height to bell diameter (Colin and Costello, 2002). An important distinction can be made at the swimming mechanism level between both these categories. Prolate medusae swim using jetting propulsion while oblate medusae use rowing propulsion. Oblate medusae are also found to reach greater dimensions which can be attributed to their swimming mechanism (Dabiri et al. 2007). The rowing mechanism utilizes the limited force available from subumbrellar muscles more efficiently to displace larger amount of water for a given bell diameter creating enough thrust to propel larger jellyfish. Rowing has been found to be more energy efficient and therefore better for long distance travel (Dabiri et al., 2007). However, the rowing mechanism is more complex as it relies on the precise formation of opposing vortices and requires greater deformations then jetting. The oblate medusae were chosen for this study due to their higher energy efficiencies and the potential to reach greater vehicle dimensions for a given force capability. Figure 2.1.3 shows the relaxed and contracted bell profile of an Aurelia aurita which is member of the oblate category. Only half of the cross-section is shown here since jellyfish can be assumed as axisymmetric. During contraction, the bell deformation is approximately 42% in the radial direction (x-axis) and 50% in the axial direction (y-axis).

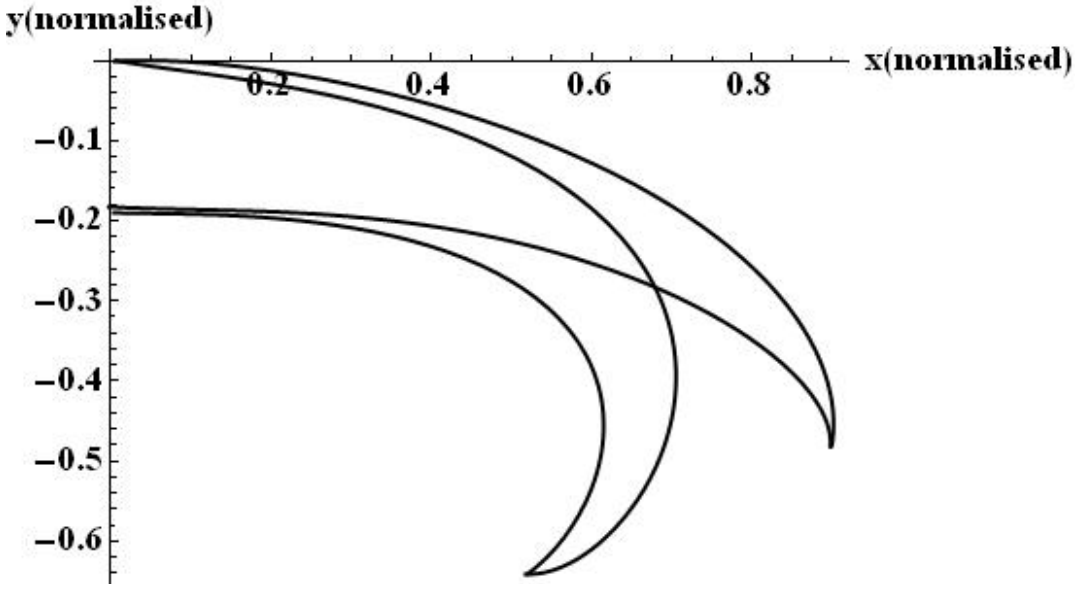

Figure 2.1.3: A. aurita bell profile in the contracted and relaxed configuration. Profiles are normalized by the bell margin radius in the relaxed configuration.

2.1.3 Jellyfish Prototype Design

2.1.3.1 Prototype I – "JetSam"

The aim of this first prototype was to investigate the system requirements of underwater SMA actuation based jellyfish for producing controlled thrust. The overall frame of the bell was designed to replicate the shape of real jellyfish. The cambered bell segments as well as the hydrodynamic main body structure were fabricated by using 3D printer. The bell segments were attached to the periphery of the main body using thin aluminum plates. As shown in Fig. 2.1.2, each SMA wire passes through a brass tube and is fixed to the attachment point on a bell segment creating a moment arm about the fixed end. Upon applying current, the bell segments contract inwards resulting in a pressure increase inside the bell. JetSam was designed to mimic the propulsion mechanics of the "jetting" jellyfish as opposed to "rowing" jellyfish.

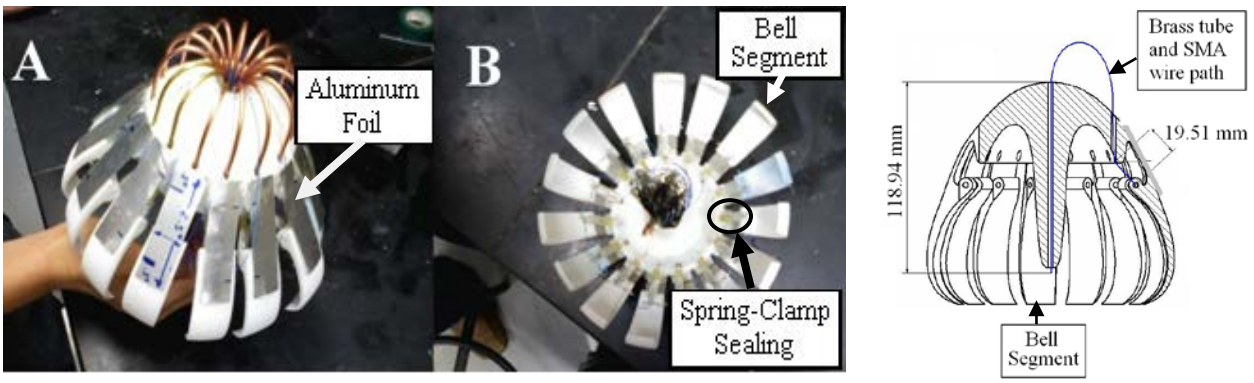

Figure 2.1.4: (a) Depicts the aluminum leaf spring and brass tubes (b) Demonstrates the bell segments and the location of the spring-clamp mechanism, (c) Cross-section of JetSam showing the relative assembly of the wires, brass tube guides and aluminum plates.

One of the main challenges in using SMA wires is that they need to be insulated from water. Heat loss due to convection from operating an SMA wire in water can diminish the performance of its temperature-driven actuation. In fact, a 20 cm long SMA wire that produced a 0.8 cm actuation when supplied with the recommended current of 0.25 A, failed to actuate, when placed in water at room-temperature and supplied with the same current. Therefore, a compressible sealing clamp with an integrated compression spring was designed. The compression spring was included to keep tension in the SMA while also preventing the sealing structure from touching the SMA. Unfortunately, this structure did not insulate the SMA wires properly and was one of the design flaws resulting in the poor performance of the JetSam.

In order to overcome the limit on allowable SMA radius of curvature, brass tubes were bent in a circular pattern and used as guides while keeping the same maximum bend radius. However, the extended curvature increases the contact area between the tube and SMA thereby increasing friction. To reduce friction with the brass and avoid potential electrical shorting, PTFE tubes were inserted as intermediate layer between the brass and SMA. This type of tube was used for its flexibility, low friction and high operating temperatures. The full system of 15 bell segments required 14 volts to achieve a current of 0.3 A in each SMA (Power supply: HP

6632B). However, the contractions for JetSam were found to be asymmetrical and inconsistent in magnitude for each segment. Theoretical bell segment tip movement was calculated to be 3.9 cm while the measured contraction was in the range of 0.1 cm to 0.5 cm on all of the 15 bell segments. Thus, JetSam had limited to no propulsion in the water. Some of the key problems were found to be: (i) required radius of curvature for SMA path resulted in high friction even with PTFE tubes, and (ii) the combination of compression spring and sealing material exerted too much resistance to the SMA deformation. These two factors resulted in a force that was larger than the 0.7 N pulling strength of 1 SMA. However, results on JetSam provided useful information on implementation of SMA in underwater vehicles and lead to the development of JetSum.

2.1.3.2 Prototype II – "JetSum"

Figure 2.1.5 shows the picture of the prolate-inspired JetSum which also utilizes SMA wires as artificial muscles to drive the jetting-type propulsion. However unlike JetSam, the "hub-style" design isolates the actuator wires from water in a central location. The bell segments were attached to the main body with a hinge joint, and a spring on the outside of the body maintained the SMA wire in tension throughout the actuation and relaxation cycle. The spring also stored energy for returning the bell segment to its original position. The SMA wires were attached near the hinge where the high mechanical strength of the SMA was exploited and the small deformation was fully utilized. Thrust depends on the actuation speed of the bell segments which is proportional to the magnitude of current passing through the SMAs. It is desirable to actuate fast and relax slowly which results in maximum thrust and minimum drag in the direction of motion. JetSum's hub design was compact and addresses the primary causes of JetSam's poor

performance by having: adequate thermal insulation of SMA wires, buoyancy control, proper pre-stress in SMA wires, efficient use of total deformation, and low SMA/tube friction.

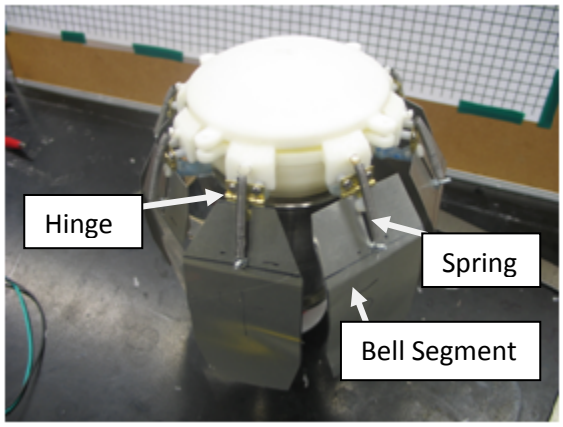

Total Mass (g)	324
Volume (cm^3)	450
Diameter (At hinge) (cm)	14.2
Bell diameter (open) (cm)	16.5
Bell diameter (contracted) (cm)	10.2
Payload mass (g)	84.8
Number of SMA	8
Single SMA length (cm)	25
Total vehicle resistance (ohm)	4.4

Figure 2.1.5: Fully constructed JetSum (left) and corresponding design specifications (right).

The primary feature of the redesign was the complete enclosure of SMA actuator wires within the central body. The central body was hollow allowing the SMA actuators to be installed across the diameter as shown in Fig. 2.1.6 (a) and (b). The straight line configuration of SMA wires helps to maximize actuation and minimize friction loss from contact with the PTFE tubing. The role of PTFE tubing was to provide electrical and thermal insulation. As can be seen in Fig. 2.1.6, the SMAs were clamped to the body by bolts and washer which also serve as the positive and negative terminals. The clamping method makes it much easier to install and adjust SMA wires when necessary. Additionally, the central body was designed such that a single SMA wire (approximately 25 cm in length) is looped from a positive terminal to a bell segment and back to the negative terminal. This eliminates the problem of losing tension in SMA and allows for initial angle of the bell segment to be changed simply by adjusting the length of SMA at either wire junction.

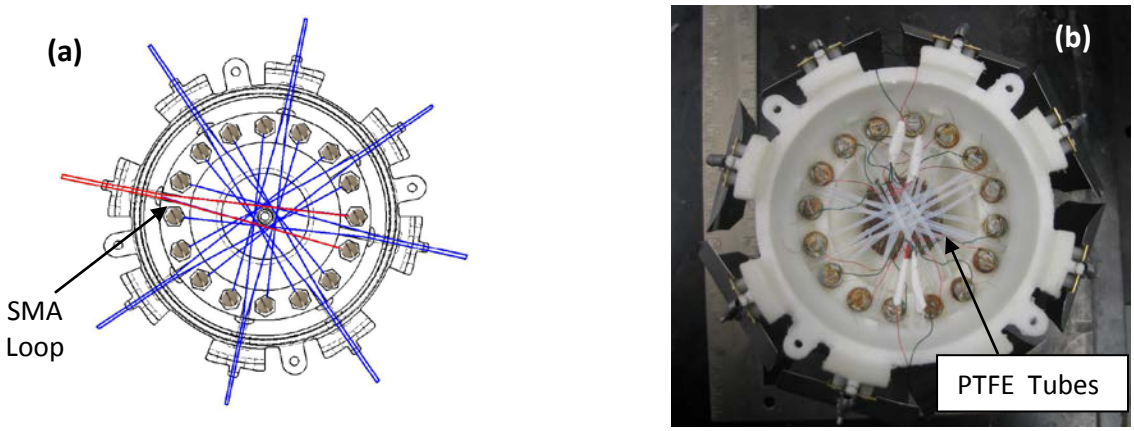

Figure 2.1.6: (a) Top view of central body as a CAD model and (b) fully constructed model. Note the straight line SMA configuration to the bell segments, built-in wire junctions, and PTFE tubes as white tubes inside the hub.

The portion of SMA wire between the bell segment and hub was sealed from exposure to cold water by a compressible "boot" as shown in Fig. 2.1.7 (a). This boot was designed to meet the actuation and isolation requirements. JetSum uses tension springs instead of compression springs that are attached from the central hub exterior to each bell segment which significantly improves the ease of contraction. The attachment point of the tension springs on the bell segments can be moved to adjust the pre-stress applied to the SMAs. The performance of SMA's can be optimized by adjusting the applied pre-stress.

The elastic silicone rubber used in this design allows the SMA to freely actuate and create a seal around the barrel used to connect the SMA to the bell segment and the knob from which SMA passes into the central hub Fig. 2.1.7 (a). Silicone was chosen due to its high operating temperature, low thermal conductivity, flexibility, compressibility, and ease of manufacturing. In addition to new electrical and thermal isolation connections, the design of bell segments was revisited. A drag approximation of flat bell segment showed that the number of SMA's required to contract full bell area could be greatly reduced. In fact, the new design used only eight SMA's and corresponding bell segments. The reduction in SMA wires also translated into drastic reduction in power consumption. Although the number of bell segments was

reduced, the overall surface area was increased. The eight bell segments nearly form a complete bell as can be seen in Fig. 2.1.7 (b). The bell segments used in this prototype were made of aluminum foil and designed to cover a large surface area for simulating a continuous bell shape. The inward bend of the aluminum foil acts to create less resistance during relaxation and a more hydrodynamic shape in the traveling direction.

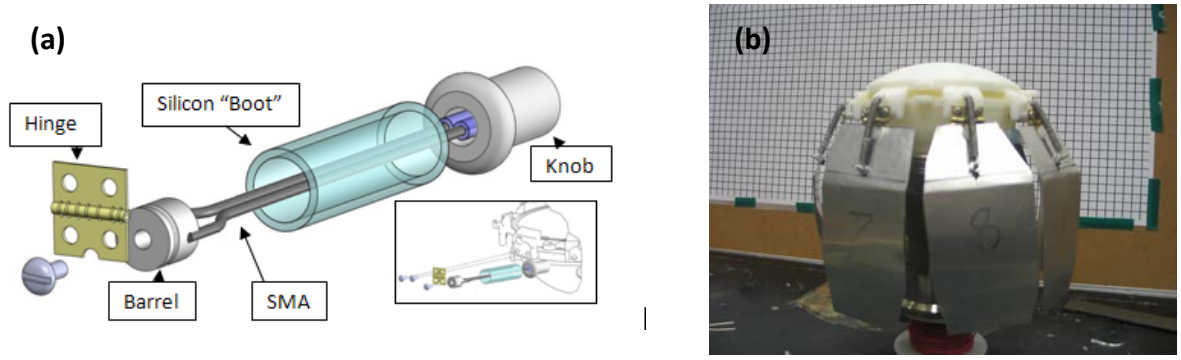

Figure 2.1.7: (a) CAD model of exploded connection assembly for the bell segment and main body junction, (b) Side view of fully constructed JetSum.

Another aspect of the hub design was the buoyancy force created by the hollow chamber. The volume of this chamber was designed so that JetSum operated at neutral buoyancy with a payload of 85 gm. This payload represents the mass of driving circuits and batteries that will be required to make the vehicle autonomous. If the actual weight of future payloads is higher, a larger top can be used to increase the buoyancy force. Since all of the functional components of this design are built into the bottom "hub", a redesign of the top will not affect the functionality of vehicle so long the center of gravity is kept under the center of buoyancy.

2.1.4 Experimental Methods

The characterization of JetSum was conducted using a video camera from Imitech with 30 FPS and 640 x 860 black and white images to record the vehicle motion. A 75 gallon glass aquarium with length, width, and height of 48" x 18" x 20" respectively was used as a test bed.

A grid board was positioned in the background for reference during image processing. A NI cDAQ card was used to record the voltage drop across JetSum as the bell segments were actuated and a HP 6632B power supply was used to provide current to the SMAs. A schematic of the experimental setup is shown in Fig. 2.1.8. Individual bell segment deformation was measured using a Micro – Epsilon optoNCDT 1401-50 displacement laser as shown in Fig. 2.1.8. The laser was positioned 5 cm outside the aquarium from the bell segment being tested for recording the lateral displacement. Bell segment displacement was measured in the water while the vehicle was anchored to the bottom. This prevented the vehicle from propelling itself during actuation and hence affecting the measurements.

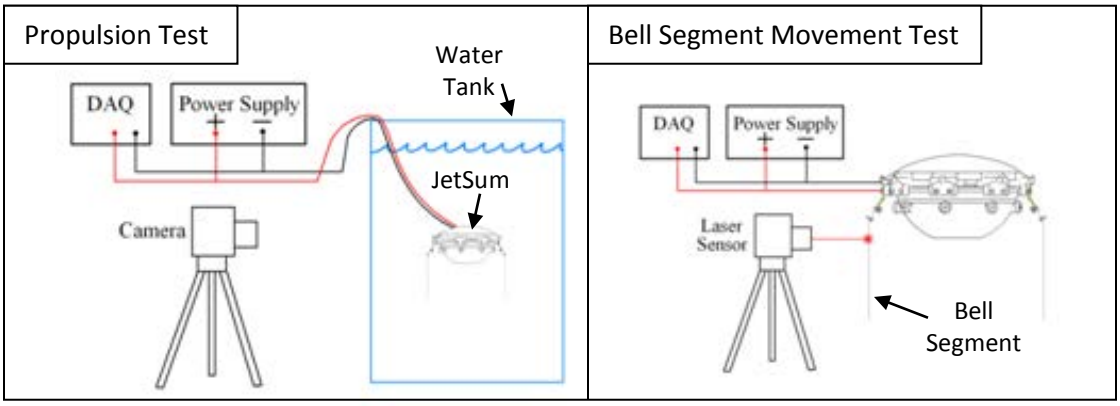

Figure 2.1.8: Schematic diagram of thrust test (left) and schematic diagram of bell segment displacement test (right).

2.1.5 Result and Discussion

2.1.5.1 Vehicle Motion Characterization

The dynamic motion of the vehicle was characterized by using the recorded real-time video file and analyzing the data at each frame using Matlab. The position at specific time period was determined by tracking a marked point on top of the bell cover. The time domain of input voltage and position was correlated by matching the frame at which the bell segment first began

actuation to the instant when voltage was turned on. Only the vertical motion of the vehicle was analyzed since the bell segments were designed to provide unidirectional movement and the motion in the other directions was considered to be negligible. Figure 2.1.9 shows snap-shots of JetSum during a full cycle. The motion was captured after 3 pulses with an input current of 3A and initial sinking state (See Fig. 2.1.11 for the corresponding position plot).

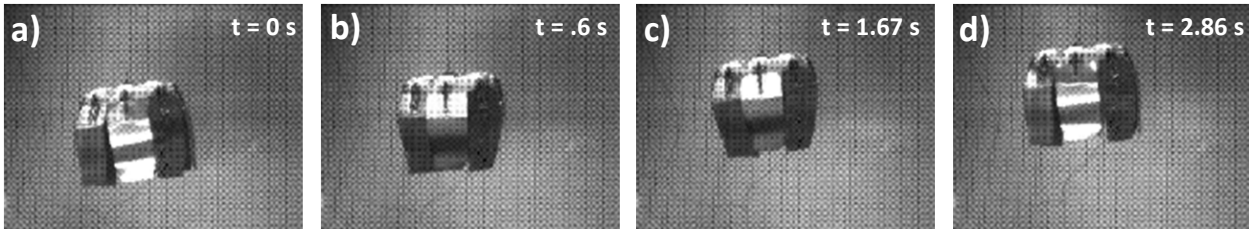

Figure 2.1.9: Demonstration of frame-by-frame analysis of JetSum's vertical motion with an input current of 3A over the course of full operation cycle. All four stages are shown: (a) relaxed state before contraction, (b) bell fully contracted, (c) end of contraction phase after cruise, and (d) return to fully relaxed state.

Preliminary testing was done by applying the voltage manually until the bell segments visually stopped contracting. It was found that an optimum distance can be traveled partly depending upon the duration in which bell segments stay in their actuated position. Figure 2.1.10 shows the relationship between input voltage and position of the vehicle inside the test tank. Voltage data was filtered with a low-pass Butterworth filter with a cutoff frequency of 100Hz. As observed in Fig. 2.1.10, for a series of step input voltage with amplitude of 10 V and frequency of approximately 1 Hz, the vehicle climbs 23 cm in 9 sec after the beginning of actuation. The position versus time data was differentiated to obtain the instantaneous velocity over the course of the vehicle's underwater locomotion. The profile indicates that the velocity attained harmonic behavior around 1 Hz. Slight distortion in profile may be due to the data extraction which was done at every 0.17s. It should be noted here that data was taken for a short

time before current was applied to the system and during that time the vehicle exhibited small vertical motion which depicts the buoyancy state of the vehicle during its trajectory.

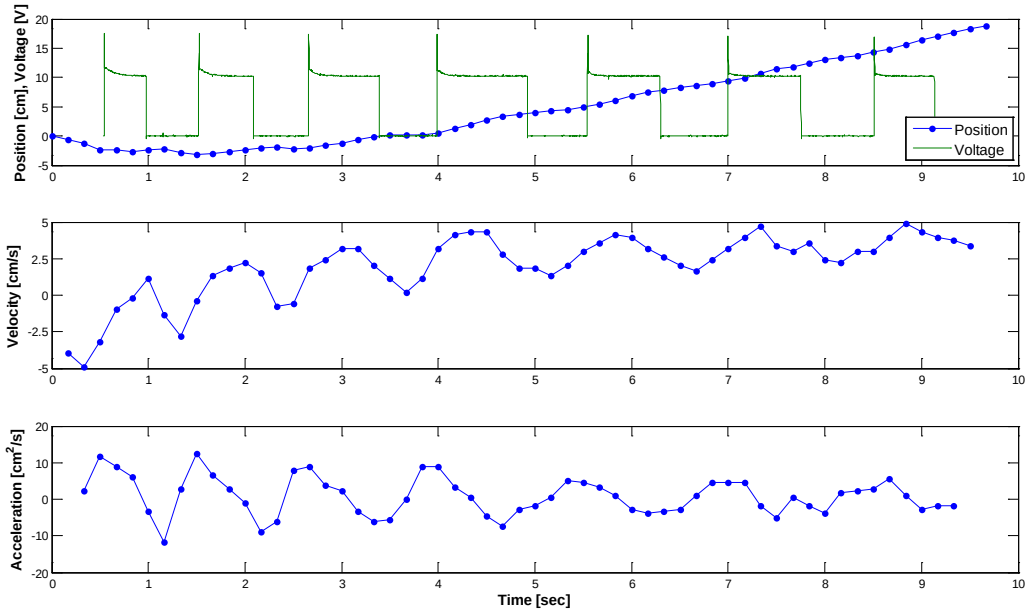

Figure 2.1.10: Applied voltage with an average current of 2.75A and resulting vehicle position in the vertical axis (top) along with corresponding instantaneous velocity (middle) and instantaneous acceleration (bottom).

While neutral buoyancy was desired for JetSum, minor water leakages and pressure gradient as a function of depth resulted in buoyancy changes during operation. The majority of tests started with small sinking rates before the application of current. This is represented by negative velocity in the beginning of the velocity profile as shown in Fig. 2.1.10(b). After a few pulses, the jellyfish prototype was able to build momentum; maintaining a positive velocity. Video data was taken for input currents of 2.50, 2.75, 3.00, 3.25 and 3.50 A. The velocities obtained by applying current in the range of 2.50 A to 2.75 A were up to 5.6 cm/s and accelerations of 20.6 cm/s^2. The tests with applied current of 3A and 3.5A produced instantaneous velocities of up to 7.8 cm/s and instantaneous accelerations of 22.2 cm/s^2. The relationship between vehicle position and input currents is explained in Fig. 2.1.11. At low

currents, the pulse frequency was limited and the vehicle took longer to build momentum resulting in lower velocities (shallower position slopes). As the input power was increased, pulse frequency increased due to faster contraction rates resulting in increased velocity (sharper position slopes). However, at 3.5 A the performance starts to level due to decrease in pulse frequency caused by additional time needed to cool the over-heated SMA wires. From the experimental data collected on JetSum, an input current of 3A was found to provide optimum performance.

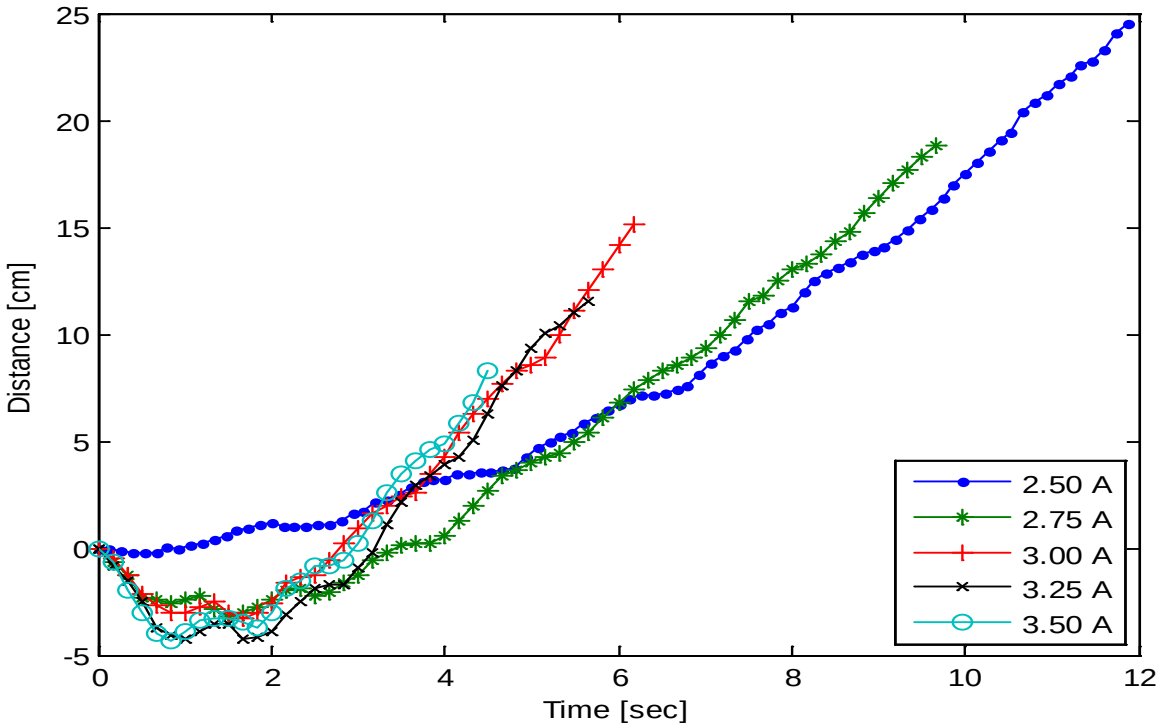

Figure 2.1.11: Plot of vertical position of JetSum during underwater operation. Data from increasing input current shows increase in slope representing increase in velocity.

2.1.5.2 Bell Segment Deformation

SMA wire actuation drives the vehicle by causing contraction of each bell segment. Displacement data was taken at 3 cm from the hinge of individual bell segments during contractions at various applied input currents. Since the bell segments can be assumed to be

rigid bodies, the deformation was extrapolated to the bell margin. This is a good representation of deformation throughout the entire bell segment. The deformation follows the expected pattern from SMA actuator performance as shown in Fig. 2.1.12(a). The response time of SMA is not instantaneous. Rather, there is a delay depending upon the applied current amplitude. As voltage spikes up and starts decreasing, the deformation keeps increasing since the temperature rises. Similarly, when the current is switched off, the SMA wires take time to regain their original length. As expected, this delay in response was found to be dependent on the magnitude of tension applied to the wire and rate of heat dissipation. As shown in Fig. 2.1.12, immediately after input voltage is switched off, the bell segment did not fully recover its original position due to residual heating. This residual heating contributes to the deformation in the next voltage step. It can be observed that deformation increases with each step corresponding to the increase in SMA temperature. The relaxation time for activation at 10 V was on the order of 1.6 sec which limits the pulsing frequency of the vehicle.

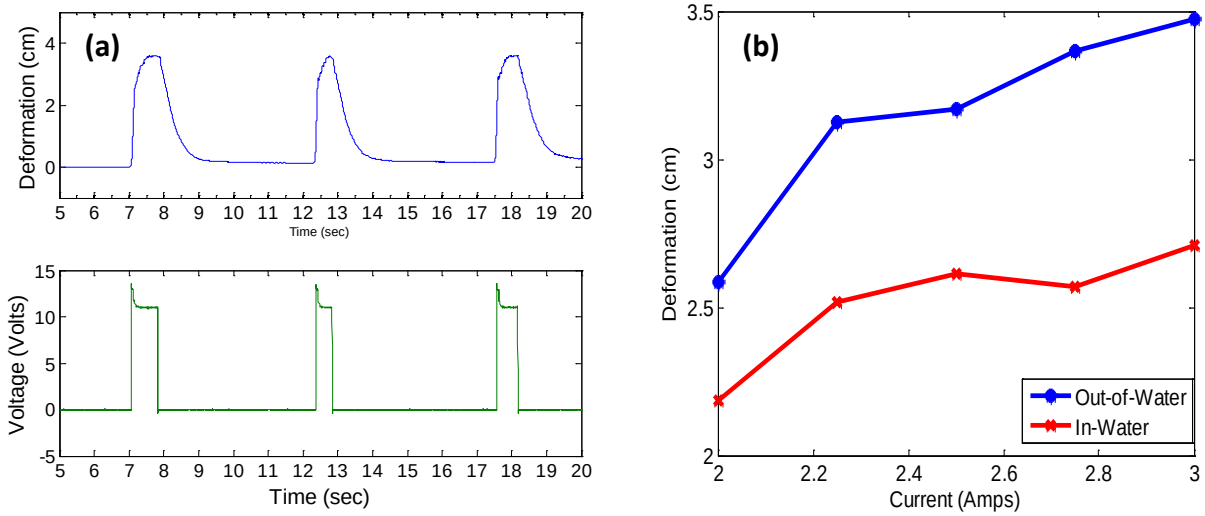

Figure 2.1.12: (a) Input voltage applied to SMA (bottom) and resulting bell margin deformation (top), (b) Average bell margin deformation as a function of input current for both in and out of water.

Water has greater heat conductivity than air; therefore the heat coming from the SMA is dissipated to the surrounding more rapidly when submerged in water. This reduces the temperature reached in the SMAs for an applied magnitude of current as shown in Fig. 2.1.12(b). It can also be seen in this figure that the difference in average deformation achieved by bell segment is around 0.5 cm at the bell margin. Thus, larger current magnitude is required in underwater condition; increasing the overall power consumption. In parallel to the heating issue, a cooling issue occurs when using high currents for extended operating time. In underwater tests, it was observed that at input current of 3.5A, long relaxation times of more than 1 sec occurred that reduced the momentum significantly and the overall motion of vehicle was worst then at lower current amplitudes. This problem can be overcome by designing a control system which limits the magnitude of the applied current and time of actuation for certain surrounding heat dissipation rate.

2.2 Bio-Inspired Shape Memory Alloy Composite (BISMAC) Actuator

2.2.1 Understanding the Radial Deformation Mechanism

In order to improve the deformation behavior of SMAs a novel composite actuator was designed. A commercially available SMA wire, BioMetal Fiber (BMF) 100 (Toki Corp., Japan) was selected for the design of bio-inspired SMA composite (BISMAC) actuators. BMF exhibits a contraction of ~4% of its original length when heated to a temperature of ~70°C. Pre-stress and active heating techniques can be used to maximize the deformation up to 6%; however this affects the SMA life span. The contraction time can be controlled by the magnitude of current passing through the actuators. The extension time depends on how rapidly heat can be dissipated

away from the actuators. Recently, active cooling mechanisms have been shown to achieve expansion times of milliseconds however their implementation on UUV platform is cumbersome (Tadesse et al., 2010). SMAs have previously been used for jellyfish like vehicles (Guo et al., 2003; Yang et al., 2007; Villanueva et al. 2009) where SMA wires were either used to a create moment arm on a bell segment or to reduce the bell diameter to create jet. Rigid bodies actuated by moments restrict the ability to create rowing propulsion due to the required active deformation along the span. Other types of actuators have also been demonstrated in underwater propulsion concepts (Abdelnour et al., 2009; Yeom and Oh, 2009) for directly creating the deformation which often results in smaller thrust, far from that required for deep ocean waters.

Available literature reveals that circular muscles are used for propulsion in both jetters and rowers (Gladfelter, 1972; Gladfelter, 1973; Satterlie et al., 2005). Therefore the first concept considered for the propulsion mechanism consisted of actuators positioned along the inner bell circumference. The bell diameter contraction can be determined using the simple expression $D=2\pi x(y)$, where D is the length of actuator and x(y) is the radius of the bell as a function of the axial direction (y-axis). During full contraction, the bell margin radius reduces by 42% for *Aurelia aurita*. This would require SMA contractions of the same amount which is approximately 10X greater than what can be achieved by available SMAs. Clearly, another mechanism for implementation of SMAs is required to realize such large deformations. Gladfelter demonstrated that *Cyanea capillata* uses radial muscles to create up to 50% of the total required deformation during swimming cycles while the rest of the deformation comes from circular muscles. These radial muscles contract about 20% while exerting a deformation reaching up to 90^0 below the horizontal. Motivated from this result, several conceptual experiments were

conducted to understand how medusae use radial muscles to contract their bell and whether it could be replicated using SMAs.

A 15 cm curved aluminum plate in a cantilever configuration was used to represent a bell fraction. One end of the SMA wire was attached to the tip of the aluminum plate while the other end was anchored to the rigid base at 0.2 cm below the plate mounting position as shown in Fig. 2.2.1.

(a)

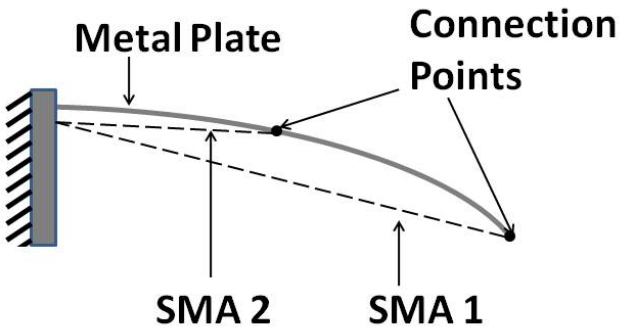

(b)

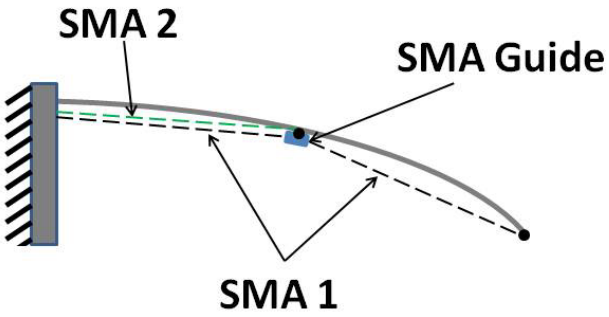

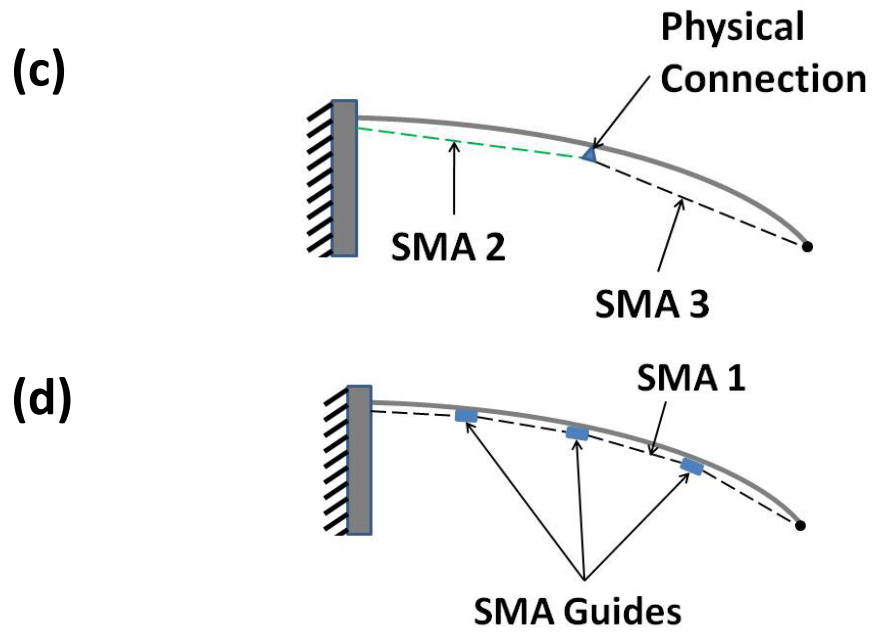

Figure 2.2.1: (a) Configuration 1, two SMA positioned in parallel, SMA 1 is connected at 10 cm from the root and SMA 2 at 5 cm. (b) Configuration 2, same as configuration 1 with SMA 1 passing through a plastic guide 0.5 cm long and 0.3 cm in diameter positioned at 5 cm from the root. (c) Configuration 3, SMA 2 and 3 are physically connected in series through an insulated connector positioned at 5 cm. (d) Configuration 4, SMA 1 passes through 3 guides positioned at 5, 10 and 15 cm from the root.

Various wire configurations, as shown in Fig. 2.2.1 (a) – 3(d), were tested to determine the arrangement that results in the highest deformation. Configuration 1 shown in Fig. 2.2.1 (a) consists of SMA wire 1 and 2 (SMA 1 and SMA 2) physically connected in parallel and electrically independent from each other. Table 2.2.1 shows the deformation results for each SMA actuated independently and then simultaneously (1 & 2).

Table 2.2.1: Results of aluminum beam experiments showing the x and y percent deformation. The percent deformation is based on the initial x and y position of the tip relative to the root.

Config.	SMA	% Def (x)	% Def (y)
1	1	9.42	22.55
	2	13.31	42.86
	1 & 2	18.70	48.96

2	1	24.26	61.54
	2	17.74	59.82
	1 & 2	27.22	71.04
3	2	18.06	55.16
	3	6.08	9.91
	2 & 3	26.48	59.82
4	1	28.96	76.06

The results show that the performance increases for configuration 2 shown in Fig. 2.2.1(b), due to an added guide. The guide is a plastic tube allowing the SMA to travel freely and maintaining a separation of 0.3 cm from the aluminum beam. SMA 1 achieves a larger deformation in configuration 2 then when both SMA 1 and 2 are operated together in configuration 1. In configuration 2, SMA 2 only increases the performance of SMA 1 by a few percent approximately 3% in the x-axis and 10% in the y-axis. In configuration 3 shown in Fig. 2.2.1(c), the SMAs are physically connected in series but electrically they are independent from each other. This means they can be operated independently and act as one SMA with a guide spanning the length of the beam. Configuration 3 demonstrates that SMA 2 and 3 achieve similar performance as SMA 1 shown in configuration 2. The slight decrease in deformation may be related to the clamps used for connecting the SMAs. The overall SMA length is reduced relative to SMA 1 allowing a smaller contraction. The advantage of configuration 3 is the additional control, as different parts of the beam can be actuated independently while maintaining the high deformation. In configuration 4 shown in Fig. 2.2.1(d), SMA 1 is connected to the aluminum plate along with three guides.

The additional number of guides enhances the performance as SMA is kept closer to the aluminum beam. Figure 2.2.2 shows the relaxed and contracted position obtained in

configuration 4 before and during the actuation cycle. The results of Fig. 2.2.1 are summarized in Table 2.2.1. It should be noted that when SMA 2 is actuated by itself the percent deformation varies from one configuration to another. This is due to initial tension exerted by other SMA wires which changes the profile of the aluminum beam and changes the tension in SMA 2. A small change in wire tension has a strong impact on the final deformation of the structure since a certain fraction of the 4% contraction is lost in recovering tension before the structure can be further actuated. In these experiments the metal strip acts as an incompressible beam and the interaction between the beam and SMA can partly be explained by kinematics. Initially, SMA and metal lengths are equal as shown in Fig. 2.2.3(a).

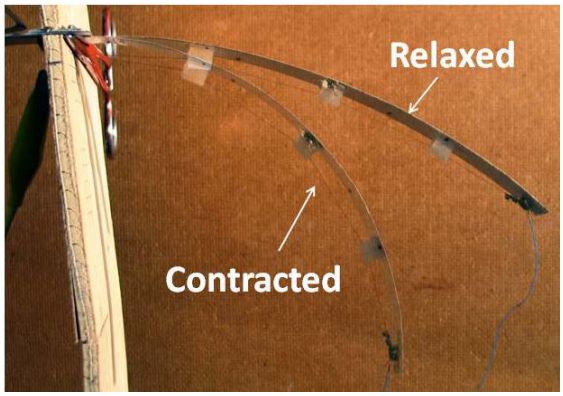

Figure 2.2.2: Picture of configuration 4 in the relaxed and contracted position.

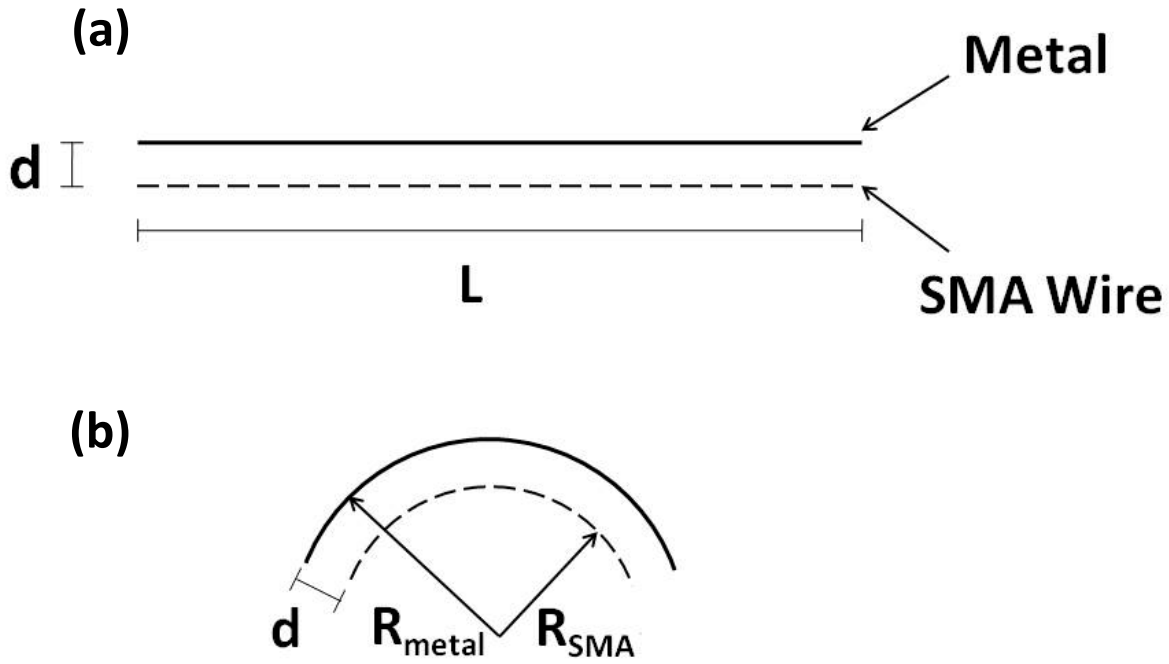

Figure 2.2.3: Beam kinematics concept diagram showing the (a) undeformed and (b) deformed configuration.

During actuation it can be assumed that the SMA contracts by 4% and the metal strip is incompressible giving the following relation: $L_{SMA}{}'=0.96*L_{SMA}$, where L_{SMA} is the initial length of the SMA and $L_{SMA}{}'$ is the SMA length after contraction. Assuming the composite beam bends kinematically without any resistance then the following can be obtained:

$$\frac{R_{SMA}}{R_{metal}} = \frac{\frac{L'_{SMA}}{\alpha_l}}{\frac{L_{metal}}{\alpha_l}} = \frac{0.96*L_{SMA}}{L_{metal}} = 0.96\,, \qquad (2.1)$$

where R_{SMA} and R_{metal} represent the radius of curvature of the SMA and metal as described in Fig. 2.2.3(b). The distance d between the SMA and metal beam is a known parameter and correlates the two radii of curvatures as:

$$R_{metal} = R_{SMA} + d, \qquad (2.2)$$

Using Eqs. (1) and (2), it can be shown that :

$$R_{metal} = 25d\ . \qquad (2.3)$$

Equation 3 shows the kinematic relation between d and the radius of curvature for an actuation of 4% which indicates that R_{Metal} can be manipulated by changing d and further implies that R_{metal} can be varied as a function of span (s) to achieve complex deformation profiles.

2.2.2 Design of the Bio-Inspired Shape Memory Alloy Composite (BISMAC) Actuators

The results from the previous section were utilized to arrive at the design of BISMAC actuators. The key design parameter found to dictate the final deformation was the SMA guides (distance d). A SMA guiding method that can keep the SMAs at specific distances from the incompressible beam was sought. Ideally, a number of small guides would be distributed along the beam length to maintain the desired separation (d) to maximize the deformation. As the number of guides is increased they eventually start to resemble the profile of a tube. Tubes keep the SMA at a constant d but add to the second moment of inertia of the beam and create resistance to bending. To overcome this problem, the SMA wire was embedded in a soft room temperature vulcanized (RTV) silicone. RTV silicone was chosen in particular due to its ability to set at room temperature. Thermosetting rubbers must be molded at high temperatures which distorts the SMA from its desired molding configuration. Silicone was also used to contain the incompressible beam and form a unified structure. The selected silicone had an elastic modulus of 56 kPa in compression and 98 kPa in tension with a density of 982 kg/m^3. Spring steel was selected for the incompressible beam due to its high flexibility and resilience. The resulting design is shown in Fig. 2.2.4 (a).

A constant cross-section (CC) BISMAC actuator is shown in Fig. 2.2.4(a). The CC-BISMAC actuator consists of four SMAs 100 μm in diameter, connected as shown in Fig.

2.2.4(a). The SMAs were placed at a distance (d) of 0.14 cm from the spring steel along 15 cm of overall length. The electrical connections at the tip and root were sealed with silicone adding 1 cm at the tip and 1.5 cm at the root. Three more beams were tested each with varying design parameters. The variable silicone (VS) BISMAC actuator consisted of different thickness of silicone above the incompressible beam while keeping the same SMA and spring steel configuration as for the CC-BISMAC actuator shown in Fig. 2.2.4(b). Next, a variable cross section BISMAC actuator with variable d and silicone thickness (VD) was tested as shown in Fig. 2.2.4(c). Another BISMAC actuator consisted of a constant silicone thickness with three layers of spring steel of different lengths (VL) as shown in Fig. 2.2.4(d). The last BISMAC tested consisted of a varying silicone thickness, spring steel distance, and SMA distance while keeping a constant d (VSSS), see Fig. 2.2.4(e). Figure 2.2.4(f) shows the Aurelia aurita (AA) BISMAC which was designed to mimic the deformation profile of the actual medusa. This is further discussed in the following sections. Figure 2.2.5 shows the picture of the fabricated samples used to analyze the effect of structural parameters on the deformation profile.

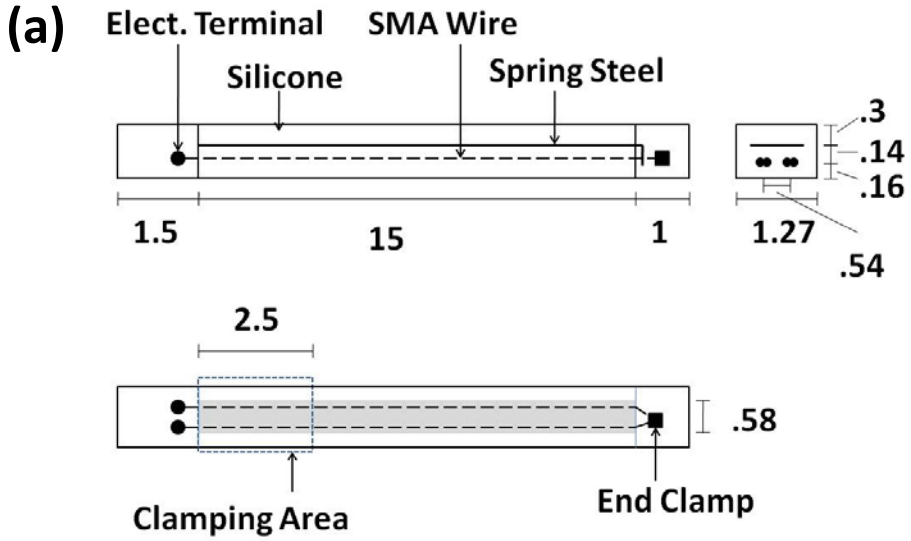

(b)

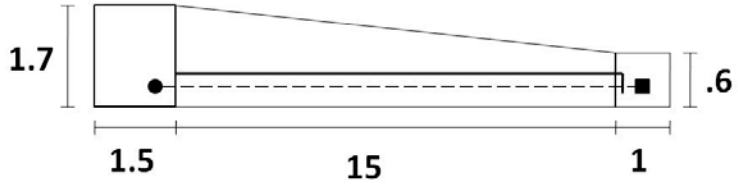

(c)

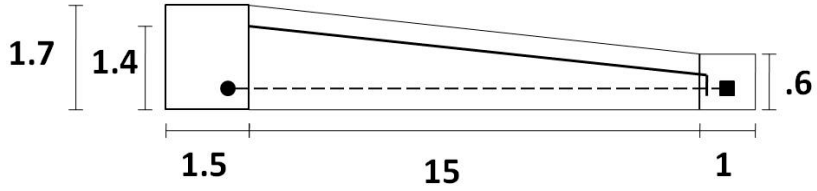

(d)

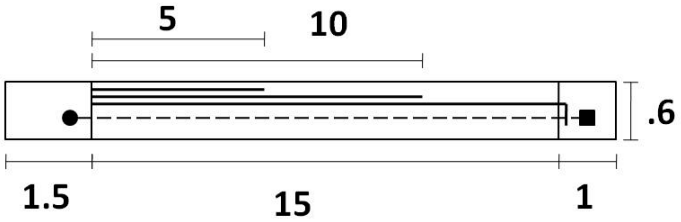

(e)

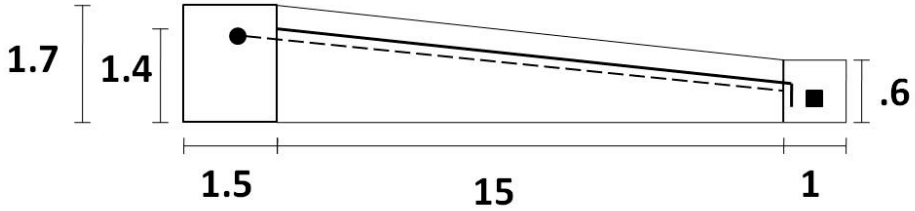

(f)

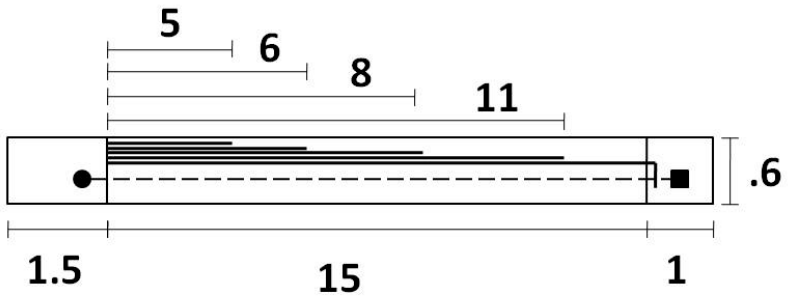

Figure 2.2.4: Diagram of the (a) CC-BISMAC, (b) VS-BISMAC, (c) VD-BISMAC, (d) VL-BISMAC, (e) VSSS-BISMAC, (f) AA-BISMAC. All dimensions are in cm. Unspecified dimensions are same as in (a).

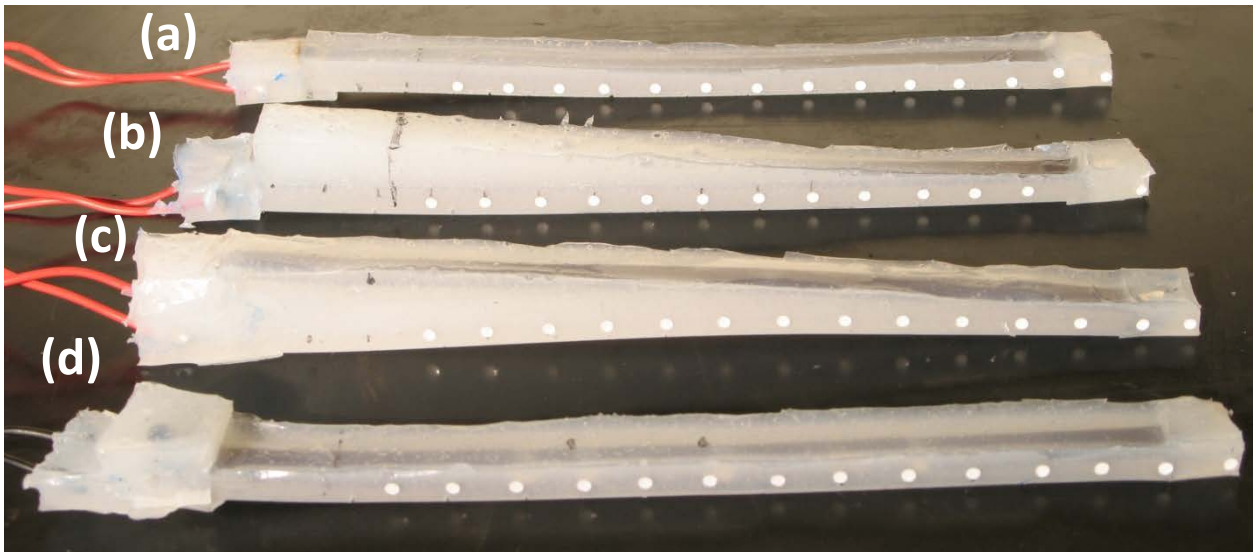

Figure 2.2.5: Picture of the (a) CC-BISMAC, (b) VS-BISMAC, c) VD-BISMAC, (d) VL-BISMAC.

2.2.3 Experimental Methods

BISMAC actuator testing was conducted by submerging specimens in water at room temperature (22°C). A glass aquarium of dimensions 122 x 46 x 51 cm was used as test bed. The actuator was clamped at a distance of 16.5 cm from the wall, 29 cm from the bottom, and 15 cm from the water surface. It was driven by an excitation signal generated from function generator

(Agilent 33120A) which was amplified by power amplifier (NF HAS 4052). The input power magnitude was measured by using a data acquisition system (NI cDAQ 9172 – NI 9221). A high-speed camera (Fastec Imaging IN250) was used to capture the actuator deformation. Figure 2.2.6(a) and (b) shows the schematic and picture of the experimental setup.

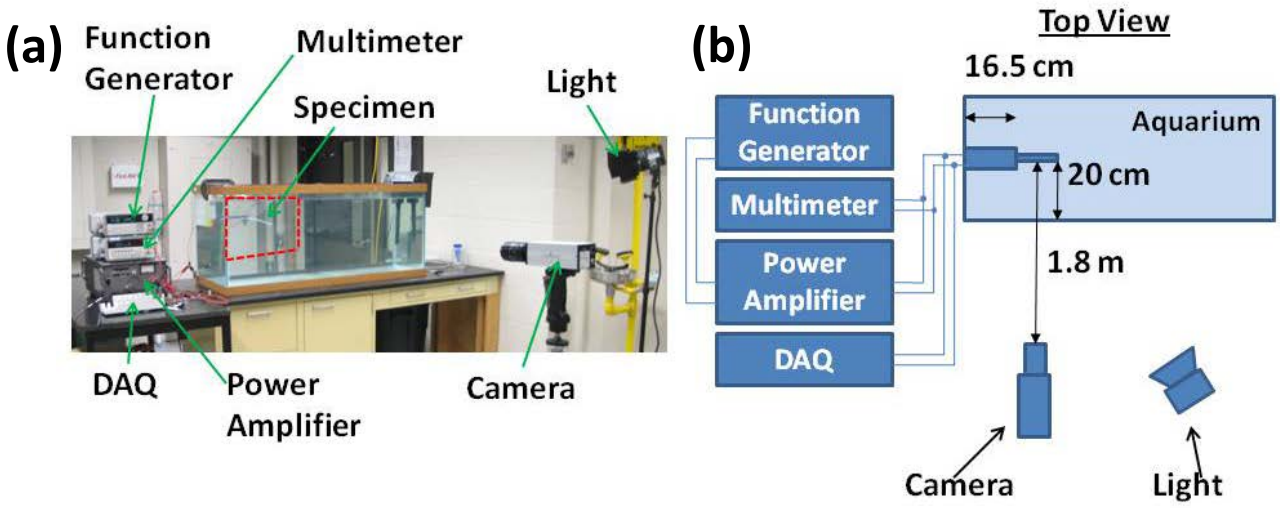

Figure 2.2.6: (a) Test setup picture, and (b) test setup diagram.

In order to precisely capture the actuator motion during excitation, 14 reflective dots with 0.25 cm in diameter were positioned on a side surface at 1 cm intervals. Background lighting was turned off during testing while a spot light was directed towards the reflective dots in order to increase the image contrast. The dots were tracked using an image processing code developed in MATLAB. Each frame was converted to a binary image and the individual points were labeled using a method described in (Haralick, 1992). To keep track of the actuator motion, the points were transformed to polar coordinates and numerical conditions were applied. The angle and magnitude of each point was compared and the points were kept in the same order as their position on the actuators.

2.2.4 BISMAC Characterization

Initially, measurements were conducted to determine the maximum deformation the actuators can achieve. This was done by driving the SMA with relatively high current until the deformation came to equilibrium. The condition for maximum deformation was set as when no additional movement could be seen by inspection of the images. During these tests, a constant voltage was maintained across the SMA wires. As SMAs underwent phase transformation from martensite to austenite, a change in resistance occurs. Since the driving voltage was kept constant during these experiments, the decrease in resistance resulted in current increase. Figure 2.2.7 demonstrates the actuators' profiles in the relaxed and fully contracted condition. The applied voltages, time of actuation and resistance magnitude are listed in Table 2.2.2. It should be noted that the SMA resistance in Table 2.2.2 is reported in terms of initial SMA resistance measured before actuation.

Table 2.2.2: Operating parameters used during the BISMAC maximum deformation test.

	Voltage (V)	Time (s)	Resistance (ohm)
CC-BISMAC	14.7	3.4	19.8
VS-BISMAC	16.7	2.9	19.7
VD-BISMAC	16.3	6.0	20.3
VL-BISMAC	16.1	3.0	19.2
VSSS-BISMAC	16.2	5.8	19.5
AA-BISMAC	16.3	6.0	19.1

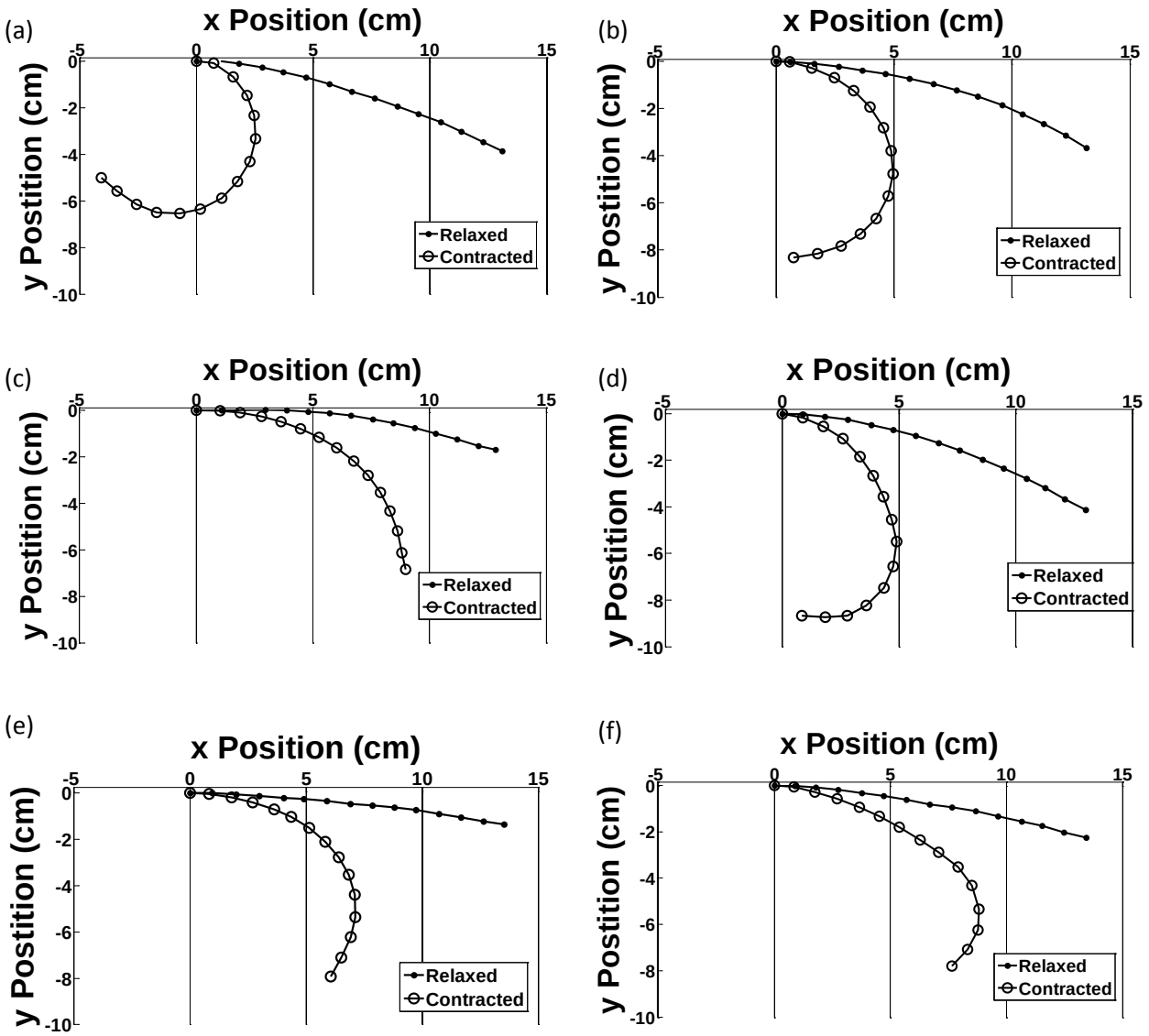

Figure 2.2.7: Relaxed and contracted configuration of the (a) CC-BISMAC, (b) VS-BISMAC, c) VD-BISMAC, (d) VL-BISMAC, (e) VSSS-BISMAC and (f) AA-BISMAC.

The CC-BISMAC actuator achieved the highest deformation as expected from its lowest second moment of inertia. The other four actuator designs achieved a smaller deformation and exhibited different profiles. To better compare the different profiles achieved by each actuator, the radius of curvature was calculated. This method was developed by K. Joshi and is described

in Villanueva et. al (2010). The results for radius of curvature as function of length “s” is shown in Fig. 2.2.8 which helps in quantifying the degree of deformation achieved by BISMACs.

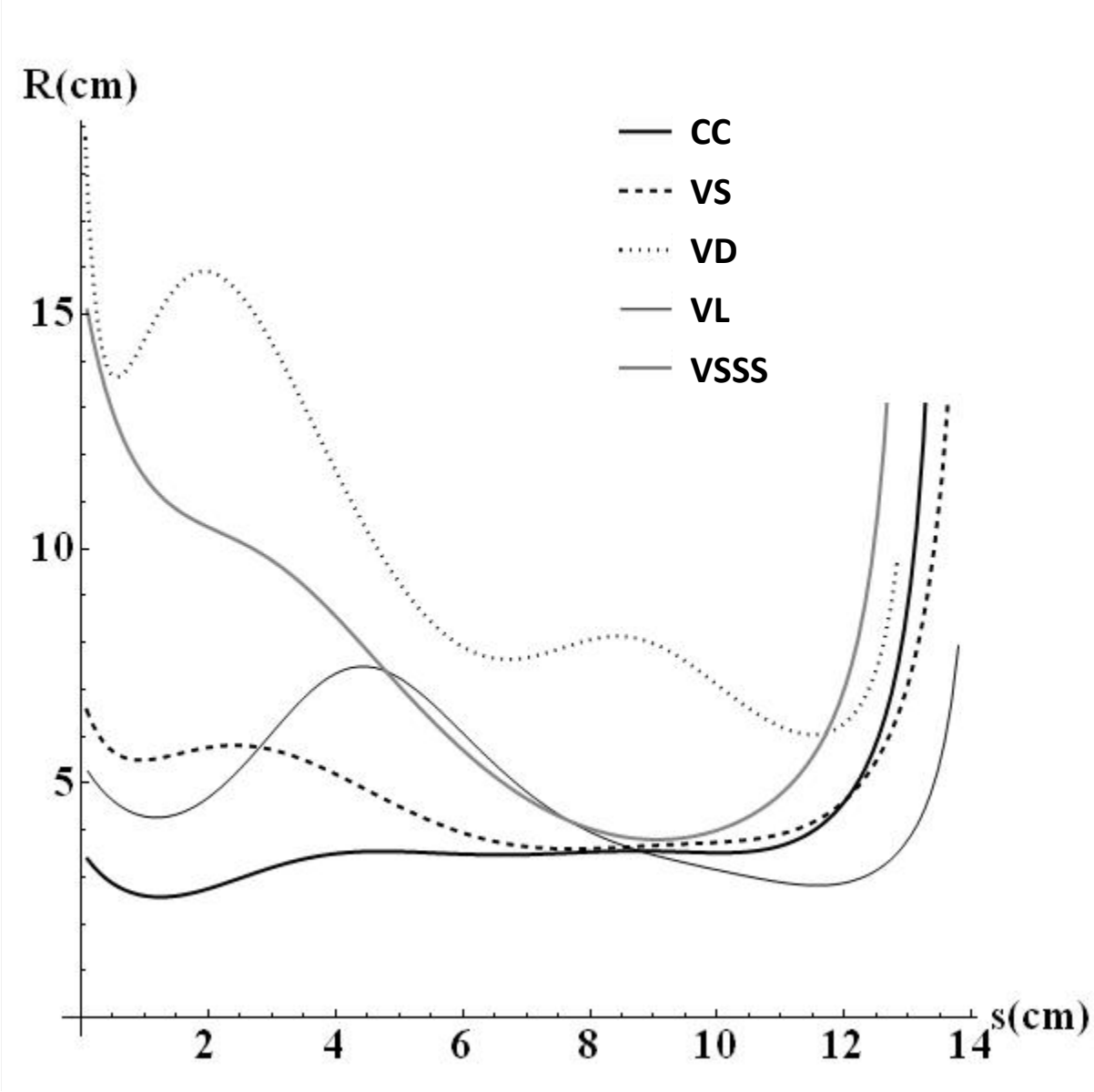

Figure 2.2.8: Radius of curvature as a function of position along s for the various BISMAC designs. This figure was made by K. Joshi in Villanueva et. al (2010).

The CC-BISMAC’s radius of curvature profile demonstrates a constant curve between 4 and 10.5 cm agreeing with what is expected from kinematics theory. An initial dip was observed in

the curve prior to 4 cm. This region is referred to as the support affected region. The radius of curvature increases significantly at the tip of the beam. This is due to the fact that the end section of the BISMAC is only a seal which does not undergo any SMA actuation. Also, the radius of curvature is affected by the initial location of reflective points. If the points are not positioned exactly in a straight line, their relative position will affect the final radius of curvature. The lowest radius of curvature is observed at 1.25 cm with a magnitude of 2.5 cm. To truly evaluate the performance of the CC-BISMAC, the region past the support affected region must be analyzed and the lowest radius of curvature becomes 3.5 cm. The VS-BISMAC achieves a different deformation profile from that of the CC-BISMAC, as expected due to the change in silicone thickness. It has a higher initial radius of curvature and beyond the support affected region (~2.5 cm), the radius of curvature reduces as the thickness of silicone decreases and approaches that of the CC-BISMAC. The VD-BISMAC shows the curvature's dependency on the distance d. Starting from the root, the greater distance d adds to the effect of larger silicone thickness resulting in a low curvature. The increased moment of inertia affects the curvature all the way up to the tip where the actuator is unable to achieve the same radius of curvature as the CC-BISMAC. This is probably due to the lack of force in the actuator as a consequence of the added resistance to deformation. The VL-BISMAC also shows a different profile then the CC-BISMAC's. After the support affected region which is taken to end at 4.5 cm in this case, the radius of curvature progressively decreases to 3 cm at 11.75 cm. Since the stacked springs steel strips are not bonded, they are allowed to shear axially relative to each other which reduces their effectiveness at resisting bending. Lastly, the VSSS-BISMAC shows the effect of having the SMA and spring steel start from a higher location on the y-axis as compared to the VS-BISMAC. The results show an initial increase in radius of curvature which progressively becomes similar

to the pattern followed by the VS-BISMAC. The results in Fig. 2.2.8 confirm that for a set SMA strength, the final profile of a BISMAC can be manipulated by changing the silicone thickness, distance d and spring steel thickness.

Since the SMA deformation is dependent on temperature, heat dissipation to the surrounding greatly affects the final beam deformation. When embedded in silicone, the SMA wires dissipate heat more rapidly than in air due to the fact that thermal conductivity of air $0.0263\,\mathrm{W/m \cdot K}$ is lower than that for RTV silicone $0.146 - 0.314\,\mathrm{W/m \cdot K}$ (Incropera, 2006). When submerged in water, silicone serves as an insulator since the thermal conductivity for water is of the order of $0.613\,W/m \cdot K$. The silicone matrix absorbs heat and its temperature increases during actuation which results in slower relaxation times due to residual heat. This phenomenon becomes an important factor through successive actuation cycles. Figure 2.2.9 and 2.2.10 demonstrate how the maximum deformation during contraction and recovery is affected over actuation cycles.

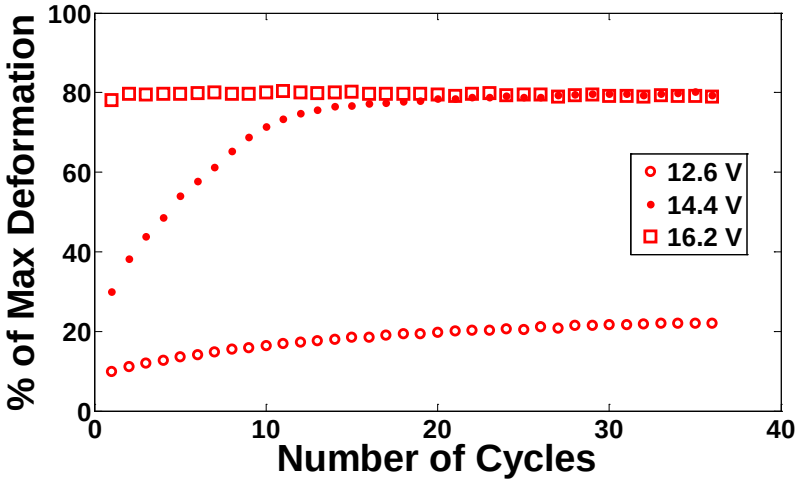

Figure 2.2.9: CC-BISMAC – percent of maximum deformation as a function of actuation cycles.

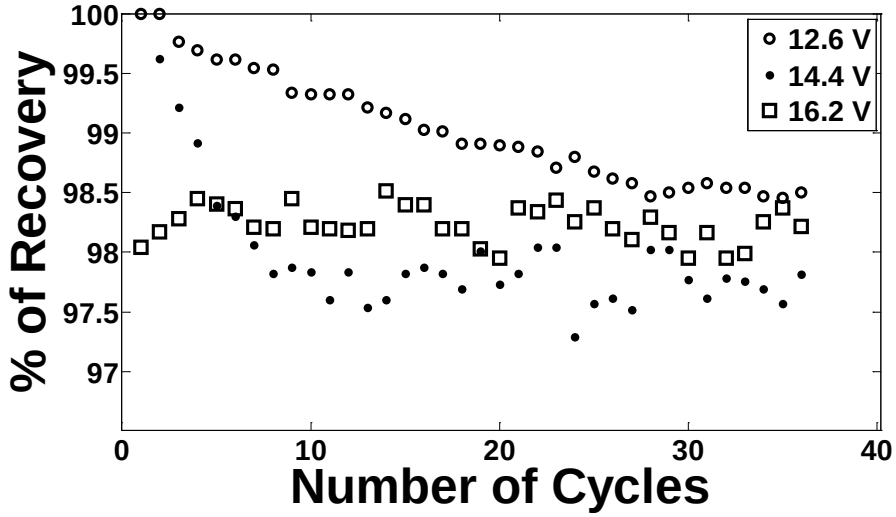

Figure 2.2.10: CC-BISMAC – percent of recovery as a function of actuation cycles.

Measurements for these figures were taken for three different voltage amplitudes at a frequency of 0.25 Hz and duty cycle of 20%. The percent of maximum deformation is based on the angle of rotation achieved by a point. The angle of rotation was compared to the maximum contraction recorded during the profile testing. Similarly, the percent recovery is based on the initial position of the actuator at the beginning of testing. As the number of actuation cycle increases, the maximum deformation eventually reaches equilibrium. This equilibrium is achieved at different percent deformation for applied voltages of 12.6 V and 14.4 V, but it was approximately the same for applied voltages of 14.4 V and 16.2 V. As the driving voltage amplitude is increased, the equilibrium was found to be achieved over fewer cycles. Higher driving voltage amplitudes and number of cycles also mean greater residual heat and consequently the actuator recovery was reduced. Similar to the percentage maximum deformation, the percent recovery also reaches equilibrium faster as the driving voltage amplitude increases. Residual heat helps the actuators reach higher deformation but causes hysteresis and delay in reaching the original position. If

duty cycle is increased than residual heat will become a more important constraint in the performance of the actuator since more time will be spent heating SMAs and less time in dissipation.

The equilibrium for maximum deformation and recovery reflects the fundamental behavior of SMA. On a temperature vs. strain plot it can be seen that SMAs achieve most of their deformation over a small temperature range (Tadesse et al., 2010). Once higher than this critical temperature range, additional deformation requires an exponential increase in temperature. The maximum deformation of 80% was achieved at the driving voltage amplitudes of 14.4 V and 16.2 V leading to the conclusion that critical temperature is reached during each cycle but heat dissipation is large enough that it restricts higher temperatures and thus the maximum contraction. At a specific frequency, the maximum deformation could be achieved by increasing the duty cycle or driving voltage amplitude. Recovery was also affected by the temperature dependent strain properties of SMA. About 1 to 3% loss in recovery was observed over time corresponding to the exponential decrease in temperature required for SMAs to regain their initial length. Furthermore, the voltage amplitude affects the contraction time and therefore the velocity at which the actuators deform. This results in a profile change as the actuator moves through the water. Figure 2.2.11(a)-(c) shows the path followed by each point on the beam during contraction and relaxation. The plots were recorded for the 25^{th} cycle of the CC-BISMAC.

A few observations can be made based on the BISMAC motion. The path followed by the actuator during contraction is different than during relaxation. The actuator contracts with a curved configuration. During relaxation the curvature decreases, and the actuator extends to follow an outer path. Also, the actuator builds up momentum during contraction and therefore

keeps bending after the SMA wires have stopped contracting. This causes an oscillation which can be observed in Fig. 2.2.11(c)-(d) through a loop occurring in the path. The contraction times for each case are listed in Table 2.2.3 along with the power consumed per cycle. Power was consumed only during the actuation period.

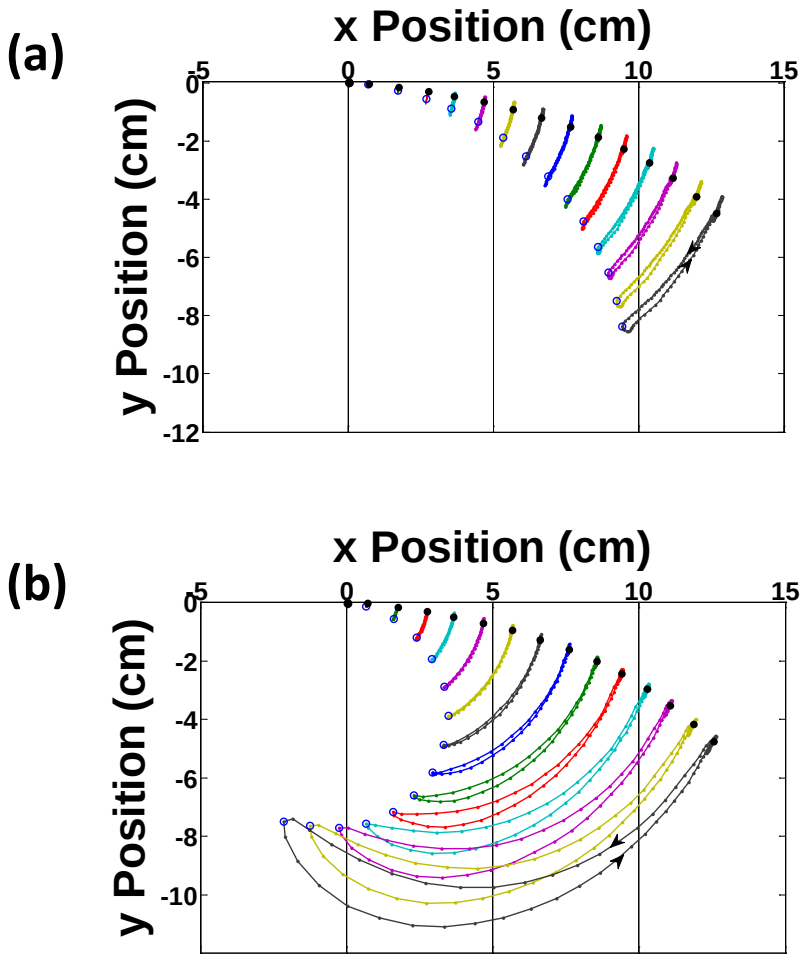

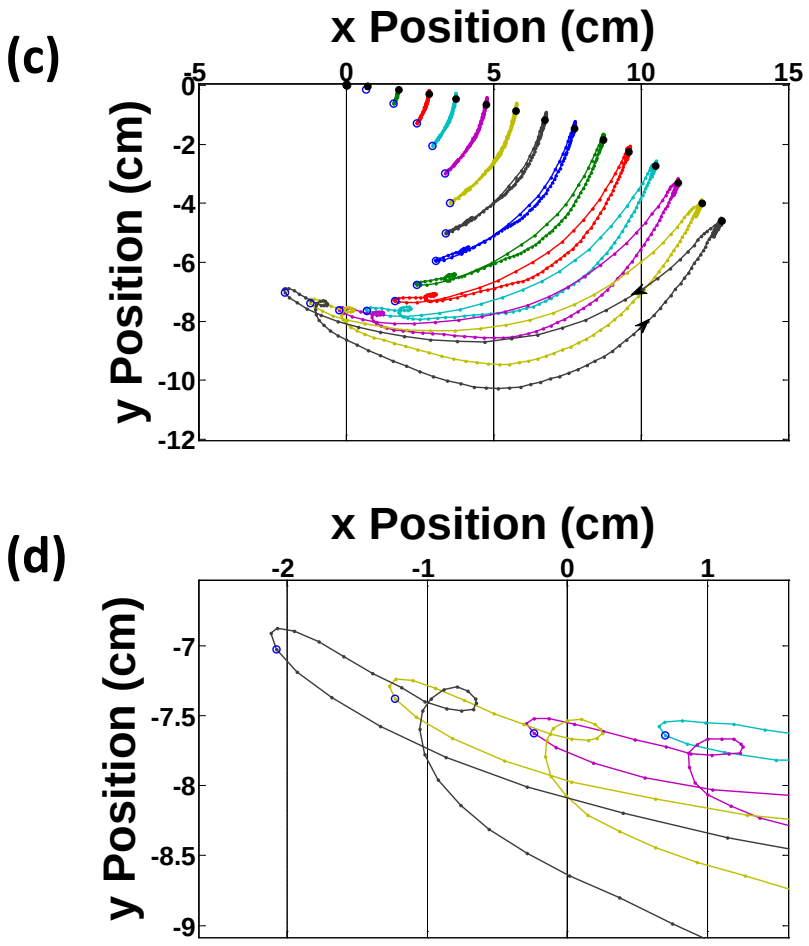

Figure 2.2.11: Path followed by CC-BISMAC during actuation of the 25th cycle for voltage amplitude of (a) 12.6 V, (b) 14.4 V, (c) 16.2 V. (d) Zoom of (c) demonstrating the loop occurring due to actuator momentum.

Table 2.2.3: Power consumption, contraction time, Joules per cycle and maximum deformation for the corresponding voltage amplitudes of the CC-BISMAC during the 25th cycle.

Voltage (V)	Current (A)	Power (W)	Contraction time (s)	Energy (J/cycle)	% of Max Deformation
12.6	0.775	9.8	0.77	7.5	20.4
14.4	0.875	12.6	0.83	10.5	78.8
16.2	0.975	15.8	0.50	7.9	79.6

As the voltage amplitude increases, the contraction time decreases. The results show that the amount of energy used per cycle can actually be decreased as the voltage amplitude was

increased. The power consumption at 16.2 V excitation was less than that at 14.4 V and a greater deformation was achieved. Current readings were taken in the fully transformed phase of the SMA where resistance magnitude was lower. Figure 2.2.12 demonstrates the CC-BIMSAC in the testing setup for both its relaxed and contracted configuration.

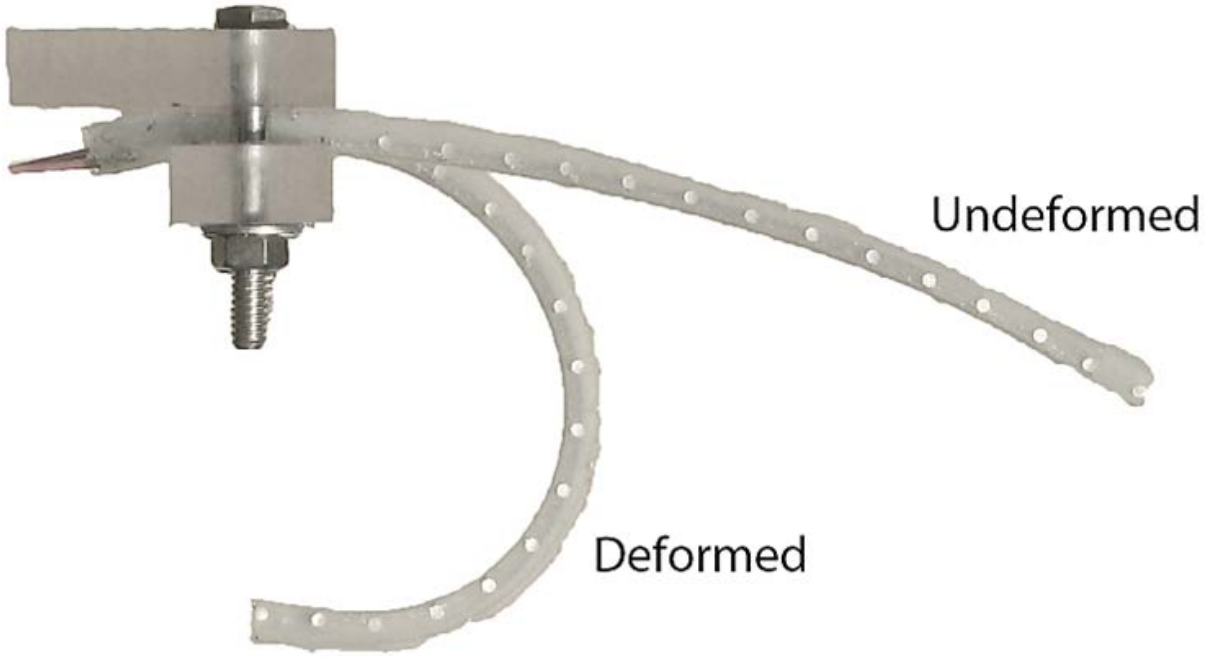

Figure 2.2.12: The CC-BISMAC is shown underwater in the undeformed and deformed configurations.

2.2.5 BISMAC Optimization

The VL-BISMAC was optimized to mimic the deformation profile of an *Aurelia aurita.* The bell subumbrella profile was chosen since it contains the actuators in the natural jellyfish. The particular profile chosen is shown in Fig. 2.1.2. The optimization method was developed by K. Joshi and is explained in Villanueva et. al (2010). The second moment of inertia of the beam was optimized to match the deformation profile of the *A. Aurelia*. The second moment of inertia was tailored by changing the amount of spring steel thickness in the VL-BISMAC. Adding strips

of spring steel of different thicknesses allows the tailoring of curvature. The resulting optimized BISMAC (AA-BISMAC) is shown in Fig. 2.2.13.

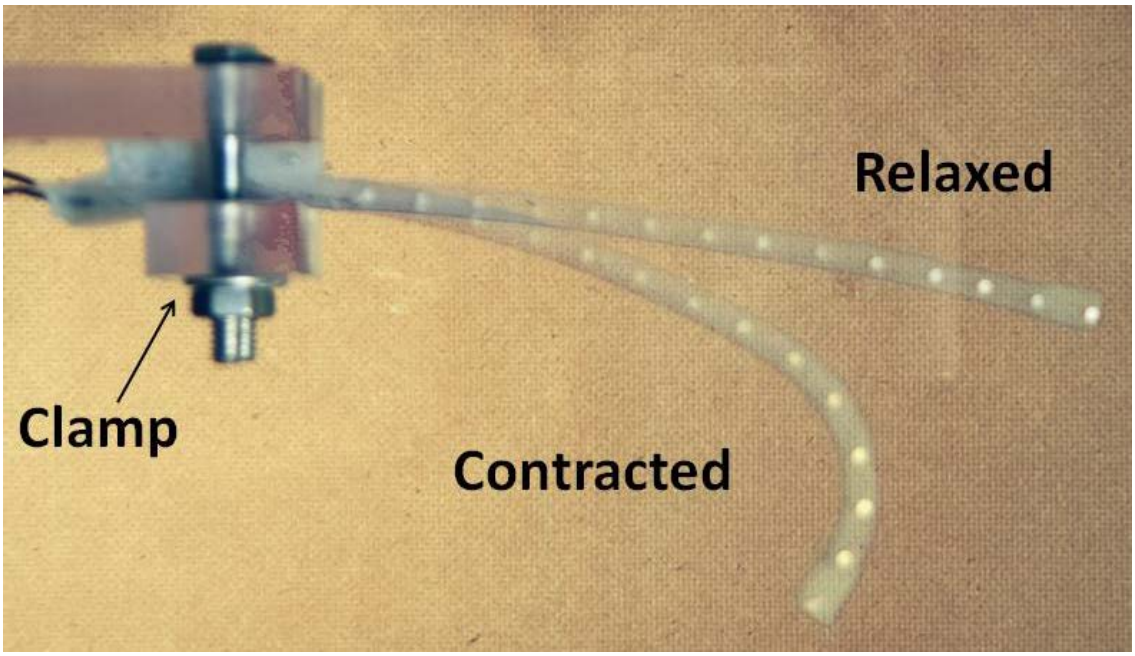

Figure 2.2.13: Picture of the AA-BISMAC in the relaxed and contracted configuration. Also shown is the clamping apparatus used during testing.

The results are compared to the actual jellyfish subumbrella profile in Fig. 2.2.14. It can be seen in Fig. 2.2.14(a) that the AA-BISMAC ends at a lower position then the jellyfish profile. The curvature comparison in Fig. 2.2.14(b) shows a strong match starting at 10 cm. The first 2.5 cm starting at the root of the radius of curvature plot shows a large discrepancy and an unexpected behavior. The reason for such a curvature difference in the first is related to the profile plot used for the jellyfish. The bell shape profile was replicated by inspection which led to some discrepancy. This is magnified in the curvature plot. Curvature should be approximately zero for that region. After 3.5 cm, the AA-BISMAC radius of curvature is less than the jellyfish's. This explains why the AA-BISMAC terminates at a different location then the jellyfish profile.

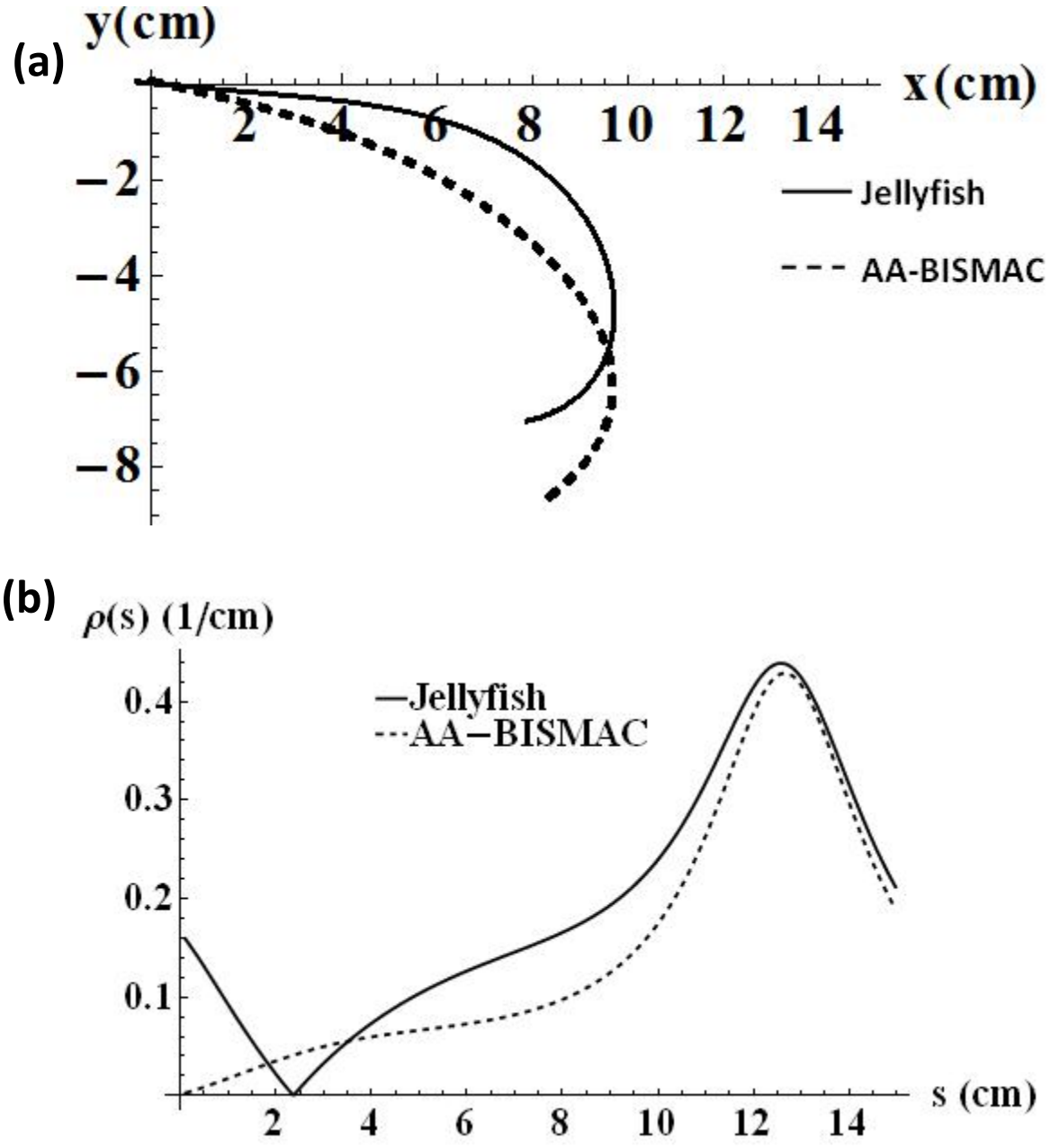

Figure 2.2.14: Comparison of the (a) deformed profile and (c) curvature between the *A. aurita* and AA-BISMAC. This figure was developed by K. Joshi in Villanueva et. al (2010).

2.3 FlexLegs – Flexible Legs Actuated by Shape Memory Alloy

In order to extend the range of application for the BISMAC we designed a new configuration to achieve bidirectional deformation. This is not required for jellyfish robotics but would enable the design of variety of walking and crawling organisms. BISMAC actuators are unidirectional flexible actuators capable of exhibiting high curvature. The new bidirectional actuators termed as “BiFlex” actuators, have the capability to achieve large deformation in two directions. The FlexLegs consist of six segments which can be actuated individually. Two different sets of legs were constructed to determine the effect of size. Biped designs usually are inspired by human morphology and are larger in dimension (Ogura et al. 2005; Scarfogliero et al., 2004). These designs offer good maneuverability and adaptability as we know it but are highly complex in their control and stability. Birds are also bipeds but have a much simpler walking algorithm (Hugel et al., 2011). Multiple leg designs often inspired by insects are more stable and offer a better alternative to wheels for rough terrains (Nelson et al., 1997; Flannigan et al., 1998; Delcomyn et al., 2000; Saranli et al., 2001). These designs are usually bulky and offer more ground agility than an autonomous vehicle would usually require before taking flight.

Flexible actuators alleviate the need for gears, joints, bearings, shafts and other cumbersome features found in conventional mechanical designs. This is one of the main reasons why flexible actuators are often used in biomimetic robotic designs. There exist various types of flexible actuators, in some cases, also referred as artificial muscles. These include pneumatic (Daerden and Lefeber, 2002), polyvinylidene fluoride (Kornbluh et al., 2000), microfiber composite, ionic polymer metal composites (Maden et al., 2004; Akle et al., 2006) and shape memory alloy (Kornbluh et al., 1998). See Tadesse et. al (2009) for a survey of the different artificial muscles and their characteristics. The main advantage of SMA based flexible actuator

over other technologies is their high power density and large force capability. This allows the design of low profile mechanisms which are problematic with conventional actuators. Work done on small biomimetic aircrafts show the importance of small, lightweight components onboard the vehicles (Fearinget al., 2000; Tanaka et al., 2005; Madangopal et al., 2005; Bunget et al., 2008) and illustrate the potential of flexible actuators. Autonomous flying vehicles must be able to land from flight, maneuver on ground and takeoff. Their landing gear must therefore be versatile while keeping mass to a minimum. Some jumping techniques have been proposed for small flying vehicles which simplifies the displacement method (Birch et al., 2000; Lakasanacharoen et al., 2000; Li et al., 2009). These techniques are used by some insects to overcome obstacles but it provides limited maneuverability. Birds use their two legs to jump, walk, and land. This provides the best options for a medium scale autonomous vehicle and was selected in our design. The development of Flexible Legs (FlexLegs) will provide the opportunities for developing new dexterous robots designs and allow us to study the physiological and neurological behavior biped animals. In order for the FlexLegs to achieve the different biped gates, considerable bending deformation in two opposite directions is required. BISMAC actuators were adapted to achieve this bidirectional deformation as described in the next section.

2.3.1 Bidirectional Actuators

2.3.1.1 Design of Bidirectional BISMAC Actuators

Unidirectional BISMACs were modified to become bidirectional by adding SMA wires on the other side of the actuator. This dual arrangement of SMA wires allowed bidirectional motion by contracting one side or the other as shown in Fig. 2.3.1. The initial concern with this bidirectional BISMAC was the resistance in tension of the SMA wire on the side opposing

actuation. This method was tested with the same parameters (mold, material, dimensions) as for the single sided BISMAC (Villanueva et al., 2010a). The thickness was 9.6 mm as opposed to 5.4mm for the single sided BISMAC due to extra material for the added side. The actuator in Fig. 2.3.1 produced a deformation of -24 % and 35 % in the x-direction and 5 % and 13 % in the y-direction respectively for both directions using a driving current of 0.65 A.

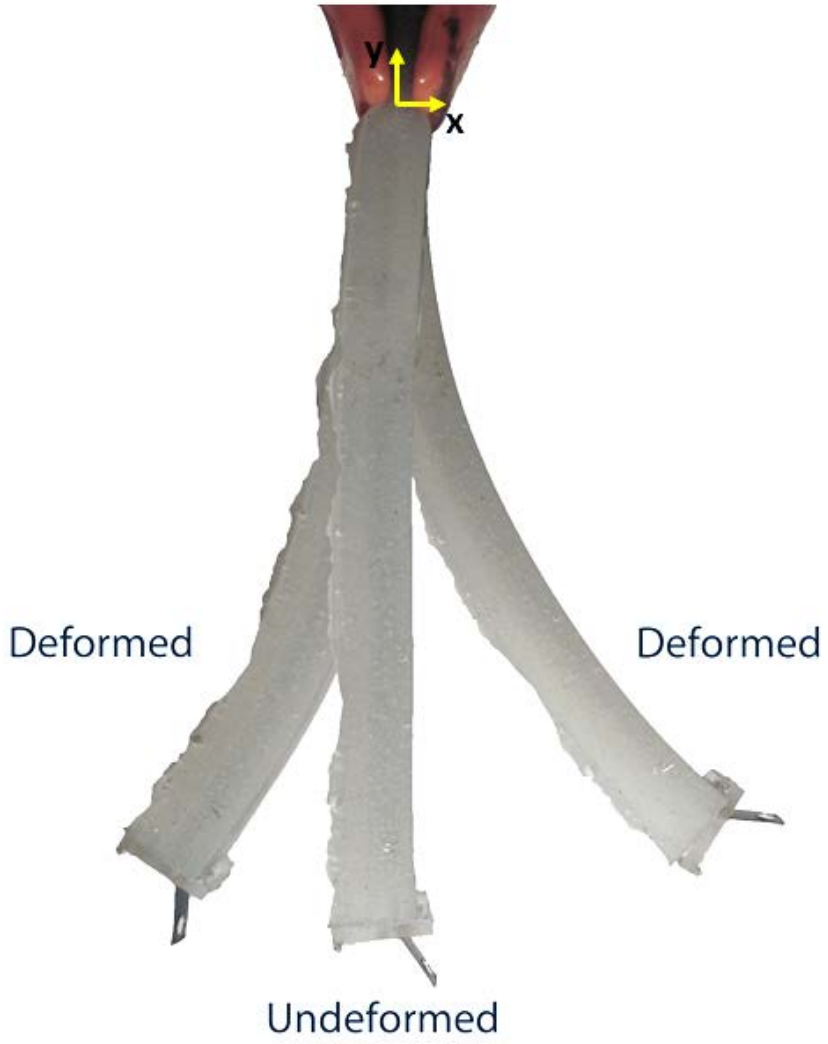

Figure 2.3.1: Top view of a Bidirectional BISMAC in the undeformed and deformed positions. The different profiles are overlaid for comparison. This BISMAC was operated in air and was clamped at one end allowing is to deform in the horizontal plane (gravity going through the figure).

These results show that BISMAC actuators can be transformed into bidirectional actuators. The super elastic property of SMA allows the wires in tension to stretch when the structure bends on the opposite side. This prototype has structural advantages due to silicone that adds compression stability along the axial direction. The main drawback of silicone is that it resists deformation and thus demands more force for the SMA wires to undergo complete contraction. Silicone also increases the power consumption of the actuators due to its higher dissipation rate. For this study, it was desired to maximize deformation and minimize power consumption and thus BISMAC design was modified to accommodate these requirements.

2.3.1.2 BiFlex Actuators

The design of BiFlex (bidirectional flexible) actuators is similar to the bidirectional BISMAC design. The main difference is that silicone is removed and instead, plastic guides keep the SMA wires in contact with the spring steel. The plastic guides consist of a central slit for the spring steel and holes for the SMA wires. The double sided SMA guides (Fig. 2.3.2(a)) were placed along the spring steel as shown in Fig. 2.3.2(b). The guides allow BISMACs to function without the need of silicone. A total of two SMA wires are used for each leg. The two wires originate at the terminal end of the leg, pass through the guides along the length and then through a hole in the spring steel, see Fig. 2.3.2(b). The wires are then passed on the opposite side through the guides and are crimped at the terminal end of the beam to create a second terminal. Two wires are used for strength and are kept separately for a better cooling rate. Passing the wires through spring steel tip creates a point of electrical conduction. This electrical connection is used as ground for the individual sides of the BiFlex which further reduces the number of electrical terminals required on each segment from eight to four.

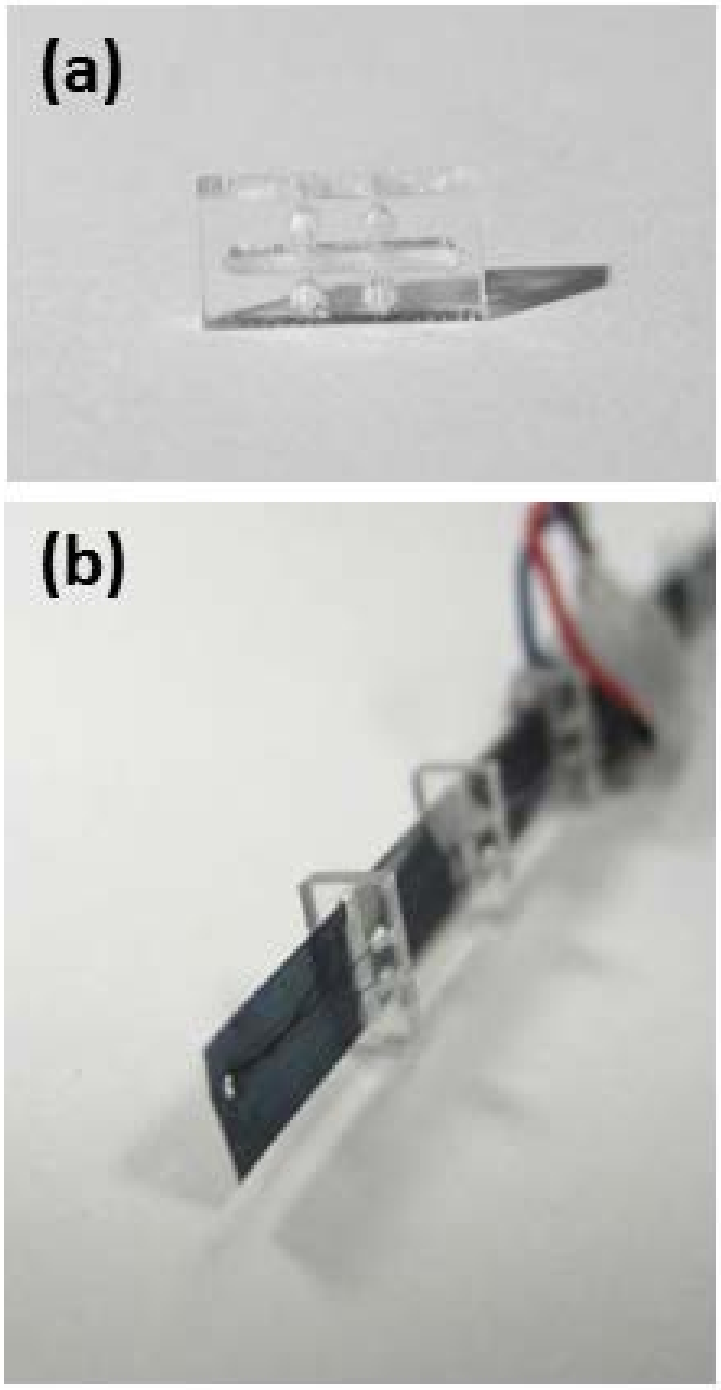

Figure 2.3.2: (a) Double sided SMA wire guide, (b) BiFlex actuator showing SMA guides and SMA wire passing through the spring steel via a hole at the tip of the actuator.

Figure 2.3.3 demonstrates the curvature results for a BiFlex of 94 mm from the first guide to the tip hole. The BiFlex was able to deform -47 % and 58 % in the x-direction and 30 % and 30 % in the y-direction for both directions respectively using a current of 0.4 A. The same coordinate system as in Fig. 2.3.2 is used. Guide density along the actuator affects deformation. Increasing the number of guides increases the deformation by keeping the SMA close to spring steel. Previously, the effect of distance between the SMA wires and spring steel has been modeled and experimentally quantified (Villanueva et al., 2010a; Villanueva et al., 2010b; Smith et al., 2011). A larger guide density tends to produce a more even curvature, however too many guides increase the stiffness of beam and reduce the deformation. The guides also create an area of added stiffness around the bonding location on the spring steel. Combinations of higher and lower guide density were tested experimentally and it was found that one guide per 1.25 cm provided an adequate deformation magnitude and constant deformation throughout the length. The BiFlex were actuated from one side to another at approximately 0.5 Hz. At higher frequencies, the relaxing actuator does not enough time to cool and stretch while the opposite actuator contracts. This causes snapping effect in the structure which comes from the buckling of the spring steel.

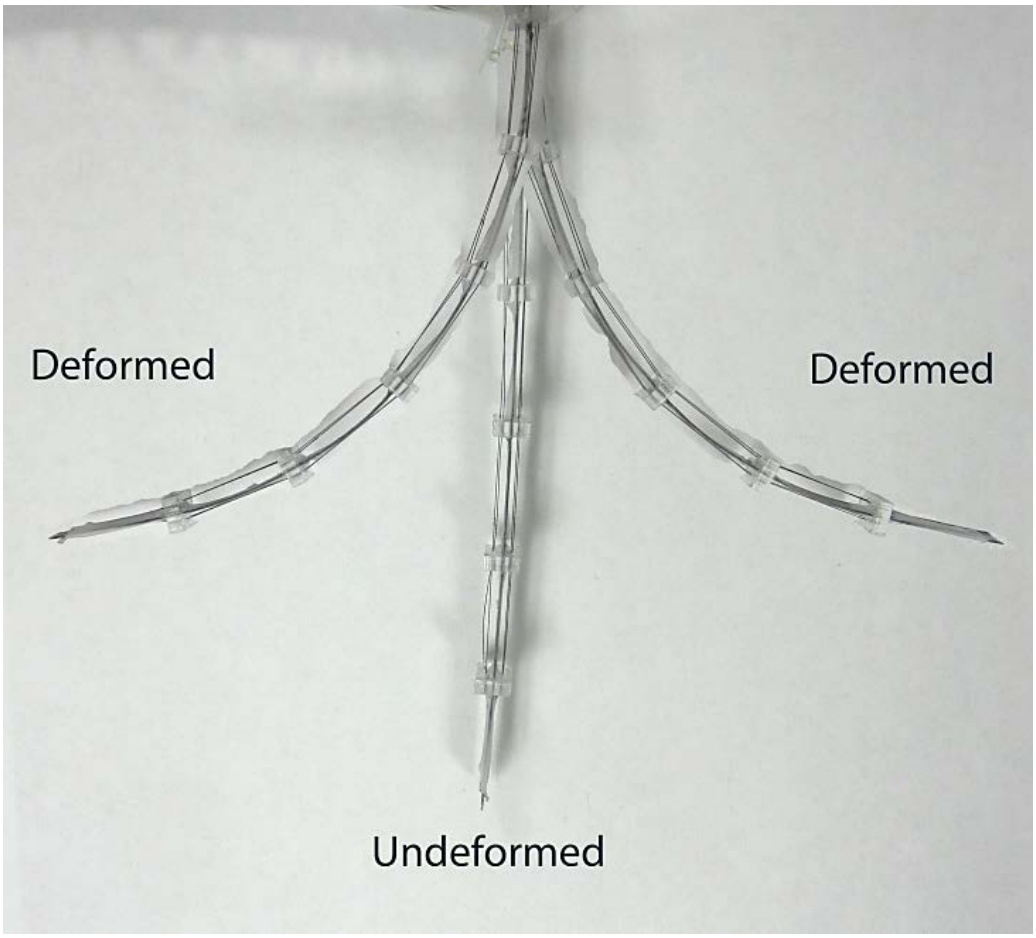

Figure 2.3.3: BiFlex, 94 mm in height with double sided guides and 2 SMA wires grounded on spring steel. (a) undeformed, (b) and (c) deformed on each side.

2.3.2 Flexlegs

Two different versions of legs were fabricated using the BiFlex design. The first version was large scale which measured a total of 97.4 mm in height and 165.4 mm in width. The second version of legs was smaller with a total height of 35.8 mm and width of 63.2 mm.

2.3.2.1 Manufacturing

The FlexLegs were built using the same process as followed for the BiFlex actuators. Each vertical segment (leg) and the horizontal segment (hip) consist of a single strip of spring steel. Each leg is split into two segments for a total of 6 segments which can all be actuated

individually. Each segment is double sided and act as positive terminal while the spring steel pieces are attached to each other so they are electrically connected and act as the ground terminal. The single wire then connects to the spring steel structure for a total of 13 wires. Each electrical terminal and spring steel had to be properly insulated to prevent electrical shorts. Figure 2.3.4 shows the small FlexLegs and the nomenclature used for the rest of the analysis. The dimensions in Fig. 2.3.4 do not take include the excess material which does not contribute to the mechanics. The FlexLegs have plastic guides which measure 7.7 mm in width, 1.7 mm in thickness and 4 mm in height. For the small FlexLegs, the guides are separated by 4.5 mm on the leg segments and 9 mm on the hip segments. For the large FlexLegs, the guides are separated by 14.3 mm on the leg segments and 12 mm on the hip segments.

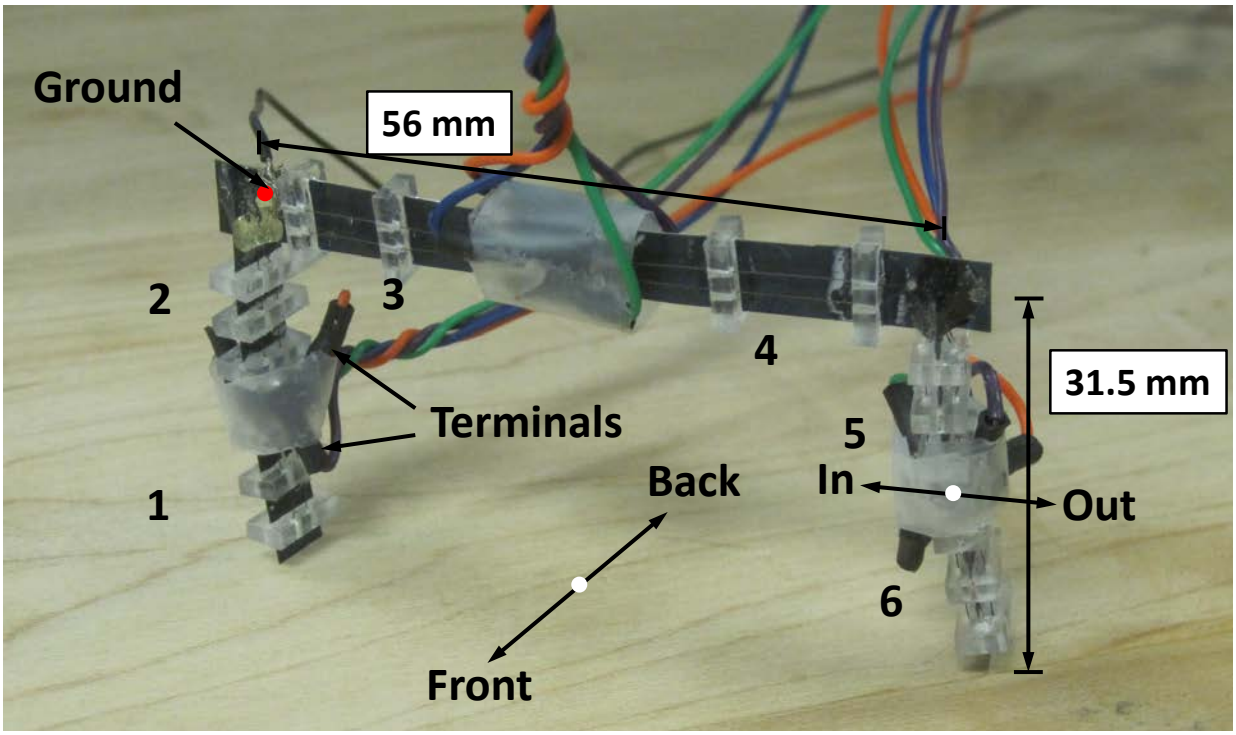

Figure 2.3.4: Small FlexLegs showing dimensions, segment labels (1-6), front/back and in/out directions. The width was measured where the two legs are connected to the hips and height was measured from the mid hip to the tip of the leg.

2.3.2.2 Deformation

Maximum deformation was tested for both sets of legs by driving the SMA using a power supply (HP 6632b). Deformation was recorded using high speed camera and then analyzed using image processing. Images were taken of the legs perpendicular to the plan of deformation and then digitized using ImageJ. Deformation was normalized by the respective leg or hip length. Segments were tested individually first and then in combination for the required walking action. Figure 2.3.5 shows the test setup used for measuring deformation.

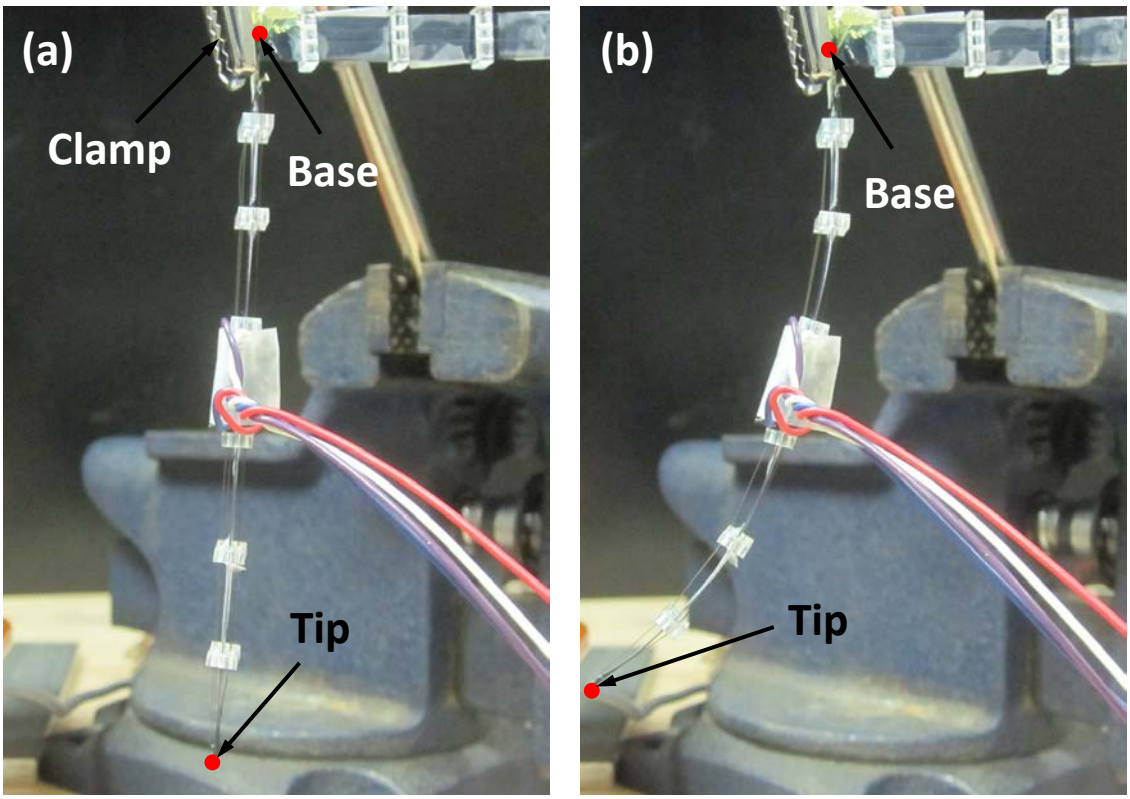

Figure 2.3.5: Large leg deformation of segment 5 out and 6 out. (a) undeformed, and (b) deformed.

FlexLegs were clamped directly above the leg that was being tested. The wires were held away from the moving parts while keeping enough looseness so that they would not create

tension on the legs. Hip deformation was tested by using the same clamping location. Deformation was measured at the tip of the leg or hip as shown in Fig. 2.3.5. All the measurements were taken relative to the base. Deformation results are shown in Tables 2.3.1 and 2.3.2 for the large and small FlexLegs respectively.

Table 2.3.1: Small FlexLegs test results for individual segments.

Segments	Deformation		Force (N)	Power (mW)
	x %	y %		
5 out	4	1	0.022	352
6 out	4	1	0.007	299
6 in	-4	2	N/A	330
5 out, 6 in	1	0	0.004	750
5 out, 6 out	10	2	0.023	767
3 Front	8	1	0.020	322
4 Front	8	2	0.008	363
4 Back	-12	3	N/A	392
3 Front, 4 Back	-6	3	N/A	754
3 Front, 4 Front	12	4	0.021	708

Table 2.3.2: Large FlexLegs test results for individual segments.

Segments	Deformation		Force (N)	Power (mW)
	x %	y %		
5 out	20	3	0.029	685

6 out	16	7	0.017	636
6 in	-21	7	N/A	667
5 out, 6 in	-8	1	N/A	1771
5 out, 6 out	29	9	0.045	1762
3 Front	50	22	0.021	1806
4 Front	14	9	0.018	1785
4 Back	-12	8	N/A	1771
3 Back, 4 Front	34	11	0.011	3059
3 Front, 4 Front	57	39	0.035	3035

Deformation results clearly show that the large legs had much better deformation as compared to that of small legs. It is important to note that the deformations have been normalized by respective leg or hip length. The largest deformation was 57 % and 39 % in the x- and y-direction respectively achieved by segments 4 and 3 when actuated in the same direction. The largest deformation corresponds to the longest segment tested. The net deformation measured at the tip for the case of 5 out, 6 in, actually canceled itself. Figure 2.3.7 demonstrates this phenomenon. This cancelation effect is due to that fact that both segments are not deforming the same amount and since they are connected to each other, the deformation of segment 5 orients that of segment 6. Segment 5 did not deform as much as segment 6 which could be due to added weight from segment 6. It should be noted that even though segment 5-out and 6-in have similar deformation magnitude, segment 5 deformation is amplified by a lever arm since deformation is measured at the leg tip. The hips (3-front, 4-back) did not have such cancelation in deformation. In case, where both sides of leg were tested such as 3-front and back, and 6-in and out, deformation is similar for both sides. There is some discrepancy between each side

which mainly comes from manufacturing. The wires created significant resistance to deformation due to stiffness and weight.

The difference in deformation between the small and large legs comes from the fact that the guides were not scaled with the rest of the structure. The distance between the SMA wire and spring steel is critical. The guides are responsible for keeping that distance to a minimum. When scaling the legs, the guide dimensions were not changed. This result in same radius of curvature applied over a shorter distance, thus a smaller net deformation. To replicate the deformation of the large legs, the guides would have to be made smaller keeping the SMA closer to the spring steel.

2.3.2.3 Walking Schemes

Different walking schemes can be achieved by actuating different segments in sequence, see Fig. 2.3.6. Stepping requires segments 3 and 4 (hips) to be actuated in opposite directions (one front and one back) in cyclic motion, see Fig. 2.3.6(c-d). Yawing requires segments 3 and 4 to be actuated in the same direction (front/front or back/back), see Fig. 2.3.6(a). The crabbing motion requires segments 1, 6 in and 2, 5 out to be actuated followed by the reverse cycle, see Fig. 2.3.6(e-f).

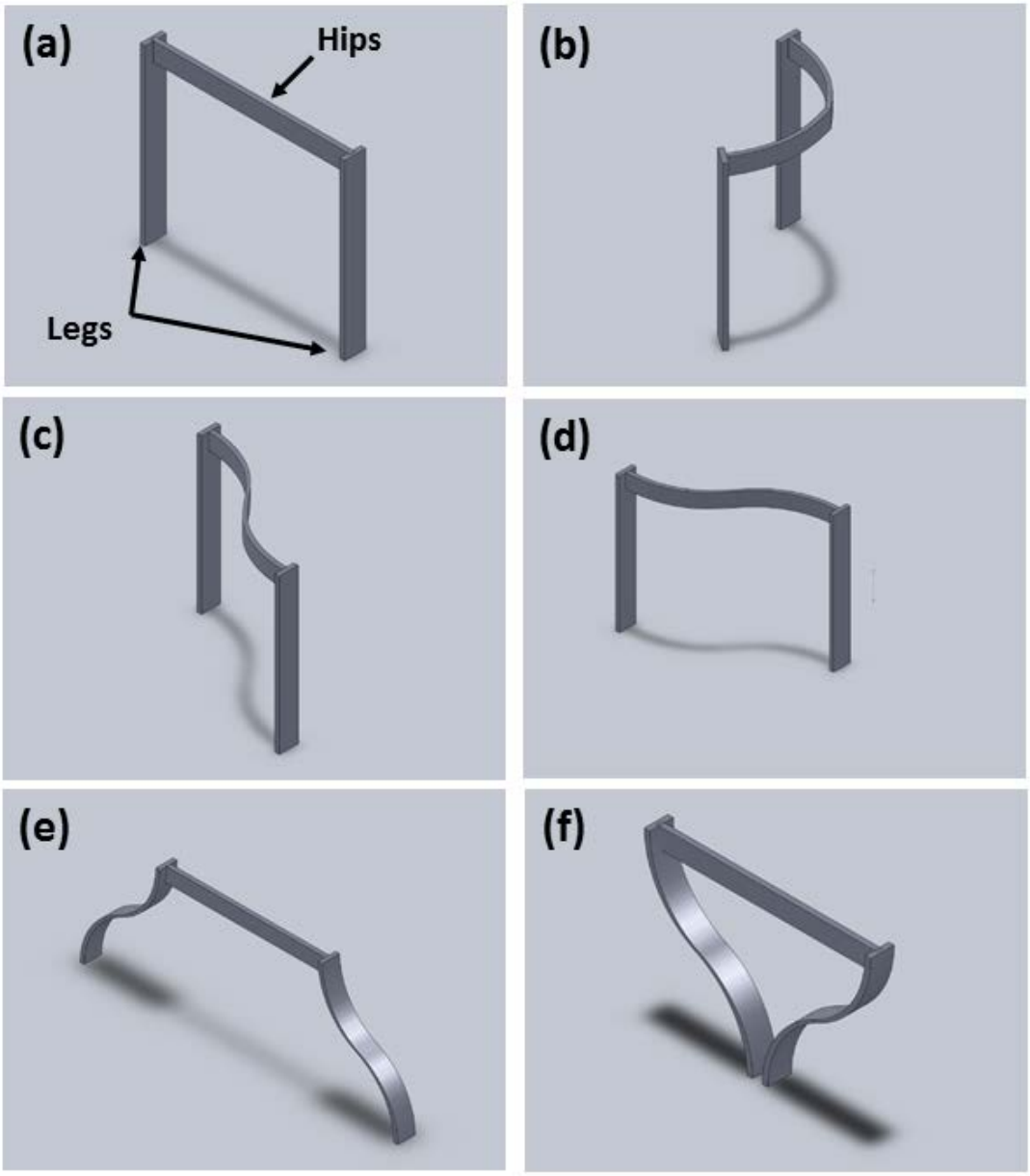

Figure 2.3.6: CAD drawings of the FlexLegs in the various walking schemes. Undeformed (a), turning (b), stepping (c) and (d), crabbing (e) and (f).

The stepping, yawing and crabbing sequences are shown for the small FlexLegs in Fig. 2.3.8 – 10. These figures show that the actuators are able to deform in both directions to provide the sequences required for walking. For comparison, Fig. 2.3.11 shows the stepping sequence for

the large FlexLegs. The large FlexLegs had better displacement as reported in Table 2.3.2 but curvature was about the same as for the small FlexLegs since they use the same guides and spring steel. In some cases, the segments had a non-constant curvature throughout their lengths. This is seen in Fig. 2.3.9 (c) where segment 4 does not achieve an even curvature. This could be due to excess initial tension in the SMA causing the segment to have a pre-deformation which opposes curvature. Other possible factors are a pre-deformation due to spring steel shape or the guides' orientation.

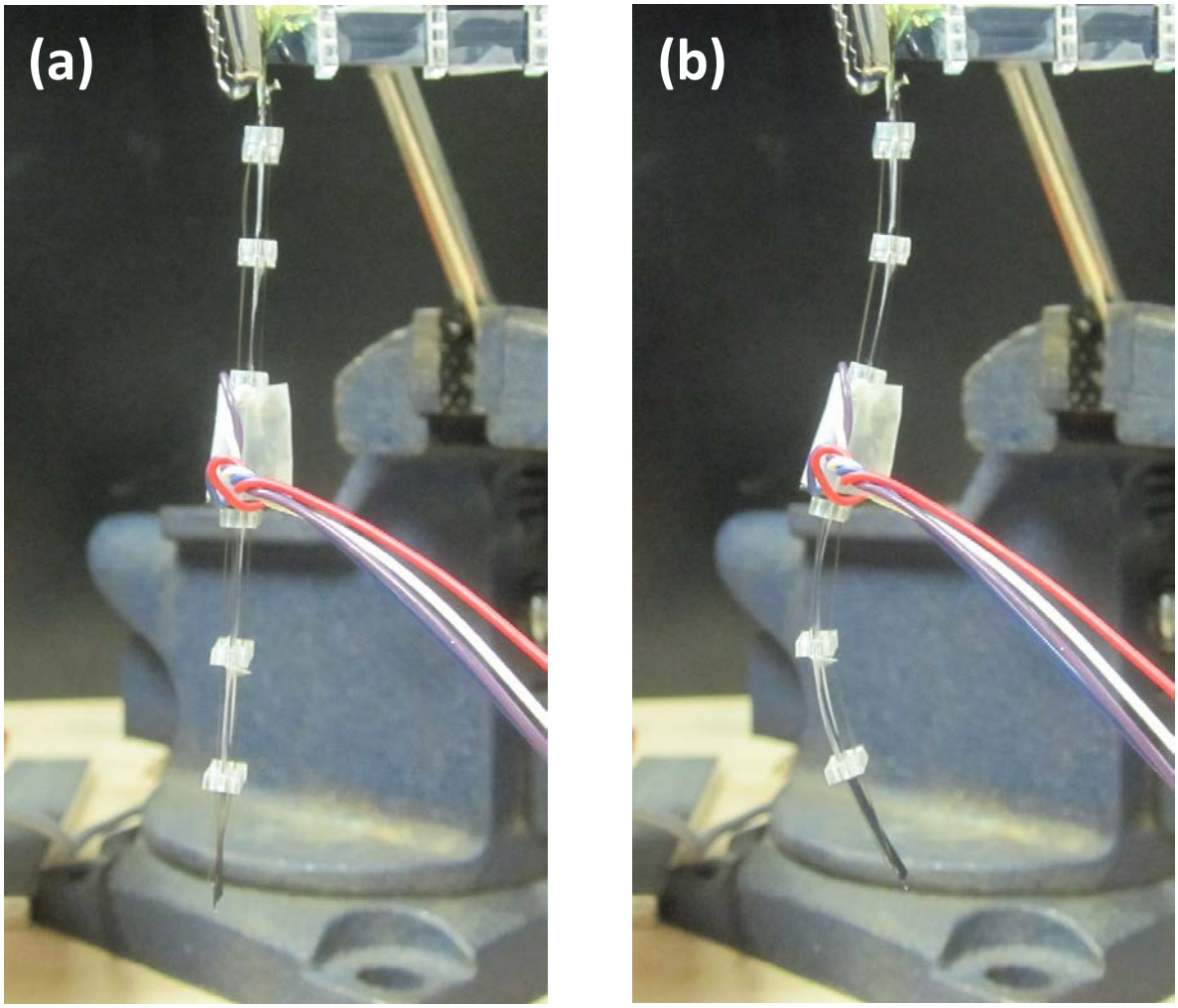

Figure 2.3.7: Large leg deformation showing s-shape deformation for the crabbing sequence, (a) undeformed, and (b) deformed (segments 5 out and 6 in).

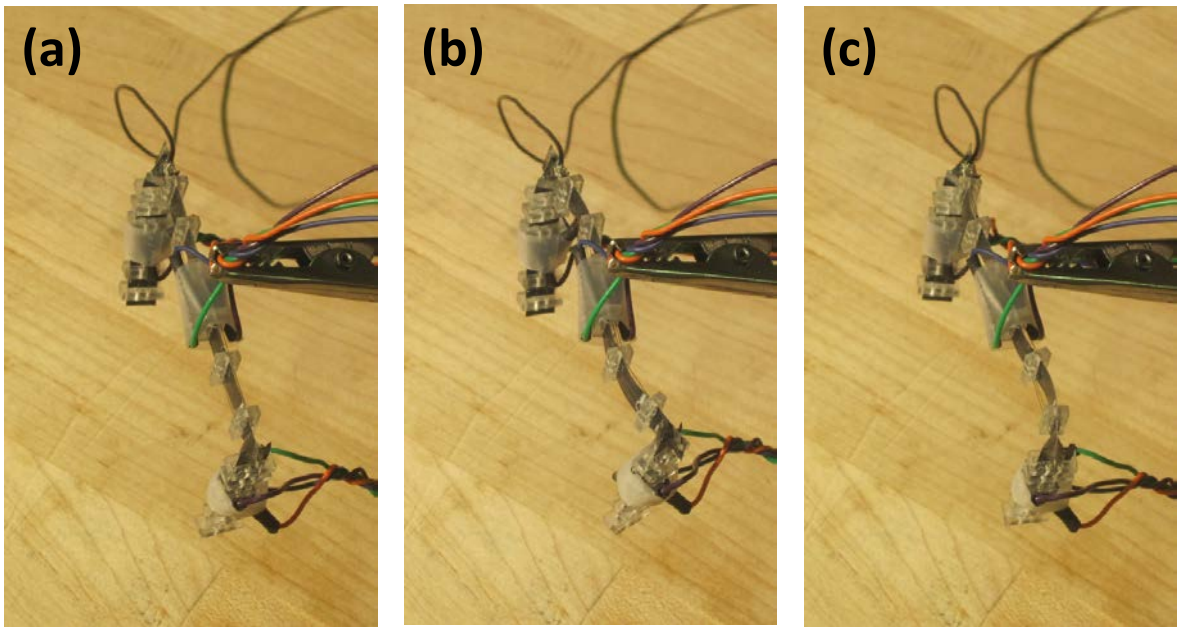

Figure 2.3.8: Small FlexLegs demonstrating stepping sequence. (a) undeformed, (b) segments 3 front and 4 back actuated, (c) segments 3 back and 4 front actuated.

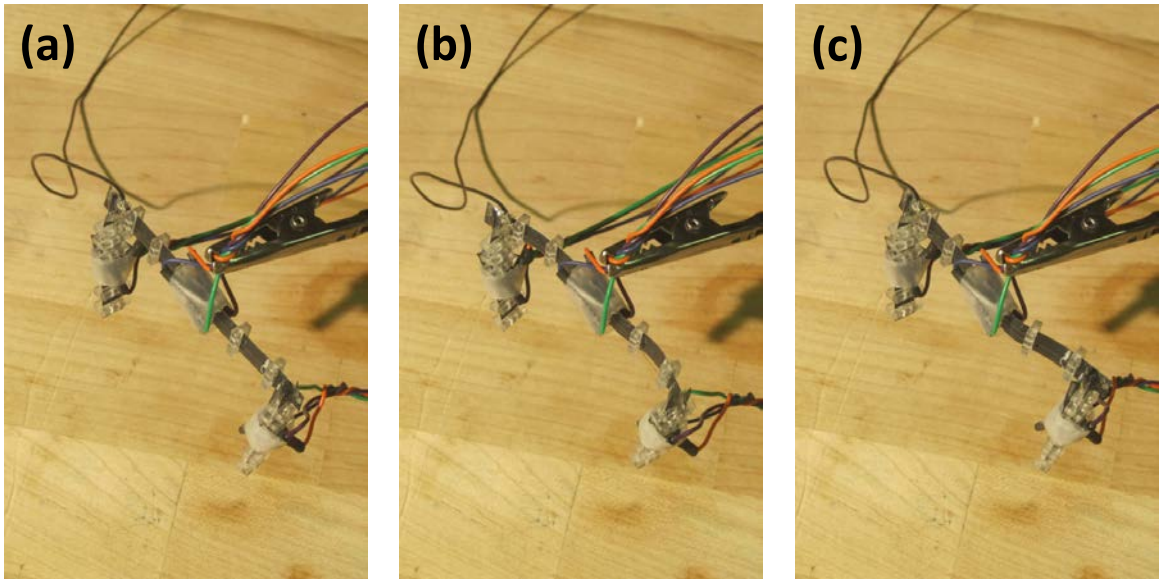

Figure 2.3.9: Small FlexLegs demonstrating yawing sequence. (a) undeformed, (b) segments 3 front and 4 front actuated, (c) segments 3 back and 4 back actuated.

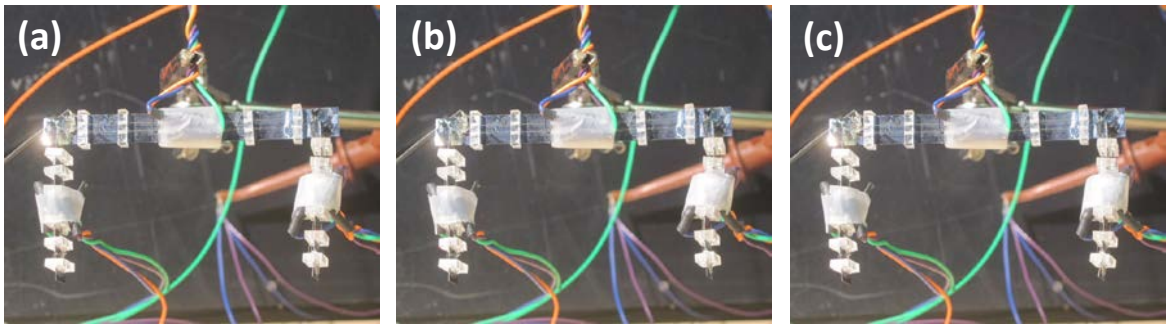

Figure 2.3.10: Small FlexLegs demonstrating crabbing sequence. (a) undeformed, (b) segments 1 out, 2 in, 5 in and 6 out actuated, (c) segments 1 in, 2 out, 5 out and 6 in actuated.

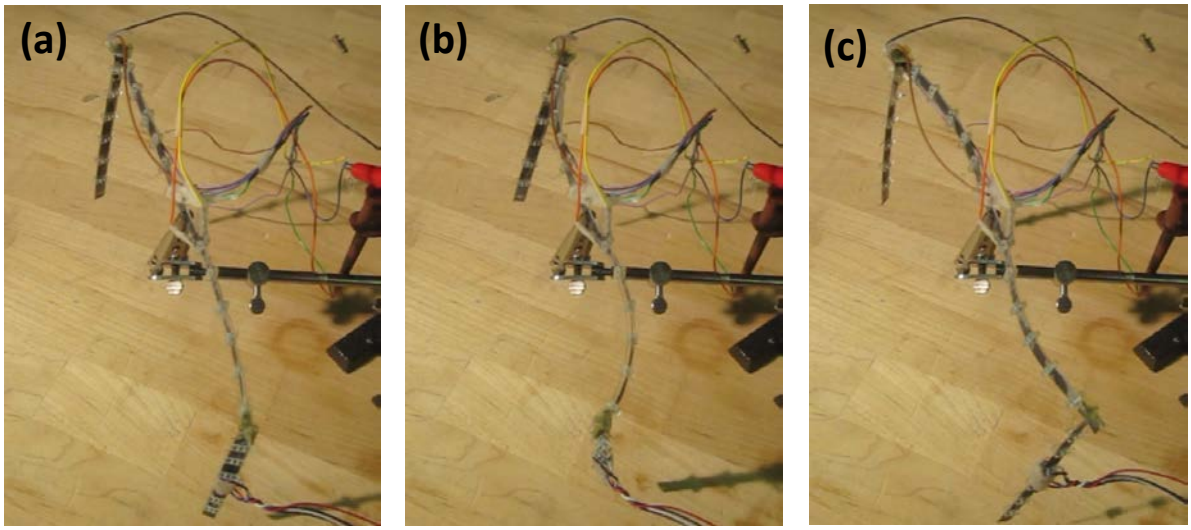

Figure 2.3.11: Large FlexLegs demonstrating stepping sequence. (a) undeformed, (b) segments 1 out, 2 in, 5 in and 6 out actuated, (c) segments 1 in, 2 out, 5 out and 6 in actuated.

2.3.3 Force, Moment, and Power Consumption

Force measurements were made using a 10 g load cell (Transducer Techniques – GSO 10). The FlexLegs applied load on the sensor parallel to the direction of deformation. The initial distance between the leg and sensor was kept less than a millimeter. Previous BISMAC studies

have shown that the actuator is strongest at zero deformation (Smith et al. 2010). The FlexLegs were clamped in a similar way as for deformation testing, see Fig. 2.3.12 for the test setup.

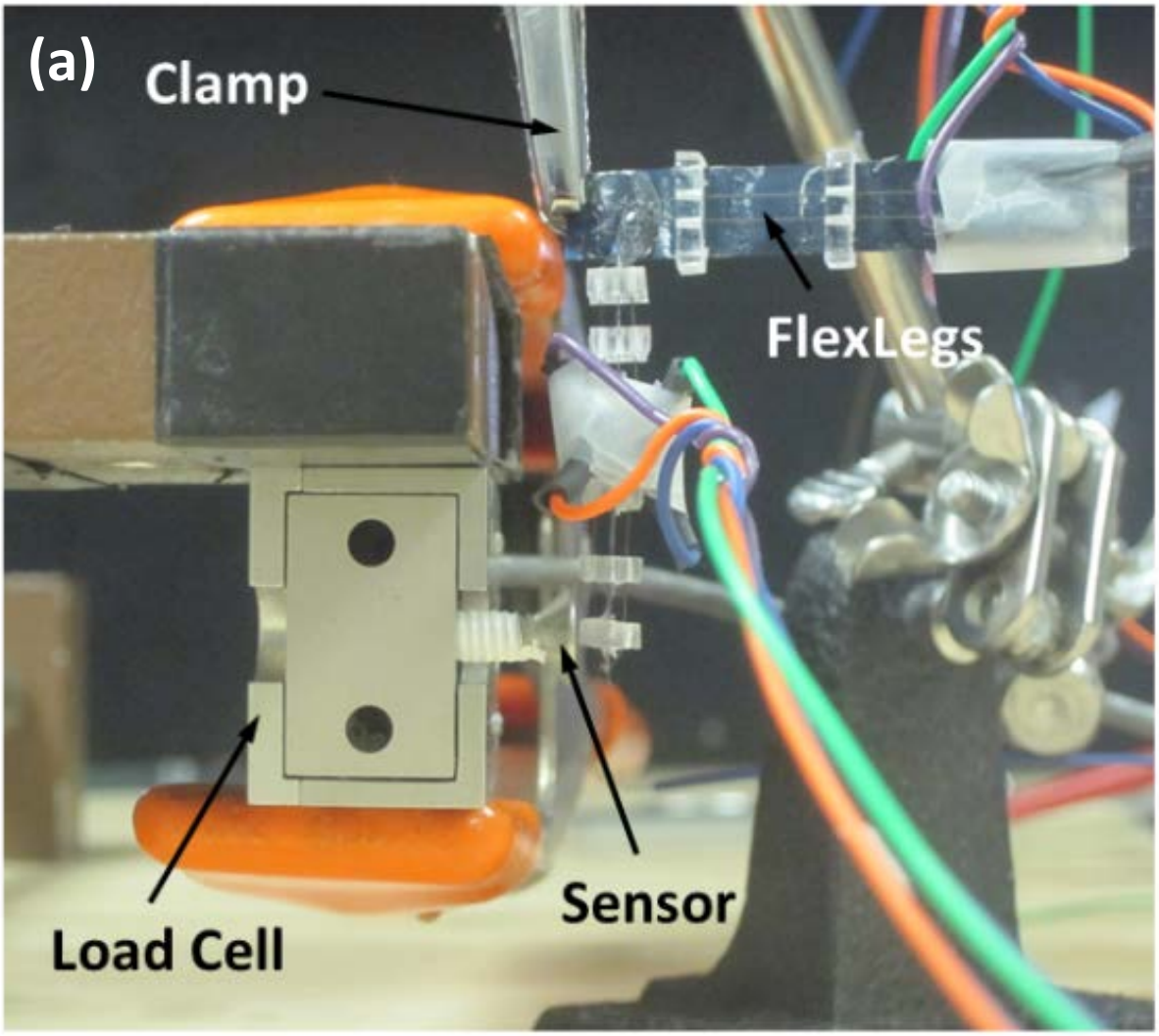

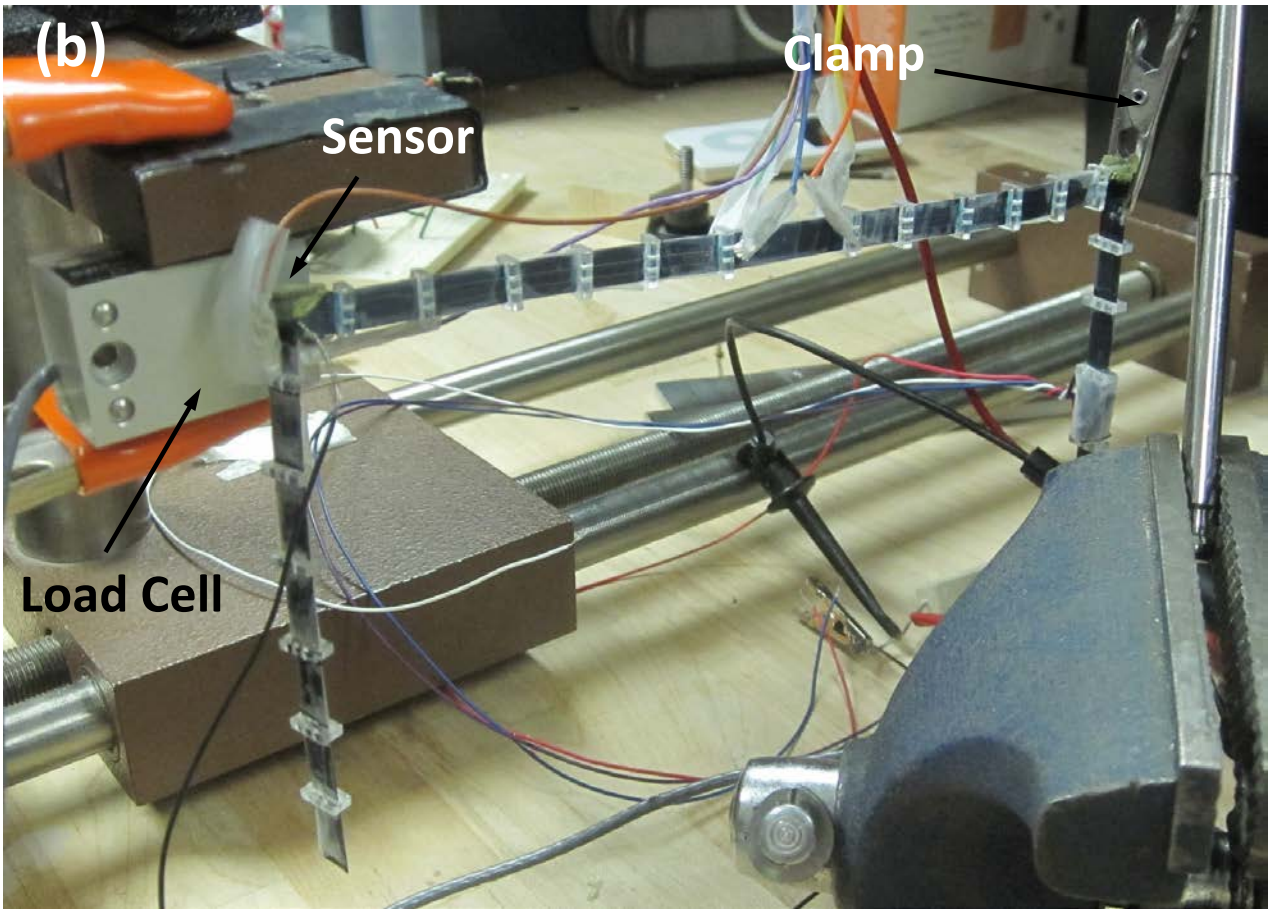

Figure 2.3.12: (a) Force test setup showing small FlexLegs pre-actuation for force measurement, and (b) Force test setup showing Large FlexLegs pre-actuation for hip force measurements.

Force results for both FlexLegs are shown in Table 2.3.1 and 2.3.2. Force was not recorded for the situations where the legs would move in the negative x-direction which is opposite to that of sensor location. The results for those cases are filled with N/A (not applicable). The small FlexLegs achieved a maximum force of 0.023 N when segment 5 and 6 were actuated in the same direction. The large FlexLegs achieved a maximum force of 0.045 N when segment 5 and 6 were actuated in the same direction. When segments 5 and 6 or 3 and 4 were actuated in opposite direction (s-shape), less load or no load was applied on the cell. When segments 6-in or 3-forward are actuated, they deform and force is produced in the opposite direction of the sensor.

The maximum tip force was achieved by segments 5 and 6-out with 0.023 N and 0.045 N for the s mall and large FlexLegs respectively. The maximum moment achieved by the hip was 1.17e-3 N-m and 5.68e-3 N-m for the small and large FlexLegs respectively. The legs were allowed to deform which means some of the force was lost in deforming the structure. Also, the legs created force in both the x- and y-directions due to curvature but was only recorded in one the y-direction. This mainly affects cases where deformation was large such as for the 3-front and 4-front case. Force is a function of number of SMA wires. Therefore, the FlexLegs could be made stronger by adding more SMA wires or using greater diameter wires. The disadvantage is that more power will be required for actuation. With systems such as BISMACs or FlexLegs, it is difficult to determine if the force is limited by deformation or by the maximum force available (Smith et al. 2011).

Power consumption was recorded during actuation and is listed in Tables 2.3.1 and 2.3.2. For each case, voltage was set constant and current was allowed to vary. Power was found by measuring current and voltage in the circuit when legs were at maximum deformation. With these results we can see that the power for small FlexLegs to achieve stepping and yawing is 760 mW and 731 mW for crabbing. The large FlexLegs needed 1766 mW for stepping and yawing, and 3047 mW for crabbing. The small legs used 50 to 80 % less power than the large FlexLegs.

The legs were also tested to see how much load they could support. Weight was applied to the structure on the hip segment as evenly as possible, see Fig. 2.3.13. The FlexLegs were tested with only the legs clamped down representing the legs gripping the surface. They were also tested with supports (pin roller) at both side of the hip to increase stability and prevented the structure from falling side to side.

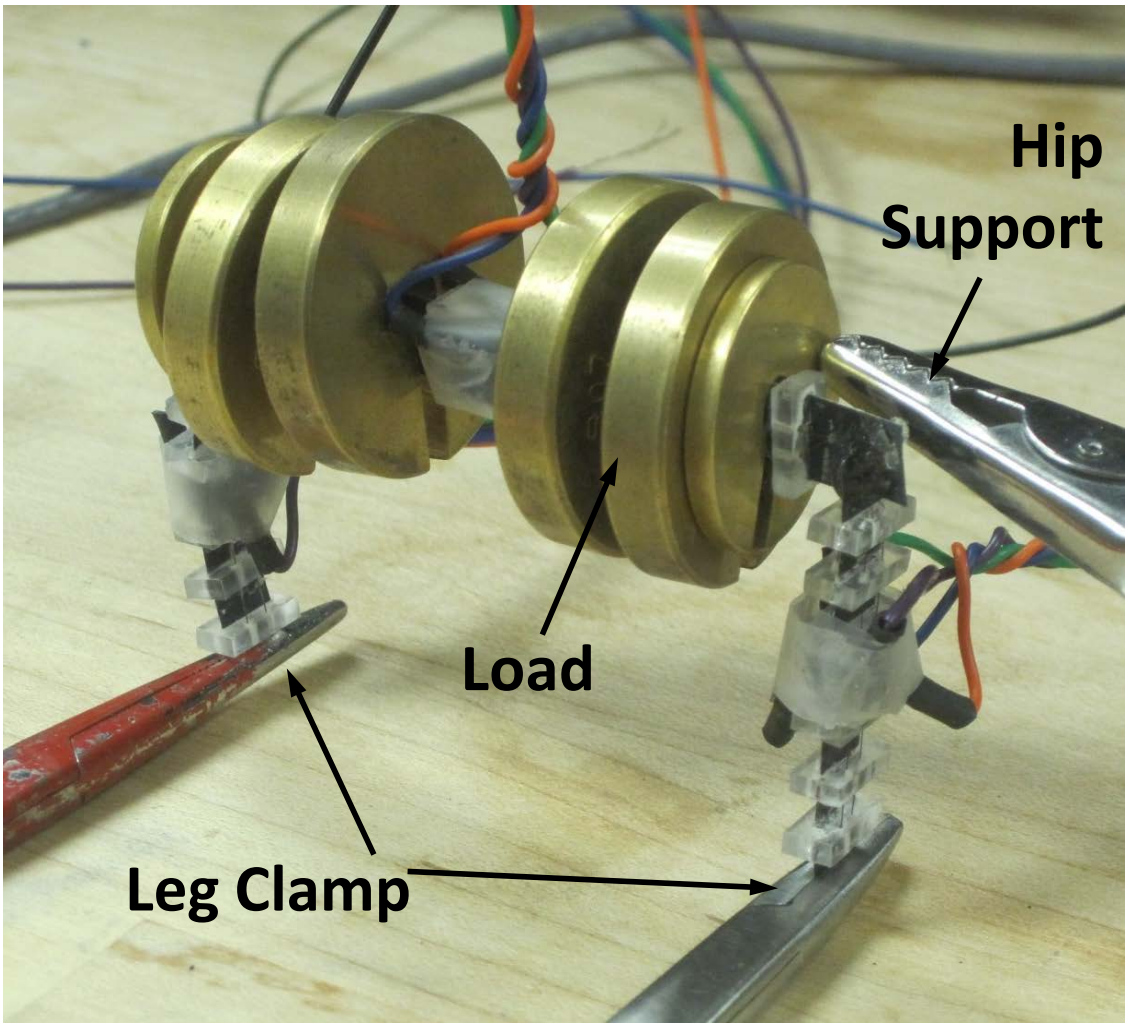

Figure 2.3.13: Load bearing test setup. The small FlexLegs are shown with two leg clamps and one hip support. Load is distributed through the hip segment.

With no hip support the small FlexLegs were able to withstand a load of 1.18 N before becoming unstable. The large FlexLegs were able to withstand 0.25 N in the same setup. For this case, the central beam buckled first and the structure collapsed. With hip supports on both sides, the small FlexLegs withstood a load of 2.94 N while the large FlexLegs withstood 0.79 N. The larger structure became unstable much more easily due to the long segments. Both structures are very sensitive to eccentric loading making it critical as to where and how the load is applied.

2.4 Chapter Summary

UUV mimicking the jetting propulsion was designed by using Biometal Fiber actuators. The use of SMA for an underwater vehicle was demonstrated to offer several advantages: (i) high force density reducing mechanism complexity, (ii) more room for payload, and (iii) simple electrical drive system. The main disadvantage in using SMA was found to be its high power consumption. Preliminary characterization indicated that jellyfish prototype designed with overall mass of 324 gm was able to thrust itself up with velocity of 7.8 cm/s under an applied current of 3.5 A at 1 Hz. The overall performance of the vehicle was also found to be highly dependent on the bell segment design.

In order to mimic the rowing propulsion, BISMAC actuators were designed and fabricated to achieve large deformation. The optimized BISMAC actuator exceeded the requirements for *Aurelia aurita* jellyfish species in terms of maximum deformation profile during swimming cycle. The actuator deformation was found to be highly dependent on distance (d) between the SMA wires and incompressible beam. The deformation is a function of the moment of inertia and can be manipulated by varying the spring steel and silicone thicknesses. Five BISMAC configurations were tested to see the effects of varying design parameters on the maximum deformation profiles. The varied design parameters were silicone, spring steel thickness, the distance d and SMA location. The operating voltage amplitude was varied to minimize power consumption and maximize deformation. For CC-BISMAC, a driving voltage amplitude of 16.2 V and current of 0.975 A was found to provide highest deformation with lowest power consumption. Furthermore, this leads to the conclusion that power impulses can be used to reduce the actuators' power consumption. Also, the SMA-silicone interfaces allowed heat to

dissipate at a faster rate than it would in air. Residual heat has an important effect on the performance of the actuators and could also influence the actuator's lifespan.

In order to expand the application regime of BISMAC actuators and provide them with bi-directional actuation capability, BiFlex actuators were developed. BiFlex demonstrated the ability to achieve large curvature in two directions. Using these actuators, two sets of FlexLegs were developed, one measuring a total of 35.8 mm in height and 63.2 mm in width and the other 97.4 mm in height and 165.4 mm in width. Both sets of legs could achieve crabbing, stepping and yawing. Reducing the size for the large FlexLegs had a significant impact on deformation since not all components were scaled. The small FlexLegs achieved a maximum deformation of 12 % and 4 % in the x- and y- direction respectively using a power of 0.7 W. They produced a maximum force of 0.023 N and were able to withstand a load of 1.18 N. The large FlexLegs had a maximum deformation of 57 % and 39 % in the x- and y-direction respectively using a power of 3 W. They produced a force of 0.045 N but were able to withstand a lesser load of 0.25 N.

2.5 References

Abdelnour, K., Mancia, E., Peterson, S. D. and Porfiri, M., (2009). Hydrodynamics of underwater propulsors based on ionic polymer metal composites: a numerical study, *Smart Mat. and Struct.* 18(8), 085006

Akle, B. J., Bennett, M. D. and Leo, D. J. (2006). High-strain ionomeric–ionic liquid electroactive actuators, *Sensors Actuat. A*, 126 173–81

Birch, M. C., Quinn, R. D., Hahm, G., Phillips, S., Drennan, B., Fife, A., Verma, H. and Beer, R. D. (2000). Design of a cricket microrobot. *IEEE Conf. on Robotics and Automation*

Blottman, J. B. and Richards, R. T. (2006) The Jellyfish: smart electro-active polymers for an autonomous distributed sensing node. *Proc. SPIE*, 6231, 62311E

Bunget, G., Seelecke, S. and Place, T. J. (2008). Design and Fabrication of a Bio-Inspired Flapping Flight Micro-Air Vehicle, *ASME 2008 Conference on Smart Materials, Adaptive Structures and Intelligent Systems*, 647-654

Colin, S. P. and Costello, J. H. (2002). Morphology, swimming performance and propulsive mode of six co-occurring hydromedusae. *J. Exp. Bio.* 205, 427-437

Costello, J. H., Colin, S. P., Dabiri, J. O. (2008) The medusan morphospace: phylogenetic constraints, biomechanical solutions and ecological consequences. *Inverteb. Biol.* 127 (3): 265-290.

Dabiri, J. P., Colin, S. P. and Costello, J. H. (2007) Morphological diversity of medusan lineages constrained by animal-fluid interactions. *J. Exp. Biol.* 210, 1868-1873

Dabiri, J. P., Colin, S. P. and Costello, J. H. (2005). Flow patterns generated by oblate medusan jellyfish: field measurements and laboratory analyses. *J. Exp. Biol.* 208, 1257–1265

Daniel, T. L. (1983). Mechanics and energetics of medusan jet propulsion. *Can. J. Zool.* 61,1406 -1420

Daniel, T. L. (1985). Cost of locomotion: unsteady medusa swimming. *J. Exp. Biol.* 119, 149–164

Daerden, F. and Lefeber, D. (2002). Pneumatic artificial muscles: actuators for robotics and automation. *Euro J. Mech. Env. Eng*. 47, 10–21

Delcomyn, F. and Nelson, M. E. (2000). Architectures for a biomimetic hexapod robot. *Rob. And Aut Syst.* 5-15

ePedia [Online] December 9, 2008. [Cited: March 3, 2009.] http://epedia.pbwiki.com/Box-Jellyfish

Fearing, R. S., Chiang, K. H., Dickinson, M. H., Pick, D. L., Sitti, M. and Yan, J. A. (2000). Wing transmission for a micromechanical flying insect. *IEEE Proc. ICRA'00 Int. Conf. on Robotics and Automation.* 2, 1509–16

Flannigan, W. C., Nelson, G. M., Quinn, R. D. (1998). Locomotion controller for a crab-like robot. *In Proceedings of the IEEE International Conference on Robotics and Automation* 152-156

Gladfelter, W. G. (1972). Structure and function of the locomotory system of Polyorchis montereyensis (Cnidaria, Hydrozoa) Helgol. Wiss. Meeresunters. 23, 38–79

Gladfelter, W. G. (1973). Structure and function of the locomotory system of the Scyphomedusa Cyanea capillata. *Mar. Biol.* 14, 150–160

Guo, S., Fukuda, T., Asaka, K. (2003). A new type of fish-like underwater microrobot *IEEE/ASME Trans Mechatronics*, 136–141

Haralick, R. M. and Shapiro, L. G. (1992). Computer and Robot Vision. Vol. I, 28-48, Addison-Wesley,

Hugel, V., Hackert, R. and Abourachid, A. (2011). Kinematic Modeling of Bird Locomotion from Experimental Data. *Robotics, IEEE Transactions on* , 27(2), 185-200

Incropera, F. P. (2006). Fundamentals of Heat and Mass Transfer, John Wiley & Sons

Jung, J., Kim, B., Tak, Y., Park, J.-Oh. (2003). Undulatory Tadpole Robot (TadRob) using ionic polymer metal composite (IPMC) actuator. *Proc. IEEE/RJS Intl. Conf. Intel. Rob. Syst.*

Kornbluh, R., Perline, R., Eckerle, J. and Joseph, J. (1998). Electrostrictive polymer artificial muscle, *Proc. IEEE Robot. Autom.* 3, 2147–54

Kornbluh, R., Pelrine, R., Pei, Q., Oh, S. and Joseph, J. (2000). Ultrahigh strain response of field-actuated elastomeric polymers. *Proc. SPIE*, 3987, 51–64

Lakasanacharoen, S., Pollack, A. J., Nelson, G. M., Quinn, R. D. and Ritzmann, R. E. (2000) Biomechanics and Simulation of Cricket for Microrobot Design. *Proc. Intern. Conf. Rob. Autom.* 1088-1094

Li, F., Bonsignori, G., Scarfogliero, U., Chen, D., Stefanini, C., Liu, W., Dario, P. and Fu, X. (2009). Jumping mini-robot with bio-inspired legs, *Proc. IEEE Intern. Conf. Rob. Biomim.*, 933-938

Madden, J. D., Vandesteeg, N. A., Anquetil, P. A., Madden, P. G., Takshi, A, Pytel, R. Z., Lafontaine, S. R., Wierenga, P. A. and Hunter, I. W. (2004). Artificial muscle technology: physical principles and naval perspects. *IEEE J. Ocean. Eng.* 29. 706–28

McHenry, M. J. (2007). Comparative Biomechanics: The Jellyfish Paradox Resolved. *Current Biol.*17(16), R632-R633

Megill, W. M., Gosline, J. M., Blake, R. W. (2005). The modulus of elasticity of the fibrillin-containing microfibrils from the mesoglea of the hydromedusa: Polyorchis penicillatus. J. *Exp Biol*. 208, 3819-3834

Nelson, G. M., Quinn, R. D., Bachmann, R. J. and Flannigan, W. C. (1997). Design and simulation of a cockroach-like hexapod robot. *Proc. IEEE Intern. Conf. Rob. Autom.* 1106-1111

Ogura, Y., Kataoka, T., Aikawa, H., Shimomura, K., Lim, H. and Takanishi, A. (2005). Evaluation of various walking patterns of biped humanoid robot. *Proc. IEEE Intern. Conf. Rob. Autom.* 605-610

Madangopal, R., Student, G., Khan, Z. and Agrawal, S. (2005). Biologically inspired design of small flapping wing air vehicles using four-bar mechanisms and quasi-steady aerodynamics, *J. Mech. Des.* 127, 809

Punning, A., Anton, M., Kruusmaa, M., and Aabloo, A. (2004). A Biologically Inspired Ray-like Underwater Robot with Electroactive Polymer Pectoral Fins. IEEE Conf. Mechat. Rob. 241 - 245

Satterlie, R. A., Thomas, K. S., and Gray, G. C. (2005). Muscle Organization of the Cubozoan Jellyfish Tripedalia cystophora Conant 1897. *Biol. Bull.* 209, 154-163

Saranli, U., Buehler, M. and Koditschek, D. E. (2001). RHex: A simple and highly mobile hexapod robot. *Int. J. Robot. Res.* 20, 616-631

Scarfogliero, U., Folgheraiter, M. and Gini, G. (2004). Advanced steps in biped robotics: innovative design and intuitive control through spring damper actuator. Proc. IEEE Conf. Humanoids 196-214

Smith, C., Villanueva, A., Joshi, K., Tadesse, Y. and Priya, S. (2011). Working principle of bio-inspired shape memory alloy composite actuators. *Smart Mater. Struct.* 20, 012001

Stoll, W. (2008). Festo - Bionic Learning Network". *Festo.* [Online] [Cited: October 20, 2008.] www.festo.com/de/bionic.

Tadesse, Y., Grange, R. W. and Priya, S. (2009). Synthesis and cyclic force characterization of helical polypyrrole actuators for artificial facial muscles. *Smart Mater. Struct.* 18, 085008

Tadesse, Y., Thayer, N., and Priya, S. (2010) Tailoring the Response Time of Shape Memory Alloy Wires through Active Cooling and Pre-Stress. J. Intel. Mat. Struct. 21, 19-40

Tanaka, H., Hoshino, K., Matsumoto, K. and Shimoyama. (2005). Flight dynamics of a butterfly-type ornithopter. *IEEE/RSJ Int. Conf. Intel. Rob. Syst.* 2706–11

Villanueva, A., Bresser, S., Chung, S., Tadesse, Y. and Priya, S. (2009). Jellyfish inspired underwater unmanned vehicle. *Proc. SPIE,* 7287

Villanueva, A. A., Joshi, K. B., Blottman, J. B. and Priya, S. (2010a). A bio-inspired shape memory alloy composite (BISMAC) actuator. *Smart Mater. Struct.* 19, 025013

Villanueva, A., Priya, S., Anna, C. and Smith, C. (2010b). Robojelly bell kinematics and resistance feedback control. *IEEE Intern. Conf. Rob. Biomim. (ROBIO),* 1124-1129

Vogel, S. (2008). Modes and scaling in aquatic locomotion. *Integr. Compar. Biol.* 48(6), 702-712

Yang, Y., Ye, X., Guo, S. (2007). A New Type of Jellyfish-Like Microrobot. *Proc. IEEE Intl. Conf. Integ. Tech. 673-378*

Yeom, S. W. and Oh, Il.-K. (2009). A biomimetic jellyfish robot based on ionic polymer metal composite actuators. *Smart Mat. and Struct.* 18(8), 085002

Chapter 3

BISMAC Actuator Control System and Power Reduction Techniques

As shown in the previous chapter, shape memory alloy based composite actuators are highly promising for bio-inspired robotics. However, they do have some drawbacks which restrict their deployment. These drawbacks are non-linear response and high power consumption. Large cyclic hysteresis in deformation causes difficulty in controlling the actuators and large power consumption lowers the life time of the robots due to the limited onboard energy supply. Another drawback of SMA actuators is the cooling time required for the actuators to regain their original configuration which lowers the frequency of operation. This is not a problem in the application of the robotic jellyfish where cyclic frequencies are below 1 Hz.

In this chapter, Section 3.1 describes the development of a rapid heating controller with resistance feedback for BISMAC actuators designed to lower the power consumption. The hysteretic deformation behavior of SMA requires the use of sensors capable of monitoring their state for control purposes. Sensors are not feasible in applications such as the robotic jellyfish or "Robojelly". Complex control system can be applied to determine the state of the actuators without the need of sensors. Section 3.2 describes the effort towards reducing the power consumption of SMA by reducing the transition temperature and thermal hysteresis. The governing parameters related to power consumption were identified based upon the deformation cycle. Synthesis of new SMA compositions was pursued by using a RF induction furnace based method to validate the hypothesis.

3.1 BISMAC Control Using SMA Resistance Feedback

As described in previous chapter, bio-inspired shape memory alloy composite (BISMAC) actuators are promising for the design of medusae rowing propulsion. BISMAC actuators were able to recreate bell deformation of *Aurelia aurita* by controlling shape memory alloy (SMA) deformation that allowed matching the contraction-relaxation deformation profile. However, a suitable control system is needed to lower their power requirement. In this section, a feedback control system using SMA wire resistance feedback to decrease contraction time and power consumption is described. The controller requires the knowledge of threshold resistance and safe current inputs which were determined experimentally.

The overheating effect of SMA wires was analyzed for BioMetal Fiber (BMF) and Flexinol 100 µm diameter wires revealing an increase in resistance as the wire gets overheated. The controller was first characterized on a SMA wire with bias spring system for a BMF 100 using $I_{hi} = 0.5$ A and $I_{low} = 0.2$ A, where hi corresponds to peak current for fast actuation and low corresponds to the safe current which prevents overheating and maintains desired deformation. A contraction of 4.59% was achieved in 0.06 s using the controller and the deformation was maintained for 2 s at low current. The BISMAC actuator was operated using the controller with $I_{hi} = 1.1$ A and $I_{low} = 0.65$ A achieving a 67% decrease in contraction time compared to using a constant driving current of $I_{low} = 0.2$ A and a 60% decrease in energy consumption compared to using constant $I_{hi} = 0.5$ A while still exceeding the contraction requirements of the *Aurelia aurita*.

3.1.1 Controller Problem Description

One of the goals in mimicking jellyfish propulsion is to match or exceed its efficiency. To do so, the jellyfish bell motion must be matched by replicating the bell kinematics. Jellyfish undergo cyclic propulsion which uses power during contraction followed by a passive relaxation. A rapid contraction followed with a slower relaxation is needed for better thrust production. The SMA wire contraction time can be tailored by controlling the amplitude of drive current used for resistive heating. The relaxation time is passive and depends on the resilience of the structure and its ability to dissipate heat. Previous BISMAC characterization and vehicle testing was done by using a constant current magnitude during contraction. Due to the high amplitude of current required for fast deformation, residual heat in silicone becomes a problem affecting the relaxation time and heat accumulates through subsequent cycles. High currents also lead to higher power consumption. For these reasons, a control system managing the input current was required. The objective was to develop a control system that can actuate BISMAC actuators within 1 s and maintain a constant deformation using minimal current.

Several controller concepts for SMA wires have previously been proposed in literature. Kuribayashi has proposed a technique that utilizes direct temperature measurement of SMA wires using small thermocouples (Kuribayashi, 1991). Several other studies have proposed technique that is now widely used and is based on the SMA resistance feedback (Webb, G. et al., 2000; Featherstone and The, 2004; The and Featherstone, 2008; Mukherjee et al., 1996; Raparelli et al., 2002; Song et. al., 2007). This technique is possible due to phase change occurring in NiTi alloy. As the SMA undergoes phase transformation from martensite to austenite, its overall resistance changes. The change in resistance is used to monitor the state of

SMA actuation. This correlation between the electrical properties and phase transformation provides a fundamental criterion for controller design.

3.1.2 Experimental Methods

The controller software was developed in LabView and the measurements were conducted using an NI cDAQ 9172. The calculated output voltage was sent by a NI-9263 analog output card to a NF HAS 4052 power amplifier set to a fixed gain of 20. The voltage drop across the current-to-voltage converter was measured using a NI-9215 16-bit isolated card. Isolation was found to be a necessity for this measurement with high precision. The NI-9221 card was used to measure the voltage drop across the SMA due to voltages reaching amplitudes greater than 10V. SMA contraction was measured using a Micro – Epsilon optoNCDT 1401-50 displacement laser. The output was read as an analog signal by the NI-9215. The input data was sampled at a rate of 10,000 samples/s with 100,000 sample buffer and 100 samples per channel were read in each cycle. The input voltage drops from the SMA and resistor were averaged over 100 samples for more accurate readings and precise control. An Agilent 33120A function generator was used to output a square wave. The controller was first developed and tested on single SMA wires attached to a bias spring as shown in Fig. 3.1.1(a). Two different types of SMA wires of diameter of 100 μm were tested, BioMetal Fiber (BMF) 100 from Toki Corporation and Flexinol 90 from Dynalloy. BISMAC testing was conducted using the same controller setup with the addition of an IN250 high-speed camera from Fastec Imaging to track the deformation during actuation. The BISMAC was placed underwater in a 75 gallon aquarium. The actuator was clamped at one end in a cantilever configuration. Reflective points on the actuators were tracked individually using software developed in Matlab (Villanueva et al., 2010) [Point Detection, Appendix A].

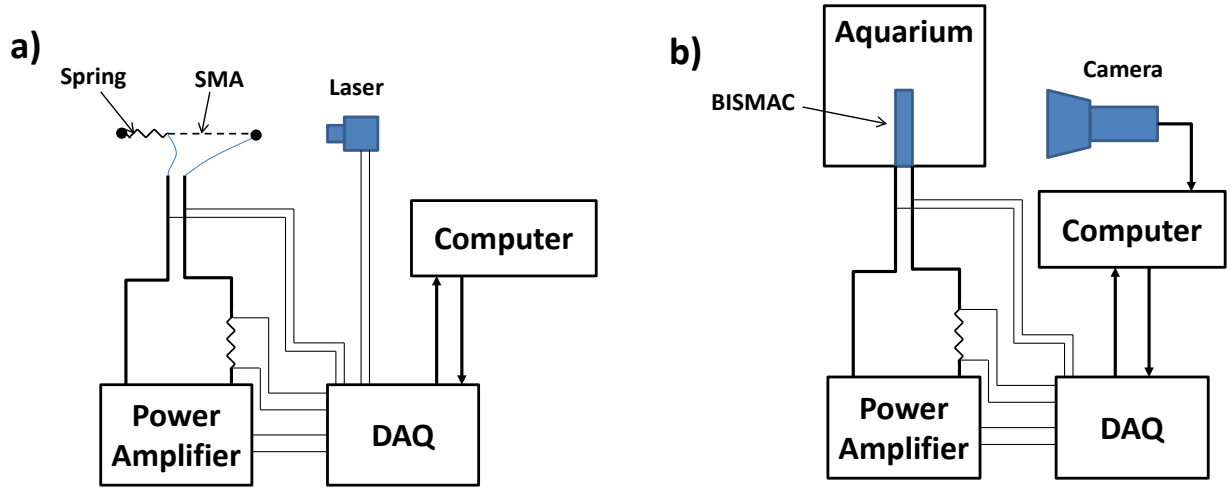

Figure 3.1.1: Experimental test setup for (a) SMA wire and bias spring system and (b) BISMAC actuator.

3.1.3 Controller Design

The goal of controller was to initially send a high impulse of current for fast contraction and then maintain deformation using a safe current magnitude. The controller consists of three main parts, the input function, the current limiter and the current regulator. Figure 3.1.2 shows a block diagram of the controller. The input function serves multiple purposes; it controls the actuation frequency, cruising time and allowed relaxation time which are all critical to the swimming performance of vehicle (Villanueva et al., 2009). An external function generator was used to output the required square wave during the experiments which serves the dual purpose of an external clock. It was found that internal clock was inadequate for these tests due to processor delays affecting the output function.

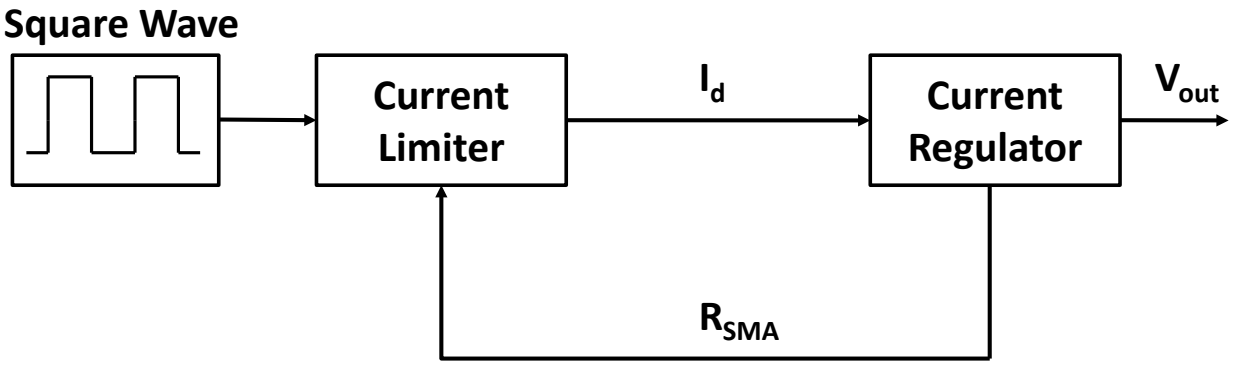

Figure 3.1.2: Controller schematic showing the square wave input, current limiter and current regulator.

The current limiter reads the function generator output as an "on" or "off" signal. When on, it takes the SMA resistance feedback and determines if it is above the threshold resistance. Based on these inputs, the following decision is made:

$$R_{SMA} = \begin{cases} > R_t, \ I_d = I_{hi} \\ \leq R_t, \ I_d = I_{low} \end{cases}, \qquad (3.1.1)$$

where R_{SMA} is the resistance of SMA wire, and R_T is the SMA threshold resistance. R_T was determined using a preliminary test as explained in Section 4. I_{hi} is the high impulse current sent for fast contraction and I_{low} is the safe current amplitude chosen to maintain deformation and prevent overheating. The desired current I_d is then sent out to the current regulator which does most of the work as shown in Fig. 3.1.3. R_{SMA} was calculated using the voltage drop across the resistor and current was measured by a passive current-to-voltage converter with a 1 Ω resistor. The output voltage was calculated from the SMA resistance and desired current. R_o which was equal to 1.79 Ω, takes into account the resistance of the current-to-voltage converter and the added resistance of cables and clamps.

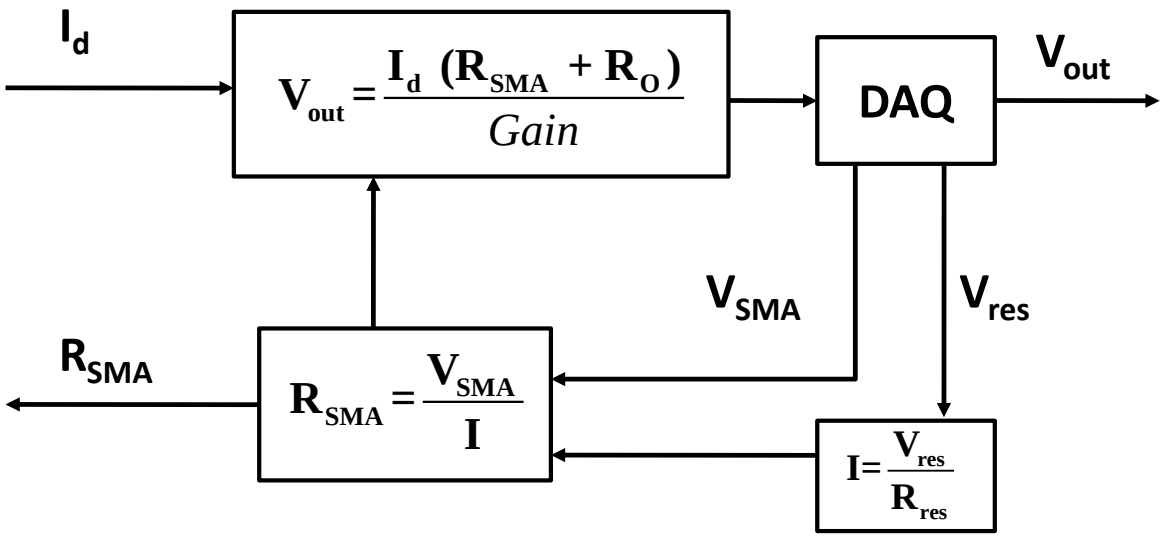

Figure 3.1.3: Schematic of the current regulator.

The voltage output was divided by "Gain" which is the amplifier gain such that the amplified value equals to the desired output voltage. Minimum and maximum resistance values were set as limits in order to prevent any arithmetic computation overload encountered when little or no current is flowing through the circuit. Due to the computation done using the two input voltages, noise would lead to excessive arithmetic computations. This would lead to slowing down of the data acquisition system and poor performance of the controller.

3.1.4 Controller Performance Characterization

The controller requires knowledge of few SMA parameters. A threshold resistance R_t refers to the point where the SMA undergoes most of its phase transition. This value is commonly taken as 80% of the initial SMA resistance since they undergo a resistance drop of

approximately 20% at full contraction. The initial SMA wire resistance varies with length and diameter while resistance drop varies with SMA composition. To obtain a precise value of R_t, a preliminary property measurement test was conducted on the SMA wires and BISMAC, before utilizing them for controller testing.

3.1.4.1 SMA Wire: R_t Measurements

This test was done by heating the SMA wire under constant current amplitude recommended by the manufacturers. For BMF 100 a current of 0.2 A was recommended, while 0.18 A was recommended for the Flexinol wire. Figure 3.1.4 shows the resistance and displacement results of both wires as a function of the applied current. The threshold resistance was taken as the steady state resistance of the wires under recommended current amplitudes. The results are listed in Table 1 along with the properties of the respective SMA wire.

Table 3.1.1: Numerical results of R_t measurement tests

	BMF 100	**Flexinol**
R_i (Ω)	13.25	12.13
R_i Measured using DMM (Ω)	13	12.1
R_t (Ω)	10.32	10.46
Max Contraction (%)	4.12	4.16
SMA Length (mm)	93	93
Contraction time (s) (4.0%)	1.24	1.79
Contraction time (s) (4.1%)	3.47	2.33

It can be observed that the SMA resistance starts at 15 Ω which is related to the method in which resistance is measured and calculated. When there is no current in the circuit, the voltage readings are noise and the maximum and minimum resistance limits are set. For this test, a maximum of 15 Ω and minimum of 1 Ω was set for R_{SMA}. The spikes seen in resistance results

are caused by V_{SMA}. V_{res} readings were quite small initially due to low current resulting in a large calculated R_{SMA} and causing a large voltage output or vice-versa when current decreases. The results show that both wires achieved a similar maximum deformation for the applied voltage. The resistance of Flexinol wire increases initially before decreasing while that for BMF resistance decreases immediately.

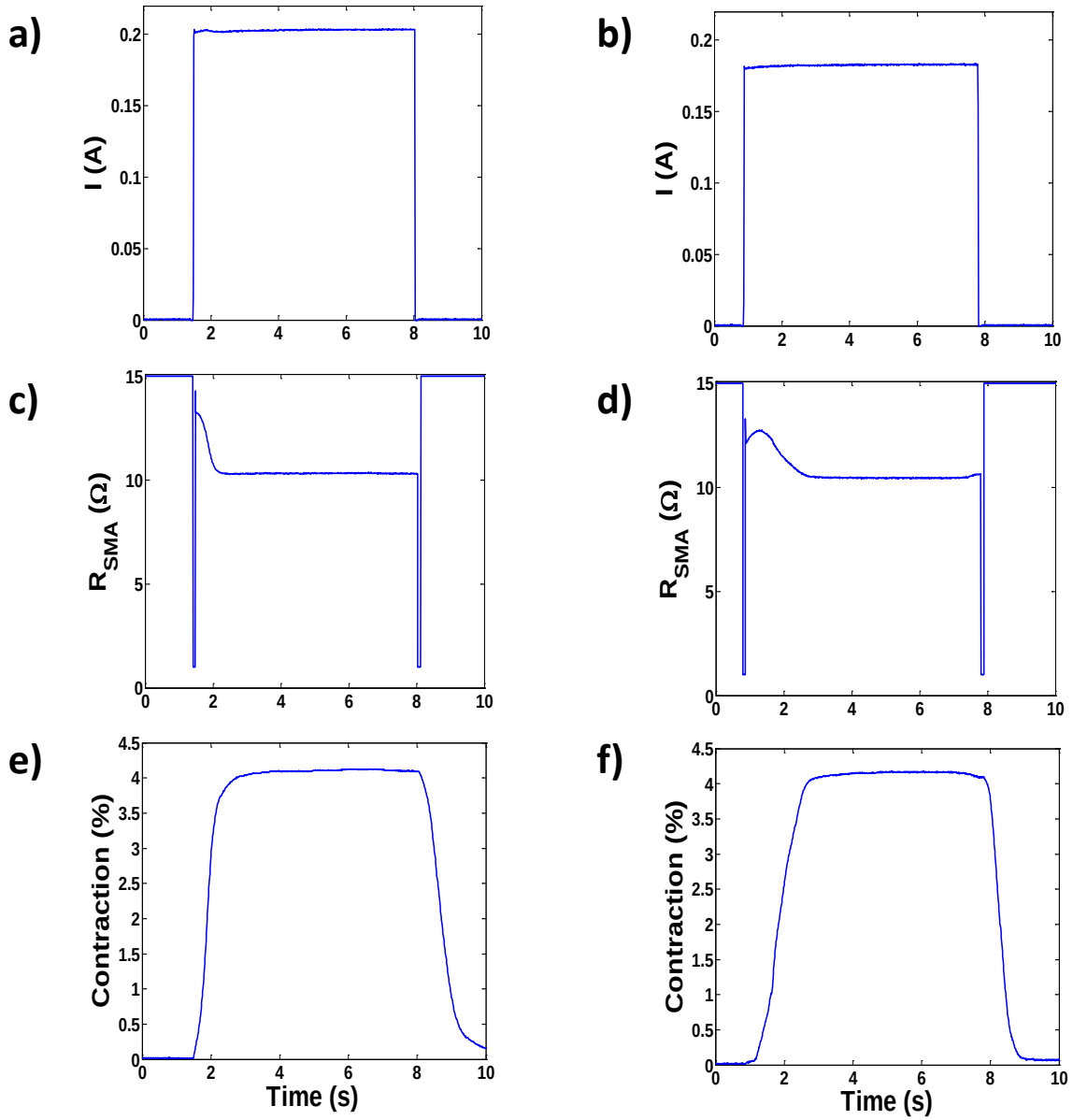

Figure 3.1.4: SMA wire and bias spring threshold test results showing input current, SMA resistance and displacement for BMF a), c), e) and Flexinol b), d), f) respectively.

Preliminary control testing revealed an interesting SMA behavior. The controller would heat the wires at I_{hi} and then drop down to I_{low} as expected but due to noise or very small threshold margin, I_{hi} would be reapplied and would stay on. Short I_{hi} impulses were expected throughout the cycle for the same two reasons mentioned, but it was not expected for I_{hi} to stay on during the entire cycle. Consequently, overheating tests were done to understand the behavior of the SMA under excessive heating conditions.

3.1.4.2 SMA Wire: Overheating Effects

Two different types of SMA wires were tested to compare their behavior upon overheating. A constant current of 0.5 A was chosen to heat the SMA wires. The results are shown in Fig. 3.1.5. For both cases, resistance readings quickly reaches R_i and then undergoes a rapid decrease as expected from the phase change. This is followed by a resistance increase back to 91.37% of R_i for BMF and 95.99 % for Flexinol which then saturates. The BMF displacement reaches a peak value higher than the recommended currents and then achieves steady state. Once current is switched-off, the BMF contraction increases as temperature drops and then regains its original length. The Flexinol wire initially has the same maximum deformation as it did under recommended current and then the deformation decreases. The displacement decreases progressively as it overheats until current is switched-off. A slight increase in displacement was observed for the BMF at the end and the wire did not regain its original length. Table 3.1.2 summarizes the experimental results.

Table 3.1.2: Overheating effect test results

	BMF 100	**Flexinol**
Ri (Ω)	13.28	12.64
Rmin (Ω)	9.76	10.34
Roh	12	12.12
Max Contraction (%)	4.66	4.36
Contraction oh (%)	4.27	3.5
Recovery (%)	100	99.62

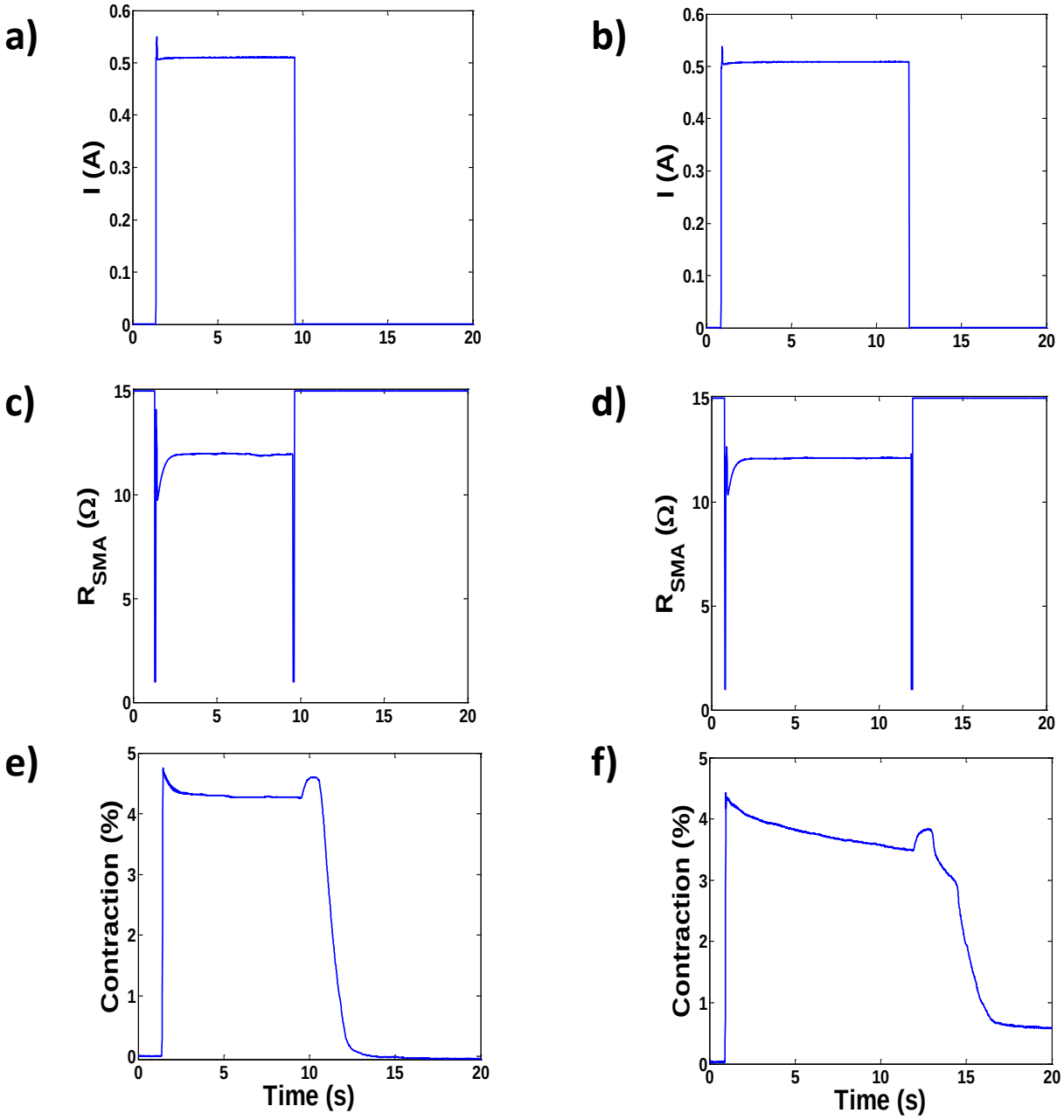

Figure 3.1.5: SMA resistance, current input, and displacement for high input currents. BMF a), c), e) and Flexinol b), d), f).

3.1.4.3 SMA Wire: Controller Characterization

The controller was applied to the SMA wire and bias spring system to evaluate its performance. The SMA used during this test was the same BMF wire that was previously tested

for R_t and overheating. The following current amplitudes were chosen for this experiment: $I_{hi} = 0.5\,A$ and $I_{low} = 0.2\,A$ with $R_t = 10.53\,\Omega$. The selected threshold resistance includes a margin of 2%. This is to take into account the noise in the system which could cause SMA resistance to appear greater than the threshold resistance and cause the controller to overheat the wire at which point resistance kept increasing. The current, resistance and displacement results are shown in Fig. 3.1.6.

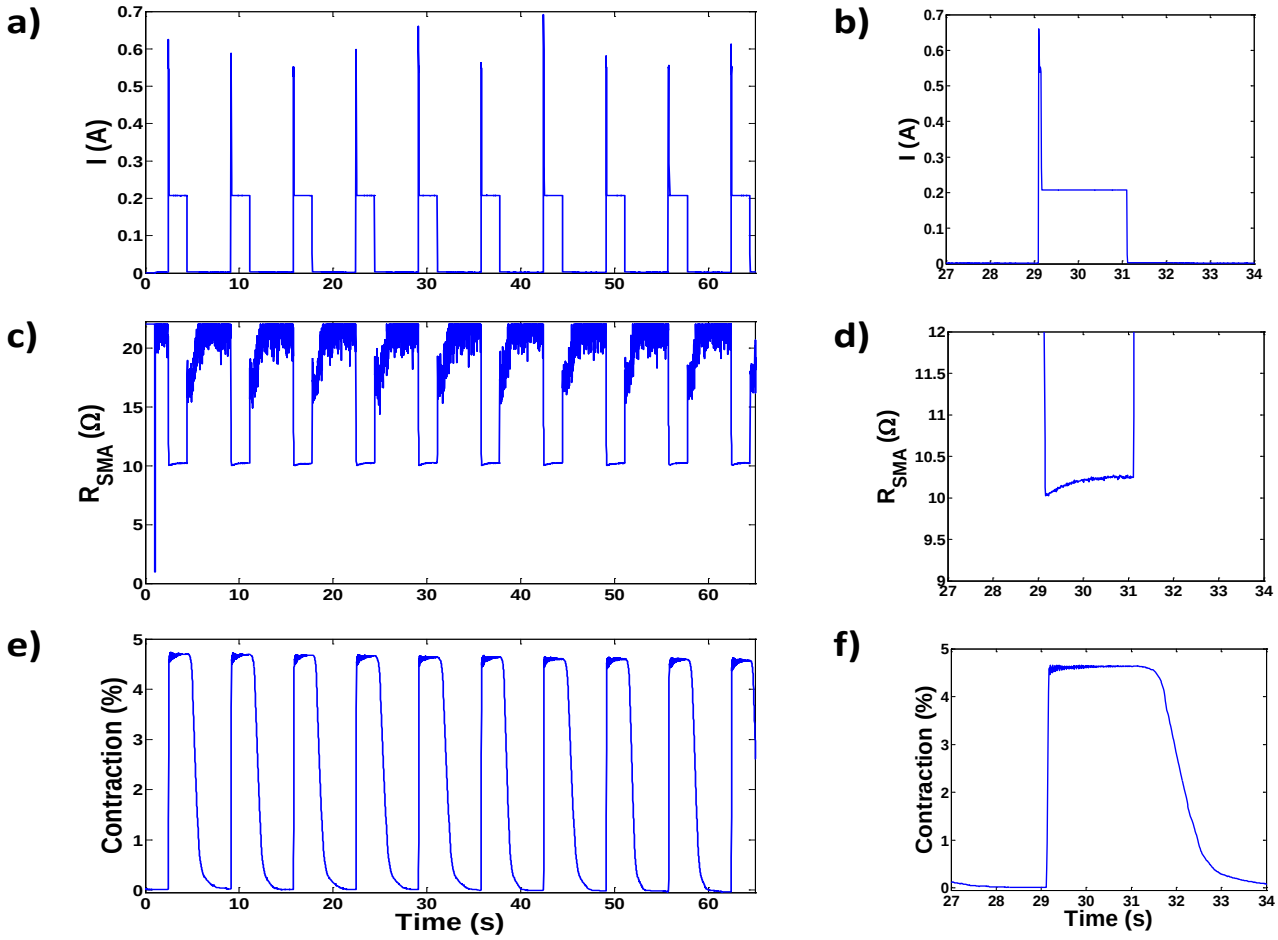

Figure 3.1.6: SMA resistance, current input, and displacement with applied controller for currents settings of $I_{hi} = 0.5$ A and $I_{low} = 0.2$ A BMF a), c), e) along with respective close up views of the 5th cycle in b), d), f).

The controller demonstrated its capability of sending current impulses allowing the actuator to reach a deformation of 4.56 % in 0.06 s. Operating the SMA with constant $I_{low} = 0.2\ A$ input achieved a deformation of 4.1 % in 3.47 s and with the controller the SMA wire deformed 4.1% in 0.05 s, which is a contraction time reduction of 98.55 %. The deformation was then maintained with a safe current magnitude. As shown in Fig. 3.1.6 (d), R_{SMA} initially goes below R_t but then increases to the threshold resistance. Once the threshold magnitude has been achieved, R_{SMA} does not further increases indicating that the SMA is not overheating. Upon relaxation, the SMA had enough time to dissipate its heat and regain its original length before the next contraction as seen in Fig. 3.1.6 f). Figure 3.1.6 a) shows the current impulses reaching higher amplitudes than the desired I_{hi}. This is due to the initial low current causing imprecise V_{SMA} and V_{res} readings and output voltage overshoot as explained in the previous section. This could be solved by using a more accurate maximum R_{SMA} limit.

3.1.4.4 BISMAC: R_t Measurement

Similarly to the SMA wire and spring system, the BISMAC actuator was characterized for threshold resistance. The heat dissipation is larger in silicone and water than in air by an order of magnitude. Consequently large currents were required to heat the SMA to temperatures necessary for contraction and thus the recommended current magnitude was not enough to heat the SMA wire embedded in silicone and submerged in water. Since there is currently no thermal model of temperature distribution inside BISMACs, a safe current was determined experimentally. Three current amplitudes were tested corresponding to, $I = 0.5, 0.6$ and $0.7\ A$. As with the SMA wires, current was applied and maintained at constant amplitude until resistance reached a steady state. The resistance and displacement results are shown in Fig. 3.1.7

with the appropriate current readings. BISMAC x-deformation is the percent deformation of the actuator tip in the x-direction relative to the maximum contraction achieved. The maximum is taken as the steady state deformation achieved at 0.7 A and the minimum in the relaxed state. For $I = 0.6$ and $0.7\ A$, R_{SMA} reaches a steady state allowing us to pick $R_t = 16.9\ \Omega$.

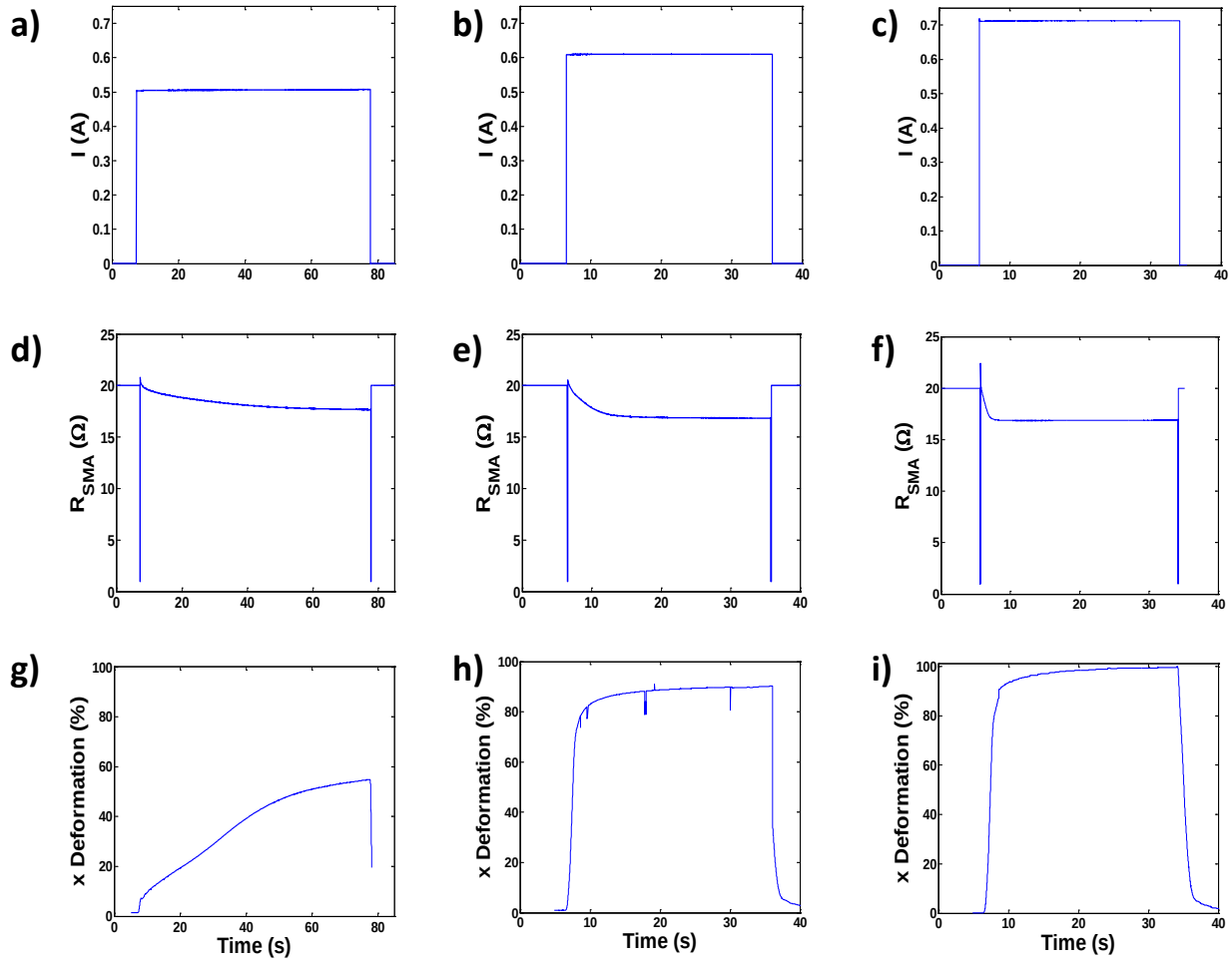

Figure 3.1.7: BISMAC threshold test results showing input current, SMA resistance and displacement for constant $I = 0.5\ A$ in a), d), g), $I = 0.5\ A$ in b), e), h) and $I = 0.7\ A$ in c), f), i) respectively.

3.1.4.5 BISMAC: Controller Characterization

The impulse current used for this test was limited by the power amplifier capability giving $I_{hi} = 1.1\ A$. The threshold resistance was determined in the previous test but little insight could be obtained on the required I_{low}. Therefore I_{low} was determined by trial and error to get an idea of what current level would maintain the contraction after I_{hi} has been applied. The controller was tested with $I_{low} = 0.6\ A$ and the actuator was unable to maintain a constant deformation. This is shown in Fig. 3.1.8 a) where the current spikes following the expected initial one are a result of the resistance increasing above the threshold. This implies that the actuator lost its deformation when I_{low} is unable to provide enough temperature change. Though corrective impulses could be a way to maintain contraction, they cause unwanted oscillation in the actuator. The current magnitude corresponding to $I_{low} = 0.7\ A$, caused the actuator to achieve contraction without any actuator oscillation. A current amplitude of $I_{low} = 0.65\ A$ was then tested and had the best performance as shown in Fig. 3.1.8 b).

A close-up view of the controlled results with $I_{hi} = 1.1\ A$ and $I_{low} = 0.65\ A$ are shown in Fig. 3.1.9. The results were compared to the BISMAC being actuated at a constant $I = 0.65$ and $I = 0.7\ A$ to identify the advantages of the controller. For constant $I = 0.65\ A$, deformation occurs throughout the actuation cycle and a maximum of 72 % was reached after 2 s of actuation as shown in Table 3.1.3. For constant $I = 1.1\ A$, the contraction was done in 0.58 s and an average deformation of 95% was achieved. The initial deformation exceeds 100 % because the momentum of the actuator causes it to go farther than its capability. The controlled actuation reaches a deformation of 72 % in 0.66 s. The smaller deformation is related to the fact that at $I = 1.1\ A$, deformation continues to occur once R passes R_t. The controlled actuation was able to achieve a contraction of 72% reducing contraction time by 67 % as compared to constant I_{low}

and increasing energy consumption by 13%. In comparison to constant I_{hi}, the controlled actuation reduced energy consumption by 60 % at a loss of 29 % contraction.

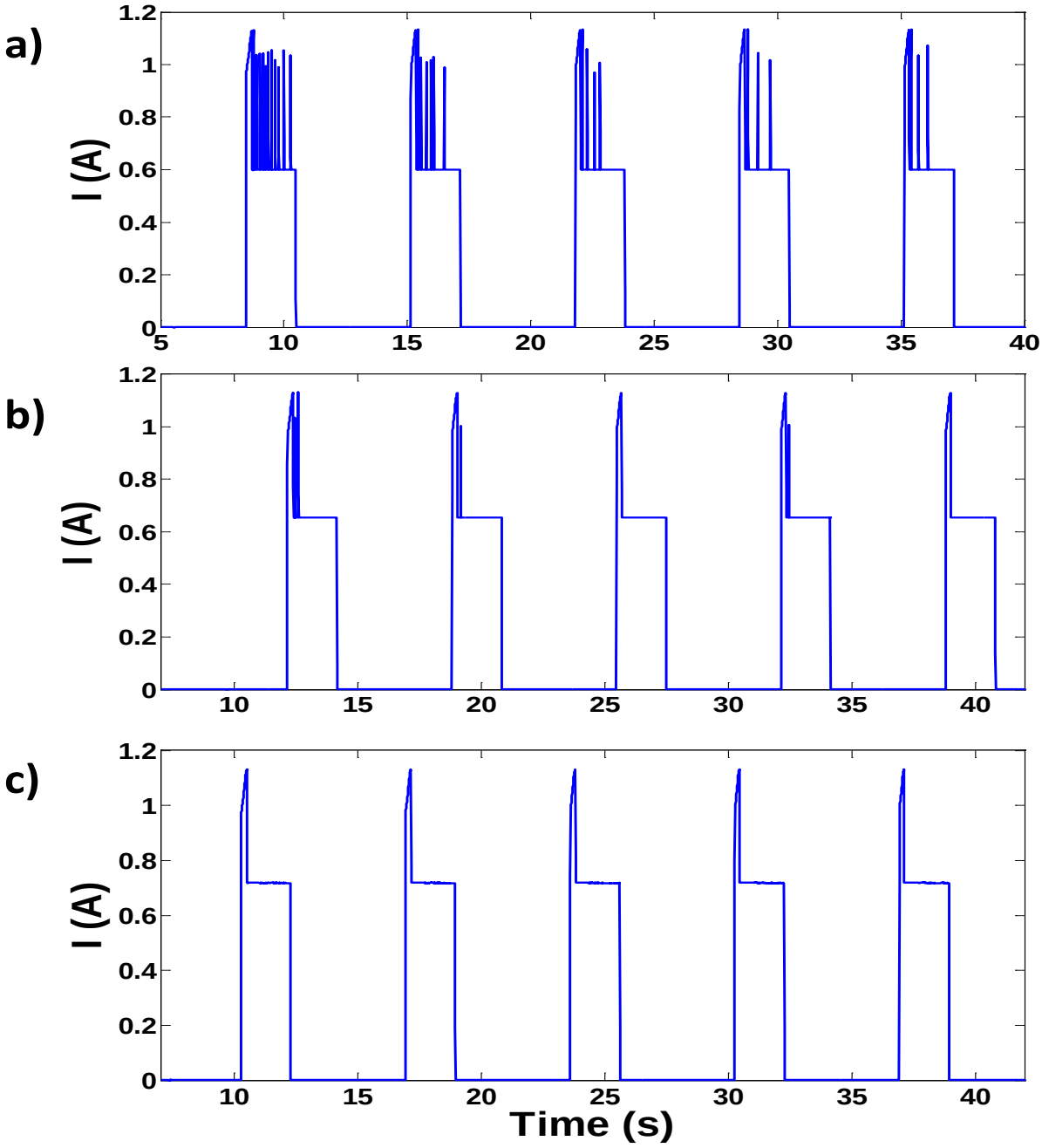

Figure 3.1.8: Current output results of the first five cycles for BISMAC actuator controlled with $I_{hi} = 1.1\ A$ and different I_{low}: a) $I_{low} = 0.6\ A$, b) $I_{low} = 0.65\ A$ and c) $I_{low} = 0.7\ A$.

Table 3.1.3: BISMAC control test results

I (A)	0.65	I_{low}=0.65, I_{hi}=1.1	1.1
Energy Consumption/cycle (J)	15.28	17.22	43.42
Contraction Time (s)	2.01	0.66	0.58
Initial Contraction (%)	71.87	72.4	101.6
Max Contraction (%)	71.87	77.87	101.6
Recovery (%)	98.3	99.36	98.4

In the controlled test, a total deformation of 5 % continued to occur even when I_{low} was applied. This means, a lower current would have to be applied if deformation was to be kept constant. In these tests, a maximum resistance of 22 Ω was set as the upper SMA resistance limit and 1 Ω as the lower limit. Resistance was not monitored during relaxation, it is therefore important that the BISMAC was designed properly so that it is able to relax in the given time for a given set of frequency and duty cycle. Most importantly, it must be able to dissipate heat at a high enough rate for the prescribed actuation conditions. Hysteresis effects were not considered because resistance was not monitored during relaxation which was achieved passively.

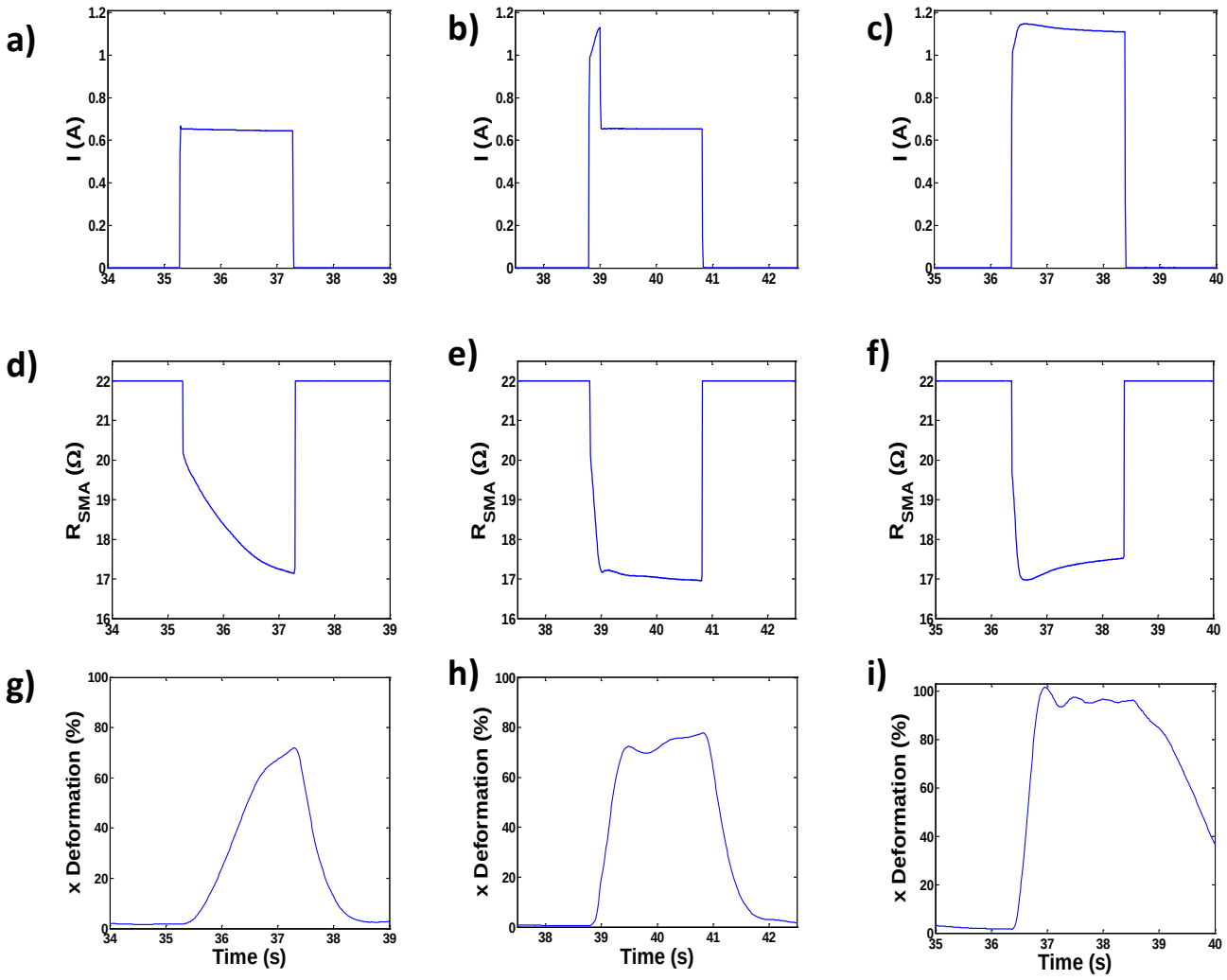

Figure 3.1.9: Close up view of the BISMAC control results. Current, resistance and percent x deformation for constant I = 0.6 A a), d) c), controlled current levels I_{hi} = 1.1 and I_{lo} = 0.65 A b), e), h), constant I = 1.2 A c), f), i).

3.2 Lowering the Power Consumption of Ni-Ti Shape Memory Alloy by Compositional Modification

Shape memory alloys (SMAs) are capable of undergoing shape memory effect and exhibiting superelasticity. Upon the application of heat, SMAs undergo shape change. Such behavior is caused by phase transformation of the crystalline material from martensite to austenite phase. The change in geometry is result of a diffusionless phase transformation in which atoms rearrange in a shear strain dominated displacement (Yamauchi et al., 2011). The transformation occurs when the material is heated beyond the austenite start transformation temperature (A_s) as shown in Fig. 3.2.1. The strain increases until the entire material has transformed to austenite phase at temperature A_f. During cooling, the material begins transition to martensite at the martensite start temperature (M_s) and completes transformation at the martensite finish temperature (M_f). While cooling down, the material regains its original shape. In order to obtain a specific geometry change, a series of cold work and annealing processes named training need to be followed.

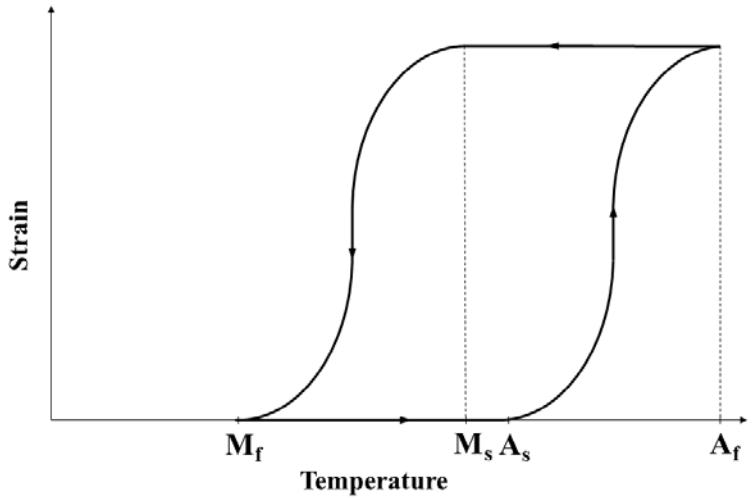

Figure 3.2.1: Schematic diagram for SMA showing strain as a function of temperature. This behavior is called the shape memory effect. A_s represents the austenite start transition

temperature while A_f represents the fully transformed material to austenite. During cooling, M_s represents the martensite start temperature while M_f is the martensite final temperature.

In order to undergo martensite to austenite phase transformation, most commercially available actuators need to be heated to 70-90ºC (Dynalloy, Toki Corp.). Robotic vehicles such as Robojelly will mostly operate near room temperature. This implies that significant energy is required to heat the wires and thus it is imperative that the transition temperature should be lowered. Significant research has been conducted on Ni-Ti based alloys but to our knowledge none have directly attempted reducing the power consumption through modulation of phase transformation temperatures. The first strategy can be reducing the thermal hysteresis during heating and cooling as shown in Fig. 3.2.2 (a). The thermal hysteresis here is taken as the difference between A_f and M_f but is has also been defined as $A_f - M_s$ (Zarinejad and Liu, 2008). This represents the amount of heat needed for the alloy to undergo a full contraction and relaxation cycle. Reducing the thermal hysteresis will reduce power required for actuation while at the same time less heat will be dissipated in the surrounding matrix which will result in higher actuation frequencies. The second strategy relies on reducing the transition temperatures as shown in Fig. 3.2.2 (b). This will reduce the heating required to undergo the transformation.

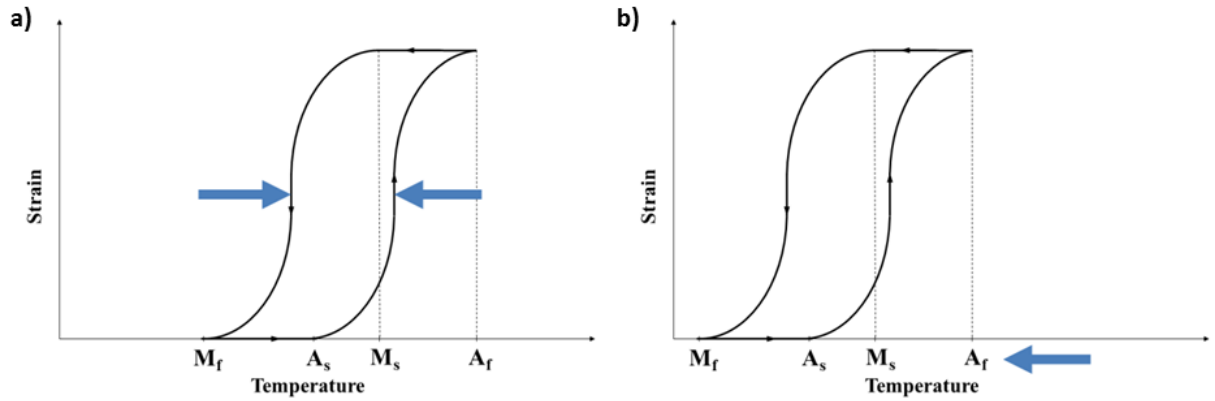

Figure 3.2.2: Schematic description of (a) the thermal hysteresis reduction and (b) the lowering of the transition temperatures relative to Fig. 3.2.1.

Different methods have been investigated in literature to modify the transition temperatures including high temperature annealing, cooling rate and compositional changes. Huang and Liu (Huang and Liu, 2001) have investigated the effects of annealing temperature on commercially available Ni-Ti based SMA. Their analysis revealed an increase in R_s and R_f temperature up to 623 K followed by a decrease (R-phase represents an intermediate which appears during the cooling cycle between austenite and martensite when the annealing is conducted below the recrystallization temperature). When annealing was done above 923 K, the R-phase disappeared and a direct transformation between martensite and austenite occurred. (Motemani et al., 2009) have analyzed the effects of cooling rate after melting the alloy given by composition $Ni_{50.7}Ti_{49.3}$ (at%). They studied three cooling techniques and concluded that A_f decreases with increasing cooling rates while M_f increases. The dominant factor controlling the transition temperature in Ni-Ti alloys is the percent of Ni. Transition temperature will vary by 10 K for each 0.1 % Ni difference for Ni-Ti alloys with Ni composition greater than 50 at% (Yamauchi et al., 2011; Buehler and Wang, 1968).

Transformation sequences for the Ni-Ti alloy are well documented in literature. An equiatomic Ni-Ti alloy transforms from a cubic austenite (B2) to monoclinic martensite (B19') phase. Adding copper can lead to a two stage transformation from cubic (B2) to orthorhombic martensite (B19) and then to a monoclinic martensite (B19'). The two stage transformation only occurs for certain compositions of Ni-Ti-Cu alloys (Shugo et al., 1985; Kudoh et al., 1985; Nam et al., 1990). The B2 to B19 phase transformation start and finish temperatures are defined as Ms' and Mf' respectively. Similarly, the B19 to B2 phase start and final transformation temperatures are defined as As' and Af' respectively. (Nam et al., 1990) have shown that for a $Ni_{40}Ti_{50}Cu_{10}$, most of the deformation occurs during the transformation between the B19 and B2 phase as shown in Fig. 3.2.3. Also, during that deformation, a very small thermal hysteresis of 11 K was observed. Our focus in this study is on increasing the efficiency of the SMA by reducing the joule heating required to achieve complete transformation. Thus, the results of (Nam et al., 1990) schematically depicted in Fig. 3.2.3 provide an important starting point towards the design of alloy composition.

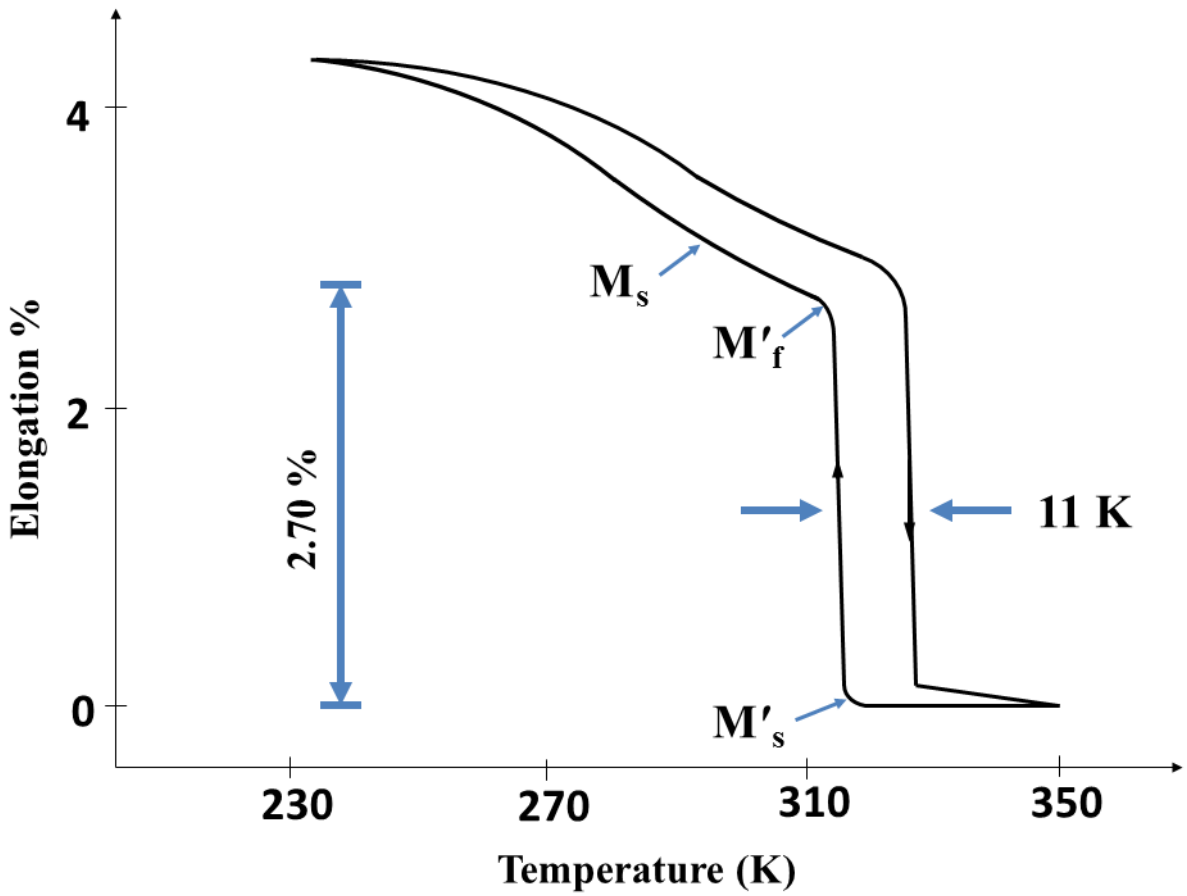

Figure 3.2.3: Elongation vs. temperature for a $Ni_{40}Ti_{50}Cu_{10}$ alloy under a load of 40 MPa. This plot shows most of the deformation occurring during the B19 – B2 transformation with a small hysteresis. Some of the transformation temperatures are not shown for clarity. Redrawn from Nam et al. (1990) [16].

(Nam et al., 1990) have analyzed the effect of copper in the alloy $Ni_{40-x}Ti_{50}Cu_x$ (at%) with x = 5, 7.5, 10, 12.5, 15, 20). For $x < 10$, the difference between A_f and M_f (A_f'and M_f' not present) increases with increasing x. For $x \geq 10$, the difference between A_f' and M_f' stayed near constant at an average of 26K. Increasing copper content in $Ni_{40-x}Ti_{50}Cu_x$ higher than 10 % is known to significantly increase brittleness (Otsuka and Wayman, 1998). Brittleness becomes a significant problem when forming SMA into a desired geometry such as a wire using cold work (Grossmann et al., 2008). The $Ni_{40}Ti_{50}Cu_{10}$ alloy has transformation temperatures of M_f' = 300

K and A_f' = 324 K under no load (Nam et al., 1990). This alloy has therefore transition temperatures close to room temperature. Also, for a $Ni_{50}Ti_{50}$ (at%) alloy, the difference between A_f' and M_f' is reduced by approximately 25 K when nickel is substituted with 10 at% copper which is a 50% reduction (Nam et al., 1990; Grossmann et al., 2008). The alloy $Ni_{40}Ti_{50}Cu_{10}$ was therefore used as base composition in our study where nickel and titanium compositions are varied to analyze their effects on transition temperature and thermal hysteresis using the formulation:

$$Ni_{40+x}Ti_{50-x}Cu_{10} \text{ (at\%)}, \qquad (3.2.1)$$

for x = 0, ±1, ±2, ±3, ±4, ±5. In this composition range, copper does not have a significant impact on transition temperature but significantly reduces A_f' - M_f'. Nickel concentration was varied since it influences the transition temperature most.

During synthesis of SMA it is important to consider several factors which can significantly alter the composition of the alloy and thereby change its performance. Oxygen and carbon contamination which is commonly present in SMA manufacturing, is known to deteriorate Ni-Ti performance (Shugo et al., 1985; Frenzel et al., 2004). Oxygen will form the secondary Ti_4Ni_2O phase which uses twice as much Ti than Ni, resulting in a Ni-rich alloy. The subsequent effect of an increased Ni in the matrix is a linear decrease in M_s. Oxidation can also cause samples to become more brittle (Frenzel et al., 2004; Mentz et al. 2006; Otubo et al., 2008). Oxygen contamination can be reduced by heat treating the samples in a vacuum or inert gas environment. (Frenzel et al., 2004) have studied the effect of graphite crucible during melting of Ni - Ti samples. They found that carbon from the graphite did contaminate their samples up to 0.25 at% and proposed a technique to reduce carbon contamination. After melting, a layer of TiC was

found to form on the contact walls (Frenzel et al., 2004). This layer was found to stabilize after melting of 10 samples preventing the diffusion of more carbon in the samples. A cladding technique was introduced to prepare the crucible. This involved adding Ti pieces on the crucible wall to promote the formation of TiC layer. (Grossmann et al., 2008) have reported the synthesis process of NiTi and $Ni_{40}Ti_{50}Cu_{10}$ (at%) wires. The synthesis consisted of melting, homogenization, swaging, rolling, wire drawing and shape setting with intermediate annealing between most of the steps. Annealing helps in removing the residual stress which occurs when working on the alloy. Residual stress can cause a significant increase in transformation temperature[22].

3.2.1 Synthesis and Characterization Procedure

3.2.1.1 Raw Material

The raw material used to synthesize alloy was in the form of powders. Titanium powder had a purity of 99.7 % (mesh -325), and the copper had a purity of 99 % (mesh -325). The nickel powder consisted of spherical particles with a purity of 99.9 % (mesh -100). The powder mass was measured using a Mettler-Toledo JB1603-C/Fact balance with and average error of 0.028 %. Weighted powders were mixed by simple stirring. This crude method was complimented by the magnetic stirring that occurs when the liquid metals are exposed to a magnetic field. When the powders are melted in the inductive furnace, circulating currents occur through the metal which promotes the mixing in the alloy.

3.2.1.2 Melting

The high melting temperature of nickel (1450°C) and titanium (1670°C) requires the use of high temperature crucibles. We decided to use graphite crucibles. The crucibles were manufactured by using a raw graphite circular rod. The rod was cut in half to a length of 7.5 cm. Two compartments with half-circular cross sections were milled using a 3.175 cm end mill with ball end as shown in Fig. 3.2.4. The compartments spanned the full diameter of the end mill and had a depth of 1.4 cm. The two compartments separated by a small graphite segment spanned a total length of 6.5 cm. Each compartment was filled to the surface with 10 gm of powder mixture.

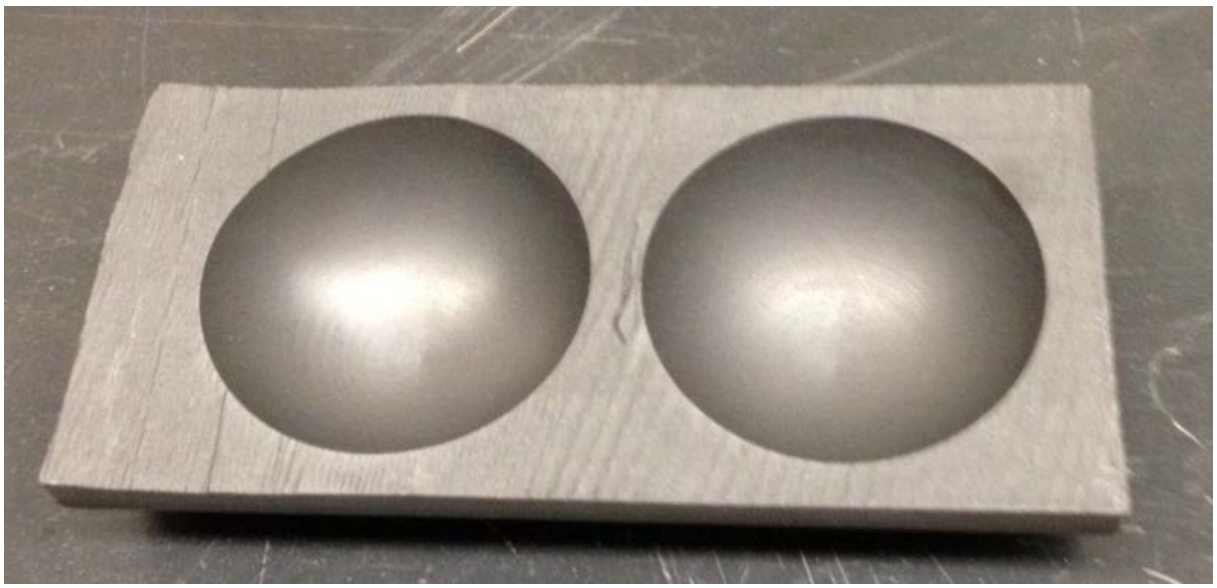

Figure 3.2.4: Graphite crucible for melting powders showing two compartments of 3.175 cm in diameter and 1.27 cm in depth.

The powders were melted using an RF induction furnace from Ameritherm Inc. as shown in Fig. 3.2.5. The furnace had an inductive coil spanning 6.5 cm with an inner diameter of 64.7 mm and a coil diameter of 6.49 mm. An argon atmosphere was produced around the sample to prevent

the oxidation. This was accomplished by inserting a quartz tube inside the inductive coil. The tube had dimensions of 61.5 mm in diameter, a wall thickness of 2 mm and a length of 48.5 mm. The two ends of the pipe were sealed with aluminum inserts. Each insert had a high temperature rubber gasket to maintain desired pressure. A hole through the central axis houses a ceramic tube which distributes the argon inside the quartz tube. A flow meter (King Instrument Company) was used in series to the outlet flow to measure the pressure. Oxygen was flushed from the quartz tube by flowing argon for 15 min before melting. A flow of 10 SCFH was maintained during flushing and melting. The same melting procedure was followed for all samples. The samples were heated at maximum voltage for 5 min at a frequency of 141 Hz. After the 5 min melting, argon was flushed for another 15 min. After cooling, the samples were removed from the quartz chamber.

3.2.1.3 Differential scanning calorimetry (DSC)

DSC was conducted to identify the transition temperatures. In this technique, amount of heat required to change the temperature of sample is measured as a function of temperature with respect to a reference sample having phase stability and known heat capacity in the temperature range of interest. Being either exothermic or endothermic in nature, any phase transition in the sample results in presence of either positive or negative peak in heat flow vs. temperature profile, and hence can be determined accurately. For our analysis a commercially available differential scanning calorimeter, TA Instruments DSC Q2000, was used. All the samples were analyzed in the temperature range of -90°C to 100°C with heating and cooling rates being 10°C /min. Sample were held for three minutes at maximum and minimum temperatures before reversing the heating

cycles. DSC was performed on small size samples having mass ranging from 10 mg – 25 mg. To avoid any discrepancy due to contamination of oxides and carbon, these small samples were taken from the core of the ingot. This was done by breaking the samples into halves and then chipping off a small piece from the core after removing about 1 mm thick layer from the top and bottom.

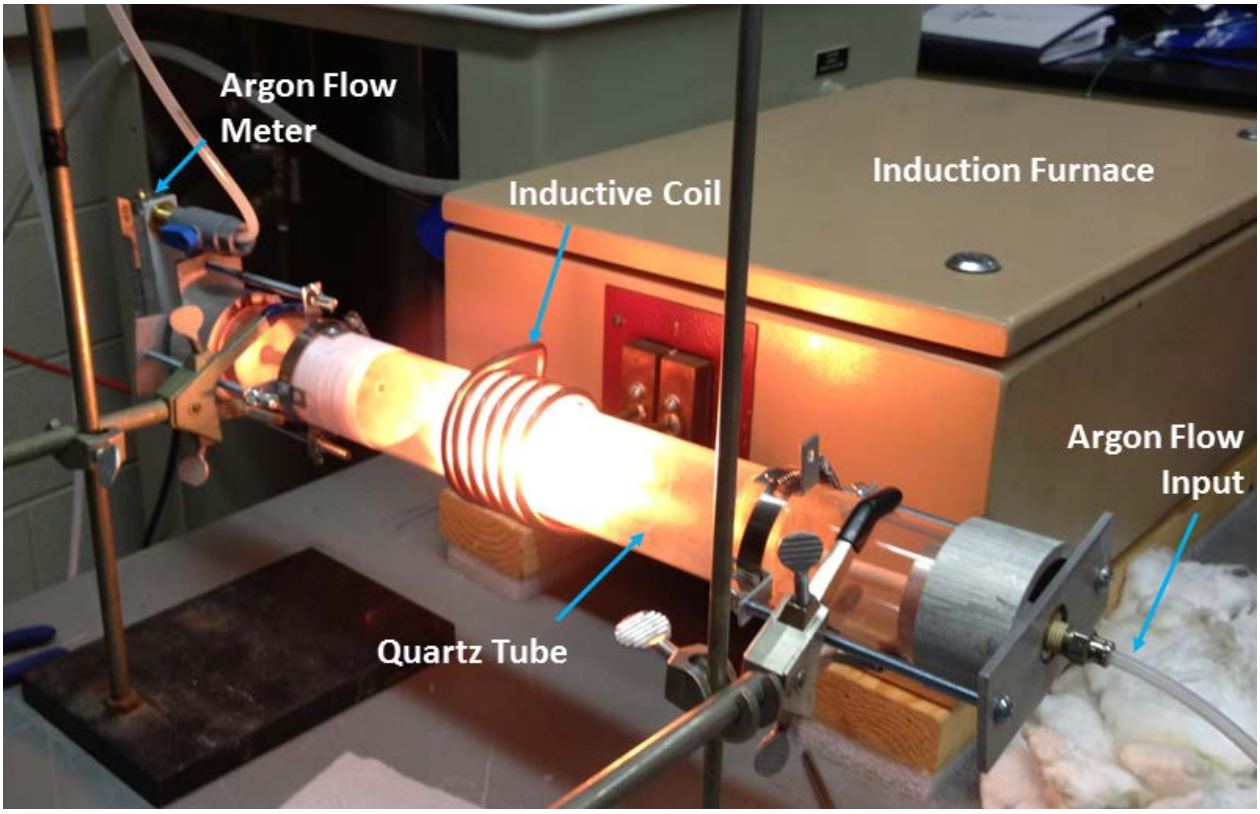

Figure 3.2.5: Induction furnace setup for melting of metal powders. A specimen is being melted inside the quartz tube under argon atmosphere.

3.2.2 Experimental Results

3.2.2.1 Sample Synthesis

After melting as shown in Fig. 3.2.6, most samples were found to stay attached to the graphite crucibles. The crucibles had to be broken in order to release the samples. Once removed,

the surface touching the graphite crucible had small fragments of graphite bonded to the alloy as shown see Fig. 3.2.7. This could be due to the porosity of the graphite. Lower porosity graphite could lead to less interaction between the samples and the crucible (Frenzel et al., 2004). Flow was kept relatively high at 10 SCFH to maintain the stability around the quartz chamber. It is speculated that a higher flow condition can lead to powder being blown away and therefore result in composition change. The sample surface in contact with flow had a visibly different color as shown in Fig. 3.2.6. The surface also shows streaks due to the gas flow. These defects should be minimized to achieve desired performance from the alloy. We are in the process of optimizing the synthesis process and thus the results shown here are just for the purposes of illustrating the simplicity and promise of RF induction based approach.

Figure 3.2.6: Crucible with melted samples. Left sample x = -4, right sample x = +4.

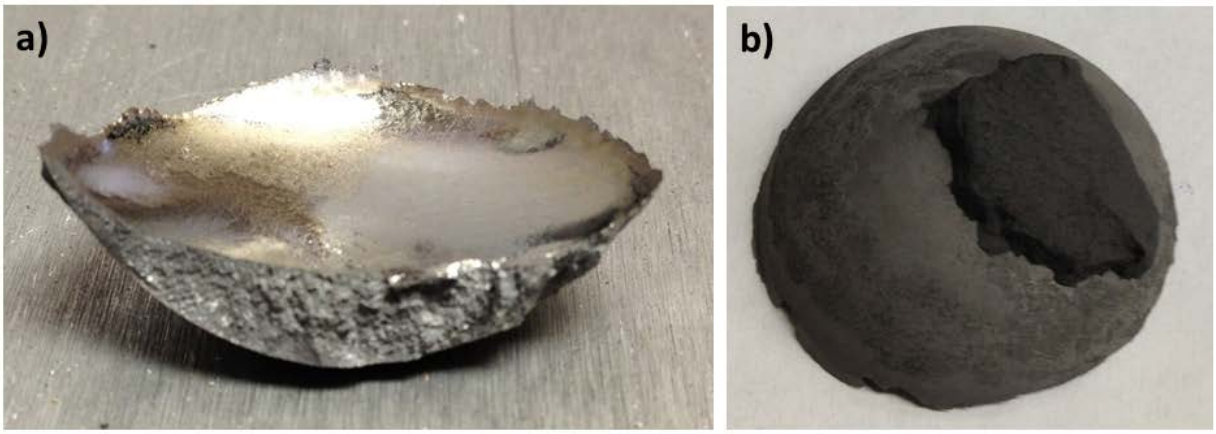

Figure 3.2.7: (a) Cross section of a specimen broken in half, (b) Specimen upside down showing piece of graphite crucible bonded on the sample.

3.2.2.2 Microstructure

Scanning electron microscope (SEM) FEI Quanta 600 FEG, Philips was used to observe the microstructure of different samples. All the samples taken from the core of the melted alloy showed dense microstructure without any significant porosity. Figure 3.2.8 shows the microstructures of fractured surfaces of representative samples (x = 0, ±3). Presence of crack on one of the sample (x = -3) is localized and appears to be produced during fracture. All the samples were found to have grain size on the order of few microns. This grain size is quite small as compared to previous reports on Ni – Ti and Ni – Ti – Cu alloys, reported to have grain size of the order of few hundred microns (Grossmann et al., 2008; Frenzel et al., 2004). This major difference in grain size can be attributed to the difference in cooling profile of the melt. We are currently optimizing the synthesis parameters and a detailed study on this subject will be published elsewhere.

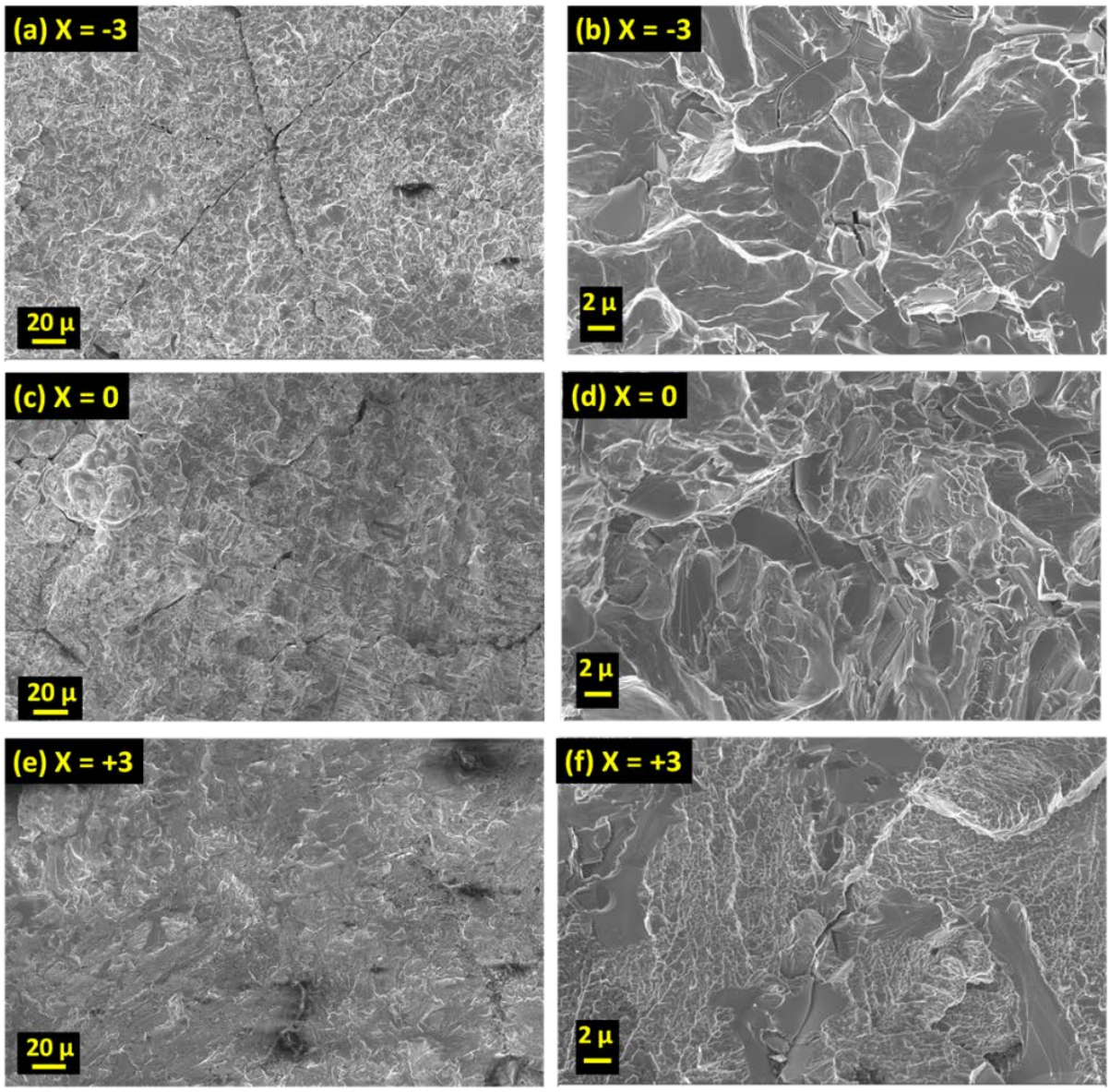

Figure 3.2.8: SEM images of various samples at different magnifications. (a) & (b) x = -3, (c) & (d) x = 0 and (e) & (f) x = +3.

3.2.2.3 Transition Temperature

The transition temperatures of the different alloys were identified from the DSC curves using the extrapolation technique as described by (Kwarciak and Marowiec, 1988). This technique is illustrated in Fig. 3.2.9 for x = -5. The transformation start temperature was taken at

the beginning of a peak and the final temperature at the end. Tangent lines were drawn from the baseline of the DSC curve to the peak. The intersection of the tangent lines is where the transformation temperature was taken. Figure 9(a) shows the DSC curves for x = 0, -1, -2, -3, -4, -5 while Fig. 9(b) shows the results for x = 0, +2, +3, +4, +5. The DSC curve for sample x = -5 shows clear peaks with A_s = 62.84ºC, A_f = 78.91ºC, M_s = 65.37ºC and M_f = 45.97ºC.

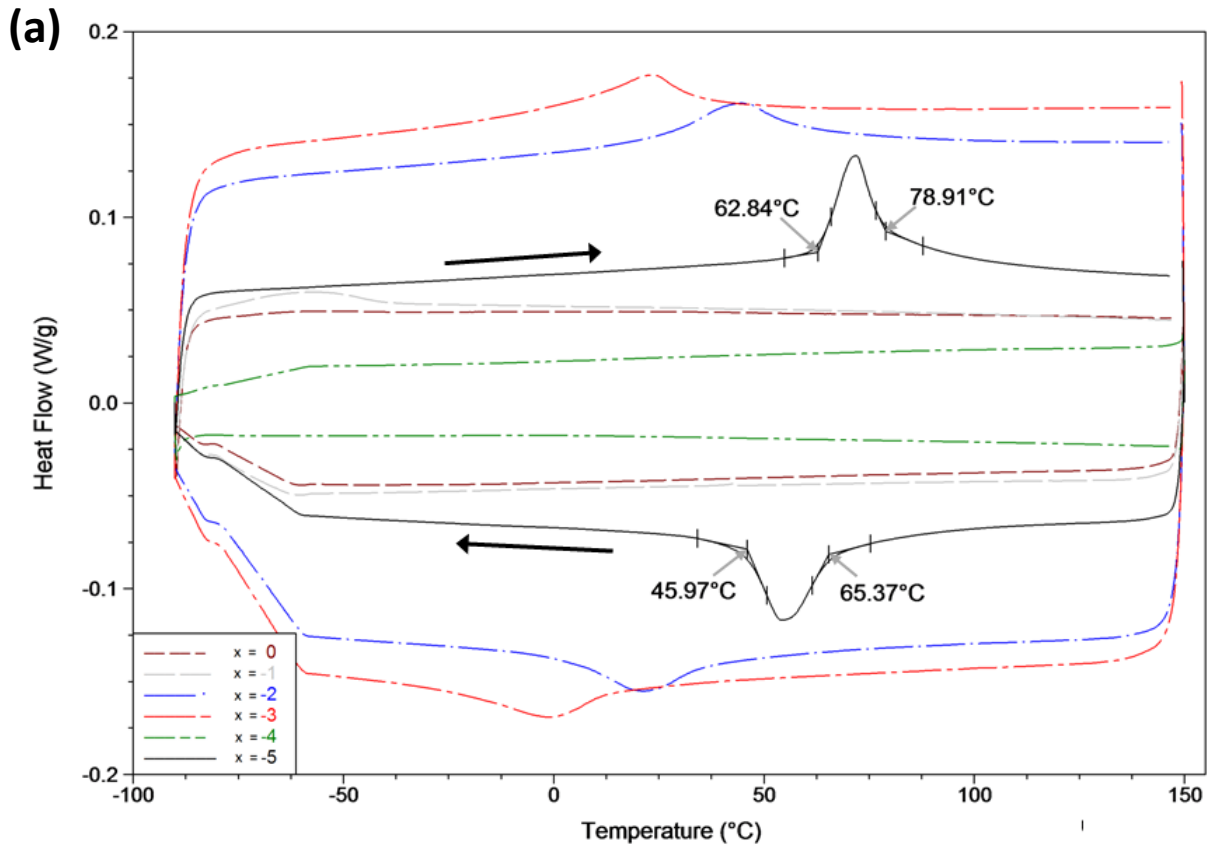

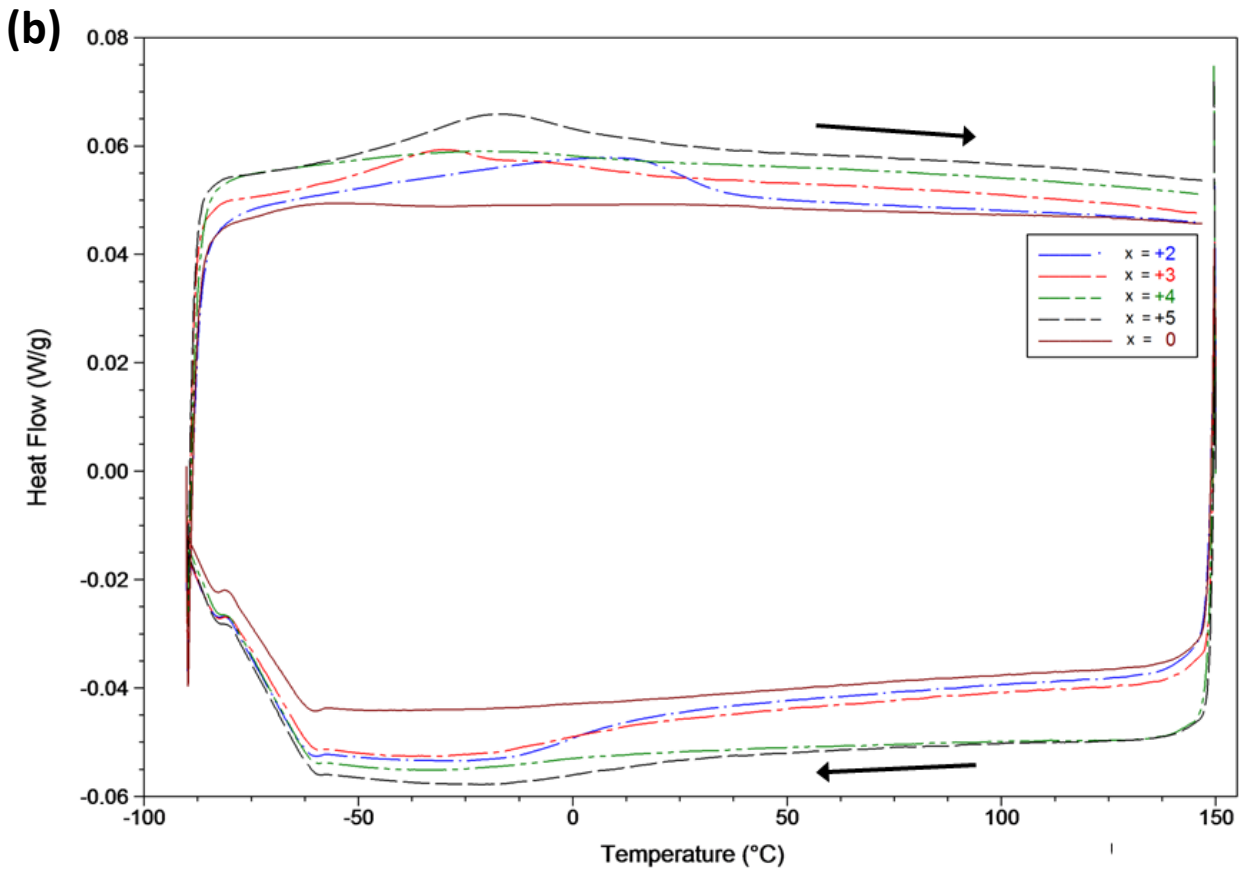

Figure 3.2.9: (a) DSC curves for $Ni_{40+x}Ti_{50-x}Cu_{10}$ (at%) and x = 0, -1, -2, -3, -4, -5. The black arrows indicate the heating and cooling directions. The transformation temperatures are labeled for x = -5. (b) DSC curves for $Ni_{40+x}Ti_{50-x}Cu_{10}$ (at%) and x = 0, +2, +3, +4, +5. The black arrows indicate the heating and cooling directions.

During quenching of melt, formation of nickel rich phases (Ti_3Ni_4 and $TiNi_3$) is a concern in Ni – Ti – Cu based alloys (Ren and Miura, 2001). These secondary phases give rise to nickel deficient matrix which influences the martensitic transformation of alloy and can alter the transition temperatures. XRD analysis is required to confirm the presence of secondary phases in our samples and this study is ongoing. We are also in the process of optimizing the melting and quenching cycle to reduce the possibility of formation of the secondary phases. The peaks for the other alloy compositions in Fig. 3.2.9 were not as prominent as that for sample x = -5, and some

of the compositions did not exhibit any peaks. If we compare the heat flow profiles of different samples, it is evident that samples having Ni > 40 at% have similar heat flow values while samples with Ni < 40 at% have abrupt values of heat flow. Absence of transformation peaks in some of the samples and discrepancy in heat flow values for different samples could be because of compositional inhomogeneity in the samples resulting due to insufficient homogenization of melt at high temperature. The transition temperatures which could be distinguished from the DSC curves are recorded in Table 3.2.1.

Table 3.2.1: Transition temperatures for the different x values based on DSC measurements.

x	**A_s**	**A_f**	**M_s**	**M_f**
-5	62.84	78.91	65.37	45.97
-4	-	-	-	-
-3	-0.7	35.26	12.02	-
-2	25.94	58.98	36.71	3.59
-1	-	-39.68	-	-
0	-	-	-	-
1	-	-	-	-
2	-30.59	36.15	-	-
3	-55.15	13.09	-	-
4	-	-	-	-
5	-50.08	17.89	-	-

The thermal hysteresis $A_f - M_f$ could only be calculated for x = -2, -5 as 55.39 and 32.94 ^oC respectively. These values are higher than expected as compared with the results from Nam et al. (1990) [16]. It is possible that the change in titanium and nickel concentration during

synthesis process could be the factor for higher thermal hysteresis. Further analysis will have to be conducted before making any conclusion.

3.3 Chapter Summary

A resistance feedback controller was developed and applied to SMA, bias spring system and BISMAC actuator. The controller operates on an input square wave which determines frequency and duty cycle and requires a threshold resistance which was determined experimentally by measuring the steady state resistance at a safe current value. The controller showed that the SMA wire was able to contract 4.56 % in 0.06 s and maintain its deformation with current of 0.2 A. The controller was also applied to a BISMAC actuator and demonstrated an improvement in contraction time of 67 % relative to using a constant I_{low} and reduced power consumption by 60 % relative to using a constant I_{hi} and still achieving a deformation exceeding the requirements for the *A. aurita* biomimetic vehicle. This controller will reduce power consumption of the UUV without compromising the deformation and cycle time. Future extension of this study will consist of improving the controller by relating SMA resistance to overall deformation by including the hysteresis and thermal model of the SMA actuators. Also, the capability of handling a more complex waveform will be added to the controller which will result in an adaptive current output.

The factors affecting the power consumption in Ni-Ti shape memory alloys were identified. It was found that power consumption can be reduced by lowering the thermal hysteresis and the phase transition temperatures. Based upon literature survey, the most effective way of lowering transition temperatures for Ni – Ti based alloys is by increasing the concentration of Ni. In the present work, alloys with composition $Ni_{40+x}Ti_{50-x}Cu_{10}$ for x = 0, ±1, ±2, ±3, ±4, ±5 were

synthesized and characterized for their phase transition temperatures by using DSC analysis. Since x = 0 sample provides a near room temperature transition temperature and low thermal hysteresis, it is desirable to understand how these factors vary with composition to produce more efficient actuators. SMA samples were synthesized by melting powders in an inductive furnace with argon atmosphere. Preliminary results show that the transition temperature decreases with the concentration of Ni. DSC curves showed a single phase transformation for samples x = -5, -3, -2, -1, 2, 3, 5 and no transformation for samples x = -4, 0, 1, 4. An in-depth composition and structural analysis of the samples is required to confirm the homogeneity of samples.

3.4 References

Buehler, W., Wang, F. (1968). A summary of Recent Research on the Nitinol Alloys and their Potential Application in Ocean Engineering. *Ocean Engng*. 1, 105-120

Daniel, T. L. (1985). Cost of Locomotion: Unsteady Medusan Swimming. *J. Exp. Biol*. 119 149-164

Bunget, G., Seelecke S., et al. (2009). Design and Fabrication of a Bio-Inspired Flapping Flight Micro-Air Vehicle. *Proc. ASME Conf. SMASIS* 2, 647-654720.

Featherstone, R. and The, Y. H. (2004). Improving the Speed of Shape Memory Alloy Actuators by Faster Electrical Heating. *Int. Symp. Experimental Robotics (ISER'04),* 18-21

Frenzel, J., Zhang, Z., Neuking, K. and Eggeler, G. (2004). High quality vacuum induction melting of small quantities of NiTi shape memory alloys in graphite crucibles. *J. Alloys and Compd.* 385, 214-223

Goldstein, D., Kabacoff, L. and Tydings, J. (1987). Stress Effects on Nitinol Phase Transformations. *J. Met.* 39(3),19-26

Grossmann, Ch., Frenzel, J., Sampath, V., Depka, T., Oppenkowski, A., Somsen, Ch., Neuking, K., Theisen, W. and Eggeler, G. (2008). Processing and property assessment of NiTi and NiTiCu shape memory actuator springs. *Mat.-wiss. U. Werkstofftech.* 39, 8

Guo, S., Fukuda, T., Asaka, K. (2003). A new type of fish-like underwater microrobot. *IEEE/ASME Trans Mechats*. 136–141

Huang, X., Liu, Y. (2001). Effect of annealing on the transformation behavior and superelasticity of NiTi shape memory alloy. *Scripta. Mat*. 45, 153-160

Kudoh, Y., Tokonami, M., Miyazaki, S., Otsuka, K. (1985). Crystal structure of the martensite in Ti-49.2 at.%Ni alloy analyzed by the single crystal X-ray diffraction method. *Inst. of Mat. Sci.* 33, 11

Kuribayashi, K. (1991). Improvement of the Response of an SMA Actuator Using a Temperature Sensor. Intern. J. Rob. Resear. 10(1), 13-20

Kwarciak, J., Morawiec, H. (1988). Some interpretation problems of thermal studies of the reversible martensitic transformation. *J. Matl. Sci*. 23, 551-557

Nguyen, B. and Kyoung, K. (2006). Position Control of Shape Memory Alloy Actuators by Using Self Tuning Fuzzy PID Controller". *IEEE ICIEA* 1-5

Ma, N., Song, G., Lee, H. (2003). Position control of SMA actuators with internal electrical resistance feedback, *SPIE Smt. Struc. Mat.* 5049

Mentz, J., Bram, M., Buchkremer, H. and Stover, D. (2006). Improvement of Mechanical Properties of Powder Metallurgical NiTi Shape Memory Alloys. *Adv. Eng. Mat*. 3, 247

Motemani, Y., Nili-Ahmadabdi, M., Tan, M., Bornapour, M., Rayagan, S. (2008). Effect of cooling rate on the phase transformation behavior and mechanical properties of Ni-rich NiTi shape memory alloy. *J. Alloy Comp*. 469, 164-168

Mukherjee, R., T. F. Christian, et al. (1996). An actuation system for the control of multiple shape memory alloy actuators. *Sensors Actuat.* 55(2-3), 185-192

Nam, T., Saburi, T., Shimizu, K. (1990). Cu-Content Dependence of Shape Memory Characteristics in Ti-Ni-Cu Alloys. *Mat. Trans. JIM*, 31(11), 959-967

Otsuka and Wayman (1998). Shape Memory Materials. Cambridge University Press, Cambridge

Otubo, J., Rigo, O., Coelho, A., Neto, C., Mei, P. (2008). The influence of carbon and oxygen content on the martensitic transformation temperatures and enthalpies of NiTi shape memory alloy. *Mat. Sci. Eng. A*, 481-482, 639-642

Raparelli, T., P. B. Zobel, et al. (2002). A robot actuated by shape memory alloy wires.: Proc. IEEE Intern. Symp. Indus. Elect. 1-4, 420-423

Ren, A., Miura, N. (2001) A comparative study of elastic constants of Ti–Ni-based alloys prior to martensitic transformation *Mat. Sci. Eng. A*, 312, 196 – 206

Shugo, Y., Hasegawa, F. and Honma, T. (1985). Effects of Copper Addition on the Martensitic Transformation of TiNi Alloy. *Bull. Res. Inst. Min. Dressing Metall. Tohoku Univ.* 37(1), 79-88

Smith, C., Villanueva, A., Joshi, K., Tadesse, Y. and Priya, S. (2011). Working principle of Bio-Inspired Shape Memory Alloy Composite actuators. *IOP Smart Mat. Struct.* 20, 012001

Song, G. B., N. Ma, et al. (2007). Position estimation and control of SMA actuators based on electrical resistance measurement. *IOP Smart Struct. Syst.* 3(2), 189-200

Tadesse, Y., Thayer, N. and Priya, S. (2010). Tailoring the Response Time of Shape Memory Alloy Wires through Active Cooling and Pre-stress. *J. Int. Mat. Syst. Struct.* 21

Teh, Y. H. and R. Featherstone (2008). An architecture for fast and accurate control of shape memory alloy actuators. Intern. *J. Robot. Res.* 27(5), 595-611

Villanueva, A., Joshi, K., Blottman, J., Priya, S. (2010). A bio-inspired shape memory alloy composite (BISMAC) actuator. *IOP. Smart Mat. Sturct*. 19, 025013

Villanueva, A., Smith, C., Priya, S. (2011). Biomimetic Robotic Jellyfish (Robojelly) using Shape Memory Alloy. *IOP Bioinspir. Biomim.* 6, 036004

Villanueva, A., Bresser, S., Chung, S., Tadesse, Y. and Priya, S. (2009). Jellyfish inspired underwater unmanned vehicle. *Proc. SPIE* 7287

Wang, Z., Hang, G. W. and Li, Y., Du, J., Wei (2008). Embedded SMA wire actuated biomimetic fin: a module for biomimetic underwater propulsion, *IOP, Smart Mat. Struct.* 17,025039

Webb, G., Wilson, L., Lagoudas, D. C. and Rediniotis, O. (2000). Adaptive control of shape memory alloy actuators for underwater biomimetic applications. *AIAA J.*, 38(2), 325-334

Yamauchi, K., Ohkata, I., Tsuchiya, K., Miyazaki, S. (2011). Shape memory and superelastic alloys: Technologies and applications. *Woodhead Publishing in Materials*

Yang, Y., Ye, X., Guo, S. (2007). A New Type of Jellyfish-Like Microrobot Proceeding of the *IEEE Intl. Conference on Integ. Tech.*

Zarinejad, M. and Liu, Y. (2008). Dependence of Transformation Temperatures of NiTi-based Shape-Memory Alloys on the Number and Concentration of Valence Electrons. *Adv. Funct. Mater.* 18, 1–6

Chapter 4

Robojelly Design, Performance and Control

Unmanned underwater vehicles (UUVs) serve a valuable function in monitoring of animals, humans, and environmental activity. Several applications can be cited for small UUVs including monitoring of ocean currents and chemical agents, study of animal migration, depth measurements, and military functions. Current technologies deployed for many of these applications suffer from practical limitations including cost-effectiveness, lifetime, and range. Buoys deployed in ocean environments are normally tethered and thus have limited operation range. The typically passive, distributed, battery operated wireless sensor nodes are not desirable as they have limited station-keeping capability and fixed lifetime. Large vehicles such as submarines and boats require high operating costs. These large vehicles can also be intrusive to the natural habitat and disturb the course of the local environment.

The goal of this chapter was to develop an unmanned vehicle that is capable of conducting autonomous surveillance over large distances for extensive periods of time. The strategy adopted to accomplish this goal was to implement methods of underwater propulsion found in biological species. Nature is comprised of a variety of animal designs that show promise for surveillance of underwater environments. They can be mobile and small with various sensory functions, networked as nodes with other units, as well as possess adaptability, maneuverability, and intelligence. Out of the broad range of choices, jellyfish were selected due to attributes such as their ability to consume little energy owing to a lower metabolic rate than other marine species (Seibel and Drazen 2007), survivability in varying water conditions, and possession of adequate morphology for carrying payload. Jellyfish inhabit every major oceanic area of the world (Cook

2010) and are capable of withstanding a wide range of temperatures and salinities (Arai 1997). Most species are found in shallow coastal waters, but some have been found in depths of 7,000 meters (Kramp 1959). Furthermore, jellyfish are found in a wide variety of sizes ranging from a few millimeters to over 2 meters in diameter (Omori and Kitamura 2004) as well as display a multitude of shapes and colors. They have the ability to move vertically but depend mainly upon ocean currents for horizontal movement (Cook 2010). They possess an elementary nervous system, which consists of receptors capable of detecting touch, light, inclination, and other stimuli (Arai 1997).

Using the BISMAC actuators described in Chapter 2 and rapid controller described in Chapter 3, a bio-inspired robotic jellyfish named Robojelly was designed, fabricated and characterized. This robot was designed based on the morphology and functionality of *Aurelia aurita*. It uses BISMAC actuators to achieve the kinematics of*A. aurita*. An interaction between the starting and stopping vortices is the foundation for the *A. aurita* mode of propulsion. It is therefore desired for the robotic vehicle to replicate these hydrodynamic structures in order to achieve the same performance as the natural animal. Section 4.1 is dedicated at explaining the design of the Robojelly and its performance. Section 4.2 goes into characterizing the kinematics of the vehicle as well as the implementation of a rapid heating controller. The controller allows the optimization of control parameters for a better performance.

4.1 Biomimetic Robotic Jellyfish (Robojelly)

Aurelia aurita (Linnaeus, 1758) is a species of Scyphozoa found in oceans around the world. The medusa is the adult stage in its life cycle which is commonly referred to as a

"jellyfish". Jellyfish can be separated into two categories based on their propulsion mechanism. These categories consist of "jetters" which exhibit relatively proficient propulsion and "rowers" which are more efficient swimmers (Ford and Costello 2000, Sahin et al. 2009). Jetting propulsion consists of water being squeezed out of the bell due to a decrease in volume. On the other hand, rowing propulsion relies on the interaction between starting and stopping vortices that allow a greater body of water to be displaced and therefore produce more thrust (Colin and Costello 2002). For this reason, rowers can reach much bigger dimensions. *A. aurita* are rowers which use circular muscles located in their subumbrella for locomotion (Chapman 1999). When the subumbrella muscles undergo a deformation cycle (contraction followed by passive relaxation), water flows out of the bell resulting in the formation of a stopping vortex and a starting vortex which are essential to achieve high efficiency (Dabiri et al. 2005). The bell diameter for *Aurelia* usually ranges between 5 and 26 cm (Dawson 2003). As discussed later in this chapter, there are several structural features which also have significant influence on the propulsive efficiency of the jellyfish.

4.1.1 Underwater Vehicle Design

The vehicle design was initiated by understanding the physical characteristics of *A. aurita*. The actual geometry of *A. aurita* was replicated by processing experimental results made available from biologist Dr. J. Costello, Providence College. Images from videos of the actual animal were digitized to obtain the bell profile, see Figure 4.1.1(a) and (b). *A. aurita* can be assumed as axis-symmetric. Therefore, a cross-section of the bell can be used to digitally recreate the full bell geometry. In order to match the performance of the natural medusa with

Robojelly (Figure 4.1.1(c)-(d)), we paid particular attention in quantifying the bell deformation over a full cycle. The actuation cycle was controlled by modifying the non-linear displacement of BISMAC actuators through a feedback controller. Jellyfish are limited in actuation power due to single cell layer muscles that provide all the thrust for the animal (McHenry 2007). High energy density, low-profile BISMAC actuators can be used to achieve an optimum combination of displacement and force generation for mimicking jellyfish bell deformation.

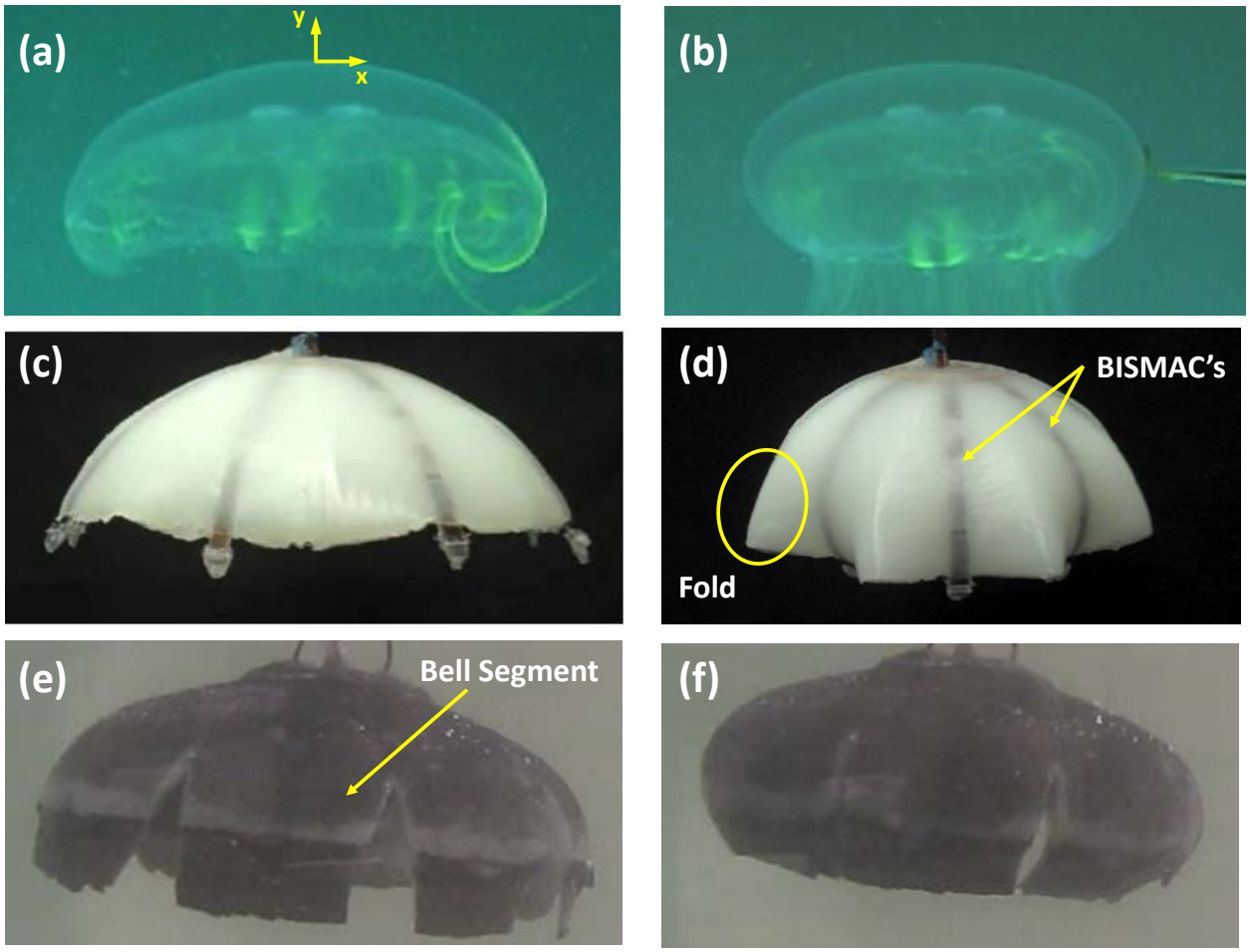

Figure 4.1.1: Natural *A. aurita* shown during a dye test in (a) relaxed, and (b) contracted state. Robojelly in the (c) relaxed state, and d) contracted state showing the folding effect and location of BISMAC actuators. Segmented Robojelly with flap in the (e) relaxed state showing bell segments, and in the (e) contracted state. Natural animal images (a) and (b) were provided by Dr. Jack Costello at Providence College. (a) shows the coordinate system used throughout this work. The coordinates are (0,0) at the bell apex.

4.1.1.1 Medusa Features

Table 4.1.1 shows various design parameters of the Robojelly vehicle. A bell dimension of 164 mm was chosen for the design of Robojelly which is within the range of naturally occurring *Aurelia*. During swimming, a medusa contracts its subumbrellar muscles reducing bell diameter and ejecting water. The *A. aurita* deforms its bell by about 50 % of the initial radius at the margin (Villanueva et al. 2010a). This means its circular muscles must contract by approximately the same magnitude. Consequently, this also implies that we cannot replicate the *A. aurita* swimming mechanism by simply replacing the circular muscles with current SMA wire technology due to their limited contraction capability. An alternate method for mimicking the muscular deformation of *A. aurita* was required and is a complex task due to the large overall magnitude of deformation.

Table 4.1.1: Robojelly vehicle parameters and their respective values.

Parameters	Values
Bell Diameter (mm)	164
Mass – Uniform bell (g)	235
Mass – Segmented bell (g)	242
Mass – Flap (g)	10
Volume (cm^3)	200
Float volume (cm^3)	11.8
Electrical resistance (Ω)	78

The *A. aurita* and *Polyorchis montereyensis* species use circular muscles for their propulsive locomotion. Circular muscles are distributed in a circular fashion throughout the subumbrella while radial muscles start at the apex of the subumbrella and run toward the bell margin. The *Polyorchis montereyensis* uses radial muscles to achieve tasks requiring larger deformations such as bringing captured food from the tentacles to its mouth (Satterlie et al. 2005). The *Cyanea*

capillata uses a combination of circular and radial muscles during its swimming stroke (Gladfelter 1973). Circular muscles are used for the first 30 to 45 degrees of bell contraction while radial muscles help with contraction up to 90 degrees. These contractions are achieved by muscle shortening of 20 to 25%. The contraction mechanism of the circular muscles is simple; as they shorten, the bell diameter decreases. The radial muscles undergo a more intricate process to create the deformation. The buttress is a region of the bell above the radial muscles. When the radial muscles actuate, the buttress resists axial deformation and induces a bending deformation, see Figure 4.1.2(a). This principle is also the underlying mechanism of BISMAC actuators where the buttress is replaced by spring steel, mesoglea by silicone, and muscles by SMA wires, see Figure 4.1.2(b).

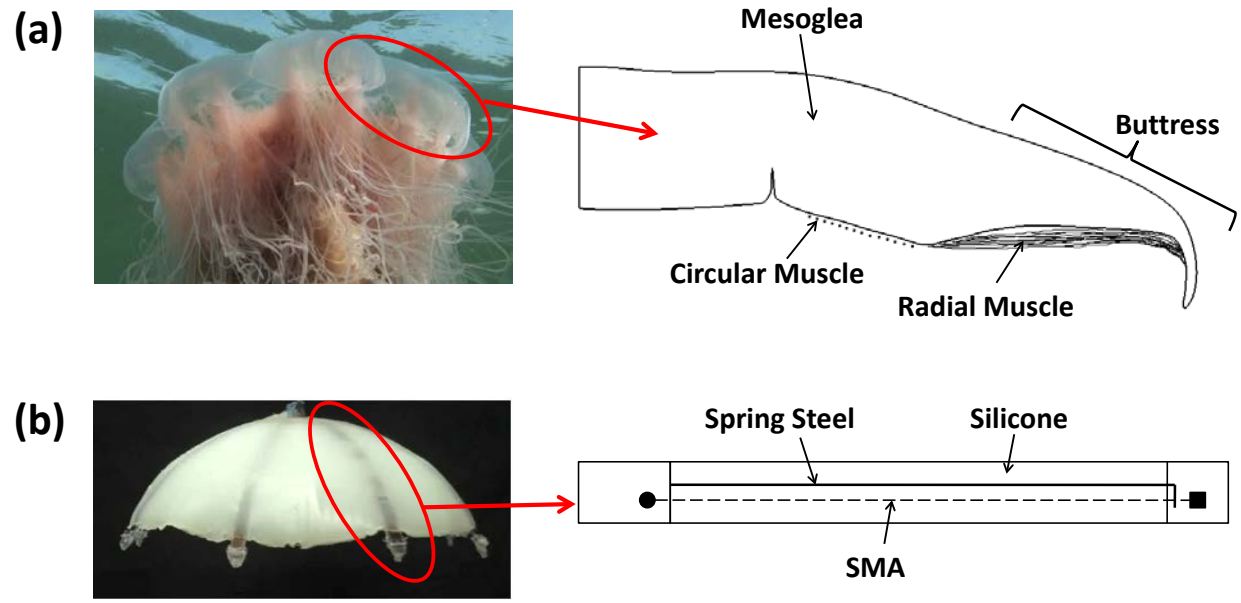

Figure 4.1.2: (a) Half bell cross-section of a *C. capillata* at the perradius. The *C. capillata* image is courtesy of Dr. Jack Costello at Providence College and the bell schematic was redrawn from (Gladfelter 1973). (b) Robojelly image and BISMAC actuator schematic (Villanueva et al. 2010a).

Jellyfish utilize a passive mechanism to regain the original bell profile after contraction (Gladfelter 1972). The passive mechanism relies on elastic energy stored in the bell. In the case of *C. capillata* during contraction, the mesoglea is compressed only slightly axially. Instead, the mesoglea is mostly relocated between the exumbrellar and subumbrellar epidermises. Upon mesoglea relocation, a thickening of the bell occurs which causes micro fibrils anchored across the exumbrellar and subumbrellar epidermises to elongate (Gladfelter 1972). These fibrils poses a high modulus of elasticity and are highly resilient which allows them to store the elastic energy required to return the bell to its relaxed state. The mesoglea relocation is controlled by an anatomical feature called joints. The joints are indentations in the mesoglea which allow the surrounding material to fold more easily at these locations. These joints are observed at various locations throughout the bell depending on the species. For example, *P. montereyensis* has apical joints located at the inner portion of the top of the bell which allows bending of the entire bell wall. The adradial joints are located through the length of the bell at four different locations and allow relocation of the mesoglea over the circumference of the bell (Gladfelter 1973).

4.1.1.2 Robojelly Design

The approach taken for the Robojelly design was to replicate the most important features related to the morphology and kinematics of the *A. aurita*. Some features had to be approximated due to limited amount of information available for *A. aurita* and limitations of current technology. The circular propulsion muscles of *A. aurita* could not be mimicked directly by SMA wires due to the required deformation of 44 % for the specimen observed in this study. SMA wires can only achieve 4 % strain. Thus another mechanism had to be used to achieve the

required deformation. BISMAC actuators have shown the capability to achieve deformations which exceeds the requirements of the *A. aurita* (Chapter 2) and were chosen to serve as propulsion actuators for Robojelly. These actuators are flexible and provide high curvature which can easily be tailored. The high power density of SMA provides an overall non-intrusive geometry which blends very well in the *A. aurita* body.

Robojelly consists of a silicone matrix bell. It has eight BISMAC actuators embedded inside the silicone which are radially distributed around the bell as seen in Figure 4.1.1(d). The eight BISMAC actuators were arranged to function as a single system converging at the central mount. The mount acts as a clamp for BISMACs and also serves the purpose of housing the electronic circuitry. The bell geometry was retrieved from *A. aurita* in the relaxed position, Figure 4.1.1(a). The cross-section was fully digitized by taking advantage of the axi-symmetric and transparent traits of the *A. aurita*. The vehicle bell design was separated into two components: active and passive. In Chapter 2, the *A. aurita*'s bell kinematics was presented and showed that the deformation profile of jellyfish consists of a "passive" region referred to as "flap" which does not actively take part in the actuation and an "active" region which drives the swimming motion. The two regions are separated by the "inflexion point" which is located approximately 91% of the subumbrellar arclength from the bell apex. This measurement was based on a qualitative analysis of the deformation profile during swimming. The bell at the location of the inflexion point deforms 44 % of the initial radius while the bell margin deforms 51 %. These results are for the specimen used in this study and will vary depending on the specimen. The exact variation of this parameter is not reported in literature for *A. aurita*.

Spring steel of 0.05 mm thickness and 0.6 mm width were used in the construction of the BISMAC actuators. Figure 4.1.2(b) shows the configuration of a BISMAC actuator. The SMA

wires used in this study are Biometal Fiber 100 (100 μm in diameter). A total of four Biometal Fiber wires were used in each actuator, two wires constitute one set and there are a total of two sets. Each set was physically positioned in parallel and are electrically connected in series. Furthermore, the eight individual actuators were all connected in series around the bell. This allows for an even current distribution across all SMA wires and provides a synchronized contraction of the bell. The passive relaxation mechanism design was also replicated from jellyfish. No actuators were used to regain the original bell position after contraction. Instead, this was done by molding the bell in the relaxed configuration. Upon actuation, the silicone and spring steel structure undergoes bending and stores elastic energy, similar to the micro fibrils, which is released during bell relaxation. Natural jellyfish are neutrally buoyant since most of their body mass is water. This feature was replicated in Robojelly by compensating for the excess weight with low density extruded polystyrene foam embedded inside the bell.

Adradial joints were integrated in the bell design to reduce material compression and to induce a localized fold (Smith and Priya 2010). To our knowledge, joint geometry is not available in literature for *A. aurita*. For this reason, Robojelly's joint geometry was inspired by the adradial joints of *P. montereyensis*, see Figure 4.1.3. The joints were scaled to the proper bell diameter and the geometry was kept the same.

The BISMAC design used for construction of Robojelly varies from the ones characterized in Chapter 2. The actuators have an initial curvature as required by the relaxed *A. aurita* bell profile. Besides this initial curvature, they follow a similar design as the VSSS-BISMAC. The silicone thickness varies along the length and the SMA wires were kept at a constant distance under the spring steel. Figure 4.1.4 shows the internal structure of the Robojelly. The cross-section shows the spring steel location inside the silicone.

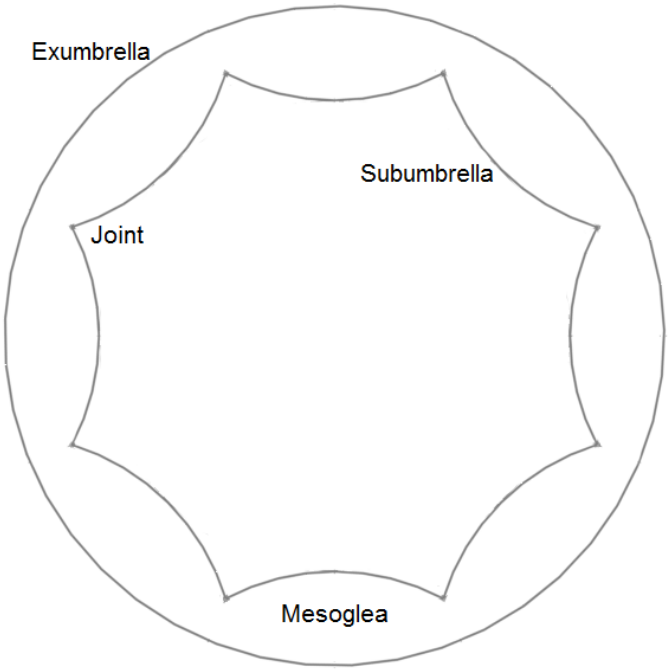

Figure 4.1.3: Schematic of adradial joint geometry used for Robojelly. This is a bell cross-section at distance of 2 cm from the bell margin.

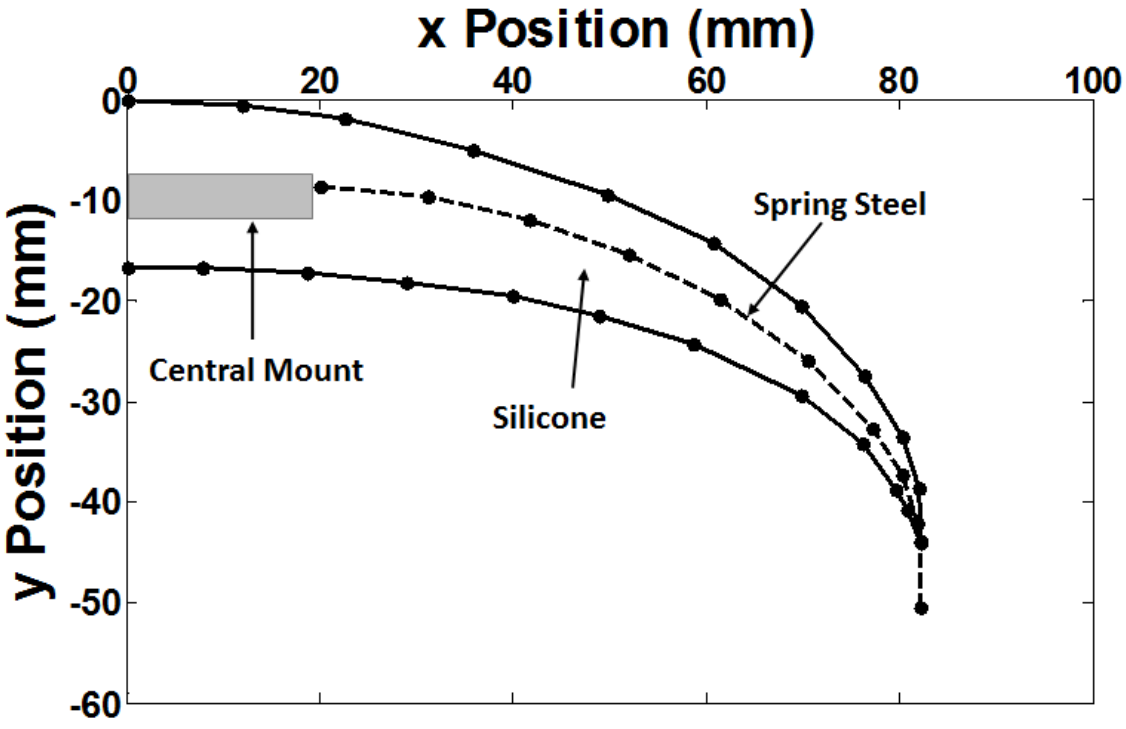

Figure 4.1.4: Cross-section of the robotic bell at the location of BISMAC actuator. The location of the central mount inside silicone is shown along with the location of spring steel. The silicone profile is taken from the natural *A. aurita*. It should be noted that the spring steel extends past the edge of the silicone by 6 mm at the bell margin.

4.1.1.3 Fabrication of Robojelly

The concept of BISMAC actuators was extended to the hemi-elliptical geometry of the *A. aurita*. This was done by joining actuators at a central mount. This central mount is located towards the bell apex. This part of the jellyfish hardly goes under any deformation making it a good location for the mount. Another issue encountered was the required initial curvature of the structure. The *A. aurita* has a curved relaxed profile, Fig. 4.1.4. The BISMACs had to be molded in this curved configuration which meant that the SMA wires would not be under tension as they are when molding linear BISMACS. Small plastic pieces were used to guide the SMA wires along the curved profile Fig. 4.1.6(a). The guides were anchored on the spring steel using a slit made in the guides. The guides put the SMA wires in the proper configuration and help in holding them in position during molding. These concepts along with radial joints were integrated in a replica of the *A. aurelia* geometry shown in Fig. 4.1.5 using a fabrication technique developed by C. Smith described in Villanueva et al. 2011.

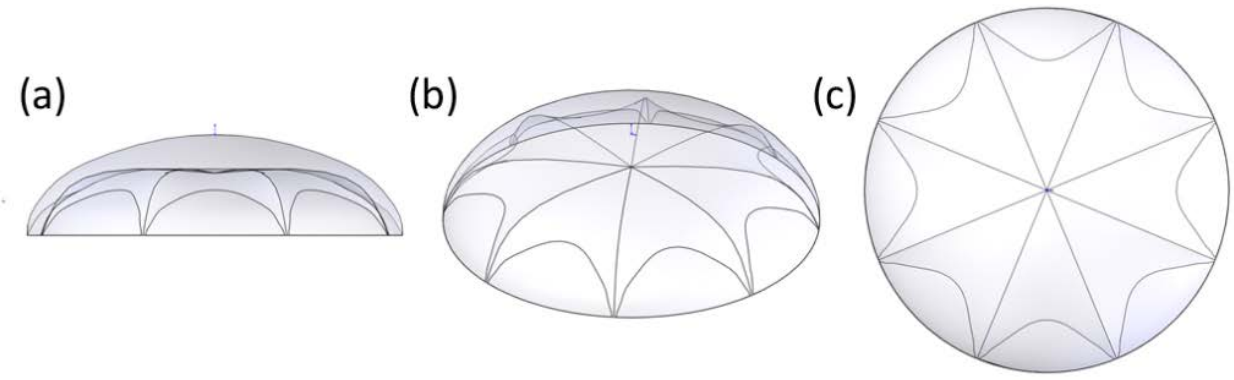

Figure 4.1.5: CAD drawing of Robojelly without internal structure showing the (a) front, (b) trimetric, and (c) top view. This figure was developed by C. Smith (Villanueva et al. 2011).

The fabrication of Robojelly consists of a multistep molding process. The first step was to assemble the internal structure consisting of BISMACs, the central mount and SMA guides as shown in Fig. 4.1.6(b). Once assembled, the internal structure was put on a plastic mold which is filled with soft 00-10 Ecoflex silicone (Smooth-On) as shown in Fig. 4.1.6(b) and (c).

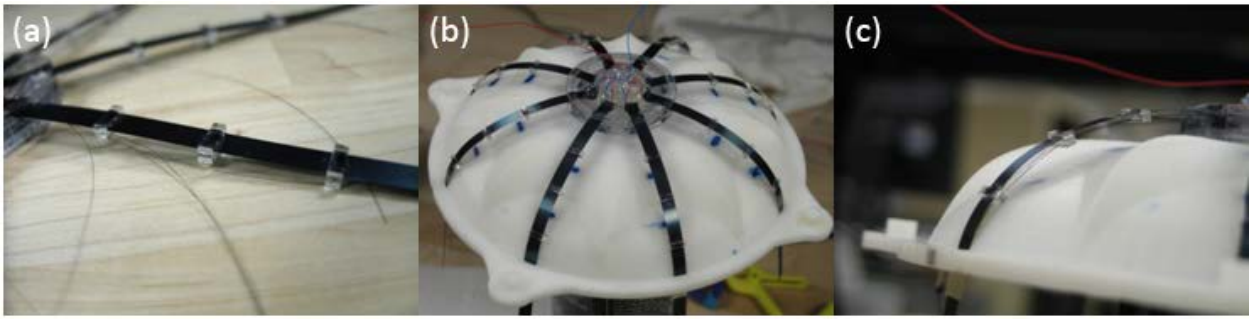

Figure 4.1.6: (a) SMA wires being threaded through the plastic guides. (b) Completed internal structure set on the plastic mold. (c) Side view of BISMAC with plastic guides. Also showing the internal structure anchored to the plastic mold. This figure was developed by C. Smith (Villanueva et al. 2011).

4.1.1.4 Neutral Buoyancy, Flap and Bell Segments

A. aurita is neutrally buoyant which is a desired feature for Robojelly. The buoyancy was kept close to zero by adding a piece of polystyrene foam in the bell. Two pieces of polystyrene foam 5 mm in thickness and 45 mm in diameter were used to achieve the neutrally buoyant condition. One disc was inserted at the bell apex and the other directly parallel to the subumbrella as shown in Figure 4.1.7. These locations were chosen because they would not affect the motion of the vehicle due to the limited amount of deformation occurring in these areas during actuation. The floats were made into two pieces to bring the center of buoyancy as close as possible to the center of mass, yet still above it. This improves maneuverability while keeping the vehicle stable in an upright position.

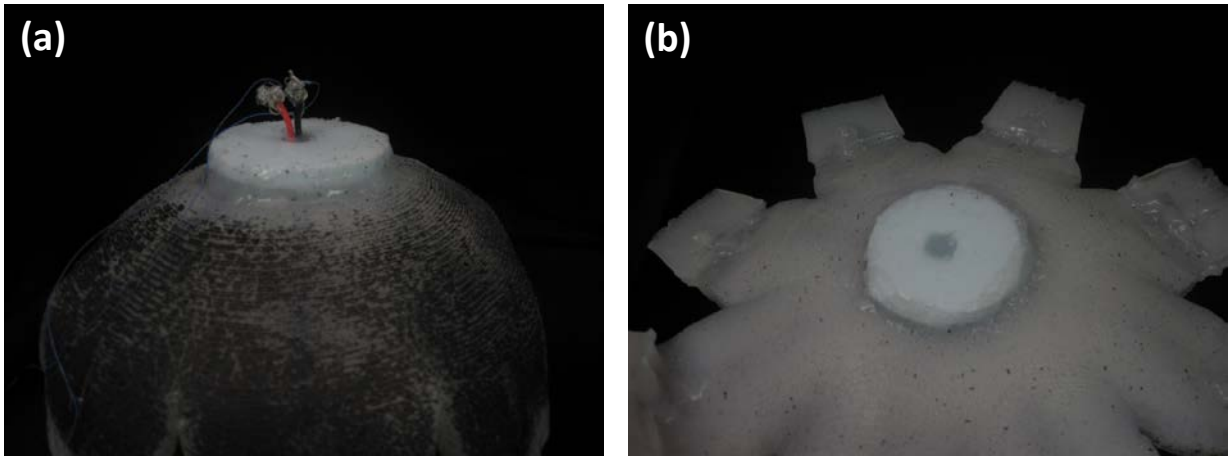

Figure 4.1.7: Robojelly in air showing (a) apex float and the (b) subumbrella float. The float is made out of Styrofoam and is sealed to the Robojelly using silicone.

The passive flap was added to the vehicle in a subsequent molding step. The flap design was taken directly from the same natural specimen digitized for the bell geometry. The flap of the natural specimen was 9 % of the active subumbrella length. The Robojelly flap was made 18% of the active subumbrella length to account for the added stiffness coming from the terminal connection and to allow proper flexibility. The active subumbrella refers to the subumbrellar region which is part of the active section of the bell. Silicone was poured into a mold which had the desired flap geometry. Robojelly was then placed on top of the mold while silicone cured and bonded to the rest of the bell margin. The passive flap can be interchanged with multiple geometries or silicone formulations by cutting out the old one and repeating the flap molding process.

One of the configurations for the bell used a biological trait found in *C. capillata*. *C. capillata* has a segmented bell structure as opposed to the continuous bell found in most medusa. The segmentations result in eight individual parts which can be actuated independently. Segmentation was achieved by cutting sections of the bell between actuators after the curing process. The bell

cutouts were proportional to the bell deformation which is exponential. More material was removed at the margin and less material centripetally until halfway up the umbrella. This can be seen in Figure 4.1.8(b) and (c) along with the other Robojelly configurations.

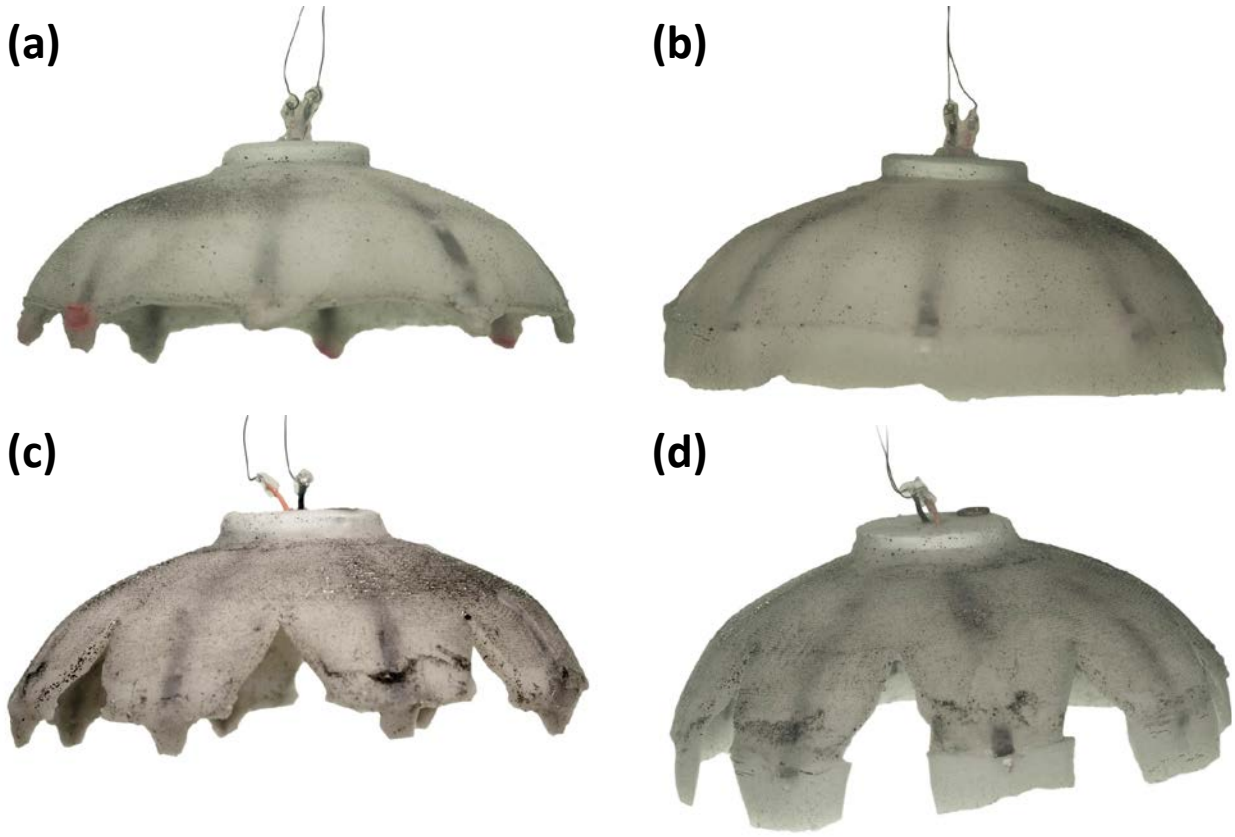

Figure 4.1.8: Robojelly in various configurations: (a) Uniform bell with no flap, (b) Uniform bell with flap, (c) Segmented bell no flap, (d) Segmented bell with flap. In all configurations Robojelly is in relaxed and underwater condition.

4.1.2 Methods

4.1.2.1 Profile Deformation

Bell deformation underwater was measured by clamping the vehicle. The vehicle was positioned on a flat surface which was small enough that it did not obstruct bell deformation. The bottom float on the subumbrella was resting on a cylindrical support. Similarly, a cylindrical support was applied on the top float of the vehicle clamping it down to the bottom support, see Figure 4.1.9. Bell deformation was tracked by positioning the specific part of the bell perpendicular to a digital camera located at a distance of 80 cm. Pins with small beads attached at the head were inserted in the silicone to a depth of 1-2 mm. The initial bead position and the location where the pin intersected the silicone (silicone surface) were recorded. After deformation, the location of the bead and a point on the pin shaft were recorded. The bead and pin angle are used to solve for the position of the silicone surface using the pin length in the relaxed configuration. This method was used since bell folds or other bell segments obstructed the location of interest during contraction. The deformation profiles were recorded both on the BISMAC surface and at fold locations for all configurations.

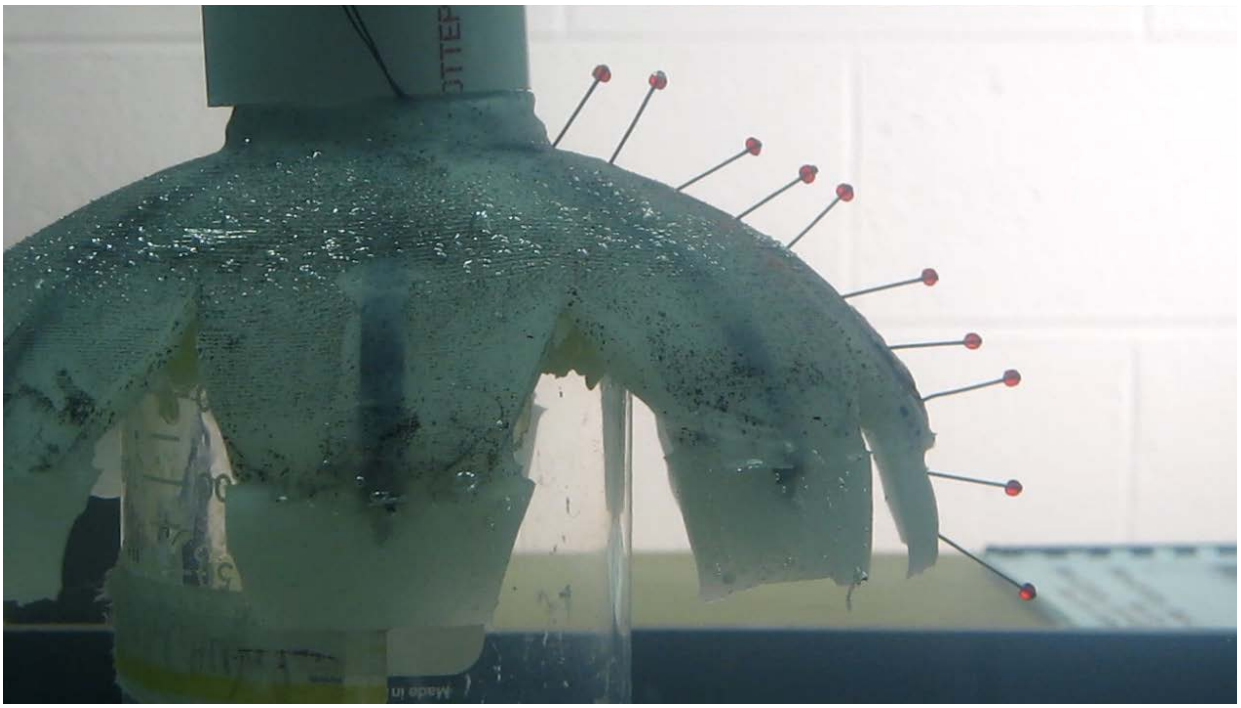

Figure 4.1.9: Deformation test setup showing the Robojelly segment with flap in water. The Robojelly was clamped from top and bottom and pins with beads were used to track the deformation profile.

4.1.2.2 Swimming Test and Operating Parameters

The vehicle performance was analyzed by tracking its position over time by using a high speed camera (Fastec Imaging IN250) operating at 60 FPS. The bell centroid was tracked by using a software developed in MATLAB which uses high contrast images as shown in Fig. 4.1.10.

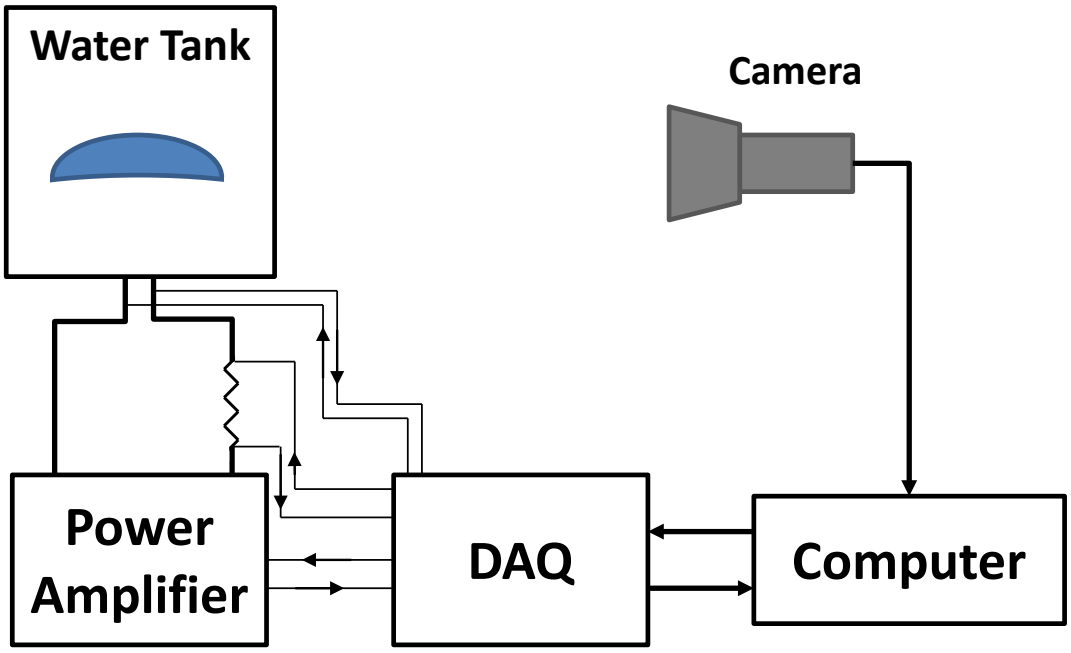

Figure 4.1.10: Schematic of the test setup for characterizing Robojelly during vertical swimming test.

Details on the image processing algorithm can be found elsewhere, see (Villanueva et al. 2010a, Villanueva et al. 2009). Shape memory alloy actuation was controlled as a function of input current, the higher the current amplitude, the faster the SMA contraction. A rapid heating controller described in Chapter 3 was used to actuate the Robojelly segments. The controller sends a high current impulse for the initial contraction. Once the actuators were fully contracted, a low current maintained this deformation. SMAs undergo a resistance change upon contraction which was used as feedback to determine the contraction state of the wire. A threshold resistance was set at 80 % of the original resistance and the following decision was made:

$$R_{SMA}\begin{cases} > R_t, \ I_d = I_{high} \\ \leq R_t, \ I_d = I_{low} \end{cases}, \tag{4.1.1}$$

where R_{SMA} is the SMA resistance, R_t is the threshold resistance, I_d is the desired current, I_{high} and I_{low} are the high and low current amplitudes. This controller allows for fast contraction and minimal power consumption (Villanueva and Priya 2010). A data acquisition system from National Instruments (NI cDAQ 9172) was used to monitor the state of the circuit and to send the output. The controller software was developed in LabView. The card output was amplified by a power amplifier (NF HAS 4052) and the vehicle was tested in an aquarium of dimensions 122 cm x 46 cm x 51 cm with tap water at 22^0C (Figure 4.1.10).

The vehicle was operated at a frequency of 0.5 Hz and a duty cycle of 35 % which refers to the cycle percentage at which the bell is contracting. These values were found to produce the best performance for the segmented bell configuration in (Villanueva et al. 2010b). A duty cycle of 35 % corresponds approximately to a 1:2 contraction to relaxation ratio which is consistent with the *A. aurita* specimen used in this research and is within the usual range for this species (Costello and Colin 1994, McHenry and Jed 2003, Bajcar et al. 2009). The actuation frequency varies with size but the data for *A. aurita* of the same dimension as that of Robojelly is not available and variation of actuation frequency as a function of size has not been reported. *A. aurita* of the same dimensions as Robojelly would have a mass of approximately 200 g. extrapolating the trends found by McHenry and Jed (2003) leads to a predicted frequency of 0.2 Hz which is a close match and reflects the similarities between the robot and natural animal.

4.1.2.3 Thrust

The method chosen to approximate the thrust production of Robojelly combines a theoretical model and experimental measurements. The theoretical model was based on techniques developed for jetting jellyfish by Daniel (1983). An attempt at adapting this method

to rowing medusae, particularly *A. aurita*, was made by McHenry and Jed (2003). They considered that the thrust produced by jetting includes the effect of flapping. The results showed that the effect of flapping was negligible and therefore this effect was not considered in this study. Though this method is a crude way of approximating the thrust production, it provides a good method of comparison between each vehicle configuration. This thrust calculation method was utilized in (Villanueva 2010b) and is reiterated here for clarity. Thrust was calculated by using the following equation:

$$T + D + F + G + F_b + W = 0, \tag{4.1.2}$$

where T is the net useful thrust produced by the vehicle, D is drag, F is the vehicle change in momentum, G is the acceleration reaction of the fluid, F_b is the buoyancy force on the vehicle, and W is the vehicle weight. The vehicle weight is defined as: $W = -g \cdot m$, where g is gravity and m is the vehicle mass. We define the individual force components for the vehicle moving in the y-direction. Drag was calculated using the following equation (Batchelor 1967):

$$D = -0.5 c_{bell} \rho_w s_{bell} u^2, \tag{4.1.3}$$

where u is the vehicle instantaneous velocity in the y-direction, c_{bell} is the drag coefficient taken as 0.42 for $u > 0$ and 1.17 for $u < 0$ (Hoerner 1965), ρ_w is the water density, s_{bell} is the instantaneous projected bell area given as $s_{bell} = 0.25\pi d^2$, and where d is the bell instantaneous diameter. The drag coefficients are determined for a three dimensional hemisphere. The change in momentum was calculated using the following equation:

$$F = -m\frac{\Delta u}{\Delta t}. \tag{4.1.4}$$

The acceleration reaction force was calculated using the following equation (Batchelor 1967):

$$G = -\alpha\rho_w V\frac{\Delta u}{\Delta t}, \tag{4.1.5}$$

where α is the added mass coefficient and V is the subumbrellar cavity volume. The shape of Robojelly can be approximated as a hemiellipsoid with internal cavity. The cavity volume is then defined as (Daniel 1983):

$$V = \pi d^2 h_{cav}/6, \tag{4.1.6}$$

where h_{cav} is the cavity height. The added mass coefficient of Robojelly was approximated as (Daniel 1983, Daniel 1985, McHenry and Jed 2003):

$$\alpha = \left(\frac{h}{r}\right)^{-1.4}, \tag{4.1.7}$$

where h and r are the instantaneous bell height and radius respectively. This added mass coefficient was determined from experimental results for hemiellipsoids. The weight of the vehicle and the buoyancy force varies from one run to another and can have a drastic effect on the performance of the vehicle. The difference of these two forces was calculated by using the following expression:

$$F_b + W = -F_s - D_s - G_s, \tag{4.1.8}$$

where the subscript, s, refers to the state of sinking before actuation. The value of $F_b + W$ was assumed to be constant throughout a run and was measured experimentally.

4.1.3 Results

4.1.3.1 Profile Deformation

Upon actuation, the Robojelly BISMAC actuators curve inwards and the passive membrane attempts to follow the curvature. Since actuators are only present at eight locations in the bell, the remaining membrane does not follow the BISMAC curvature completely. Instead, there is a folding effect occurring between the actuators, see Fig. 4.1.1(d). This phenomenon is not present in the natural *A. aurita* because its circular muscles cover the entire circumference of the subumbrella. During contraction every part of the bell is pulled inward instead of only along eight strips as in the Robojelly. This affects the deformation profile as shown in Fig. 4.1.11. Each deformation profile presented was taken during the 25^{th} cycle at the end of the contraction phase. This was done so that the actuators had time to reach a thermal steady state. The cycle number was determined by experimental cycle tests and it was found that the BISMAC thermal steady state for the given geometry and water conditions occurs at around 20 cycles (Villanueva et al, 2010a and 2010b). A transient phase occurs until the actuators reach a thermal steady state. The exumbrellar (surface) profile of Robojelly was measured over a BISMAC actuator which represents the location of greatest deformation. It was also measured over a joint which represents the location of smallest deformation. The deformation was recorded over the BISMAC and fold locations for the uniform and segmented bell configurations. Folds of the segmented bell are shorter in length because bell cutouts were removed at those regions.

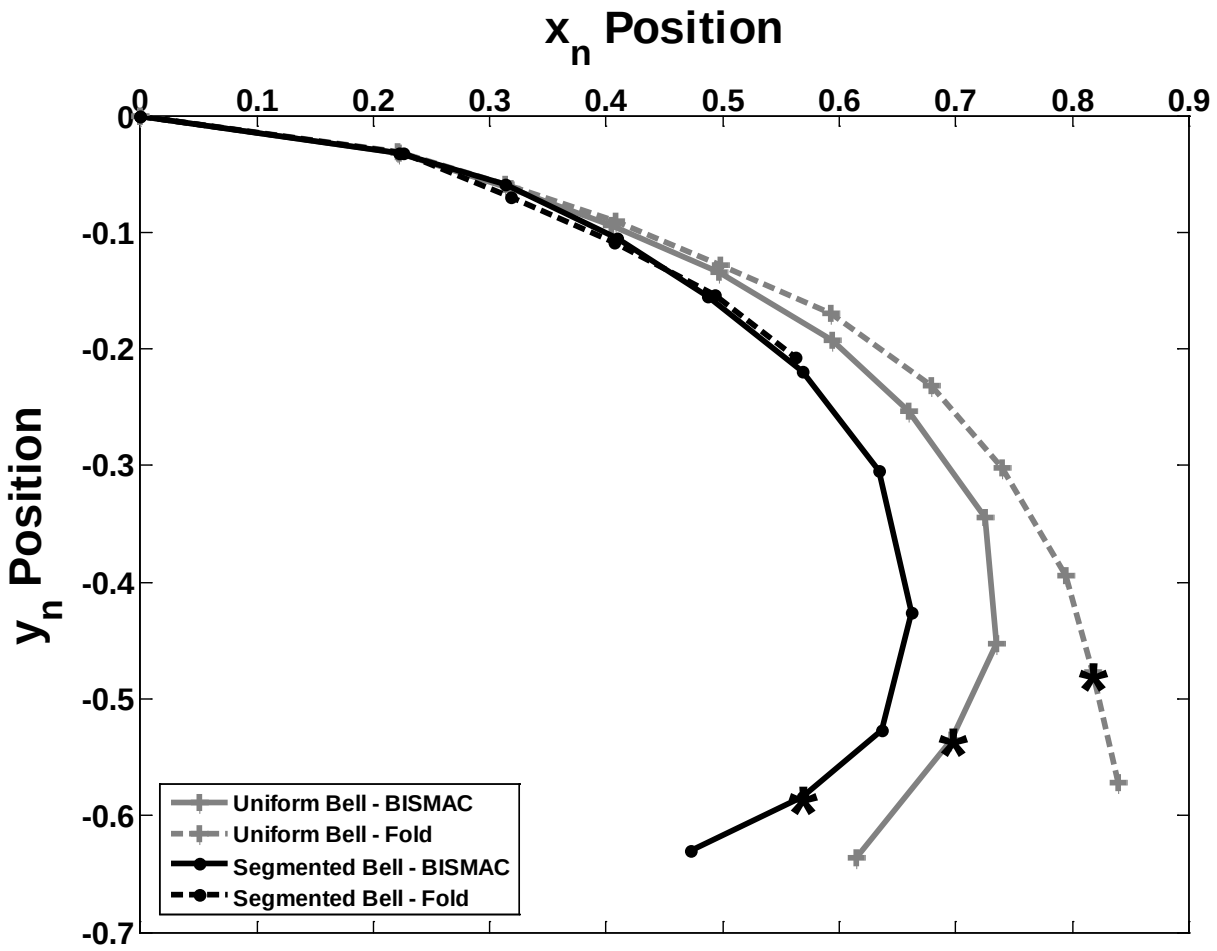

Figure 4.1.11: Exumbrellar deformation profile of Robojelly with uniform and segmented bell configuration. Deformations are shown at the BISMAC and fold location. Inflection points are shown by black stars. The deformation profiles were taken at the end of the contraction period of the 25th actuation cycle. The x- and y-positions were normalized by the relaxed exumbrellar length.

The fold in the uniform bell configuration did not contract as much as the region with BISMAC actuators. For the segmented bell, there was no significant folding as silicone followed the BISMAC deformation. The segmented bell showed an increase in deformation as compared to the uniform bell. This is mainly due to the decrease in resistance to deformation which previously occurred due to the surplus silicone folding on itself. Segmenting the bell increased the deformation by 13 % in the x-direction and 2 % in the y-direction. Table 4.1.2 provides the

quantitative comparison of deformation profiles by analyzing the bell margin and inflexion point. The inflexion point marks the transition between active and passive regions of the bell. The bell margin simply refers to the bell outer tip. The Robojelly segmented configuration was also tested after overheating the actuators. The vehicle was actuated with 1.5 A current for 10 sec which is drastically more power than is recommended for the SMA wire and overheats them. After cooling down, the vehicle was run through a 25 cycle deformation test. Post overheating results show a decrease of 60 % deformation in the x-direction at the inflection point.

Table 4.1.2: The deformation (u) results are shown for different Robojelly bell configurations in the x- and y-direction. The vehicle was actuated for 25 cycles in a clamped configuration. Deformation is shown at the inflection point and bell margin. Results are also shown for deformation at BISMAC and fold locations. Post overheating results are shown under Segmented BISMAC-Post.

			Inflection Point Deformation		Margin Deformation	
	Bell	Location	u_x (%)	u_y (%)	u_x (%)	u_y (%)
Robojelly	Uniform	BISMAC	16.05	7.26	27.67	3.49
		Fold	2.95	2.88	3.91	2.46
	Segmented	BISMAC	29.14	9.59	40.13	1.30
		Fold	0.42	2.06		
		BISMAC – Post	11.49	5.14	17.53	2.54
A. aurita	Uniform		42.32	19.78	51.59	17.15

The first step in matching the full motion of the natural medusa was to match the deformation profile. The relaxed and contracted robotic bell profiles were characterized to identify the similarities with the natural jellyfish. The deformation profiles for both the real and robotic jellyfish are compared in Fig. 4.1.12. The segmented Robojelly is chosen for comparison even though the *A. aurita* is not segmented, because it offers the greatest deformation. Limitations caused by the folding effect do not allow the full contraction of the BISMAC actuators. The relaxed profile for the natural jellyfish was the same as the one used for creating

the Robojelly casting mold. Its contracted profile was obtained by using the maximum contraction observed during a swimming cycle.

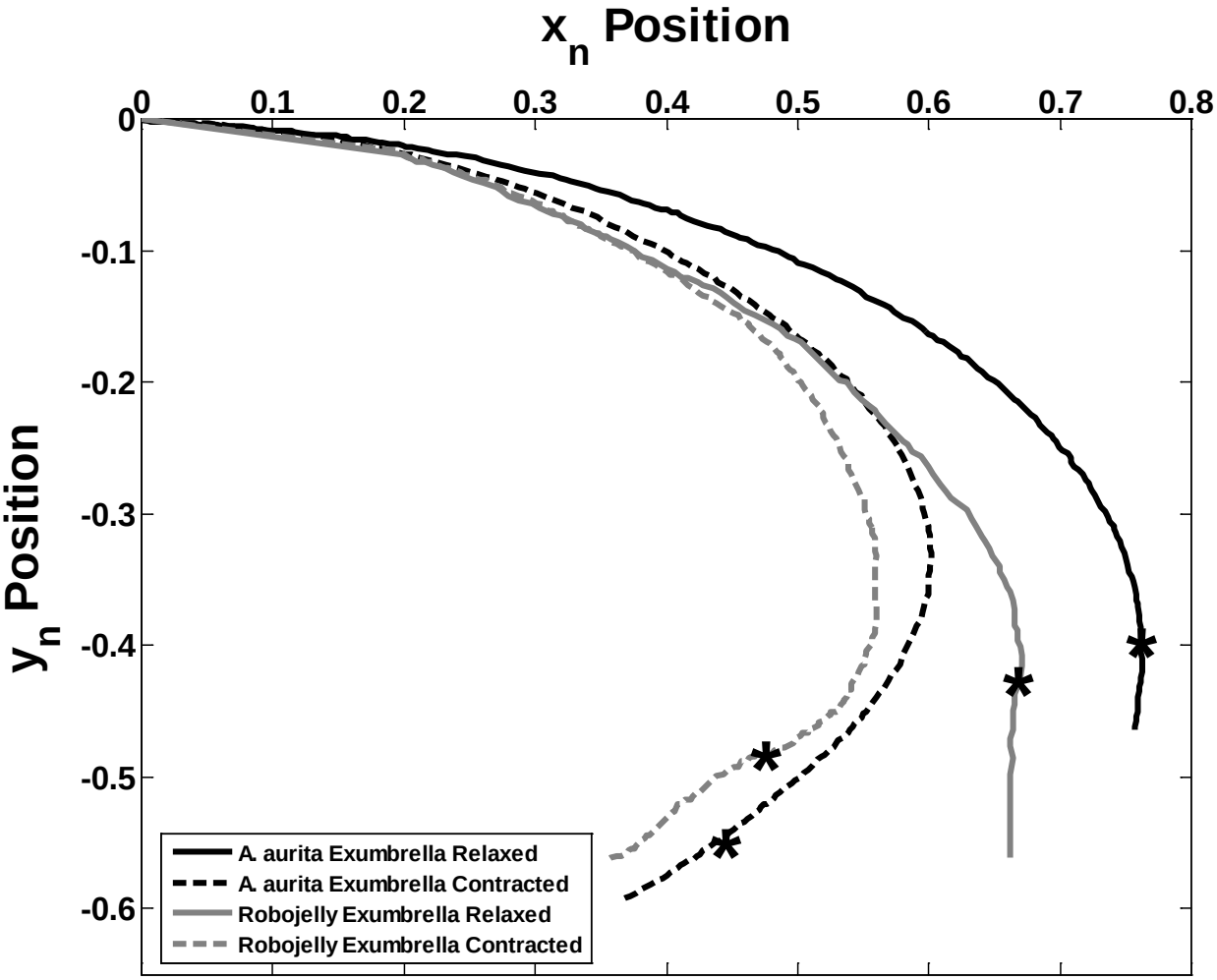

Figure 4.1.12: Exumbrellar deformation profile of natural *A. aurita* and Robojelly in the segmented configuration. Deformations are shown at the BISMAC and fold location. Inflection points are shown by black stars. The deformation profiles were taken at the end of the contraction period of the 25th actuation cycle. The x- and y-positions were normalized by the relaxed exumbrellar length.

The main difference in deformation profile was the initial position of the Robojelly bell. The bell starts at a much lower position. At the inflection point the robotic bell deforms 29 % while the natural bell deforms 42%. BISMAC actuators are capable of deforming over 110 % which means

that the Robojelly bell has the potential to be modified to achieve higher deformation. The y-deformation was significantly less, about half of that of the natural medusa. This requires an adjustment in the structural design of the BISMAC actuators using the guidelines pointed out in Villanueva et al. (2010a). The *A. aurita* exumbrellar length during contraction was found to stretch by 9.7 % while the subumbrella contracted by 4.3 %. For Robojelly, the exumbrellar length stretches by 7.2 %. The subumbrella was not measured because our current technique does not allow us to track the subumbrella profile. The bell profiles were normalized by their respective relaxed exumbrellar arc lengths. The natural jellyfish profile was also normalized by its relaxed exumbrellar length. The deformation profile was analyzed in terms of position along the x-axis.

4.1.3.2 Performance of Robojelly

The performance of Robojelly was evaluated in terms of its ability to generate thrust. The vehicle was positioned in the middle of the water tank and was allowed to swim in the vertical direction. An initial sinking state was induced by adding weights on the order of 1 to 4 g until the vehicle was visibly moving downwards. This was done to ensure that any thrust produced was a result of vehicle thrust production and not due to a net positive buoyancy force. Robojelly can be seen swimming over a full cycle in Fig. 4.1.13.

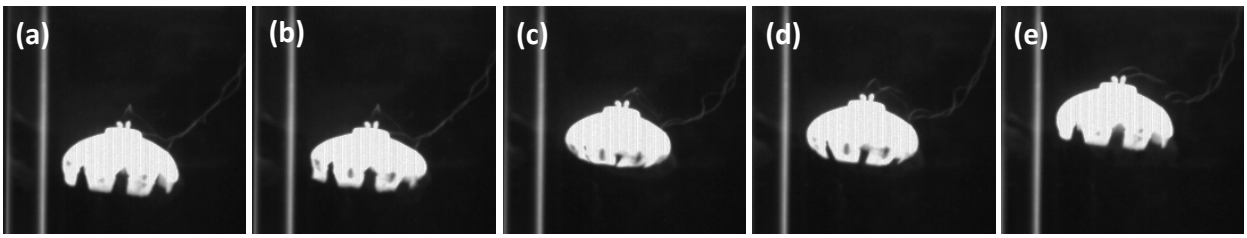

Figure 4.1.13: Swimming cycle of Robojelly in the segmented with flap configuration: (a) Fully relaxed, (b) contracting, (c) fully contracted, (d) relaxing, (e) fully relaxed. These high contrasts images are used to track vehicle position over time.

The change in position as a function of time is shown in Fig. 4.1.14(a). The velocity and acceleration of the vehicle were extracted from the position results using a first order and second order central finite difference, see Fig. 4.1.14(a) and (c). Video was recorded at 60 FPS but only 10 FPS (10 Hz) were used for analysis. Skipping frames smoothed the noise associated with the tracking software. Small variations in the tracking location from one frame to another result in high instantaneous velocities and acceleration spikes. This recording frequency is adequate for the jellyfish since it actuates at a low frequency of 0.5 Hz and for this test we are mainly interested in the total vehicle motion. Using a lower frame rate gives a lower estimate of the maximum velocity and acceleration but a better perspective of the total vehicle movement.

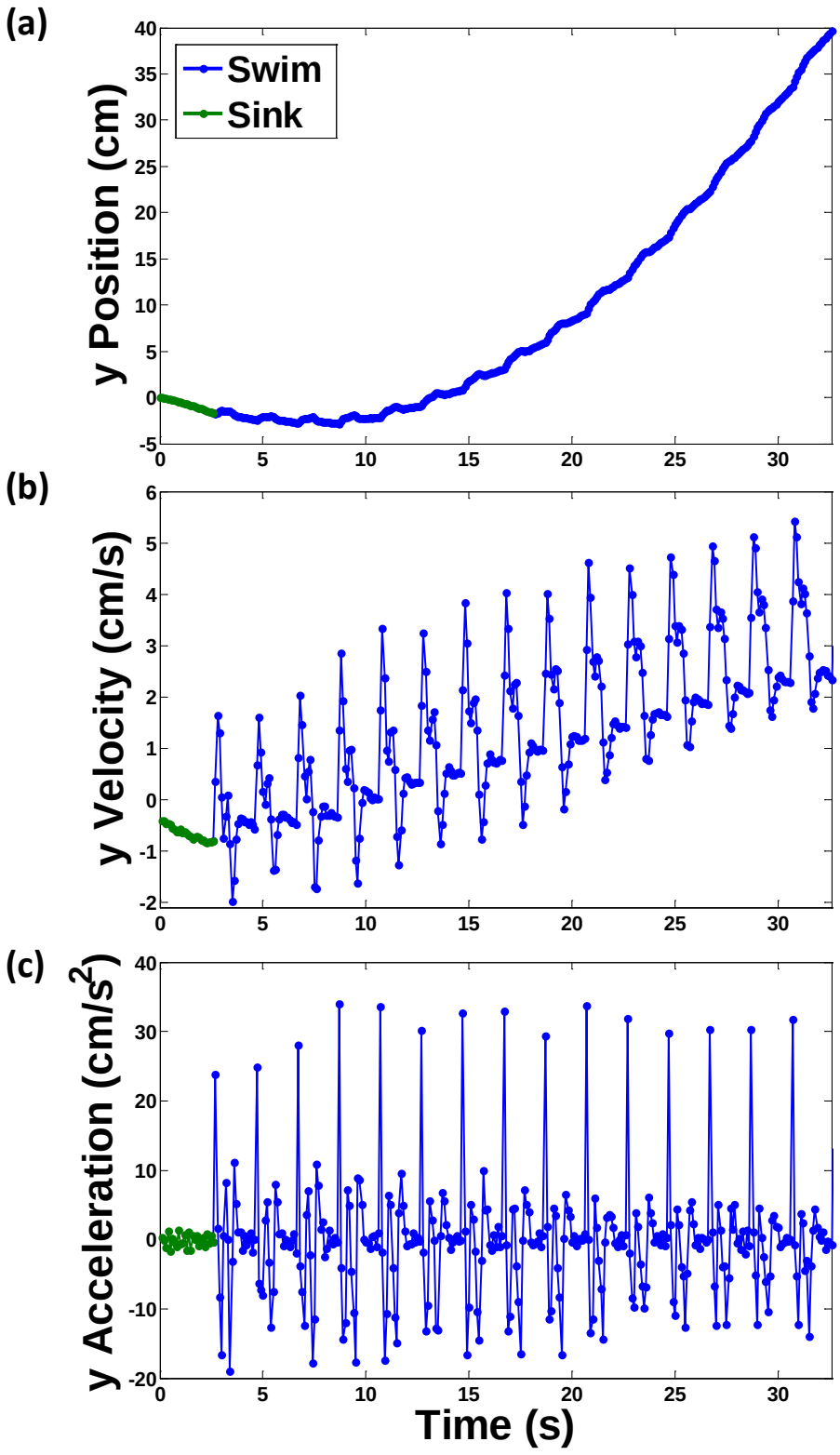

Figure 4.1.14: Position, velocity, and acceleration in the vertical direction as a function of time. Robojelly begins in a sinking state as noted by the green data points.

The position plot Fig. 4.1.14(a), demonstrates that the vehicle started with a sinking state and was able to create enough thrust to propel itself upwards. The cyclic propulsion of Robojelly can be seen in Fig. 4.1.14(a) where an upward motion during contraction is followed by a downward motion during relaxation. The vehicle has a near constant acceleration over a cycle throughout its ascent and does not reach a steady state velocity before reaching the surface of the water. The maximum instantaneous velocity and acceleration achieved were 5.42 cm/s and 34.01 cm/s^2 respectively. The natural jellyfish analyzed in this study was able to achieve a proficiency of 0.25 s^{-1} while Robojelly achieved a proficiency of 0.19 s^{-1} in the segmented with flap configuration. This proficiency was computed by taking the average velocity of the 14^{th} cycle of actuation normalized by the bell diameter. The experimental uncertainty in the measured values of the performance analysis mainly comes from the tracking software. During tracking, slight variations occur when the vehicle is tracked from one frame to another due to the pixel resolution. This variation is on the order of +/- 0.1 cm.

4.1.3.3 Thrust production of Robojelly

Proficiency of the robotic vehicle was greatly dependent on its initial state of buoyancy. If the vehicle sinks more initially, the maximum speed achieved will be less. A better method to compare the performance is to look at thrust production. The thrust produced by Robojelly was approximated by summation of the acceleration reaction, drag, change in momentum, buoyancy force and weight. The results for each of these components are shown in Fig. 4.1.15 for the segmented Robojelly with flap.

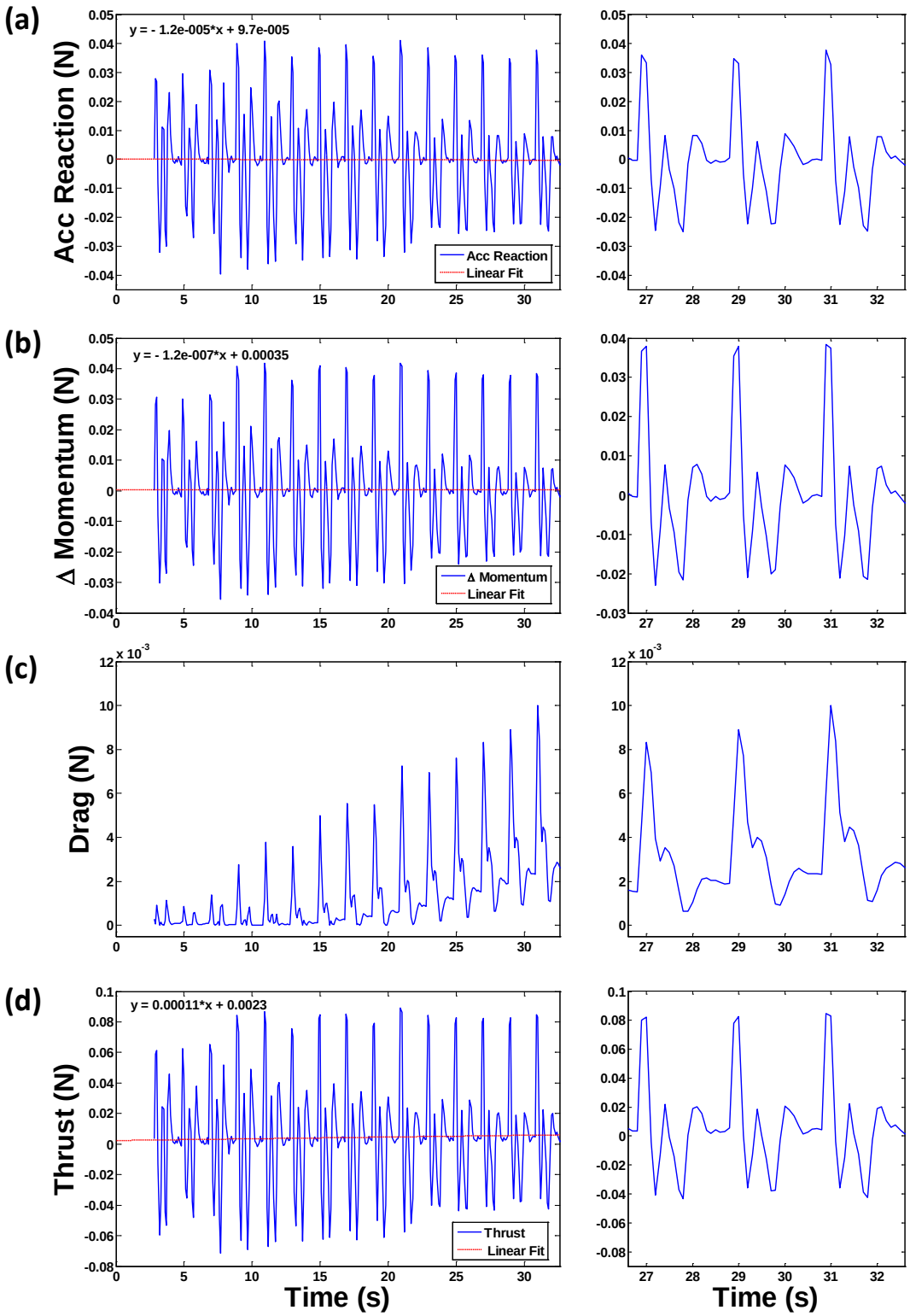

Figure 4.1.15: Segmented Robojelly with flap operating with parameters: I_{hi} = 1.5 A, I_{low} = 0.65 A, duty cycle = 35 %, F = 0.5 Hz. Results are shown for the acceleration reaction (a), change in momentum (b), drag (c), and thrust (d). The right column is a close up view for the last three actuation cycles.

The acceleration reaction and change in momentum predicted by the model shows a small decrease as the vehicle builds momentum. Drag increases with vehicle velocity and is highest at the beginning of cycle when the robot is contracting and reaches top velocity. The predicted thrust results show a small increase with time which for the segmented bell with flap peaks at 0.09 N. The average thrust for the first 4 and 14 cycles was $2.8x10^{-3}$ N and $3.9x10^{-3}$ N respectively as shown in Table 4.1.3 along with the results for three other configurations. Figure 4.1.16 compares the average thrust production for all four configurations. The average thrust was measured over two sets of cycles because of the varying swimming behavior associated with the transient phase of the SMA. The 4^{th} cycle was chosen since the uniform bell with no flap configuration reached the bottom of the tank at that point. The segmented bell with flap reached the water surface after 14^{th} cycles which is the least amount of cycles required of all the different configurations and thus this cycle was also chosen for comparison. Actuator contraction speed and total deformation increases as the thermal steady state is reached. The average thrust over the first 14 cycles shows how the performance was increased for two of the three configurations (uniform bell with flap and segmented bell with flap) in comparison to the first 4 cycles. The segmented bell with no flap exhibited a small decrease in thrust production (24%) with increasing cycle number which could be related to a slight inclination in the bell during swimming. Adding a flap to the uniform bell and segmented bell configurations increased the average thrust over the first 4 cycles of actuation by 352 % and 685 % respectively. Adding a flap to the segmented bell increased the average thrust over the first 14 cycles by 1340 %. Segmenting the uniform bell without and with flap increased the average thrust by 34 % and 133 % respectively over the first 4 cycles. Segmenting the uniform bell with flap increased the average thrust by 116 % over the first 14 cycles. The results show that segmenting the bell

allows the flap to increase the performance even more. Segmenting the bell allows the flap to move freely as folding no longer take place.

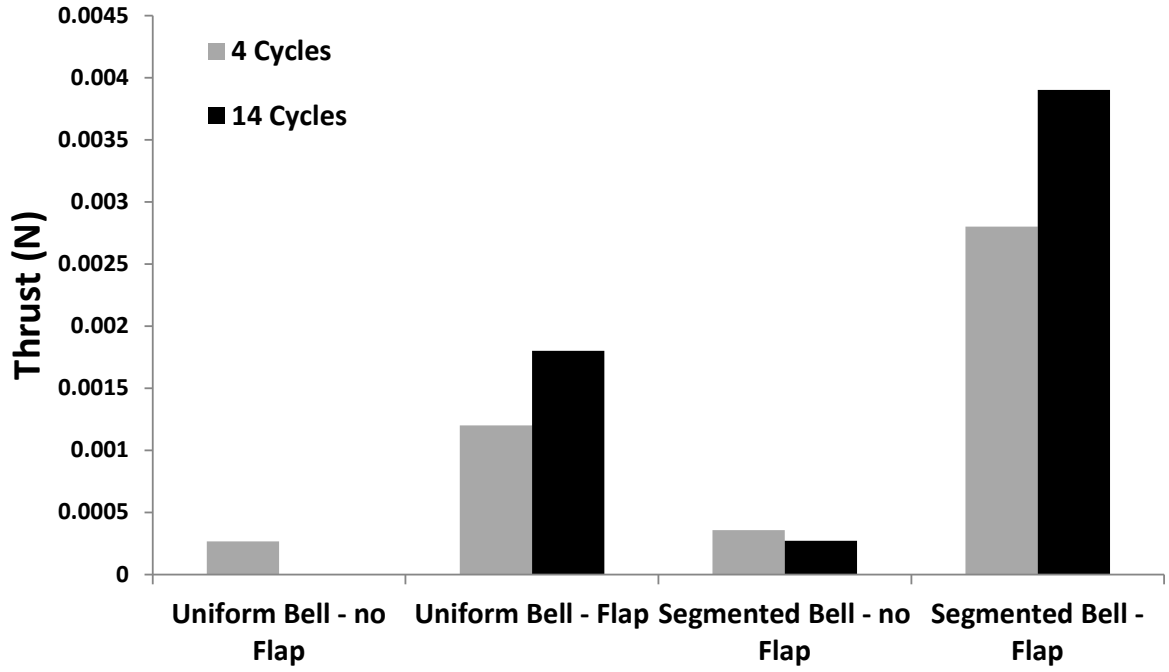

Figure 4.1.16: Average thrust comparison after 4 and 14 cycles of actuation between all four Robojelly configurations. The Uniform Bell – no Flap configuration reached the bottom of the tank before actuating for 14 cycles and is therefore not reported.

4.1.3.4 Power consumption

The rapid heating controller sends a high current to the SMA wires causing them to contract rapidly. Once contracted, a low current is sent to maintain deformation. Robojelly operating current and power are shown in Fig. 4.1.17.

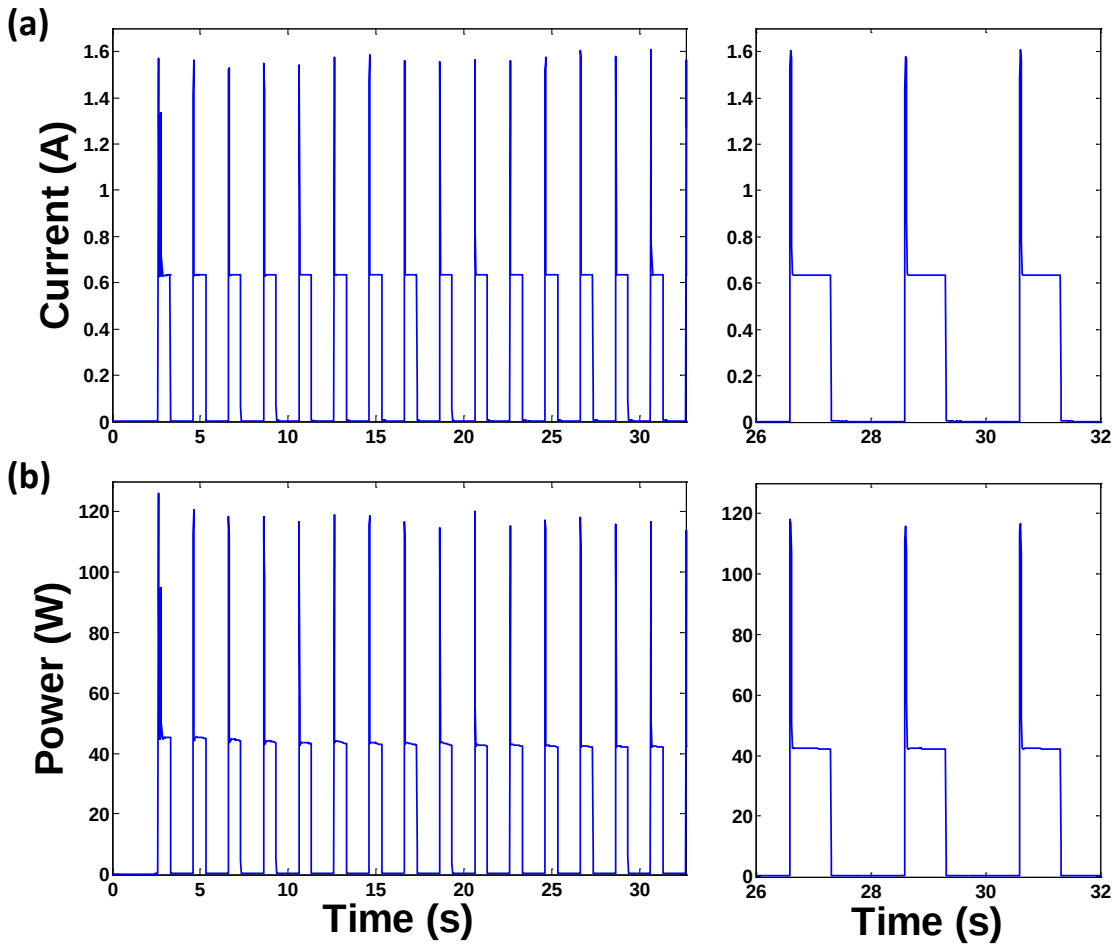

Figure 4.1.17: Robojelly segmented with flap, and operating with parameters: I_{hi} = 1.5 A, I_{low} = 0.65 A, duty cycle = 35 %, F = 0.5 Hz. Results are shown for current (a), and power consumption (b). The right column is a close up view for the last three actuation cycles.

Power consumption decreases with cycle number and eventually reaches a steady state. Residual heat accumulates in the silicone surrounding SMA wires and increases its temperature over time until a steady state is reached. Less heat is therefore required to contract the SMA wires in subsequent actuation cycles. This causes the bell to have a larger deformation over set cycle parameters but also to recover less of its original position at each relaxation cycle. The average power consumed for the segmented bell with flap was 16.74 W during its 14^{th} actuation cycle.

This power consumption as well as power requirements for other configurations are shown in Table 4.1.3.

Table 4.1.3: Average thrust over the first 4 and 14 cycles along with the respective SMA power consumption for the different Robojelly bell configurations.

	Cycle #	Tavg (N)	P (W)
Uniform Bell - no Flap	4	2.66E-04	20.32
Uniform Bell - Flap	4	1.20E-03	18.85
Segmented Bell - no Flap	4	3.57E-04	17.57
Segmented Bell - Flap	4	2.80E-03	17.34
Uniform Bell - Flap	14	1.80E-03	17.95
Segmented Bell - no Flap	14	2.71E-04	16.95
Segmented Bell - Flap	14	3.90E-03	16.74

More energy is required to power the vehicle until the actuators reach a thermal steady state. This pattern can be seen in Figure 4.1.17(b). The overall propulsive efficiency of the vehicle is calculated using:

$$\eta_o = \frac{\overline{Tu}}{\overline{P}} \ , \tag{4.1.9}$$

where P is the power consumption and the over bar represents the time average. For the segmented bell with flap configuration along with measured power consumption, the estimated thrust calculations and measured vehicle velocity, the efficiency of the vehicle is calculated to be 7e-6 over the first 14 actuation cycles.

4.1.4 Discussion

The difference in swimming performance of Robojelly and *A. aurita* can be attributed to various factors in fabrication and actuation. One of the prime structural differences was the

presence of a folding effect in the Robojelly bell. Some of the membrane in Robojelly was unable to follow the BISMAC path during contraction. This was corrected by cutting segments into the bell creating enough space between the segments for unobstructed contraction. Consequently, that created openings where water could escape reducing thrust. An important aspect of the *A. aurita* wake fluid structure is its axi-symmetry. The stopping and starting vortices form vortex rings which cannot be perfectly replicated in the current Robojelly configuration due to bell folding or bell cutouts.

Another difference between the natural and robotic jellyfish was the relaxed profile of the bell in water. The profile was less extended for the Robojelly than for the natural jellyfish even though the exact contours of the natural jellyfish were used to create the casting mold. Gravity acts on the bell and causes it to sag relative to the desired position. Also, BISMACs tend to settle into a lower position because of the interaction between silicone and spring steel during contraction. The same initial profile as the natural medusa could be achieved by molding Robojelly in a more extended fashion to account for the effect of gravity.

Figure 4.1.12 shows that the deformation of Robojelly was quite similar to that of the natural animal. The BISMAC actuator design maximized deformation by minimizing the distance, d, between the SMA wires and spring steel. The final deformation profile achieved demonstrates that the bell geometry was able to tailor the deformation well even without an optimization of the other BISMAC parameters. This is expected from the results reported for the VS-BISMAC (Villanueva et al. 2010a). The varying distance between the subumbrella and spring steel also helps in tailoring the deformation as predicted by the measurement on VSSS-BISMAC. The maximum deformation achieved at the BISMAC locations was still less than that for natural

animal. This problem could be resolved by optimizing the BISMAC structure and spring steel location inside the silicone.

The operating parameters used in this study were previously found to produce the best Robojelly performance but the bell kinematics of the natural animal are not matched completely (Villanueva and Priya 2010, Villanueva et al. 2010b). Robojelly's maximum deformation is held constant during most of the contraction period instead of being immediately released like the *A. aurita*. This actuation pattern was found to produce a better performance for the frequency used and the deformation capability of the current design. Differences between the natural and robotic jellyfish ultimately affect the hydrodynamic performance. Further work will have to be conducted on the wake structure created by the robotic jellyfish to evaluate how the differences in bell kinematics and structure affect flow.

The Robojelly design was also found to show sensitivity to SMA wire overheating. Overheating the SMA wires decreased deformation in the x-direction by 60 %. Most of this deformation loss could come from a decrease in the fraction of martensite to austenite transformation due to overheating of the alloy. The rapid heating controller subjects the SMA wires to overheating due to the high currents used during actuation. Slight error in the controller could cause high currents to deteriorate the actuation capability of the SMA wires. Thus, the shape memory alloys and controller used in the vehicle must be properly characterized to understand and prevent the effects of overheating.

Power consumption was high for the vehicle size and performance. We believe that power consumption could be reduced by properly designing the thermal properties of the bell material. It could be optimized so that less heat is dissipated during contraction while enough is released

for proper relaxation. Another way to reduce power consumption comes from the shape memory alloy used. Some shape memory alloys have a lower transformation temperature. Such alloy would require less heat to actuate and thereby reduce power consumption. Thrust results show the drastic increase in performance without the need for additional power when Robojelly was equipped with a passive flap. This passive piece of material was able to increase thrust production by over 1300 % in the segmented configuration. This feature is crucial to the vehicle and presumably to the natural jellyfish. Its role and mechanics need to be better understood so that it can be properly duplicated and implemented in the robotic model.

The low efficiency of Robojelly can be attributed to a few factors. The average power consumed over the 14 cycles was in the range of 17 W. This quite large power consumption is due to the SMA actuators which require high current for creating maximum deformation in underwater applications due to the higher heat capacity of water over air. The thrust calculation method used in this analysis takes into account buoyancy and velocity which gives a better description of performance than proficiency. It provides a good method of comparison between each vehicle configuration, but we believe that the thrust predicted by this method is low and the accuracy will be validated in future work.

4.2 Robojelly Bell Kinematics and Resistance Feedback Control

Initially, Robojelly was actuated by square wave for simplicity. However, significant overheating was observed due to incomplete heat dissipation in the actuators between contraction cycles. A jellyfish controller was consequently needed to inhibit the overheating problem, reduce power consumption and match the kinematics of the natural animal both in speed and deformation profile. Jellyfish undergo cyclic propulsion consuming energy during the contraction followed by a passive relaxation. This method enhances the thrust production of animal. The SMA contraction time can be tailored by controlling the amplitude of drive current used for resistive heating. The relaxation is passive and depends on the resilience of the structure and ability to dissipate heat. Several controller concepts for SMA actuators have been proposed in literature. Kuribayashi has proposed a technique that utilizes direct temperature measurement of SMA wires using thermocouples (Kuribayashi, 1991). Several other studies have proposed a technique based on SMA resistance feedback that is now widely investigated (Webb and Wilson, 2000; Featherstone and The, 2004; The and Featherstone, 2008; Mukherjee et al., 1996; Raparelli et al., 2002; Song et al., 2007; Takeda et al., 2008). This technique is related to the phase change that occurs in NiTi alloy during heating. As the SMA undergoes martensite to austenite phase transformation its overall resistance changes. This correlation between the electrical property and phase transformation provides a fundamental criterion for controller design.

Figure. 4.2.1: Picture of Robojelly in water in fully relaxed configuration.

4.2.1 Methods

4.2.1.1 Aurelia aurita digitization

A video of swimming *Aurelia aurita* was provided by biologist (Sean Colin, Roger Williams University). The 30 FPS video was converted into images which were then digitized to extract the necessary information. An average of 90 manually-selected points along the bell exumbrella was extracted using ImageJ as shown in Fig. 4.2.2 and used to interpolate points at 5% intervals along the exumbrella. This was done so that the same points could be tracked during deformation. A total of 20 points from the bell margin to the apex were analyzed since we can assume the bell to be axi-symmetric.

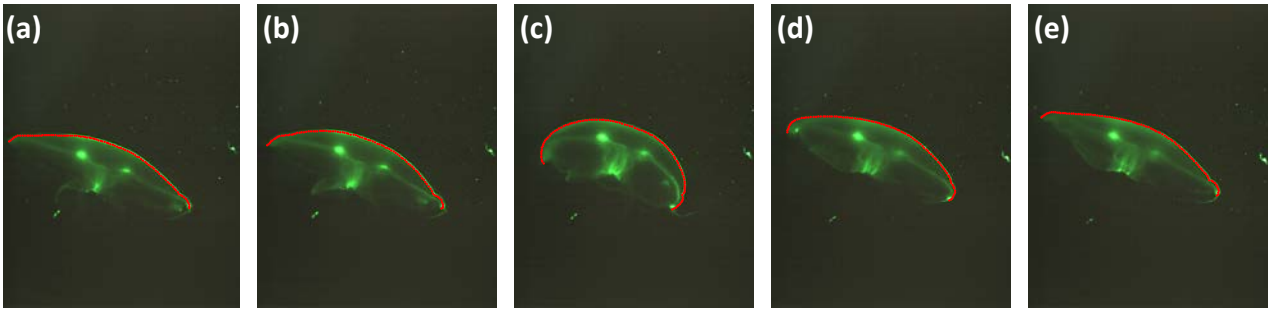

Figure 4.2.2: Image sequence of *A. aurita* specimen over a full contraction cycle. The fish is shown with bell in (a) fully relaxed, (b) contracting, (c) fully contracted, (d) relaxing and (e) fully relaxed position. The points manually picked on the exumbrellar surface are shown as red dots.

For each frame, all points were zeroed at the bell apex. This was accomplished by measuring the x- and y-displacement of the apex at each frame relative to the initial frame, and subtracting that motion from each subsequent frame. This is analogous to making the specimen swim in place. To account for rotation, the rectangular x-y coordinates were first converted to polar r-θ and the angle between the left and right bell tips was measured at each frame. Plotting this angle against the frame number revealed that the specimen rotated (rolled) a total of 3.365° over one cycle. Rotation started about halfway through the cycle at a constant rate and was subtracted from all subsequent frames.

4.2.1.2 Controller

The speed of SMA wire contraction depends on heating rate. A faster actuation can be achieved by high driving current impulses. To prevent overheating of the SMA wires during actuation cycle, the current level can be reduced once the actuator has reached desired contraction. This allows the actuator to maintain deformation without using more power. It also helps in reducing residual heat from being accumulated inside the material. This type of

controller can be for in-air or in-water applications (Webb and Wilson, 2000; Featherstone and Teh, 2004; Teh and Featherstone, 2008). In the previous chapter, a rapid heating controller was applied to BISMAC actuators immersed in water (Villanueva et al., 2010). This controller was modified to meet Robojelly's requirements. The rapid heating controller uses SMA wire resistance feedback to monitor the state of contraction. A schematic is shown in Fig. 4.2.3. The controller consists of three main parts, the input function, the current limiter and the current regulator. The input function serves multiple purposes: controls the actuation frequency, cruising time and relaxation time which are all critical for vehicle performance (Villanueva et al., 2009).

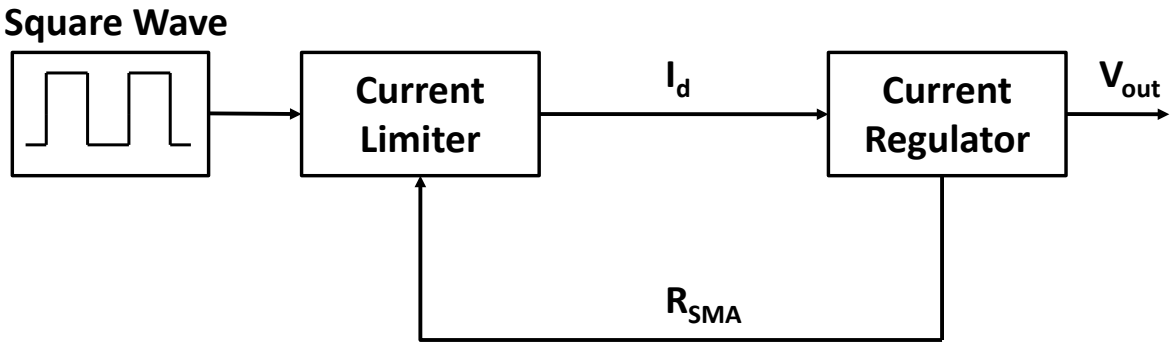

Figure 4.2.3: Schematic of rapid heating controller(Villanueva et al., 2009).

The current limiter reads the function generator output as an "on" or "off" signal. When on, it takes the SMA resistance feedback and determines if it is above the threshold resistance. The following decision is then made:

$$R_{SMA} = \begin{cases} > R_t, \ I_d = I_{hi} \\ \leq R_t, \ I_d = I_{lo} \end{cases} \quad (4.1.1)$$

where R_{SMA} is the resistance of SMA wire, and R_T is the SMA threshold resistance. R_T is determined using a preliminary test which consists of sending a safe current that fully contracts the actuators without overheating them. A safety margin (~2%) is then added to steady state

resistance and taken as the threshold resistance. I_{hi} is the high impulse current sent for fast contraction and I_{lo} is the safe current amplitude chosen to maintain deformation. The desired current I_d is determined based on the resistance values and sent to the current regulator as shown in Fig. 4.2.4. R_{SMA} is calculated using the voltage drop across the SMA and current is measured by a passive current-to-voltage converter across a 1 Ω resistor. The output voltage was calculated from the SMA resistance and desired current. R_o takes into account the resistance of the current-to-voltage converter and the added resistance of cables and was equal to 2 Ω.

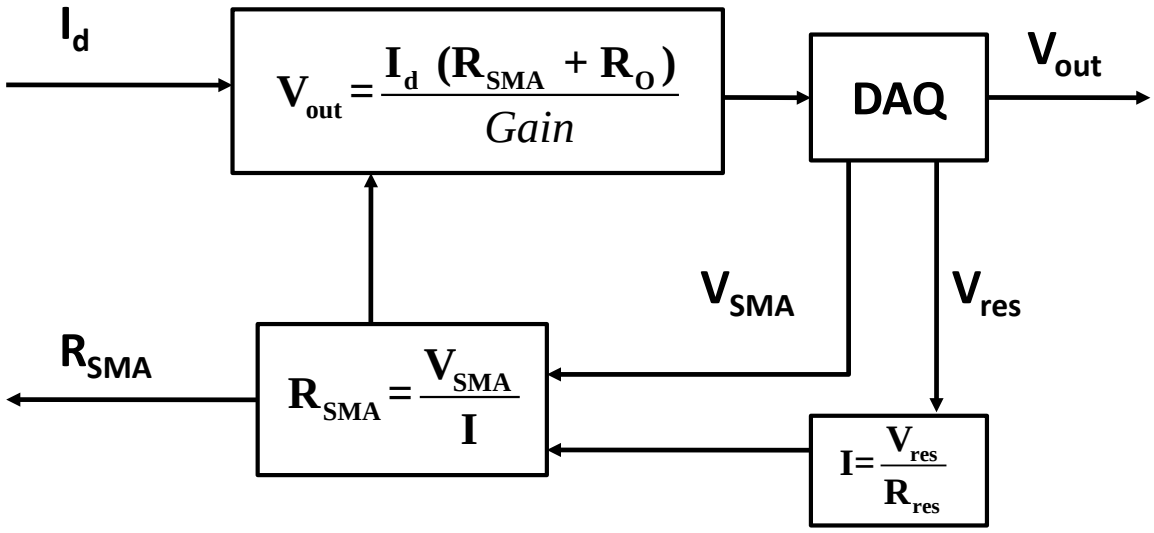

Figure 4.2.4: Schematic of the current regulator(Villanueva et al., 2009).

The voltage output was divided by "Gain" which is the amplifier gain so that the amplified value equals the desired output voltage. Minimum and maximum resistance values were set as limits in order to prevent any arithmetic computation overload encountered when little or no current is flowing through the circuit.

4.2.1.3 Experimental Setup

The controller software was developed in LabView and the measurements were conducted using an NI cDAQ 9172. The calculated output voltage was sent by using a NI-9263 analog output card to a NF HAS 4052 power amplifier set to a fixed gain of 200. The voltage drop across the current-to-voltage converter was measured by using a NI-9215 16-bit isolated card. The voltage drop across the SMA was measured indirectly through a current divider and voltage divider using the NI-9215. These dividers were required since voltage drop across the SMA wires exceeds the capability of the DAQ cards. The input data was sampled at a rate of 10,000 samples/s with 100,000 sample buffer and 100 samples per channel were read in each cycle. The input voltage drop from the SMA and resistor were averaged over 100 samples for more accurate readings and precise control. An Agilent 33120A function generator was used to generate the square wave.

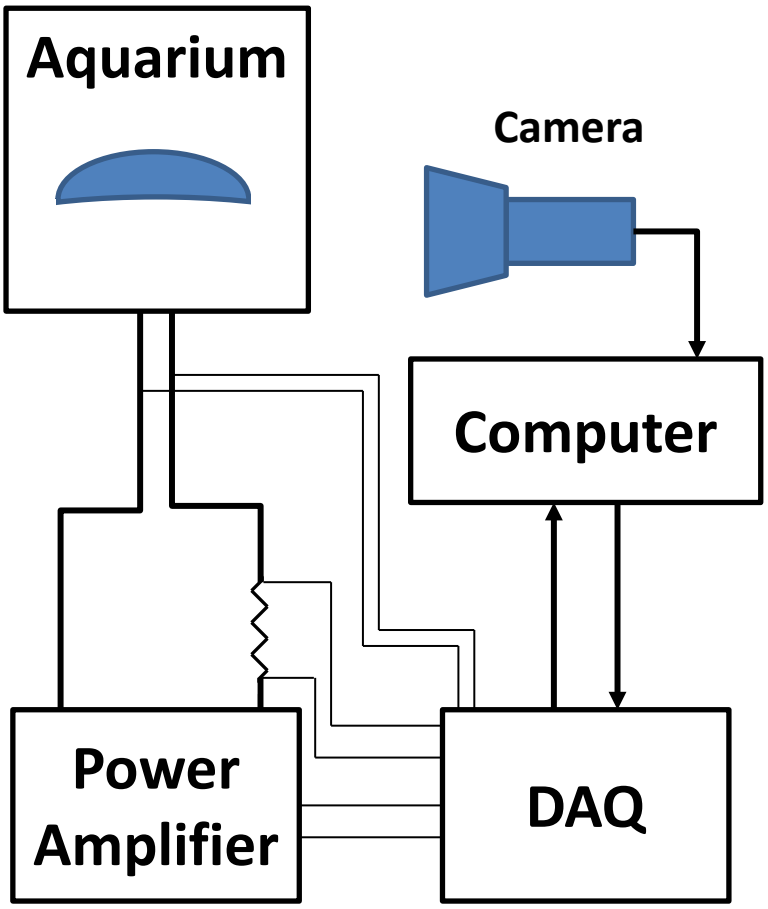

Figure 4.2.5: Schematic diagram of the test setup for Robojelly testing.

Robojelly motion was captured by using an IN250 high-speed camera from Fastec Imaging. The vehicle was placed underwater in an aquarium of dimensions 50 x 50 x 80 cm as shown in Fig. 4.2.5. Reflective points on the vehicle were tracked individually using software developed in Matlab (Villanueva et al., 2011).

4.2.1.4 Performance and Kinematics Test

During the performance test, a single reflective point was put at the bell apex which was tracked throughout the vehicle trajectory. For the bell kinematics tracking, four points were monitored. Three reflective points were positioned at the top of the vehicle where little deformation occurs during contraction and took into account the vehicle's roll and yaw. Pitch was found to be negligible in previous experiments and was neglected for this 2D analysis. Robojelly was positioned on a fixed column and was free to move upwards as shown in Fig. 4.2.6. The column reduces the overall vehicle motion which was not of interest for this analysis while allowing it to contract freely and swim upward.

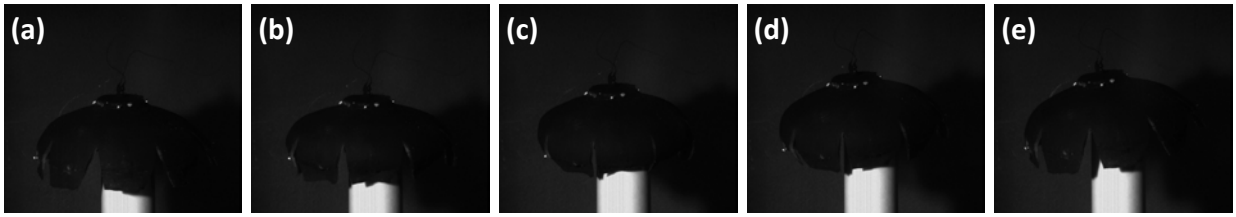

Figure 4.2.6: Image sequence of Robojelly over a full contraction cycle during a kinematics test. Robojelly is shown with bell in (a) fully relaxed, (b) contracting, (c) fully contracted, (d) relaxing and (e) fully relaxed condition.

The fourth reflective point was marked at the inflexion point. This point captures the bell deformation during actuation cycles and provides information on the overall bell deformation. Videos were recorded at 60 FPS but only every 6 frames were used during data processing. Velocity and acceleration were calculated using first order and second order central finite difference respectively. The vehicle motion was subtracted from the bell deformation using a similar algorithm as used for the natural jellyfish.

4.2.2 Results

4.2.2.1 Bell Kinematics

A. *Aurelia aurita*

The *A. aurita* bell kinematics were analyzed by tracking points along the exumbrella. The trajectories of three different points during one full cycle are plotted in Fig. 4.2.7. The data has been normalized by initial bell radius at the bell margin and zeroed about the bell apex. The close up view shows three different trajectories. During contraction at the point 20 % up the exumbrella, the bell follows a trajectory more inwards than when it relaxes. At a point 10% up the exumbrella, the bell follows the same general trend but the difference in path is reduced at the mid-section of the trajectory. The bell margin follows a different trend with an outward trajectory during contraction and inward trajectory during relaxation. This indicates that the flap converts an inner trajectory during contraction into an outer one.

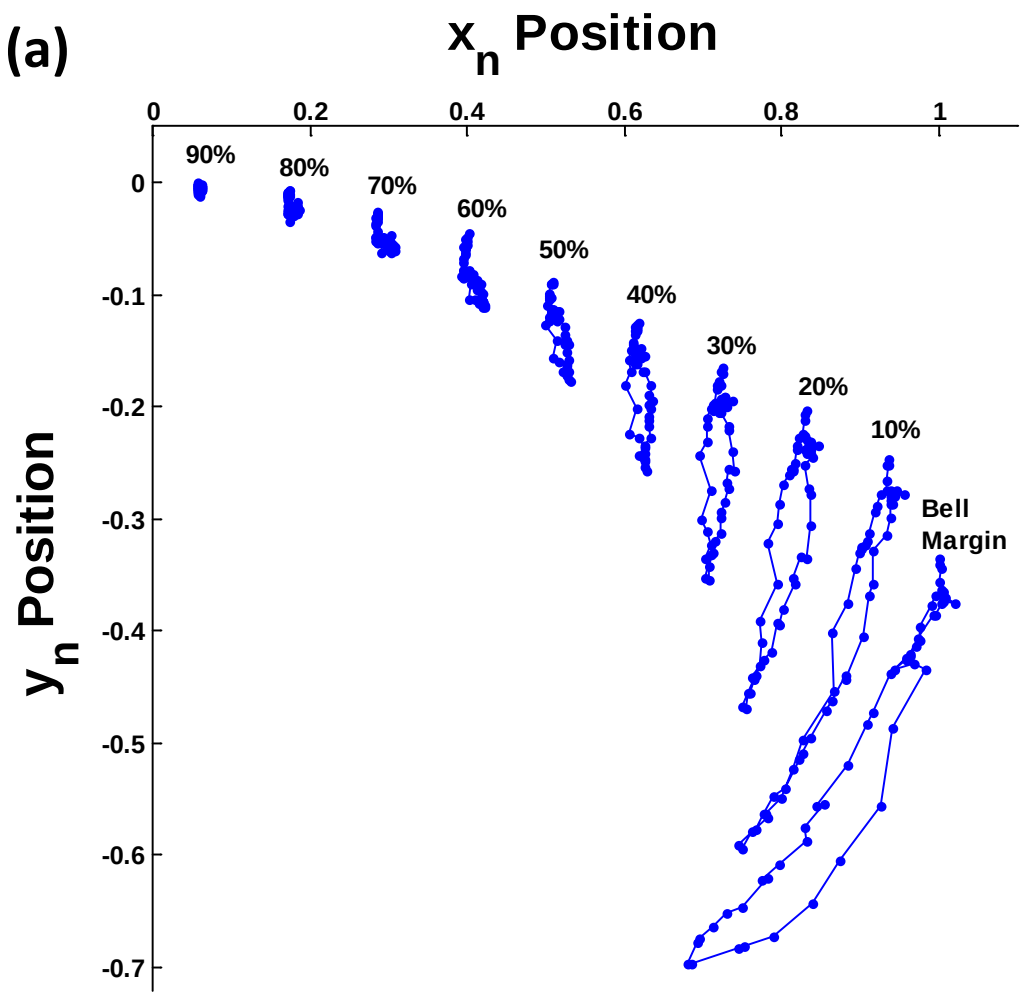
(a)
x_n Position
y_n Position
0
0.2
0.4
0.6
0.8
1
0
-0.1
-0.2
-0.3
-0.4
-0.5
-0.6
-0.7
90%
80%
70%
60%
50%
40%
30%
20%
10%
Bell
Margin

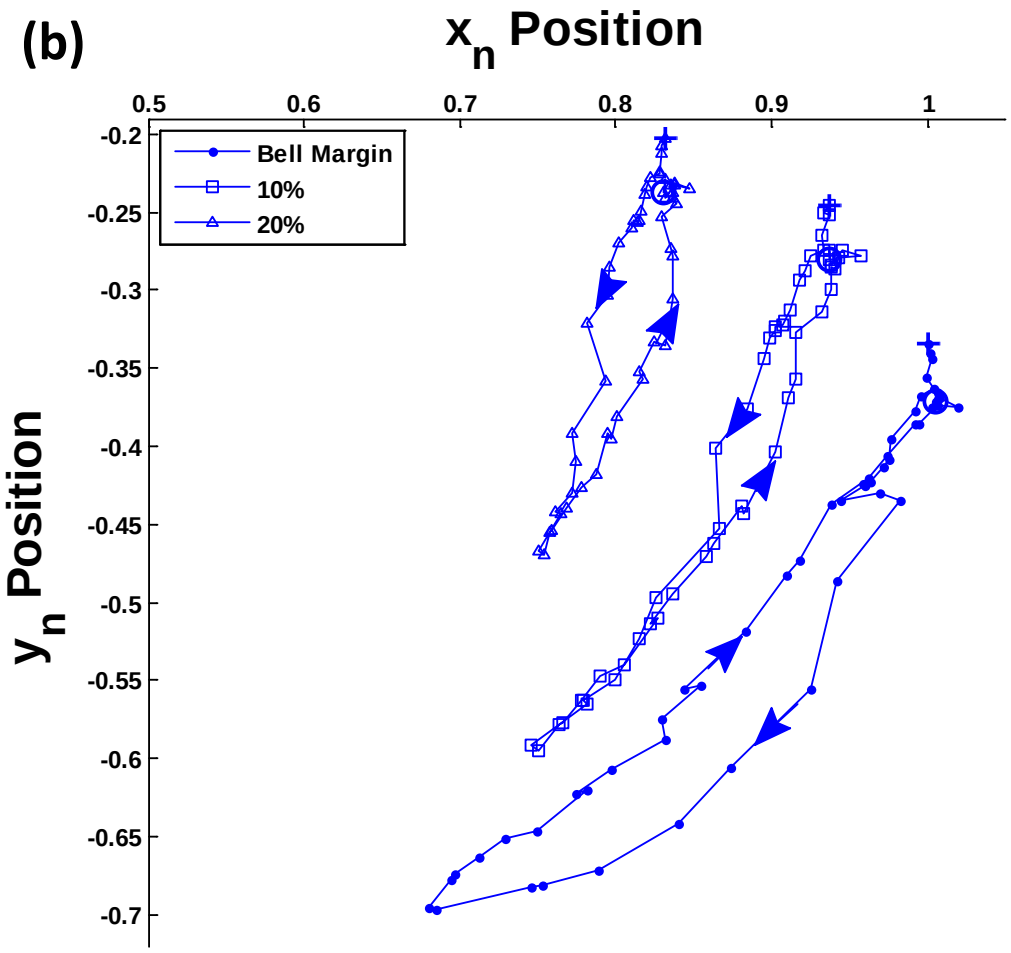

Figure 4.2.7: *B*ell kinematics of the exumbrella for one full cycle showing the x and y positions normalized by initial bell margin radius. (a) The trajectories are shown for points on the exumbrella at 10% intervals starting at the bell margin and ending at the bell apex. The intervals are calculated in terms of exumbrellar length. (b) Close up view of (a) showing the bell margin, 10% and 20% points. The arrows depict the direction of motion, the + is the start location and **O** is the final location.

Points higher than 20% up the bell follow the same trend as that at 20% with the degree of deformation gradually reducing. The different trajectories followed by the bell during contraction show how the *A. aurita* deforms its body for swimming. An outer trajectory upon contraction causes the bell to extend over a larger radius. This creates more area perpendicular to water in the direction of bell motion and allows more water displacement to produce thrust. With an inner trajectory during relaxation, the bell has a smaller radius which leads to a smaller surface area

acting perpendicular to motion, thus reducing drag.

The subumbrella can be separated into two sections: active and passive where the transition is marked by the inflexion point. We hypothesize that the active region has propulsive muscles while the passive region does not, and inflexion point is located at muscle terminals. The passive section, referred as flap, deforms differently than the rest of the bell. From our analysis, the inflexion point is approximately 10 % up the subumbrella. Robojelly design used in this study has a flap length which is 18 % of its subumbrella. The extra length was used to compensate for the added stiffness from the overshooting BISMAC actuators in the soft flap.

B. Robojelly

Robojelly bell kinematics were measured and analyzed in a similar way as that of *A. aurita*. The inflexion point was tracked along with the bell margin. The change in SMA performance due to residual heat affects the bell deformation which can be observed by comparing 1^{st} and 20^{th} cycle. A total of 20 cycles were chosen to ensure steady state deformation. The bell margin and inflexion point trajectory are shown in Fig. 4.2.8. The effect of residual heat is shown by the difference in point trajectory of the 1^{st} and 20^{th} cycle. In the 20^{th} cycle, the bell margin does not fully recover the initial position but achieves a larger x-deformation than previous cycles. At the start of 20^{th} cycle, an upward motion is seen in the trajectories which were not present during the1^{st} cycle. The bell margin then follows an upward motion while the inflection point continues down. Residual heat causes the SMA wires to contract further during the cycle and the parts with more silicone to contract faster than others. During both the 1^{st} and 20^{th} cycle, the inflexion point follows an inner trajectory during contraction like the *A. aurita*'s 10% and greater points. Robojelly bell margin follows an inner

trajectory during the first 2/3 of its contraction unlike the *A. aurita* and outer trajectory for the last 1/3. This means the flap properties should be modified to fully replicate the outer trajectory during contraction.

During the 20th cycle, Robojelly inflexion point contracts 3% less in the x-direction then the *A. aurita* and 30% less in the y-direction. Similarly at the bell margin, we observe a difference of 7% in the x-direction and 41% in the y-direction. The initial bump observed in the 20th cycle trajectory indicates that the bell does not contract in an even motion. The bump in the data occurs because of the apex moving down slightly and bell point moving up during the initial part of the contraction. From the deformation trajectories, we can see in the 1st cycle results that the initial position of the inflection point begins much lower than that of the *A. aurita* at -0.50 as opposed to -0.35. The same pattern was observed at the bell margin. This could be because the bell profile used for vehicle design was taken from a different specimen. It could also be due to the structure bending under gravity load.

(a)

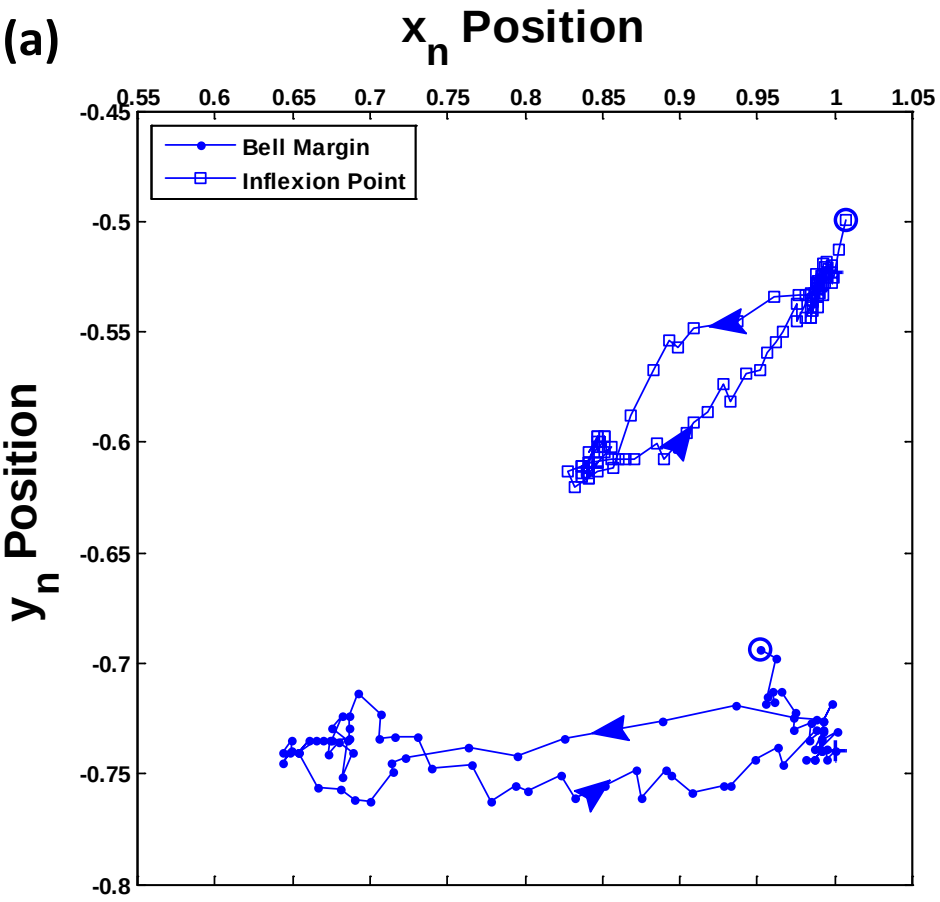
x_n Position
y_n Position
Bell Margin
Inflexion Point
0.55
0.6
0.65
0.7
0.75
0.8
0.85
0.9
0.95
1
1.05
-0.45
-0.5
-0.55
-0.6
-0.65
-0.7
-0.75
-0.8

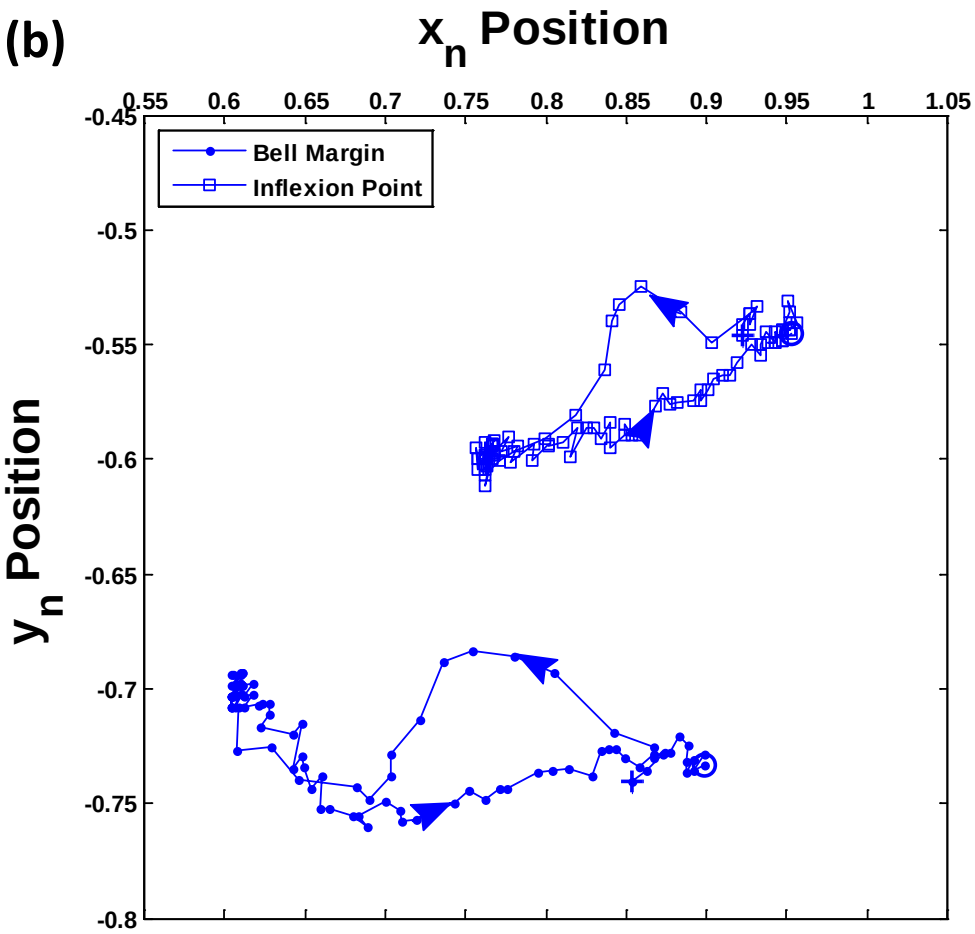

Figure 4.2.8: Robojelly bell kinematics, x and y positions normalized by initial bell margin radius for the inflexion point and bell margin during the (a) 1st cycle and (b) 20th cycle. The Robojelly was actuated using I_{hi} = 1.2 A, I_{lo} = 0.65 A and duty cycle = 0.35 %.

Another important aspect of bell kinematics is contraction and relaxation time as shown in Fig. 4.2.9. These times vary with the size of the animal with larger specimens contracting and relaxing more slowly but the ratio of contraction to relaxation time staying near 1:2 (McHenry, and Jed, 2003; Bajaca et al., 2009; Costello and Colin, 1984). The inflexion points show the x_n position over time for the natural jellyfish and Robojelly during its 1st and 25th actuation cycle.

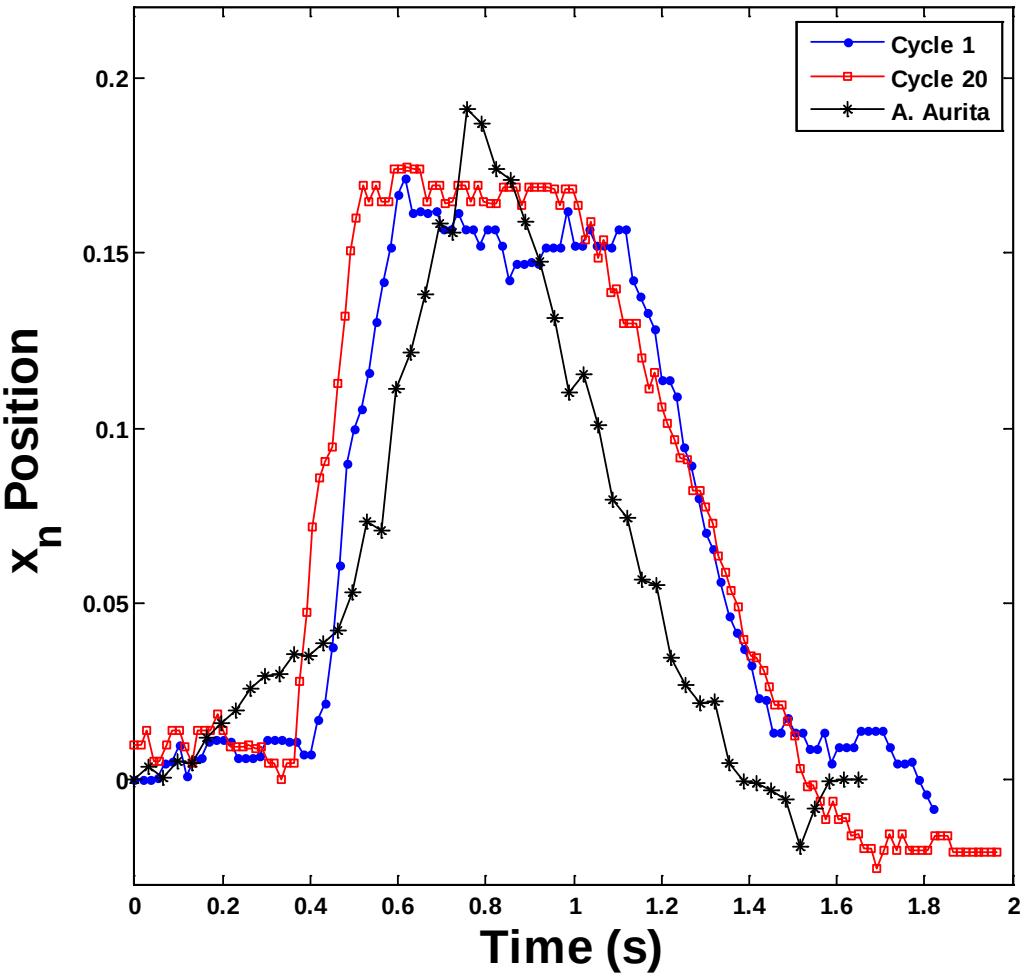

Figure 4.2.9: Plot of the x-position normalized by initial bell margin radius against time of the point 10% up the *A. aurita* exumbrella from the bell margin and Robojelly inflexion point for one full propulsive cycle. The Robojelly was actuated with I_{hi} = 1.2 A, I_{lo} = 0.65 A and duty cycle = 0.35 %.

Based on the x_n-deformation, *A. aurita* contracts at an increasing rate and immediately starts relaxing once it reaches a maximum deformation. Its average contracting rate was 0.3 s^{-1}. Robojelly with I_{hi} = 1.2 A has a very fast contraction at rate of 0.9 s^{-1} during its 20th cycle. The deformation was then maintained for the rest of the actuation time. *A. aurita*'s average relaxation rate was 3.28 s^{-1} while the Robojelly ranges from 2.32 s^{-1} to 3.15 s^{-1} for the 1st and 20th cycle respectively.

4.2.2.2 Swimming Performance

Video recording was started as the Robojelly initially sank due to induced negative buoyancy. The performance of Robojelly was compared after 12 cycles of pulsation since for some cases this was enough to reach the water surface. A total of 12 cycles were not enough to reach the steady state velocity and deformation. An I_{lo} of 0.65 A was experimentally found to be optimum for maintaining deformation for a constant cross-section BISMAC actuator of 0.6 cm thickness in same water conditions (Villanueva et al., 2009). I_{lo} was chosen as the lowest magnitude that is able to maintain deformation after rapid heating. An I_{lo} of 0.65 A was applied to Robojelly and was found to properly maintain deformation as it did for BISMAC actuators.

The natural jellyfish can achieve a proficiency of 0.25 s^{-1} which is calculated as the average velocity over multiple cycles divided by the bell diameter. During testing of the Robojelly, steady state velocity was not reached during vertical swimming, thus proficiency is not a good method for performance comparison in this case. The thrust produced (**T)** was used to compare the vehicle performance. Fig. 4.2.10 shows the thrust production for various values of I_{hi} with corresponding power consumption. Power consumption is defined as the average power used over the first 12 cycles.

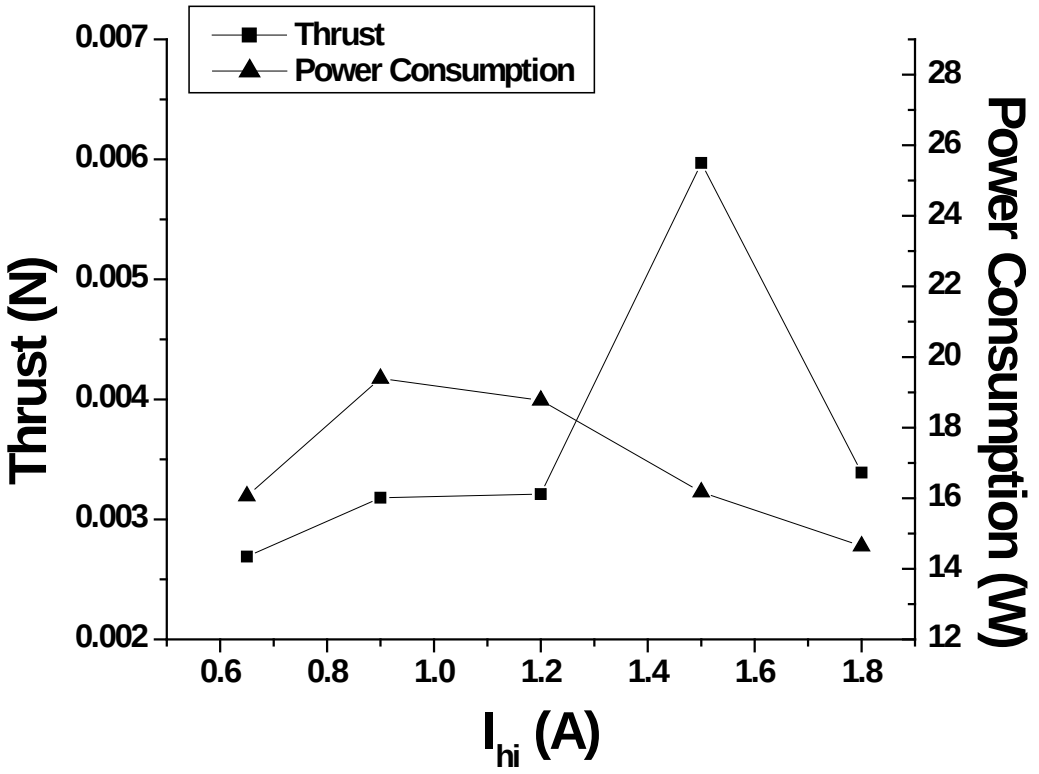

Figure 4.2.10: Average instantaneous thrust and average instantaneous power consumption as a function of I_{hi} . All values are for I_{lo} of 0.65 A and duty cycle of 35% over 12 cycles of actuation.

The results show that a maximum thrust was achieved with I_{hi} = 1.5A. Rapid heating with I_{hi} = 0.9 A increases thrust but also power consumption. Increasing I_{hi} further reduces power consumption while still increasing thrust. At I_{hi} = 1.5A, thrust peaks and then decreases. Higher currents may cause too rapid of a contraction and lead to poor bell kinematics and hydrodynamics. At I_{hi} of 1.5A, thrust was >120% higher than without rapid heating (I_{hi} = 0.65A) and power consumption was only increased by 1.28%. To see the effect of duty cycle, tests were conducted with I_{hi} = 1.5A and I_{lo} = 0.65A as duty cycle was varied, see Fig. 4.2.11. Maximum thrust occurs at a duty cycle of 35%. This agrees with the 33.3% duty cycle (1:2 contraction to relaxation ratio) of the natural jellyfish. Increasing duty cycle further increases power consumption but not thrust. Too small of a duty cycle causes the bell to relax early and the

vehicle assumes a more oblate shape which is less hydrodynamic. A large duty cycle causes excess residual heat in the actuators. The thrust produced with I_{hi} = 1.5A and 35 % duty cycle first appears as an peak in Fig. 4.2.10 since it does not follow the expected trend but the results of constant I_{hi} = 1.5A and varying duty cycle in Fig. 4.2.11 show a trend with less deviation and confirm its accuracy.

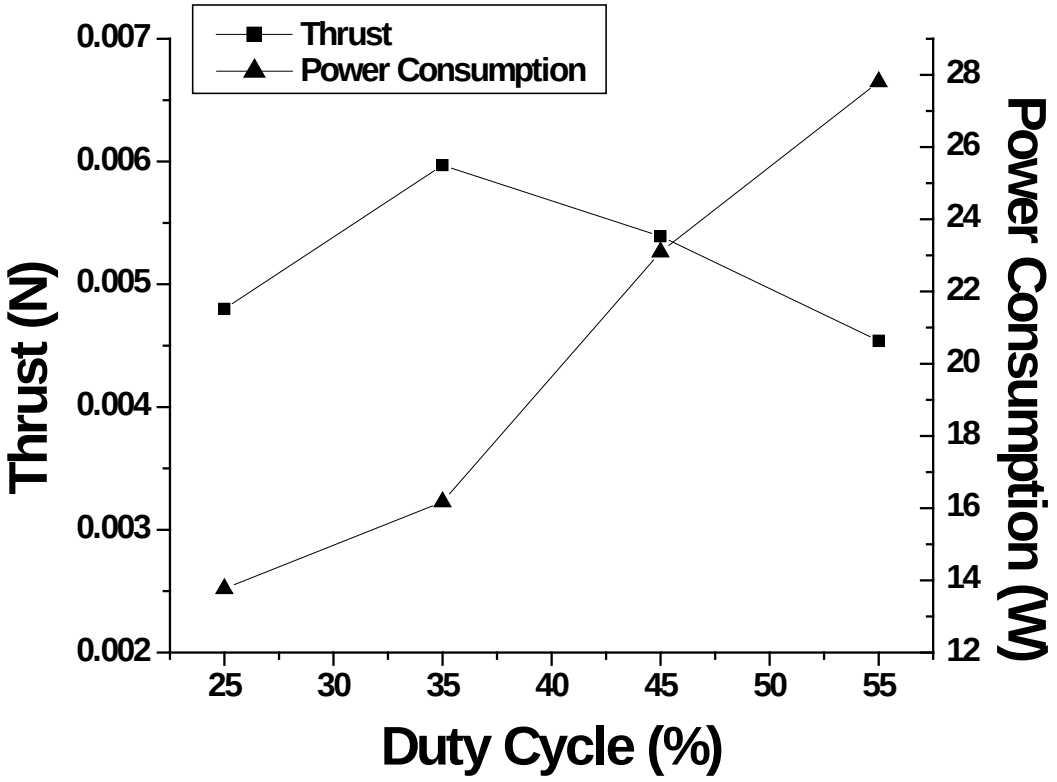

Figure 4.2.11: Average instantaneous thrust and average instantaneous power consumption as a function of percentage duty cycle. All values are for I_{hi} = 1.5 A, I_{lo} = 0.65 A and after 12 cycles of actuation.

The y-position over time of the Robojelly swimming for an I_{hi} = 1.8 A, I_{lo} = 0.65 A and duty cycle = 35 % is shown in Fig. 4.2.12 with corresponding velocity and acceleration. Results show the initial sinking followed by a series of actuations which produce small bumps in the y-position vs. time plot. The velocity and acceleration plots show an increasing velocity as well as average acceleration that remain constant over 26 cycles.

(a)

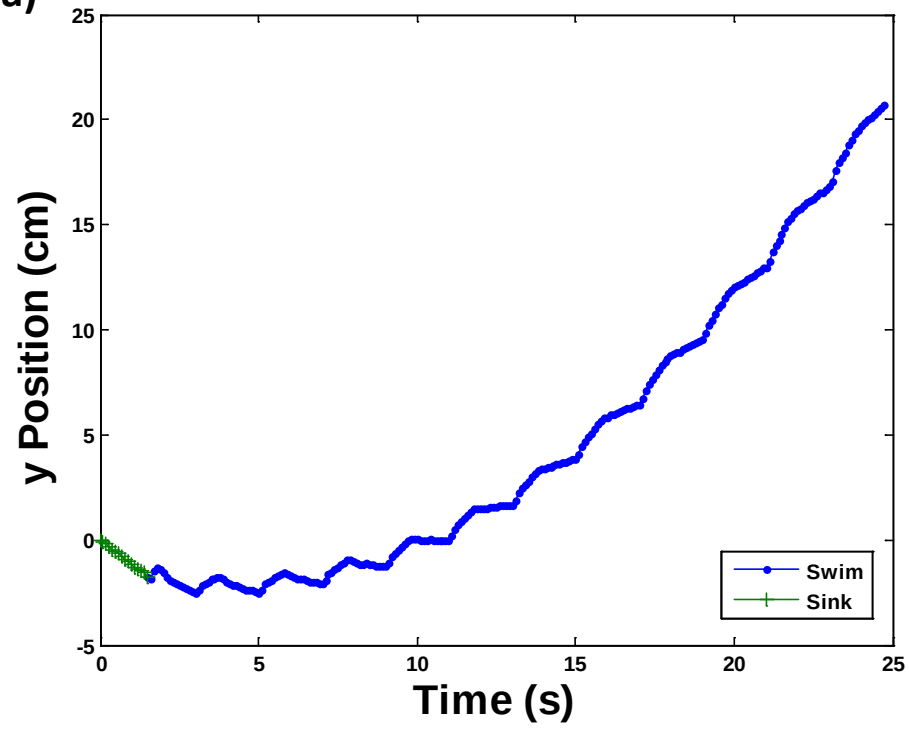
y Position (cm)
Time (s)
Swim
Sink

(b)

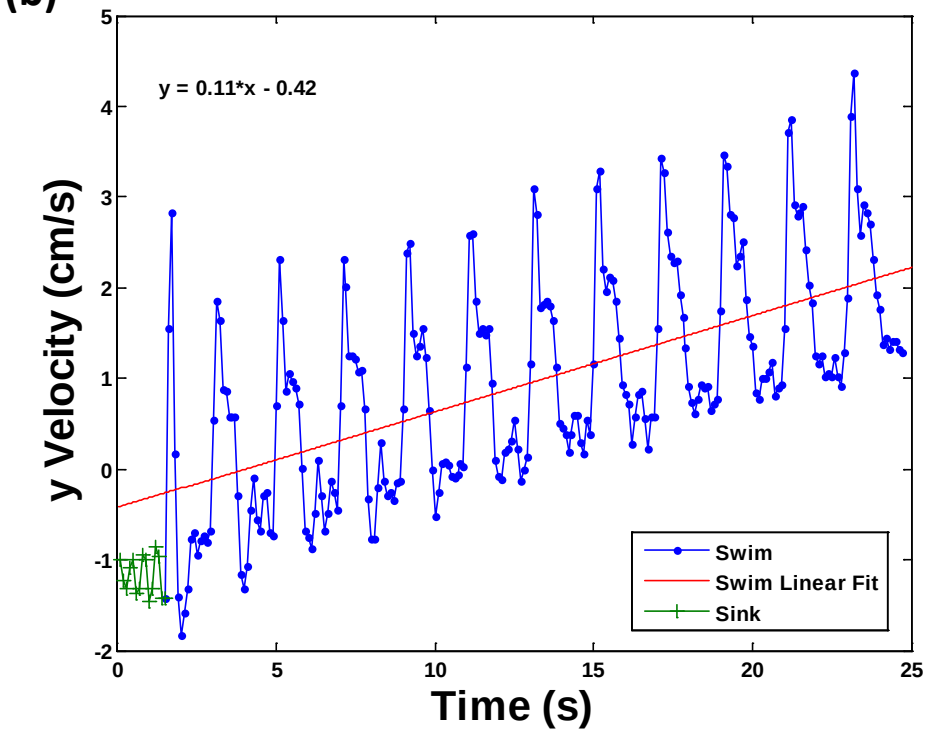
y = 0.11*x - 0.42
y Velocity (cm/s)
Time (s)
Swim
Swim Linear Fit
Sink

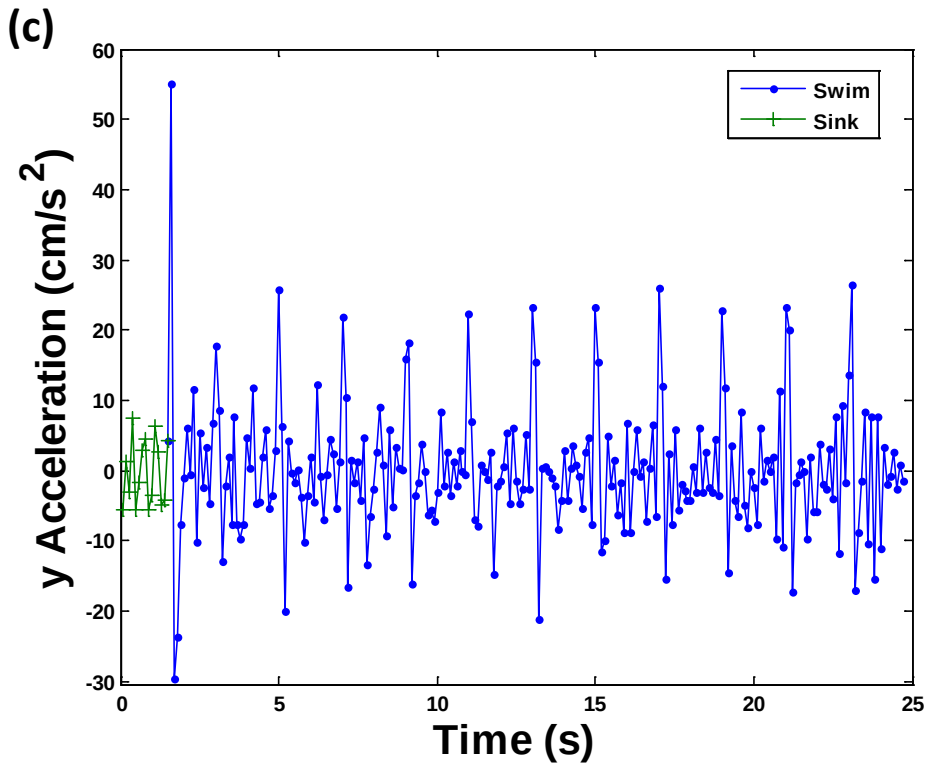

Figure 4.2.12: Robojelly y-position over time and corresponding velocity and acceleration for 12 cycles of actuation with an initial sinking rate of -0.078 cm/s^2, initial velocity of -1.42 cm/s upon first actuation, I_{hi} = 1.8 A, I_{lo} = 0.65 A and duty cycle = 35 %.

The maximum proficiency for Robojelly was found to be 0.178 s^{-1}, which was achieved with an I_{hi} of 1.8 A and duty cycle of 35 % after 15 cycles. A maximum thrust of 0.006 N was achieved with an I_{hi} of 1.5A and duty cycle of 35 % with corresponding power consumption of 16.2 W. The maximum proficiency was not produced by the maximum thrust because for the 1.8 A run, the vehicle was sinking less and was able to reach greater velocity.

4.3 Chapter Summary

A systematic method for the design and fabrication of a robotic jellyfish "Robojelly" with SMA based BISMAC actuators was developed. Robojelly mimics the natural *A. aurita*'s bell

geometry, passive relaxation mechanism, neutral buoyancy, duty cycle, actuation frequency, flap and deformation profile. The joint geometry was approximated for *A. aurita* and the actuation mechanism utilizes a radial configuration instead of the natural circular configuration. The results clearly show that Robojelly was able to produce enough thrust to propel itself and achieve a proficiency of 0.19 s^{-1} which is comparable to the natural medusa at 0.25 s^{-1}. A folding effect was observed in the silicone bell which was found to decrease performance. This problem was fixed by segmenting the bell allowing a more uniform deformation. Adding a passive flap to the segmented bell configuration was found to increase average thrust by over 1300 %. The vehicle consumed an average of 16.74 W over its 14^{th} cycle of actuation. The concept of BISMAC actuators was implemented but was not fully optimized for this vehicle. Future work will include optimizing the BISMAC actuators to match the *A. aurita* deformation profile and kinematics more accurately to increase vehicle performance. Robojelly average thrust reached a maximum of 0.006 N at I_{hi} = 1.5A and duty cycle of 35 %. The rapid heating technique increased thrust by 120 % and power consumption by only 1.28 %. Duty cycle compared favorably to the natural jellyfish which demonstrates the benefits of biomimetics.

4.4 References

Arai, M. N. (1997). A Functional Biology of Scyphozoa *London: Chapman & Hall* 35, 188-193

Bajaca, T., Malacic, V., Malej, A. and Sirok, B. (2009). Kinematic properties of jellyfish *Aurelia* sp.. *Hydrobiologia,* 616, 279-289

Batchelor, G. K. (1967). An Introduction to Fluid Dynamics *New York: Cambridge University Press.*

Bhushan, B., Koch, K. and Jung, Y. C. (2008). Biomimetic hierarchical structure for self-cleaning. *Appl. Phys. Lett.* 93 093101

Bunget ,G., Seelecke, S. and Place, T. J. (2008). Design and Fabrication of a Bio-Inspired Flapping Flight Micro-Air Vehicle *ASME 2008 Conference on Smart Materials, Adaptive Structures and Intelligent Systems,* 647-654

Chapman, D. M. (1998). Microanatomy of the bell rim of *Aurelia aurita* (Cnidaria: Scyphozoa) *Can. J. Zool.* 77, 34-46

Colin, S. P. and Costello, J. H. (2002). Morphology, swimming performance and propulsive mode of six co-occurring hydromedusae. *J. Exp. Biol.* 205, 427-437

Cook, S. (2010). New Zealand Coastal Marine Invertebrates *Christchurch: Canterbury University Press.* 229-230

Costello, J., and Colin, S. (1984). Morphology, fluid motion and predation by the scyphomedusa *Aurelia aurita*. *Marine Biol.*327–334

Dabiri, J. P., Colin, S. P. and Costello, J. H. (2005). Flow patterns generated by oblate medusan jellyfish: field measurements and laboratory analyses. *J. Exp. Biol.* 208, 1257–1265

Daniel, T. L. (1983). Mechanics and energetics of medusan jet propulsion. *Can. J. Zool.* 61, 1406 -1420

Dawson, M. N. (2003). Macro-morphological variation among cryptic species of the moon jellyfish, Aurelia (Cnidaria: Scyphozoa). *Mar. Biol.* 143, 369–379

Featherstone, R. and The, Y. H. (2004). Improving the Speed of Shape Memory Alloy Actuators by Faster Electrical Heating. *Int. Symp. Experimental Robotics (ISER'04),* 18-21

Ford, M. D. and Costello, J. H. (2000). Kinematic comparison of bell contraction by four species of hydromedusae. *Sci. Mar*. 64, 47-53

Gladfelter, W. G. (1972). Structure and function of the locomotory system of Polyorchis montereyensis (Cnidaria, Hydrozoa). *Helgol. Wiss. Meeresunters.* 2,3 38–79

Gladfelter, W. G. (1973). Structure and function of the locomotory system of the Scyphomedusa Cyanea capillata, *Mar. Biol.* 14, 150–160

Guo, S., Fukuda, T. and Asaka, K. (2003). A new type of fish-like underwater microrobot. *IEEE/ASME Trans Mechatronics,* 136–141

Gust, D., Moore, T. A. and Moore, A. L. (2001). Mimicking Photosynthetic Solar Energy Transduction *Acc. Chem. Res.* 34, 40–48

Hoerner, S. F. (1965). Fluid-Dynamic Drag. Brick Town, NJ: Hoerner Fluid Dynamics.

Kramp, P. L. (1959). Stephanoscyphus (Scyphozoa) *Galatea Report* 1, 173-185

Kuribayashi, K. (1991). Improvement of the Response of an SMA Actuator Using a Temperature Sensor. Intern. *J. Rob. Research* 10(1), 13-20

Lazaris, A., Arcidiacono, S., Huang, Y., Zhou, J., Duguay, F., Chretien, N., Welsh, E. A., Soares J. W. and Karatzas, C. N. (2002). Spider Silk Fibers Spun from Soluble Recombinant Silk Produced in Mammalian Cells ,*Science* 295 472-476

Lee, H., Lee, B. P. and Messersmith, P. B. (2007). A reversible wet/dry adhesive inspired by mussels and geckos. *Nature* 44**8** 338-341

McHenry, M. J. (2007). Comparitive Biomechanics: The Jellyfish Paradox Resolved. *Current Biology*, 17 R632-R633

McHenry, M. J. and Jed, J. (2003). The ontogenetic scaling of hydrodynamics and swimming performance in jellyfish (Aurelia aurita). *J. Exp. Biol.* 206, 4125-4137,

Menciassi, A. and Dario, P. (2003). Bio-inspired solutions for locomotion in the gastrointestinal tract: background and perspectives. *Phil. Trans. R. Soc. Lond. A* 361, 2287-2298,

Mukherjee, R., Christian ,T. F., et al. (1996). An actuation system for the control of multiple shape memory alloy actuators. *Sensors Actuat.* 55(2-3), 185-192

Omori, M. and Kitamura, M. (2004). Taxonomic review of three Japanese species of edible jellyfish (Scyphozoa: Rhizostomeae). *Plankton Biol. Ecol.* 51, 36–51

Raparelli, T., P. B. Zobel, et al. (2002). A robot actuated by shape memory alloy wires. *Proc. IEEE Intern. Symp. Indus. Elect*. 1-4, 420-423

Satterlie, R. A., Thomas, K. S. and Gray, G. C. (2005). Muscle Organization of the Cubozoan Jellyfish Tripedalia cystophora Conant 1897. *Biol. Bull.* 209, 154-163

Sahin, M., Mohseni, K. and Colin, S. P. (2009). The numerical comparison of flow patterns and propulsive performances for the hydromedusae *Sarsia tubulosa* and *Aequorea victoria. J. Exp. Biol.* 212, 2656-2667

Seibel, B. A. and Drazen, J. C. (2007). The rate of metabolism in marine animals: environmental constraints, ecological demands and energetic opportunities. *Phil. Trans. R. Soc. B,* 362 2061-2078

Smith, C. and Priya, S. (2010). Bio-inspired unmanned undersea vehicle. *Proc. SPIE* 7644 76442A

Song, G. B., N. Ma, et al. (2007). Position estimation and control of SMA actuators based on electrical resistance measurement. *IOP Smart Struct. Syst.* 3(2), 189-200

Takeda, Y., Cho and Yamamoto H. T. (2008). Control Characteristics of Shape Memory Alloy Actuator Using Resistance Feedback Control Method. *Advances in Sci. Tech.* 59, 178-183

Teh, Y. H. and R. Featherstone (2008). An architecture for fast and accurate control of shape memory alloy actuators. *Intern. J. Robot. Res.* 27(5), 595-611

Trask, R. S., Williams, H. R. and Bond, I. P. (2007). Self-healing polymer composites: mimicking nature to enhance performance. *Bioinspir. Biomim.* 2, P1

Villanueva, A., Bresser, S., Chung, S., Tadesse, Y. and Priya, S. (2009). Jellyfish inspired underwater unmanned vehicle, *Proc. SPIE,* 7287, 72871G

Villanueva, A. and Priya, S. (2010). BISMAC control using SMA resistance feedback *Proc. SPIE,* 7642, 76421Z

Villanueva, A. A., Joshi, K. B., Blottman, J. B. and Priya, S. (2010a). A bio-inspired shape memory alloy composite (BISMAC) actuator, *Smart Mater. Struct.* 19, 025013

Villanueva, A., Priya, S., Anna, C. and Smith, C. (2010b). Robojelly bell kinematics and resistance feedback control. *IEEE Intern. Conf. Robot. Biomim.*, 1124-1129

Villanueva, A., Smith, C. and Priya, S. (2010c). BISMAC control using SMA resistance feedback. *Proc. SPIE* 7642, 76421Z

Villanueva, A., Smith, C., Priya, S. (2011). Biomimetic Robotic Jellyfish (Robojelly) using Shape Memory Alloy. *IOP Bioinspir. Biomim.* 6, 036004

Wang, Z., Hang, G., Wang, Y., Li, J. and Wei, D. (2008). Embedded SMA wire actuated biomimetic fin: a module for biomimetic underwater propulsion. *Smart Mater. Struct.* 17, 025039

Webb, G., Wilson, L., Lagoudas, D. C. and Rediniotis, O. (2000). Adaptive control of shape memory alloy actuators for underwater biomimetic applications. *AIAA J.*, 38(2), 325-334

Yang, Y., Ye, X. and Guo, S. (2007). A New Type of Jellyfish-Like Microrobot. *Proc. IEEE Intl. Conf. Integr. Tech.*

Yasrebi, M., Kim, G. H., Gunnison, K. E., Milius, D. L., Sarikaya, M. and Aksay, I. A. (1990). Biomimetic processing of ceramics and ceramic-metal composites. *Better Ceramics through Chemistry IV,* 180, 625–635

Chapter 5

Cyanea capillata Kinematics

For some ocean surveillance applications, large vehicles with more payload room can be desirable. A goal of replicating one of the largest species of jellyfish was set to study the effect of scale on the hydrodynamics and mechanics of such large animal in order to understand its impact on biomimetic jellyfish vehicle. The *Cyanea capillata* was chosen as model species and a biomimetic robot presented in Chapter 6 was developed to serve as a scientific platform. This robot termed Cyro had for objective to mimic the performance, motion and morphology of the natural animal and be greater than 1.5 m in bell diameter. The morphology of the *C. capillata* could be replicated using images and anatomical diagrams but the performance and motion required kinematic data. Limited information is available on *C. capillata* and no information is available on the kinematics of large specimen. An in situ video of a *C. capillata* 50 cm in diameter was found to have the best potential for providing the necessary kinematics. The in situ video had a series of artifacts which required corrections before being able to extract the necessary kinematics. Novel correction techniques for in situ video are presented in Section 5.2 which allows the analysis of animal kinematics. This is followed by a novel approach at analyzing jellyfish bell kinematics in Section 5.3 where discretization methods and modeling methods are developed. The resulting kinematics are then analyzed to provide insights for the development of Cyro.

5.1 Correction Techniques for In Situ Animal Kinematics

The ability to analyze in situ video from field recordings is crucial to the study of many organisms which are either too large or too delicate to work within the laboratory environment. In addition, field recordings allow observation of animals in their natural habitat, thus reducing the probability of behavioral alterations and other effects common in laboratory studies such as wall effects (Webb, 1993). High quality kinematic data is required for many biological studies as well as for the development of biomimetic and bio-inspired systems. In a controlled environment, two-dimensional (2D) analysis can often provide suitable kinematics of a specimen (Norberg, 1976; Sfakiotakis et al., 1999; Rosenberg, 2001; Colin and Costello, 2002; Sathirapongsasuti et al., 2004; Poelma et al. 2006; Ijspeert et al, 2007). Three-dimensional (3D) methods, such as multiple integrated 2D cameras can capture more complex kinematics where substantial motion is occurring in all three planes (Tian et al., 2006; Fry et al., 2006; Tobalske et al., 2006). However, these techniques are difficult to apply in most field settings where animal locations are often random and their presence is spontaneous. In these situations a single camera operated by hand often provides the only means for recording animal behavior. This problem is exemplified in situations where a free-swimming scuba diver needs to record large free-swimming animals such as fish, marine mammals, sea turtles or jellyfish. In this scenario, not only is the animal moving freely in 3D but so is the diver. The simultaneous multi-axis motion of both the animal and diver make using traditional methods of kinematic analysis unfeasible.

In this section a novel method for obtaining accurate kinematics from in situ underwater recordings is presented, using the jellyfish *Cyanea capillata* as an example. Large *C. capillata* are animals which cannot feasibly be analyzed in a controlled environment and as a result, little information is available in the literature on their behavior and swimming kinematics. These

techniques will help deriving accurate kinematics from video recordings obtained in sub-optimal conditions. This provides the ability to extract potentially valuable biological information from future recordings and existing footage.

5.1.1 Materials and methods

An in situ video of a large *C. capillata* was used to elucidate the swimming kinematics of the animal. The video was obtained from the Ocean Footage video library and was filmed in the Atlantic Ocean off the coast of Norway. The exact animal size is unknown but is approximated to be 50 cm in diameter using a diver nearby as reference.

The analysis can be visualized to take place on a 2D surface perpendicular to the camera. Traditionally, in order to capture animal kinematics accurately, several criteria are required: (1) The animal motion must occur in a 2D plane parallel to the camera plane. Due to the asymmetry of animals such as the *C. capillata*, the angle at which the animal faces the camera is important. The animal consists of 8 bell segments and to extract proper bell kinematics, two opposing bell segments need to be perpendicular to the field of view. (2) The 2D plane must be at a constant distance from the camera during the duration of the analysis. Otherwise, the animal scale changes over time. (3) The animal must not rotate about the x- or y-axis of the camera. Rotation out of plane causes part of the profile information to be lost when projected on the 2D camera plane. The later criteria cannot be compensated during post-processing if only one view of the motion is available.

5.1.1.1 Profile tracking

In a dynamic environment such as the ocean, it is difficult to achieve all the aforementioned criteria. The selected video of *C. capillata* meets criteria (1) and (3) with negligible rotation about the x- and y-axis but does not meet criteria (2). The footage begins with the jellyfish's bell fully contracted and covers two full cycles. It was filmed at 25 fps with image resolution of 640 x 360 pixels. The entire exumbrella from one margin to another was digitized manually for every 5 frames using ImageJ resulting in a number of points i for each frame j. Selected raw profiles after digitization are shown in Fig. 5.2.1.

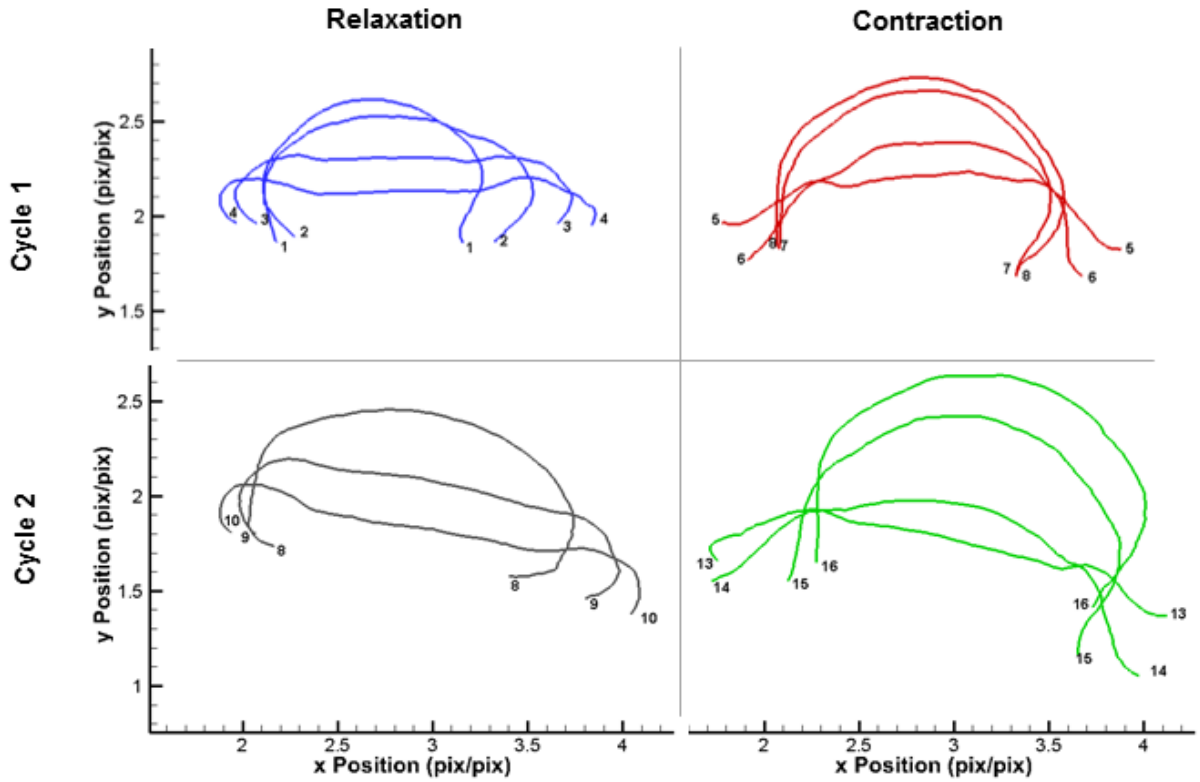

Figure 5.1.1: *Cyanea capillata* exumbrella profiles over two full swimming cycles before processing. Profile tips are numerically labeled in order of occurrence. Note the change in apparent animal size over just two swimming cycles. The profiles displayed were manually selected in order to fully display the bell kinematics at different instances. Each contraction and relaxation phases for both cycles are represented by a different color. The position has been normalized by the half exumbrella arclength in the relaxed position of the first cycle.

5.1.1.2 Body tracking

The digitized profiles were post-processed in order to obtain a set of half profiles which can be used for kinematic analysis. The data was first zeroed about the bell apex. The apex was found by measuring the exumbrella arclength in the fully contracted position and then finding the middle point. Post-processing strongly relies on the location of the apex. It is therefore crucial to obtain an apex location over time which is as accurate as possible. Tracking of the apex using the

exumbrella arclength over time leads to significant error due to complexity in locating the bell margins on some frames. Margin location largely affects the exumbrella length and therefore the apex location. The apex was tracked over time by tracking a visible point on the bell near the apex and then shifting the point accordingly. The point positions were normalized by the exumbrella arclength of the half profile in the relaxed position of the first cycle.

5.1.1.3 Magnification

The chosen video sequence was recorded from a camera that moves relative to the animal. The animal itself is moving relative to the ocean floor and the camera moves closer to the animal during the sequence. These factors affect the magnification of the animal and must be accounted for in order to resolve the correct bell kinematics. Two different techniques are used to account for magnification. The first technique uses the reference in the background to estimate the motion of the camera relative to the background *(a)*. The second method uses a dimension on the animal itself *(b)*.

a) Background reference

A significant image magnification occurs in the sequence which is due to the camera moving relative to the ocean floor. A rock on the ocean floor was used as a reference to estimate the ground position relative to the camera. The rock moves out of frame as the camera is moving toward the rock, see Fig. 5.2.2A.

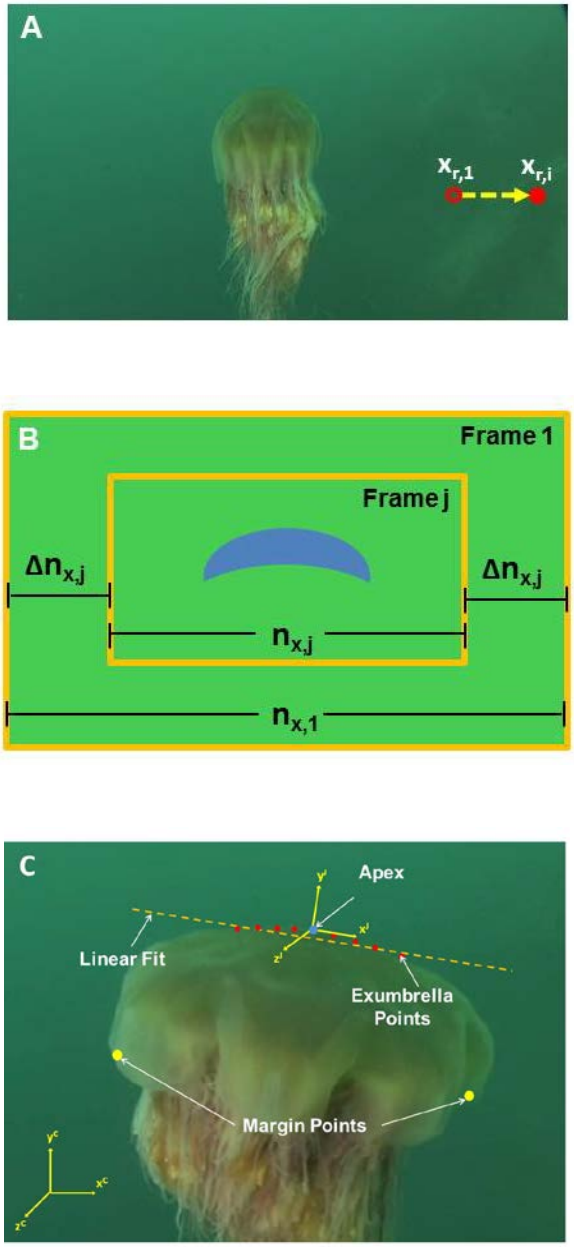

Figure 5.1.2: Illustrations of how image magnification was compensated for by using a reference point on the ocean floor. (A) Frame of the *Cyanea capillata* footage used for bell kinematics digitization with reference rock highlighted by a red hollow dot in the first frame and red dot in frame j>1. (B) Schematic of magnification correction technique using a background reference point. (C) Schematic of the method used to account for the body rotation about the z^J-axis and z^C-axis. The red dots represent the exumbrella points $c \le i \le d$ which meet the 24% criteria. The linear fit was calculated from these exumbrella points.

The total number of pixels is constant for each frame. In the x-direction, the following is true:

$$n_{x,1} = n_{x,j} \qquad (5.1.1),$$

where $n_{x,1}$ and $n_{x,j}$ are the number of pixels in frame 1 and j respectively. Frame 1 is taken as the reference frame where the rest of the frames will be adjusted to match its scale. Eq. 5.1.1 is illustrated in Fig. 2B. As the jellyfish is magnified in the camera frame, the rock moves out of frame by a distance of:

$$\Delta n_{x,j} = x_{r,1} - x_{r,j} \qquad (5.1.2),$$

where $x_{r,1}$ and $x_{r,j}$ are the x-position of the reference rock in frame 1 and j respectively. The magnification results in an increase in resolution where more pixels represent the jellyfish. This increase in pixel is proportional to the rock displacement by:

$$s_j = \frac{n_{x,j} + 2\Delta n_{x,j}}{n_{x,1}} \qquad (5.1.3),$$

where s_j is the scale for frame j by which the profile coordinates are multiplied in order to keep the same scale as in the reference frame. Eq. 5.1.3 assumes the camera moves with the jellyfish centered in its frame. The displacement of the rock in the y-direction is negligible in this image sequence. The same analysis could be conducted with displacement in the y-direction. The analysis also assumes that the camera is moving only in the z-axis. Displacement in the x-axis or rotation about the y-axis of the camera would result in error.

b) Animal dimension

The exumbrella arclength can be used to assess the scale change over time. The arclength is calculated using:

$$S_{i,j} = 0, \quad i = 1$$

$$S_{i,j} = \sum_{b=2}^{i} \sqrt{\left(x_{i,j} - x_{i-1,j}\right)^2 + \left(y_{i,j} - y_{i-1,j}\right)^2}, \quad i > 1 \qquad (5.1.4),$$

where $x_{i,j}$ and $y_{i,j}$ are the coordinates of the exumbrella point i. To account for the displacement of the jellyfish relative to the camera, the animal itself can be used as a reference. The *C. capillata* specimen has no anatomical features of fix length which can be used as a reference point to determine scale. Exumbrella arclength can be used as a size reference but the exumbrella naturally undergoes an increase in length during contraction and a decrease in length during relaxation. Therefore, the arclength cannot be used directly to scale the images but the exumbrella will have the same length at a given stage of different swimming cycles. The exumbrella length in the fully contracted position is used at three different times in the swimming sequence. A linear fit of those three points gives a correction scale by which the exumbrella profiles can be adjusted.

5.1.1.4 Body rotation

Body rotation can be quantified for analysis or for removal. To account for body rotation, two coordinate systems must be established. The first coordinate system labeled C, is fixed on the camera lenses and the second coordinate system labeled J, is a body fixed coordinate system

which is centered on the jellyfish apex as shown in Fig. 5.2.2C. The *C. capillata* specimen rotates about the z^{C}-axis during its two swimming cycles. We assume that the z^{C}-axis and z^{J}-axis are parallel. In this application, the rotation angle is calculated so it can be removed from the bell kinematics. In other words, we want to analyze the jellyfish motion from the jellyfish coordinate system.

Two different methods were considered to calculate body rotation of the jellyfish relative to the camera coordinate system. The first method uses the angle formed by a line passing through the margin points. As the animal stabilizes itself, it undergoes small non-axisymmetric kinematics. This causes the margin to deform at different rates on each side and therefore causes this method to result in incorrect angles. Also, the slightest discrepancy in margin position will significantly affect the angle. The second method uses the fact that the area in proximity of the apex undergoes very small deformation during swimming and is also not affected significantly by non-axisymmetric deformation (Ford and Costello, 2000; Bajcar et al., 2009; Villanueva et al., 2010). A linear fit of points in that region can be used to produce a line from which the angle of the animal is calculated as shown in Fig. 5.1.2C.

The points falling within ±24% of the exumbrella arclength on each side where $c \le i \le d$, were selected for this calculation. N_{cd} is the total number of points from c to d. The mean location of these points was calculated as follows:

$$\overline{x}_j^{C} = \frac{1}{N_{cd}} \sum_{i=c}^{d} x_{i,j}^{C} \qquad (5.1.5),$$

$$\overline{y}_j^{C} = \frac{1}{N_{cd}} \sum_{i=c}^{d} y_{i,j}^{C} \qquad (5.1.6).$$

A linear fit was calculated using the following equation:

$$y_{LF,j}^{\mathrm{C}} = a_j x_{LF,j}^{\mathrm{C}} \qquad (5.1.7),$$

where:

$$a_j = \frac{\sum_{i=c}^{d}\left(x_{i,j}^{\mathrm{C}} - \overline{x}_{LF,j}^{\mathrm{C}}\right)\left(y_{i,j}^{\mathrm{C}} - \overline{y}_{LF,j}^{\mathrm{C}}\right)}{\sum_{i=c}^{d}\left(x_{i,j}^{\mathrm{C}} - \overline{x}_{LF,j}^{\mathrm{C}}\right)^2} \qquad (5.1.8),$$

and $x_{LF,j}^{\mathrm{C}}$ and $y_{LF,j}^{\mathrm{C}}$ are the components of the linear fit. The rotation angle about the z^{J}-axis is:

$$\phi_j = \tan^{-1}\left(a_j\right) \qquad (5.1.9).$$

The exumbrella points in the jellyfish coordinate system are:

$$\mathbf{d}_{i,j}^{\mathrm{J}} = \mathbf{R}_{\mathrm{C}}^{\mathrm{J}}\mathbf{d}_{i,j}^{\mathrm{C}} \qquad (5.1.10),$$

where:

$$\mathbf{d}_{i,j}^{\mathrm{J}} = \begin{bmatrix} x_{i,j}^{\mathrm{J}} \\ y_{i,j}^{\mathrm{J}} \\ z_{i,j}^{\mathrm{J}} \end{bmatrix} \qquad (5.1.11),$$

$$\mathbf{d}_{i,j}^{\mathrm{C}} = \begin{bmatrix} x_{i,j}^{\mathrm{C}} \\ y_{i,j}^{\mathrm{C}} \\ z_{i,j}^{\mathrm{C}} \end{bmatrix} \qquad (12),$$

are the position vectors for each point in the jellyfish and camera coordinate systems respectively and:

$$\mathbf{R}_{\mathrm{C}}^{\mathrm{J}} = \begin{bmatrix} \cos(\phi_j) & \sin(\phi_j) & 0 \\ -\sin(\phi_j) & \cos(\phi_j) & 0 \\ 0 & 0 & 1 \end{bmatrix} \qquad (5.1.13),$$

is the rotation matrix between the camera and jellyfish coordinate system. The profiles were then divided into two sides, left and right with apex as the root of each profile. The data was then filtered with a second order Butterworth low pass filter with cut-off frequency of 20% of the Nyquist frequency which varied from 0.28 to 0.44 samples per pixel. This filter was applied to the points when converted into polar coordinates due to the curvature of the bell. The points were then converted back to Cartesian coordinates.

5.1.1.5 Profile discretization by interpolation

A random number of points were collected for each profile during digitization. A fixed number of points for each profile are desired to allow the analysis of a given point on the exumbrella. Since the exumbrella deforms during a swimming cycle, this method assumes it deforms equally throughout its arclength. A cubic spline was fitted to each half profile and by interpolating points (b) for a total of N_b=51 points per profile. The points span from the apex b=0 to the margin b=51. A description of cubic spline interpolation can be found in (Chapra, 2005) and can be implemented using built-in functions in software such as Matlab.

5.1.2 Results

5.1.2.1 Magnification

The total exumbrella arclength $S_{n,j}$ as a function of time is shown in Fig. 5.1.3. The original data showed a large increase in length. Once adjusted for magnification, the length magnitudes were better but still showed a significant increase over time. This increase could be related to the animal movement relative to the camera. This was accounted for by calculating the exumbrella length in the fully contracted position at three different times in the swimming sequence. The exumbrella length should be the same at those three instances. A linear fit was made through those three points and the data was scaled accordingly as shown in Fig. 5.1.3 by the LF Adjusted curve. This adjustment assumes that the magnification due to jellyfish movement relative to the camera was constant over the two swimming cycles. The adjusted result shows only minor discrepancies which could be due to rotation of the animal during swimming.

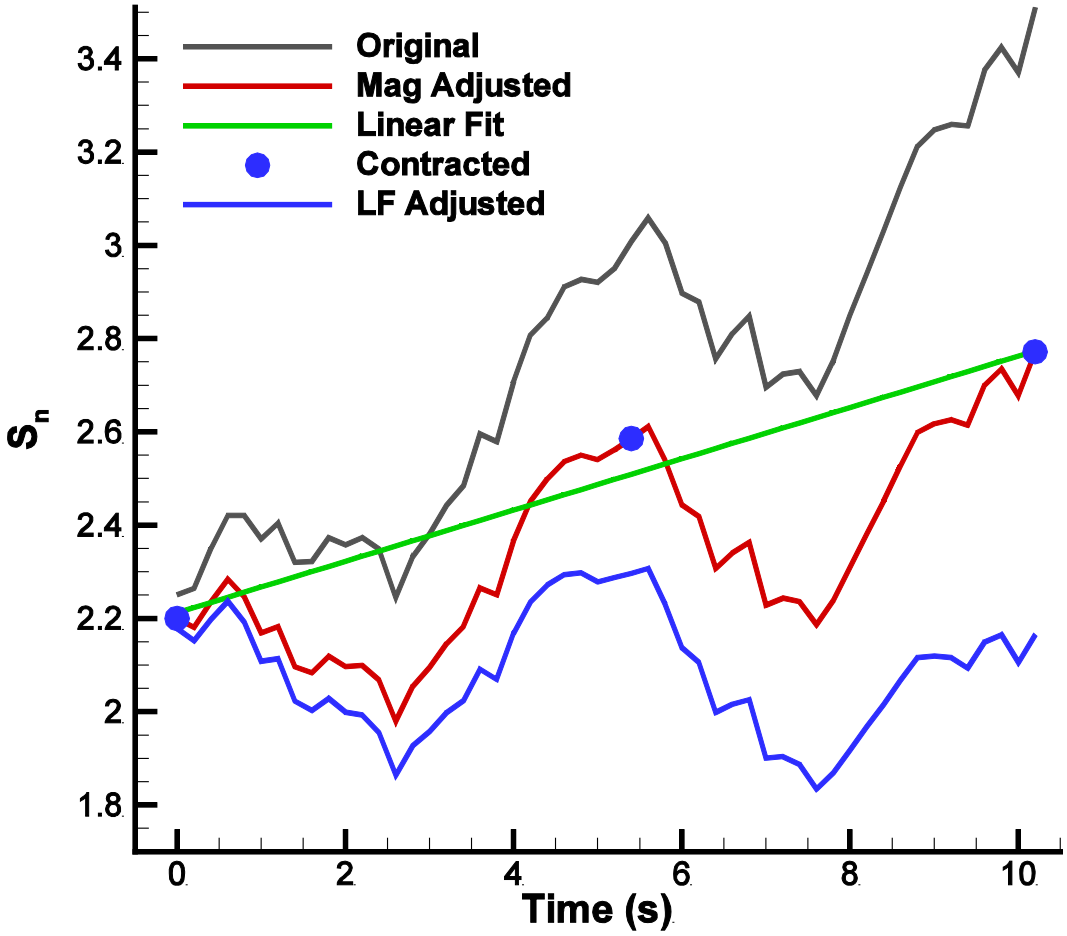

Figure 5.1.3: Normalized exumbrella arclength as a function of time for two full swimming cycles starting fully contracted. The Original lengths correspond to the raw digitized profiles. The Mag Adjusted lengths are the Original lengths corrected for magnification based on camera movement relative to the background. The Linear Fit accounts for the distance change between the jellyfish and camera by fitting a line through the exumbrella lengths in the fully contracted states at three different instances. The LF Adjusted lengths are the Mag Adjusted lengths with additional LF adjustment.

5.1.2.2 Bell kinematics

Selected profiles after processing are shown in Fig. 5.1.4A during a full cycle. The bell margin trajectory is also shown for two consecutive cycles. The overlay of the margin trajectory shows the accuracy at which the correction methods were able to account for the different video artifacts. The margin trajectories between the two cycles overlay well which means the bell is following a similar path during both cycles. In order for this to occur, magnification and rotation had to be properly compensated. Some minor variation is seen after processing. This can be due to the animal reacting to its environment and the resulting inconsistency in deformation, minor errors from the manual digitization process, the footage not fully meeting criteria (1) and (3) through the two cycles and the assumption of linear motion between the animal and camera.

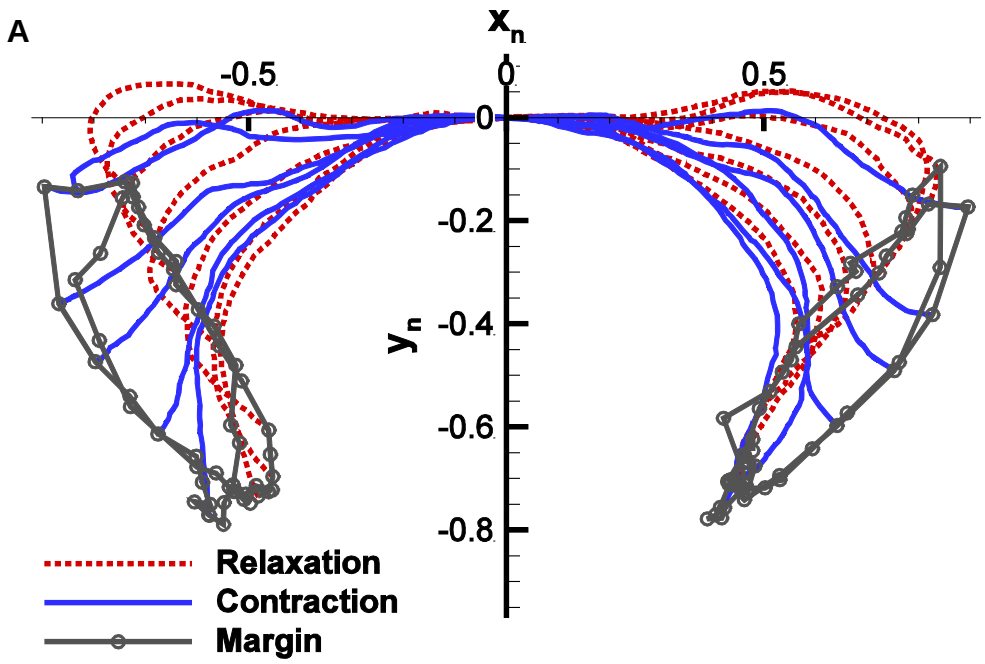

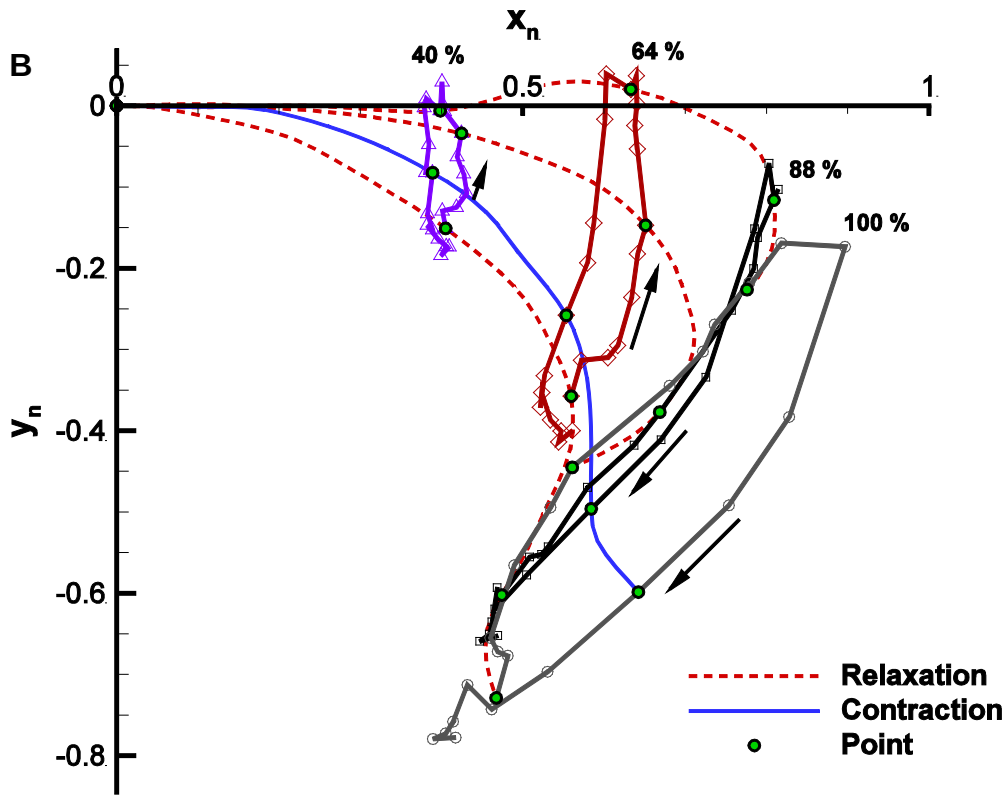

Figure 5.1.4: (A) *Cyanea capillata* exumbrella bell profiles are shown during a full cycle which includes contraction and relaxation. The profiles were arbitrarily selected over the first cycle of the digitized swimming sequence to demonstrate the different geometries encountered. Bell margin trajectory is shown for two consecutive cycles. The positions are normalized by the half exumbrella arclength in the relaxed position. (B) Bell trajectory at different exumbrella point locations based on arclength percentage. Trajectories are shown during the first swimming cycle along with selected profiles.

5.1.3 Discussion

Profile discretization by interpolation gives the trajectory of additional points along the exumbrella. The results for different point locations based on exumbrella arclength percentage are shown in Fig. 5.1.4B. These point trajectories allows the analysis of different locations along the bell and give a more complete understanding of how the bell deforms.

Many large or delicate marine animals are poorly studied and understood due to our lack of ability to acquire accurate data about them in their natural environment. The ability to use in situ recordings to obtain accurate kinematics provides insight into how these animals interact with their environment as well as potential for growth and reproduction. For jellyfish, swimming not only provides locomotion but also affects prey encounter (Acuña et al., 2011). However, very little is known about the influence of larger species. Therefore, understanding kinematics of swimming in these large specimens will provide insight into their influence on trophic ecology within marine ecosystems. The kinematics can also be used to model the fluid response of the animal's motion and the animal's structural response to the fluid interaction. Information about the two-way fluid-structure interaction is important for developing a bio-inspired system. Jellyfish hydrodynamics can be studied directly from live specimen but the analysis is limited since it is difficult to change parameters on a live animal. Having a kinematic model of an animal allows for the manipulation of many physical parameters that can guide the design of experiments as well as computational analysis (Pivkin et al., 2005; Mittal et al., 2006; Poelma et al., 2006; Ijspeert et al., 2007).

The *C. capillata* can reach sizes of over 2 m in diameter (Russell, 1970). Vehicles sizes on that order are desirable for certain applications. Jellyfish are known to change kinematics as they change size (Gladfelter, 1973) which will affect hydrodynamics and therefore vehicle thrust and efficiency. This indicates the importance of understanding an animal's kinematics and how they vary with size. The kinematic changes describe how the different robotic parts need to move. This dictates what kind of mechanism needs to be used, where the actuators need to be placed and what kind of actuators to use. Since such large jellyfish cannot feasibly be analyzed in a

controlled environment, in situ video processing techniques are necessary to capture and model animal kinematics.

5.2 *Cyanea capillata* bell kinematics analysis and modeling using strategic discretization techniques

Jellyfish have a unique propulsion mechanism which is of interest to a diverse group of researchers from disciplines such as biology, materials science and engineering. The mechanism by which jellyfish generates thrust in combination with other essential functions required to grow and reproduce can provide insight for a variety of applications such as vehicle propulsion, energy harvesting, synthetic heart valves and animal foraging. In our studies, we are particularly interested in using jellyfish as inspiration for the development of unmanned underwater vehicles (UUVs).

The *Cyanea capillata*, see Figure 5.2.1A, was chosen as model for the design of a UUV. This species is an advantageous model because it grows to large diameters (≥ 2m) making it one of the largest jellyfish species (Russell 1970). This model therefore provides the understanding required for the design of a larger biomimetic vehicle for tasks where large instruments or payloads are required. It is important to understand the implications of size on the propulsion mechanism of jellyfish but there is very little information available in literature addressing this issue.

McHenry and Jed (2003) investigated the scaling effects of *Aurelia aurita* on hydrodynamic performance. The specimen diameters ranged from 1.57 to 9.51 cm. Herschlag and Miller (2011)

have studied the effect of Reynolds number on *A. aurita* specimen ranging from 0.36 to 10.2 cm in diameter. *C. capillata* can reach dimensions over an order of magnitude from what has been analyzed and there is currently no hydrodynamic analysis of such large medusa.

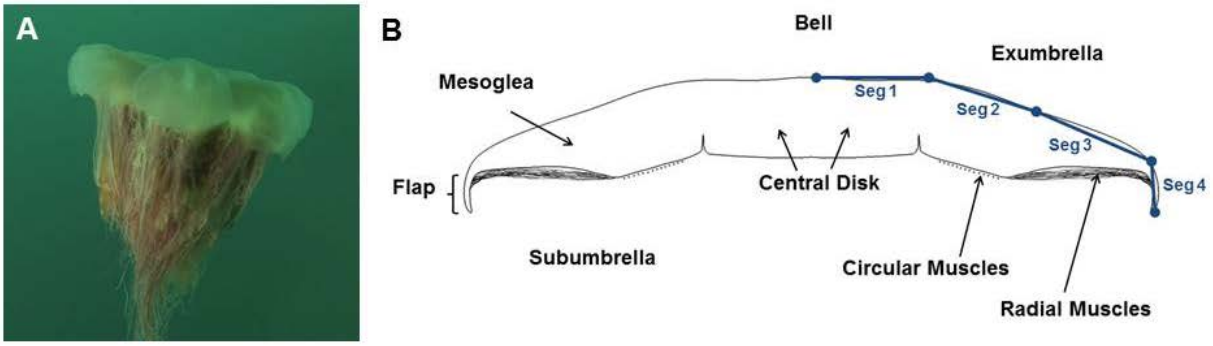

Figure 5.2.1: (A), image of a *Cyanea capillata* in the relaxed position. (B), Schematic of a *C. capillata* bell cross section showing different anatomical parts and a four-segment model of the exumbrella.

Jellyfish swim in an oscillating fashion which consists of a two phase cycle: contraction and relaxation. Contraction is achieved by muscles located in the subumbrella as shown in Fig. 5.2.1B, which cause a circumference decrease. The bell thickness then increases non-linearly and strains the radial mesogleal fibres (DeMont and Gosline, 1988). These fibres store elastic energy which is used to passively relax the bell to its original geometry. Jellyfish can be separated into two main categories based on their propulsion mechanism. Rowing jellyfish are oblate and can reach large dimensions, while jetting jellyfish are prolate and smaller (Ford and Costello, 2000). Rowers and jetters produce a starting vortex during contraction. During relaxation, jetters refill their bells in no particular way while rowers create a stopping vortex in the subumbrella. The interaction between the starting and stopping vortices results in larger thrust and efficiency which enables the rower's large dimensions (Dabiri et al., 2005; Dabiri et al., 2007, Sahin et al., 2009). This vortex interaction is of importance for vehicle performance and in the design of

UUVs. In order to replicate the vortex interaction in a biomimetic approach, the bell kinematics of rowers must be matched. Several investigations have been conducted regarding bell kinematics of rowers (Costello and Colin, 1994; Costello and Colin, 1995; Ford and Costello, 2000; Costello and Colin, 2002; Bajcar et al., 2009; Villanueva et al., 2010; Dabiri and Gharib, 2003), however, none have provided a time dependent model which can be used to replicate the jellyfish kinematics of the whole bell over a full cycle. This is often required to model the structural mechanics, hydrodynamics and mechanism for UUV design.

Jellyfish bell kinematics vary significantly from other animals. The locomotion is performed by a bell that is nearly uniform in structure and has high flexibility which undergoes large curvature change. This is different than most animals where motion occurs by actuating rigid internal structures about a pivot point such as in bone and joint mechanisms. The lack of rigid structures demands new kinematics tracking and analysis methods. Flexible structures can be discretized in order to estimate their deformation and motion such as done in finite element analysis (FEA) and computational fluid dynamics (CFD). Jellyfish bells have previously been discretized for CFD applications (Sahin et al., 2009; Wilson and Eldredge, 2011; Herschlag and Miller, 2011). In those instances, nodes are prescribed a certain displacement or force and the structure's resulting kinematics interacts with a surrounding fluid. A similar discretization process used to model in FEA and CFD can be used to describe the motion of live jellyfish.

A discrete kinematic bell model can be useful for several applications such as to analyze the function of different anatomical features. In this application, a discrete kinematic bell model should have segmentation representing the anatomical features of interest. A discrete kinematic bell model can also be used for CFD where a minimum number of nodes are used to mimic the kinematics. The discrete kinematic bell model can also be used to design a robotic analogue

which serves as a biomimetic UUV translating the swimming performance of the natural animal. The kinematics of the robot must match the natural jellyfish in order to achieve the same hydrodynamic performance.

Cyanea capillata are found in the North Atlantic, Pacific and Artic Oceans (Mayer, 1910). They can reach dimensions exceeding 2 m in bell diameter and tentacles of 36 m long (Russell, 1970). *Cyanea capillata* have one significant difference from most other jellyfish species; they have a segmented bell as opposed to a uniform bell. Segmentation allows flaps surrounding each of the bell segments to fold on itself during relaxation and expand during contraction. A maximum form area is therefore achieved during contraction while minimized during relaxation. Circular muscles in jellyfish subumbrella are typically responsible for propulsion. The *C. capillata* uses a combination of circular muscles and radial muscles to contract its bell and create propulsion (Gladfelter, 1973). Gladfelter reported that the circular muscles contract the bell for the first 30°-45° below the horizontal and the radial muscles further contract the bell up to a total of 90°. The *C. capillata* features long tentacles originating from the subumbrella. These tentacles are used to capture prey as they come in contact with the nematocysts on the tentacles. The subumbrella also has four oral arms with length of about a bell diameter (Mayor, 1910; Russell, 1970). *C. capillata* are usually a reddish-brown or yellowish color (Kramp, 1961).

5.2.1 Materials and methods

Information in literature is sparse for large *C. capillata* as they cannot be kept in captivity to conduct controlled experiments. Thus video imaging in natural waters is the only means to acquire kinematic information on the largest individuals. Footage taken in an uncontrolled environment can result in artifacts which can mask the desired animal kinematics.

5.2.1.1 Bell Kinematics

Footage of a large *C. capillata* was obtained from Ocean Footage. The video had a frame rate of 25 fps with image resolution of 640 x 360 pixels. This video was recorded in the Atlantic Ocean off the Norwegian shore. A swimming sequence is shown in Fig. 5.2.2. This footage features the jellyfish swimming as desired but has several artifacts which prevented a proper bell kinematic analysis. The animal moved relative to the camera as well as relative to the ocean floor. This caused a change in magnification throughout the sequence. The animal also had body rotation which needed to be compensated for in order to capture the bell motion used for swimming kinematics.

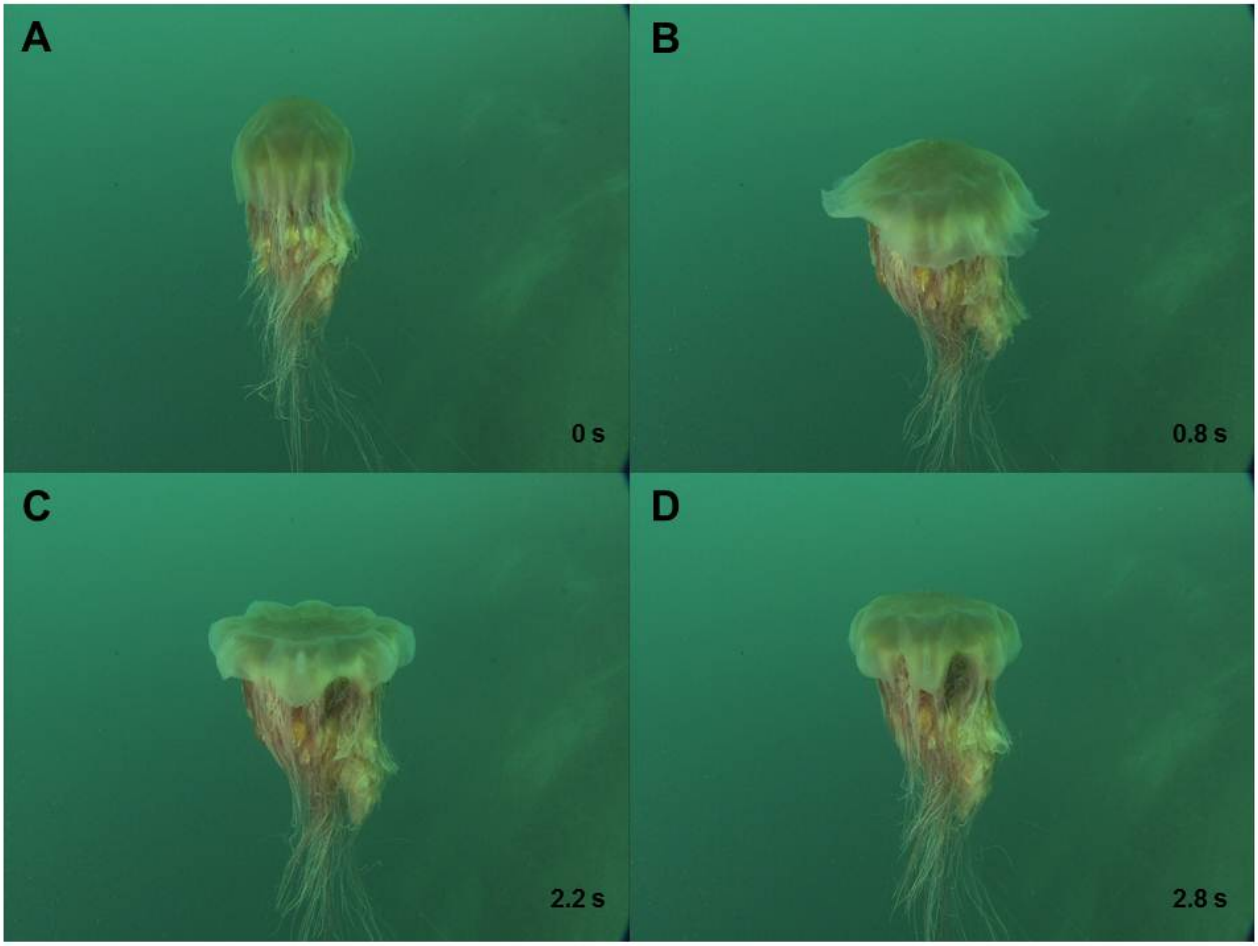

Figure 5.2.2: Swimming sequence of a large *C. capillata* in the Atlantic Ocean off the Norwegian shore. The animal is shown in the (A), fully contracted, (B), relaxing, (C) fully relaxed and (D) contracting states. The swimming cycle shown is the first of two digitized cycles.

The exumbrella profiles were digitized manually at every 5 frames for two consecutive swimming cycles using ImageJ for a total number of N = 52 frames. Magnification and rotation were corrected as described in Section 5.1. The digitized points were then zeroed about the apex and split into left and right half profiles. The half profiles were filtered and interpolated to give a fixed number of 51 points per profile. The profiles were normalized by the half exumbrella arclength in the fully relaxed state of the first swimming cycle.

5.2.1.2 Strategic bell discretization

Three discretization methods were explored to create a model of the *C. capillata* exumbrella. The first method is referred to as the tangent angle method and uses a series of bell profile to determine where most of the deformation occurs over time. The second method consists of observing the animal's anatomy to identify where the variations in structure and anatomical features might affect deformation. The third method consists of optimizing the node location for a set of segments by minimizing the error found between the discrete model and natural profiles.

(a) Tangent angle

Node location can be determined from the bell profiles by analyzing the change in deformation as a function of time. The two lines plotted on the bell profile in Fig. 5.2.3 isolate a node. The lines lie on sections of the bell where little deformation occurs and they intersect over the center of the node.

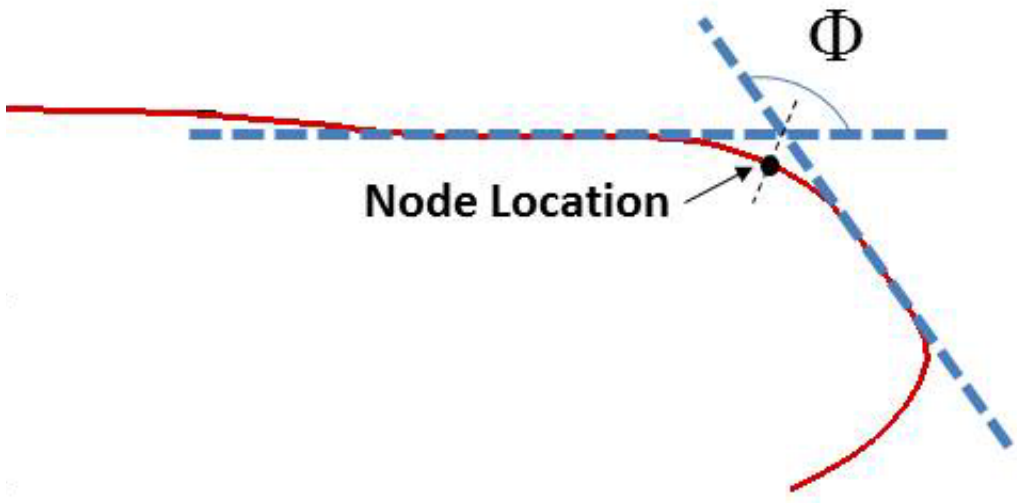

Figure 5.2.3: Schematic of the tangent angle method used to find node locations on *C. capillata* exumbrella profiles.

This method is achieved mathematically using the following procedure. The lines in Fig. 5.2.3 are determined at every point i by a line tangent to the curve. The angle created by the tangent lines with the x-axis can be found using the following equations:

$$\phi_{i,j} = \tan^{-1}\left(\frac{y_{i+h,j} - y_{i,j}}{x_{i+h,j} - x_{i,j}}\right), \quad i \le h$$

$$\phi_{i,j} = \tan^{-1}\left(\frac{y_{i+h,j} - y_{i-h,j}}{x_{i+h,j} - x_{i-h,j}}\right), \quad h < i < n_j - h \qquad (5.2.1),$$

$$\phi_i = \tan^{-1}\left(\frac{y_{i,j} - y_{i-h,j}}{x_{i,j} - x_{i-h,j}}\right), \quad i \ge n_j - h$$

where n_j is the total number of points per profile j and h is the step size used for this calculation. The lines used to find the angles in Eq. 5.1.1 were found using a forward finite difference and a backward finite difference at the two boundaries while a central finite difference was used for the rest of the points. The angle Φ formed by both lines was named the tangent angle and was calculated as follows:

$$\Phi_{i,j} = \pi - \left(\phi_{i-k,j} - \phi_{i+k,j}\right), \quad k < i < s - k \qquad (5.2.2),$$

where k is the step size for the lines used on each side of point i. The derivative of the tangent angle with respect to the arclength was then taken as follows:

$$\frac{d\Phi_{i,j}}{dS_{i,j}} = \frac{\Phi_{i+1,j} - \Phi_{i,j}}{S_{i+1,j}}, \quad i \le k$$

$$\frac{d\Phi_{i,j}}{dS_{i,j}} = \frac{\Phi_{i+1,j} - \Phi_{i-1,j}}{S_{i+1,j} - S_{i-1,j}}, \quad k < i < n_j - k \qquad (5.2.3),$$

$$\frac{d\Phi_{i,j}}{dS_{i,j}} = \frac{\Phi_{i,j} - \Phi_{i-1,j}}{S_{i-1,j}}, \quad i \geq n_j - k$$

where the arclength at each point i was calculated as:

$$S_{i,j} = 0, \quad i = 1$$

$$S_{i,j} = \sum_{b=2}^{i} \sqrt{\left(x_{b,j} - x_{b-1,j}\right)^2 + \left(y_{b,j} - y_{b-1,j}\right)^2}, \quad i > 1 \qquad (5.2.4),$$

The potential node locations can be found by setting the tangent angle derivative equal to zero. The derivative of the tangent angle effectively identifies the locations on the exumbrella where the tangent angle varies most with respect to surrounding parts on the bell.

(b) Anatomical analysis

The second method used to determine node locations consisted of analyzing the anatomical features of the natural animal to learn about the musculature and joint arrangements. Gladfelter (1973) studied the anatomy of *C. capillata* ranging from 2 to 30 cm in diameter. A specimen laying on its exumbrella with tentacles removed was used to obtain feature dimensions. The features of interests were the central disk, circular muscles, radial muscles and flap, see Fig. 5.2.1B. The dimensions were taken from the center of the bell to the different features and normalized by the bell radius.

(c) Error analysis

An error analysis was conducted to determine a segment configuration which best matched the natural animal's bell kinematics. It also allowed the evaluation of the other two different node detection methods. The area formed between the *C. capillata* bell profile and the segment representation was used to quantify the discrepancy between both profiles. This discrepancy or error is calculated using the following expression:

$$e_j = \int_0^{\zeta_j} \left| f_C\left(S_{i,j}\right) - f_m\left(S_{i,j}\right) \right| dS_{i,j} \qquad (5.2.5),$$

where ζ_j is the total arclength for each bell profile j, f_C and f_m are the bell profile and discrete bell model functions respectively. The error of each profile for both cycles was then summed as follows:

$$E = \sum_{j=0}^{N} e_j \qquad (5.2.6),$$

This gives the total error E for a given discrete bell model. It should be noted that the error is dimensionless since Eq. 5.1.10 is also dimensionless due to the normalized profiles.

5.2.1.3 Subumbrella Volume Change

Medusa propulsion is often modeled as a function of subumbrella volume change. The subumbrella volume can be approximated using the exumbrella profiles. This approximation neglects the bell thickness between the exumbrella and subumbrella and the tentacles attached to the subumbrella. The mesoglea volume is near constant during actuation and the tentacles are

fixed to the subumbrella. Therefore, this method provides a good estimation of the water volume during swimming. The subumbrella volume is defined as the space delimited by the exumbrella profile and a horizontal line passing through the minimum exumbrella y-position for each profile, $y_{\min,j}$. The subumbrella volume for a given profile was calculated using the following equation:

$$V_j = \pi \int_0^{n_j} \left(y_{i,j}\left(x_{i,j}\right) - y_{\min,j} \right)^2 dx_{i,j} \qquad (5.2.7),$$

Equation 12 assumes the *C. capillata* bell is axi-symmetric which is a crude representation of the bell geometry but gives a good approximation for this analysis.

5.2.2 Results

5.2.2.1 Bell kinematics

The processed exumbrella profiles are shown in Fig. 5.2.4 for the first of two digitized swimming cycles. Selected bell profiles at different instances are shown along with the bell margin trajectory.

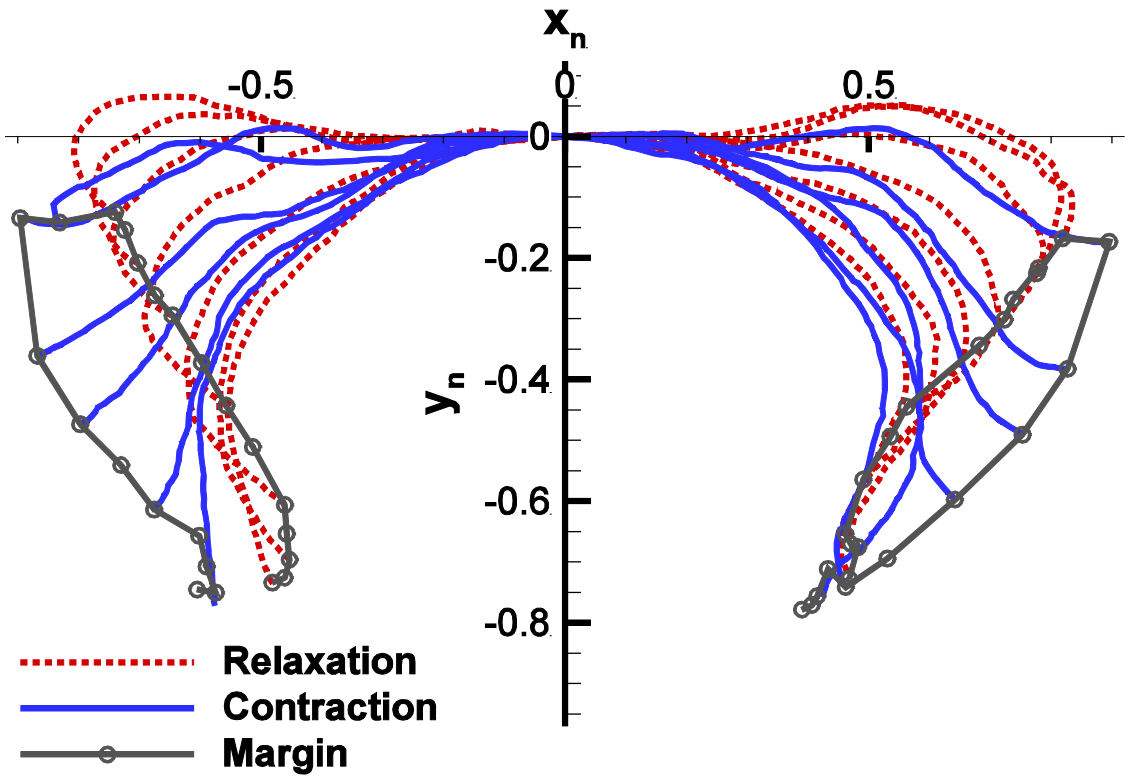

Figure 5.2.4: *Cyanea capillata* exumbrella bell profiles during the first digitized swimming cycle. The profiles were arbitrarily selected to demonstrate the different geometries encountered during a cycle. The bell margin trajectories are also shown. The positions are normalized by the half exumbrella arclength in the relaxed position.

During relaxation, the bell goes over the apex as seen at $x_n = 0.5$. This is not common in most jellyfish which do not relax higher than their apex (Costello and Colin, 1994; Costello and Colin, 1995; Ford and Costello, 2000; Costello and Colin, 2002; Bajcar et al., 2009). Also, most of the motion occurs in the y-direction with an average distance for both cycles on each side of $y_n = 0.62$ and $x_n = 0.28$ at the bell margin between the relaxed and contracted positions. The flap flares outwards during contraction and is bent inwards during relaxation. This results in an outer trajectory during contraction and inner trajectory during relaxation. The same observation has been made with *A. aurita* (Villanueva et. al, 2010).

5.2.2.2 Strategic bell discretization

The anatomical analysis revealed five important locations which set the delimitation for a four-segment anatomical kinematic model. The 0% location corresponds to the bell apex which is at the center of the central disk. The central disk region is passive and consists of mesoglea and gonads. It is delimited by the coronal joint and circular muscles at 40%. This joint eases deformation at that location when the circular muscles actuate. The radial muscles begin at the outer edge of the circular muscles which is at 64%. This location of actuator transition will be less stiff then the surrounding area due to the lack of muscles. It is therefore also considered as a node location. The flap starts where the radial muscles end at 88%. This is a location of mechanical transition from active to passive. The flap is also more flexible due to its lack of muscles which will result in more compliance during contraction and relaxation. The fifth node is taken as the bell margin 100%, which also marks the end of the flap.

The tangent angle was calculated for each point on each digitized profile. The tangent angle of a given point was then averaged over the 52 profiles. The average tangent angle for the right side of the bell is shown in Fig. 5.2.5 along with the first variance. The peaks and valleys correspond to the highest deformation on average. The variance indicates to what extent deformation changes during swimming.

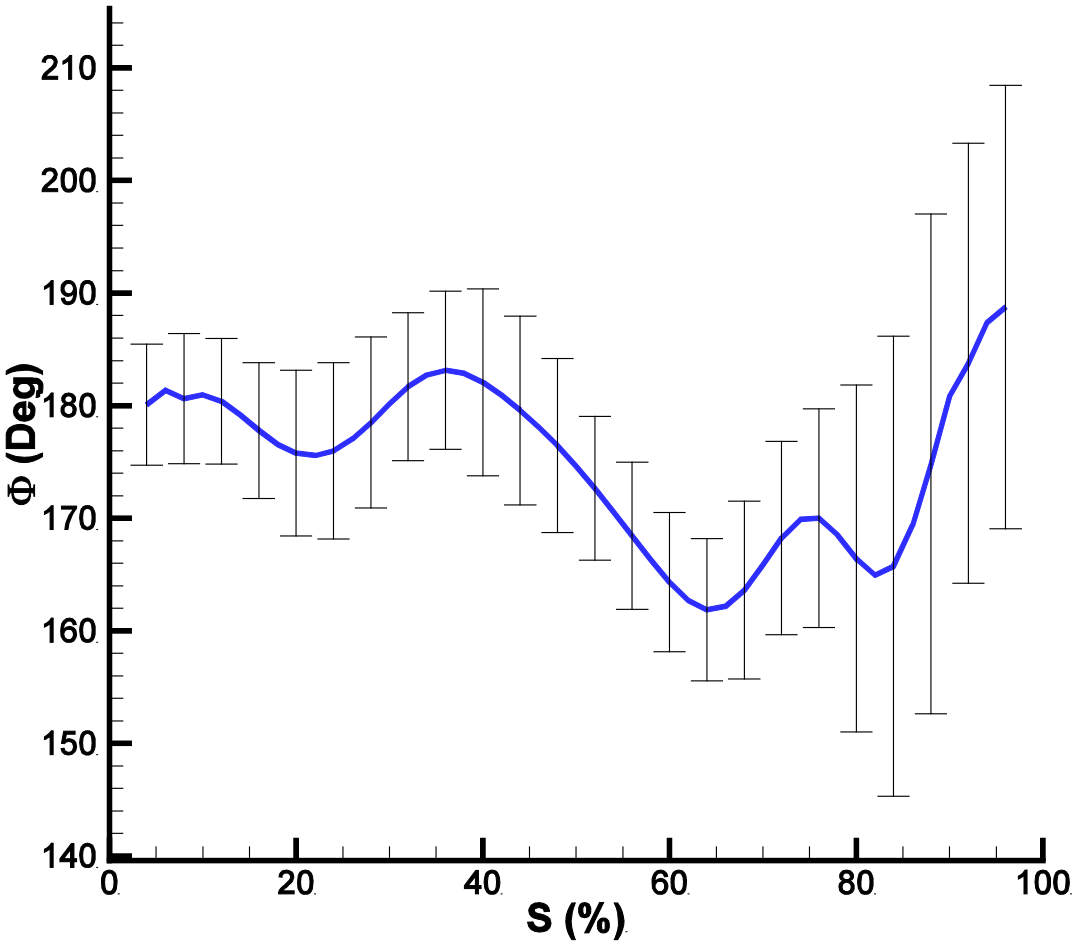

Figure 5.2.5: Average tangent angle as a function of exumbrella arclength for two full cycles. The arclength is in percentage of the total relaxed exumbrella arclength. Error bars show the first variance. Peaks and valleys represent potential node locations.

The tangent angle curve shows that there are five main peaks and valleys at 22, 36, 64, 76, and 82% of exumbrella arclength starting at the apex. These peaks and valleys correspond to potential node locations. The points corresponding to these peaks and valleys were found by identifying the points where Eq. 5.2.3 is closest to zero. Comparing the five potential node locations with the location of the anatomical features we can see that three of the locations match well. Point 36% matches with the beginning of the circular muscle start location with an error of

10%, point 64% matches exactly with the beginning of the radial muscles start location and point 82% matches with the flap start location with an error of 7%.

Most points along the active part of the bell undergo a similar variation in deformation. Variation increases significantly near Point 82%. Comparing with the anatomical measurements, we can see that this point is close to the 88% point which marks the end of radial muscles and the beginning on the flap. The flap corresponds to a passive part of the bell beginning at the end of the swimming muscles up to the bell margin. The flap undergoes large deformation and movement during swimming but areas on the flap should not be considered node locations from a robotic perspective since this deformation can be achieved by a passive material as shown in Chapter 7. The root of the flap which was found to be at 82% with the kinematic analysis and 88% with the anatomical analysis is considered as a node location. The discrepancies between the anatomical and tangent angle node location may be due to several factors. Anatomy ratio variation with size is unknown for *C. capillata*. It is possible that the anatomical ratios measured varied between the two animals analyzed. Discrepancies in the footage processing can also have led to error in tangent angle analysis.

5.2.2.3 Node location optimization

When modeling the kinematics of the *C. capillata*, it is desired to reduce the error between the natural profiles and the model. Depending on the application, the number of segments used to represent the motion might differ. The error analysis technique was used to find which node location on the bell profile minimizes error for a given number of segments. This was done for 1 to 6 segments and the optimized results are shown in Table 5.2.1.

Table 5.2.1: Node locations found by the error analysis node detection method for discrete models representing the *C. capillata* exumbrella geometry. Node locations are given in exumbrella half arclength percentages starting from the bell apex. The associated error found by the error analysis between digitized and model exumbrella are listed.

	Node Location (%)							
Model	**1**	**2**	**3**	**4**	**5**	**6**	**7**	**E**
One- Seg	0	100						8.30
Two- Seg Opt	0	60	100					2.10
Three-Seg Opt	0	32	66	100				1.11
Four-Seg Opt	0	26	60	80	100			0.63
Five-Seg Opt	0	24	50	66	84	100		0.41
Six-Seg	0	22	42	58	70	84	100	0.29

As expected, the error decreases with increasing number of segments. This is illustrated in Fig. 5.2.6. The relationship between error and increasing segment number has the following power function: $E = 8.11 L_n^{-1.85}$ with $R^2 = 0.999$ where L_n is the number of segments. The optimized four-segment discrete model along with the original *C. capillata* profiles are shown in Fig. 5.2.7. The five possible node locations found by the tangent angle method were optimized to find which combination of these five possible locations will result in the least amount of error for a given number of segments. The results are shown in Table 5.2.2. The error follows a similar trend as with the fully optimized results. A power function was fitted to the error results and has the following parameters: $E = 2.23 L_n^{-1.043}$ and $R^2 = 0.995$. Node location has a small effect on error for the locations analyzed. The number of node has a stronger influence on error as shown in Fig. 5.2.6. The node locations found from the anatomical analysis were also tested for error. The results are reported in Table 5.2.2. Out of the three different four-segment models, the anatomical results yielded the highest error with 0.74, the tangent angle optimized results had a 0.71 error and the fully optimized results had a 0.63 error.

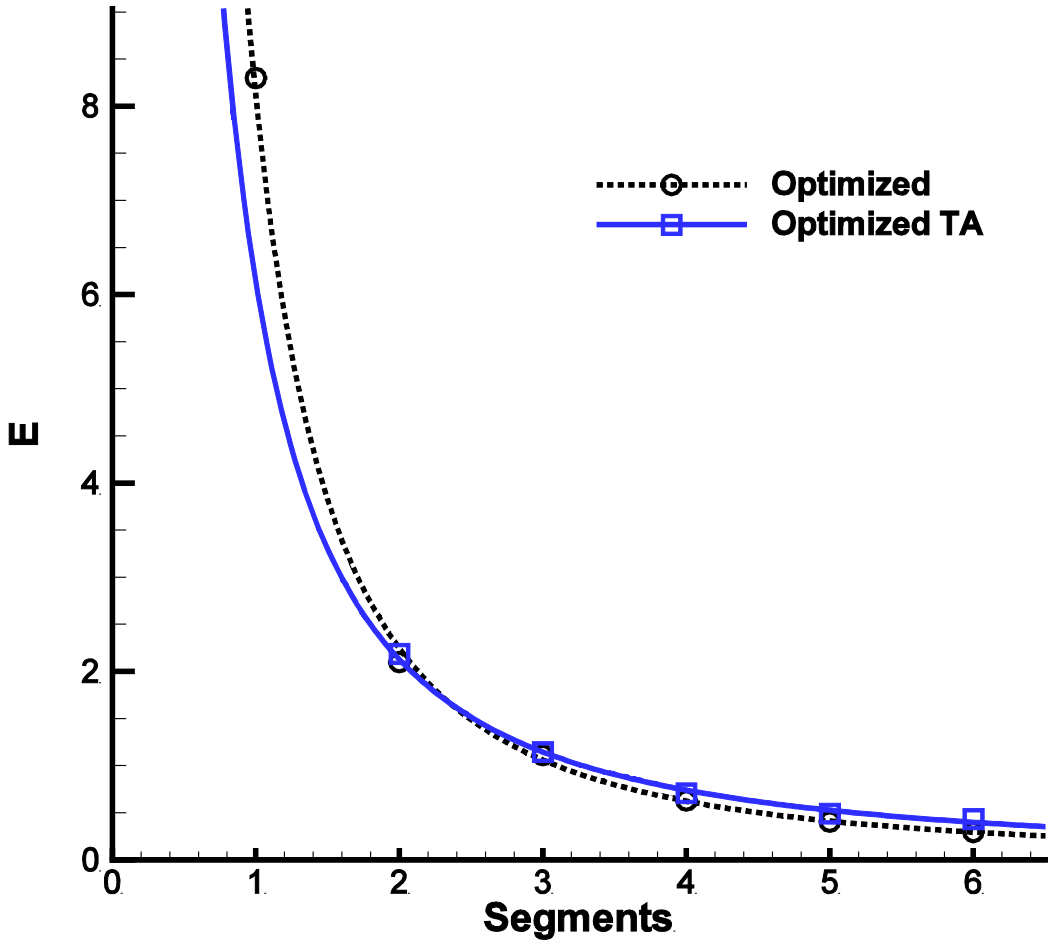

Figure 5.2.6: Error (E) for different number of segments for the four-segment optimized discrete model whose node locations were found by the error analysis method and the four-segment optimized TA discrete model whose node locations were found by the tangent angle node detection method and then optimized. The data has been fitted with power curves with equations $E = 8.11L_n^{-1.85}$ with a coefficient of determination of $R^2 = 0.999$ for the optimized data and $E = 2.23L_n^{-1.043}$ with a coefficient of determination of $R^2 = 0.995$ for the optimized kinematic results.

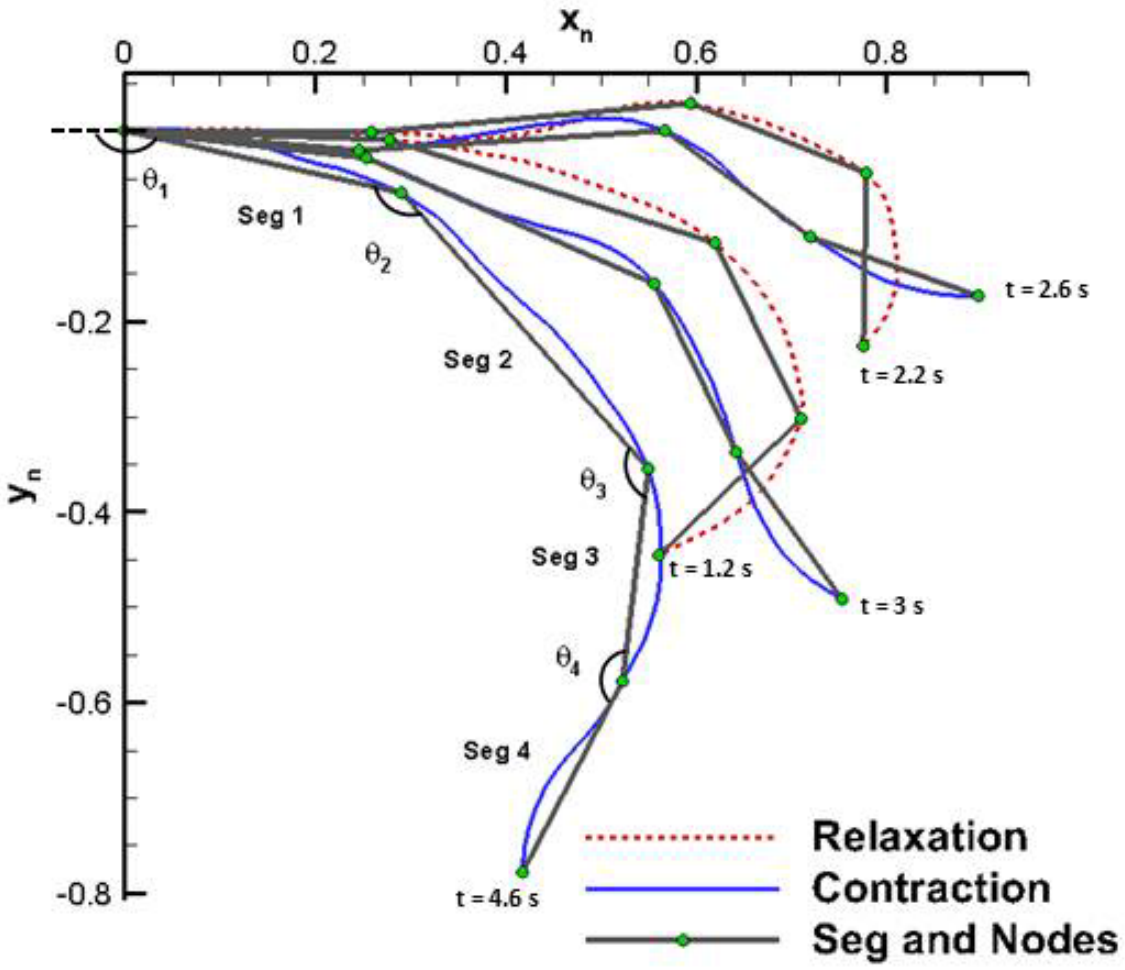

Figure 5.2.7: The optimized four-segment discrete model and selected *C. capillata* exumbrella profiles. The time at which each profile occurs from the beginning of relaxation phase are labeled. The segments and angles formed between each segment are also labeled.

Table 5.2.2: Node locations found by the tangent angle node detection method for discrete models representing the *C. capillata* exumbrella geometry. The five different node locations found by the tangent angle method were optimized using the error analysis to see which set of segments would yield in the least amount of error for a given number of segments. Node locations are given in exumbrella half arclength percentage starting from the bell apex. The associated error found by the error analysis between digitized and model exumbrella are listed.

	Node Location (%)							
Model	**1**	**2**	**3**	**4**	**5**	**6**	**7**	**E**
Two- Seg	0	64	100					2.19
Three-Seg	0	36	64	100				1.15
Four-Seg	0	36	64	82	100			0.71
Five-Seg	0	22	36	64	82	100		0.50
Six-Seg	0	22	36	64	76	82	100	0.43
Four-Seg Anat	0	40	64	88	100			0.74

5.2.2.4 Kinematic models

Kinematic models of the optimized four-segment discrete model and the four-segment anatomical discrete model were developed using Fourier series. The segment lengths and angles θ between segments were fitted with Fourier series. The fit was done on the second digitized cycle. This cycle was clipped and shifted in time so that the contraction occurred first followed by cruise and relaxation. It was then repeated nine times and fitted with a Fourier series. The Fourier coefficients for both kinematic models are shown in Tables A1-A4. Using these coefficients, one can recreate the bell kinematics of a *C. capillata* approximated by four segments for any number of cycles using the following equations:

$$\theta_m(t) = a_0 + \sum_{p=1}^{r} a_p \cos(r\omega t) + b_p \sin(r\omega t) \qquad (5.2.8),$$

$$L_m(t) = a_0 + \sum_{p=1}^{r} a_p \cos(r\omega t) + b_p \sin(r\omega t) \qquad (5.2.9),$$

where θ_m is the angles between each segments, L_m is the segment lengths, p is the order of the Fourier transform used and $\omega = {}^{2\pi}\!/_{T}$ is the angular frequency where T is the period of the swimming cycle.

5.2.2.5 Discretized bell kinematics analysis

A discrete representation of the *C. capillata* bell allows for an analysis of individual parts of the bell. We look at the four-segment anatomical kinematic model to gain an understanding of how the different anatomical regions behave during a swimming cycle. The angles formed between each segment are plotted as a function of time in Fig. 5.2.8 for one full cycle. The second cycle of the *C. capillata* was used for this analysis and is also the same cycle used for the Fourier model. The original data was clipped and shifted in time so that the contraction occurs first instead of relaxation. Figure 5.2.8 also shows the corresponding four-segment anatomical kinematic model.

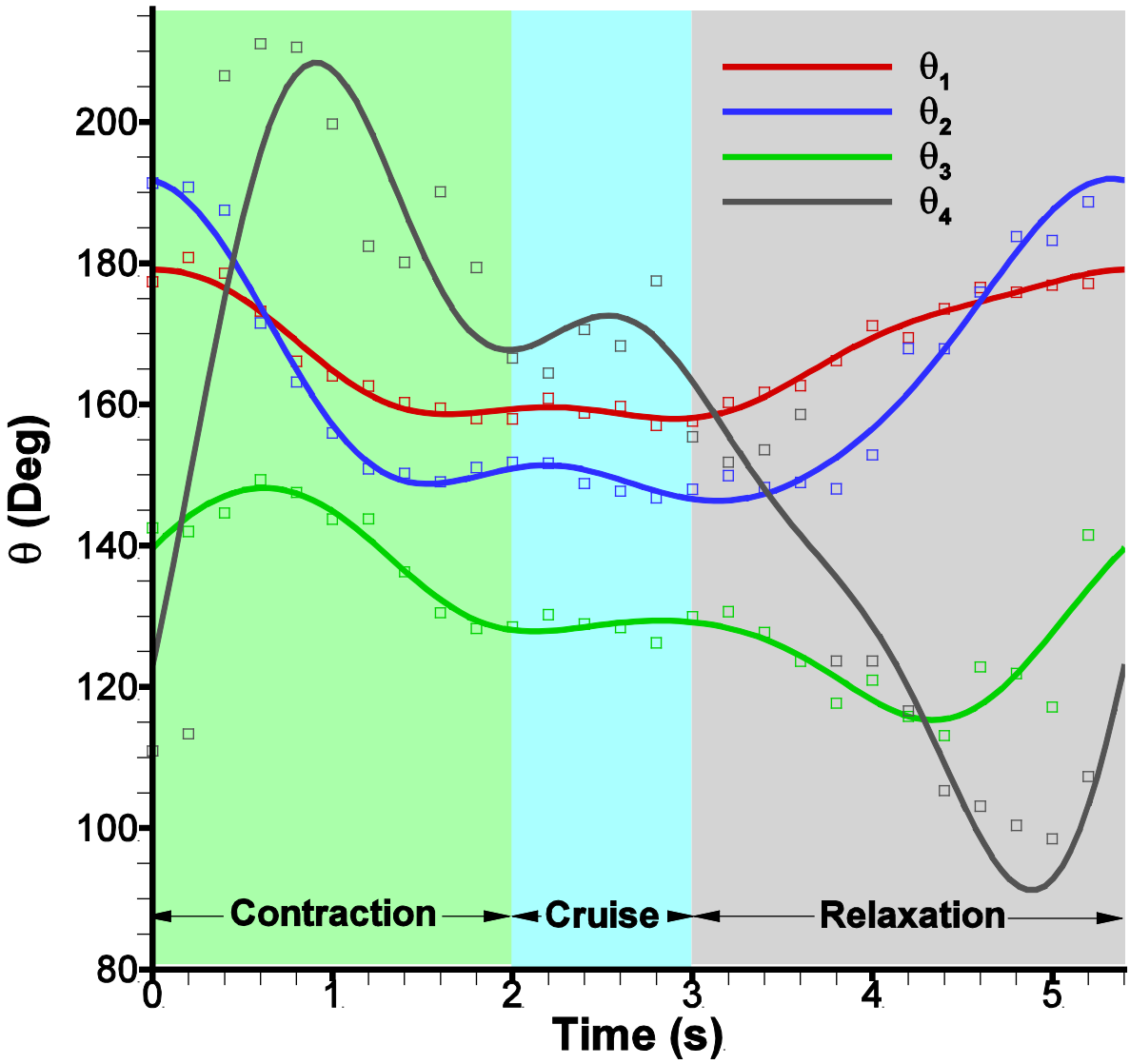

Figure 5.2.8: Angles between adjacent segments of the anatomical segment configuration over a full cycle. Squares represent digitized *C. capillata* profile points and lines represent the four-segment anatomical kinematic model.

Contraction is taken as the period when the active sections of the bell are moving inwards. This occurs when the circular or radial muscles cause the bell to contract. Figure 5.2.8 shows that the contraction lasts for 2 s which ends when the radial muscles stop moving the bell inward. Following contraction, the bell undergoes little movement for 1 s. This period is referred to as cruise time. It is unknown if the muscles are still actuating during cruise time or if the

hydrodynamic forces are enough to keep the bell contracted. Cruise is followed by the relaxation phase where the elastic energy stored in the bell allows the bell to return to its fully relaxed position. Relaxation is first seen in Segment 1 and 2. Segment 3 sees further inward motion initially and then starts relaxing. The circular muscles might be causing this additional pivoting or the hydrodynamic forces accompanied with a less stiff structure result in partial relaxation. Counting the cruise time as the relaxation phase, the duty cycle is 38% which is similar to other rowing jellyfish which range from 32% to 42% (Costello and Colin, 1994; Ford and Costello, 2000; Colin and Costello, 2001; Bajcar et al., 2009; Blough et al., 2011). With the cruise time part of the contraction phase, the duty cycle is 58% which would be the duty cycle used if actuators are powered to maintain deformation.

In the four-segment anatomical discrete model, Fig. 5.2.8, Segment 1 represents the central disk, Segment 2 represents the circular muscles, Segment 3 represents the radial muscles and Segment 4 represents the passive flap. Figure 5.2.1 shows a schematic of segment locations and associated anatomical features which is summarized in Table 5.2.3 along with their functions during a swim cycle. The contraction phase is initiated by the circular muscles at which point the radial muscles and flap are still expanding. The circular muscles undergo a total angle change of 42°. The radial muscles start contracting 0.6 s after the circular muscles and bend the bell by an additional 20°. Though the central disk is passive, it undergoes an angle change of about 20° due to contraction of the circular and radial muscles. Segment 4, which corresponds to the flap, undergoes significant lag during all phases of the swimming cycle. As angles θ_1 and θ_2 are decreasing during contraction, the flap angle θ_4 is increasing. About halfway during the contraction, the flap angle starts decreasing. During relaxation, the flap angle decreases further until 5 s where it then starts increasing. This sudden increase is associated with the deceleration of segment 2 and this

allows the elastic energy in the flap along with its inertia to move the structure to its original position.

Table 5.2.3: Anatomical features with corresponding discrete model analog. The Motion column describes if the motion of a given feature is done passively of actively. Contraction and relaxation columns describe the angle change during each phase and the associated lag period if any. Cruise was omitted from the table since negligible angle change occurs.

Anatomical Feature	**Model**	**Motion**	**Contraction**	**Relaxation**
Central Disk	Segment 1	Passive	20° ↓	20°↑
Circular Muscles	Segment 2	Active	42° ↓	46°↑
			8°↑, 20°↓ 0.6 s	13°↓, 25°↑ 1.3 s
Radial Muscles	Segment 3	Active	Lag	Lag
			85°↑, 41°↓ 0.9 s	72°↓, 32°↑ 1.9 s
Flap	Segment 4	Passive	Lag	Lag

The bell trajectories at the anatomical node locations during a full swimming cycle are plotted in Fig. 5.2.9. Each node trajectory has hysteresis between contraction and relaxation. The bell margin consisting of node location 100% has the largest hysteresis. The margin contracts with outer trajectory and relaxes with an inner trajectory. The 88% node consisting of the flap beginning undergoes almost no hysteresis during most of the cycle. Nodes 64% and 40% have hysteresis and their trajectory is inner during contraction and outer during relaxation. The flap therefore turns an inner trajectory during contraction into an outer trajectory and vice versa during relaxation. An outer trajectory during contraction increases the surface area used to produce thrust while an inner trajectory during relaxation reduces the surface area subjected to drag forces. These trajectory patterns are consistent with observations made on *Aurelia aurita* (Villanueva et. al, 2010). Figure 5.2.10 is the equivalent plot for the four-segment anatomical kinematic model. The segment angles for this plot are the same as shown in Fig. 5.2.8. The kinematic model trajectories have the same behavior as the original *C. capillata* kinematics.

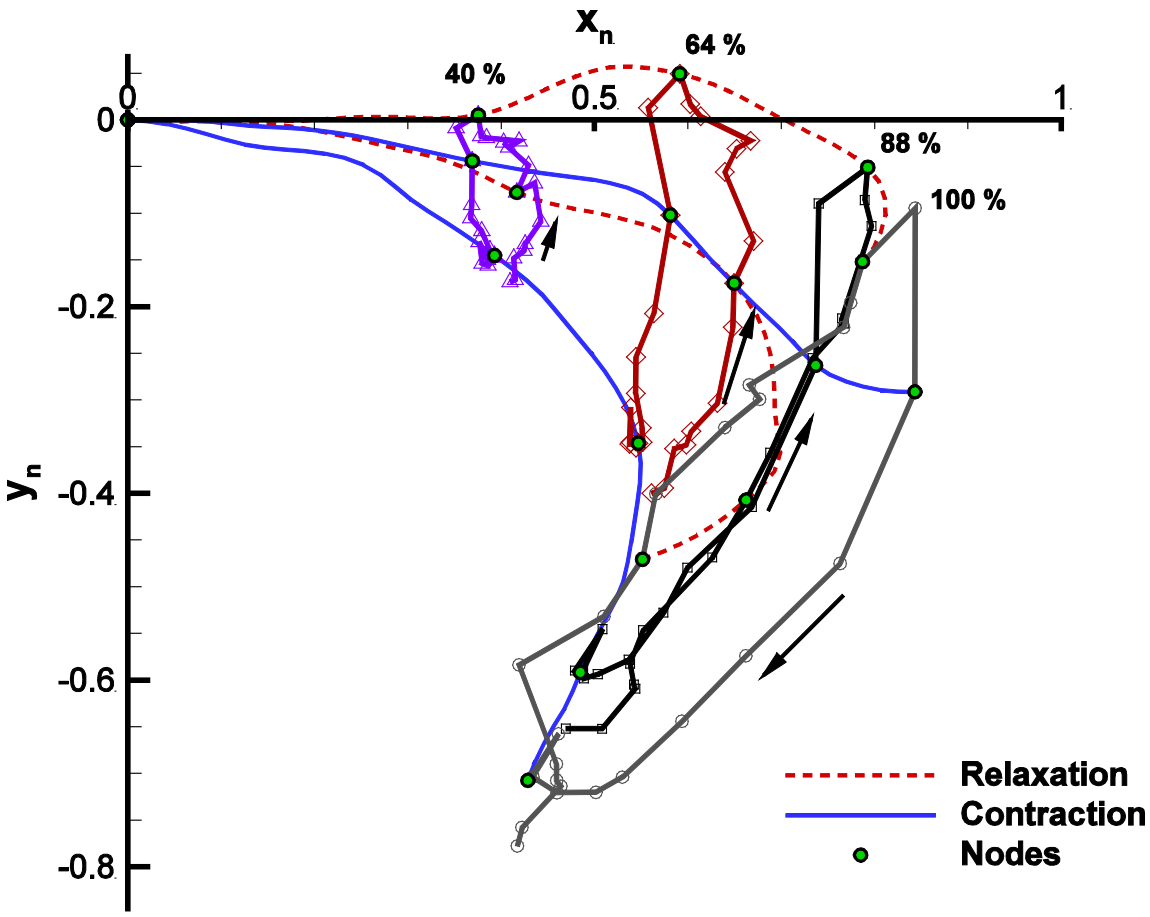

Figure 5.2.9: Bell trajectory at node locations of the four-segment anatomical discrete model during the second swimming cycle.

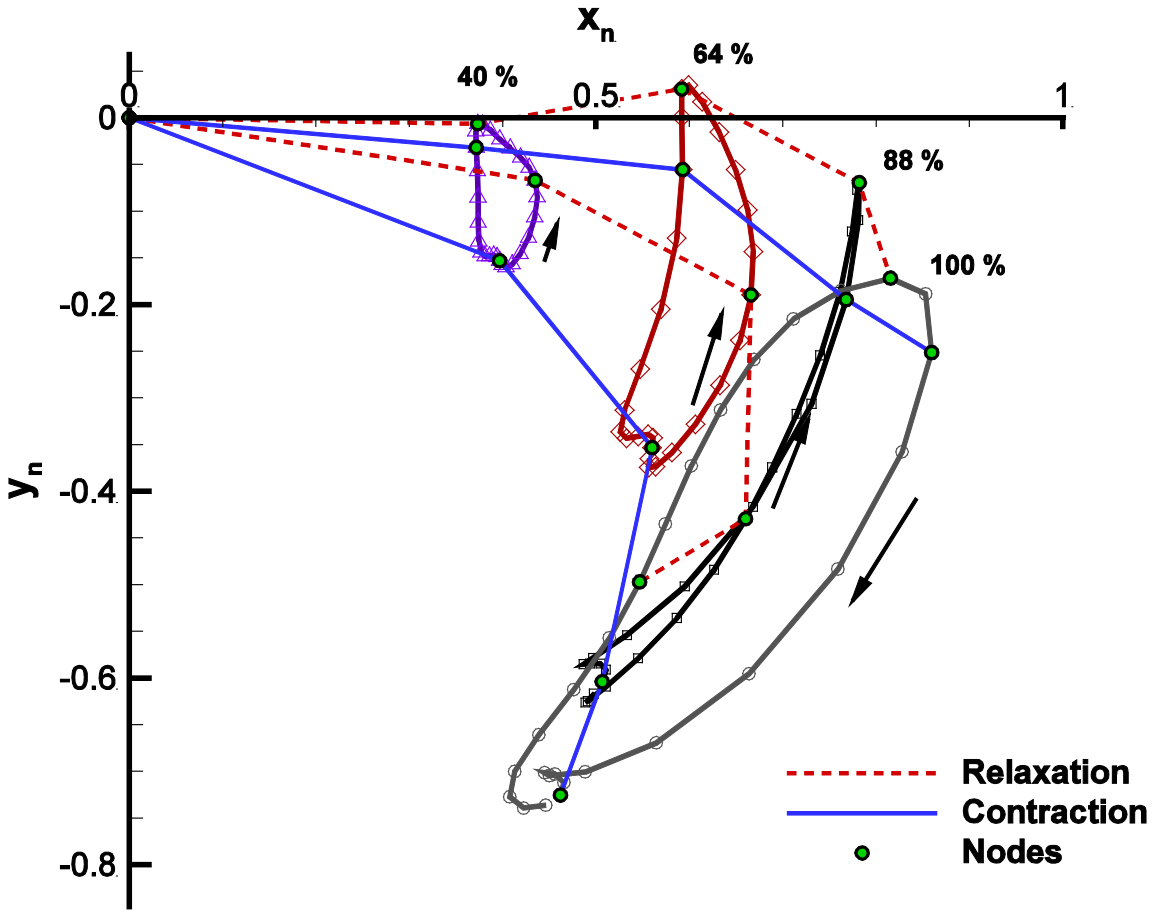

Figure 5.2.10: Bell trajectory at node locations of the four-segment anatomical kinematic model during the second swimming cycle.

5.2.2.6 Subumbrella volume change

The subumbrella volume and bell diameter as a function of time for one full cycle are plotted in Fig. 5.2.11. The subumbrella volume is approximated using the exumbrella profiles and the bell diameter is taken at the bell margin. The results in Fig. 5.2.11 show that the volume decreases briefly as the *C. capillata* begins to contract. This is due to the bell extending and flattening as contraction begins. When the radial muscles start contracting at 0.6 s, the subumbrella volume then starts increasing. The volume fluctuates slightly while cruising and

starts decreasing during relaxation. This goes against current hydrodynamic models of medusa propulsion. Bell diameter as a function of time is inversely proportional to the volume of water enclosed by the subumbrella. The cycle shown in Fig. 5.2.11 is the same as in Fig. 5.2.8.

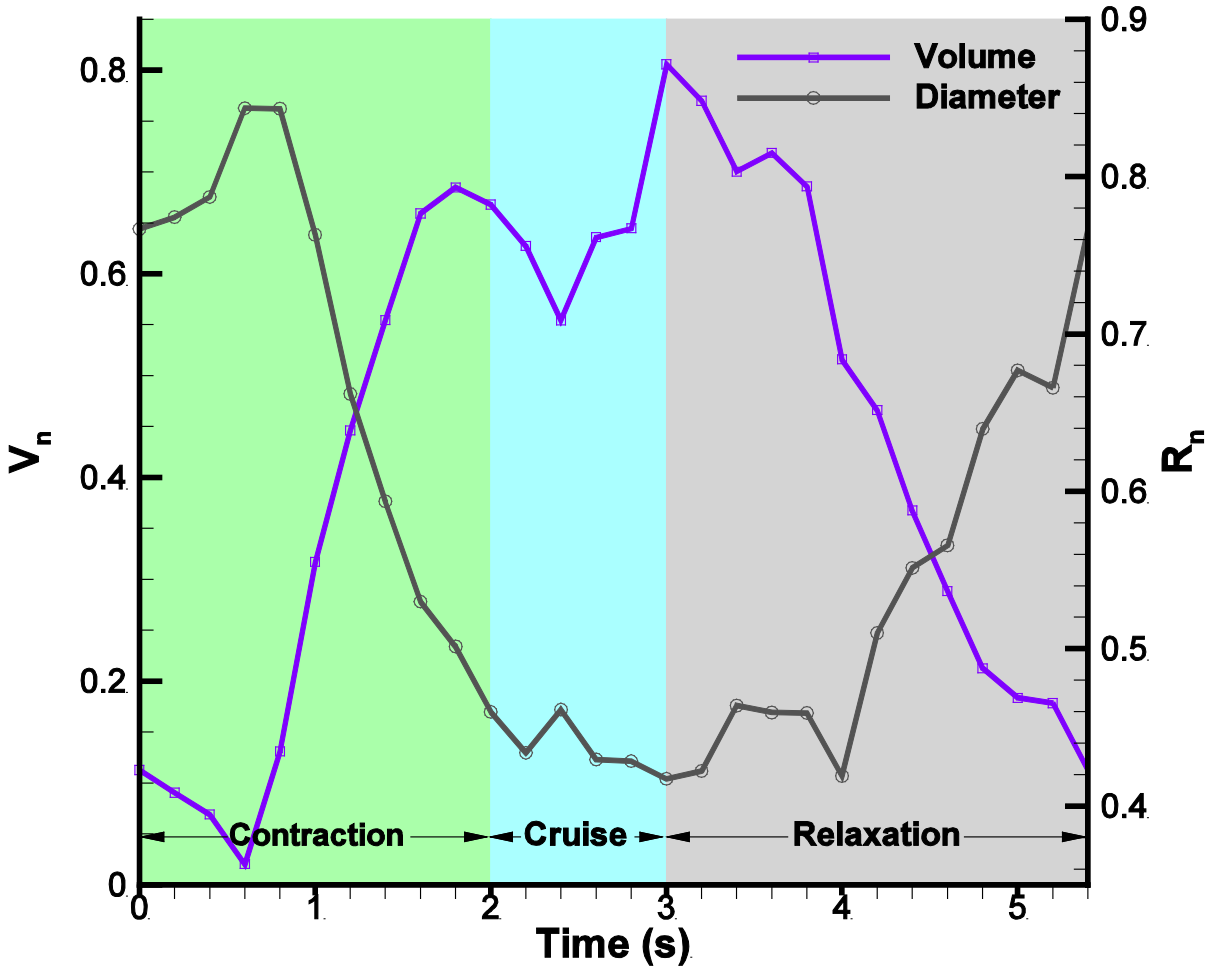

Figure 5.2.11: Subumbrella volume and bell radius as a function of time for one full swimming cycle. The diameter is taken as the x-position of the bell margin.

5.2.4 Discussion

The three node detection methods presented in this study offer different benefits. The tangent angle method determines where the areas of highest deformation occur. With this method, there is no need to actually look at the animal anatomy. Footage of the animal kinematics satisfying the three selection criteria presented in Section 5.1.1 is the only information required. The error analysis method provides the best node and segment representation of the exumbrella for a given number of segments. This can be especially useful for modeling the bell as a discrete representation in computational applications. On the other hand, it does not take into account the mechanics of the bell which would be necessary in a robotic application. To reproduce the same kinematics and morphology of the *C. capillata*, the material behavior and mechanics must also be taken into account. For such application, the dimensions given by the anatomical analysis might have better results. This method shows where artificial actuators should be located if they were able to recreate the same deformation assuming they have the same form factor as the natural muscles. A downside of this method is the required analysis of the natural animal's anatomy which can be significantly more demanding then recording an in situ footage. For some specimens such as the *C. capillata*, the kinematics scale with size in an unknown fashion. Visual inspection of small ~5 cm in diameter free swimming *C. capillata* shows different bell kinematics then larger ~40 cm ones. Gladfelter also pointed out anatomical feature variations with size which could affect swimming mechanics and therefore kinematics.

The kinematic models provided can be used as a time dependent representation of the *C. capillata* bell motion. The four-segment optimized kinematic model best matches the exumbrella

kinematic representation for four segments. The four-segment anatomical kinematic model gives the kinematics of the bell at locations where important anatomical features act.

The four-segment anatomical kinematic model revealed important features of the *C. capillata* bell kinematics. It was found that the bell does not deform uniformly. The radial muscles actuate with a lag period from the circular muscles and also lag behind the circular muscles during relaxation. The passive flap was found to have significant lag behind all the other sections. This leads to hysteresis in the bell margin causing the bell to have an outer trajectory during contraction and inner trajectory during relaxation. The kinematics analysis also revealed that the *C. capillata* has a cruise time which lasts for $1/5^{th}$ of its swimming cycle where the bell geometry stays near constant. Rowers such as the *A. aurita* do not undergo cruise time. Their contraction is followed by an immediate relaxation (Costello and Colin, 1994; Ford and Costello, 2000; Colin and Costello, 2002; Bajcar et al., 2009). Jetters, conversely, usually undergo a cruise time after having fully relaxed. Cruise time after contraction has shown to increase the performance of a segmented bell Robojelly (Villanueva et al., 2011). This leads to the hypothesis that cruise time improves the performance of segmented bell jellyfish. Cruise time may also be a function of size. The *C. capillata* kinematic models found in this study coupled with a hydrodynamic analysis will allow investigation of these hypotheses.

Rowing medusa propulsion has been modeled as a combination of jetting and paddling (McHenry and Jed, 2003; Dabiri et al., 2007). Jetting is a function of subumbrella volume change between the relaxed state and fully contracted state (Daniel, 1983). McHenry and Jed (2003) found that jetting was responsible for most of the thrust. However, jetting depends on a decrease in subumbrella volume during contraction which is not the case for the *C. capillata* as was found in this analysis. According to the jetting model this should result in a negative thrust.

A jetting model is therefore inappropriate for representing the propulsion mechanism of *C. capillata*. The starting and stopping vortex interaction between the contraction and relaxation phase described by Dabiri et al. (2005) is likely to play a more prominent role in the thrust production of *C. capillata*.

An important aspect of *C. capillata* bell kinematics which requires further exploration is the kinematics of individual bell segments. Bell segments have a three-dimensional deformation which comes from the presence of a passive flap that surrounds the circumference of each bell segments. Also, the tentacles and oral arms being a prominent mass portion of the animal will influence the dynamics and therefore kinematics of the animal. The extent to which they contribute to the kinematics will require further investigation.

5.3 References

Acuña J. L., López A., Colin S. (2011). Faking Giants: The Evolution of High Prey Clearance Rates in Jellyfishes. *Nature* 333, 1627, DOI: 10.1126/science.1205134

Bajcar, T., Malacic, V., Malej, A., and Sirok, B. (2009). Kinematic properties of jellyfish Aurelia sp.. *Hydrobiologia* 616, 279-289

Blough, T., Colin, S. P., Costello, J. H., Marques, A. C. (2011). Ontogenetic changes in the bell morphology and kinematics and swimming behavior of rowing medusae: the special case of the limnomedusa Liriope tetraphylla. *Biol. Bull*. 220(1), 6-14

Chapra, S. C. (2005). Applied Numerical Methods with MATLAB for Engineering and Science. McGraw-Hill, New-York

Costello, J. and Colin, S. (1994). Morphology, fluid motion and predation by the scyphomedusa Aurelia aurita. *Mar. Biol.* 121, 327–334

Colin, S. P., and Costello, J. H. (2002). Morphology, swimming performance and propulsive mode of six co-occurring hydromedusae. *J. Exp. Biol.* 205, 427–437

Dabiri, J. and Gharib, M. (2003). Sensitivity analysis of kinematic approximations in dynamic medusan swimming models. *J. Exp. Biol.* 206, 3675-3680

Dabiri, J. P., Colin, S. P. and Costello, J. H. (2005). Flow patterns generated by oblate medusan jellyfish: field measurements and laboratory analyses. *J. Exp. Biol*. 208, 1257–1265

Dabiri, J. O., Colin, S. P., and Costello, J. H. (2007). Morphological diversity of medusan lineages constrained by animal–fluid interactions. *J. Exp. Biol.* 210, 1868–1873

Daniel, T. L. (1983). Mechanics and energetics of medusa jet propulsion. *Can. J. Zool*. 61, 1406-1420

DeMont, M. E. and Gosline, J. M. (1988). Mechanics of jet propulsion in the hydromedusan jellyfish, Polyorchis penicillatus. I. Mechanical properties of the locomotion structure. *J. Exp. Biol.* 134, 313–332

Ford, M. D. and Costello, J. H. (2000). Kinematic comparison of bell contraction by four species of hydromedusae. *Sci. Mar*. 64, 47-53

Fry, S. N., Sayaman, R. and Dickinson. M. H. (2005). The aerodynamics of hovering flight in Drosophila. *J. Exp. Biol.* 208, 2303-2318. DOI:10.1242/jeb.01612

Ijspeert, A. J., Crespi, A., Ryczko, D., Cabelguen, J. M. (2007). From Swimming to Walking with a Salamander Robot Driven by a Spinal Cord Model. *Science* 315, 1416. DOI: 10.1126/science.1138353

Gladfelter, W. G. (1973). Structure and function of the locomotory system of the Scyphomedusa Cyanea capillata. *Mar. Biol.* 14, 150–160

Herschlag, G. and Miller, L. (2011). Reynolds number limits for jet propulsion: a numerical study of simplified jellyfish. *J. Theor. Biol.* 285(1), 84-95

Kramp, P. L. (1961). Synopsis of the Medusae of the World Journal of the Marine Biological Association of the United Kingdom, 40, 469.

Mayor, A. G. (1910). Medusae of the world. III. The Scyphomedusae. Publication of the Carnegie Institute of Washington, Washington DC

McHenry, M. and Jed, J. (2003). The ontogenetic scaling of hydrodynamics and swimming performance in jellyfish (Aurelia aurita). *J. Exp. Biol.* 206, 4125-4137

Mittal, R., Dong, H., Bozkurttas, M., Lauder, G. and Madden, P. (2006). Locomotion with flexible propulsors: II. Computational modeling of pectoral fin swimming in sunfish. *Bioinsp. Biomim.* 1, S35–S41. DOI:10.1088/1748-3182/1/4/S05

Norberg, U. M. (1976). Aerodynamics, kinematics, and energetics of horizontal flapping flight in the long-eared bat Plecotus auritus. *J. Exp. Biol.* 65, 179-212

Pivkin, I. V., Hueso, E., Weinstein, R., Laidlaw, D. H., Swartz, S. and Karniadakis, G. E. (2005). Simulation and Visualization of Air Flow Around Bat Wings During Flight. *ICCS 2005*. LNCS 3515. pp. 689-694

Poelma, C., Dickson, W. B., Dickinson, M. H. (2006). Time-resolved reconstruction of the full velocity field around a dynamically-scaled flapping wing. *J. Exp. Fluids* 41, 213–225, DOI 10.1007/s00348-006-0172-3

Russell, F. S. (1970). The medusae of the British Isles. II. Pelagic Scyphozoa. Cambridge University Press, Cambridge, UK

Rosenberger, L. (2001). Pectoral fin locomotion in batoid fishes : undulation versus oscillation. *J. Exp. Biol.* 204, 379–394

Sathirapongsasuti, J., Punnanithi, N., Wimonkittiwat, P. (2004). A mathematical explanation of millipede's walk: Walking with a Millipede. *Intel ISEF*. Bangkok, Thailand

Sfakiotakis, M., Lane, D. M. and Davies, B. C. (1999). Review of Fish Swimming Modes for Aquatic Locomotion. J. Ocean Eng. 24, 2

Tian, X., Iriarte, J., Middleton, K., et al. (2006). Direct measurements of the kinematics and dynamics of bat flight. Bioinsp. Biomim. 1, S10–S18. DOI:10.1088/1748-3182/1/4/S02

Tobalske, B. W., Hedrick, T. L. and Biewener, A. A. (2003). Wing kinematics of avian flight across speeds. J. Avian Bio. 34, 177-184

Villanueva, A., Priya S., Anna, C., and Smith. C, (2010). Robojelly bell kinematics and resistance feedback control. Robotics and Biomimetics (ROBIO), 2010 IEEE International Conference on, 1124-1129

Villanueva, A. A., Smith, C. F., Priya, S. (2011). Biomimetic Robotic Jellyfish (Robojelly) using Shape Memory Alloy. Bioinspir. Biomim. 6, 3

Webb, P. W. (1993). The effect of solid and porous channel walls on steady swimming of steelhead trout Oncorhynchus mykiss. J.Exp. Biol. 178(1), 97-108.

Wilson, M. M. and Eldredge, J. D. (2011). Performance improvement through passive mechanics in jellyfish-inspired swimming. Int. J. Non-Linear Mech. 40(4), 557–567

Chapter 6

Biomimetic Autonomous Robot Inspired by the *Cyanea capillata* (Cyro)

6.1 Introduction

Underwater surveillance through autonomous underwater vehicles (AUVs) has been limited by factors such as operation time, depth of operation and range of operation. Existing AUVs that can operate for extended periods of time have limited operational depth. For example, the Wave Glider (Liquid Robotics) can operate almost indefinitely but is limited to operation on the surface. Conversely, the REMUS 100 and REMUS 6000 can reach depths of 100 and 6000 m respectively but can only operate for a period of approximately 8 and 12 hours respectively. A combination of long operation time and high efficiency would result in a vehicle that could perform more demanding tasks and reduce operation cost. If a vehicle's operation time is short, an entire crew and servicing vehicles must attend to the AUVs deployment, operation and recuperation in remote sea locations. Nature has already developed mechanisms and methods to achieve this desired level of performance. Different species of fish and mammals are able to swim for extended periods of time, reach high depth and travel long distances. Whales are able to reach depths greater than 1800 m (Tyack et al. 2006) and tunas have been known to swim over 5800 km during migration (Stokesbury et al. 2007). One particular type of animal that can swim with low cost of transportation (COT) and reach depths down to 7000 m is the medusa (Kramp, 1959). This meets many of the criterions set forth for future generation AUVs.

Medusa also known as jellyfish, are able to travel using very little energy even though their oscillating mode of propulsion is not necessarily the most efficient in terms of hydrodynamics.

Jellyfish Froude efficiency ranges from 0.09-0.53 (Daniel, 1985; Dabiri et al., 2010), compared to approximately 0.8 in fish (Webb et al., 1984; Videler and Hess 1984). Gemmell et al. (unpublished) and Larson (1987) have shown that the jellyfish COT is one of the lowest in the animal kingdom. The cost of transportation is the amount of energy used to travel a certain distance and is calculated as:

$$\mathrm{COT} = \frac{P}{mV}, \qquad (6.1)$$

where P is the input power, V is the vehicle velocity and m is the mass. Larson found that the COT for a 1 kg *Stomolophus meleagris* was 1 J/kg·m. This low COT is due to several factors. Rowing jellyfish, defined by their propulsion mechanism (Dabiri et al., 2005), are known to be more efficient swimmers in comparison to their jetting counterparts (Sahin et al., 2009). In rowers, the interaction of starting and stopping vortices results in larger thrust and efficiency (Dabiri et al., 2005). Additionally, this propulsion method is responsible for their feeding mechanism. As jellyfish swim, they capture prey from the same water flow that is used to create thrust. The microscopic preys get caught and immobilized in the tentacles from where they are transported to the mouth and digested. This simultaneous locomotion and feeding mechanism makes the animal even more energy efficient but foraging is not taken into the calculation of COT. The jellyfish's low energy consumption comes in great part from its low metabolic rate. Larson (1987) quantified the metabolic rate by measuring the weight specific respiration rates which he found to be 48 mL/h·kg for active medusae.

An AUV capable of such low energy consumption is highly desirable for military and civilian applications. The objective of our research is to design an autonomous underwater vehicle that mimics the morphology, motion and performance of jellyfish. In this paper, we focus on

replicating the kinematics of the *Cyanea capillata* with Cyro to achieve similar hydrodynamic performance while keeping the same general morphology.

In most cases jellyfish have a uniform bell, implying that it is nearly axi-symmetric. The bell as shown in Figure 1, consists largely of mesoglea which is a very soft gel-like material enclosed by the epidermis. The bell also houses sensory organs called rhopalia and digestive organs called gonads. The swimming muscles are located in the region under the bell called subumbrella. Jellyfish are limited in their muscle structure as they only have a single layer of swimming muscles. Tentacles passive in motion extrude from the bell margin or from the subumbrella and are primarily used for capturing prey (Mayor 1910). Jellyfish consists of more than 95 % water (Lowndes, 1942) and are nearly neutrally buoyant.

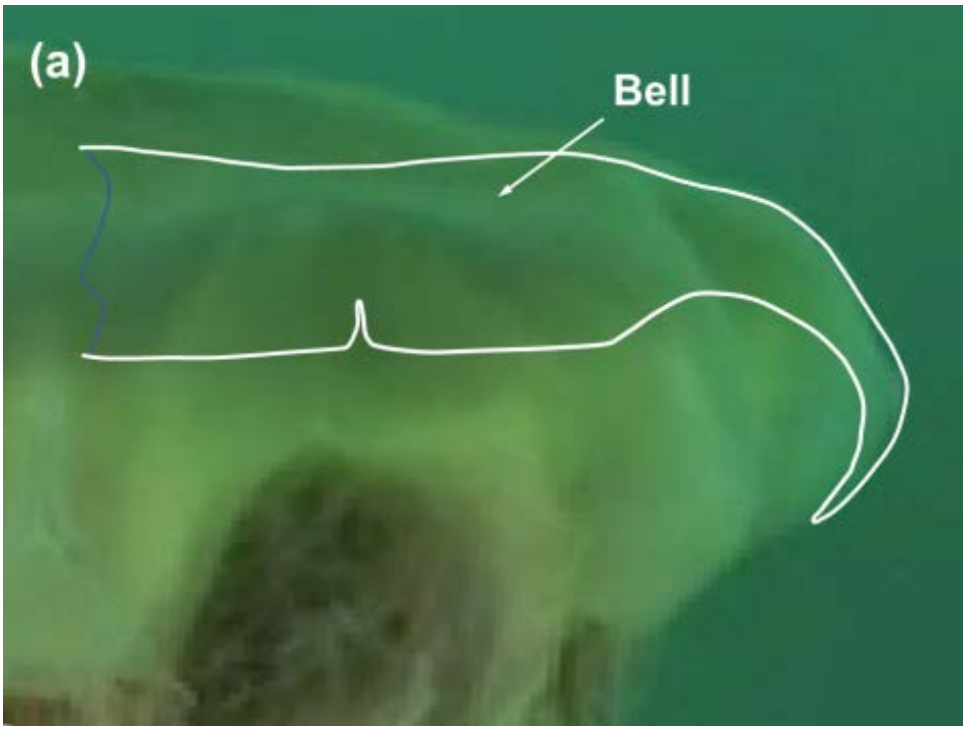

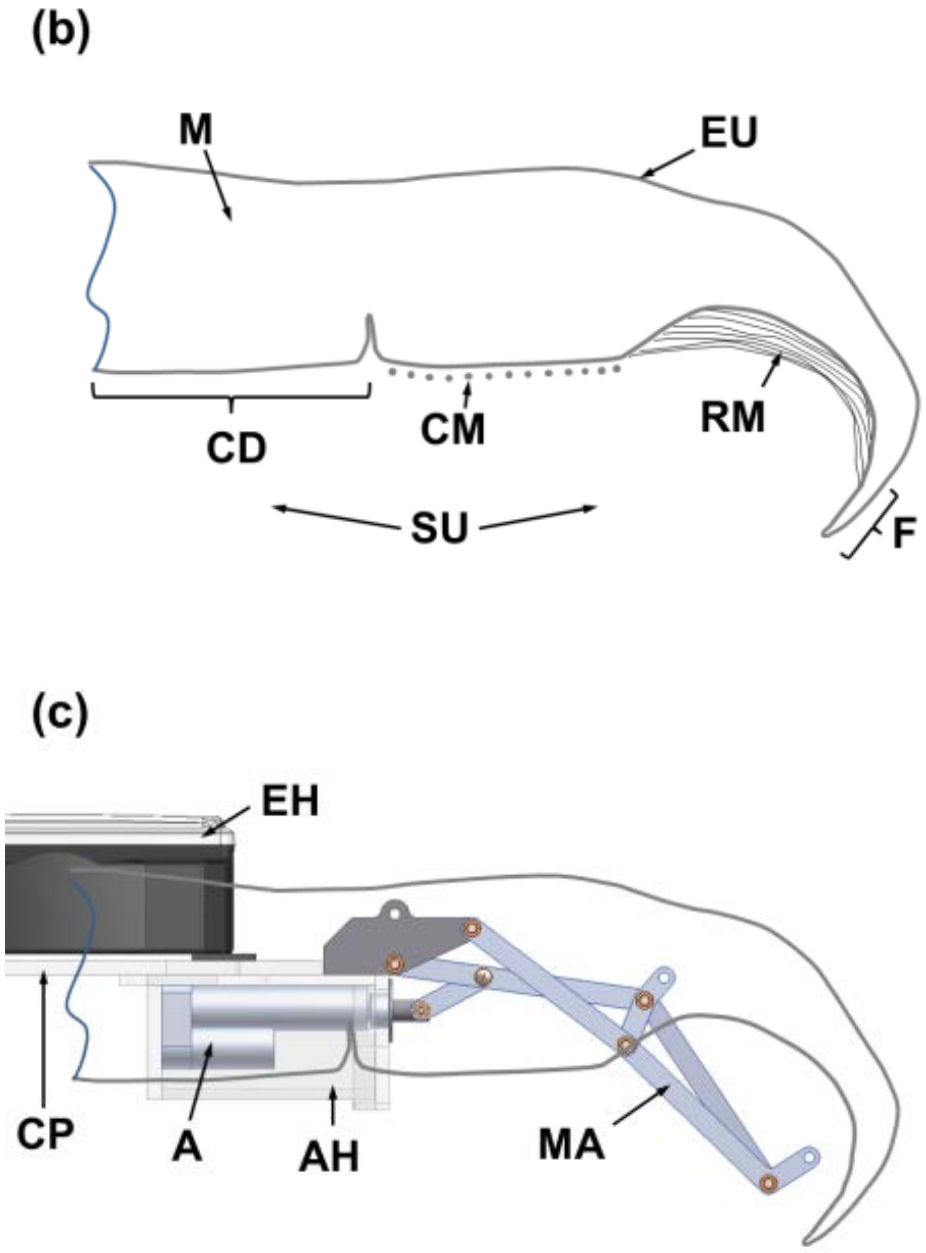

Figure 6.1: (a) Image of a 50 cm *C. capillata* in ocean water with digitized profile. The exumbrella was digitized directly from the image shown and the subumbrella profile was approximated based on Gladfelter's (1973) anatomical analysis. (b) Schematic of a *C. capillata* cross-section showing the mesoglea (M), exumbrella (EU), central disk (CD), circular muscles (CM), radial muscles (RM), Flap (F) and subumbrella (SU). (c) Mechanical arm (MA) with linear actuator (A), actuator housing (AH), central plate (CP) and electronics housing (EH). A superposition of the *C. capillata* subumbrella and exumbrella profiles shows the robotic analogs to the different anatomical parts.

Several vehicles inspired by jellyfish have been reported in literature (Guo et al. 2003; Yang et al. 2007; Villanueva et al 2009, Yeom and Oh 2009; Najem et al. 2012; Nawroth et al. 2012; Marut et al. 2012). The designs of these vehicles are mainly a function of the actuators employed for achieving deformation. Limitations in mimicking the morphology and maintaining biomimetic kinematics are related to the difficulty in replicating the circular contraction of jellyfish. Jellyfish are capable of contracting their subumbrellar muscles up to 50% (Villanueva et al. 2010) which results in uniform deformation of the bell during swimming. In addition to the small form factor in which a jellyfish is able to achieve this deformation, the flexible nature of its body creates a difficult engineering challenge. The jellyfish robots reported in literature are smaller than approximately 17 cm in diameter even though some jellyfish can reach dimension over an order of magnitude greater.

Bell segmentation helps alleviate mechanical issues that occur when trying to replicate a uniform bell with artificial materials. In a previous study (Villanueva et al. 2011), Robojelly was developed to mimic the *Aurelia aurita* species which has a uniform bell structure. Radial actuators were used to deform the Robojelly bell as opposed to circular actuators utilized by *A. aurita*. Deforming a uniform bell with a discrete number of radial actuators causes a folding effect in the bell material between each actuator. The *Cyanea capillata* species has a segmented bell design (Mayor 1910, Kramp 1961, Russell, 1970) which can be replicated more authentically than a uniform bell given current limitations in actuator technology. The effects of bell segmentation on the resulting hydrodynamics have not been quantified in literature. Cyro was developed and characterized with intent to serve as a research platform to further the understanding on hydrodynamic, kinematic and morphology traits of this particular species and large medusa in general.

6.2 Design and Fabrication

Cyro was designed to be modular for the ease of accessing the mechanical and electrical components as required for parametric studies. The actuator housing was more prone to water leaking then the electronic boxes due to the active motion of the actuators. Thus, separating the actuator housing prevented water leaks from reaching the electronics. Another motivation for modularity is the reduction in complexity for fabrication. Initially, a central hub design was considered for housing all the electronics and actuation mechanism. The large scale of the vehicle caused issues with fabricating a large central hub that could accomplish all the required functions. The vehicle modules included the actuation mechanism, electronics, artificial mesoglea, central plate, mechanical arms and actuator housing as shown in Fig. 6.1, 2 and 3. There are eight arm assemblies representing the eight *C. capillata* bell segments. Each arm assembly comprises of a mechanical arm, actuator and actuator housings that attach to a central plate. The electronics housing is positioned at the center of the vehicle and clamped on the central disk. The artificial mesoglea consists of a large single piece of silicone and is attached to the mechanical arms and central plate. The artificial mesoglea is passive and is responsible for generating the hydrodynamic forces which propel the vehicle. The design and fabrication of the of the different components are described in the following subsections while the electronics for the vehicle developed by K. Marut are described in Villanueva et al. (unpublished).

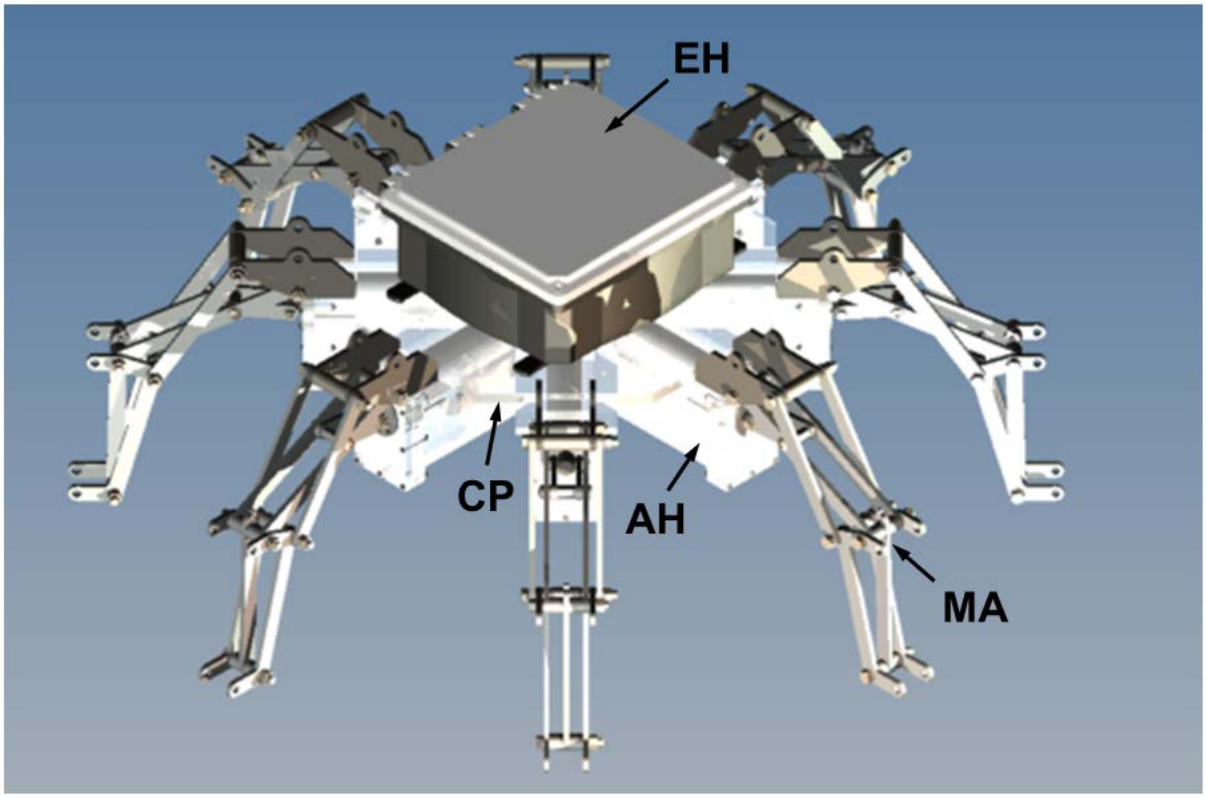

Figure 6.2: CAD model of Cyro without the artificial mesoglea. Shown in the figure are the electronics housing (EH), mechanical arms (MA), actuator housing (AH) and central plate (CP).

6.2.1 Mechanical Arms

Limitations in actuator technology prevent the direct substitution of artificial actuators in biomimetic robots to achieve the same function and morphology as natural muscles. Therefore, other actuation strategies need to be employed in order to mimic the motion and morphology of natural animal. Gladfelter (1973) has analyzed the locomotion system of the *C. capillata*. The *C. capillata* uses two different sets of muscles to swim; circular muscles and radial muscles. Gladfelter observed that the circular muscles were first to contract followed by the radial muscles at the beginning of swim cycle. The circular muscles brought the bell from a near horizontal angle to 45° while the radial muscles deformed it to near 90°.

A kinematic analysis of the *C. capillata* bell in Chapter 6 provides details on the function of the different anatomical parts during swimming. The animal analyzed was 50 cm in bell diameter and was filmed in the Atlantic Ocean off the Norway shore. The kinematic analysis was made using a four-segment representation of the *C. capillata* exumbrella. Segments here represent discretized sections of the bell exumbrella as opposed to bell segments which refer to the eight "arms" of the *C. capillata*. The exumbrella is the outer surface of the bell as shown in Fig. 6.4(b). In this model, Segment 1 is the analogue to the central disk (CD) which is a passive region at the center of the mesoglea as shown in Figs. 1 and 3. Segment 2 and 3 are the analogs to the radial muscles (RM) and circular muscles (CM) respectively. Segment 4 is analog to the flap (F) which is a passive section of mesoglea that spans from the end of the radial muscles to the bell margin.

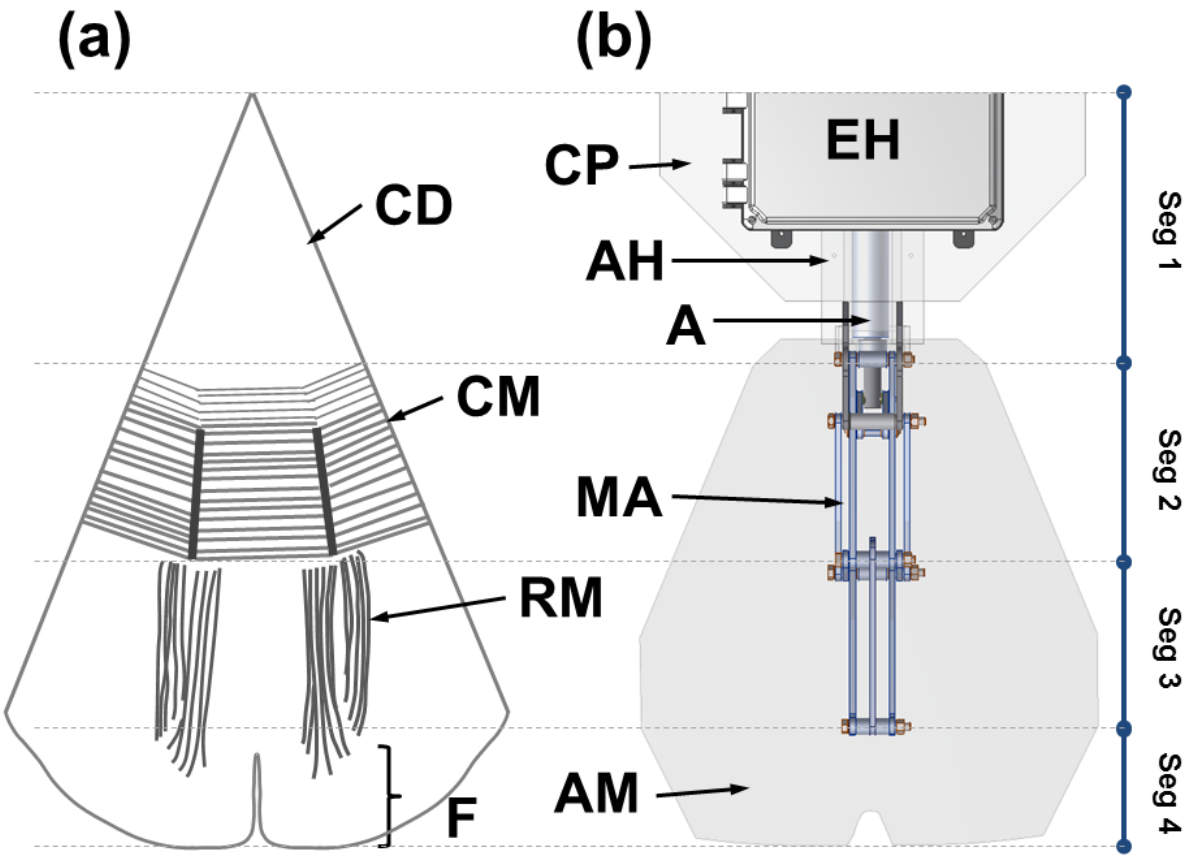

Figure 6.3: (a) Anatomical schematic of the bottom view of a *C. capillata* bell section (1/8th). This image is redrawn from Gladfelter (1973) and the labels are described as: circular disk (CD), circular muscle (CM), radial muscles (RM) and flap (F). (b) CAD drawing showing the bottom view of a robotic bell segment that includes the artificial mesoglea (AM), mechanical arm (ME), actuator (A), actuator housing (AH), electronics housing (EH) and central plate (CP). The side-by-side comparison of *C. capillata* and robotic bell segment shows the robotic analogs to the different anatomical parts for each segment (Seg).

The kinematics of the natural animal was analyzed in terms of the angle formed between two exumbrella segments as shown in Fig. 6.4. The central disk angle (θ_1) is formed between the horizontal and Segment 1. The circular muscle angle (θ_2) is formed between Segment 1 and 2, and so on. See Section 5.2 for a clear depiction of the angles and their behavior as a function of time. It was found that the circular muscles initiate contraction with a total change in angle of 42°. When contraction begins, the radial muscles and flap are still relaxing. In the 5.4 s

swimming cycle of the 50 cm *C. capillata* analyzed for the prior kinematics study, the radial muscles started to contract 0.6 s after the circular muscles and decreased its angle by 20°. The passive central disk also underwent a 20° decrease due to the compliance of the structure resulting from the actuation of both muscle sets. The flap conversely, undergoes an increase in angle during contraction. This is seen as a flaring outward geometry during contraction. A 1 s "cruise time" is present after contraction where the bell holds its contracted position. This is followed by the relaxation phase which is initiated by the circular muscles whose angle starts increasing. At that moment, the central disk angle also increases but the radial muscle angle further decreases. This could be due to further muscle contraction or the hydrodynamic forces overpowering the elastic energy of the structure as it relaxes. The flap follows a similar trend as the radial muscle segment. The flap angle decreases for the first 2 s of relaxation and then starts increasing.

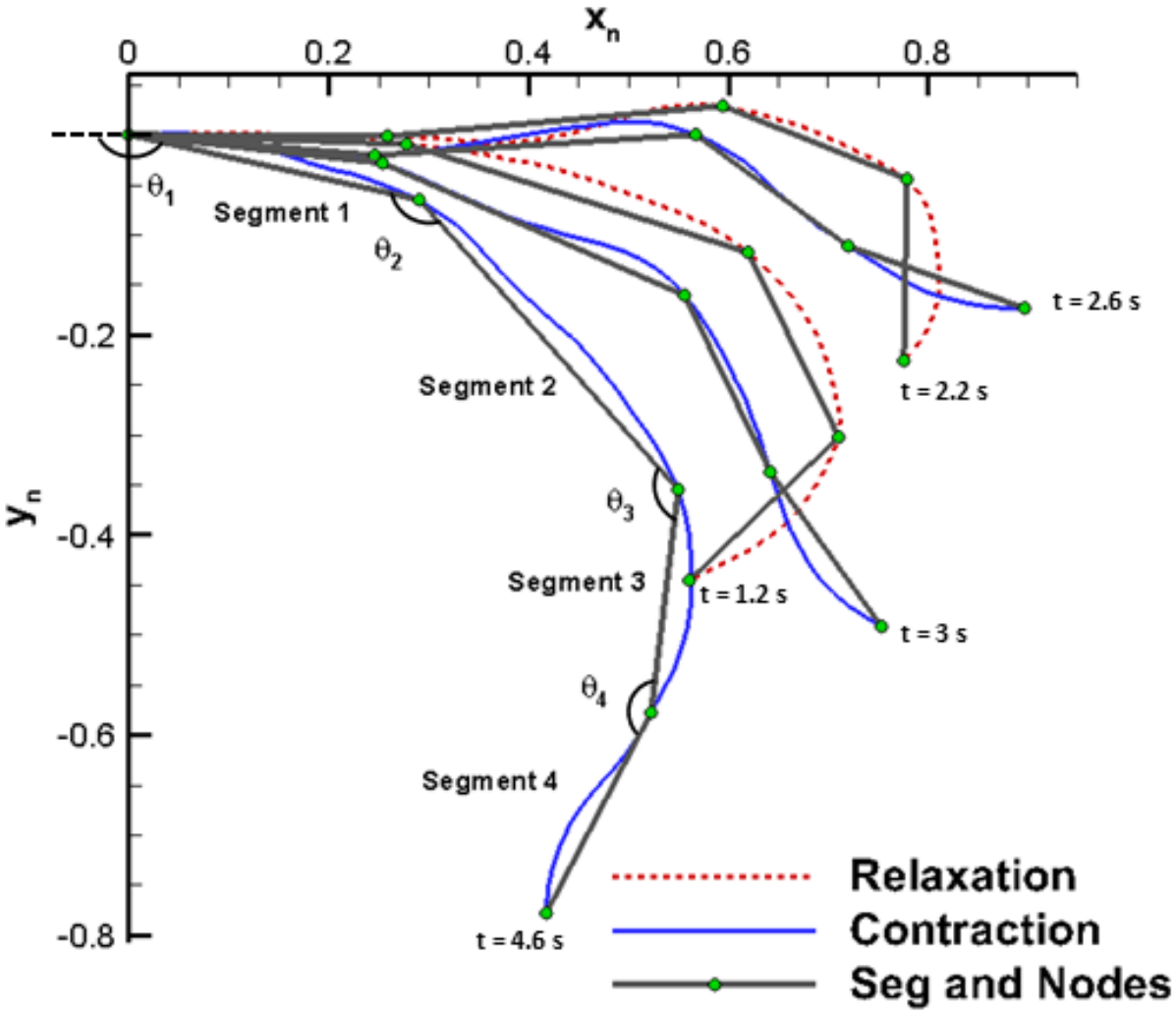

Figure 6.4: Selected *C. capillata* exumbrella profiles during contraction and relaxation over a swimming cycle. The cycle begins with relaxation, and the time at which each profile occurs is labeled. Segments and nodes were found using the optimization node detection method described in Section 5.2 . The angles formed between segments for kinematics analysis are labeled.

For Cyro, the number of actuators was minimized while keeping control over the eight different bell segments. The mechanisms for replicating the circular contraction based on linear or rotary actuators resulted in overly complex and energy consuming designs. A system consisting of one linear actuator and a mechanical arm per bell segment resulted in the desired performance and

fitted within the space constraints of the *C. capillata* morphology as shown in Fig. 6.1 and 3. Eight independent control platforms are therefore present on the vehicle.

The central disk (Segment 1) is passive and undergoes the least amount of rotation in a swimming cycle. This region of the mechanical system was set as a fixed segment as shown in Figs. 1(c) and 3(b). This provides a mounting location for the rigid components of the vehicle. The fixed segment is covered by mesoglea which is free to move passively similar to the natural animal. The circular muscles (Segment 2) are replaced by the mechanical arm and linear actuator which directly actuates this segment. The mechanical arm in this segment consists of a four-bar mechanism. The radial muscles (Segment 3) are replaced by the mechanical arm which actuates this section of the bell also based on the motion of the four-bar mechanism as shown in Fig 1(c), 2 and 3(b). The arm is connected to a linear actuator (PA-14-4-50, Progressive Automations) (L_{AB}) by a transfer link (L_{BC}). CAD images of the mechanical arm are shown in Fig. 6.5 with the arm in the contracted (a) and relaxed positions (b). The different links are labeled in Fig. 6.5 by the joint locations such as link L_{BC} which is the link between joints B and C. The flap region (Segment 4) is replaced by passive artificial mesoglea extending past the mechanical arm. The lag in Segment 3 and 4 during relaxation is critical for the reproduction of the hydrodynamics of the *C. capillata*. The mechanical arm was designed with added passivity in Segment 3 in order to replicate this motion. The passive link consists of a slotted link (L_{GH}), as shown in Figs. 5(a) and 6 which allows the segment to move further inwards during relaxation. A string attaches to L_{GH} near joint G and becomes taut as the arm fully relaxes. This causes tension on the slotted link and pulls Segment 3 to a fully relaxed position. Segment 4 is designed to passively replicate the lagging effect using the compliance of the artificial mesoglea.

The *C. capillata* has natural joints which are indentations in the mesoglea to reduce the force required for deformation. Mechanical joints in Cyro serve a similar purpose as they allow the motion of the linkage system. The link lengths were determined based on the kinematic and anatomical analysis of the *C. capillata* in Section 5.2. Exumbrella profiles over two full swimming cycles were obtained through video digitization of the natural animal in Section 5.1. An example of exumbrella profile with reconstructed subumbrella profile is shown in Fig. 6.1(a). Kinematic artifacts due to the rotation of the animal and motion between the camera and animal were corrected using a video correction technique described in Section 5.1. Three joint detection methods were then developed to find possible mechanical joint locations. Joint locations are quantified in terms of exumbrella arclength from the apex divided by the total exumbrella arclength in the relaxed position. The first joint detection method consists of analyzing the anatomy of a small *C. capillata* in Gladfelter (1973) (with exact diameter unknown). The properties and functions of anatomical feature led to four possible mechanical joint locations. At 40% subumbrella arclength with animal laid flat on its exumbrella, a circular joint in the mesoglea separates the central disk and circular muscles. This location is prone to deformation and is considered as a good location for a mechanical joint analog. Similarly, at 64% there is a transition between the circular muscles and radial muscles. The change in actuator type is also a location prone to more deformation. Lastly, at 88% is the end point of the radial muscles and beginning of the flap. This location marks a transition from a passive to an active region and was also chosen as a mechanical joint location. In addition, the lack of muscles in the passive region causes the flap to be more compliant which affects its dynamics during swimming. The second method is the tangent angle method which consists of finding the areas of the exumbrella with largest deformation over a full cycle. The third method consists of an error analysis between a

discrete bell model and the natural exumbrella profiles. This method resulted in joint locations at 26%, 60% and 80% which are illustrated in Fig. 6.4 and listed in Table 6.1 along with the results of the other joint detection methods. The joint locations from the error analysis method give the most accurate representation of the natural kinematics. However, this method does not take into account several factors relevant to vehicle design such as material properties and structural mechanics involved in creating the kinematics. It assumes that the joints will be placed on the exumbrella. This is also true for the tangent angle joint detection method. In the case of Cyro, a rigid mechanical structure deforms the artificial mesoglea which is located above the structure. In other words, the joint will be located closer to the subumbrella as in the natural animal then the exumbrella as assumed in the optimization method and tangent angle method. Therefore, the anatomical joint detection method should provide a better prediction for the location of Cyro's mechanical joints. The subumbrella arclength percentages found from the anatomical analysis were used directly to establish the joint locations on the mechanical arm.

Table 6.1: Joint locations as determined by the *C. capillata* anatomy from Gladfelter (1973), the *C. capillata* tangent angle joint detection method and the *C. capillata* error analysis joint detection method from Section 5.2. Mechanical joint locations of the mechanical arm (Cyro Arm) are given assuming a flap length of 12%. The joint locations measured on the artificial mesoglea (Cyro Exumbrella) are also shown. Joint locations are given in percentages of exumbrella arclength and relaxed position. Joint 1 for all methods is taken at 0% which corresponds to the bell apex. The last joint or node is at the bell margin (100%).

Joint Detection Method	**Joint 2**	**Joint 3**	**Joint 4**
C. capillata Anatomy	40	64	88
C. capillata Tangent Angle	36	64	82
C. capillata Error Analysis	26	60	80
Cyro Arm	38	65	88
Cyro Exumbrella	39	66	88

The chosen joint locations for Cyro's mechanical arm design are shown in Table 6.1. The joint locations were chosen to account for the structural mechanics and material properties of the mesoglea. The error between the robotic and natural jellyfish only resulted in a maximum of 3% error. The lengths of each link from joint to joint used to construct the mechanical arm are shown in Fig. 6.5 and listed in Table 6.2. The linkages were made of 0.64 cm thick aluminum sheets and were milled out of plates using a CNC. Stainless steel bolts and aluminum spacers were used at the joints. The resulting mechanical arm is shown in Figs. 5(c).

Table 6.2: Lengths of the different links in the mechanical arm between joints. Link L_{AB} represents the linear actuator which changes length from 0.64 to 4.45 cm.

Link	Length (cm)
$\mathbf{L_{AB}}$	0.64-4.45
$\mathbf{L_{BC}}$	8.36
$\mathbf{L_{CD}}$	10.03
$\mathbf{L_{DA}}$	5.12
$\mathbf{L_{DE}}$	7.59
$\mathbf{L_{EF}}$	17.27
$\mathbf{L_{FG}}$	4.32
$\mathbf{L_{GD}}$	22.53
$\mathbf{L_{GH}}$	18.59
$\mathbf{L_{FH}}$	17.72

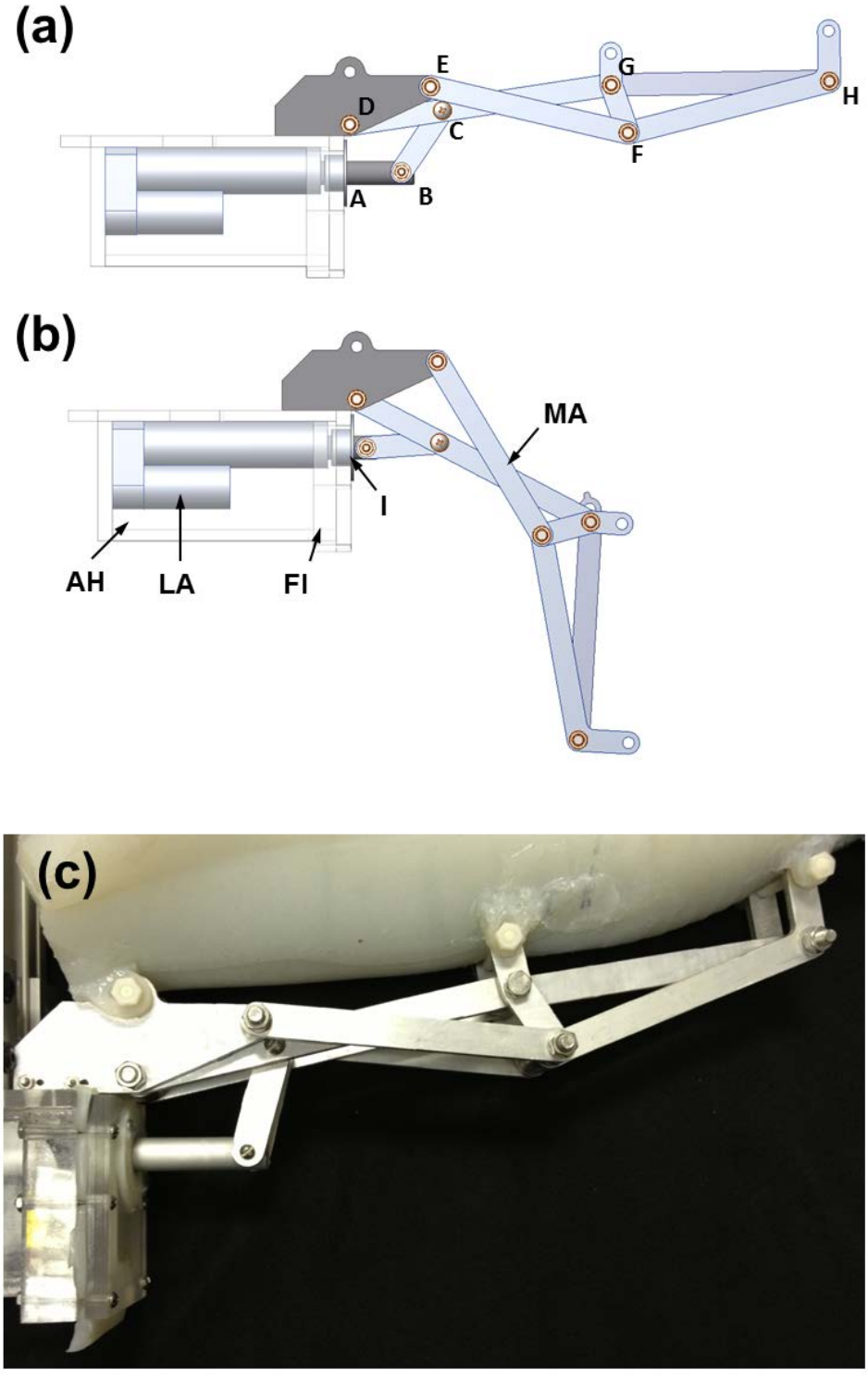

Figure 6.5: Mechanical arm (MA) in the (a) relaxed and (b) contracted positions. Also shown is the actuator housing (AH), linear actuator (LA), Flange (Fl) and insert (I). (c) Picture of the assembled mechanical arm, actuator housing and artificial mesoglea.

Figure 6.6: Slotted link (L_{GH}) for added passivity in Segment 3 during relaxation. The string attachment allows the link to regain its fully relaxed position as the rest of the arm relaxes.

6.2.2 Artificial Mesoglea

The artificial mesoglea was designed based on thickness percentages from Gladfelter's (1973) and Dawson's (2005) prior studies. The dimensions were scaled assuming a linear trend with bell diameter. Cyro's bell diameter was chosen to be 170 cm which was determined by the dimension of the selected motors, mechanical architecture and objective vehicle dimension. Each bell segment was fabricated individually along with the central hub. Individual bell segments were further divided into four separate sections in order to create the 3D shape shown in Fig. 6.7. Figure 7(a) shows the complex geometry of the *C. capillata* in the relaxed position and CAD model of the artificial mesoglea with individual pieces color coded are shown in (b) and (c). Molds were created for each section by milling the proper geometric cavities from lumber blocks. The individual artificial mesoglea sections were made out of Ecoflex® 0010 (Smooth-On®) silicone. This material was chosen because of its mechanical properties and its casting characteristics. The silicone is soft and has a density of 1040 kg/m^3 which is close to that of water (1000 kg/m^3) and helps to achieve the neutral buoyancy of the vehicle. This material was also chosen because of its tear strength of 3850 N/m, which adds to the robustness of the vehicle.

When assembled, the bell segments have a concave geometry with cavity in the subumbrella to promote the same folding effect during relaxation and expansion during contraction.

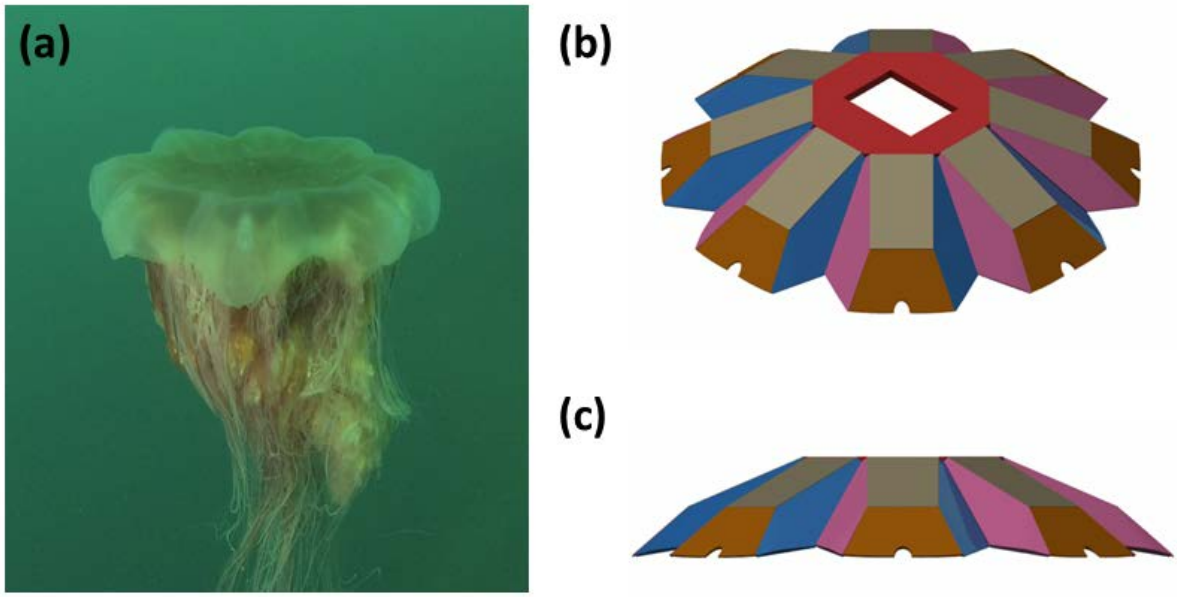

Figure 7: (a) *C. capillata* in the relaxed position. CAD model of the artificial mesoglea showing (b) an isometric and (c) front view. The different colors of the artificial mesoglea represent the sections fabricated separately.

6.2.3 Actuators and Structures

Eight DC linear actuators (PA-14-4-50, Progressive Automations) were selected to drive each arm segment of the robot. The actuators have a maximum force output of 23 kg and originally had a 10 cm stroke length. Due to the design of the mechanical arms, it was necessary to adjust the maximum and minimum stroke limits of each actuator in order to prevent collisions between mechanical parts. This was done by rearranging the two limit switches inside each motor to achieve the exact stroke length necessary to drive the arm segments to their proper relaxed and contracted positions.

Each of the eight actuators was housed in a custom made acrylic box, as shown in Fig. 6.1, 2 and 3. The dimensions for the inside of the box were 5 cm x 10 cm x 20 cm. The acrylic on the top, bottom and sides was 0.8 cm thick, while the front and back panels were 1.27 cm thick. Flanges made of 1.27 cm acrylic were attached at the front of the side plates and were used for attaching the front plate. IPS Weld-On #16 Acrylic Solvent Cement was used to bond all the edges of the box together. The actuator was secured to the back plate of the box with three screws. The front plate was made removable for access to the motors and was secured in place with bolts running through the front plate and the side flanges. A soft silicon gasket provided the seal between the front plate and flanges. The actuator rod passed through an aluminum insert that held a dynamic seal (Type B Polypak, Parker). The dynamics seal allowed linear motion of the rod during actuation while sealing the box from water. A 1.27 cm acrylic central plate was used as the base platform to secure the electronics box and each of the actuator boxes. This plate was octagonal in shape with each side having dimension of 19.7 cm in length. Actuator boxes were bolted to the underside of the plate while the electronics box was bolted on the topside.

The electronics box measured approximately 30 x 25 x 10 cm and was located at the apex of the vehicle to assist the wireless communication and maintenance during operation. The sixteen cell battery pack was placed at the bottom of the box in a separate acrylic housing to further protect it against water. By laying the battery cells horizontally, instead of grouping it vertically as the stock battery is arranged, additional space within the box was created to house the remaining electronics. The electronics were located on top of the battery housing within the box. Waterproof connectors on two sides of the box allowed power to be transferred from the battery to each actuator.

6.2.4 Full Vehicle Assembly

A CAD model of the fully assembled vehicle and an image of the actual vehicle are shown in Fig. 6.8. The center of mass (CM) and center of buoyancy (CB) were initially designed to keep the vehicle stable during upward swimming. This was achieved by designing the CG to be lower than the CB by a distance of 7.87 cm. Table 6.3 lists the buoyancy force for each component. The vehicle's moments of inertia were taken about the CG and are reported in Table 6.4. The chosen coordinate system is centered at the CG and is shown in Fig. 6.9.

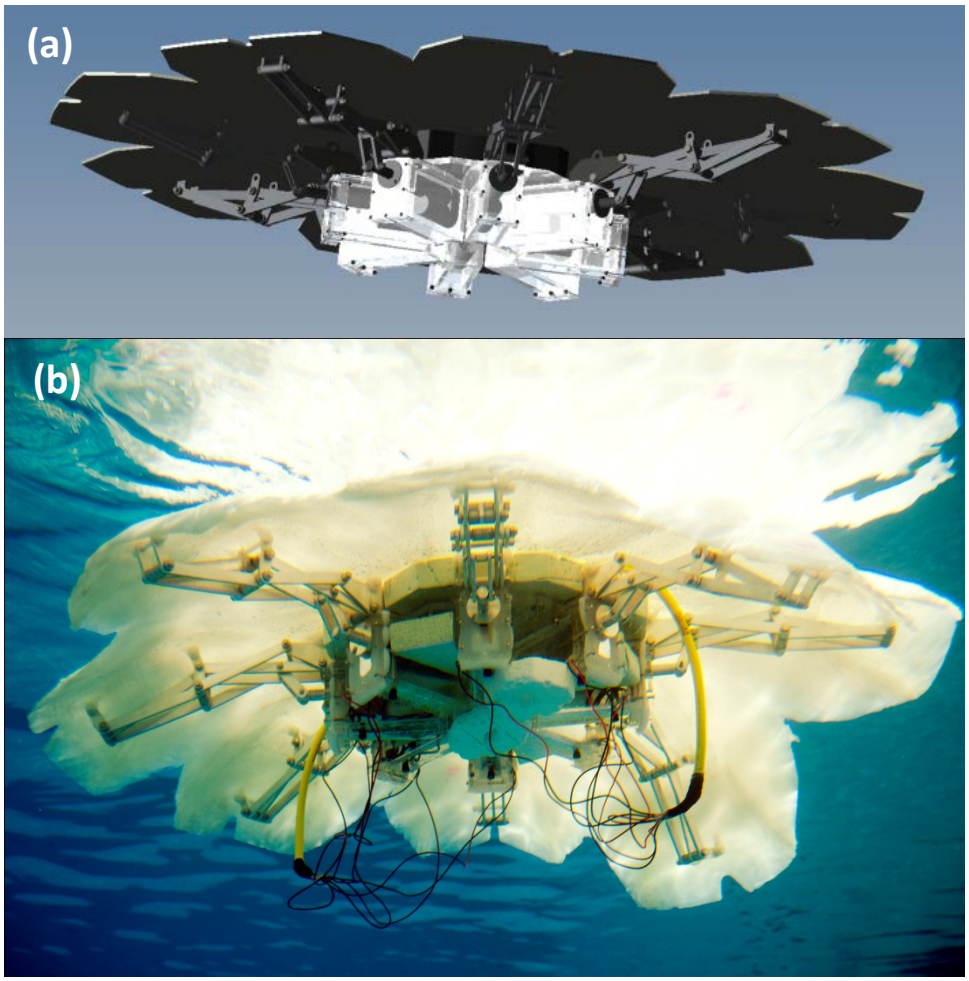

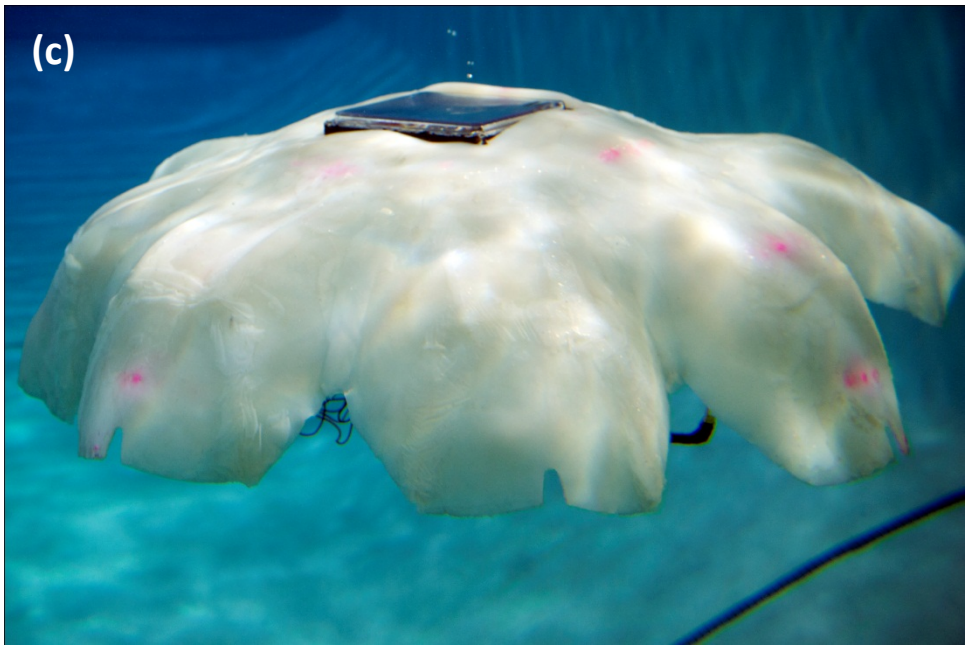

Figure 6.8: (a) CAD model of Cyro, and fully assembled Cyro deployed in water showing a view of the (b) subumbrella and (c) exumbrella.

Table 6.3: Specification for the different components on Cyro.

Component	Volume (cm^3)	Mass (kg)	Buoyancy Force (N)
Mesoglea Bell	36964	38.41	-15.12
Electronics Box / Wires	10219	7.79	23.57
Arm Assembly (x8)	17711	25.28	-74.73
Center Plate / Fasteners	2452	3.71	-12.45
Arm / Tentacles	115	0.45	-4.00
Buoyancy Foam (Top)	9349	0.32	88.52
Buoyancy Foam (Bottom)	1688	0.09	15.57
Totals:	78498	76.06	21.35

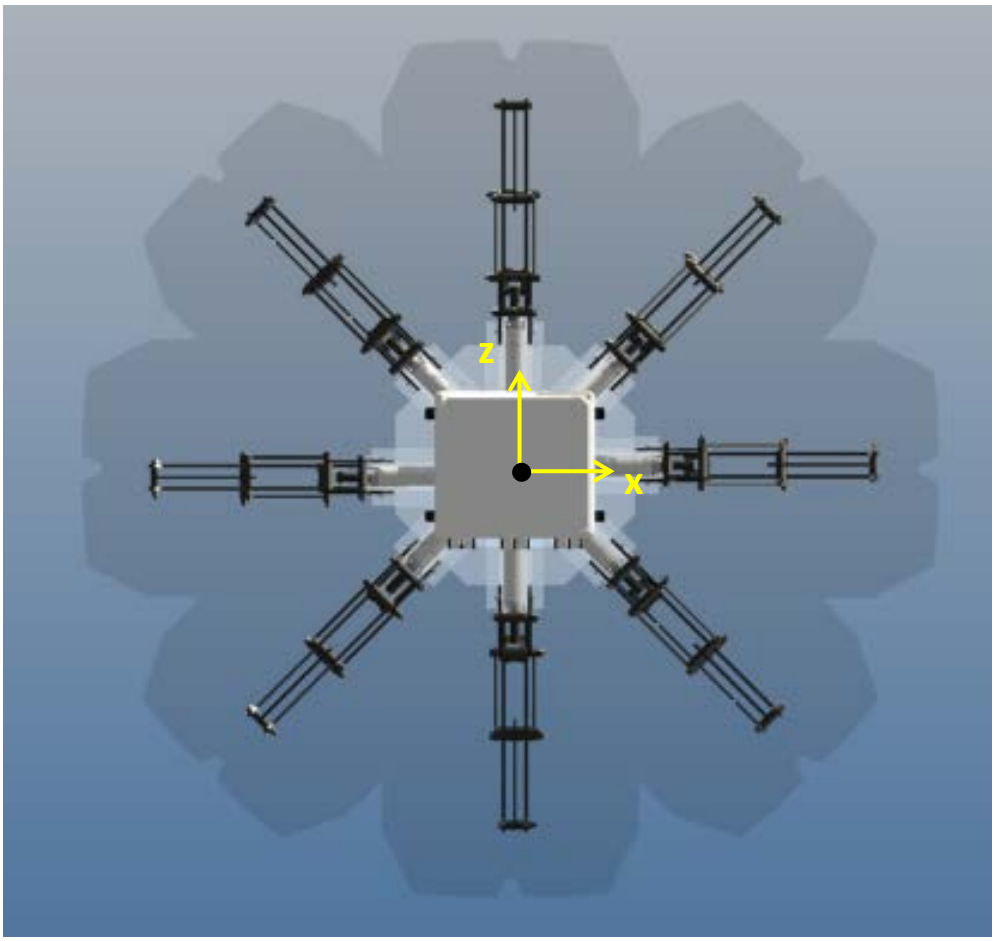

Figure 6.9: Coordinate system of the vehicle centered at the CG. The y-axis points into the page.

Table 6.4: Moments of inertia (kg·cm^2) calculations for the full vehicle with respect to vehicle's CG and coordinate system shown in Fig. 6.9.

I_{xx} = 82208.33	I_{xy} = 35.12	I_{xz} = 49.75
I_{yx} = 35.12	I_{yy} = 144681	I_{yz} = -3031.75
I_{zx} = 49.75	I_{zy} = -3031.75	I_{zz} = 82237.6

6.3 Methods and Materials

6.3.1 Mechanical Arm Model

The mechanical arm design consists of a set of rigid links that pivot about joints. A simplified representation of the link and joint mechanism is shown in Fig. 6.10. The arm mechanism can be split into three different sections on a 2D plane. The first section consists of points A-D and is referred as the translating mechanism. Link AB (L_{AB}) consists of a linear actuator which drives the arm and L_{DA} is fixed. The section defined by points D-G is a four-bar mechanism. The section defined by points FGH is passive and contains a link L_{GH} which is a slotted link. The slotted link will be considered as a regular link with a prescribed elongation during simulation.

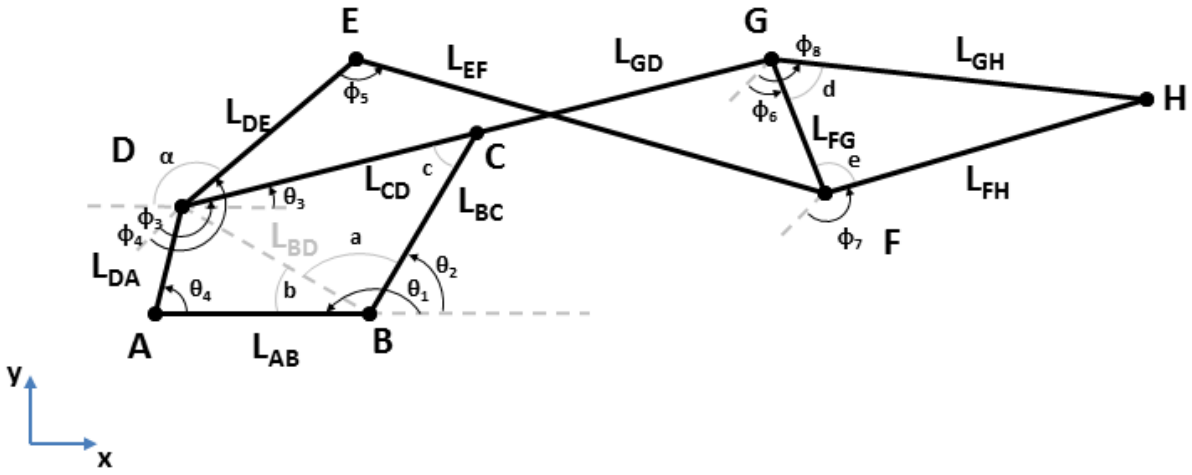

Figure 6.10: Diagram of the arm mechanism model. Joint locations are labeled by letters A-H while the links are labeled by L and the joints bounding them such as L_{AB}. L_{BD} is an artificial link used only for computation. Angles θ_1-θ_4 and ϕ_3-ϕ_8 are the angles formed by links. Angles a-e are artificial angles used for computation. The coordinate system shown is the global coordinate system used for solving arm model.

In order to derive the model, we start by solving for the kinematics of the translating mechanism. The translating mechanism is a four bar mechanism which can be simplified since L_{DA} is fixed and L_{AB} does not rotate. The driving variable of the mechanical arm is L_{AB}, which is the varying length of the translating actuator. The distance between B and D is defined as L_{BD} and is not an actual link. It separates the quadrilateral formed by the translating mechanism into two separate triangles whose angles can be solved by the law of cosines as follows:

$$\cos(\theta_4) = \frac{L_{AB}^2 + L_{DA}^2 - L_{BD}^2}{2L_{DA}L_{AB}}, \quad (6.2)$$

$$\cos(a) = \frac{L_{BD}^2 + L_{BC}^2 - L_{CD}^2}{2L_{BD}L_{BC}}, \quad (6.3)$$

$$\cos(b) = \frac{L_{AB}^2 + L_{BD}^2 - L_{DA}^2}{2L_{AB}L_{BD}}, \quad (6.4)$$

$$\cos(c) = \frac{L_{BC}^2 + L_{CD}^2 - L_{BD}^2}{2L_{BC}L_{CD}}, \quad (6.5)$$

where:

$$L_{BD} = \sqrt{L_{AB}^2 + L_{DA}^2}, \quad (6.6)$$

The angles are in the global coordinate system shown in Fig. 6.10. This gives θ_2:

$$\theta_2 = 180° - a - b, \quad (6.7)$$

and the angle of interest θ_3:

$$\theta_3 = \theta_2 - c, \quad (6.8)$$

Next, the four-bar mechanism can be solved in terms of L_{AB}. The loop closure equations of the four-bar mechanism are:

$$L_{DE}\cos(\phi_4) + L_{EF}\cos(\phi_5) - L_{FG}\cos(\phi_6) - L_{GD}\cos(\phi_3) = 0, \quad (6.9)$$

$$L_{DE}\sin(\phi_4) + L_{EF}\sin(\phi_5) - L_{FG}\sin(\phi_6) - L_{GD}\sin(\phi_3) = 0, \quad (6.10)$$

where ϕ_4 is set equal to $180°$ in order to simplify the system. We are interested in solving for ϕ_5. To do so, ϕ_6 is isolated and both sides of Eqs. 6.9 and 6.10 are squared:

$$\left(L_{FG}\cos(\phi_6)\right)^2 = \left(-L_{DE} + L_{EF}\cos(\phi_5) - L_{GD}\cos(\phi_3)\right)^2, \quad (6.11)$$

$$\left(L_{FG}\sin(\phi_6)\right)^2 = \left(L_{EF}\sin(\phi_5) - L_{GD}\sin(\phi_3)\right)^2, \quad (6.12)$$

Equations 6.11 and 6.12 are then expanded and added. After grouping the terms, the following form can be obtained:

$$k_1\cos(\phi_3) - k_2\cos(\phi_5) + k_3 = \sin(\phi_5)\sin(\phi_3) + \cos(\phi_5)\cos(\phi_3), \quad (6.13)$$

where:

$$k_1 = \frac{L_{DE}}{L_{EF}}, \quad (6.14)$$

$$k_2 = \frac{L_{DE}}{L_{GD}}, \quad (6.15)$$

$$k_3 = \frac{L_{DE}^2 + L_{EF}^2 + L_{FG}^2 - L_{GD}^2}{2L_{EF}L_{GD}}, \quad (6.16)$$

Equation 6.13 is known as the Freudenstein equation. The following trigonometric properties are then substituted in Eq. 6.13:

$$\sin\left(\phi_5\right) = \frac{2\tan\left(\frac{1}{2}\phi_5\right)}{1+\tan^2\left(\frac{1}{2}\phi_5\right)}, \qquad (6.17)$$

$$\cos\left(\phi_5\right) = \frac{1-\tan^2\left(\frac{1}{2}\phi_5\right)}{1+\tan^2\left(\frac{1}{2}\phi_5\right)}, \qquad (6.18)$$

Grouping the terms, we arrive at the following equation:

$$A\tan^2\left(\tfrac{1}{2}\phi_5\right) + B\tan\left(\tfrac{1}{2}\phi_5\right) + C = 0, \quad (6.19)$$

where:

$$A = \cos\left(\phi_3\right)\left(k_1+1\right) + k_2 + k_3, \quad (6.20)$$

$$B = -2\sin\left(\phi_3\right), \qquad (6.21)$$

$$C = \cos\left(\phi_3\right)\left(k_1-1\right) - k_2 + k_3, \quad (6.22)$$

Equation 6.19 is a quadratic equation which can be solved using:

$$\phi_5 = 2\tan^{-1}\left(\frac{-B \pm \sqrt{B^2 - 4AC}}{2A}\right), \quad (6.23)$$

Similarly, we can solve for ϕ_6 and obtain the following:

$$\phi_6 = 2\tan^{-1}\left(\frac{-E \pm \sqrt{E^2 - 4DF}}{2D}\right), \qquad (6.24)$$

where:

$$D = k_5 + k_2 - \cos(\phi_3)(k_4 - 1), \qquad (6.25)$$

$$E = -2\sin(\phi_3)$$

$$F = k_5 - k_2 - \cos(\phi_3)(k_4 + 1), \qquad (6.26)$$

and:

$$k_4 = \frac{L_{DE}}{L_{FG}}, \qquad (6.27)$$

$$k_5 = \frac{L_{EF}^2 - L_{DE}^2 - L_{FG}^2 - L_{GD}^2}{2L_{FG}L_{GD}}, \qquad (6.28)$$

Next, we solve for the passive section of the mechanical arm. The angles ϕ_8 and ϕ_7 can be solved by noticing that the passive section is a triangle with constant location with respect to L_{FG}. Using the law of cosine we obtain the angles determining the triangle:

$$\cos(e) = \frac{L_{GH}^2 + L_{FG}^2 - L_{FH}^2}{2L_{GH}L_{FG}}, \qquad (6.29)$$

$$\cos(d) = \frac{L_{FG}^2 + L_{FH}^2 - L_{GH}^2}{2L_{FG}L_{FH}}, \qquad (6.30)$$

The angles dictating the position of L_{GH} and L_{FH} are then determined using:

$$\phi_7 = 180 + \phi_6 - d\,, \qquad (6.31)$$

$$\phi_8 = e + \phi_6\,, \qquad (6.32)$$

The four-bar mechanism and passive section are related to the translational mechanism using the following relationship:

$$\theta_3 = \phi_3 - \alpha\,, \qquad (6.33)$$

where α is used to convert the coordinate system to the global coordinate system used in solving for the translational mechanism. α can also be used to convert angles ϕ_4 - ϕ_8 into the global coordinate system as follows:

$$\theta_i = \phi_i - \alpha, \quad 3 \le i \le 8\,. \qquad (6.34)$$

These angles along with the different link lengths L, fully describe the position of the arm mechanism as a function of L_{AB}.

6.3.2 Thrust Quantification

A thrust stand was developed to quantify the forces produced by a single bell segment during swimming. This can be extrapolated to approximate the thrust produced by the full vehicle which provides an assessment of the vehicle's capability to propel itself. Design requirements for the thrust stand included the ability to measure force underwater and to isolate the x- and y-components of force during contraction and relaxation. Figure 11 shows a free body diagram of the force created by the bell segment during actuation along with a schematic and experimental setup of the thrust stand.

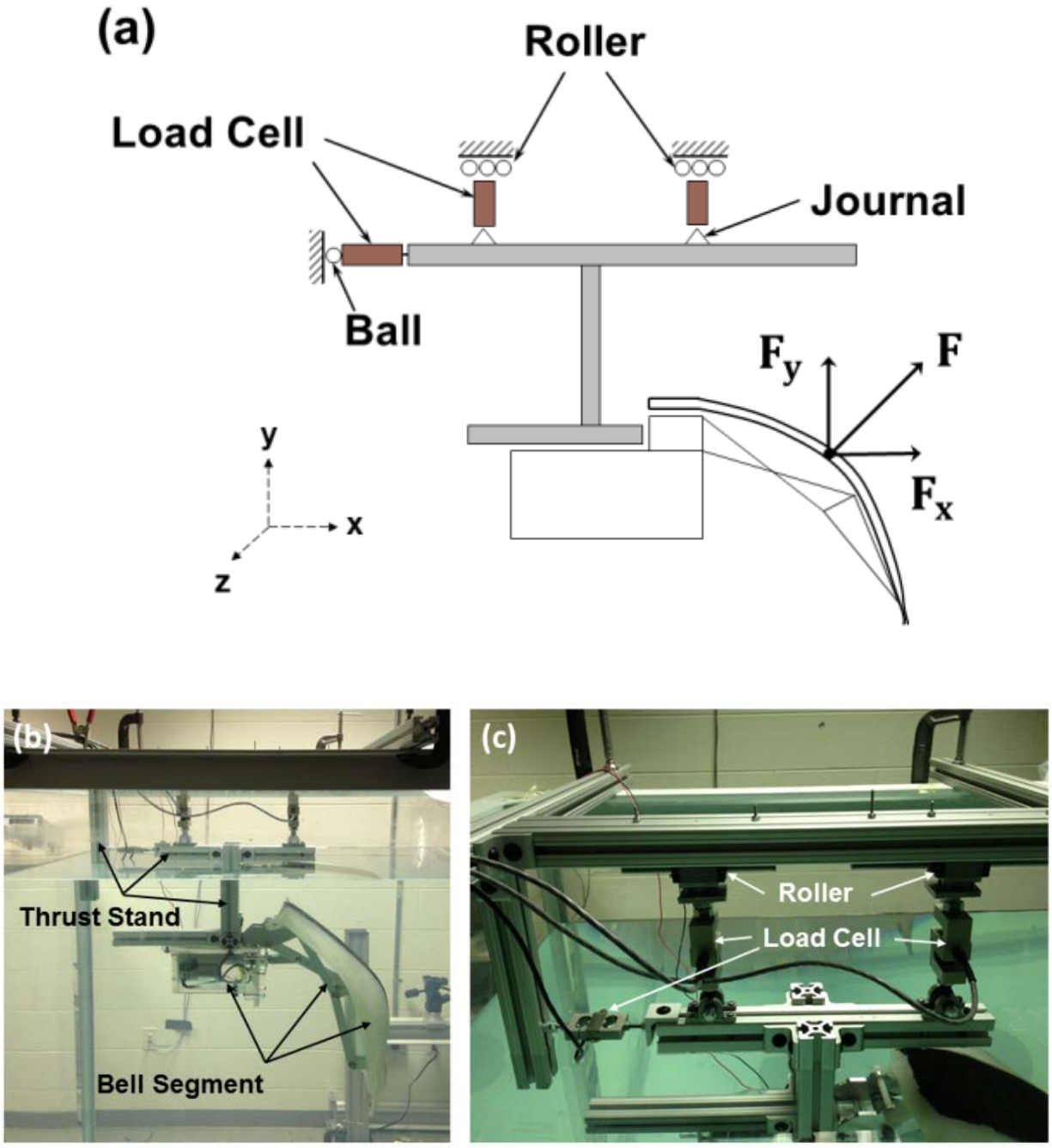

Figure 6.11. (a) Schematic of the thrust stand showing the rollers, ball and socket joint, journal bearings and load cells. (b) Image of the experimental setup with thrust stand and bell segment in water. (c) Close-up view of the thrust stand.

The thrust stand design consists of two vertical 110 kg S-load cells (LC101-250, Omegadyne) for measuring the force in the y-direction. Each vertical load cell is on a slider at one end and on

bearings at the other. This provides a degree of freedom in the x-direction and about the z-axis. One 23 kg S-load cell (LC101-50, Omegadyne) measures force in the x-direction. This load cell is positioned on a ball joint which allows rotation about the x-, y- and z-axis. This design assumes small displacement in the y-direction and neglects the effects of friction at the supports. The load cells are kept out of water and the forces are distributed through t-slotted aluminum beams of 3.8 x 3.8 cm in cross-section. The y-component of force is the sum of both y-direction load cells. The x-component of force is measured directly by the 23 kg load cell. The hydrodynamic center and center of mass movement of the mechanical arm over an actuation cycle significantly changes the direction of the reaction forces causing oscillation in the system. The two-vertical-load cell setup adds stability and reduces oscillation as the arm rotates. This thrust stand also prevents the need for submerging force measuring devices. The output of the load cells were recorded with a data acquisition card (NI 9215, National Instruments) at a sampling rate of 1000 bits per second (bps). A hundred samples were averaged giving 10 samples per second which were then filtered with a second order low pass Butterworth filter. The 56 x 50 x 3 cm bell segment was tested in a tank measuring 170 x 150 x 80 cm.

6.3.3 Swim Testing and Kinematics Tracking

The vehicle was tested for its ability to swim autonomously. This test was conducted in a swimming pool which had a 120 cm shallow end and a 420 cm drop off. See Fig. 6.12 for a schematic of the test setup. A camera (HDR-CX260, Sony) in an underwater case (SPK-HCG, Sony) was setup on a tripod positioned in the shallow end and recorded the vehicle kinematics at 30 fps. A 23 cm diameter buoy was used to keep the vehicle steady at a depth of 182 cm before

actuation. The buoy was attached to the vehicle via a rope and four attachment points on the central plate. The rope was kept slack during active testing to prevent the buoyancy force from the buoy to act on the vehicle. The camera and its weighted tripod were placed on the flat surface of the shallow end of the diving well.

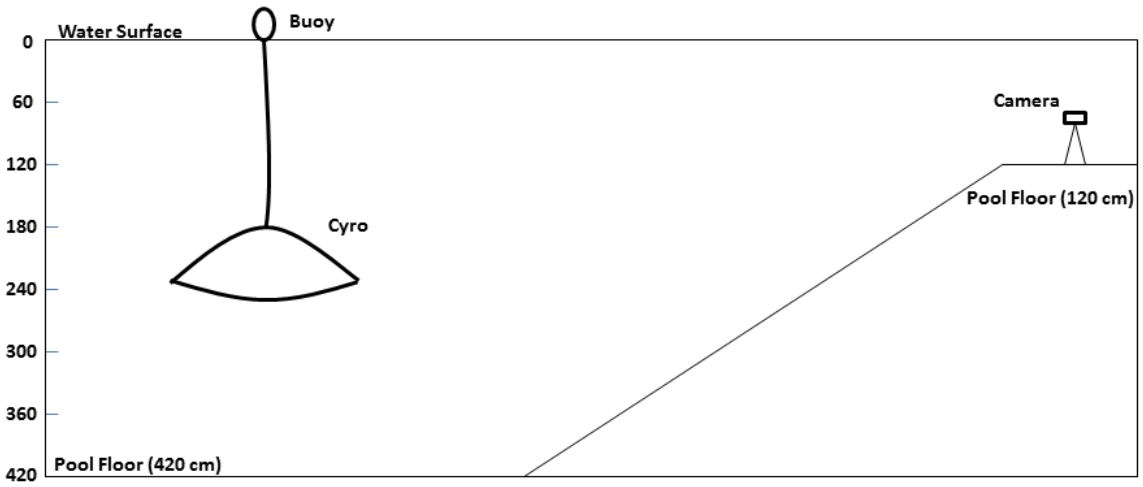

Figure 6.12: The image shows a representation of the indoor pool used for vehicle testing. The objects in the image are not to scale. The deepest part of the pool is 420 cm and accounts for the majority of the pool area. There is a small 120 cm shallow section on one end of the pool, where the camera was placed.

Preliminary testing inside the pool was done to determine suitable operating parameters for swimming. The following sets of parameters were varied: relaxation rate, relaxed pause time, contraction rate and cruise time. A LabView program was developed and utilized to vary these parameters by wirelessly updating the onboard controller using two Xbee wireless transceivers. Tracking markers shown in Fig. 6.13 were positioned on the artificial mesoglea for tracking the vehicle and bell kinematics. The markers were perforated hollow plastic balls with negligible buoyancy force and were dark in color for high contrast with the mesoglea edging and pool background. Markers were placed along the actuating arms at the margin (1, 9, 13), apex (5), the

mechanical arm tips (2, 8, 12) and over the joints (3, 4, 6, 7, 10, 11) of Cyro's mesoglea. The video used for bell kinematics analysis was chosen so that the tracking balls numbered 1 through 9 in Fig. 6.13 were aligned parallel with the image plane of the camera for an accurate perspective on the vehicle's kinematics. Bell kinematics of Cyro were tracked by digitizing the position of the tracking balls over a full swimming cycle. The positions were digitized from the recorded video using ImageJ and corrected for vehicle rotation using the procedure described in Section 5.1. The points were zeroed about the apex (tracking ball 5) and normalized by the exumbrella arclength in the relaxed position. The power consumption of the vehicle was monitored during swim testing using a cascading op-amp circuit. Current and voltage across the battery were sampled at 20 Hz using this circuit and then stored as analog voltage signals in the onboard memory module. The cascading op-amp circuit was designed to withstand a maximum current of 40 A.

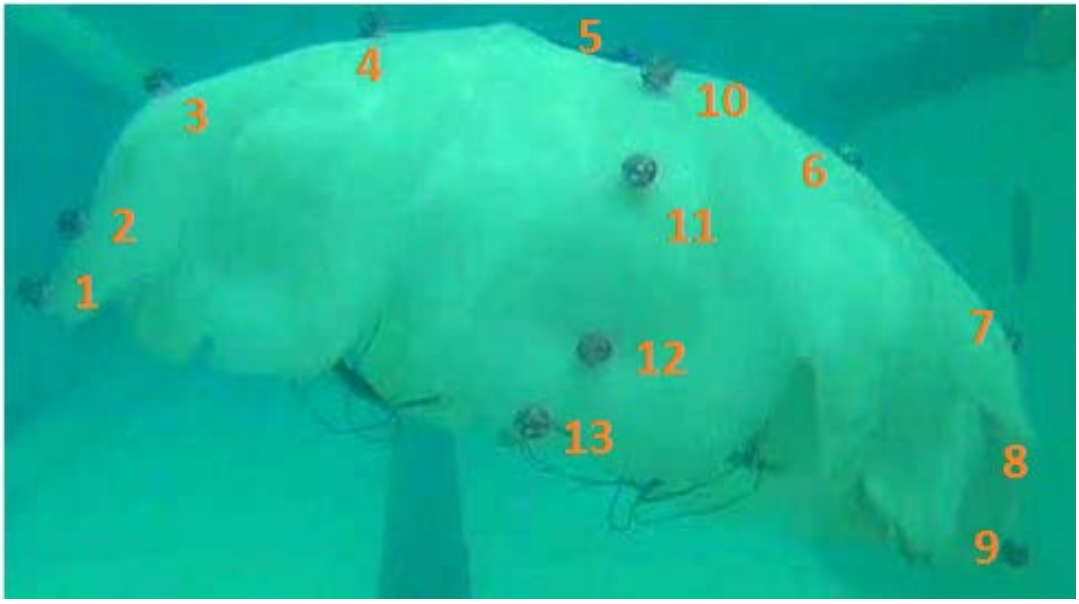

Figure 6.13: Picture of Cyro in the fully contracted position illustrating the position of the tracking balls used to generate discrete representations of the vehicle's bell kinematics.

6.4 Results

6.4.1 Bell Kinematics

The *C. capillata* bell profiles obtained in Chapter 6 are shown in Fig. 6.14 along with margin and flexion point trajectories. The flexion point is defined as the location where the flap begins and corresponds to the mechanical arm tip on Cyro. The *C. capillata'*s bell margin follows an outer path during contraction and an inner path during relaxation. This hysteresis helps in increasing thrust during contraction while reducing drag during relaxation. The kinematics are also important for the formation of starting and stopping vortices and the interaction between the vortices is a crucial aspect of the rowing propulsion (Dabiri et al. 2005). Cyro's margin trajectory stays nearly constant during contraction and relaxation. The lack of hysteresis is due to Segments 3 and 4 not bending inwards by a large enough angle during relaxation. Segment 3 has the slotted link which is designed to allow inwards bending during relaxation but the stiffness of the artificial mesoglea when stretched during contraction prevents it from passively doing so. The hysteresis at the flexion point is much less then at the bell margin and Cyro mimics this well. Comparing the trajectories of both natural animal and robot, we can see that the *C. capillata* is able to achieve more displacement in the x- and y-directions. The *C. capillata* achieves 0.14 and 0.19 units more deformation in the x- and y-direction respectively than Cyro. This is mainly due to Segment 1 being fixed on Cyro and not allowing the 20° rotation of the central disk region during swimming. To show this clearly, the *C. capillata* kinematics are shown in Fig. 6.14(c) with Segment 1 fixed. The resulting trajectories are compared with Cyro and the original *C. capillata* kinematics in Fig. 6.14(d). The flexion point trajectory of the *C. capillata* with fixed Segment 1 now has a displacement difference of 0.16 units in the x-direction and only 0.03 units difference in the y-direction then Cyro. This is closer

to Cyro and confirms the limitation of having a fixed Segment 1 in the y-direction but it does not account for the lack of deformation in the x-direction. The limitation in the x-direction is related to the design of the mechanical arm. The trajectories in Fig. 6.14(d) also show discrepancies between the location of the natural and robotic profiles. This is due to variation in the initial exumbrella profiles which is used to normalize each subsequent profile. This is seen in Fig. 6.14(a) and (b).

The results in Fig. 6.14(d) show the tip trajectory of the mechanical arm model. Results are shown with and without the passive link simulated. The passivity adds hysteresis to the trajectory. It is difficult to compare the trajectory with the natural animal since the error in processing of the natural profiles is of the same order as the hysteresis of the arm model with passivity. Also, the model trajectories are lower than that of Cyro. This is because the trajectories were tracked on the artificial mesoglea of the robot as opposed to directly on the mechanical arm as done in the simulation. After accounting for these differences and the error in tracking Cyro profiles, the model shows a good representation of the mechanical arm.

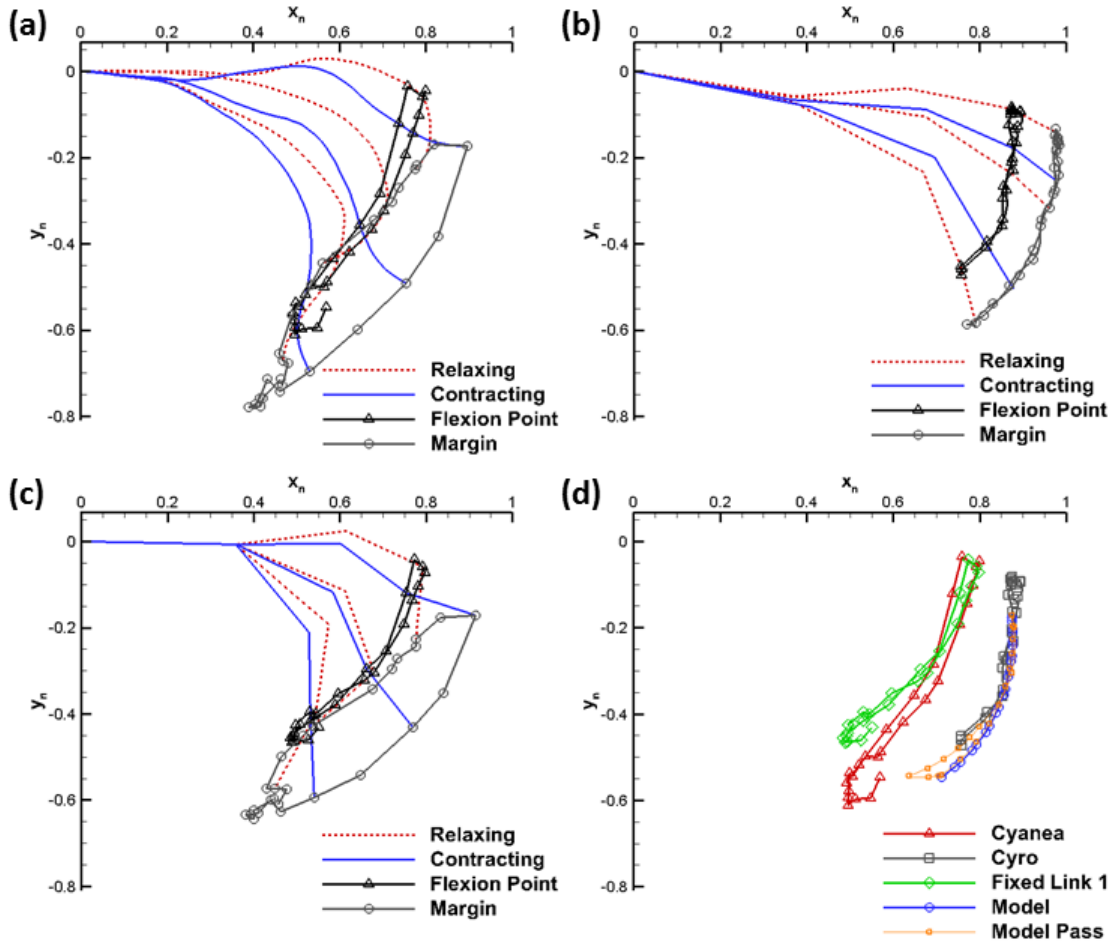

Figure 6.14: Selected bell profiles with flexion point and margin trajectories for (a) the *C. capillata*, (b) Cyro and (c) *C. capillata* with fixed Segment 1. (d) Flexion point trajectories for Cyro, *C. capillata*, *C. capillata* with fixed Segment 1, and arm model with and without prescribed passivity.

6.4.2 Thrust

The forces exhibited by a single bell segment were measured using a thrust stand in static water. The x- and y-components were measured over one actuation cycle and are shown in Fig. 6.15. The cycle begins with relaxation where the arm moves upwards and creates a negative force in the x- and y-directions. The average force magnitude in the x-direction is higher than the y-direction for this phase as shown in Table 6.5. The contraction phase results in positive forces

in both directions. Cruise time results in very low magnitude forces as can be expected since the arm is not moving. The contraction phase produced average forces approximately 3X and 11X larger in the x- and y-components respectively than in the relaxation phase. Overall, this resulted in an average force of -0.1 N in the x-component and 3.49 N in the y-component over the full cycle. Multiplying the y-component by eight for the other bell segments, we can approximate the total thrust produced by the vehicle to be 27.9 N during one cycle. These results predict that the vehicle will be able to produce a positive force which will yield net forward displacement assuming it is near neutral buoyancy. Part of the force in the x-direction will be directed towards the y-component force since water in the subumbrella will face hydrodynamic forces equal in magnitude and opposite in direction in the x-component due to symmetry. Most of the thrust is produced during the last half of the contraction cycle when the bell's contraction rate reaches its peak. The slower contraction rate at the beginning of the contraction cycle is related to the transfer link (L_{BC}) which engages the mechanical arm into rotary motion driven by the linear actuator. See power consumption results in Fig. 6.16(a) for a corresponding delay which explains the smaller hydrodynamic load at the beginning of contraction.

Some oscillation is seen in the system as the linear actuator reaches its maximum position at the end of the relaxation and end of the contraction. This is an artifact of the segment being clamped. Some noise in the y-component is due to the load cell being rated for a much higher magnitude than the forces measured. Load cells with higher sensitivity at lower magnitudes would help improve the signal to noise ratio.

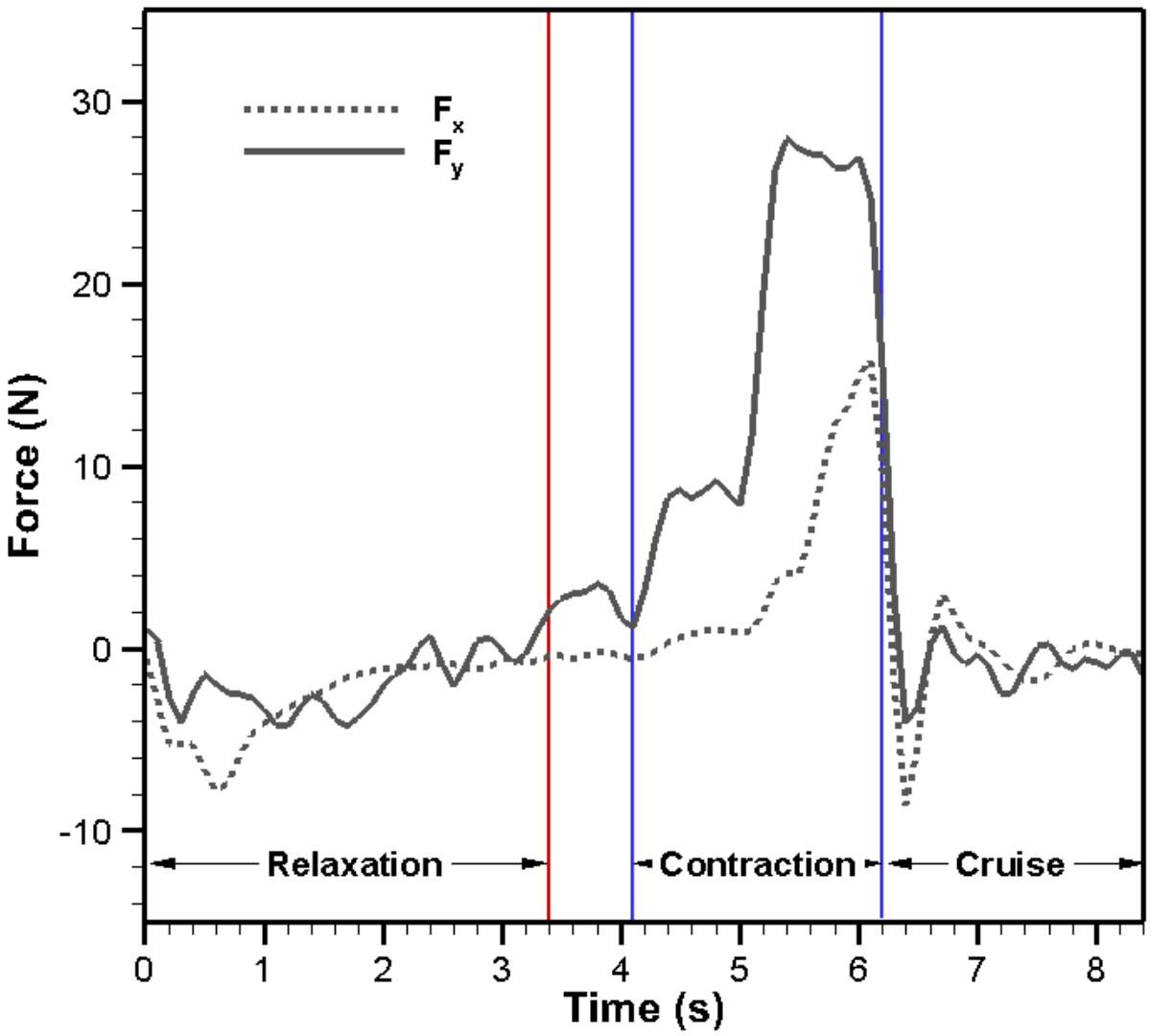

Figure 6.15: x and y force components of one bell segment over an actuation cycle. Relaxation and contraction refer to the linear actuator pulling and pushing respectively. Cruise time is a period when the actuator is off and in the contracted position. The actuator is also off for a short period (0.7 s) between relaxation and contraction.

Table 6.5: Time and average force components as measured with the thrust stand for each actuation cycle phase and for a full cycle.

	Relaxation	Contraction	Cruise	Full Cycle
Time (s)	3.4	2.1	2.2	8.4
F_x (N)	-2.58	4.85	-0.411	0.1
F_y (N)	-1.7	16.9	0.155	3.81

6.4.3 Upward Swimming Performance

Cyro was tested in a pool for its overall swimming ability. Initial actuation settings were chosen to match that of a natural *C. capillata* of the same size as Cyro which were found by extrapolating the contraction time over the cycle period of smaller animals. The biomimetic projections were then adjusted based on visual inspection of preliminary testing to improve the robot's performance. The chosen parameters for upward swimming was done with a relaxation time of 3.4 s, a relaxation pause time of 0.7 s, contraction time of 2.1 s and cruise time of 2.2 s. The contraction corresponds to the highest pulse width signal (100% duty cycle) of the motors and a slower pulse width signal (55% duty cycle) during relaxation.

The vehicle was put at a depth of 182 cm. Prior to actuation, the vehicle was raised slightly to remove tension from the rope and buoy and allowed to drift for approximately 2 s which is the time prior to zero in Fig. 6.16. It can be seen from the drifting time that the vehicle had a near neutral buoyant state. Cyro was then powered at (t = 0 s) and allowed to swim freely to the surface. The apex of the vehicle was tracked over time and the resulting position, velocity and acceleration in the y-direction as a function of time are plotted in Fig. 6.16 along with the associated power consumption. Upon actuation, the vehicle is initially in a contracted state. The bell creates a negative (down) force as it relaxes which sends the vehicle below its initial position. The cycle continues with a contraction that gives positive (up towards the water surface) displacement. This cycle repeats itself five times before the vehicle breaks the water surface. The overall displacement of the AUV for five actuation cycles was 177 cm and the maximum displacement achieved by one complete stroke cycle was 63 cm on the last stroke, as shown Fig. 6.16. The vehicle built momentum throughout swimming but did not reach a steady state velocity. The velocity plot with power consumption curve shows where in the cycle the

motors were actuating. The vehicle continued positive motion in the y-direction during cruise time. As the bell relaxed, the vehicle underwent a negative velocity until the fifth cycle where it stayed near 0 cm/s. The average velocity and acceleration were 4.2 cm/s and 0.17 cm/s^2 respectively over the five cycles. The maximum velocity and maximum acceleration were 25.5 cm/s and 18 cm/s^2 respectively which were achieved during the last stroke. These results prove the vehicle's ability to propel itself autonomously.

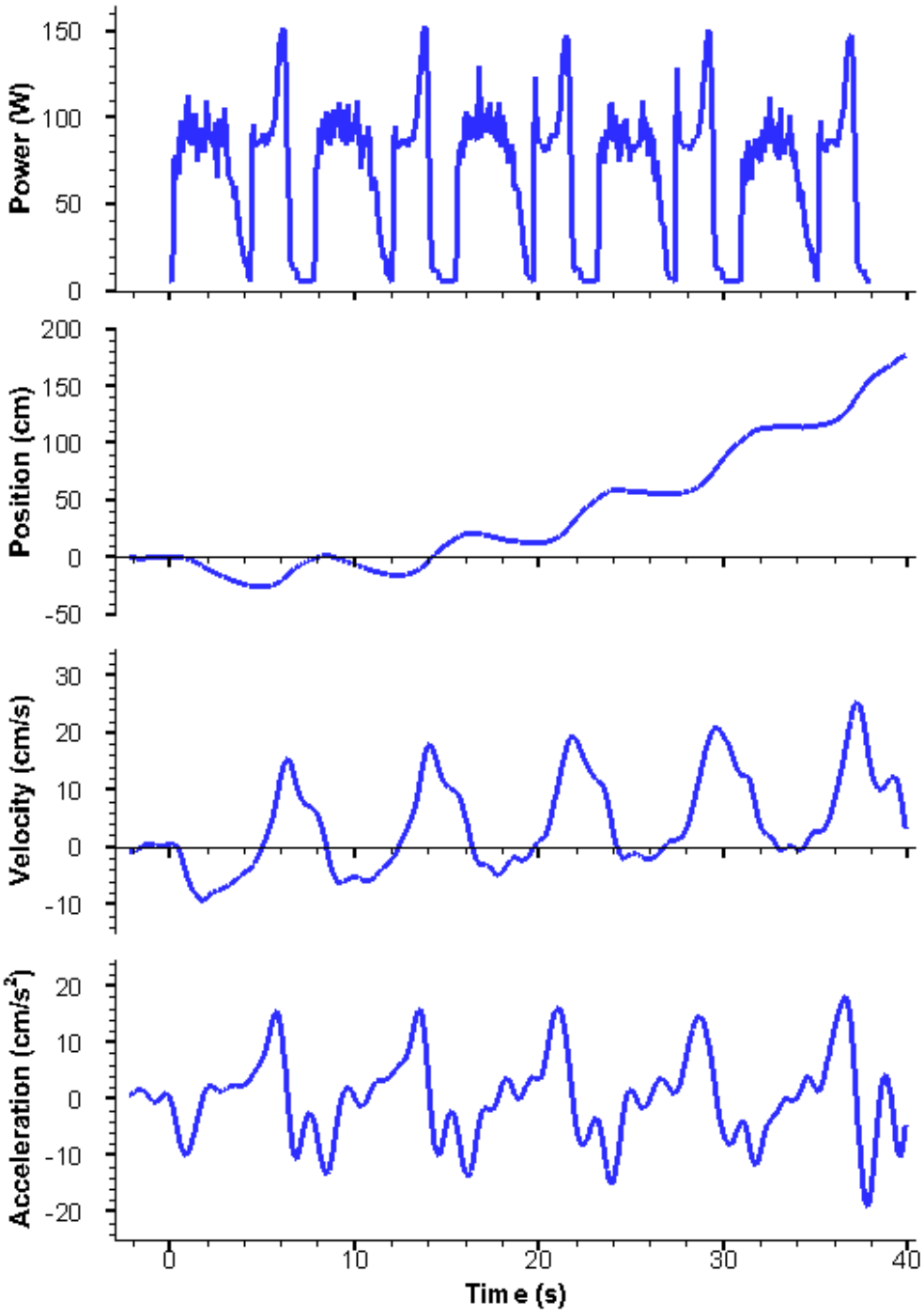

Figure 6.16: Power consumption and vehicle kinematics over five cycles of actuation. The results show that the vehicle is near neutral buoyancy before actuation ($t < 0$ s). Cyro swims until it reaches a distance of approximately 5 cm below the water surface which marked the end of the fifth cycle. The bell is initially in the contracted state.

6.4.4 Power Consumption

A cascading op-amp circuit on-board the AUV measured the power drawn from the battery. Instantaneous values of current (i_i) and voltage (V_i) were recorded at a sampling rate of 20 Hz. These numbers were recorded through two analog-to-digital converters on the microcontroller. Power consumption was then calculated as $P_i = V_i i_i$. Figure 16(a) shows the resulting plot of power consumption over time for the five actuation cycles recorded during the swim test. The controller and sensor use 5 W which is seen as an off-set when the actuators are off in the power consumption results. The resulting power data was processed using a second order Butterworth filter. The average power consumption over one full swimming cycle was 70 W. The average power consumption in-air without artificial mesoglea was 48 W. Therefore, 22 W was consumed in moving the artificial mesoglea and generating the hydrodynamic forces. Out of the 48 W required for in-air actuation, 5 W was for the electronics and therefore, 43 W was required for moving the mechanical arm and compensating for mechanical losses. The total energy consumed during contraction was 218 J and 314 J during relaxation. The vehicle's total efficiency can be calculated using:

$$e = \frac{P_{out}}{P_{in}} = \frac{VT}{P}, \qquad (6.34)$$

where P and T are the average power consumption and thrust of vehicle over the 5th cycle. The average thrust was approximated to be 27.9 N which results in an efficiency of 3%. The COT for Cyro was 10.9 J/kg·m, as defined by Eq. 6.1 with an average velocity of 8.47 cm/s taken during the 5th cycle, average power consumption of 70 W and body mass of 76 kg.

6.5 Discussion

Cyro showed its ability to swim autonomously while maintaining a similar physical appearance and kinematics as the *Cyanea capillata*. Measurements of *C. capillata*'s performance were not available for animals of similar dimensions as Cyro. Therefore, the main metric used to evaluate the degree of mimicry is the bell kinematics. The number of actuators in Cyro's design was reduced from one set of circular muscles and one set of radial muscles per bell segment to a single linear actuator. Also, Segment 1 of the *C. capillata* was set as a fixed plate which limited the bell's range of motion. The passivity of Segments 3 and 4 of the *C. capillata* was replicated but the kinematic results showed that the motion was not matched. The bell margin trajectory of Cyro did not have as much hysteresis as the *C. capillata* and the mechanical arms did not bend passively as desired during relaxation. This is due to the artificial mesoglea keeping too much tension in the arm which reduces the compliance with hydrodynamic forces. The improvement of passivity will be the subject of future work since the bell kinematics directly affects the hydrodynamics of the vehicle and therefore its performance as seen in natural jellyfish (Costello and Colin, 1994; Costello and Colin, 1995; Colin and Costello, 2002; Bajcar et al., 2009; Sahin et al., 2009; Wilson and Eldredge, 2011). Also, the bell segments of the *C. capillata* have a complex 3D geometry which was roughly approximated in this study. Natural *C. capillata* will have to be scanned in order to replicate its bell geometry with higher accuracy. Further, the bell kinematics of this 3D structure will require more analysis as only one plane in the spanwise (radial) direction of a bell segment was considered in this work.

Thrust measurements of a single bell segment provided an approximation of thrust production for the whole vehicle. Several assumptions were made for this approximation. The mesoglea of the bell segment does not have a central disk region covering the top portion of the arm though

this should not have much effect when the arm is clamped. It also does not have adjacent segments on each side. These limitations allow water to flow in regions where it would not be able to do so in the fully enclosed bell. Water in the subumbrella flowing in the x-component is able to keep moving in the x-direction without being met by equal and opposite forces due to the symmetry of the full vehicle. These limitations will likely underestimate force in the y-component. The thrust stand design used for this experiment was able to seclude the x- and y-components of the total force upon actuation. This design was also able to reduce oscillation in the system due to the pitching motion of the bell segment. The thrust stand will serve as a method to test different artificial mesoglea and mechanical arm designs in order to increase performance and efficiency.

Poor hysteresis in the Cyro's bell trajectory should result in higher drag. This is compensated by a faster contraction rate as seen when comparing the contraction time over one full cycle of the *C. capillata* and Cyro which are 37% and 25% respectively. The jellyfish is limited by its single layer of muscles while Cyro is not. It is possible that for an artificial system such as the *C. capillata* the optimal contraction rate is not the same as the natural animal due to different losses in the mechanical and electrical systems. The swimming performance of Cyro was observed to improve with contraction rate but further characterization will be required to determine an optimum which maximizes proficiency or efficiency. The total vehicle efficiency and COT were found to be 3% and 10.9 J/kg·m respectively but these numbers rely on the average velocity of the fifth cycle of actuation where the vehicle had not yet reached a steady state velocity. The average velocity at steady state would likely be higher and therefore increase the efficiency and COT calculations.

Energy expenditures of relaxation and contraction are 314 J and 218 J respectively. More energy is therefore spent in opening the bell then contracting it. Though the arms move at a faster rate during contraction, they move for a longer time during relaxation. The mechanical loses and opposing gravitational force on the arm cause this higher energy consumption. The natural jellyfish's approach is to spend more energy during contraction and store enough elastic energy in its structure to passively relax. The level to which this is advantageous in an artificial design will be the source of future investigation.

Power consumption is an important criterion for this type of vehicle. The current design can last for over three hours of continuous swimming. The power consumption analysis revealed the high losses of energy in the mechanical system. Removing the need for actuators during relaxation could help reduce the losses associated with the actuators. The COT was found to be approximately one order of magnitude larger than the natural jellyfish. Several strategies will have to be employed in order to decrease the COT for missions lasting on the order of weeks and months. The robot will need to be more biomimetic by reducing power consumption and adding the ability to harvest energy. As pointed out in the introduction section, the jellyfish are able to swim with a very low metabolic rate. Therefore, more attention needs to be paid towards replicating the bell kinematics at a low energy cost. Energy harvesting from the ocean environment will be required to replenish the energy supply of Cyro for extended mission time and range. Some energy harvesting strategies have already been investigated for this vehicle (Joshi et al. 2011).

Cyro has shown the ability to achieve a basic level of autonomy. This platform can be expanded to accommodate more autonomous capabilities. Sensory feedback coupled with adaptive control and the ability to turn will allow the vehicle to achieve more complex objectives. The

understanding of turning mechanism is currently an ongoing research with both natural and robotic jellyfish.

6.6 References

Bajcar, T., Malacic, V., Malej, A. and Sirok, B. (2009). Kinematic properties of jellyfish Aurelia sp.. *Hydrobiologia* 616, 279-289

Dabiri, J. P., Colin S. P. and Costello J.H. (2005). Flow patterns generated by oblate medusan jellyfish: field measurements and laboratory analyses *J. Exp. Biol.* 208, 1257–1265

Colin, S. P. and Costello, J. H. (2002). Morphology, swimming performance and propulsive mode of six co-occurring hydromedusae. *J. Exp. Biol.* 205, 427–437

Costello, J. H. and Colin, S. P. (1994). Morphology, fluid motion and predation by the scyphomedusa Aurelia aurita. *Mar. Biol.* 121, 327–334

Costello, J.H. and Colin S. P. (1995). Flow and feeding by swimming scyphomedusae. *Marine Biol.* 124, 399-406

Dabiri, J. O., Colin, S.P., Ktija, K. and Costello, J. H. (2010). A wake-based correlate of swimming performance and foraging behavior in seven co-occurring jellyfish species. *J. Exp. Biol.* 213, 1217-1225

Daniel, T. L. (1985). Cost of locomotion: unsteady medusan swimming. *J. Exp. Biol.* 119, 149–164

Dawson, M. N. (2005). Cyanea capillata is not a cosmopolitan jellyfish: morphological and molecular evidence for C. annaskala and C. rosea (Scyphozoa: Swmaeostomeae: Cyaneidae) in south-eastern Australia. *Invert. Systemat.* 19, 361-370

Gladfelter, W. G. (1973). Structure and function of the locomotory system of the Scyphomedusa Cyanea capillata. *Mar. Biol.* 14, 150–160

Guo, S., Fukuda, T. and Asaka, K. (2003). A new type of fish-like underwater microrobot *IEEE/ASME Trans Mechatronics* 136–141

Kramp, P. L. (1961). Synopsis of the Medusae of the World Journal of the Marine Biological Association of the United Kingdom, 40, 469

Joshi K., Costello, J. H. and Priya, S. (2011). Estimation of Solar Energy Harvested for Autonomous Jellyfish Vehicles (AJVs). *IEEE J. Ocean. Eng*. 36, 4

Larson, R. J. (1987). Costs of transport for the scyphomedusa Stomolophus meleagris L. Agassiz. *Can. J. of Zool.* 65, 11, 2690-2695

Lowndes, A. G. (1942). Percentage of Water in Jelly-Fish. *Nature*, 150, 234–235.

Marut, K., Stewart, C., Villanueva, A., Avirovic, D. and Priya, S. (2012). A biomimetic Jellyfish-inspired Jet Propulsion System Using an Iris Mechanism. *AMSE Conference Proceeding SMASIS* 5134

Mayor, A. G. (1910). Medusae of the world. III. The Scyphomedusae. Publication of the Carnegie Institute of Washington, Washington DC

Najem, J., Sarles, S. A., Akle, B. and Leo, D. J. (2012). Biomimetic jellyfish-inspired underwater vehicle actuated by ionic polymer metal composite actuators. *Smart Mater. Struct.* 21

Nawroth, J., Lee, H., Feinberg, A., Ripplinger, C., McCain, M., Grosberg, A., Dabiri, J. and Parker, K. (2012). A tissue-engineered jellyfish with biomimetic propulsion. *Nature Biotechnology* 30, 792-797

Russell, F. S. (1970). The medusae of the British Isles. II. Pelagic Scyphozoa. Cambridge University Press, Cambridge, UK

Sahin, M., Mohseni, K. and Colin, S. P. (2009). The numerical comparison of flow patterns and propulsive performances for the hydromedusae *Sarsia tubulosa* and *Aequorea Victoria. J. Exp. Biol.* 212, 2656-2667

Stokesbury, M., Cosgrove, R., Boustany, A., Browne, D., Teo, S., O'Dor, R. K., Block, B. A. (2007). Results of satellite tagging of Atlantic bluefin tuna, Thunnus thynnus, off the coast of Ireland. *Hydrobiologia* 582, 91–97

Tyack, P. L., Johnson, M., Soto, N. A., Sturlese, A., Madsen, P. T. (2006). Extreme diving of beaked whales. *J. Exp. Biol.* 209, 4238-4253

Videler, J. J. and Hess, F. (1984). Fast continuous swimming of two pelagic predators, saithe (*Pollachius virens*) and mackerel (*Scomber scombrus*): a kinematic analysis. *J. Exp. Biol.* 109, 209-22

Villanueva, A., Bresser, S., Chung, S., Tadesse, Y. and Priya, S. (2009). Jellyfish inspired underwater unmanned vehicle. *Electroactive Polymer Actuators and Devices (EAPAD), SPIE*, 7287

Villanueva, A. and Priya, S. (2010). BISMAC control using SMA resistance feedback. *Proc. SPIE* 7642 76421Z

Villanueva, A., Smith, C. and Priya, S. (2011). A biomimetic robotic jellyfish (Robojelly) actuated by shape memory alloy composite actuators. *Bioinspi. Biomim.* 6, 3

Webb, P. W. (1993). The effect of solid and porous channel walls on steady swimming of steelhead trout Oncorhynchus mykiss. *J.Exp. Biol.* 178(1), 97-108.

Wilson, M. M. and Eldredge, J. D. (2011). Performance improvement through passive mechanics in jellyfish-inspired swimming. *Int. J. Non-Linear Mech.* 40(4), 557–567

Yang, Y., Ye, X. and Guo, S. (2007). A New Type of Jellyfish-Like Microrobot *Proceeding of the 2007 IEEE Intl. Conference on Integration Technology*

Yeom, S., Oh, K. (2009). A biomimetic jellyfish robot based on ionic polymer metal composite actuators. *Smart Mater. Struct.* 18, 8

Chapter 7

Flexible Margin

7.1 Effects of a flexible margin on a jellyfish inspired robotic vehicle

7.1.1 Introduction

Underwater vehicles have a crucial need of long period operation. Underwater mission require long range coverage at remote locations. Current technology either consists of stationary platform or time limited vehicles. Stationary platforms offer a limited range of coverage and therefore limited applications. Unmanned underwater vehicles offer wider range of applications but are still limited by important factors. Short operation life ranging between a few hours to a day limits the vehicle range. This also means a costly service vehicle with crew must be readily available to transport UUV at the location of interest. A self-sustainable vehicle is therefore highly desirable. Vehicle self-sustainability consists of autonomous control, robustness and also energy independence. Autonomous control allows the vehicle to achieve mission without input from an operator. Robustness prevents the vehicle from degrading for long periods of time in different environments. Energy independence is achieved from two different angles: energy harvesting and vehicle efficiency. Several energy sources can be harvested in oceans waters such as wave energy, solar energy, and chemical energy from nutrients. Given these sources, the amount of energy harvested is still limited due to harvester technology and a decrease in harvestable energy with increasing depth. Vehicle efficiency is therefore very important to reduce the amount of energy needed to power the vehicle. Several factors come into play including, mechanical, electrical and hydrodynamic. Electronic systems have had significant improvements over the years and are relatively efficient. In a biomimetic vehicle, mechanical

efficiency includes the actuation system and the structural system. Both of these can have significant losses which include actuation efficiency, mechanical friction and structural resistance and are generally a consequence of high vehicle flexibility and deformation for propulsion. Lastly, the hydrodynamic efficiency is also very important for a UUV. The ability to create useful hydrodynamic forces for little energy is critical. Overall, biological systems have been able to answer these problems better than any engineered system. We therefore look at biology for answers to solve these problems.

Advancements in actuator technology have made the mimicry of animals more feasible. Animal dynamics and kinematics can be studied by replicating their morphology and mechanics by creating an artificial surrogate. This allows the variation of parameters which would not be possible on animals without disrupting their physiological functions. In this study, medusa also known as jellyfish, are studied. These animals have relatively simple mechanics allowing the more easily isolating and studying of different parameters. A robotic jellyfish named Robojelly was developed to mimic the morphology and propulsion mechanism of the *Aurelia aurita* jellyfish species. The vehicle dynamics have been characterized and it has shown the ability to propel itself.

Jellyfish can be separated into two categories based on their mode of propulsion, namely jetting and rowing. Jetting is found on smaller species of prolate medusa generally not exceeding a few centimeters in diameter. This method of propulsion is known for a higher proficiency or higher velocities and accelerations. Rowing is found on larger jellyfish which are also more oblate in geometry. This is a more efficient mode of propulsion (Dabiri et al., 2005). Aurelia aurita fall in the category of rowers. There swimming mechanism is achieved by muscles located in their subumbrella contracting the bell. The relaxation phase is done passively by elastic energy stored

in the bell. The flexible body of this jellyfish undergoes interesting kinematics during swimming. Some of the observations made from this animal and robotic counterpart raised questions which are also applicable to a variety of fish and birds using oscillating and undulating based propulsion.

7.1.2. Methods and Materials

7.1.2.1 Flap

When designing Robojelly, the morphology of an *Aurelia aurita* was first replicated by digitizing the relaxed geometry of the natural animal. The bell kinematics were then analyzed in order to determine where to position the actuators. It was noticed that the bell margin did not follow the same deformation pattern as the rest of the bell. Figure 1 shows the jellyfish in the relaxed, contracting and fully contracted states. These images of *Aureila aurita* were taken during a flow characterization test using dye. This test was conducted in ocean waters the dye is seen as bright green in the images.

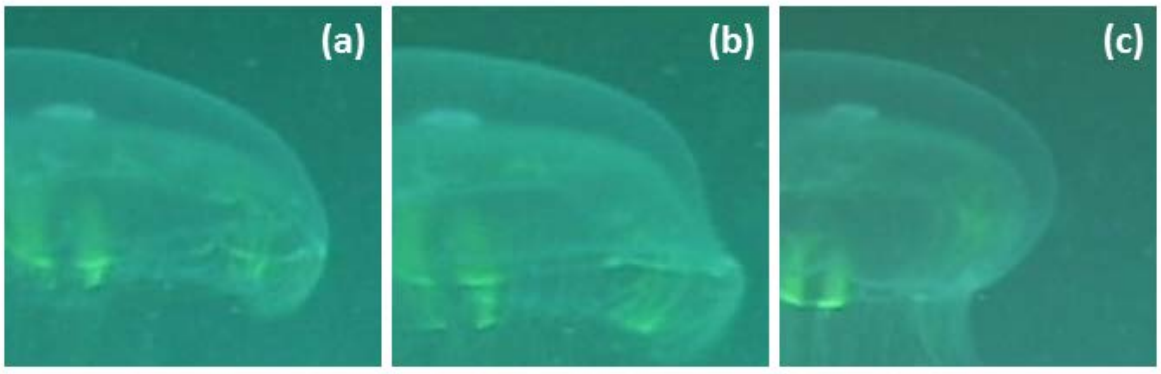

Figure 7.1.1: *Aurelia aurita* half bell profile in the (a) relaxed, (b) Contracting and (c) contracted position.

Figure 7.1.1(b) shows the flaring occurring at the bell margin. To better demonstrate this phenomenon, the exumbrella of the different configurations were digitized and are shown in Fig. 7.1.2(a). The pixel locations of the exumbrella was converted to polar coordinates and filtered using second order lowpass filter. The first derivative of the profiles was taken using central difference.

7.1.2.2 BISMAC

Before looking at the flap's role on hydrodynamics, it is required to replicate the proper kinematics. The observations made from the bell kinematics lead to the hypothesis that it can be recreated using a passive flexible margin. This means that no actuators would be required in the section between the flexion point and the bell margin. A BISMAC actuator capable of high curvature was used to test this hypothesis. The BISMAC actuator used was optimized to recreate the same deformation as the *Aurelia aurita*. Further description on BISMAC actuator design and characterization can be found in Villanueva et al. (2010(b); 2011).

Three flap designs were tested as shown in Fig. 7.1.2. The first flap configuration tested is a rectangular cross section with length of 3 cm as shown in Fig. 7.1.2 (a). The second flap configuration has a tapered cross section and length of 3 cm as shown in Fig. 7.1.2 (b). The taper gives a varying stiffness through the span of the flap. The third configuration has a taper and curvature which is more representative of the natural *Aurelia aurita* flap and measures 4 cm extended.

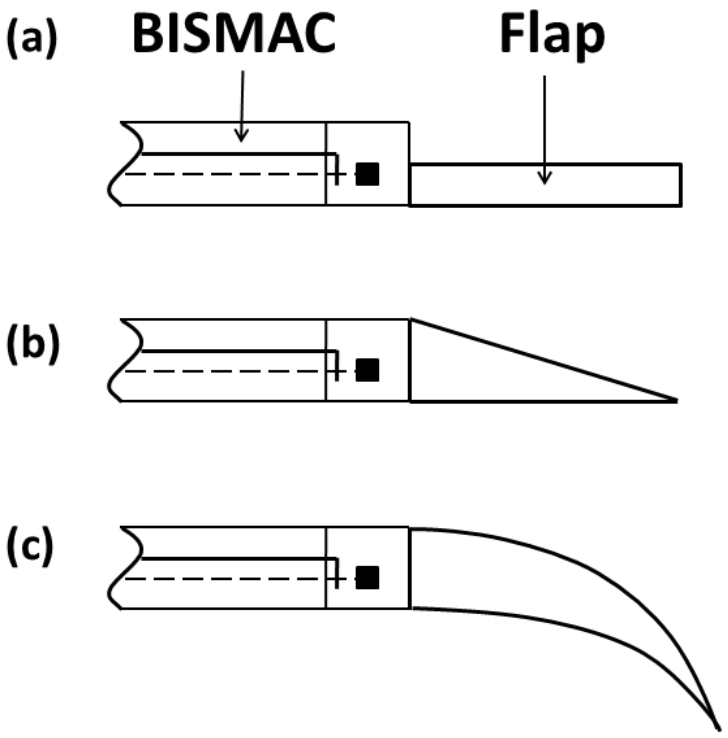

Figure 7.1.2: Cross section of BISMAC actuators with flaps of (a) rectangular, (b) tapered and (c) curved and tapered cross section.

The BISMAC actuators with flap were tested in water clamped at the base. Reflective points distributed evenly along the actuator and flap were later tracked using image processing in Matlab. The BISMAC were all actuated under the same conditions. Further information on the experimental procedure can be found in Villanueva et al. (2010a).

7.1.2.3 Robojelly

When designing the Robojelly, the flap was left out of the active section which contains BISMAC actuators. A thorough description of the Robojelly design can be found in Villanueva et al. (2011). The flap was added to the design on a separate step allowing the analysis of both configurations individually. Figure 3 shows the two Robojelly configurations. It should be noted that the bell is segmented as opposed to the uniform bell found in Aurelia aurita. The segmentation was made to alleviate a folding effect occurring in the artificial uniform bell. The flap added to Robojelly in Fig. 7.1.3(b) is designed to replicate the natural flap.

Figure 7.1.3: Robojelly with (a) no flap and (b) flap.

Both robot configurations were tested for their swimming performance. The vehicles were put in a water tank with static water and were allowed to swim upwards. The robots were actuated both using 0.65 A and 14 V. The vehicles were initially in a state of sinking to show that any thrust produced was from the propulsion mechanism and not positive buoyance. The vehicle is very sensitive to buoyancy which discards the typical proficiency analysis techniques utilized for

natural jellyfish. A thrust analysis was therefore used in order to compare performance. The thrust method used consists of measuring position over time to quantify vehicle momentum and the buoyancy state. The hydrodynamic forces are approximated using a jetting model and empirical models for drag and added mass. This method is further explained elsewhere (Bachelor, 1967; Daniel, 1983; Villanueva et al., 2011). The accuracy of thrust magnitude predicted by this method has not yet been validated for a rowing jellyfish mechanism but it offers a good method of comparison between the different vehicle designs since it accounts for the major forces on the vehicle.

7.1.2.4 Vortex

The Robojelly performance results show the importance of a flap in rowing jellyfish propulsion. An initial attempt was made at understanding the flap's role on the hydrodynamic structure produced by jellyfish during swimming. A flap of constant cross section with lengths of 33, 66, 100, 133, and 200% of the natural flap length was analyzed on the Robojelly. This was also compared to a "No flap" and "Bio flap" configuration which as previously described. This flap has the same length as the *A. aurita*'s flap and the 100 % constant cross section flap but is tapered and curved. The robot was tested with the Bio flap first, it was then removed and the 200 % flap was put on. The robot was then tested for each flap length by cutting out section of the flap to proper lengths until no flap was left.

The Robojelly wake was analyzed using a Time Resolved Digital Particle Image Velocimetry (TRDPIV) system. The system consisted of a continuous laser forming a sheet on the Robojelly's side. A high speed camera recording 1028x1028 pix images at a rate of 400 FPS was set perpendicular to the laser sheet as shown in Fig. 7.1.4. The Robojelly was clamped at the

apex inside a 122 x 46 x 51 cm water tank. Near neutrally buoyant glass particles with average diameter of 10 μm were used as flow tracers. The robot was actuated for 19 cycles before a full cycle was recorded for analysis. Preliminary actuation was necessary for the shape memory alloy (SMA) actuators to reach a thermal steady state. The thermal state of the SMA actuators affects the robot's bell deformation (Villanueva et al., 2010a, Villanueva et al., 2011).

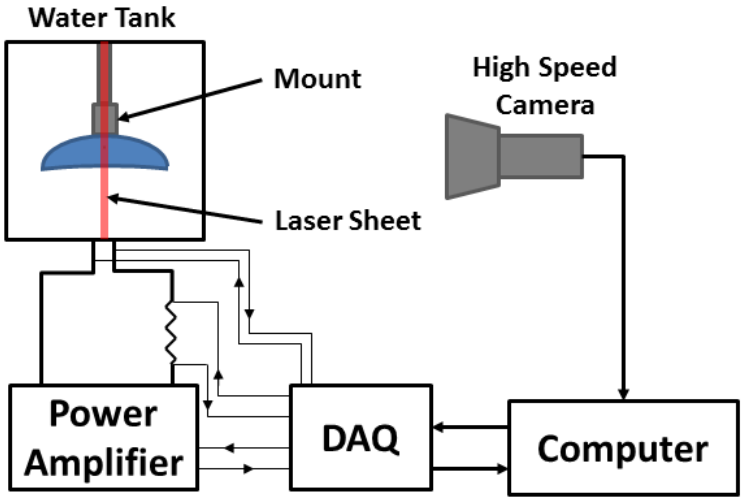

Figure 7.1.4: (a) Robojelly with 200 % flap setup on a mount in the water tank. The laser sheet is pointed at the bell. (b) PIV test setup schematic.

Cross correlation was done on the high speed images to obtain the corresponding velocity fields ($\mathbf{v}$). The data was processed using three passes of a Robust Phase Correlation (RPC) deformation method with window resolution of 32x32 vectors, widow size of 64x64 vectors and a grid resolution of 4x4 pix (Eckstein and Vlachos 2009, Scarano 2002, Eckstein and Vlachos 2009b, Eckstein et al. 2008). The mean error of this technique is estimated to range between 0.05-0.15 pix (Eckstein and Vlachos 2009a). A Proper Orthogonal Decomposition (POD) was used to post process the TRDPIV results to reduce the high frequency noise (Sirovich 1987, Doligalski et al. 1994). The fundamental eigenmodes containing 90 % of the total energy in the system were kept.

A vortex identification algorithm was used to identify the starting vortex through each frame. Vortex identification was done using a method described by Holden (2011) which consists of two different identification methods and comparing the results of both. The first method is based on Sperner's lemma which is adapted for vortex identification in Jiang et al. (2002). For this method, a first pass is done on the velocity field to label each velocity vectors in one of three equally spaced direction ranges. The second pass looks at the surrounding neighbors of every grid point and determines if all three direction labels are present. If so, the current point is identified as a vortex center.

After identifying possible vortex locations with Sperner labeling, the λ_{ci} method was used to calculate the swirling strength of each possible vortex (Zhou et al., 1999, Chakraborty et al., 2005). The swirling strength is taken as the imaginary eigenvalue of $\nabla\mathbf{v}$. This is based on the fact that local streamlines can be represented as a function of real and complex eigenvalues. See Zhou et al. (1999) for more details and a visual representation of this method. The maximum swirling strength over the velocity fields was determined. Any potential vortex center having a

swirling strength within 5% of this maximum was characterized as a vortex center. Vortex locations varying from the general path of the starting vortex were manually removed.

7.1.2.5 Circulation and Force

Once the vortex centers were identified, the vortex area A was determined using the regions which fell within the 5% swirling strength threshold. Circulation of the starting vortex was computed using the line integral of the velocity field $\mathbf{v}$, over the identified contour C delimiting the vortex area (Bachelor, 1967):

$$\Gamma = \oint_C \mathbf{v} \cdot d\mathbf{l}, \qquad (7.1.1)$$

where $d\mathbf{l}$ is the discrete contour length vector. Vortex circulation and area were filtered using a second order Butterworth low pass filter.

For scaling purposes, the bell margin was tracked as a function of time. Starting at rest, the margin position was digitized manually using ImageJ. The distance traveled between each point was then calculated. The digitized distances where then smoothed using a second order Butterworth low pass filter.

The force generated by a jellyfish during swimming can be estimated using its vorticity field of its wake and the added mass contribution from the vortices (Dabiri, 2005b). This is represented by the following equation (Shaffman, 1992):

$$\mathbf{F} = \rho \frac{\partial}{\partial t} \int \mathbf{x} \times \boldsymbol{\omega} dV_V + \rho \frac{\partial}{\partial t} \int \phi \mathbf{n} dS_V \,, \qquad (7.1.2)$$

where ρ is the fluid density, $\mathbf{x}$ is the vector position relative to a point of origin, $\boldsymbol{\omega}$ is vorticity, V_V and S_V are the vortex volume and surface respectively, and $\boldsymbol{\varphi}$ is the velocity potential. The first term of Eq. 7.1.2 takes into account the force created by the wake momentum. The second term is related to the added mass contribution of the wake vortex. The added mass term is neglected since the 3 dimensional vortex structure of the segmented Robojelly is not well known at this point. The momentum term should capture the majority of the force produced by the Robojelly and will serve as a good method for comparison between each flap configurations. The vortex momentum is approximated using the following (Drucker and Lauder 1999, Dabiri 2005):

$$\rho \frac{\partial}{\partial t} \int \mathbf{x} \times \boldsymbol{\omega} dV_V \approx \rho \frac{d}{dt} A\Gamma \,. \qquad (7.1.3)$$

This simplification assumes that the starting vortex is composed of thin rings. For the instantaneous force, Eq. 7.1.3 simplifies further to:

$$\begin{aligned} F &= \frac{\rho\left[A(t_{i+1})\Gamma(t_{i+1}) - A(t_i)\Gamma(t_i)\right]}{t_{i+1} - t_i}, \quad i = 1 \\ F &= \frac{\rho\left[A(t_{i+1})\Gamma(t_{i+1}) - A(t_{i-1})\Gamma(t_{i-1})\right]}{t_{i+1} - t_{i-1}}, \quad 1 < i < s \,, \\ F &= \frac{\rho\left[A(t_i)\Gamma(t_i) - A(t_{i-1})\Gamma(t_{i-1})\right]}{t_i - t_{i-1}}, \quad i = s \end{aligned} \qquad (7.1.4)$$

where s is the length of each circulation and area array.

7.1.3 Results

7.1.3.1 Aurelia aurita Kinematics

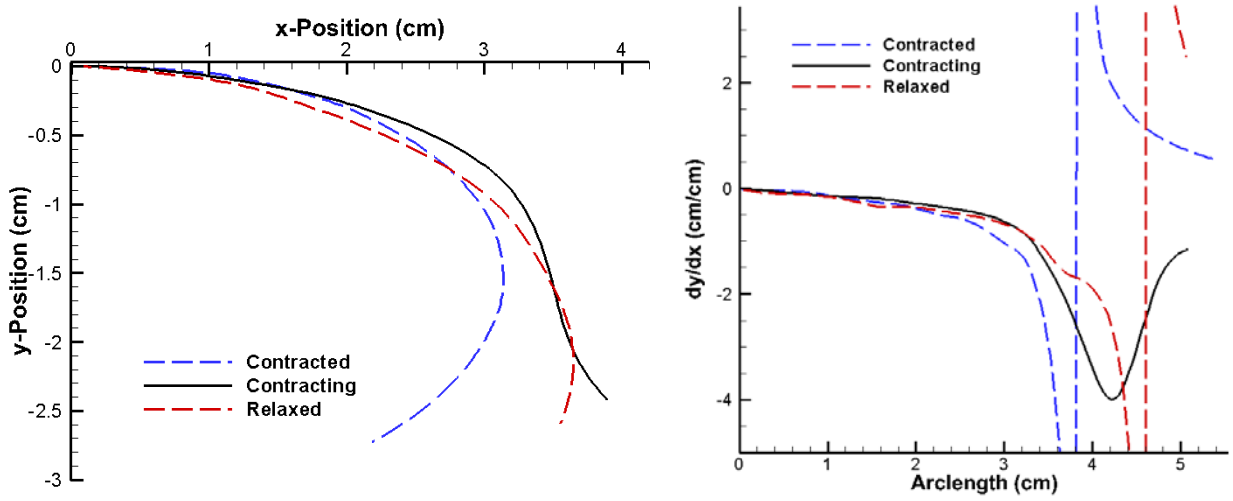

Figure 7.1.5: (a) Digitized *Aurelia aurita* exumbrella profile for different bell configurations and the (b) corresponding derivative as a function of arclength.

The digitized *A. aurita* profiles at three different stages in the actuation cycle is shown in Fig. 7.1.5(a). The profiles' first derivative shows if the bell is deforming in a convex or concave fashion based on the slop of the first derivative. For the relaxed and contracted cases, curvature is convex which translates to a negative slope in Fig. 7.1.5(b) throughout the exumbrella profile. For the contracting case, it can be seen that the slope becomes positive (concave curvature) towards the bell margin. This is referred to as the flexion point and is located at a distance of 4.2 cm along the arclength starting from the bell apex which is 83% of the total arclength of this specimen. The bell section located past this point is referred to as the flap or flexible margin. This is further depicted in Fig. 7.1.6(a) where the digitized exumbrella profile and flexion point location are superimposed on the respective *A. aurita* image. The Robojelly flexion point does not fall exactly at the actuator tip or flap start location as shown in Fig. 7.1.6(b). This is mainly due to an increase in local stiffness due to manufacturing requirements at the actuator end.

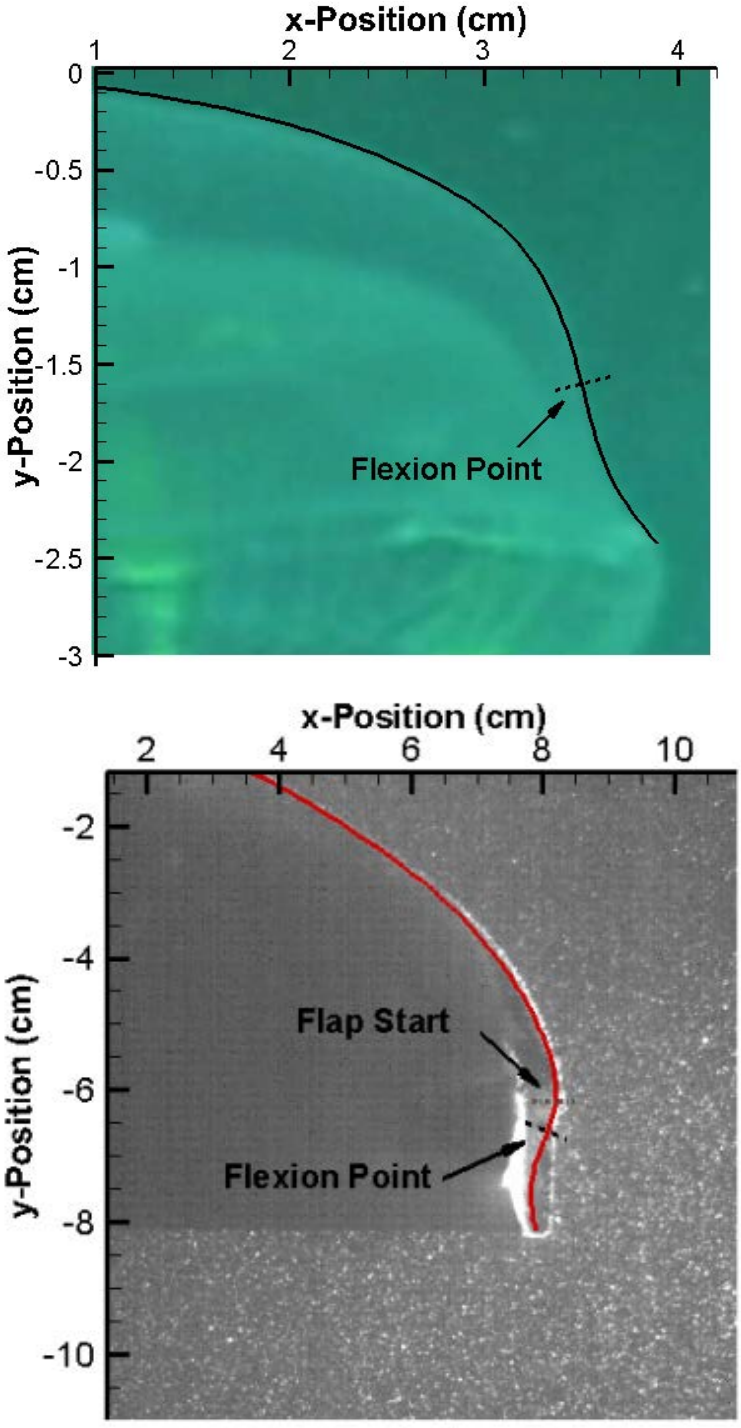

Figure 7.1.6: Superimposed exumbrellar profile with flexion point location for the contracting (a) *Aurelia aurita* and (b) Robojelly. The actual Robojelly flap start location which was based off the *Aurelia aurita* flexion point is also shown in (b).

The bell kinematics of an *Aurelia aurita* specimen, different than the one presented previously, during a full swimming cycle was analyzed. The exumbrella profiles were digitized from a video taken a 30 FPS and the data was zeroed and compensated for small rotations during the swim cycle. Further details on how this data was processed can be found in Villanueva et al. (2010b). The bell kinematics of the *A. aurita* for a full circle can be seen in Fig. 7.1.7.

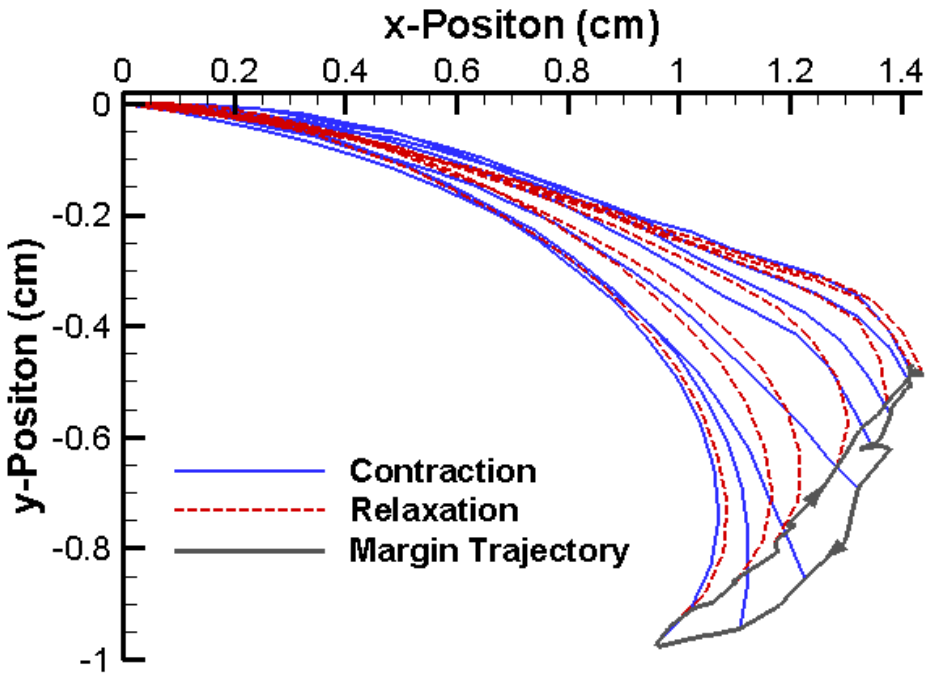

Figure 7.1.7: *Aurelia aurita* bell kinematics showing the half exumbrella profiles over a full swimming cycle. The plotted data was down sampled for clarity and the time between each profile is arbitrary. The margin trajectory is also shown with its direction.

The margin trajectory shows that the extended bell configuration during contraction leads to an outer path and the bent configuration during relaxation leads to an inner path. In Villanueva et al. (2010b), it was found that this outer and inner trajectory becomes opposite when moving on

point further up the bell. At the flexion point the contraction and relaxation paths are practically the same and further up they are inner during contraction and outer during relaxation. The flap has an extended profile during contraction and a bent profile during relaxations. An increase in surface area perpendicular to the direction of motion due to the extended flap will help create thrust while a smaller surface area during relaxation will help reduce drag.

7.1.3.2 BISMAC Kinematics

The actuator profiles at different times over a full cycle are plotted in Fig. 7.1.8 along with the margin path.

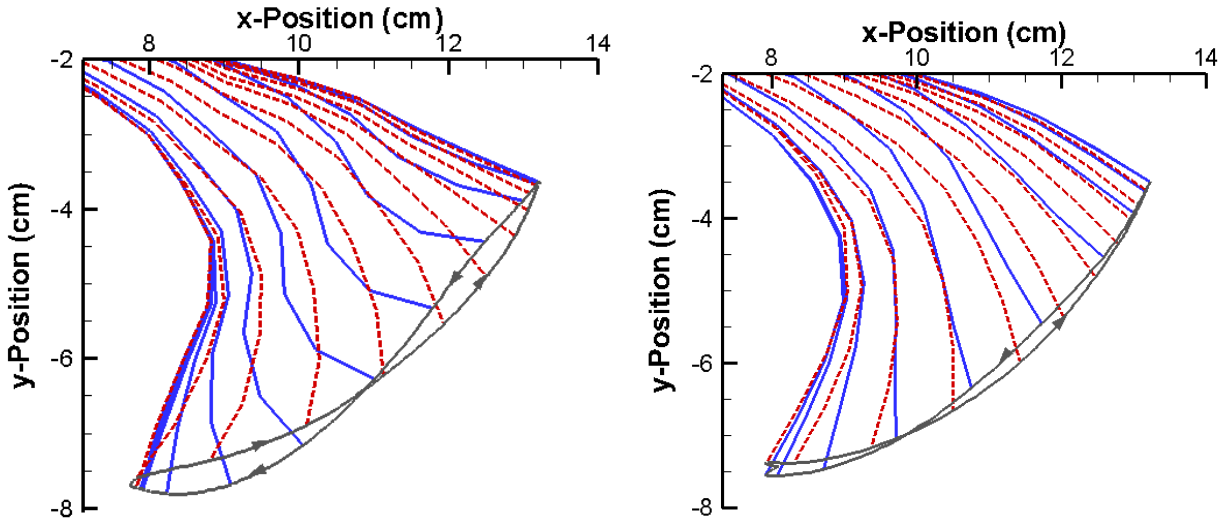

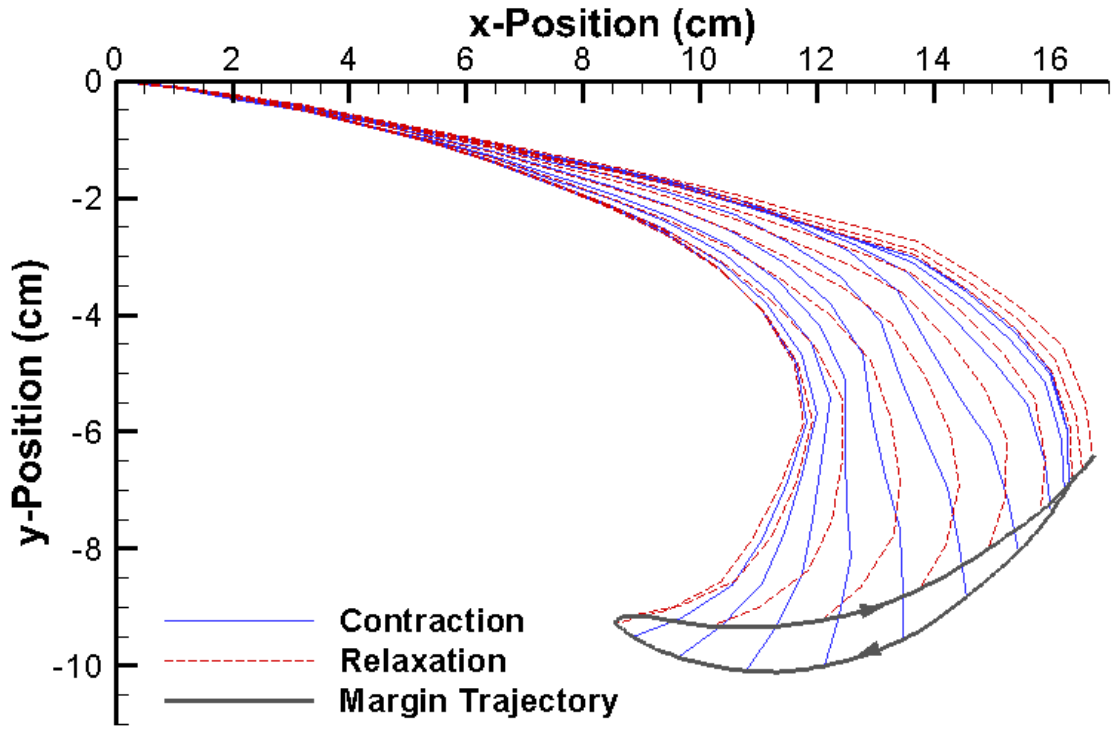

Figure 7.1.8: BISMAC actuator profile deformation with (a) constant, (b) tapered and (c) curved and tapered cross section. Margin trajectory with direction is also shown. Profiles where down sampled from 250 FPS in this figure for clarity.

The actuator and flap kinematics show different behavior for the different flap configurations. The rectangular cross section flap which was the least stiff configuration had a margin path resembling a Fig. 7.1.8. The beginning of the contraction starts with an inner path and transitions about half way into an outer path. The same is true for the relaxation phase. The flap exhibits large deflections during actuation which is beyond what is achieved by the *Aurelia aurita*. The deformation profile of the tapered flap (Fig. 7.1.8(b)) does not vary much during contraction and relaxation where the margin trajectory is almost the same. The increased stiffness prevented the flap to undergo enough curvature during relaxation. Adding a curvature to this profile caused the flap to already have a curvature during relaxation. During contraction, the

curved and tapered flap extended due to water resistance. The profile result of the curved and tapered flap is shown in Fig. 7.1.8(c). The margin path shows an outer path during contraction and an inner path during relaxation as achieved by the *Aurelia aurita*. The kinematics results of the BISMAC with flap show that it is indeed possible to replicate flap kinematic characteristics of the *Aurelia aurita* using a passive flexible margin.

In terms robotic design, limiting the amount of actuators reduces the complexity of the design dramatically and ultimately can lead to more efficient vehicles. If the flap deformation can be achieved with a passive material, less actuators need to be use and a simpler more efficient design can be achieved. The transition from active to passive would be where the muscles stop but this will not always be the case if ever. The *Aurelia aurita*'s subumbrella has muscles all the way to its margin. The extent at which they contribute during swimming is unknown. We hypothesis that the muscles in the flap help maintain a desirable stiffness depending on if the animal is contracting or relaxing. But judging from the BISMAC results, it can be hypothesized that the flap muscles do not actuate much if at all during uniform swimming. Their role could be justified during a turning maneuver where the bell needs to achieve an asymmetric configuration.

7.1.3.3 Robojelly

When testing both configurations, a significant improvement on thrust was observed with the addition of a flap as shown in Fig. 7.1.9. Thrust increased by 1340 % from the no flap to with flap configuration of the segmented bell Robojelly causing the vehicle to swim up.

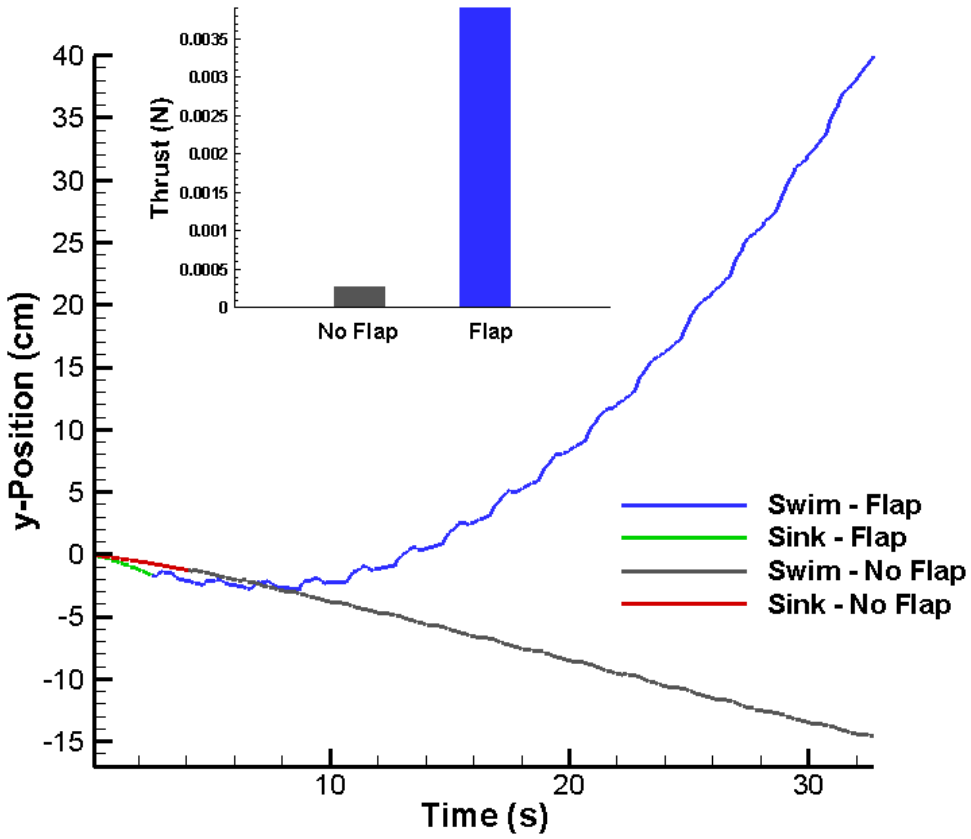

Figure 7.1.9: Y-position as a function of time for Robojelly with and without flap during vertical swimming. The initial sinking state of the robot is shown along with the robot swimming phase. Average thrust production over the full 14th actuation cycle is shown in the subplot.

7.1.3.4 Circulation and Force

Dimensional circulation as a function of time is show in Fig. 7.1.10 for the different flap configurations. The constant cross section flaps show a general increase in peak vortex strength as a function of flap length. The time it takes for the vortex to reach peak circulation also increased with flap length.

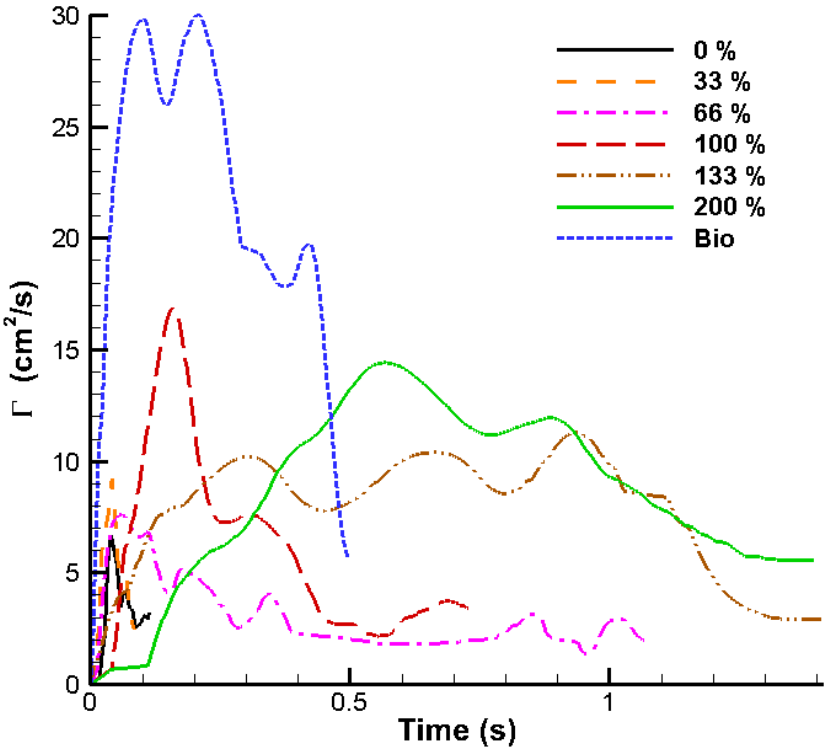

Figure 7.1.10: Robojelly circulation as a function of time for different flap configurations.

The bio flap had a much higher circulation then the other flaps though it was the same length as the bio flap. Figure 11 shows that the bio flap and 100% flap were actuated at different rates and covered different distances. This actuation difference between these two flap configurations is mainly related to the actuators. The flap margin displacement as a function of time for all flap configurations is shown in Fig. 7.1.11.

The longer peak time with increasing flap length in Fig. 7.1.11 can be attributed to the the flap structural dynamics. The longer the flap, the more bending it undergoes due to drag. As a result, a larger lag occurs at the margin relative to the flap start location. The Robojelly was actuated at

a constant power input for each configuration but the velocity at which the bell deformed varied due to the increased drag and inertia with flap length.

In order to analyze the role of flap length and geometry, the effects of the SMA actuators must be considered. The SMA actuators were set to a constant controlling scheme for all flap configurations. Despite the constant actuation scheme, the SMA actuators gave a different performance through testing as shown by the displacement and actuation rate of the 100% and bio flap. The force of the SMA actuators is limited which can lead to slower actuation time under higher loads. The SMA can also undergo performance degradation over high stress and overheating which is present in the Robojelly. The bio flap was tested first which means the actuators were in best condition. The constant cross section flap at 200% was then tested followed by the 133% and so on until the no flap configuration. The added mass to the bell from the flap may also cause it to not regain a fully relaxed position causing the actuation cycle to be smaller as flap length increase. This is not captured by Fig. 7.1.11 since the flap margin is passive and acts as an extension of actuator itself.

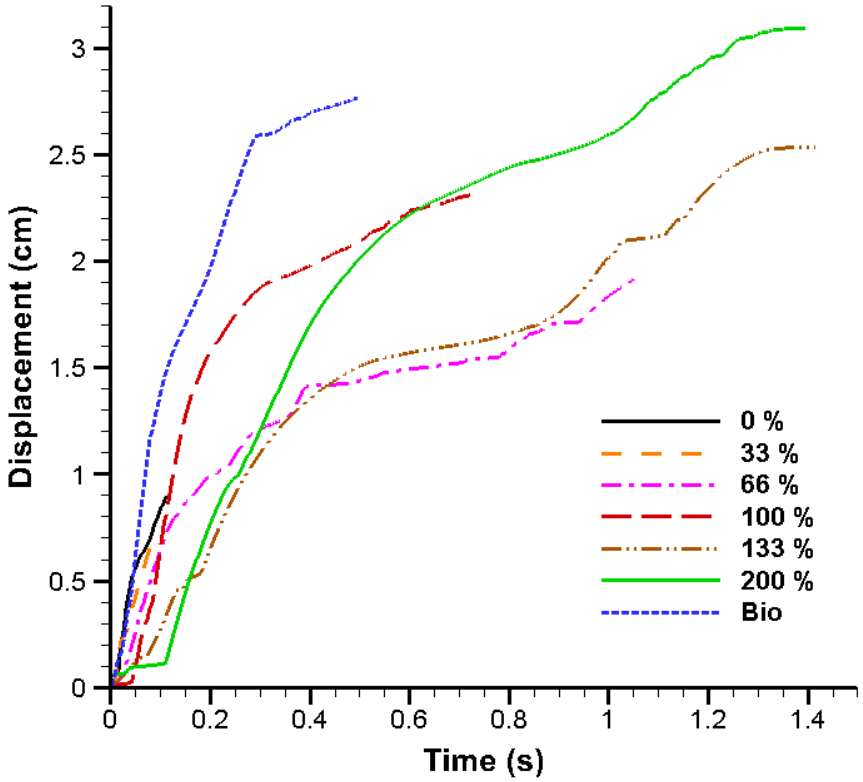

Figure 7.1.11: Bell margin displacement as a funciton of time during actuation for the different flap lenghts. Displacments are shown from the beginning of actuation till the end of positive displacement.

An interesting phenomenon is observed as flap length increases. As the actuator tip which is the beginning of the flap, begins actuation, the flap margin starts moving at a delay do to the flexibility of the structure. This is seen clearly for the 200% flap in Fig. 7.1.11.

To determine the underlying principles of flap length, circulation and time are made non-dimensional. The Robojelly flap is scaled using two different methods. The first method considered the Robojelly with flap as an axi-symmetric body which ejects water from a varying orifice during contraction. A good starting point for this method is the work done on varying

orifice pistons (Dabiri, 2005; Allen and Naitoh, 2005). In this work, circulation and time or scaled as a function of piston velocity and orifice diameter as a function of time. Robojelly has a varying diameter but not a moving piston. Water displacement on the Robojelly is due to actuation of the bell or walls which contract or reduce the diameter of the Robojelly. The non-dimensional equations in Dabiri and Gharib (2005) can be modified to take into account water displacement due to wall deformation:

$$\Gamma_n = \frac{\Gamma\left(\overline{U}/S_b\right)}{\overline{U^2}}, \qquad (7.1.5)$$

$$t_n = \left(\frac{\overline{U_{xy}}}{S_b}\right)t, \qquad (7.1.6)$$

where U is the magnitude of the flap tip velocity $\mathbf{U}$ and:

$$\overline{U} = \frac{1}{t}\int_0^t U(\tau)\,d\tau, \qquad (7.1.7)$$

is the time average velocity. S_b is the arclength of the exumbrella from the bell apex to the flap tip. The resulting non-dimensional circulation is shown in Fig. 7.1.12. The results show a poor collapse of the circulation peaks as is expected for similar systems (Dabiri and Gharib, 2005). This method proves to not be adequate to scale the circulation of the Robojelly starting vortex.

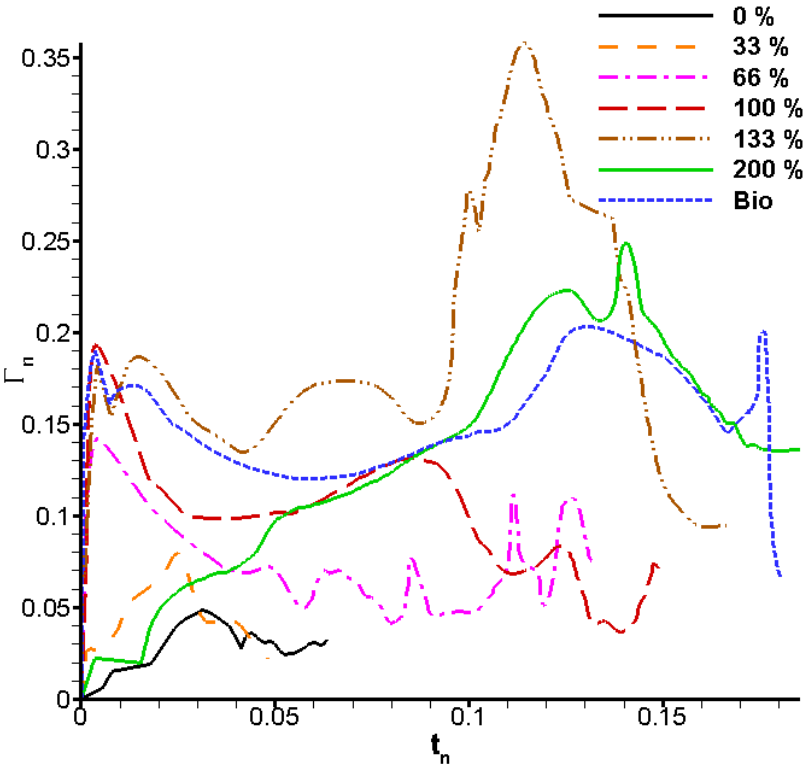

Figure 7.1.12: Non-dimensional circulation as a function of time scaled by orifice diameter bell margin trajectory and bell arclength form apex to bell margin.

The second method for scaling circulation analyzes the Robojelly as a set of pitching panels distributed circularly about the bell apex. The segmented bell can be approximated as a set of panels pitching about hinges. The bell deformation during contraction consists of a curvature which varies along the span of the bell. The hinge location of the pitching panel representation of Robojelly is approximated as the point where the highest rate of deformation as a function of arclength occurs. The hinge location was found to be at 1.5 cm exumbrella arclength above the flexion point. The length S_h is defined as the arclength between the hinge location and the flap margin. Work on rigid pitching panels serve as a good starting point for scaling of the flexible

Robojelly flap. Buchholz and Smits (2008) demonstrated the importance of the panel aspect ratio (AR) which is the chord over span of the panel, and the ratio A/S which is the panel maximum amplitude over span. Green and Smits (2008) have found that the coefficient of pressure C_p of a pitching panel was best scaled by:

$$C_{p,n} = C_p\left(1+\beta\frac{A}{S}\right), \qquad (7.1.8)$$

where β is an arbitrarily chosen constant to collapse the results. It was found that a value of $\beta = 7$ best collapse the coefficient of pressure and coefficient of thrust. Buchholz et al. (2011) expanded this method to the scaling of circulation for pitching panels:

$$\Gamma_{GS,n} = \frac{\Gamma}{fA^2}\left(1+\beta\frac{A}{S}\right), \qquad (7.1.9)$$

where f is the frequency of actuation. This scaling method therefore takes into account the geometry and kinematics of the pitching panel. This method can be adapted to the Robojelly as follows:

$$\Gamma_n = \frac{\Gamma}{d_{\max}^2/T}\left(1+\beta\frac{d_{\max}}{S_h}\right), \qquad (7.1.10)$$

$$t_n = \frac{t}{T}\left(1+\beta\frac{d_{\max}}{S_h}\right), \qquad (7.1.11)$$

where d_{max} is the maximum distance traveled by the flap margin during contraction before its starts moving backwards. T is the time taken from the beginning of actuation to reach d_{max}. The non-dimensional circulation and time for the different flap configurations is shown in Fig. 7.1.13 for $\beta = 15$.

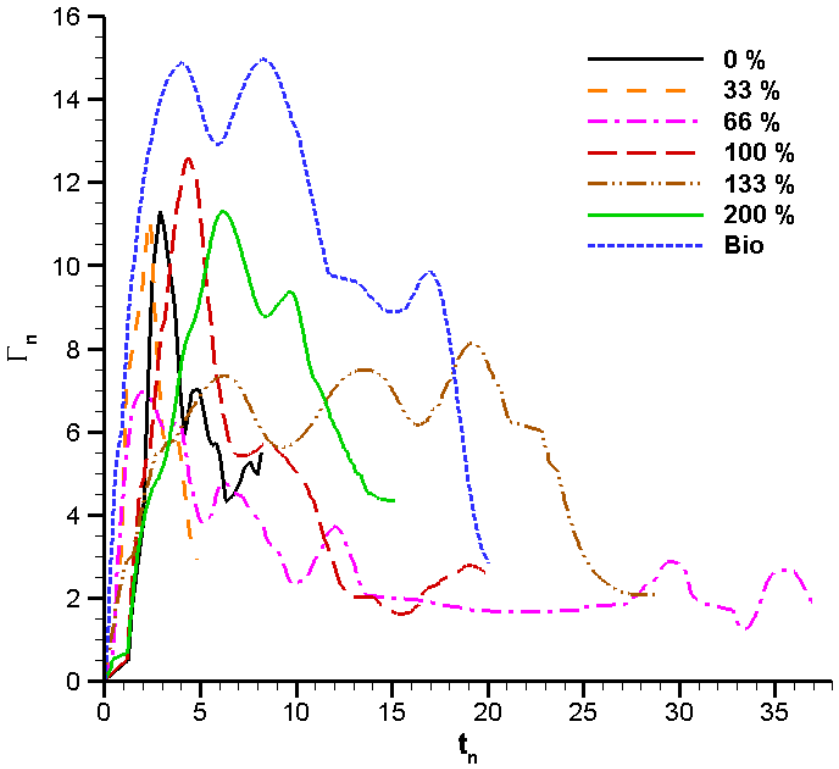

Figure 7.1.13: Non-dimensional circulation as a function of non-dimensional time for different flap configurations.

β was chosen based on the normalized standard deviation value of the first peak of the non-dimensional circulation:

$$\bar{\sigma}_\Gamma = \frac{\sigma_\Gamma}{\bar{\bar{\Gamma}}_n}. \qquad (7.1.12)$$

The normalized standard deviation converged to 0.2298 as shown in Fig. 7.1.14. At β = 15, $\bar{\sigma}_\Gamma = 0.23$ as shown in Fig. 7.1.15 and has a convergence of 0.04%. These values are calculated for the constant cross section flaps of different lengths. The bio flap is excluded from the results in Figs. 14 and 15 since it has a different geometry.

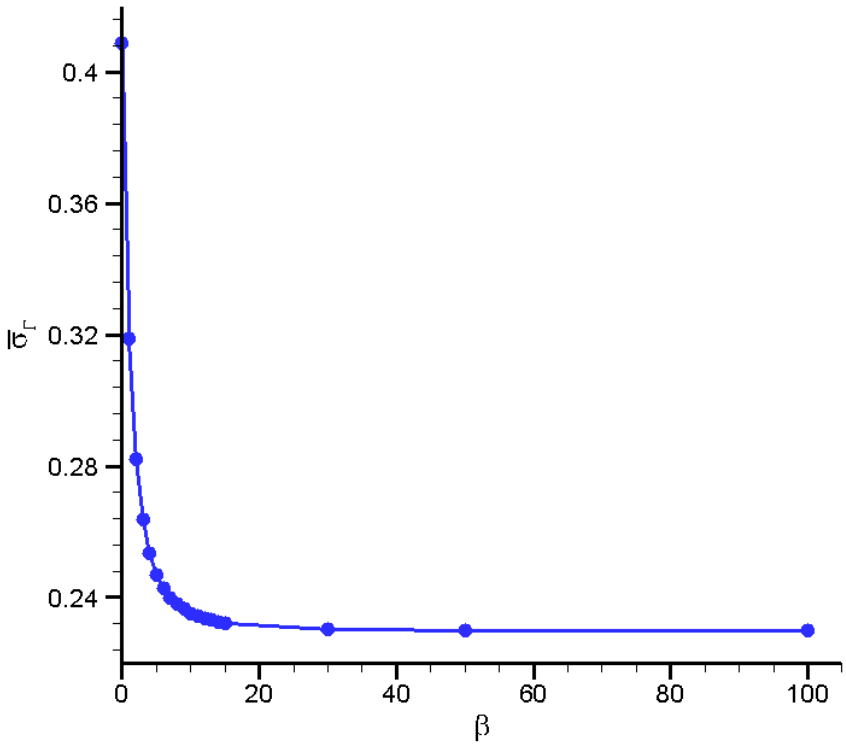

Figure 7.1.14: Normalized standard deviation of non-dimensional circulation at first peak as a function of β.

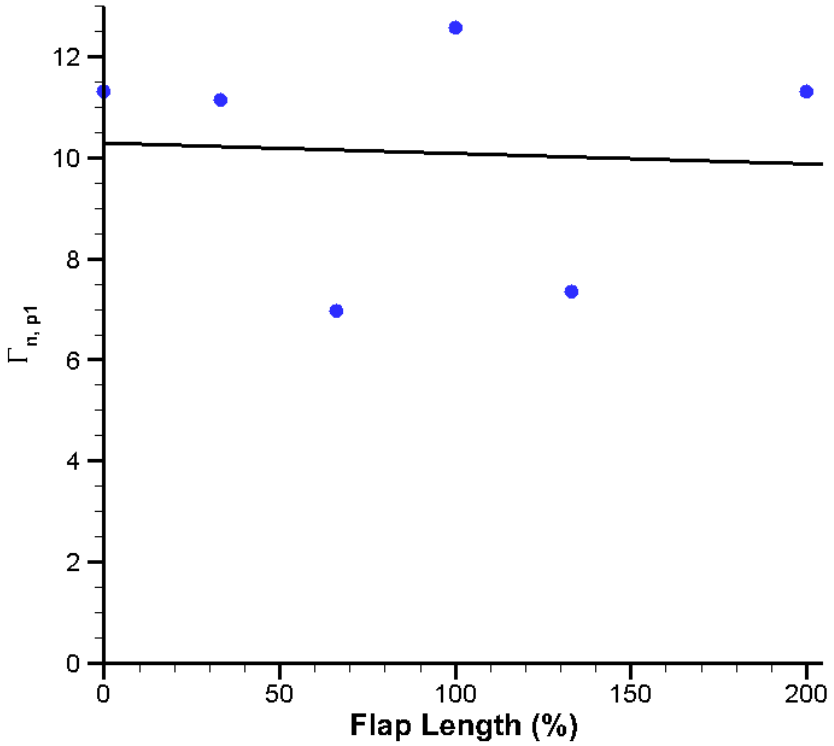

Figure 7.1.15: Circulation of the first peak as a function of flap length for β = 15. This does not include the bio flap. The normalize standard deviation is 0.23.

The non-dimensional circulation results show a good collapse with β = 15. The rigid pitching panels collapse better with a normalized standard deviation of 0.15 and 0.04 for beta = 7 and 2 respectively. The higher standard deviation of the flaps could be due to the fact that they are flexible. Flexibility causes the panel base and tip to move at a different phase. Also, flexibility allows the flap to deform and assume different curvature profiles. A better understanding of the effects of curvature and varying curvature as a function of time is therefore necessary to better scale circulation. In addition, an understanding of the flap compliance for a given stiffness is necessary to know its instantaneous geometry over time. The 66% and 133% flap act as outliers

from the rest of the non-dimensional circulation results. It is possible that the poor flow resolution during these particular flap tests disrupted vortex identification and resulted in lower circulation amplitudes to be detected.

The bio flap has a curve and taper which creates a different deformation profile upon actuation. The non-dimensional circulation results of Fig. 7.1.13 show that the bio flap follows a slightly different scaling then the constant cross section flaps.

The vortex area was computed to approximate the force generated by Robojelly. Figure 16 shows a high speed PIV image of the bio flap used for processing. The starting vortex tracked during contraction is dipicted by blue circles. The circle diameter is representative of the vortex area relative to one another. These results show that the vortex path is diagonal or down and towards the central axis. The starting vortex formed by the *Aureila aurita* are usually oriented downward in a vertical direction and move slowly outwards (Dabiri et al., 2005). For the bio flap, high vortex area with low circulation occurs at the very beginning of the contraction phase. The high initial area could be due to artifacts from light reflection of the flap. The vortex area then starts small and grows over time up to 0.24 s. A decrease is then observe followed by a peak again at 0.44 s which leads to vortex dissipation. The ocasional dissipation seen as large oscillation in the area and circlation results could be due to surrounding flow structures momentarly disturbing the starting vortex preventing the tracking algorithm from fully resolving the vortex area.

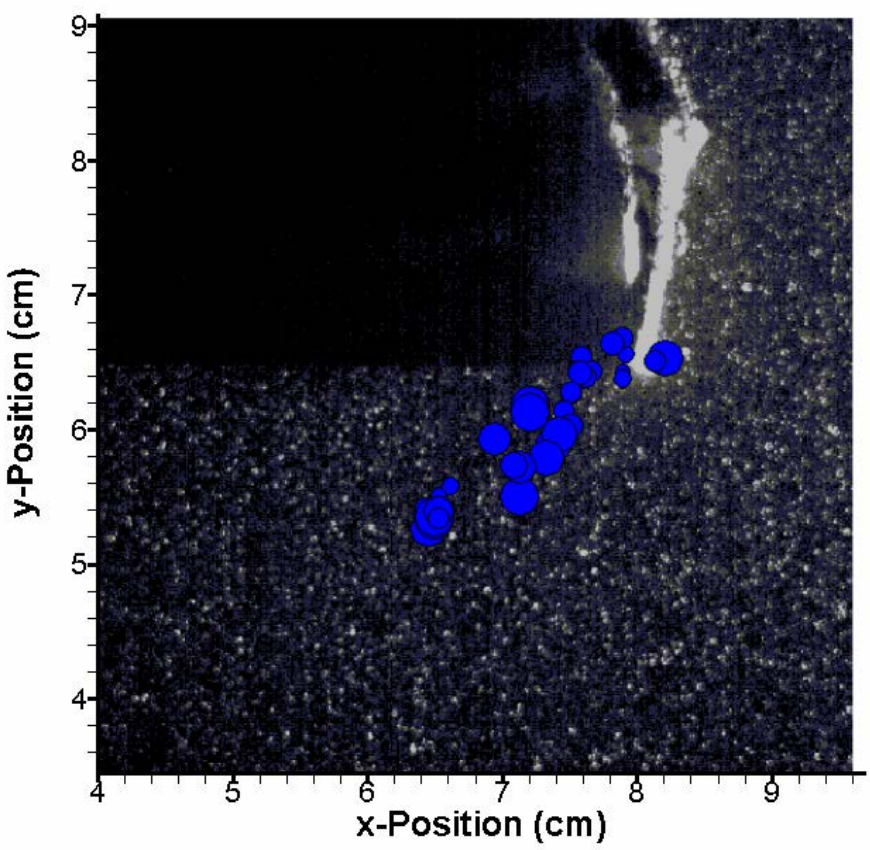

Figure 7.1.16: Image for PIV of Robojelly with bio flap configuration. Vortex position over a full contraction is shown by blue circles where the area is proportional to the vortex area but does not represent the actual area size.

The force generated by Robojelly was approximated based on the momentum of its wake. This was calculated using Eq. 7.1.4 which uses the starting vortex momentum to approximat force. The dimesional results are shown in Fig. 7.1.17.

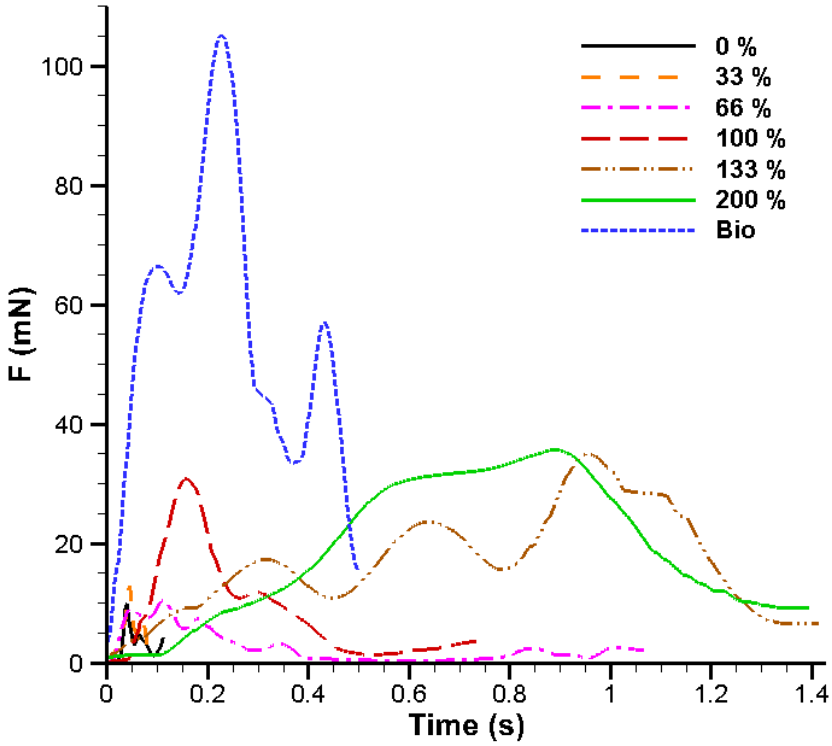

Figure 7.1.17: Dimensional force as approximated from the circulation of the Robojelly wake as a function of time for the different flap configurations.

The dimensional force results show an increase force with flap length. Also, the time at which peak force occurs increases with flap length. The bio flap has a drastically different force profile which means the actuator kinematics likely plays a large role in the force generated. A similar scalling strategy as for circulation is used for force in order to account for actuator kinematics and flap length. The instantaneous force is made non-dimensional using:

$$F_n = \frac{F T^2}{m d_{\max}} \left(1 + \beta \frac{d_{\max}}{S} \right), \qquad (7.1.13)$$

where *m* is the Robojelly mass without flap. The results are shown in Fig. 7.1.18.

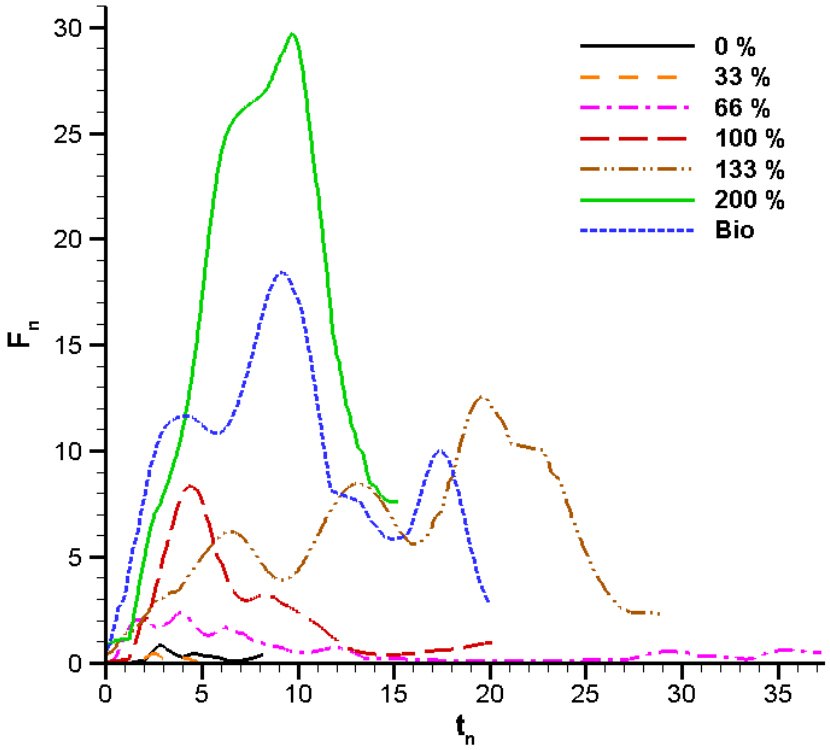

Figure 7.1.18: Non-dimensional force as a function of non-dimensional time for the different flap configurations.

The non-dimensional force results show a poor collapse of the peak force magnitude as well as the time of peaking. This shows that the flap kinematics and geometry are not the only parameters dictating the force created by Robojelly and that the force approximation does not scale using the kinematic and geometry relations in Eq. 7.1.13. Perhaps a better parameter to scale force would be flap stiffeness and flap instantaneous geometry. The way curvature affects vortex formation and force will have to be characterized in order to properly collapse the Robojelly force results.

7.1.4 Discussion

Flaps are observed in many animals which use an oscillating or undulating propulsion mechanism. Jellyfish and the Robojelly revealed the importance of flaps for such propulsion mechanism. The Robojelly was found to have a thrust increase of 1340 % when adding a flap. The flap was defined as the bell region bounded by the flexion point and bell margin. The flexion point is the location where the structure undergoes a different compliance and therefore where the slope of the exumbrella changes direction during the actuation phase. This should correspond to a different structural composition where actuators end. The *Aurelia aurita* flap length is 17% of the exumbrella arclength. Using a BIMSAC actuator, it was found that the flap kinematics could be replicated closely using a passive flap with a curved and tapered geometry.

Further work will have to be conducted on other animals to determine if the flexion point correlates to the structural composition change and muscle location. In terms of kinematics, it was observed that the flap has a few important parameters. During contraction, the flap begins with a convex geometry or bent inwards, changes into a concave geometry and regains a convex shape at the end of contraction. During relaxation, the initial curved convex geometry is increased. As a result to the geometry change, the margin trajectory during contraction follows an outer path and an inner path during relaxation.

The ability to change flap kinematics by varying the stiffness using different geometries was shown. Material composition could also be used to change the flap stiffness and match a desired kinematics profile. The passive flap deforms at a different phase then the rest of the active bell. The flap kinematics results show that this can be achieved with a simple passive structure and

alleviate the need for a separate set of actuators. The fact that the flap can be recreated artificially by a passive structures raises the following question: “Do *Aurelia aurita* actuate their flap during swimming?” It is known that muscles are located inside the flap but the extent at which they actuate during bell contraction is unknown (Chapman, 1998). Further research in the animal’s histology will have to be conducted in order to answer this question.

The margin trajectory of the BISMAC with tapered and curved flap show strong resemblances with the *A. aurita*’s margin trajectory. Differences between the two can still be observed such as the *A. aurita* margin path which is more diagonal as opposed to the horizontal trajectory of the BISMAC and Robojelly’s curved and tapered flaps (Villanueva et al., 2010b).

An important aspect to consider for replicating the flap kinematics of the *A. aurita* is its axisymmetry. The axisymmetry of the natural flap causes additional structural integrity which affects the kinematics during contraction and relaxation as opposed to the discrete flap of the BISMAC and Robojelly. Also, the flow escaping from the sides of the finite BISMAC is trapped by the uniform bell of the *A. aurita* and will cause additional resistance to the structure and therefore additional deformation of the flap. The BISMAC flap kinematics have shown that for a given actuation scheme, the flap kinematics can be optimized by changing the flap stiffness profile. This can be achieved by modifying the geometry and material composition. Flap kinematics will change with the velocity at which they are actuated which will therefore affect the hydrodynamic structures. The actuator dynamics must therefore be taken into account when designing a flap. This was shown by better collapse of the non-dimensional circulation which took into account actuator kinematics and flap geometry.

The force transferred to the fluid during contraction was analyzed based on starting vortex momentum. This method showed an increase in dimensional force with flap length. These results along with the Robojelly swim test show the importance of a passive structure on a bio-inspired propulsor. Force approximation based on starting vortex momentum is a good metric for comparison between the different flap configurations but does not fully describe the amount of useful thrust produced by the vehicle when changing flap geometry. It does not take into account the relaxation phase where the role of the flap was not analyzed. It also neglects the force contribution of the starting vortex added mass. The force results were not properly scaled using a similar non-dimensional form as for circulation which indicates the need for different scaling parameters.

The role of a flap was analyzed during contraction only but it could also play an important role during relaxation. The flap will affect the stopping vortex formation which is an important aspect of the rowing jellyfish propulsion mechanism. The interaction between the starting and stopping vortex is a key component of the rowing propulsion mechanism. Increasing flap length will also increase the amount of drag during relaxation. Therefore, the role of flap during relaxation is an important aspect which will also have to be looked into to quantify the net thrust produced by the Robojelly using wake structures. Robojelly does not currently create a full toroid as does the natural jellyfish due to bell segmentation. Segmentation is likely to reduce the thrust produced by jellyfish vehicles but is better than having folds in a uniform bell as shown by Villanueva et al. (2011). Force calculation assumed that a full toroid was created which overestimates the useful force but also neglected the added mass contribution of the starting vortex.

Two scaling methods were used make the Robojelly circulation non-dimensional. Approximating the robot as a jetting system with varying orifice gave inadequate results. Bell

segmentation and varying curvature as a function of arclength required a different way to model the Robojelly. A pitching panel representation of the segmented bell gave a better collapse of the circulation. This raises the possibility of using pitching panel theory to better understand the fundamental mechanism of varying orifice propulsors. In this study, the flaps were approximated as rigid panels for scaling. The effects of flexibility in pitching panels is still poorly understand and will require further research.

The 19 cycles of actuation before recording led to an increase in turbulence in the water especially since the vehicle was clamped in a finite tank preventing it to swim to undisturbed water. Turbulence was more prominent for flap configurations which created more circulation. This added turbulence in the water which made the PIV analysis and vortex tracking more difficult and less precise. It is likely that a better collapse of the non-dimensional circulation could occur if the PIV data was less noisy.

7.2 Piston-Cylinder Apparatus with Passively Varying Output

7.2.1 Introduction

A jellyfish propulsion mechanism can be approximated as a piston with varying orifice and passive flap as shown in Fig 7.2.1. The piston in this system is the main source of water flow. The varying orifice represents the actively deforming walls of the jellyfish. The passive flap is analogous to the passive flap of the jellyfish. The system allows the analysis of the main components of the jellyfish independently. A piston with varying orifice has been previously studied (Dabiri, 2005; Allen and Naitoh, 2005), but little is known about effects of passive flap.

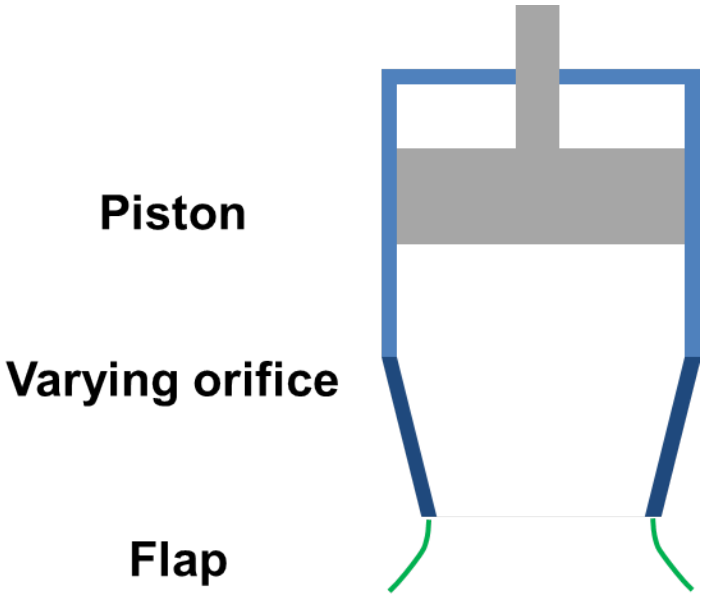

Figure 7.2.1: Simplified representation of a jellyfish with piston for fluid displacement, varying orifice and passive flap.

The piston can be coupled with the flap as shown in Fig. 7.2.2. This removes some of the intrusive parameters present when analyzing the flap of the Robojelly in Section 7.1. It has a uniform bell without collapsing walls. Therefore, the kinematics of the flap is purely due to the water flow and not the decreasing circumference of the base of the flap. Figure 7.2.2 shows four different flap configurations which will characterize the function of flaps on pulsating actuators. The flaps (a)-(c) in Fig. 7.2 have angles of 45°, 0° and 90°. The flap (d) has a taper and curvature which mimics the flap morphology of the natural animal. These flaps can also be made at different lengths to provide an parametric analysis of flap length as well as angle.

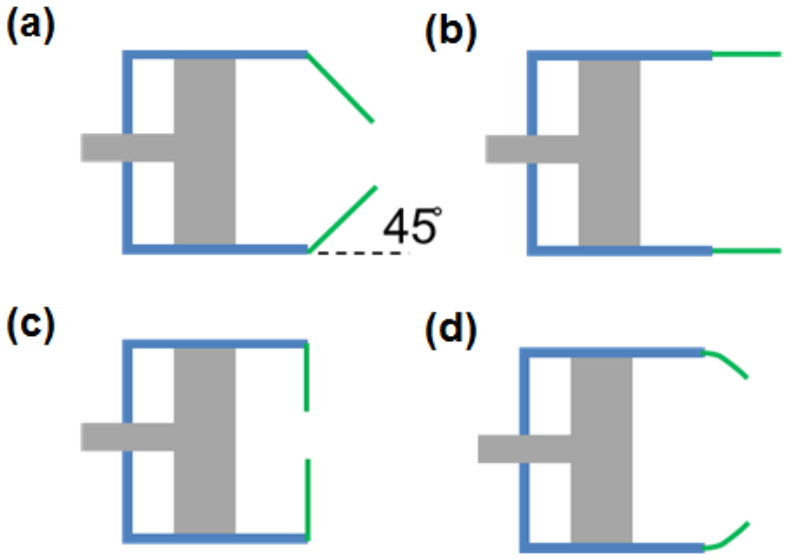

Figure 7.2.2: Different flap configurations (a) 45° angle, (b) 0° angle, (c) 90° angle and (d) bio.

7.2.2 Methods and Materials

A piston apparatus was designed to test the different flap configurations in Fig. 7.2.2. The piston was designed to mimic the same parameters as an *Aurelia aurita*. One of the most important parameters to match was the Reynolds number. Feitl et al (2009) reported Re values for *A. aurita* of different dimensions. An adult of 7.6 cm in diameter was chosen which has a corresponding Re = 2500. The volume change was calculated using the relaxed and contracted profile of an *A. aurita* subumbrella. The relaxed subumbrella volume was found to be 55.7 cm^3 and the bell undergoes a subumbrella volume change of 24.6 cm^3 during contraction. The mechanical piston shown in Fig. 7.2.3 was built from a PVC pipe with inner diameter (D) of 7.6 cm and outer diameter of 8.9 cm. A pneumatic piston with stroke length (L) of 20.6 cm give an L/D = 2.7. This exceeds the jellyfish L/D = 0.07 required to achieve the same volume change.

The piston apparatus was put on a thrust stand which measures the force produced by the piston during contraction and relaxation. A linear potentiometer connected to the piston rod by a string on pulleys measures the displacement of the piston. The system is put on sliders to prevent resistance to movement in the axial direction.

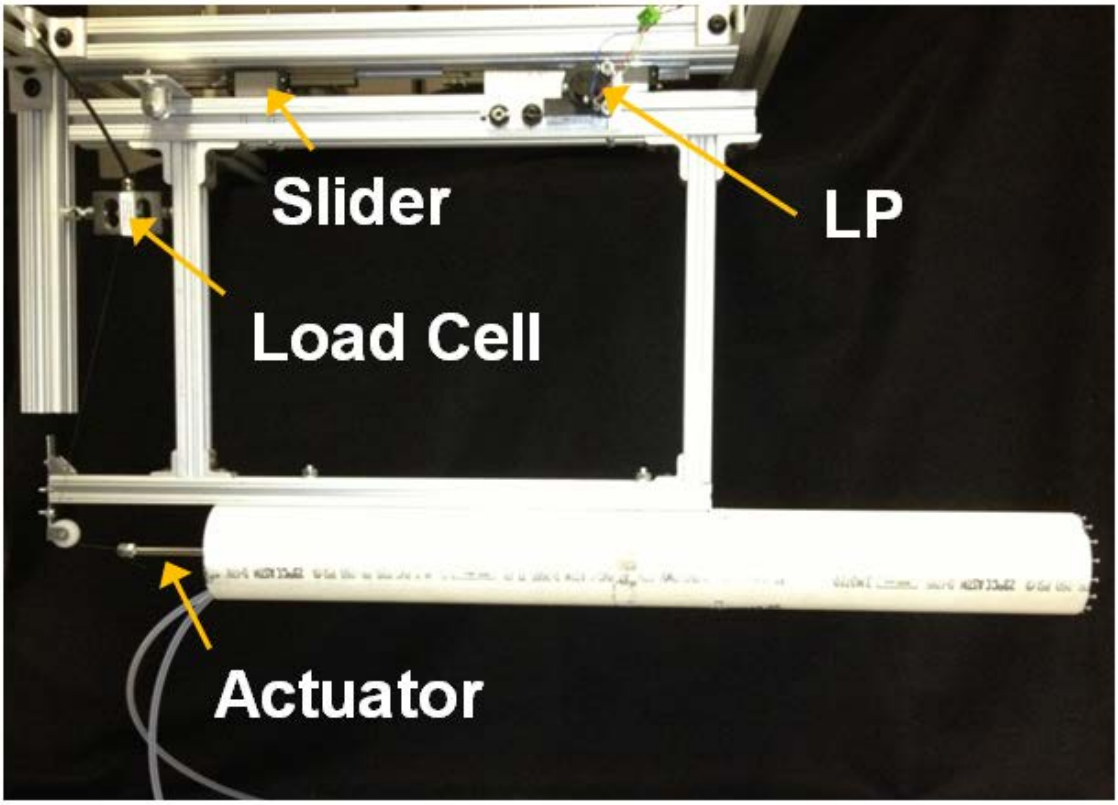

Figure 7.2.3: Experimental setup of the piston and flap apparatus showing the load cell, two sliders, and linear potentiometer (LP).

Flap lengths of 0%, 50%,100%, 150% and 200% are tested. Flap length percentage corresponds to the percentage of the natural flap of an A. aurita of the same diameter. The angle flaps have a constant cross section and thickness of 0.01 cm. They were manufactured from silicone (Ecoflex 10, Smooth-On) which is a soft room temperature vulcanization silicone with a shore hardness ratio of 0010. The flap was poured in a two part mold which was printed with a high precision

3D printer (Object Eden260V). The resulting 200% flap is shown in Fig. 7.2.4. The 200% flap is cut to desired lengths for testing. The flap is died with black silicone paint in order to reduce laser reflection during PIV testing.

Figure 7.2.4: Constant cross section flap with angle of 45°.

7.2.3 Results

Flap profiles during rest, contraction and relaxation are shown in Fig. 7.2.5 for the 45° flap at 100% length. The results show a traveling wave on the flexible flap as the water flow from the piston travels out the orifice.

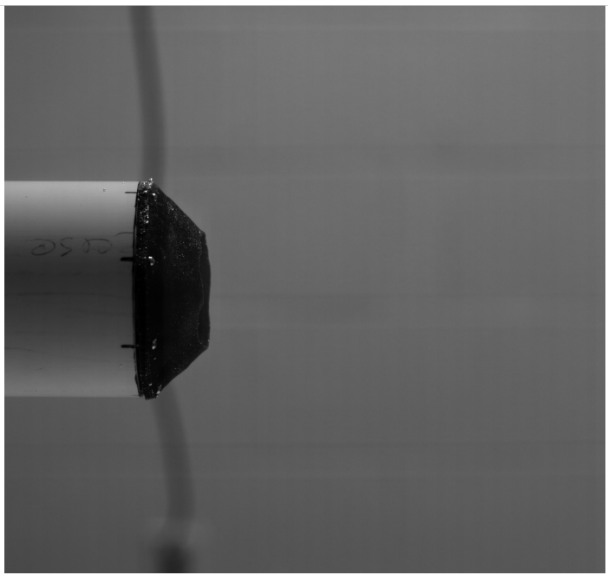

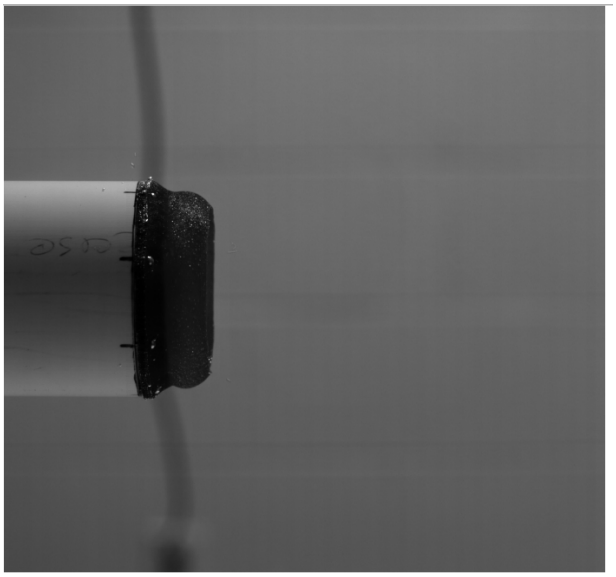

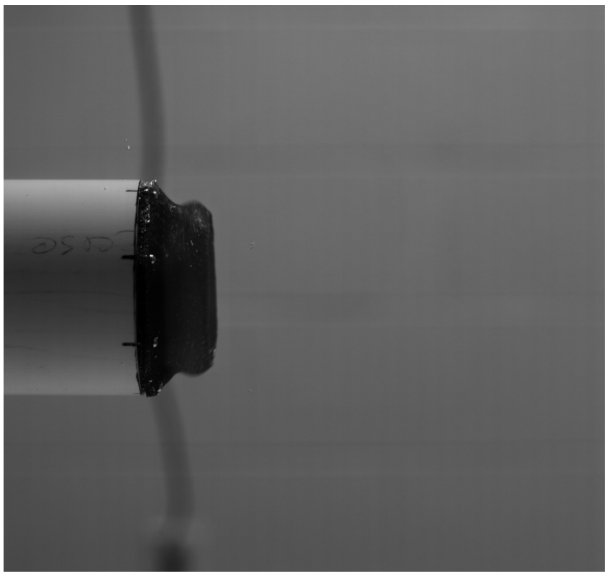

Figure 7.2.5: 45 flap at 100% length during (a) rest, (b) contraction and (c) relaxation.

The orifice diameter or flap margins were tracked as a function of time during the actuation cycle as shown in Fig. 7.2.6. It can be seen that the 45° flap had a faster response time faster deformation rate at a length of 200% then 100%. The 90° flap had the slowest deformation rate while the 0° flap had the fastest. The bio flap had a rapid deformation and stayed near constant for a long period before relaxing.

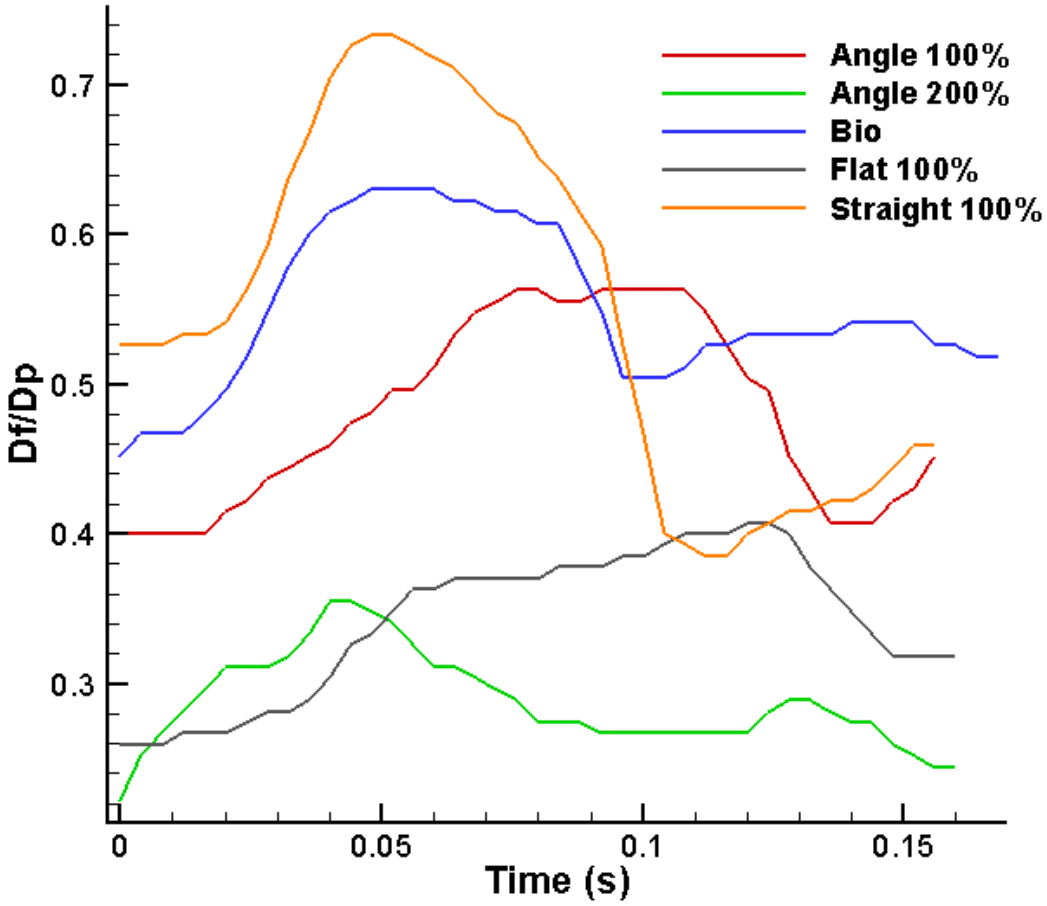

Figure 7.2.6: Flap diameter as a function of time for different flap configurations.

7.2.4 Conclusions

The preliminary flap kinematics results show the varying orifice characteristics found in jellyfish. The flap deforms non-linearly along its length. Therefore analyzing the flap as a piston with varying orifice does not take into account the varying geometry of the flap during actuation. As pointed out in Section 7.1, it might be more suitable to look at the flap as a flexible pitching

panel with axisymmetry. Future work will include looking at the vortex structure formed by the different flap configurations and scale the vortex circulation based on flap parameters.

7.3 Methodology for Characterizing Flaps and Medusa Propulsion

The previous two sections of this chapter have covered some initial work on understanding the role of flaps on oscillating propulsors. The following section serves as a guide for developing a series of experiments which can be used to further understand the role of flexible margin on oscillating propulsors.

A flexible margin (or flap) is a flexibility problem which is a fluid-structure interaction problem. To understand the different parameters involved in the fluid-structure interaction, the individual effects of the different parameters involved with flexible margins must be quantified. Complexity can then be added as fundamental understandings are achieved until the more complex jellyfish system.

The problem can be broken down into its fundamental governing parameters and analyzed individually. For example, flexibility is a complex problem in any field. By first modeling flexibility as a rigid structure of different geometries, we can remove the transient effects which can be studied later. This will give the building blocks to better understand the overall jellyfish propulsion mechanism. Figure 7.3.1 shows a schematic of the overall problem broken down into simple experiments. A possible approach is to start from **G** and work upwards.

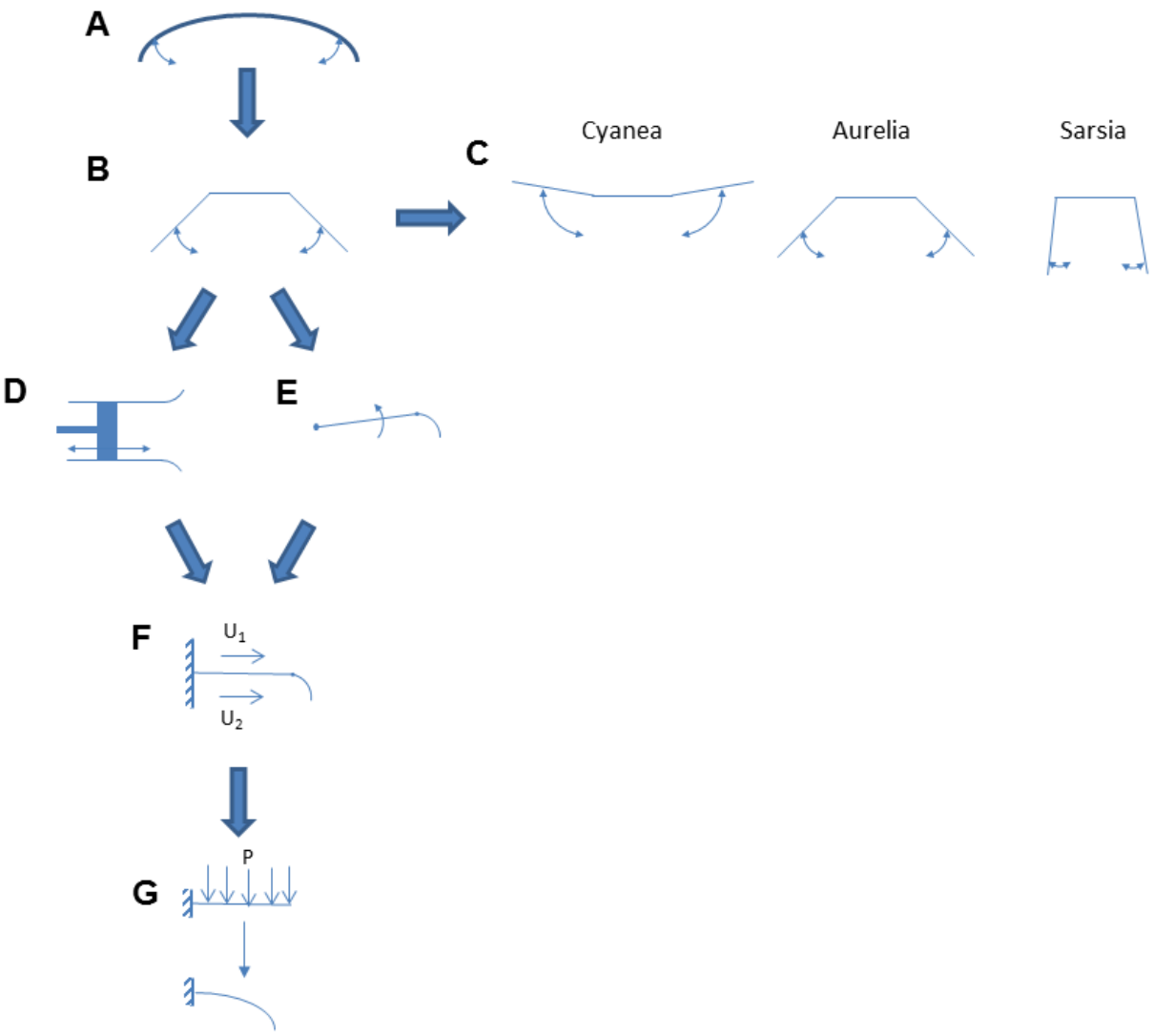

Figure 7.3.1: Schematic of the jellyfish propulsion mechanism broken down into simple experiments which can reveal fundamental parts.

Following is a description of the above figure:

A - The medusa as we know it.

B - A simplified representation of a jellyfish which consists of actuating appendages and a flat central plate at the center.

C - The different actuation schemes seen in different medusa species. As the Cyanea subumbrella volume has shown, the jetting model does not hold for all jellyfish during their entire propulsion cycle. The set of experiments in **C** would look at the effects of jetting and paddling/rowing for different medusa propulsion schemes.

D and **E** – Look at the assumption that jellyfish propulsion can be analyzed as jetting and paddling.

D - The jetting approximation of a medusa where a jet is formed with a moving piston. Vortex formation can be analyzed during contraction and relaxation for different flap configuration:

- Actuation:
    - Solid flap
        - Look at concave (bent outwards) flaps of different curvature and arclength
    - Flexible flap
        - Look at different flap geometries and stiffness
- Relaxation
    - Same as with actuation but with a convex flap (bent inwards). A clear tube is required to analyze the stopping vortex experimentally.
- Actuation-relaxation combination
    - Analyze the effect of a stopping vortex on actuation.

E - A pitching panel is analogous to a contracting wall of the medusa without creating a jet.

- Actuation
    - Solid Flap
        - Geometry: Vary curvature and arclength

        - Kinematics: Vary frequency and amplitude
    - Flexible flap
        - Vary stiffness and geometry

F – Simplified representation of **D** and **E**. This is a plate put in a flow with velocities U_1 and U_2 on top and bottom. Both velocities can be the same or differ. For a vortex analysis, we probably want to set U_2 as zero. A series of solid flap curvature and arclength can be analyzed. This will allow the study of vortex formation due to flap geometry.

G – Pressure distribution (P) along a flexible plate. We can study the structural response of a flexible flap to a given pressure distribution. This is well known and is just a matter of picking a model which suites our needs. A structural model of the flexible flap is an essential part to describe the fluid structure interaction, i.e. the curvature of flexible flaps during actuation.

7.4 References

Allen, J.J. and Naitoh T. (2005). Experimental study of the production of vortex rings using a variable diameter orifice. *Phys. Fluids* 17, 061701

Batchelor, G. K. (1967). An Introduction to Fluid Dynamics *New York: Cambridge University Press.*

Buchholz, J. H. and J. and Smits A. J. (2008). The wake structure and thrust performance of a rigid low-aspect-ratio pitching panel. *J. Fluid Mech.*603, 331-365

Buchholz, J. H., Green M. A. and J. and Smits A. J. (2011). Scaling the circulation shed by a pitching panel. *J. Fluid Mech.* 688, 591-601

Chakraborty, P., Balachandar, S. and Adrian R. (2005). On the relationships between local vortex identification schemes. *J. Fluid. Mech.* 535, 189-214

Chapman, D. M. (1998). Microanatomy of the bell rim of *Aurelia aurita* (Cnidaria: Scyphozoa) *Can. J. Zool.* **77**, 34-46

Dabiri, J. O. (2005). On the estimation of swimming and flying forces from wake measurements. *J. Exp. Biol.* 208, 3519-3532

Dabiri, J. O. and Gharib, M. (2005). Starting flow through nozzles with temporally variable exit diameter. *J. Exp. Biol.* 538, 111-136

Dabiri, J. O., Colin, S. P. and Costello, J. H. (2005). Flow patterns generated by oblate medusan jellyfish: field measurements and laboratory analyses. J. Exp. Biol. 208, 1257–1265

Danie,l T. L. (1983). Mechanics and energetics of medusan jet propulsion Can. J. Zool. 61 1406 -1420

Doligalski, T., Smith C., and Walker J. (1994). Vortex interactions with walls. *Annual Review of Fluid Mechanics*, 26(1), 573-616.

Eckstein, A. and Vlachos, P. (2009a). Digital particle image velocimetry (DPIV) robust phase correlation. *Meas. Sci. Technol*. 20, 055401

Eckstein, A. and Vlachos P. (2009b). Assessment of advanced windowing techniques for DPIV. *Meas. Sci. Technol*. 20, 075402.

Eckstein, A., Charonko, J., and Vlachos, P. (2008) Phase correlation processing for DPIV measurements. *Exp. Fluids*, 45(3), 485-500.

Feitl, K. E., Millett, A. F, Colin, S. P. Dabiri, J. O. and Costello J. H. (2009). Functional Morphology and Fluid Interactions During Early Development of the Scyphomedusa Aurelia aurita. *Biol. Bull.* 217, 283-291

Green M. A. and Smits A. J. (2008). Effects of three-dimensionality on thrust production by a pitching panel. *J. Fluid Mech.* 615, 211-220

Holden, D. (2011). Flying snakes: Aerodynamics of body cross-sectional shape. Masters of Science Thesis, Virginia Polytechnic Institute and State University

Jiang, M., Machiraju, R. and Thompson, D. (2002). A novel approach to vortex core region detection. Proc. IEEE TCVG, 217

Scarano, F. (2002), Iterative image deformation methods in PIV. *Meas. Sci. Technol.* 13, R1-R19.

Sirovich, L. (1987). Turbulence and the dynamics of coherent structures. I- Coherent structures. II- Symmetries and transformations. III- Dynamics and scaling. *Quarterly of applied mathematics*, 45, 561-571.

Villanueva, A. A., Joshi K. B., Blottman J. B. and Priya S. (2010a). A bio-inspired shape memory alloy composite (BISMAC) actuator *Smart Mater. Struct.* 19, 025013

Villanueva, A. A., Priya, S., Anna, C. and Smith, C. F. (2010b). Robojelly bell kinematics and resistance feedback control. *Robotics and Biomimetics (ROBIO), 2010 IEEE International Conference on*, 1124-1129

Villanueva, A. A., Smith, C. F., Priya, S. (2011). Biomimetic Robotic Jellyfish (Robojelly) using Shape Memory Alloy. *Bioinspir. Biomim.* 6, 3

Zhou, J., Adrian, R., Balachandar, S. and Kendall T. (1999). Mechanisms for generating coherent packets of hairpin vortices in channel flow. *J. Fluid Mech.* 387, 353-396

Chapter 8

Conclusions

8.1 Achievements

Several novel achievements were accomplished through the development of this dissertation. These include JetSum: a SMA based biomimetic jetting jellyfish robot. This robot was the first SMA based jellyfish robot and as shown the ability to propel itself.

Bio-inspired shape memory alloy composites (BISMAC) actuators capable of high deformation were developed as a foundation for robotic jellyfish. The composite actuators are partly made of silicone which adds to their robustness and allows them to function in air as well as water. They can also be used for other applications requiring soft actuators which high deformation.

BiFlex and FlexLegs were developed based on the concept of BISMAC. The BiFlex are an extension of BISMAC allowing deformation in two directions. The BiFlex were then used to develop a set of legs called FlexLegs capable of different walking gates with a low weight and small form factor.

Robojelly is the first SMA based biomimetic rowing jellyfish robot. It is inspired by the *Aurelia aurita* species and uses BISMAC actuators to deform its bell and produce thrust. This vehicle also proved the ability to propel itself while achieving a similar morphology and kinematics as the natural *A. aurita*.

Through the development of Robojelly, it was found that the *A. aurita* had a section of its bell towards the margin which deformed at a different phase. This led to the discovery of performance improvement due to a flexible margin or flap.

Further analysis of the flap revealed that it is possible to replicate the kinematics of the flexible margin using a passive flap.

A biomimetic *Mastigias* oral structure was developed. The structure was first model in CAD and then constructed out of soft silicone. This structure can be used to study the effects of the different parameters on the hydrodynamics and food capture of *Mastigias*.

Correction techniques for in situ animal kinematics were developed. This allows the analysis of videos which would otherwise be useless for quantifying animal kinematics. These techniques open new opportunities for analyzing old videos and for conducting new experiments in situ when controlled experiments are not possible.

Discretization techniques for kinematics analysis and modeling were developed. This gives a set of tools for engineers and biologist to methodologically quantify the kinematics of natural animal. This can be used to study animal behavior or to replicate its motion.

A bio-mimetic robot named Cyro measuring 170 cm in diameter was developed. The design is inspired by the *Cyanea capillata* species. The vehicle is the fully autonomous and showed the ability to swim untethered.

The following sections list a series of recognized achievements made during the course of my PhD.

8.1.1 Publications

8.1.1.1 Journal Articles

1. **Villanueva A**, Vlachos P and Priya S. Piston-Cylinder Apparatus with Passively Varying Output (under preparation)

2. **Villanueva A**, Marut K, Michael T and Priya S. *Cyanea capillata* biomimetic unmanned underwater vehicle. (provisional patent submitted)

3. **Villanueva A**, Raben S, Vlachos P and Priya S. Effects of a Flexible Margin on Robojelly Vortex Structures. (under preparation)

4. **Villanueva A**, Gemmell B, Priya S (2013). *Cyanea capillata* bell kinematics analysis and modeling using strategic discretization techniques. *J. Exp. Biol.* (submitted)

5. **Villanueva A**, Priya S (2013). Correction techniques for animal kinematics from in situ video containing substantial multi-axis motion. *J. Exp. Biol.* (submitted)

6. Smith C**, Villanueva A**, Priya S. Material properties of mesoglea in the jellyfish Aurelia aurita and comparison to artificial poly(vinyl) alcohol hydrogel with ferritin nanoparticles. *IOP Smart Mat. Struc.* (submitted)

7. Marut K, Stewart C, Michael T, **Villanueva A**, Priya S (2012). A bio-insired Jet Propulsion Robot (JetPRo) actuated by and Iris Mechanism. *Smart Mat. Struct*. (submitted)

8. Colin S, Costello H, Dabiri J, **Villanueva A**, Blottman J, Gemmell B and Priya S (2012). Biomimetic and live Medusae Reveal the Mechanistic Advantages of a Flexible Bell Margin. *PLoS ONE* 7(11), e48909

9. Smith C, **Villanueva A** and Priya S (2012). *Aurelia Aurita* Bio-inspired Tilt Sensor. *Smart Mat. Sys.* 21, 10

10. Tadesse Y, **Villanueva A**, Haines C, Novitski D, Baughman and Priya S (2012). Hydrogen Fuel-Powered Bell-Segments of Biomimetic Jellyfish undersea vehicle. *Smart Mater. Struct.* 21, 045013

11. Keyur J, **Villanueva A**, Smith C and Priya S (2011). Modeling of Artificial *Aurelia aurita* Bell Deformation. *Marine Tech Soc. Journ*., 45, 4, 165-180(16)

12. **Villanueva A**, Smith C and Priya S (2011). Biomimetic Robotic Jellyfish (Robojelly) using Shape Memory Alloy. *Bioinspir. Biomim*. 6, 036004

13. Smith C, **Villanueva A**, Joshi K, Tadesse Y and Priya S (2011). Working principle of Bio-Inspired Shape Memory Alloy Composite actuators. *Smart Mat. Struct.*, 20, 012001

14. **Villanueva A**, Joshi K, Blottman J and Priya S (2010). A Bio-Inspired Shape Memory Alloy (BISMAC) Actuator. *Smart Mat. Struct.*19, 025013

8.1.1.2 Conference Proceeding Articles

1. Michael T, **Villanueva A**, Vlachos P, Priya S. Hydrodynamics of *Mastigias* oral structure. (under preparation)

2. Marut K, Stewart C, **Villanueva A**, Avirovic D, Priya S (2012). A biomimetic Jellyfish-insired Jet Propulsion System Using an Iris Mechanism. AMSE Conference Proceeding SMASIS2011-5134

3. **Villanueva A**, Gupta S, Priya S (2012). Effects of Copper Addition and Annealing Temperature on Transition Temperature of Ni-Ti Shape Memory Alloys. *SPIE Smart Struct./NDE*, 8342-52

4. **Villanueva A**, Smith C, Priya S (2011). Flexlegs – Flexible Legs Actuated by Shape Memory Alloy. AMSE Conference Proceeding SMASIS2011-5134

5. **Villanueva A**, Priya S, Anna C, Smith C (2010). Robojelly bell kinematics and resistance feedback control. *Robotics and Biomimetics (ROBIO), 2010 IEEE International Conference on* , vol., no., pp. 1124-1129, 14-18 DOI: 10.1109/ROBIO.2010.5723486

6. **Villanueva A**, Priya S. (2010). BISMAC control using SMA resistance feedback. *Proc. SPIE.* 7642 76421Z, DOI:10.1117/12.847788

7. **Villanueva A**, Bresser S, Chung S, Tadesse Y, and Priya S (2009). Jellyfish inspired underwater unmanned vehicle Proc. SPIE. 7287, 72871G, DOI:10.1117/12.815754

8.1.2 Abstract-Based Presentations and Invited Talks

1. American Physics Society Division of Fluid Dynamics (APS – DFD). Vortex formation analysis of a piston apparatus with passively varying output inspired by jellyfish. (November 2012)

2. Virginia Military Institute, Science Technology Engineering and Math (STEM) Education Conference. Bio-inspired Jellyfish Underwater Unmanned Vehicles. (October 2012)

3. American Physics Society Division of Fluid Dynamics (APS – DFD). Effects of a Flexible Margin on Robojelly Vortex Structures. (November 2011)

4. Virginia Tech President Steger invited presentation. Biomimetic Robotic Jellyfish Research. (October 2011)

5. Annual Center for Smart Materials Systems and Structures (CIMSS) Conference. Jellyfish Propulsion Mechanics Biomechanics. (March 2010)

6. Annual Center for Smart Materials Systems and Structures (CIMSS) Conference, Jellyfish AUV. (August 2009)

8.1.3 Proposals

- National Science Foundation - Innovation Corps Program, Biomimetic surveying and Monitoring Vehicle (Priya S, Villanueva A, Coggin J), July 2012

- Office of Naval Research DURIP, "Time-resolved Particle Image Velocimetry System", ~$297K, February 2011 – February 2012, PI: Shashank Priya, Program Manager: Dr. Robert Brizzolara.

8.1.4 Patents

- "Jellyfish Autonomous Underwater Vehicle". (Villanueva A, Priya S), U. S. Provisional Application submitted

- "Shape Memory Alloy (SMA) Actuators and Devices including Bio-Inspired Shape Memory Composite (BISMAC) Actuators". (Villanueva A, Smith C, Priya S), U. S. Provisional Application 61/421,847, filed December 10, 2010

8.1.5 Research Related Recognitions

- Featured in IOP Smart Material and Structures 'Highlights of 2012' for the following paper:
    - Tadesse Y, Villanueva A, Haines C, Novitski D, Baughman and Priya S (2012). Hydrogen Fuel-Powered Bell-Segments of Biomimetic Jellyfish undersea vehicle. *Smart Mater. Struct.* 21, 045013

- Featured in IOP Smart Material and Structures 'Highlights of 2012' for the following paper:
    - Villanueva AA, Joshi KB, Blottman JB, Priya S (2010). A bio-inspired shape memory alloy composite (BISMAC) actuator. *Smart Mat. Struct.* 19, 025013

- Awarded "Outstanding Ph.D. Candidate" of the Mechanical Engineering Department at Virginia Tech, 2012

- ASME SMASIS 2011 – Best Student Hardware Competition Finalist.

- Featured in IOP Smart Material and Structures 'Highlights of 2010' for the following paper:
    - Villanueva AA, Joshi KB, Blottman JB, Priya S (2010). A bio-inspired shape memory alloy composite (BISMAC) actuator. *Smart Mat. Struct.* 19, 025013

8.2 Conclusions

Three different robotic jellyfish and supporting technology were developed. The design and analysis of these vehicles and components were covered in this dissertation. BISMAC actuators were shown experimentally to have the ability to be tailored in order to achieve a specific deformation profile. A tracking code was developed for large deformation bending beams. This code helped in characterizing the deformation of BISMAC actuators. A rapid heating controller was developed to reduce the energy consumption of Robojelly by 60% and increase its performance. Methods for further reducing the power consumption of SMA actuators were identified. This includes identifying shape memory alloy composition for reduced energy consumption. A literature review of non-linear controller for SMA was also conducted and ANFIS controller was identified to have the highest potential for biomimetic jellyfish robots.

The Robojelly operating parameters were optimized to increase performance and efficiency. The vortex structures created by Robojelly were analyzed using PIV. The results showed that the Robojelly flaps scaled well with the assumption of a pitching panel representation of the bell. The circulation scaled with actuator kinematics and flap geometry. The PIV experiments on the Robojelly showed that multiple parameters including the performance of the SMA actuators affected vortex formation. A piston apparatus was designed and fabricated to analyze the flexible margin by isolating the flap parameters.

In the development of Cyro, the kinematics of the *Cyanea capillata* was modeled using Fourier series. This can serve as a reference for the kinematics of *C. capillata* for a variety of applications including computational fluid dynamics. The method which led to the formation of this model can also serve as a methodology for modeling other jellyfish species and animals with similar kinematics.

The bell kinematics of *Aurelia aurita* and *Cyanea capillata* were both analyzed and quantified for the development of Robojelly and Cyro. The kinematics of the robotic analogs were also quantified and then compared with the natural ones. A kinematic modeled of Cyro's mechanical arms was developed. In combination with the natural animal's kinematic model, this allows for the optimization of the robotic arm in order to achieve a more biomimetic motion. A two axis test stand was designed and fabricated for Cyro's bell segment analysis and optimization.

Several important topics will require advancements before biomimetic underwater vehicles can be deployed to achieve underwater missions. The research reported in this document shows advancements in understanding the jellyfish propulsion mechanism for creating robotic analogues. Jellyfish are anatomically relatively simple animals which may mislead one to believe

they are easy to replicate mechanically. Their simplicity is what makes jellyfish so elegant, efficient and hard to replicate. Their structure is highly flexible and is designed to reduce losses during swimming. The actuators are circular muscles which are small and capable of large contraction at high efficiency while keeping the ability to undergo large deformation with the bell. No actuators currently available come close to match all the characteristics of the jellyfish muscles. Available actuators are too bulky, not efficient enough, not flexible, unable to achieve enough strain, force or speed or a combination of these. The chosen actuators ultimately dictate the morphology, performance and efficiency of a biomimetic vehicle. It is therefore the most important factor limiting biomimetic vehicles. With the current technological state of actuators, sacrifices in morphology, performance or efficiency have to be achieved for a functioning biomimetic vehicle. This can be seen from the high energy consumption of Robojelly and the mechanical morphology of Cyro. Also, current actuator technology mainly consists of rotary actuators, namely DC motors. Biomimetic vehicles require linear actuation for which there are limited options.

Shape memory alloy wires have a very good form factor and flexibility which resembles muscles but have poor contraction and energy efficiency. Dielectric elastomers have good efficiency; they are flexible and have shown the ability to form linear actuators with large deformation. Advancement in manufacturing techniques is required before these actuators can be used as artificial muscles. Electrostatic forces have shown the ability to be used as micro actuators with very high efficiency (>90%). These actuators are rigid and require complex manufacturing methods. Such high efficiency though screams for more attention. Further research could turn this functional unit into a full scale artificial muscle as does the sarcomere for natural muscles. Revolutionary new actuator technology may not be necessary in order to significantly advance

current actuator technology. The modification and adaptation of current technology could lead to significant improvements.

The interface technology between the different subsystems is also important. Rotary DC motors are highly efficient but its motion must be translated into a linear motion or converted via a mechanical system in order to be used in biomimetic vehicles. This currently comes at a great energy cost and often results in a bulky system. The measures used to seal electronics and actuators also come at a great energy loss. Strategies involving instruments that interact well with water or provide seamless integration with its surrounding could significantly reduce the power consumption. Biomimetic vehicles are flexible while most of the mechanisms researched and used today are for rigid systems or utilize rigid components to achieve flexible deformation. Reducing the complexity of these systems by directly using flexible structures could also lead to significant energy savings. Strategies diverting from this suggestion may be used and will likely result in some losses but might still lead to feasible systems.

8.3 Future Scope

As discussed in the previous section, the mechanical efficiency of biomimetic vehicles requires significant improvements before they can be deployed. A lot of focus and importance has been brought to hydrodynamic efficiency but if the mechanical system responsible for creating the motion for highly efficient hydrodynamics compensates hydrodynamic gains with mechanical energy losses, the system is no better.

Actuator technology should be improved to produce more efficient linear and circumferential contraction. Attention should also be placed towards making actuator flexible or improving

flexible actuator technology. Complimenting flexible structures must also reduce losses and improve compliance. For artificial jellyfish robots, artificial mesoglea is a topic which should be further addressed to produce a material which is flexible, can withstand salt water, is neutrally buoyant and provide the proper resilience for propulsion. Research should be done to determine if passive relaxation is more efficient then active relaxation when taking into account the added energy during actuation of a passively relaxing system.

Though jellyfish have shown to be poor swimmers, their basic propulsion mechanism allows the study of different parameters also found in other species. For example, the flexible margin and varying orifice diameter is found in a variety of animals. Scaling of pitching panel should be extended to flexible margin of different stiffness and flexion point locations to gain a better understanding of the role of flexibility in animal propulsion.

Cyro was built as a first prototype to study the effect of scale on jellyfish hydrodynamics and mechanics. The current design is not optimized. The bell kinematics could undergo significant improvements with the different models developed in this research. Cyro could also be used to study the effects of segmented bell vs. uniform bells. Is it a coincidence that segmented Cyanea capillata are known to be one of the largest jellyfish species or is there a scientific reason related to the hydrodynamics of segmented bells?

The robotic jellyfish vehicles developed are currently not able to turn due to limitations in their control systems and vehicle stability. The ability to turn is necessary to achieve missions of any significance. Therefore, more time and effort should be spent in developing a control system which allows robotic jellyfish vehicles to turn. The control system chosen partly depends on the type of actuators used.

Several jellyfish species have passive oral structures which are used for feeding. These oral structures often consists a majority of the animal's mass. They also provide a vital function which could be used to solve engineering problems. For example, oral structures on a robotic vehicle could be used for more payload space, to harvest energy or filter water for inspection or cleaning purposes. These oral structures play a significant role on the dynamics of the animal and further research should be conducted to see how it affects its overall swimming efficiency and stability.

The robots developed can only swim for a period of a few hours before needing to refuel but so do natural animals. Energy harvesting is therefore a biomimetic approach which will be required in order to have vehicles capable of operating for excessive periods ranging from weeks to months. Water filtering for nutrients is a potential source of energy when coupled with technology such as microbial fuel cells and bi-lipid layer technology. Algae growth on the vehicle can actually be a source of energy as shown by *Mastigias papua* and a possible strategy for underwater vehicles.

The image processing techniques developed could be further expanded to account for more artifacts in videos and to be applicable to different animal species. A deeper look into image processing literature could reveal strategies which could greatly improve biological image processing. The kinematic modeling techniques proposed here provide a good way to quantify biological kinematics. If such methods were used by biologist to quantify animal kinematics, they could be useful for a series of engineering and biological applications as the topic of biomimetics and bio-inspiration gains increasing interest.

Appendix A

Matlab Codes

A.1 Point Detection

```
clc
clear
close all

% Read Video

video = mmreader('AA_beam_c000004.avi');

numframes = get(video,'NumberOfFrames')

I_1 = read(video,1);

numpoints = 14;

step = 15;
skip = 0;


TH = .225;

min_area = 16;
max_area = 65;


% Normalize
Base = [56, 171]; %[55, 171];

Tip = [454, 211];

Scale_Norm = sqrt((Base(1) - Tip(1))^2 + (Base(2) - Tip(2))^2);

x11= 0;
y11 = 0;
dx = 1/Scale_Norm;

R = makerefmat(x11, y11, -dx, dx);

Clamp_Pix_Coord = Base;

e=1;
```

```
ee=1;

x_max = zeros(1,numpoints)+100;


%%

for i=1:step:numframes - skip

I = read(video,i+skip);

gray_im = rgb2gray(I);
BW_im = im2bw(gray_im,TH);

% figure
% imshow(gray_im)
% figure
% imshow(BW_im)

B = imrotate(I,90);    %Image rotation 90 degrees

% Image Convergion

gray_im_r = rgb2gray(B);
BW_im_r = im2bw(gray_im_r,TH);

% MASK
BW_im_r(569:605,127:197)=0;



% figure
% imshow(gray_im_r);
% figure
% imshow(BW_im_r);


% Point Labelling

[L_r,num] = bwlabel(BW_im_r,4);
L = rot90(L_r, -1);                %Data rotation -90 degrees
A  = regionprops(L, 'area');
s  = regionprops(L, 'centroid');
areas = cat(1, A.Area);
centroids = cat(1, s.Centroid);
```

```
b=1;
for a = 1:length(areas)
    if areas(a) >= min_area && areas(a) <= max_area
        points(b,1,e) = centroids(a,1);
        points(b,2,e) = centroids(a,2);
        b=b+1;
    end
end




[xp(:,e)] = points(:,1,e);
[yp(:,e)] = points(:,2,e);
[y_t(:,e), x_t(:,e)] = pix2map(R,[points(:,1,e)-
Clamp_Pix_Coord(1),points(:,2,e)- Clamp_Pix_Coord(2)]);  %%%%%


 theta_test(:,e) = atan(y_t(:,e)./x_t(:,e));

Mag(1,e) = sqrt( [x_t(1,e)].^2 + [y_t(1,e)].^2);
theta(1,e) = atan(y_t(1,e)/x_t(1,e)) + 2*pi;

for u = 1:200
    h=1;

for ii = 2:length(points(:,1,e))
    Mag(ii,e) = sqrt( [x_t(ii,e)].^2 + [y_t(ii,e)].^2);


%     if Mag(ii-1,e) < Mag(ii,e)


    if x_t(ii-1,e) > 0 && x_t(ii,e) > 0
        theta(ii-1,e) = atan([y_t(ii-1,e)]/[x_t(ii-1,e)]) +
2*pi;
        theta(ii,e) = atan([y_t(ii,e)]/[x_t(ii,e)]) + 2*pi;

    elseif x_t(ii-1,e) > 0 && x_t(ii,e) < 0
        theta(ii-1,e) = atan([y_t(ii-1,e)]/[x_t(ii-1,e)]) +
2*pi;
        theta(ii,e) = atan([y_t(ii,e)]/[x_t(ii,e)]) + pi;

        elseif x_t(ii-1,e) < 0 && x_t(ii,e) < 0
```

```
        theta(ii-1,e) = atan([y_t(ii-1,e)]/[x_t(ii-1,e)]) + pi;
        theta(ii,e) = atan([y_t(ii,e)]/[x_t(ii,e)]) + pi;

    end

    if x_t(6,e) > 0 && theta(ii-1,e) > theta(ii,e) && Mag(ii-
1,e) < Mag(ii,e) || (x_t(6,e) < 0 && theta(ii-1,e) >
theta(ii,e))
        [x(h,e)] = [x_t(h,e)];
        [y(h,e)] = [y_t(h,e)];
        [x(h+1,e)] = [x_t(h+1,e)];
        [y(h+1,e)] = [y_t(h+1,e)];
    else
        [x(h+1,e)] = [x_t(h,e)]; % this creates the switch
        [x(h,e)] = [x_t(h+1,e)];
        [x_t(h+1,e)] = [x(h+1,e)];
        [x_t(h,e)] = [x(h,e)];

        [y(h+1,e)] = [y_t(h,e)];
        [y(h,e)] = [y_t(h+1,e)];
        [y_t(h+1,e)] = [y(h+1,e)];
        [y_t(h,e)] = [y(h,e)];
    end

    h=h+1;

end
end

%% Finding Min and Max Positions


     [x_min] = [x(:,1)];
     [y_min] = [y(:,1)];


if  e > 1 && x(6,e) < x_max(6)
     [x_max] = [x(:,e)];
     [y_max] = [y(:,e)];
     ee = ee + 1
end

%% Differing between contraction and relaxation

if e > 1 && xp(6,e) > xp(6,e-1)
    [xp_rel(:,e)] = [xp(:,e)];
    [yp_rel(:,e)] = [yp(:,e)];
```

```
else
    [xp_cont(:,e)] = [xp(:,e)];
    [yp_cont(:,e)] = [yp(:,e)];

end

%% Figure Generation

% Using non-rotated image

% figure
% imshow(gray_im)
% hold on
%
%
% if e > 1 && xp(6,e) > xp(6,e-1)
%
% plot(points(:,1,e), points(:,2,e),
'b*',xp_rel(1,:),yp_rel(1,:),'ro',xp_rel(2,:),yp_rel(2,:),'ro',.
..
%
xp_rel(3,:),yp_rel(3,:),'ro',xp_rel(4,:),yp_rel(4,:),'ro',...
%
xp_rel(5,:),yp_rel(5,:),'ro',xp_rel(6,:),yp_rel(6,:),'ro',...
%
xp_rel(7,:),yp_rel(7,:),'ro',xp_rel(8,:),yp_rel(8,:),'ro',...
%
xp_rel(9,:),yp_rel(9,:),'ro',xp_rel(10,:),yp_rel(10,:),'ro',...
%
xp_rel(11,:),yp_rel(11,:),'ro',xp_rel(12,:),yp_rel(12,:),'ro',..
.
%
xp_rel(13,:),yp_rel(13,:),'ro',xp_rel(14,:),yp_rel(14,:),'ro',..
.
%
xp_rel(7,:),yp_rel(7,:),'ro',xp_rel(8,:),yp_rel(8,:),'ro',...
%
xp_rel(7,:),yp_rel(7,:),'ro',xp_rel(8,:),yp_rel(8,:),'ro',...
%
xp_cont(1,:),yp_cont(1,:),'go',xp_cont(2,:),yp_cont(2,:),'go',..
.
%
xp_cont(3,:),yp_cont(3,:),'go',xp_cont(4,:),yp_cont(4,:),'go',..
.
```

```
%
xp_cont(5,:),yp_cont(5,:),'go',xp_cont(6,:),yp_cont(6,:),'go',..
.
%
xp_cont(7,:),yp_cont(7,:),'go',xp_cont(8,:),yp_cont(8,:),'go',..
.
%
xp_cont(9,:),yp_cont(9,:),'go',xp_cont(10,:),yp_cont(10,:),'go',
...
%
xp_cont(11,:),yp_cont(11,:),'go',xp_cont(12,:),yp_cont(12,:),'go
',...
%
xp_cont(13,:),yp_cont(13,:),'go',xp_cont(14,:),yp_cont(14,:),'go
')
%
% hold off
%
% else
%
% plot(points(:,1,e), points(:,2,e),
'b*',xp_cont(1,:),yp_cont(1,:),'go',xp_cont(2,:),yp_cont(2,:),'g
o',...
%
xp_cont(3,:),yp_cont(3,:),'go',xp_cont(4,:),yp_cont(4,:),'go',..
.
%
xp_cont(5,:),yp_cont(5,:),'go',xp_cont(6,:),yp_cont(6,:),'go',..
.
%
xp_cont(7,:),yp_cont(7,:),'go',xp_cont(8,:),yp_cont(8,:),'go',..
.
%
xp_cont(9,:),yp_cont(9,:),'go',xp_cont(10,:),yp_cont(10,:),'go',
...
%
xp_cont(11,:),yp_cont(11,:),'go',xp_cont(12,:),yp_cont(12,:),'go
',...
%
xp_cont(13,:),yp_cont(13,:),'go',xp_cont(14,:),yp_cont(14,:),'go
')
%
%
% hold off
%
% end
%
```

```
% %
%
% M(e) = getframe;
%
e = e+1;
if e == 50 || e == 100 || e == 150
    close all
end

end


%% Max and Min vectors

Min = [[x_min] [y_min]]
Max = [[x_max] [y_max]]



%% Plot


figure
plot(x(1,:),y(1,:),x(2,:),y(2,:),x(3,:),y(3,:),x(4,:),y(4,:),x(5
,:),y(5,:),...

x(6,:),y(6,:),x(7,:),y(7,:),x(8,:),y(8,:),x(9,:),y(9,:),x(10,:),
y(10,:),...

x(11,:),y(11,:),x(12,:),y(12,:),x(13,:),y(13,:),x(14,:),y(14,:),
...
    x_max,y_max,'o',x_min,y_min,'x')
%
legend('1','2','3','4','5','6','7','8','9','10','11','12','13','
14')
xlabel('X_n_o_r_m position')
ylabel('Y_n_o_r_m position')

% figure
%
plot(xp(1,:),yp(1,:),xp(2,:),yp(2,:),xp(3,:),yp(3,:),xp(4,:),yp(
4,:),xp(5,:),yp(5,:),xp(6,:),yp(6,:),xp(7,:),yp(7,:),xp(8,:),yp(
8,:),xp(9,:),yp(9,:),xp(10,:),yp(10,:))
% legend('1','2','3','4','5','6','7','8','9','10')

% , grid on;
```

```
%% Movie

% figure
% movie(M,10,2)
% movie2avi(M,'Image Processing')
```

A.2 Mechanical Arm Model

```
clc
clear
close all

savebase = 'E:\Research\Robojelly\Cyanea\Arm Kinematics\';



R = 32.5; % Bell Radius

%% Length of Links

r1 = 2.988;
r2 = 6.8;
r3 = 1.7;
r4 = 8.87;
% r5 = is defined lower in the code
r6 = 6.976;
r7 = [1.75:-.05:.25, .25:.05:1.75];
r8 = 3.292;
r9 = 3.95;
r10 = 2.0156;



Lag = 0;
theta1 = 180 *pi/180;
theta10 = 97.125 *pi/180;

p = 1;
k = 1;
for i = 1:length(r7)

%% Lag

% This is to include the laging effect

if Lag == 1
```

```
    if i>1 && r7(i) > r7(i-1)

        r5(i) = 7.32 + p*10/length(r7);
        p = p + 1;

        if r5(i) > 8.52
            r5(i) = 8.52;
        end

        if theta4(i-1) > 5*pi/180
            r5(i) = 8.52 - k*10.8/length(r7);
            k = k+1;

            if r5(i) < 7.32
            r5(i) = 7.32;
            end
        end

    else
        r5(i) = 7.32;
    end

else
    r5(i) = 7.32;

end

theta1 = 180 *pi/180;

%% Finding Theta 9 and Theta 8

r11(i) = sqrt(-2*r10*r7(i) * cos(theta10) + r7(i)^2 + r10^2);
d(i) = acos((r7(i)^2 + r11(i)^2 - r10^2) / (2*r7(i)*r11(i)));
e(i) = acos((r11(i)^2 + r8^2 - r9^2) / (2*r11(i)*r8));

theta8(i) = pi - d(i) - e(i);

f(i) = acos((r8^2 + r9^2 - r11(i)^2) / (2*r8*r9));

theta9(i) = theta8(i) - f(i);

theta4(i) = theta9(i) + 155*pi/180;


%% Finding Theta 4

k2 = r1/r4;
k1 = r1/r2;
k3 = (-r3^2 + r1^2 + r2^2 + r4^2) / (2*r2*r4);

A2 = cos(theta4(i)) * (k1+1) + k2 + k3;
B2 = -2 * sin( theta4(i));
C2 = cos(theta4(i)) * (k1 - 1) - k2 + k3;
```

```
theta2(i) = 2 * atan2((-B2 - sqrt(B2^2 - 4*A2*C2)), (2*A2));

%% Finding Theta 3


k4 = r1/r3;
k5 = (r2^2 -r1^2 - r4^2 - r3^2 ) / (2*r3*r4);

D = k5 + k2 - cos(theta4(i)) * (k4 - 1);
E = -2 * sin(theta4(i));
F = k5 - k2 - cos(theta4(i)) * (k4 + 1);


theta3(i) = 2 * atan2((-E - sqrt(E^2 - 4*D*F)), (2*D));


%% Finding Theta 5 and 6

theta5(i) = acos((r5(i)^2 + r3^2 - r6^2)/(2*r5(i)*r3)) + theta3(i);
theta6(i) = pi + theta3(i) - acos((r3^2 + r6^2 - r5(i)^2)/(2*r3*r6));



%% Rotation

theta1 = theta1-155*pi/180;
theta2(i) = theta2(i)-155*pi/180;
theta3(i) = theta3(i)-155*pi/180;
theta4(i) = theta4(i)-155*pi/180;
theta5(i) = theta5(i)-155*pi/180;
theta6(i) = theta6(i)-155*pi/180;

%% Calculating joint coordinates for animation purposes

% The following shifts place the model at the same location as on the
% Robojelly

shift_x = 12.375/R; % Length of link 1 normalized by radius
shift_y = - 0.0827 - 2.875/R - 0.0658; % shift based on location of flexion
                                       % point on robot data, distance between
                                       % mid-golf ball in inches and joint
location,
                                       % distance between joint 1 and
                                       % flexion point


x(i,:) = [ r1*cos(theta1),  r1*cos(theta1)+r2*cos(theta2(i)),
r4*cos(theta4(i)),...
    r4*cos(theta4(i))+r3*cos(theta3(i)),
r4*cos(theta4(i))+r5(i)*cos(theta5(i)),...
    r1*cos(theta1)+r2*cos(theta2(i))+ r6*cos(theta6(i)),...
```

```
    -r10*cos(theta10), -r10*cos(theta10) + r7(i), -r10*cos(theta10) + r7(i) +
r8*cos(theta8(i))] / R + shift_x;

y(i,:) = [ r1*sin(theta1),  r1*sin(theta1)+r2*sin(theta2(i)),
r4*sin(theta4(i)),...
    r4*sin(theta4(i))+r3*sin(theta3(i)),
r4*sin(theta4(i))+r5(i)*sin(theta5(i)),...
    r1*sin(theta1)+r2*sin(theta2(i))+ r6*sin(theta6(i)),...
    -r10*sin(theta10),  -r10*sin(theta10),  -r10*sin(theta10) +
r8*sin(theta8(i))] / R + shift_y;



end



%% Plot
figure('Color', 'white');
hh = plot([shift_x, x(1,1);x(1,1), x(1,2)],...
     [shift_y, y(1,1);y(1,1), y(1,2)],...
     [x(1,2), x(1,6)],...
     [y(1,2), y(1,6)],...
     [0, x(1,3);x(1,3), x(1,4)],...
     [0, y(1,3);y(1,3), y(1,4)],...
     [x(1,3), x(1,5)],...
     [y(1,3), y(1,5)],...
     [x(1,7), x(1,8)],...
     [y(1,7), y(1,8)],...
     [x(1,8), x(1,9)],...
     [y(1,8), y(1,9)],...
    '.-', 'MarkerSize', 20, 'LineWidth', 2);
axis equal
axis([0 1.2 -1 0.1]);
hold on
hh2 = plot(x(1,5), y(1,5),'o', 'MarkerSize', 2);
hold off
ht = title(sprintf('Theta4: %0.2f Degrees', theta4(1)*180/pi));

% Get figure size
pos = get(gcf, 'Position');
width = pos(3); height = pos(4);

% Preallocate data (for storing frame data)
mov = zeros(height, width, 1, length(theta4), 'uint8');

% Loop through by changing XData and YData
for id = 1:length(theta4)
    % Update graphics data. This is more efficient than recreating plots.
    set(hh(1), 'XData', [shift_x, x(id, 1)]              , 'YData', [shift_y,
y(id, 1)]);
    set(hh(2), 'XData', [x(id, 1), x(id, 2)]       , 'YData', [y(id, 1),
y(id, 2)]);
    set(hh(3), 'XData', [shift_x, x(id, 3)]              , 'YData', [shift_y,
y(id, 3)]);
```

```
    set(hh(4), 'XData', [x(id, 3), x(id, 4)]       , 'YData', [y(id, 3),
y(id, 4)]);
    set(hh(5), 'XData', [x(id, 3), x(id, 5)]       , 'YData', [y(id, 3),
y(id, 5)]);
    set(hh(6), 'XData', [x(id, 4), x(id, 6)]       , 'YData', [y(id, 4),
y(id, 6)]);
    set(hh(7), 'XData', [x(id, 7), x(id, 8)]       , 'YData', [y(id, 7),
y(id, 8)]);
    set(hh(8), 'XData', [x(id, 8), x(id, 9)]       , 'YData', [y(id, 8),
y(id, 9)]);
    set(ht, 'String', sprintf('Theta4: %0.2f Degrees', theta4(id)*180/pi));
    set(hh2(1), 'XData', x(1:id,5)                   , 'YData', y(1:id,5));

    % Get frame as an image
    f = getframe(gcf);

    % Create a colormap for the first frame. For the rest of the frames,
    % use the same colormap
    if id == 1
        [mov(:,:,1,id), map] = rgb2ind(f.cdata, 256, 'nodither');
    else
        mov(:,:,1,id) = rgb2ind(f.cdata, map, 'nodither');
    end
end

% Create animated GIF
imwrite(mov, map, 'animation.gif', 'DelayTime', 0, 'LoopCount', inf);


FP = [x(:,5) y(:,5)];

save(strcat(savebase,'Flexion Point','.txt'),'-ASCII','-tabs','FP')

%%
Theta3 = theta3 *180/pi;
Theta4 = theta4 *180/pi;

sqrt((x(1,2)-x(1,4))^2 + (y(1,2)-y(1,4))^2);
```

A.3 Profile Analysis

```
clc
clear
close all

Mov = 0;
Mov2 = 1;

f_s = 4;

Num = 218:5:488; %598; % the 523 is limited by the scale
```

```
Filter = 1;
Spline = 1;

file = 'Anato_c1';
% file = 'FullyOpt';

test = 'Frame_';

load(strcat('E:\Research\Robojelly\Cyanea\Bell
Kinematics\Profiles\','i_a','.txt'));

savebase = 'E:\Research\Robojelly\Cyanea\Bell Kinematics\';

p = 1;
n = 51;
point = 1:n;
Jstat = zeros(n,1);
J2stat = zeros(n,1);
tri = 1;
[B,A] = butter(2,.2,'low');

%%

for q = f_s:length(Num)

    Nums = num2str(Num(q));
    Nums2 = num2str(Num(q) + 275 - (f_s-1)*5);


clear x y xy xr yr xl yl d theta dtheta d_Fil theta_Fil xr_unfil yr_unfil...
    dl thetal dthetal d_Fill theta_Fill xl_unfil yl_unfil xf po fo L_sum...
    X Y S N Z CFdata cx cy L dthtds J

xy = load(strcat('E:\Research\Robojelly\Cyanea\Bell
Kinematics\Profiles\','Frame_','xy_Cor3_',Nums,'.txt'));

x = xy(:,1);
y = xy(:,2);

s = size(xy);


%% Differing between left and right profiles

l = i_a(p);
r = 1;
for i = 1:s(1)
   if i <= i_a(p)
       xl(l,1) = -x(i);
       yl(l,1) = y(i);
       l = l-1;
   end
```

```
   if i >= i_a(p)
       xr(r,1) = x(i);
       yr(r,1) = y(i);
       r = r+1;
   end
end

xr_unfil = xr;
yr_unfil = yr;
xl_unfil = xl;
yl_unfil = yl;




%% Filter

if Filter == 1

% Right Side

for i = 1:s(1)-i_a(p)+1
    d(i,1) = sqrt(xr(i)^2 + yr(i)^2);
    theta(i) = atan2(yr(i),xr(i));
end

d_Fil(:,1) = filtfilt(B,A,d);
theta_Fil(:,1) = filtfilt(B,A,theta);

for i = 1:s(1)-i_a(p)+1
xr(i) = d_Fil(i)*cos(theta_Fil(i));
yr(i) = d_Fil(i)*sin(theta_Fil(i));
end


% Left side

for i = 1:i_a(p)
    dl(i,1) = sqrt(xl(i)^2 + yl(i)^2);
    thetal(i) = atan2(yl(i),xl(i));
end


d_Fill(:,1) = filtfilt(B,A,dl);
theta_Fill(:,1) = filtfilt(B,A,thetal);

for i = 1:i_a(p)
xl(i) = d_Fill(i)*cos(theta_Fill(i));
yl(i) = d_Fill(i)*sin(theta_Fill(i));
end


end
```

```
% xyr = [xr yr];
% xyl = [xl yl];
%
% save(strcat(savebase,'Profiles\','Right_xy_',Nums,'.txt'),'-ASCII','-
tabs','xy')
% save(strcat(savebase,'Profiles\','Left_xy_',Nums,'.txt'),'-ASCII','-
tabs','xy')

%% Length Measurement

sr = length(xr);
sl = length(xl);
L(1) = 0;
Lsum_old = 0;
Lsum_oldl = 0;

for u = 1:sr(1) - 1
    L(u+1) = sqrt((xr(u)-xr(u+1))^2 + (yr(u)-yr(u+1))^2);

    Lsum = Lsum_old + L(u+1);
    Lsum_old = Lsum;
end

Ltotr(p) = Lsum;

for u = 1:sl(1) - 1
   Ll(u+1) = sqrt((xl(u)-xl(u+1))^2 + (yl(u)-yl(u+1))^2);

    Lsuml = Lsum_oldl + Ll(u+1);
    Lsum_oldl = Lsuml;
end

Ltotl(p) = Lsuml;


% Nyquist Frequency

FN(p) = length(xr)/(Ltotr(p)) * (1/89.83 * 1/1.234) / 2; % Nyquist frequency
samples per pixel


%%

%%%%%%%%%%%%%%%%%% Temporary - Looking at left side instead of right%%%%%%
%
% clear xr yr
%
% xr = xl;
% yr = yl;

%%%%%%%%%%%%%%%%%%%%%%%%%%%%%%%%%%%%%%%%%%%%%%%%%%%%%%%%%%%%%%%%%%%%%%%%%%%
```

```
%% Spline and Interpolation

if Spline == 1

X = zeros(n, size(xr,1)/2);
Y = zeros(n, size(xr,1)/2);
CFdata = zeros(n,size(xr,1));


    Z = cumsum(sqrt([0,diff(xr')].^2+[0,diff(yr')].^2))';   % arc length

    N = linspace(0,max(Z),n);

    [cx,~,~] = fit(Z,xr,'spline');     % curve fit f(L) = X, returns cfit
object
    [cy,~,~] = fit(Z,yr,'spline');     % curve fit f(L) = Y

    clear xr yr

    xr = feval(cx,N);
    yr = feval(cy,N);



end

s = length(xr);

%% Trajectory
%
xtipr(p) = xr(45);
ytipr(p) = yr(45);

i = 1;

if file == 'Anatomic'

    if p >= 24 && p<=50

xtraj1(tri) = xr(21);
ytraj1(tri) = yr(21);
xtraj2(tri) = xr(33);
ytraj2(tri) = yr(33);
xtraj3(tri) = xr(45);
ytraj3(tri) = yr(45);
xtraj4(tri) = xr(51);
ytraj4(tri) = yr(51);

traj1 = [xtraj1' ytraj1'];
traj2 = [xtraj2' ytraj2'];
traj3 = [xtraj3' ytraj3'];
traj4 = [xtraj4' ytraj4'];
```

```
tri = tri+1;
    end

elseif file == 'Anato_c1'
        if p <= 24

xtraj1(tri) = xr(21);
ytraj1(tri) = yr(21);
xtraj2(tri) = xr(33);
ytraj2(tri) = yr(33);
xtraj3(tri) = xr(45);
ytraj3(tri) = yr(45);
xtraj4(tri) = xr(51);
ytraj4(tri) = yr(51);

traj1 = [xtraj1' ytraj1'];
traj2 = [xtraj2' ytraj2'];
traj3 = [xtraj3' ytraj3'];
traj4 = [xtraj4' ytraj4'];

tri = tri+1;
    end

elseif file == 'FullyOpt'

    if p >= 24 && p<=50

xtraj1(tri) = xr(14);
ytraj1(tri) = yr(14);
xtraj2(tri) = xr(31);
ytraj2(tri) = yr(31);
xtraj3(tri) = xr(41);
ytraj3(tri) = yr(41);
xtraj4(tri) = xr(51);
ytraj4(tri) = yr(51);

traj1 = [xtraj1' ytraj1'];
traj2 = [xtraj2' ytraj2'];
traj3 = [xtraj3' ytraj3'];
traj4 = [xtraj4' ytraj4'];

tri = tri+1;
    end

end

% xtipr(p) = xr(end);
% ytipr(p) = yr(end);

%%%% Fixed first link %%%%%
% shift_x = 0.35843603; % these shifts are based on the location of point 19
in frame 288
% shift_y = -0.0071083899;
```

```
%
% xtiprff(p) = xr(42) -xr(19) + shift_x ;
% ytiprff(p) = yr(42) -yr(19) + shift_y ;
%%%%%%%%%%%%%%%%%%%%%%%%%%%%



xtipl(p) = xl(end);
ytipl(p) = yl(end);

% xtip = [xtipr'; xtipl'];
% ytip = [ytipr'; ytipl'];

tipr = [xtipr' ytipr'];
tipl = [xtipl' ytipl'];
% tipr = [xtiprff' ytiprff'];
% tipl = [xtipl' ytipl'];

if Num(q) >= 233 && Num(q) <= 358
xtipr_1c(p) = xr(42);
ytipr_1c(p) = yr(42);
end

%% Saving

xyr = [xr yr];
save(strcat(savebase,'Profiles\','Frame_','xyr_',Nums,'.txt'),'-ASCII','-
tabs','xyr')
xyl = [-xl yl];
save(strcat(savebase,'Profiles\','Frame_','xyl_',Nums,'.txt'),'-ASCII','-
tabs','xyl')


%%

%%%%%%%%%%%%%% Analyse One Frame %%%%%%%%%%%%%%%%%%%%%%%%%%%%%%%%%%%%

% if Num(q) >= 373 && Num(q) <=403
%   if   Num(q) == 288
%       figure (700)
%       plot(xr,yr)
%
%   end

%%%%%%%%%%%%%%%%%%%%%%%%%%%%%%%%%%%%%%%%%%%%%%%%%%%%%%%%%%%%%%%%%%%%%%%

%% Polynomial Fit

% if Num(q) == 263 | Num(q) == 288 | Num(q) == 298 | Num(q) == 308 | Num(q)
== 348
%
% nn = 4;
%
% % po = polyfit(xr, yr, nn);
```

```
% % fo = polyval(po,xr);
%
% for i = 1:51
%     dp(i,1) = sqrt(xr(i)^2 + yr(i)^2);
%     thetap(i) = atan2(yr(i),xr(i));
% end
%
% po = polyfit(thetap', dp, nn)
% fo = polyval(po,thetap);
%
% for i = 1:51
% xp(i) = fo(i)*cos(thetap(i));
% yp(i) = fo(i)*sin(thetap(i));
% end
%
% order = num2str(n);
%
% % xf = [xr fo];
% xf = [xr yr];
%
% save(strcat(savebase,'Polynomial
Fits\',test,'_poly_Fully_Opt',order,'.txt'), 'xf', '-ASCII')
%
% figure
% plot(xr,fo,'r')
% plot(xp,yp,'r')
% % axis([0 150 -120 20])
% hold on
% plot(xr, yr)
% hold off
% end

%% Arclength
S(1) = 0;
Lsum_old = 0;
for u = 1:s(1)-1
    L_temp = sqrt((xr(u)-xr(u+1))^2 + (yr(u)-yr(u+1))^2);

    S(u+1) = Lsum_old + L_temp;
    Lsum_old = S(u+1);
end



%% Curvature
a = 1;
b = -a;
j = 1;
for i = 1+a:s(1) - a%s(1)-i_a(p)+1 - a

R(j,p) = ( sqrt( (xr(i+b) - xr(i))^2 + (yr(i+b) - yr(i))^2)...
    * sqrt( (xr(i) - xr(i+a))^2 + (yr(i) - yr(i+a))^2)...
    * sqrt( (xr(i+a) - xr(i+b))^2 + (yr(i+a) - yr(i+b))^2))...
    /(2 * (xr(i)*yr(i+b) - xr(i+b)*yr(i) + xr(i+a)*yr(i) - xr(i)*yr(i+a) +
xr(i+b)*yr(i+a) - xr(i+a)*yr(i+b)));

C(j,p) = 1/R(j,p);
```

```
j = j+1;
end
%


%% Change in Curvature
h = 1;
j = 1;
for i = 1:s(1)-2*a

    if i <= h
        dC(j,p) = (C(i+h,p) - C(i,p)) / (S(i+h) - S(i));
    elseif i >=s(1)-h-2*a
        dC(j,p) = (C(i,p) - C(i-h,p)) / (S(i) - S(i-h));
    else
        dC(j,p) = (C(i+h,p) - C(i-h,p)) / (S(i+h) - S(i-h));
    end


    j = j+1;
end



    [peaks J2] = findpeaks(C(:,p));
    J2 = J2';

    for j = 1:length(J2)
    for i = 1:n
        if J2(j,1) == point(i)
            J2stat(i,1) = J2stat(i,1) + 1*peaks(j);
        else
            J2stat(i,1) = J2stat(i,1) + 0;
        end
    end
end

save(strcat(savebase,'Joints\','Joints2_',Nums,'.txt'),'-ASCII','-tabs','J2')



% %    if Num(q) == 373

% figure(5)
% plot(1+a:s(1)-a, C(:,p))
% hold on
% plot(19, C(19-a,p),'.' ,'MarkerSize', 20)
% plot(33, C(33-a,p), 'r.', 'MarkerSize', 20)
% plot(42, C(42-a,p),'g.','MarkerSize', 20)
% title('Curvature 19, 33, 42')
```

```
% figure(6)
% plot(xr,yr)
% title('19, 33, 42')
% hold on
% plot(xr(19),yr(19),'.', 'MarkerSize', 20)
% plot(xr(33),yr(33), 'r.', 'MarkerSize', 20)
% plot(xr(42),yr(42),'g.', 'MarkerSize', 20)
% axis([0 1.4 -1.2 .2])
% hold off


%
% figure(77)
% plot(1+a:s(1)-a, dC(:,p))
% xlabel('i')
% ylabel('dC')
% % end


%% Derivative

h = 3;
j = 1;
for i = 1:s(1)%s(1)-i_a(p)+1 - h

    if i <= h
        dydx(j) = (yr(i+h) - yr(i)) / (xr(i+h) - xr(i));
    elseif i >=s(1)-h
        dydx(j) = (yr(i) - yr(i-h)) / (xr(i) - xr(i-h));
    else
        dydx(j) = (yr(i+h) - yr(i-h)) / (xr(i+h) - xr(i-h));
    end


    j = j+1;
end


%% Angle of Each tangent lines

% Using 2 points

h = 2;  % Uses one point located h point before and one point located h point
after
j = 1;
for i = 1:s(1)%s(1)-i_a(p)+1 - h

    if i <= h
        tht(j) = atan2((yr(i+h) - yr(i)), (xr(i+h) - xr(i)));
    elseif i >=s(1)-h
        tht(j) = atan2((yr(i) - yr(i-h)), (xr(i) - xr(i-h)));
    else
        tht(j) = atan2((yr(i+h) - yr(i-h)), (xr(i+h) - xr(i-h)));
    end
```

```
    j = j+1;
end


%% Using Linear Fit
%
% g = 1;
% m = 1;
%
% for i = 1:s(1)
%     clear kt
%     sum_xy = 0;
%     sum_xx = 0;
%
%  if i <= m
%
%     for j = 0:m+1
%         kt = 0:m+1;
%         xr_m(i+j) = xr(i+j)-xr(i+m); % adjust the /2 to zero data
accordingly
%         yr_m(i+j) = yr(i+j)-yr(i+m);
%
%         sum_xy_t = xr_m(i+j)*yr_m(i+j);
%         sum_xx_t = xr_m(i+j)*xr_m(i+j);
%
%         sum_xy = sum_xy_t + sum_xy;
%         sum_xx = sum_xx_t + sum_xx;
%
%     end
%
%  elseif i > s(1)-m
%
%     for j = -m-1:0
%         kt = -m-1:0;
%         xr_m(i+j) = xr(i+j)-xr(i-m); % adjust the /2 to zero data
accordingly
%         yr_m(i+j) = yr(i+j)-yr(i-m);
%
%         sum_xy_t = xr_m(i+j)*yr_m(i+j);
%         sum_xx_t = xr_m(i+j)*xr_m(i+j);
%
%         sum_xy = sum_xy_t + sum_xy;
%         sum_xx = sum_xx_t + sum_xx;
%
%     end
%
%  else
%     kt = -m:m;
%     xr_msum = 0;
%     yr_msum = 0;
%
%     for j = -m:m
%         xr_mt = xr(i+j);
%         xr_msum = xr_mt + xr_msum;
```

```
%         yr_mt = yr(i+j);
%         yr_msum = yr_mt + yr_msum;
%     end
%
%         xr_m(i+j) = xr(i+j) - (xr_msum) / length(kt);
%         yr_m(i+j) = yr(i+j) - (yr_msum) / length(kt);
%
%     for j = -m:m
%         sum_xy_t = xr_m(i+j)*yr_m(i+j);
%         sum_xx_t = xr_m(i+j)*xr_m(i+j);
%
%         sum_xy = sum_xy_t + sum_xy;
%         sum_xx = sum_xx_t + sum_xx;
%
%     end
%
%
% %      if xr(i + kt(1)) >= xr(i + kt(end)) && yr(i + kt(1)) >= yr(i +
kt(end))
% %      sum_xx = -sum_xx;
% %      sum_xy = -sum_xy;
% %      end
% %
% %      if xr(i + kt(1)) > xr(i + kt(end)) && yr(i + kt(1)) < yr(i +
kt(end))
% %      sum_xx = sum_xx;
% %      sum_xy = -sum_xy;
% %      end
%
%  end
%
%



% tht_l(g) = atan2(sum_xy, sum_xx);

%    if g>1 && tht_l(g) > 0.4
%        tht_l(g) =  tht_l(g) - pi;
%
% %    if tht_l(g) > pi/4
% %        tht_l(g) = tht_l(g) -pi;
% %    end
%    end

%    g = g+1;
%
% end
%
% %
% % if Num(q) == 488
% figure(500)
% plot(tht)
% hold on
% plot(tht_l)
% % hold off
```

```
% % end


%% Tangent Angle : Calculates the Angle Between two Tangent Lines

k=2;
j=1;

if p == 1
    TA_sum = zeros(length(tht)-2*k,1);
end

for i = 1+k:length(tht)-k

    TA(j,p) = pi-(tht(i-k) - tht(i+k));

    TA_sum(j) = TA(j,p) + TA_sum(j);

    j=j+1;
end




% for i = 1+k:s(1)-k
%
%     TA(j,p) = ((tht_l(i+k)) - (tht_l(i-k)));
%
% j=j+1;
% end

%% Tangent Angle Derivative

h = 1;
j = 1;
for i = 1:s(1)-2*k

    if i <=h
        dthtds(j) = (TA(i+h, p) - TA(i, p)) / (S(i+h+k));
    elseif i >=s(1)-2*k-h
        dthtds(j) = (TA(i, p) - TA(i-h, p)) / (S(i-h+k));
    else
        dthtds(j) = (TA(i+h, p) - TA(i-h, p)) / (S(i+k) - S(i-h+k));
    end

    j = j+1;
end



%
% figure(7)
% plot(point(1+k:end-k), dthtds,'r')
% hold on
```

```
% plot([0 s(1)-k],[0 0])
% % hold off


%% Joint Detection

j = 1;
for i = 1:s(1)-2*k-1
if dthtds(i) > 0 && dthtds(i+1) < 0

    if abs(dthtds(i)) < abs(dthtds(i+1))
        J(j,1) = point(i) + k;
        j = j+1;
    else
        J(j,1) = point(i+1) + k;
        j = j+1;
    end


elseif dthtds(i) < 0 && dthtds(i+1) > 0

    if abs(dthtds(i)) < abs(dthtds(i+1))
        J(j,1) = point(i) + k;
        j = j+1;
    else
        J(j,1) = point(i+1) + k;
        j = j+1;
    end

end

end

%%
% figure(8)
% % plot(1:length(xr), tht,'g')
% hold on
% % plot(1+k:length(TA(:,1))+k, -TA(:, p)/4,'r')
% plot(1+k:length(TA(:,1))+k, TA(:, p),'r')
% ylabel('TA')
% % plot(xr(1+h:end-h), (tht-pi),'r')
% % axis([0 1.4 -1.2 .2])
% % plot(J,ones(length(J)),'b.','MarkerSize',15)
% hold on
% % plot(xr, yr)
% % hold off
% % ylabel('Angle(rad*20), y')
% % xlabel('x')
% title(Nums)
% % legend('Angle', 'Profile')

%% Stastistics
```

```
for j = 1:length(J)
    for i = 1:n
        if J(j,1) == point(i)
            Jstat(i,1) = Jstat(i,1) + 1;
        else
            Jstat(i,1) = Jstat(i,1) + 0;
        end
    end
end

save(strcat(savebase,'Joints\','Joints_',Nums,'.txt'),'-ASCII','-tabs','J')

%%

%%%%%%%%%% For one frame analysis %%%%%%%%%%%%%%%%%%%%

% end
%%%%%%%%%%%%%%%%%%%%%%%%%%%%%%%%%%%%%%%%%%%%%%%%%%%%%%%%%%%%%%%%%%%%%%%

%% Angles Between Links

if file == 'FullyOpt'
FO = 1;

p1=14;
p2=31;
p3=41;
p4=51;

end

if file == 'Anatomic' | 'Anato_c1'
FO = 0;
p1=21;
p2=33;
p3=45;
p4=51;

end

        tht1_t = atan2((yr(p1) - 0), (xr(p1) - 0));
        tht2_t = atan2((yr(p2) - yr(p1)), (xr(p2) - xr(p1)));
        tht3_t = atan2((yr(p3) - yr(p2)), (xr(p3) - xr(p2)));
        tht4_t = atan2((yr(p4) - yr(p3)), (xr(p4) - xr(p3)));

tht1(p) = (pi + tht1_t)*180/pi;
tht2(p) = (pi + tht2_t - tht1_t)*180/pi;
tht3(p) = (pi + tht3_t - tht2_t)*180/pi;
tht4(p) = (pi + tht4_t - tht3_t)*180/pi;

%% Link Lengths

LL1(p) = sqrt((0 - xyr(p1,1))^2 + (0 - xyr(p1,2))^2);
LL2(p) = sqrt((xyr(p2,1) - xyr(p1,1))^2 + (xyr(p2,2) - xyr(p1,2))^2);
```

```
LL3(p) = sqrt((xyr(p3,1) - xyr(p2,1))^2 + (xyr(p3,2) - xyr(p2,2))^2);
LL4(p) = sqrt((xyr(p4,1) - xyr(p3,1))^2 + (xyr(p4,2) - xyr(p3,2))^2);



%<greek>q</greek><sub>1</sub>
% if Num(q) == 253 | Num(q) == 263 | Num(q) == 288 | Num(q) == 298 | Num(q)
== 308 | Num(q) == 348
if Num(q) == 383 | Num(q) == 418 | Num(q) == 428 | Num(q) == 478  % this is
for cycle 2
Links = [0 0; xyr(p1,1) xyr(p1,2);xyr(p2,1) xyr(p2,2); xyr(p3,1) xyr(p3,2);
xyr(p4,1) xyr(p4,2)]
save(strcat(savebase,'Links\','Links_',file,Nums,'.txt'),'-ASCII','-
tabs','Links')
end

if file == 'Anato_c1' % thsi  is for cycle 1
if Num(q) == 233 | Num(q) == 263 | Num(q) == 288 | Num(q) == 313
Links = [0 0; xyr(p1,1) xyr(p1,2);xyr(p2,1) xyr(p2,2); xyr(p3,1) xyr(p3,2);
xyr(p4,1) xyr(p4,2)]
save(strcat(savebase,'Links\','Links_',file,Nums,'.txt'),'-ASCII','-
tabs','Links')
end
end

p = p+1;
end


TA_avg = TA_sum/(length(Num)-f_s);

sig_sum = zeros(length(TA),1);
p = 1;

N = length(f_s:length(Num))

for i = 1:length(TA_avg)

    for p = 1:N
        sig_sum(i) = (TA(i,p) - TA_avg(i))^2 + sig_sum(i);
    end

    sig(i,1) = sqrt(1/N * sig_sum(i));

end




figure(8)
plot(1+k:length(TA_avg(:,1))+k, TA_avg)
hold on
plot(1+k:length(TA_avg(:,1))+k, (TA_avg + sig))
```

```
plot(1+k:length(TA_avg(:,1))+k, (TA_avg - sig))
hold off
TangentAngle = [((1+k:length(TA_avg(:,1))+k)'-1) * 2, TA_avg *180/pi,
sig*180/pi];
save(strcat(savebase,'TA\','TangentAngle_Left','.txt'),'-ASCII','-
tabs','TangentAngle')
save(strcat(savebase,'TA\','Std','.txt'),'-ASCII','-tabs','sig')

figure(81)
plot(TangentAngle(:,1), TangentAngle(:,2))
hold on
plot(TangentAngle(:,1), (TangentAngle(:,2) + TangentAngle(:,3)))
plot(TangentAngle(:,1), (TangentAngle(:,2) - TangentAngle(:,3)))
hold off



save(strcat(savebase,'Profiles\','Flexion Point
Trajectory','_Right','.txt'),'-ASCII','-tabs','tipr')
save(strcat(savebase,'Profiles\','Flexion Point
Trajectory','_Left','.txt'),'-ASCII','-tabs','tipl')

save(strcat(savebase,'Profiles\','Trajectory_',file,'_1','.txt'),'-ASCII','-
tabs','traj1')
save(strcat(savebase,'Profiles\','Trajectory_',file,'_2','.txt'),'-ASCII','-
tabs','traj2')
save(strcat(savebase,'Profiles\','Trajectory_',file,'_3','.txt'),'-ASCII','-
tabs','traj3')
save(strcat(savebase,'Profiles\','Trajectory_',file,'_4','.txt'),'-ASCII','-
tabs','traj4')


%%%% Fixed First link
% save(strcat(savebase,'Profiles\','Flexion Point Trajectory Fixed First
Link','_Right','.txt'),'-ASCII','-tabs','tipr')
% save(strcat(savebase,'Profiles\','Flexion Point Trajectory Fixed First
Link','_Left','.txt'),'-ASCII','-tabs','tipl')


tip_1c = [xtipr_1c' ytipr_1c'];
save(strcat(savebase,'Profiles\','Flexion
Point','_Right_1st_cycle','.txt'),'-ASCII','-tabs','tip_1c')

g = 1;
for j = 1:length(TA(:,1))

sum_STA = 0;
sum_SS = 0;

    for i = 1:length(TA(1,:))

        sum_STA_t = S(j)*TA(j,i);
        sum_SS_t = S(j)*S(j);
```

```
        sum_STA = sum_STA_t + sum_STA;
        sum_SS = sum_SS_t + sum_SS;

    end

    a_TA(j) = sum_STA/ sum_SS;

    TA_lf(j) = a_TA(j)*S(j);
end
% figure(400)
% plot(-TA_lf)


% dCdt

h = 1;
j = 1;


for i = 1:length(TA(:,1))
    j = 1;
    for g = 1:length(TA(1,:)) %time

    if g <= h
        dCdt(i,j) = (TA(i, g+h) - TA(i, g)) / 1;  % Change Time value for
accuracy
    elseif g >=length(TA(1,:))-h
        dCdt(i,j) = (TA(i, g) - TA(i, g-h)) / 1;
    else
        dCdt(i,j) = (TA(i, g+h) - TA(i, g-h)) / 2;
    end


    j = j+1;
end
end


% figure(401)
% plot(1:52,dCdt(:,:))
% figure(402)
% plot(C(:,:))


% Plotting angle change between links

figure(10)
% plot(Num(4:end), tht1*180/pi, Num(4:end), tht2*180/pi, Num(4:end),
tht3*180/pi, Num(4:end), tht4*180/pi, Num(4:end), tht5*180/pi)
% legend('tht1','tht2','tht3','tht4','tht5')

% plot(Num(4+22:end), tht1(23:end), Num(4+22:end), tht2(23:end),
Num(4+22:end), tht3(23:end), Num(4+22:end), tht4(23:end))
```

```
plot(Num(4:end), tht1, Num(4:end), tht2, Num(4:end), tht3, Num(4:end), tht4)
legend('\theta_1','\theta_2','\theta_3','\theta_4')
xlabel('Frame')
ylabel('Angle (Deg)')


t = (Num(4:end)-Num(4))*1/25; % 25 FPS

Angle1 = [t' tht1'];
Angle2 = [t' tht2'];
Angle3 = [t' tht3'];
Angle4 = [t' tht4'];
save(strcat(savebase,'Links\','Angle1','_4_',file,'.txt'),'-ASCII','-
tabs','Angle1')
save(strcat(savebase,'Links\','Angle2','_4_',file,'.txt'),'-ASCII','-
tabs','Angle2')
save(strcat(savebase,'Links\','Angle3','_4_',file,'.txt'),'-ASCII','-
tabs','Angle3')
save(strcat(savebase,'Links\','Angle4','_4_',file,'.txt'),'-ASCII','-
tabs','Angle4')


% Plotting Link Lenghts
figure(11)
plot(Num(4:end), LL1, Num(4:end), LL2, Num(4:end), LL3, Num(4:end), LL4)
legend('Link_1','Link_2','Link_3','Link_4')
xlabel('Frame')
ylabel('Length')


Length1 = [t' LL1'];
Length2 = [t' LL2'];
Length3 = [t' LL3'];
Length4 = [t' LL4'];
save(strcat(savebase,'Links\','Length1','_4_',file,'.txt'),'-ASCII','-
tabs','Length1')
save(strcat(savebase,'Links\','Length2','_4_',file,'.txt'),'-ASCII','-
tabs','Length2')
save(strcat(savebase,'Links\','Length3','_4_',file,'.txt'),'-ASCII','-
tabs','Length3')
save(strcat(savebase,'Links\','Length4','_4_',file,'.txt'),'-ASCII','-
tabs','Length4')


% Plotting Arclengths

figure(13)
plot(Num(f_s:end), Ltotr, Num(f_s:end), Ltotl)
legend('Right', 'Left')

% Plotting Nyquist Frequency

% figure(9)
% plot(Num(f_s:end),FN)
```

```
%% Movie Making 1
if Mov == 1

xy2 = load(strcat('E:\Research\Robojelly\Cyanea\Bell
Kinematics\Profiles\','Frame_xyr_','233','.txt'));


figure(100)
hh = plot(xy2(:,1),xy2(:,2),'r')
hold on
hh2 = plot(0, 0, '.', 'MarkerSize', 20)
xt1 = plot(xtip, ytip,'-o', 'MarkerSize', 2)
hold off
axis([0 1.4 -1.2 .2])
ht = title(sprintf('Frame: %0.2f', Num(f_s)));

% Get figure size
pos = get(gcf, 'Position');
width = pos(3); height = pos(4);

Tum = 218:5:Num(end) + 275 - (f_s-1)*5;

% Preallocate data (for storing frame data)
mov = zeros(height, width, 1, length(Tum)-f_s, 'uint8');


id = 1;
for P = f_s:length(Tum)

    clear xy2

Nums = num2str(Tum(P));

xy2 = load(strcat('E:\Research\Robojelly\Cyanea\Bell
Kinematics\Profiles\','Frame_xy2_',Nums,'.txt'));

set(hh(1), 'XData', xy2(:,1)  , 'YData', xy2(:,2));
set(hh2(1), 'XData', 0  , 'YData', 0);
set(xt1(1), 'XData', xtip(1:id)  , 'YData', ytip(1:id));
set(ht, 'String', sprintf('Frame: %0.2f', Tum(P)));

% Get frame as an image
    f = getframe(gcf);

    % Create a colormap for the first frame. For the rest of the frames,
    % use the same colormap
    if id == 1
        [mov(:,:,1,id), map] = rgb2ind(f.cdata, 256, 'nodither');
    else
        mov(:,:,1,id) = rgb2ind(f.cdata, map, 'nodither');
    end
```

```
    id = id+1;
end

% Create animated GIF
imwrite(mov, map, 'animation3.gif', 'DelayTime', 0, 'LoopCount', inf);

end

%% Movie Making 2


if Mov2 == 1


xyr = load(strcat('E:\Research\Robojelly\Cyanea\Bell
Kinematics\Profiles\','Frame_xyr_','233','.txt'));
xyl = load(strcat('E:\Research\Robojelly\Cyanea\Bell
Kinematics\Profiles\','Frame_xyl_','233','.txt'));


figure(100)
%%% Five Links
% hh = plot(xyr(:,1),xyr(:,2),'r')
% hold on
% hh2 = plot(0, 0, '.', 'MarkerSize', 20)
% hh4 = plot([0 xyr(p1,1);xyr(p1,1) xyr(23,1)],...
%     [0 xyr(p1,2);xyr(p1,2) xyr(23,2)],'.-', 'MarkerSize', 15)
% hh5 = plot([xyr(23,1) xyr(33,1);xyr(33,1) xyr(p3,1)],...
%     [xyr(23,2) xyr(33,2);xyr(33,2) xyr(p3,2)],'.-', 'MarkerSize', 15)
% hh6 = plot([xyr(p3,1) xyr(47,1)],...
%     [xyr(p3,2) xyr(47,2)],'.-', 'MarkerSize', 15)

%%% Three links

%%%% Fixed first link %%%%%
% xyrff(p2,1) = xyr(p2,1) -xyr(p1,1) + shift_x;
% xyrff(p2,2) = xyr(p2,2) -xyr(p1,2) + shift_y;
% xyrff(p3,1) = xyr(p3,1) -xyr(p1,1) + shift_x;
% xyrff(p3,2) = xyr(p3,2) -xyr(p1,2) + shift_y;
% xyrff(p4,1) = xyr(p4,1) -xyr(p1,1) + shift_x;
% xyrff(p4,2) = xyr(p4,2) -xyr(p1,2) + shift_y;
%
% xyrff(p1,1) = xyr(p1,1) -xyr(p1,1) + shift_x;
% xyrff(p1,2) = xyr(p1,2) -xyr(p1,2) + shift_y;
%%%%%%%%%%%%%%%%%%%%%%%%%%


hh = plot(xyr(:,1),xyr(:,2),'r')
hold on
hh2 = plot(0, 0, '.', 'MarkerSize', 20)
hh4 = plot([0 xyr(p1,1);xyr(p1,1) xyr(p2,1)],...
    [0 xyr(p1,2);xyr(p1,2) xyr(p2,2)],'.-', 'MarkerSize', 15)
hh5 = plot([xyr(p2,1) xyr(p3,1)],...
```

```
    [xyr(p2,2) xyr(p3,2)],'.-', 'MarkerSize', 15)

hh6 = plot([xyr(p3,1) xyr(p4,1)],...
    [xyr(p3,2) xyr(p4,2)],'.-', 'MarkerSize', 15)


xt1 = plot(xtraj1, ytraj1,'-o', 'MarkerSize', 2)
xt2 = plot(xtraj2, ytraj2,'-o', 'MarkerSize', 2)
xt3 = plot(xtraj3, ytraj3,'-o', 'MarkerSize', 2)
xt4 = plot(xtraj4, ytraj4,'-o', 'MarkerSize', 2)

%% Fixed First Link
% hh = plot(xyr(:,1),xyr(:,2),'r')
% hold on
% hh2 = plot(0, 0, '.', 'MarkerSize', 20)
% hh4 = plot([0 xyrff(p1,1);xyrff(p1,1) xyrff(p2,1)],...
%     [shift_y xyrff(p1,2);xyrff(p1,2) xyrff(p2,2)],'.-', 'MarkerSize', 15)
% hh5 = plot([xyrff(p2,1) xyrff(p3,1)],...
%     [xyrff(p2,2) xyrff(p3,2)],'.-', 'MarkerSize', 15)
% hh6 = plot([xyrff(p3,1) xyrff(p4,1)],...
%     [xyrff(p3,2) xyrff(p4,2)],'.-', 'MarkerSize', 15)
%
% xt1 = plot(xtiprff, ytiprff,'-o', 'MarkerSize', 2)

hold off
axis([0 1.4 -1.2 .2])
ht = title(sprintf('Frame: %0.2f', Num(f_s)));

% Get figure size
pos = get(gcf, 'Position');
width = pos(3); height = pos(4);

Tum = 218:5:Num(end) + 275 - (f_s-1)*5;

% Preallocate data (for storing frame data)
mov = zeros(height, width, 1, length(Num)-f_s, 'uint8');



id = 1;
for P = f_s:length(Num)

    clear xyr xyl

Nums = num2str(Num(P));

xyr = load(strcat('E:\Research\Robojelly\Cyanea\Bell
Kinematics\Profiles\','Frame_xyr_',Nums,'.txt'));
xyl = load(strcat('E:\Research\Robojelly\Cyanea\Bell
Kinematics\Profiles\','Frame_xyl_',Nums,'.txt'));


%%%% Fixed first link %%%%%
% xyrff(p2,1) = xyr(p2,1) -xyr(p1,1) + shift_x;
```

```
% xyrff(p2,2) = xyr(p2,2) -xyr(p1,2) + shift_y;
% xyrff(p3,1) = xyr(p3,1) -xyr(p1,1) + shift_x;
% xyrff(p3,2) = xyr(p3,2) -xyr(p1,2) + shift_y;
% xyrff(p4,1) = xyr(p4,1) -xyr(p1,1) + shift_x;
% xyrff(p4,2) = xyr(p4,2) -xyr(p1,2) + shift_y;
%
% xyrff(p1,1) = xyr(p1,1) -xyr(p1,1) + shift_x;
% xyrff(p1,2) = xyr(p1,2) -xyr(p1,2) + shift_y;
%%%%%%%%%%%%%%%%%%%%%%%%%%%%


set(hh(1), 'XData', xyr(:,1)  , 'YData', xyr(:,2));
% set(hh3(1), 'XData', xyl(:,1)  , 'YData', xyl(:,2));

% set(hh4(1), 'XData', [0, xyr(p1,1)]  , 'YData', [0, xyr(p1,2)]);
% set(hh4(2), 'XData', [xyr(p1,1), xyr(23,1)]  , 'YData', [xyr(p1,2),
xyr(23,2)]);
% set(hh5(1), 'XData', [xyr(23,1), xyr(33,1)]  , 'YData', [xyr(23,2),
xyr(33,2)]);
% set(hh5(2), 'XData', [xyr(33,1), xyr(p3,1)]  , 'YData', [xyr(33,2),
xyr(p3,2)]);
% set(hh6(1), 'XData', [xyr(p3,1), xyr(47,1)]  , 'YData', [xyr(p3,2),
xyr(47,2)]);

%%%%%%%%%%%% GOOD One
set(hh4(1), 'XData', [0, xyr(p1,1)]  , 'YData', [0, xyr(p1,2)]);
set(hh4(2), 'XData', [xyr(p1,1), xyr(p2,1)]  , 'YData', [xyr(p1,2),
xyr(p2,2)]);
set(hh5(1), 'XData', [xyr(p2,1), xyr(p3,1)]  , 'YData', [xyr(p2,2),
xyr(p3,2)]);

set(hh6(1), 'XData', [xyr(p3,1), xyr(p4,1)]  , 'YData', [xyr(p3,2),
xyr(p4,2)]);

set(xt1(1), 'XData', xtraj1(1:id)  , 'YData', ytraj1(1:id));
set(xt2(1), 'XData', xtraj2(1:id)  , 'YData', ytraj2(1:id));
set(xt3(1), 'XData', xtraj3(1:id)  , 'YData', ytraj3(1:id));
set(xt4(1), 'XData', xtraj4(1:id)  , 'YData', ytraj4(1:id));
%%%%%%%

%%%% Fixed First link
% set(hh4(1), 'XData', [0, xyrff(p1,1)]  , 'YData', [shift_y, xyrff(p1,2)]);
% set(hh4(2), 'XData', [xyrff(p1,1), xyrff(p2,1)]  , 'YData', [xyrff(p1,2),
xyrff(p2,2)]);
% set(hh5(1), 'XData', [xyrff(p2,1), xyrff(p3,1)]  , 'YData', [xyrff(p2,2),
xyrff(p3,2)]);
% set(hh6(1), 'XData', [xyrff(p3,1), xyrff(p4,1)]  , 'YData', [xyrff(p3,2),
xyrff(p4,2)]);
%
%
% set(xt1(1), 'XData', xtiprff(1:id)  , 'YData', ytiprff(1:id));
%%%%%%%


set(hh2(1), 'XData', 0  , 'YData', 0);
```

```
set(ht, 'String', sprintf('Frame: %0.2f', Num(P)));



% Get frame as an image
    f = getframe(gcf);

    % Create a colormap for the first frame. For the rest of the frames,
    % use the same colormap
    if id == 1
        [mov(:,:,1,id), map] = rgb2ind(f.cdata, 256, 'nodither');
    else
        mov(:,:,1,id) = rgb2ind(f.cdata, map, 'nodither');
    end

    id = id+1;
end

% Create animated GIF
imwrite(mov, map, 'animation3.gif', 'DelayTime', 0, 'LoopCount', inf);


end
%
% set(hh4(1), 'XData', [0 xyr(p1,1);xyr(p1,1) xyr(23,1);xyr(23,1)
xyr(33,1);xyr(33,1) xyr(p3,1);xyr(p3,1) xyr(47,1)]...
%     , 'YData', [0 xyr(p1,2);xyr(p1,2) xyr(23,2);xyr(23,2)
xyr(33,2);xyr(33,2) xyr(p3,2);xyr(p3,2) xyr(47,2)]);



%% Joints
%
% for P = f_s:length(Num)
%     clear J
%     Nums = num2str(Num(P));
% J = load(strcat('E:\Research\Robojelly\Cyanea\Bell
Kinematics\Joints\','Joints_',Nums,'.txt'));
% % figure(200)
% % plot(J, Num(P),'.', 'MarkerSize', 15)
% % hold on
% end
% % hold off
% %

% figure(201)
% plot(Jstat)
% title('TA')

% Running Average

h = 2;
j = 1;
    for i = 1+h:n-h
```

```
        Jstat_av(j,1) = Jstat(i-h,1) + Jstat(i-h+1,1)+Jstat(i,1)+Jstat(j+h-
1,1)+Jstat(i+h,1);
        j = j+1;
    end

% figure(203)
% plot(3:s(1)-2, Jstat_av)
% title('TA avg')



% for P = f_s:length(Num)
%     clear J
%     Nums = num2str(Num(P));
% J2 = load(strcat('E:\Research\Robojelly\Cyanea\Bell
Kinematics\Joints\','Joints2_',Nums,'.txt'));
%
% end


% figure(301)
% plot(J2stat)
% title('Curvature avg')


% Time variation

% t = 1:length(TA(3,:));
% figure(202)
% plot(t, TA(3,:), t, TA(10,:), t, TA(15,:), t, TA(19,:), t, TA(22,:), t,
TA(33,:), t, TA(42,:), t, TA(40,:), t, TA(45,:))
% hold off
% legend('3','10','15','19','22','33','42','40','45')
%
%
% t = 1:length(C(3,:));
% figure(203)
% plot(t, C(3+1,:), t, C(10+1,:), t, C(15+1,:), t, C(19+1,:), t, C(22+1,:),
t, C(31+1,:), t, C(40+1,:), t, C(42+1,:))
% hold off
% legend('3','10','15','19','22','31','40','42')
```

A.4 Angle Processing

```
clc
clear
close all




name = 'Anatomical';
% name = 'Fully_Opt';


for i = 1:4
    file = strcat('Angle',num2str(i),'_4_',name)


    if i == 1
        model = 'fourier3';
    elseif i == 2
        model = 'fourier3';
    elseif i == 3
        model = 'fourier4';
    else
        model = 'fourier3';
    end

% Cycle 1
% Num = 233:5:343;

% Cycle 2
% Num = 343:5:488;


test = 'Frame_xyr_';
Directory = 'E:\Research\Robojelly\Cyanea\Bell Kinematics\Links\';
savebase = 'E:\Research\Robojelly\Cyanea\Bell Kinematics\Links\';

tA = load(strcat(Directory,file,'.txt'));

% t = tA(1:23, 1);
% A = tA(1:23, 2);

tt = tA(23+1:52-2, 1);
At = tA(23+1:52-2, 2);
A = [At;At;At;At;At;At;At;At;At];
t =
[tt;tt+5.4;tt+5.4*2;tt+5.4*3;tt+5.4*4;tt+5.4*5;tt+5.4*6;tt+5.4*7;tt+5.4*8] -
tt(1);

figure
plot(tA(:,1), tA(:,2),'r')
hold on
```

```
plot(tt(:,1), At(:,1))
hold off
figure
plot(t(:,1), A(:,1))

% Fourier Series Fit

n = 1000%243;

    N = linspace(0,max(t),n);

    [cy,~,~] = fit(t,A,model)     % curve fit f(t) = Y

    yr = feval(cy,N);

figure
plot(t, A)
hold on
plot(N,yr,'r')
hold off


fit_f = [(N'-2.6) yr];
Orig = [(t-2.6) A];

% fit_f = [(N(55:end)'-2.6) yr(55:end)];
% Orig = [(t(14:end)-2.6) A(14:end)];
% fit_f = [N' yr];

save(strcat(savebase,file,'_Fourier_Fit','.txt'), 'fit_f', '-ASCII')
save(strcat(savebase,file,'_Original','.txt'), 'Orig', '-ASCII')

end
```

A.5 Length Processing

```
clc
clear
close all


model = 'fourier2';

name = 'Anatomical';
% name = 'Fully_Opt';


for i = 1:4
    file = strcat('Length',num2str(i),'_4_',name)
```

```
% Cycle 1
% Num = 233:5:343;

% Cycle 2
% Num = 343:5:488;

% LL1(p) = sqrt((0 - xyr(p1,1))^2 + (0 - xyr(p1,2))^2)/.2982;
% LL2(p) = sqrt((xyr(p2,1) - xyr(p1,1))^2 + (xyr(p2,2) -
xyr(p1,2))^2)/0.3899;
% LL3(p) = sqrt((xyr(p3,1) - xyr(p2,1))^2 + (xyr(p3,2) - xyr(p2,2))^2)/.2245;
% LL4(p) = sqrt((xyr(p4,1) - xyr(p3,1))^2 + (xyr(p4,2) - xyr(p3,2))^2)/.2282;


test = 'Frame_xyr_';
Directory = 'E:\Research\Robojelly\Cyanea\Bell Kinematics\Links\';
savebase = 'E:\Research\Robojelly\Cyanea\Bell Kinematics\Links\';


tA = load(strcat(Directory,file,'.txt'));

% t = tA(1:23, 1);
% A = tA(1:23, 2);

tt = tA(23+1:52-2, 1);
At = tA(23+1:52-2, 2);
A = [At;At;At;At;At;At;At;At];
t =
[tt;tt+5.4;tt+5.4*2;tt+5.4*3;tt+5.4*4;tt+5.4*5;tt+5.4*6;tt+5.4*7;tt+5.4*8] -
tt(1);

figure
plot(tA(:,1), tA(:,2),'r')
hold on
plot(tt(:,1), At(:,1))
hold off
figure
plot(t(:,1), A(:,1))

% Fourier Series Fit

n = 1000%243;

    N = linspace(0,max(t),n);

    [cy,~,~] = fit(t,A,model)     % curve fit f(t) = Y

    yr = feval(cy,N);

figure
plot(t, A)
hold on
plot(N,yr,'r')
hold off
```

```
fit_f = [N' yr];


save(strcat(savebase,file,'_Fourier_Fit','.txt'), 'fit_f', '-ASCII')

end
```

A.6 Error Analysis

```
clc
clear
close all


% Error Analysis



Num = 233:5:488;



test = 'Frame_xyr_';
Directory = 'E:\Research\Robojelly\Cyanea\Bell Kinematics\Profiles\';
savebase = 'E:\Research\Robojelly\Cyanea\Bell Kinematics\';

J0p = 1;
J4p = 51;
% J3p = 42;
% J2p = 32;

tot_err_opt = 1;

for J3p = 4:50
for J2p = 3:49
for J1p = 2:48

if J1p < J2p  && J2p < J3p

Js = [J0p J1p J2p J3p J4p];

for q = 1:length(Num)


    Nums = num2str(Num(q));
```

```
    xyc = load(strcat(Directory,test,Nums,'.txt')); % Loads the xy values of
the 51 points of the cyanea

    x = xyc(:,1);
    y = xyc(:,2);


    tht1 = atan2((y(J1p) - 0), (x(J1p) - 0));
    tht2 = atan2((y(J2p) - y(J1p)), (x(J2p) - x(J1p)));
    tht3 = atan2((y(J3p) - y(J2p)), (x(J3p) - x(J2p)));
    tht4 = atan2((y(J4p) - y(J3p)), (x(J4p) - x(J3p)));

    % Convert to Polar

    for i = 1:51
        d(i,1) = sqrt(x(i)^2 + y(i)^2);
        th(i) = atan2(y(i),x(i));
    end



    % Rotate Curve on x-axis


    for i = 1:51
    if i == J1p
        yrt(1) = d(i)*sin(th(i) - tht2);
    elseif i == J2p
        yrt(2) = d(i)*sin(th(i) - tht3);
    elseif i == J3p
        yrt(3) = d(i)*sin(th(i) - tht4);
    end
    end



    for i = 1:51
    if i <= J1p
        xr(i) = d(i)*cos(th(i) - tht1);
        yr(i) = d(i)*sin(th(i) - tht1);
    elseif i <= J2p
        xr(i) = d(i)*cos(th(i) - tht2);
        yr(i) = d(i)*sin(th(i) - tht2) - yrt(1);
    elseif i <= J3p
        xr(i) = d(i)*cos(th(i) - tht3);
        yr(i) = d(i)*sin(th(i) - tht3) - yrt(2);
    else
        xr(i) = d(i)*cos(th(i) - tht4);
        yr(i) = d(i)*sin(th(i) - tht4) - yrt(3);
    end



    end
```

```
    S(1) = 0;
    Lsum_old = 0;
    for u = 2:51
         L_temp = sqrt((x(u)-x(u-1))^2 + (y(u)-y(u-1))^2);

         S(u) = Lsum_old + L_temp;
         Lsum_old = S(u);
    end

%     figure
%     plot(S, abs(yr))


    error(q) = trapz(S,abs(yr));

end


tot_err = sum(error);

if tot_err < tot_err_opt
    J1p_opt = J1p;
    J2p_opt = J2p;
    J3p_opt = J3p;

    tot_err_opt = tot_err;
end




end

end
end
end

figure
plot(Num,error)

Js_Opt = [J0p J1p_opt J2p_opt J3p_opt J4p]
```

A.7 Profile Corrections

```
clc
clear
close all

Rotation = 0;
Rotation2p0 = 1;
Scalling = 1;
Filter = 0;

Savename = 'Frame_xy_Cor3_';

f_s = 4;

Num = 218:5:488; %598; % the 523 is limited by the scale

k = 1;
p = 1;
L(1) = 0;
r = 1+5*(f_s-1);

Full_image_width = 640;
Full_image_height = 360;

test = 'Frame_';


Apex = load(strcat('E:\Research\Robojelly\Cyanea\Bell
Kinematics\','Apex3','.txt'));
load(strcat('E:\Research\Robojelly\Cyanea\Bell Kinematics\','Scalex_Rock'));
savebase = 'E:\Research\Robojelly\Cyanea\Bell Kinematics\';


for q = f_s:length(Num)

    Nums = num2str(Num(q));

clear x y x_org y_org Org A B C D d theta d_Fil theta_Fil x y x_Fil y_Fil
x_cor y_cor x_a y_a d...
    theta x_rot y_rot x_aa

Org = load(strcat('E:\Research\Robojelly\Cyanea\Bell
Kinematics\Profiles\',test,Nums,'.txt'));

s = size(Org);


%%


x_org = Org(:,1);
y_org = Org(:,2);
```

```
x_a = Apex(q,2)+5; % need apex every five here % The 9 is a pixel correction
to move the apex to the right
y_a = -Apex(q,3) + 360;

%% Finding an apex

for i = 1:s(1)-1
    a = abs(x_org(i) - x_a);

    if i==1
        x_aa = x_org(i);
    elseif a < abs(x_aa - x_a)
        x_aa = x_org(i);
        y_a = -y_org(i)+360;
        i_a(p) = i;
    end
end


x_a = x_aa;


%% Scalling

% Normalize by Exubrella length

Norm = 1/89.83 * 1/1.234;

if Scalling == 1

dpix_x(p) = scalex(r);
old_num_pix_x = Full_image_width - (-2*dpix_x(p));
scale = old_num_pix_x/Full_image_width;

% dpix_y(p) = scalex(r) * Full_image_height/Full_image_width;
% old_num_pix_y = Full_image_height - (-2*dpix_y(p));
% scale_y = old_num_pix_y/Full_image_height;



% Scale Adjustment
    % this is based on a linear increase in size throughout the video. the
    % length at begining of relaxation was taken for each cycle and a linear
fit was
    % made

% adj_x = (Num(q)-218) * 0.217/Full_image_width;
% adj_y = (Num(q)-218) * 0.1241/Full_image_height;

adj_x = (Num(q)-218) * 0.4097/Full_image_width; % this should be scaled using
the following relation dL = sqrt(dx^2+dy^2)
adj_y = (Num(q)-218) * 0.2303/Full_image_height;
```

```
x = (x_org - x_a) * (scale - adj_x) * Norm;
y = (-y_org + 360 - y_a) * (scale - adj_y) * Norm;

x_na = (x_org - x_a) * (scale) * Norm;
y_na = (-y_org + 360 - y_a) * (scale) * Norm;

else
%     x = (x_org - x_a) * Norm;
%     y = (-y_org + 360 - y_a) * Norm;
    x = (x_org) * Norm;
    y = (-y_org + 360) * Norm;
end


%% Rotation
 % Based on the end tips

if Rotation == 1

for i = 1:s(1)
    d(i,1) = sqrt(x(i)^2 + y(i)^2); %sqrt((x(i)-x(i+1))^2+(y(i)-y(i+1))^2);
    theta(i) = atan2(y(i),x(i));
end

dtheta(p) = atan2((y(end) - y(1)),x(end) - x(1));

for i = 1:s(1)
x(i) = d(i)*cos(theta(i) - dtheta(p));
y(i) = d(i)*sin(theta(i) - dtheta(p));
end


end

% Based on a linear fit of the top of the exumbrella
sum_xy = 0;
sum_xx = 0;

if Rotation2p0 == 1
 g = 1;
 LF_mean_xsum = 0;
 LF_mean_ysum = 0;

 % Calculating the mean position of the selected points

    for i = 1:s(1)
    d(i,1) = sqrt(x(i)^2 + y(i)^2); %sqrt((x(i)-x(i+1))^2+(y(i)-y(i+1))^2);
    theta(i) = atan2(y(i),x(i));

    if x(i) >= x(i_a(p)) - 27*Norm && x(i) <= x(i_a(p)) + 27*Norm
       LF_mean_xsum = x(i) + LF_mean_xsum;
       LF_mean_ysum = y(i) + LF_mean_ysum;
```

```
    g = g+1;
    end
    end

    LF_mean_xsum = LF_mean_xsum/(g-1);
    LF_mean_ysum = LF_mean_ysum/(g-1);

g = 1;
   for i = 1:s(1)

    if x(i) >= x(i_a(p)) - 27*Norm && x(i) <= x(i_a(p)) + 27*Norm  % the
.2431 needs to be adjusted according to the scale
        sum_xy_t = (x(i)-LF_mean_xsum) * (y(i)-LF_mean_ysum);
        sum_xx_t = (x(i)-LF_mean_xsum)*(x(i)-LF_mean_xsum);

        sum_xy = sum_xy_t + sum_xy;
        sum_xx = sum_xx_t + sum_xx;

    g = g+1;
    end
    end


    a = sum_xy/ sum_xx;

    dtheta(p) = atan(a);


for i = 1:s(1)
x(i) = d(i)*cos(theta(i) - dtheta(p));
y(i) = d(i)*sin(theta(i) - dtheta(p));
end


end


%% Identifying bell tips

xtip1(p) = x(1);
ytip1(p) = y(1);
xtip2(p) = x(end);
ytip2(p) = y(end);



%% Length Measurement

Lsum_old = 0;
Lsum_old_o = 0;
Lsum_old_na = 0;
for u = 1:s(1)-1
```

```
    L_temp = sqrt((x(u)-x(u+1))^2 + (y(u)-y(u+1))^2);

    Lsum = Lsum_old + L_temp;
    Lsum_old = Lsum;

    L_temp_o = sqrt((x_org(u)-x_org(u+1))^2 + (y_org(u)-y_org(u+1))^2);

    Lsum_o = Lsum_old_o + L_temp_o;
    Lsum_old_o = Lsum_o;

    L_temp_na = sqrt((x_na(u)-x_na(u+1))^2 + (y_na(u)-y_na(u+1))^2);

    Lsum_na = Lsum_old_na + L_temp_na;
    Lsum_old_na = Lsum_na;
end

L(p) = Lsum;
L_o(p) = Lsum_o;
L_na(p) = Lsum_na;

xy = [x y];
save(strcat(savebase,'Profiles\',Savename,Nums,'.txt'),'-ASCII','-tabs','xy')
save(strcat(savebase,'Profiles\','i_a','.txt'),'-ASCII','-tabs','i_a')

p = p+1;
r = r+5;
end

%%
tipsl = [xtip1' ytip1'];
tipsr = [xtip2' ytip2'];
save(strcat(savebase,'Profiles\','Tips_Cor3_Left','.txt'),'-ASCII','-
tabs','tipsl')
save(strcat(savebase,'Profiles\','Tips_Cor3_Right','.txt'),'-ASCII','-
tabs','tipsr')

if Rotation == 1

    figure(3)
    plot(Apex(1:length(L),1), dtheta)

end


% figure(4)
% xt1 = plot(xtip1, ytip1,'-o', 'MarkerSize', 2)
% axis([-200 200 -200 50])
% hold on
% xt2 = plot(xtip2, ytip2,'-o', 'MarkerSize', 2)
% hold off
```

```
xy = load(strcat('E:\Research\Robojelly\Cyanea\Bell
Kinematics\Profiles\',Savename,'233','.txt'));


figure(100)
hh = plot(xy(:,1),xy(:,2),'r')
hold on
hh2 = plot(0, 0, '.', 'MarkerSize', 20)
xt1 = plot(xtip1, ytip1,'-o', 'MarkerSize', 2)
xt2 = plot(xtip2, ytip2,'-o', 'MarkerSize', 2)
hold off
axis([-1.4 1.4 -1.8 1])
ht = title(sprintf('Frame: %0.2f', Num(f_s)));

% Get figure size
pos = get(gcf, 'Position');
width = pos(3); height = pos(4);


% Preallocate data (for storing frame data)
mov = zeros(height, width, 1, length(Num)-f_s, 'uint8');

id = 1;
for P = f_s:length(Num)

    clear xy

Nums = num2str(Num(P));

xy = load(strcat('E:\Research\Robojelly\Cyanea\Bell
Kinematics\Profiles\',Savename,Nums,'.txt'));

set(hh(1), 'XData', xy(:,1)  , 'YData', xy(:,2));
set(hh2(1), 'XData', 0  , 'YData', 0);
set(xt1(1), 'XData', xtip1(1:id)  , 'YData', ytip1(1:id));
set(xt2(1), 'XData', xtip2(1:id)  , 'YData', ytip2(1:id));
set(ht, 'String', sprintf('Frame: %0.2f', Num(P)));

% Get frame as an image
    f = getframe(gcf);

    % Create a colormap for the first frame. For the rest of the frames,
    % use the same colormap
    if id == 1
        [mov(:,:,1,id), map] = rgb2ind(f.cdata, 256, 'nodither');
    else
        mov(:,:,1,id) = rgb2ind(f.cdata, map, 'nodither');
    end

    id = id+1;
end

% Create animated GIF
```

```
imwrite(mov, map, 'animation.gif', 'DelayTime', 0, 'LoopCount', inf);


z = [233,L_na(1);368,L_na(28);493,L_na(52)]

figure(10)
plot(Apex(f_s:length(L)+f_s-1,1), L)
xlabel('Frame')
ylabel('Length (Pix)')
hold on
plot(Apex(f_s:length(L)+f_s-1,1), L_o*Norm,'r')
plot(Apex(f_s:length(L)+f_s-1,1), L_na,'g')
plot(z(:,1),z(:,2),'.', 'MarkerSize', 20)
% axis([0 110 0.4 1.3])
hold off
legend('Length Scaled', 'Length Original')


LF = .0022*Apex(f_s:length(L)+f_s-1,1)+1.7;
t = (Num(4:end)-Num(4))*1/25;
z_t = [t(1),L_na(1); t(28),L_na(28); t(52),L_na(52)];


Length_org = [t' L'];
Length_zoomed = [t' [L_o*Norm]'];
Length_adj = [t' L_na'];
Length_LF = [t' LF];

save(strcat(savebase,'Lengths\','Length Orgiginal','.txt'),'-ASCII','-
tabs','Length_org')
save(strcat(savebase,'Lengths\','Length Zoomed','.txt'),'-ASCII','-
tabs','Length_zoomed')
save(strcat(savebase,'Lengths\','Length Adjusted','.txt'),'-ASCII','-
tabs','Length_adj')
save(strcat(savebase,'Lengths\','Length Linear Fit of Adusted','.txt'),'-
ASCII','-tabs','Length_LF')
save(strcat(savebase,'Lengths\','Linear Fit Points','.txt'),'-ASCII','-
tabs','z_t')

a = 5;
b = -a;
h = 5;
j = 1;

%% Curvature

% for i = 1-b:s(1)-a
% % R(i) = ( sqrt( (x_Fil(i) - x_Fil(i+1))^2 + (y_Fil(i) - y_Fil(i+1))^2)...
% %     * sqrt( (x_Fil(i+1) - x_Fil(i+2))^2 + (y_Fil(i+1) - y_Fil(i+2))^2)...
% %     * sqrt( (x_Fil(i+2) - x_Fil(i))^2 + (y_Fil(i+2) - y_Fil(i))^2))...
% %     /(2 * x_Fil(i+1)*y_Fil(i) - x_Fil(i)*y_Fil(i+1) +
x_Fil(i+2)*y_Fil(i+1) - x_Fil(i+1)*y_Fil(i+2) + x_Fil(i)*y_Fil(i+2) -
x_Fil(i+2)*y_Fil(i));
%
% R(j) = ( sqrt( (x_Fil(i+b) - x_Fil(i))^2 + (y_Fil(i+b) - y_Fil(i))^2)...
```

```
%     * sqrt( (x_Fil(i) - x_Fil(i+a))^2 + (y_Fil(i) - y_Fil(i+a))^2)...
%     * sqrt( (x_Fil(i+a) - x_Fil(i+b))^2 + (y_Fil(i+a) - y_Fil(i+b))^2))...
%     /(2 * x_Fil(i)*y_Fil(i+b) - x_Fil(i)*y_Fil(i) + x_Fil(i+a)*y_Fil(i) -
x_Fil(i)*y_Fil(i+a) + x_Fil(i+b)*y_Fil(i+a) - x_Fil(i+a)*y_Fil(i+b));
%
% P(j) = 1/R(j);
%
%
%     if j>1
%     bl(j) = bl(j-1) + sqrt( (x_Fil(i-h) - x_Fil(i))^2 + (y_Fil(i-h) -
y_Fil(i))^2);
%     else
%         bl(j) = sqrt( (x_Fil(i-h) - x_Fil(i))^2 + (y_Fil(i-h) -
y_Fil(i))^2);
%     end
%
%     j = j+1;
%
%
% end
%
% xy = [x_Fil' y_Fil'];

% figure(4)
% plot(P)
al(1) = 0;
cl(1) = 0;


%% Derivative

% h = 1;
% j = 1;
% for i = 1+h:s(1)-h
%
%     dydx(j) = (y_Fil(i+h) - y_Fil(i-h)) / (x_Fil(i+h) - x_Fil(i-h));
%
%     if j>1
%     al(j) = al(j-1) + sqrt( (x_Fil(i-h) - x_Fil(i))^2 + (y_Fil(i-h) -
y_Fil(i))^2);
%     cl(j) = cl(j-1) + sqrt( (x(i-h) - x(i))^2 + (y(i-h) - y(i))^2);
%     else
%         al(j) = sqrt( (x_Fil(i-h) - x_Fil(i))^2 + (y_Fil(i-h) -
y_Fil(i))^2);
%         cl(j) = sqrt( (x(i-h) - x(i))^2 + (y(i-h) - y(i))^2);
%     end
%
%     dydx_nf(j) = (y(i+h) - y(i-h)) / (x(i+h) - x(i-h));
%
%
%
%     j = j+1;
% end

% figure(5)
% plot(al,dydx)
```

```
% hold on
% plot(cl,dydx_nf)
% hold off
% ylabel('dydx')

%% Second Derivative
% h = 1;
% j = 1;
% for i = 1+h:s(1)-h
%
%     ddyddx(j) = (y_Fil(i+h) + 2*y_Fil(i)+ y_Fil(i-h)) / (x_Fil(i+h) -
x_Fil(i-h))^2;
%
% %     if j>1
% %     al(j) = al(j-1) + sqrt( (x_Fil(i-h) - x_Fil(i))^2 + (y_Fil(i-h) -
y_Fil(i))^2);
% %     else
% %         al(j) = sqrt( (x_Fil(i-h) - x_Fil(i))^2 + (y_Fil(i-h) -
y_Fil(i))^2);
% %     end
%
%     j = j+1;
% end
%
% % figure(6)
% % plot(al,ddyddx)
% % ylabel('ddyddx')
%
% xy = [x y_Fil'];
% xy_Fil = [x_Fil' y_Fil'];
% dydx = [al' dydx'];
% P = [bl' P'];

%% Saving

% % save(strcat(savebase,test,'_xy_Fil','.txt'), 'x_Fil','y_Fil', '-ASCII')
% % save(strcat(savebase,test,'_dydx','.txt'), 'al','dydx', '-ASCII')
% % save(strcat(savebase,test,'_P','.txt'), 'bl','P', '-ASCII')
%
%
%
%
% save(strcat(savebase,test,'_xy','.txt'), 'xy', '-ASCII')
% save(strcat(savebase,test,'_xy_Fil','.txt'), 'xy_Fil', '-ASCII')
% save(strcat(savebase,test,'_dydx','.txt'), 'dydx', '-ASCII')
% save(strcat(savebase,test,'_P','.txt'), 'P', '-ASCII')
%
%
%
%
%
% % for i = s(1):-1:1
% %
% %     data(k,1) = -Org(i,1)
% %     data(k,2) = Org(i,2)
% %     k = k+1;
```

```
% % end
% %
% % data(s(1)+1:s(1)*2-1,1) = Org(2:end,1)
% % data(s(1)+1:s(1)*2-1,2) = Org(2:end,2)
% %
% % figure(100)
% % plot(data(:,1),data(:,2))
% %
% %
% % save(strcat(savebase,test,'_Mirrored','.txt'), 'data', '-ASCII')
%
% % clear all


% figure(1000)
% movie(M,1)
% movie2avi(M,'Cyanea','FPS', 2)
```

Appendix B

Mastigias Oral Structure

Mastigias has an interesting oral structure which forms a significant part of its body but is believed to not have much effect on its hydrodynamic performance. This structure is appealing for adding payload volume in a robotic vehicle. The oral structure is used by *Masitgias* to filter water for food and is passive in motion. This filtering capability presents potential for applications in chemical cleaning and energy harvesting. The oral structure was replicated accurately in a CAD model. An artificial oral structure was than built and tested on the Robojelly.

B.1 Oral Structure Design

The *Mastigias papua* subspecies was chosen specifically because it is known to swim longer distances in ocean waters than other subspecies making its design evolved for swimming. Also because it has long terminal clubs which are of unknown use and can be the subject of a parametric study. In order to recreate the same hydrodynamics as the natural *M. papua*, its morphology had to be recreated as closely as possible. In general, at least three views are required to build a complex structure: top, bottom and side views. The *M. papua* oral structure is a highly complex three-dimensional geometry and requires more than three views. Uchida looked a *M. papua* from Japan. Kishinoue (1895) analyzed the *Mastigias physophora* which is thought to be a variety of the *M. papua* (Uchida, 1926). Dawson (2005) also investigated the *M. papua* amongst other species. Some views of the oral structure are given the respective references and the relevant dimensions given are summarized in Table B1. The anatomical

feature dimensions collected from Dawson (2005) are of 15 cm in diameter *M. papua* from Palau, . Dawson (2005) has the most complete set of measurements but more dimensions and views were required for an accurate replication of the oral structure. Therefore, four *Mastigias papua* were obtained from Indonesia. Their morphology was deteriorated from the travel and only one specimen was good enough for anatomical analysis.

The anatomical feature dimensions in Table B1 are given in terms of bell diameter and the respective labels are illustrated in Fig. B1-B5. A bell diameter of 16.4 cm was selected which corresponds to the diameter of Robojelly (Villanueva et al, 2011). The oral structure was to be put under the Robojelly bell for preliminary testing and therefore the features were scaled based on bell diameter. *M. papua* are usually found with bell diameter ranging between 9 to 20 cm (Uchida, 1926) but have been found to reach 30 cm according to fishermen (Kishinouye, 1895).

The oral structure was divided into four sets of parts for replication: the oral disk, oral arms, cirri and terminal clubs. The oral disk also includes oral pillars and part of the oral arms. The oral arms and oral disk were strategically divided so that each part could be molded and demolded. Having the features made modular not only eases fabrication but also enabled the variation of different parameters for analysis without having to redesign or rebuild the entire structure.

B.1.1 Oral Arms

The oral structure has eight oral arms. Each arm consists of two wings which can be visualized as flat plates connecting at their back edge and forming an angle of 60° between each other, see Fig. B1. The front, bottom and back edges are covered in cirri. The cirri sprout in all directions from the wing edges and give the arm an appearance of being full. For reconstruction, the oral arm and cirri were designed as two separate components, see Fig. B1(b)-(d). The

dimensions without cirri are given by $A_c - C_c$ and respective dimensions with cirri are given as A – C in Table B1. It should be noted that the *M. papua* in Fig. B1(a) is not as healthy as should be and as a result, the structure of the oral arm and cirri differs slightly from a healthy specimen. The cirri is less spread out and the oral arms along with cirri are more weighted down.

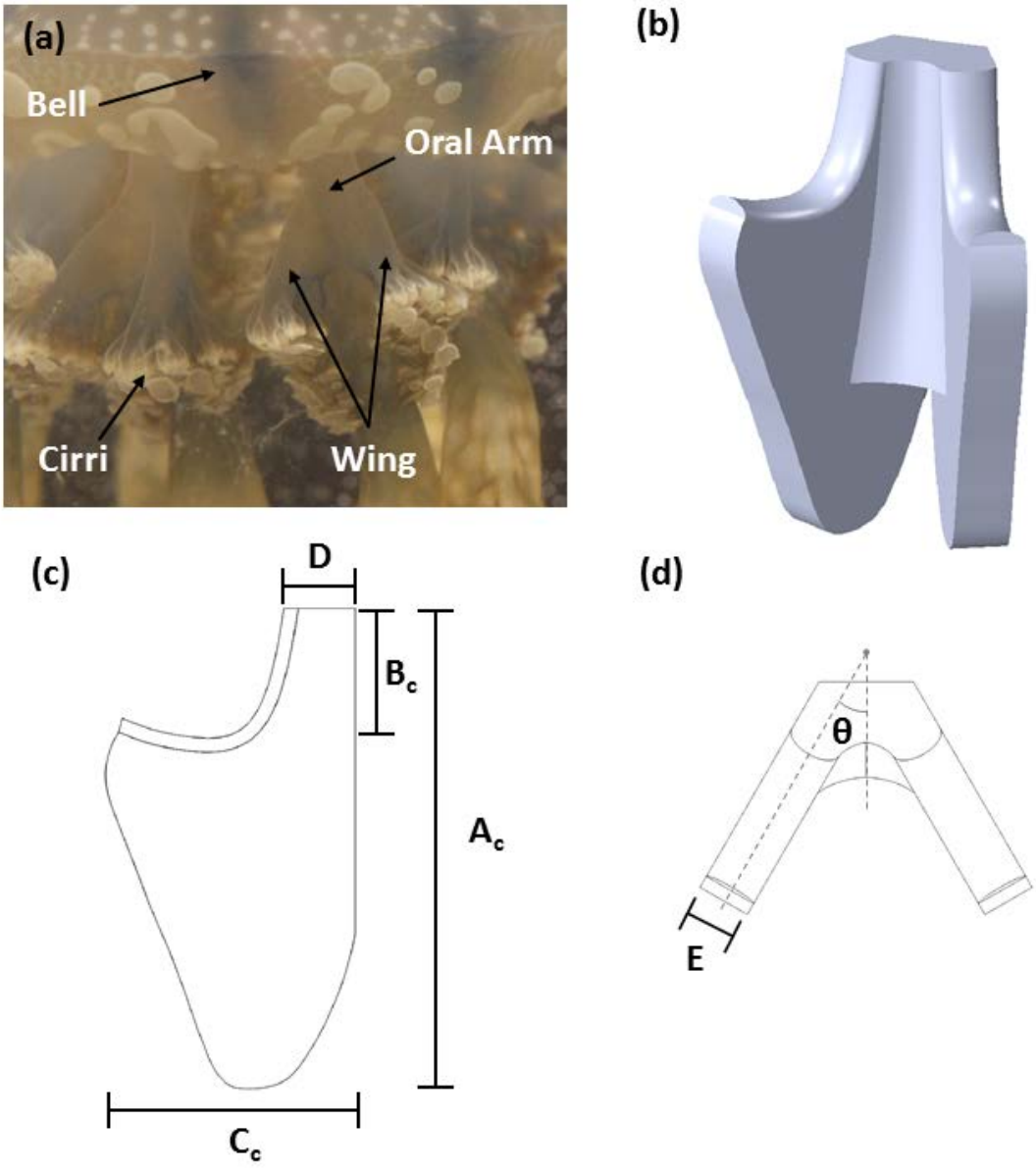

Figure B1: (a) Image of a *Mastigias papua* oral arm. (b) CAD drawing of an oral without cirri. Schematic of an oral are showing the (c) side view and (d) top view. The different dimensions are listed in B 1.

Table B1: Dimensions for oral structure dimensions of the *Mastigias papua* according to Uchida (1926), Kishinouye (1895), Dawson (2005) and this work represented by U, K, D and V respectively. The actual dimensions selected for the design of the artificial oral structure are shown in the Selected column. The dimension labels A-W and A_c-C_c are illustrated in Figs. B1-B5.

Dimensions	U	K	D	V	Selected
A	0.5	0.5	0.44	0.44	0.48
A_c					0.23
B	0.17	0.17	0.12	0.12	0.12
B_c				0.08	0.08
C				0.34	0.42
C_c				0.16	0.16
D				0.04	0.04
E				0.04	0.04
F	>0.5		0.52	0.52	0.52
G				0.1	0.04
H				0.04	0.04
I				0.04	0.04
J				0.1	0.05
K	0.1		0.11		0.12
L	0.1		0.12		0.1
M			0.04		0.04
N					0.05
O				0.08	0.02
P		0.07		0.09	0.13
Q					0.06
R					0.01
S					0.02
T	1		1	1	1
U				0.1	0.1
V				0.17	0.17
W					0.1

B.1.2 Oral Disk

The oral disk can be approximated as a square with rounded corners that is thinner at the center and has rounded edges. Each corner has an arc like structure under which connects two oral arms, see Fig. B2. The arc like structures are circularly distributed under the disk and form an octagonal shape, see Fig. B2(e). The oral disk is connected to the subumbrella via four oral pillars. The oral disk in Fig. B2(a) was of a 6 cm *M. papua*. The oral pillars and cirri have been removed but the oral arms are still present. The structure was starting to deteriorate by the general shape could still be seen. An oral disk CAD model (Fig. B2(b)-(d)) was made using the landmarks and dimensions gathered from the obtained samples and profiles in literature (Kishinoue, 1895; Uchida, 1926; Dawson, 2005).

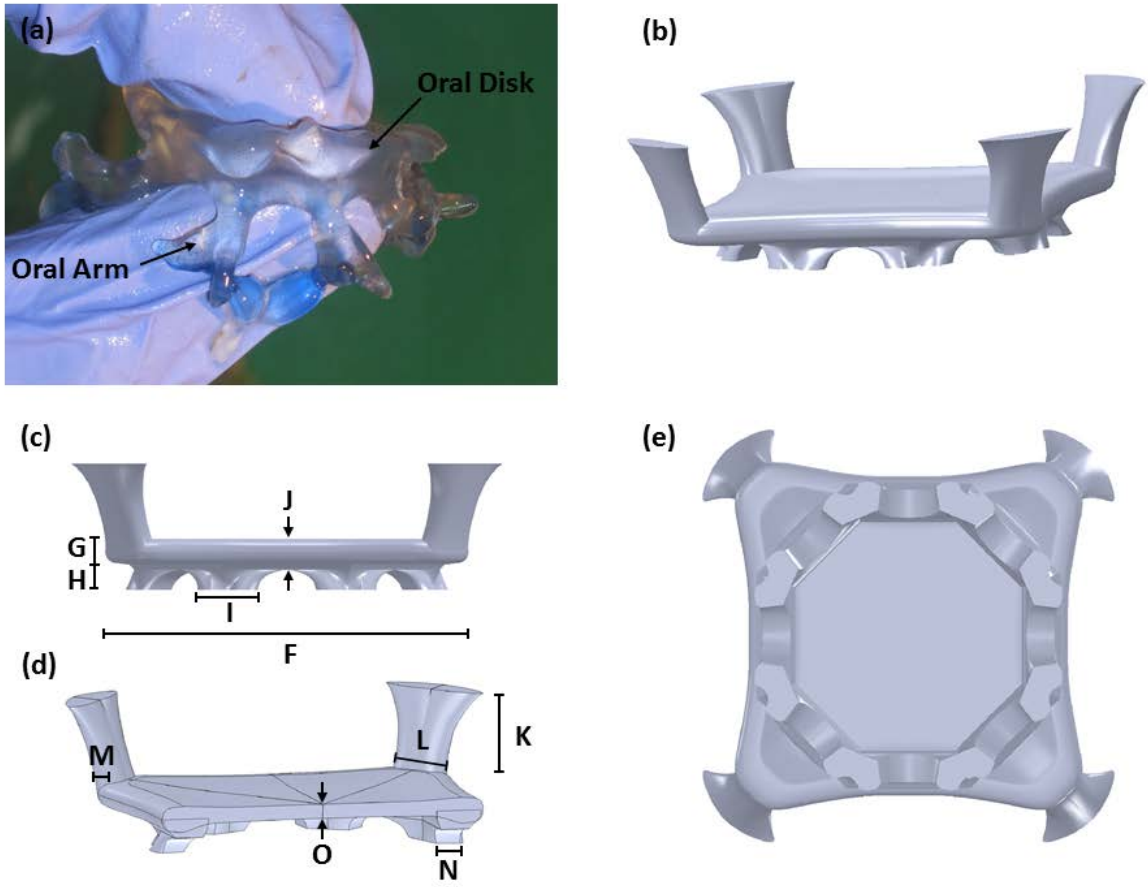

Figure B2: (a) Oral structure of *M. papua* 6 cm in bell diameter. CAD model of the oral structure showing an (b) isometric view, (c) front view, (d) cross section view at the center and (e) bottom view.

B.1.3 Cirri

The cirri can be approximated as small branches which extrude from the oral arms. They split in 2-3 folds with arms getting smaller in diameter and length each time they split, see Fig. B3(a). There is no clear pattern in the number of splits, location of the splits and orientation of each branch. The cirri sprout from the edges of the oral arm and span an area covering approximately 270°. The cirri had to be simplified for purposes of manufacturing. The pattern

was made repeatable and the number of splits was limited to two. Five larger branches split from the oral arm, and each branch splits into another five branches, see Fig. B3(a)-(b). The smaller size is limited by the viscosity of silicone used for manufacturing preventing penetration of smaller holes in the mold. The cirri was made slightly longer than the 0.07 and 0.09 which were recorded to 0.13 so they could be cut down for analysis.

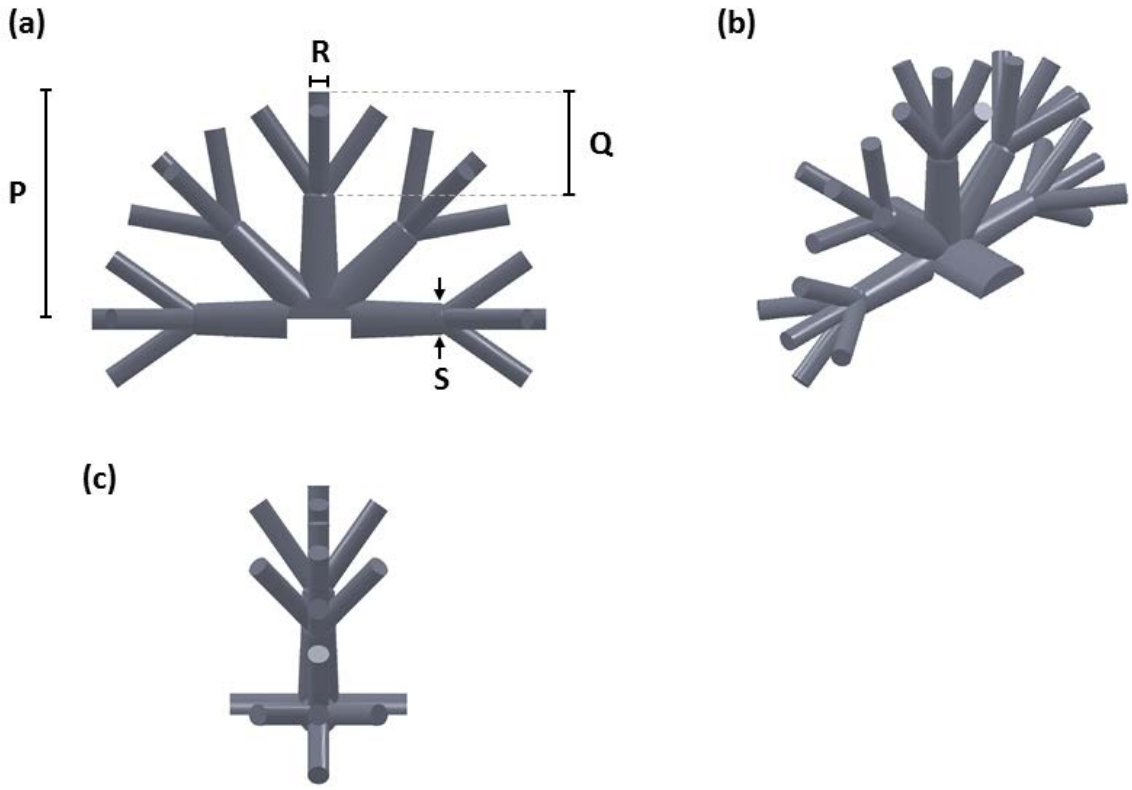

Figure B3: CAD models of cirri showing the (a) front view, (b) isometric view and (c) side view.

B.1.2 Terminal Clubs

Each of the eight terminal clubs begins at the end of an oral arm. Its cross section is triangular and the club tappers at the tips, see Fig. B4. The club length was chosen to be the

length of one bell diameter. A small piece of 0.1 connects the terminal club to the oral arm as shown in Fig. B4(a).

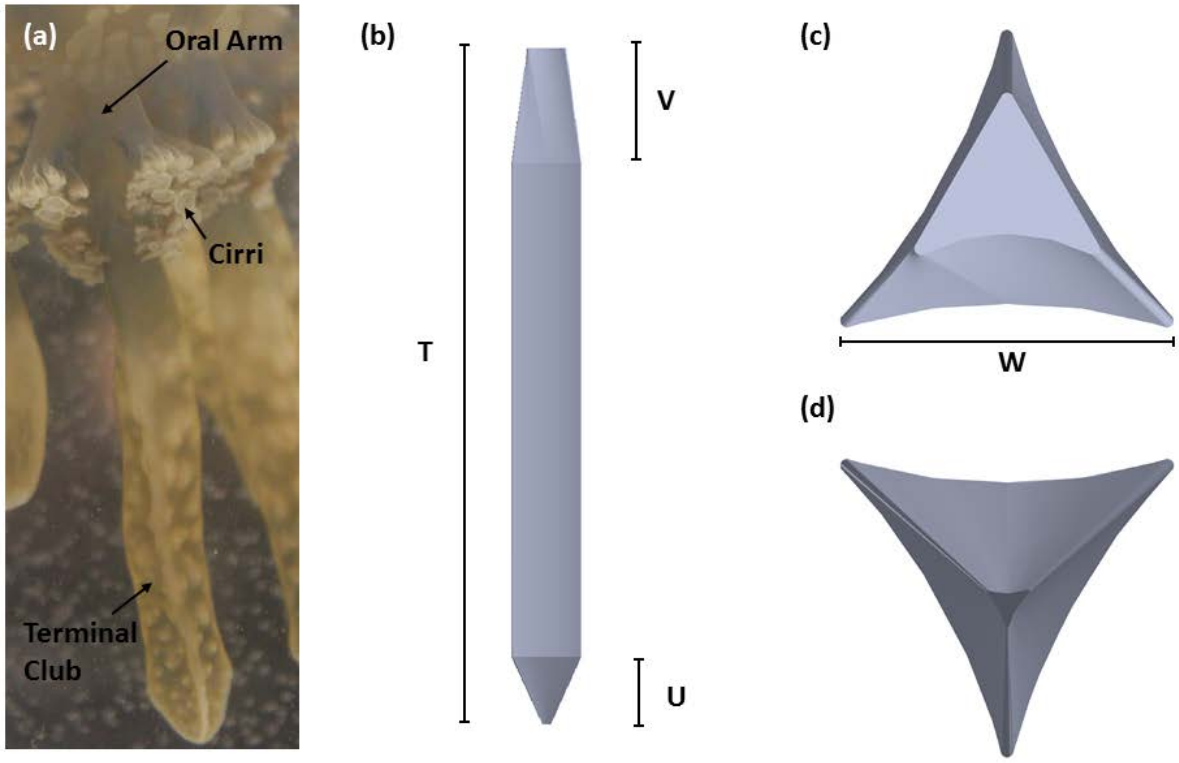

Figure B4: (a) M. papua terminal club along with the oral arm and cirri. CAD models of the terminal club showing the (b) front view, (c) side view and (d) bottom view.

B.2 Manufacturing

Two part molds where made from the CAD models of the anatomical features. The molds were 3D printed using an Object Eden260V. RTV silicone (Ecoflex 0010, Smooth-On Inc.) was poured into the molds with a black die (Silc Pig, Smooth-On). The black die is used to reduce the light reflection from the PIV laser. The different parts were assembled using more silicone. The

CAD model of the assembled oral structure without cirri is shown in Fig. B5(a) and the silicone oral structure is shown in Fig. B5(b).

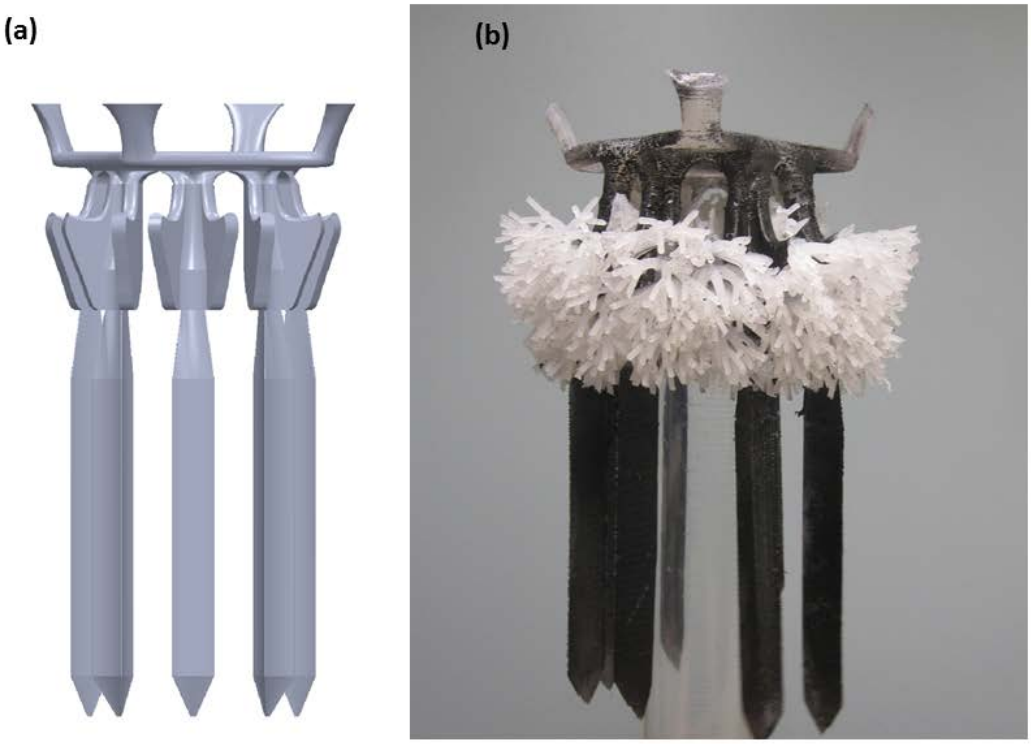

Figure B5: (a) CAD model of the oral structure without cirri. (b) Silicone oral structure.

B.3 References

Dawson, M. N., (2005). Five new subspecies of *Mastigias* (Scyphozoa: Rhizostomeae: Mastigiidae) from lakes, Palau, Micronesia. *J. Mar. Biol. Ass. U.K.*, 85, 679-694

Kishinoue, K., (1895). Description of a new Rhizostoma *Mastigias physophora* nov. spec. *Dobutsugaku Zassi*, 9, 86-88

Uchida, T. (1926). The Anatomy and Development of a Rhizostome Medusa, Mastigias papua L. Agassiz, with Observations on the Phylogeny of Rhizostomae. *J. Fac. Sci. Tokyo Univ.* (sect. IV, Zool.), 1, 45-95

Villanueva, A. Smith, C. Priya, S., (2011). Biomimetic Robotic Jellyfish (Robojelly) using Shape Memory Alloy. *Bioinspir. Biomim.*, 6, 3

Appendix C

Non-Linear Shape Memory Alloy Controller Review

A literature review was conducted to determine which type of controller is most promising for SMA actuators for robotic jellyfish applications. As shown with the rapid heating controller, the Robojelly was able to swim well with a limited state feedback of the actuator. During turning a more complex bell motion was observed. Some of the arms only partially deform depending on the degree of turning required. This requires a more precise feedback of the actuators. SMA undergoes large hysteresis during deformation (Dutta et al., 2005). If the SMA wires were always actuated with the same power cycle, there would only be a major hysteresis loop. Major hysteresis loops are easy to model and would not require much effort to control. The system gets more complex when the power cycle varies from one loop to another. This causes minor hysteresis loops as shown in Fig. C.1.

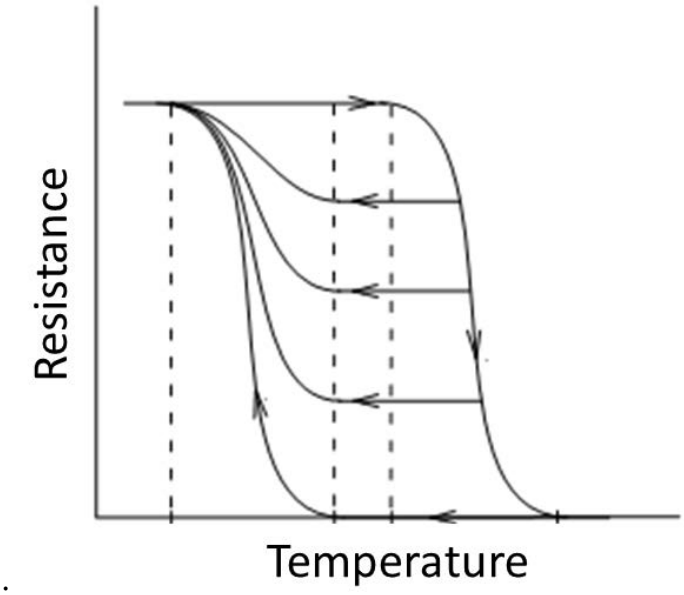

Figure C.1: Schematic of the major and minor loops of shape memory alloy (Redrawn from Dutta et al., 2005).

In order to model the minor loops more information of the current and past state of the actuators must be known. There are two main types of control algorithm used to compensate for nonlinearities. The first are dynamic algorithms which use mathematical models to compensate for hysteresis. These use thermo-mechanical models such as the ones developed by Bo and Lagoudas (1999), Dupta et al. (2004), and Shibly and Soffker (2010). These algorithms can also use hysteresis models such as the Duhem–Madelung, and Preisach and Krasnoselskee-Pokrovskii model (Webb et al. 1998; Shibly and Sofker, 2010). Dynamic models require many parameters of the system to be experimentally specified. They are not able to adapt to disturbances to the system which makes them impractical for applications in varying underwater environments.

The second type of control algorithm involves feedback control as shown in Fig. C.2. This includes the different PID configurations with displacement, strain or resistance feedback (Pons et al., 1997; Webb et al., 2000; Sreekumar et al., 2007; Ahn and Kha, 2008).

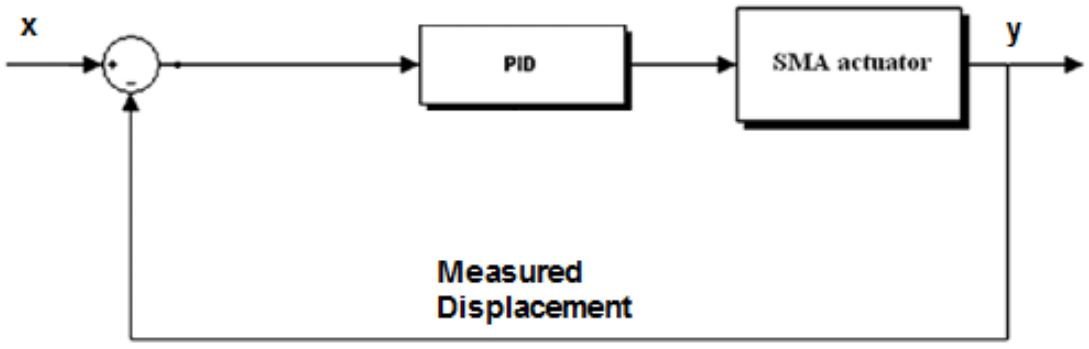

Figure C.2: Schematic diagram of a feedback controller for shape memory alloy control.

Displacement measurements offer high accuracy but require large sensors which make this type of system unfeasible for controlling the eight actuators of the Robojelly. This type of control algorithm is well developed and offers a good starting point. PID controllers are sometimes coupled with a Fuzzy logic to update the PID gains (Kha and Ahn, 2006, Bizdoaca et al., 2006). These controllers offer good accuracy and the ability to adapt to disturbances of the system.

As previously mentioned, displacement sensors are not feasible for Robojelly. Strain sensors are also not accurate enough for SMA wires due to their small size. The better state feedback is resistance feedback since it does not require external sensors. Simply monitoring the state of the electronic circuit suffices. A resistance feedback controller requires a controller such as PID with an inverse dynamic model which is used to convert resistance into position, see Fig. C.3.

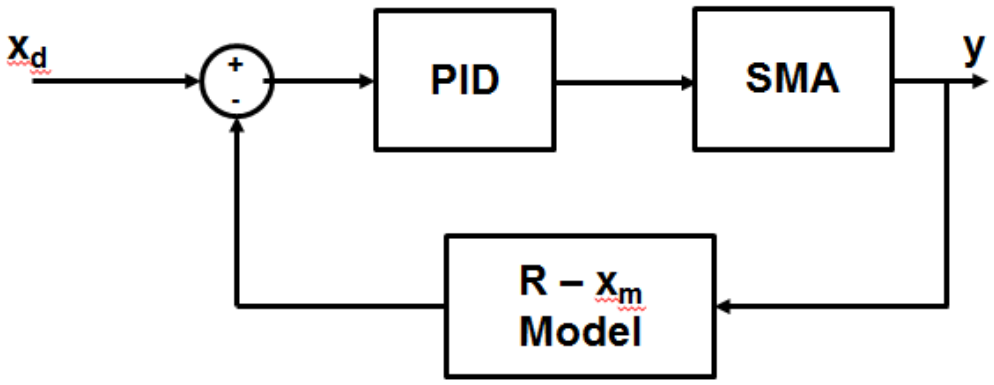

Figure C.3: PID controller with inverse dynamic model.

Several inverse dynamic models have been used for this type of applications such as linear approximation of the major loops, polynominal fit, variable sub-layers (Pons et al., 1997). The most promising models include neural network and ANFIS controllers (Ghafari et al., 2006). Neural networks work in a similar way as biological nervous systems. It is a non-algorithmic approach for processing information and can be used to model non-linear systems (Asua et al.

2010). A neural network based controller (Ma et al., 2003), could be used to model the resistance to deformation ($R - x_m$). Neural networks undergo a training phase where the system learns the behavior of the subject. Performance examples can be seen in (Ma et al., 2003). Some of the limitations of neural networks include the effects of stress and minor loop modeling. One promising method used to overcome these limitations is to add the adaptive ability of Fuzzy logic. A controller which combines both these modalities is called as Adaptive Neuro-Fuzzy Inference System (ANFIS) (Kilicarslan et al., 2011). ANFIS has shown the ability to properly account for minor loops (Kilicarslan et al., 2011).

ANFIS based controllers have shown promising results for SMA actuators. They have also been studied for controlling natural muscles in prosthetic applications. Natural muscles and SMA have a similar hysteresis behavior. For SMA applications, ANFIS has only been used as an inverse model and their performance was evaluated using displacement sensors. For controlling the Robojelly, an inverse ANFIS model could be used to convert resistance feedback into displacement. In addition, a self-tuning PID controller which combines a PID controller with Fuzzy logic could be used to compensate for disturbances in the system, see Fig. C.4. It is possible that the Fuzzy controller will not be necessary; however, experimental validation will need to be conducted.

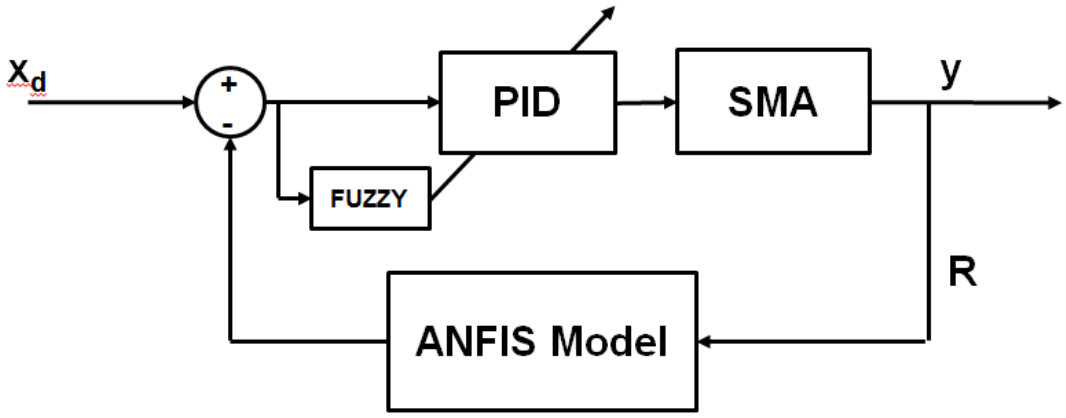

Figure C.4: Proposed SMA controller which includes an ANFIS inverse dynamic model with a self-tuning PID controller and resistance feedback.

References

Ahn, K. K. and Kha, N. B. (2008). Modeling and control of shape memory alloy actuators using Preisach model, genetic algorithm and fuzzy logic. Machatronics, 18, 141-152

Asua, E., Feutchwanger, J., Garcia-Arribas, A. and Etxebarria, V. (2010). Sensorless Control of SMA-based Actuators Using Neural Networks. *J. intl. Mat. Syst. Struct.* 21, 1809-1818

Bizdoaca, N., Hamdan, H. and Selisteanu, D. (2006). Fuzzy Logic Controller for a Shape Memory Alloy Tentacle Robotic Structure. IEEE, 0-7803-9521-2/06

Bo, Z. and Lagoudas D. C. (1999), Thermomechanical modeling of polycrystalline SMAs under cyclic loading, Part IV: modeling of minor hysteresis loops. *Int. J. Eng. Sci.* 37, 1205-1249

Dutta S. M. and Ghorbel F. H. (2005). Differential Hysteresis Modeling of a Shape Memory Alloy Wire Actuator. *IEEE/ASME Transactions on Mechatronics*, 10, 2

Kha, N. B. and Ahn, K. K. (2006). Position Control of Shape Memory Alloy Actuators by Using Self Tuning Fuzzy PID Controller. IEEE, 0-7803-9514-X/06

Kilicarslan, A., Song, G. and Grigoriadis, K. M. (2011). Modeling and Hysteresis Compensation in a thin SMA Wire Using ANFIS Methods. *J. Intel. Mat. Syst. Struct.* 22

Ma, N., Song, G. and Lee, H. J. (2003). Position control of SMA actuators with internal electrical resistance feedback. *Proceedings of SPIE, Smart Struct. Mat.* 5049

Pons, J. L., Reynaerts, D., Peirs, J., Ceres, R. and VanBrussel, H. (1997). Comparison of Different Control Approaches to Drive SMA Actuators. *IEEE ICAR*, 0-7803-4160-0-7/97

Shibly, H. and Sofker, D. (2010). Mathematical models of shape memory alloy behavior for online and fast prediction of the hysteretic behavior. *Nonlinear. Dyn.* 62, 53-66

Sreekumar, M., Singaperumal, M., Nagarajan, T., Zoppi, M. and Molfino, R. (2007). Recent advances in nonlinear control technologies for shape memory alloy actuators. *J. Zheijian Univ. Scie. A*, 8(5), 818-829

Webb G. V., Wilson, L., Lagoudas, D. C. and Rediniotis, O. (2000). Adaptive Control of Shape Memory Alloy Actuators for Underwater Biomimetic Applications. *AIAA J.* 38, 2

Webb G. V., Lagoudas, D. C. and Kurdila, A. J. (1998). Hysteresis Modeling of SMA Actuators for Control Applications. *J. Intel. Mat. Syst. Stuct*. 9, 432-448

Appendix D

Copyrights

Some of the material in this document has previously been published. The following lists each section where this is the case along with associated copyright information.

2.1 Jellyfish Inspired Unmanned Underwater Vehicle

Villanueva, A., Bresser, S., Chung, S., Tadesse, Y. and Priya, S. (2009). Jellyfish inspired underwater unmanned vehicle. Proc. SPIE, 7287, doi:10.1117/12.815754;

Copyright 2009 Society of Photo-Optical Instrumentation Engineers. One print or electronic copy may be made for personal use only. Systematic reproduction and distribution, duplication of any material in this paper for a fee or for commercial purposes, or modification of the content of the paper are prohibited.

http://dx.doi.org/10.1117/12.815754

2.2 Bio-Inspired Shape Memory Alloy Composite (BISMAC) Actuator

Villanueva, A. A., Joshi, K. B., Blottman, J. B. and Priya, S. (2010a). A bio-inspired shape memory alloy composite (BISMAC) actuator. *Smart Mater. Struct*. 19, 025013

See attached document at the end of this appendix for IOP reprint permission.

2.3 FlexLegs – Flexible Legs Actuated by Shape Memory Alloy

Villanueva, A., Smith, C. and Priya, S. (2011). Flexlegs – Flexible Legs Actuated by Shape Memory Alloy. *AMSE Conference Proceeding* SMASIS2011-5134

See attached document at the end of this appendix for ASME reprint permission.

3.1 BISMAC Control Using SMA Resistance Feedback

Villanueva A, Priya S. (2010). BISMAC control using SMA resistance feedback. *Proc. SPIE.* 7642 76421Z, doi:10.1117/12.847788

Copyright 2010 Society of Photo-Optical Instrumentation Engineers. One print or electronic copy may be made for personal use only. Systematic reproduction and distribution, duplication of any material in this paper for a fee or for commercial purposes, or modification of the content of the paper are prohibited.

http://dx.doi.org/10.1117/12.847788

3.2 Lowering the Power Consumption of Ni-Ti Shape Memory Alloy by compositional Modification

Villanueva A, Gupta S, Priya S (2012). Effects of Copper Addition and Annealing Temperature on Transition Temperature of Ni-Ti Shape Memory Alloys. *SPIE Smart Struct./NDE*, 8342-52; doi:10.1117/12.914539

Copyright 2012 Society of Photo-Optical Instrumentation Engineers. One print or electronic copy may be made for personal use only. Systematic reproduction and distribution, duplication of any material in this paper for a fee or for commercial purposes, or modification of the content of the paper are prohibited.

http://dx.doi.org/10.1117/12.914539

4.1 Biomimetic Robotic Jellyfish (Robojelly)

Villanueva A, Smith C and Priya S (2011). Biomimetic Robotic Jellyfish (Robojelly) using Shape Memory Alloy. *Bioinspir. Biomim.* 6, 036004

See attached document at the end of this appendix for IOP reprint permission.

4.2 Robojelly Bell Kinematics and Resistance Feedback Control

Villanueva A, Priya S, Anna C, Smith C (2010). Robojelly bell kinematics and resistance feedback control. Robotics and Biomimetics (ROBIO), 2010 IEEE International Conference on , vol., no., pp. 1124-1129, 14-18; doi: 10.1109/ROBIO.2010.5723486

See attached document at the end of this appendix for IEEE reprint permission.

IOP Permission

Conditions

Non-exclusive, non-transferrable, revocable, worldwide, permission to use the material in print and electronic form will be granted **subject to the following conditions:**

· Permission will be cancelled without notice if you fail to fulfil any of the conditions of this letter.

· You will make reasonable efforts to contact the author(s) to seek consent for your intended use. Contacting one author acting expressly as authorised agent for their co-authors is acceptable.

· You will reproduce the following prominently alongside the material:

o the source of the material, including author, article title, title of journal, volume number, issue number (if relevant), page range (or first page if this is the only information available) and date of first publication

o for material being published electronically, a link back to the article (via DOI)

o if practical and IN ALL CASES for works published under any of the Creative Commons licences the words "© IOP Publishing. Reproduced by permission of IOP Publishing. All rights reserved"

· The material will not, without the express permission of the author(s), be used in any way which, in the opinion of IOP Publishing, could distort or alter the author(s)' original intention(s) and meaning, be prejudicial to the honour or reputation of the author(s) and/or imply endorsement by the author(s) and/or IOP Publishing.

· Payment of £0 is received in full by IOP Publishing prior to use.

IEEE Permission

The IEEE does not require individuals working on a thesis to obtain a formal reuse license, however, you may print out this statement to be used as a permission grant:

Requirements to be followed when using any portion (e.g., figure, graph, table, or textual material) of an IEEE copyrighted paper in a thesis:

1) In the case of textual material (e.g., using short quotes or referring to the work within these papers) users must give full credit to the original source (author, paper, publication) followed by the IEEE copyright line © 2011 IEEE.
2) In the case of illustrations or tabular material, we require that the copyright line © [Year of original publication] IEEE appear prominently with each reprinted figure and/or table.
3) If a substantial portion of the original paper is to be used, and if you are not the senior author, also obtain the senior author's approval.

Requirements to be followed when using an entire IEEE copyrighted paper in a thesis:

1) The following IEEE copyright/ credit notice should be placed prominently in the references: © [year of original publication] IEEE. Reprinted, with permission, from [author names, paper title, IEEE publication title, and month/year of publication]
2) Only the accepted version of an IEEE copyrighted paper can be used when posting the paper or your thesis on-line.
3) In placing the thesis on the author's university website, please display the following message in a prominent place on the website: In reference to IEEE copyrighted material which is used with permission in this thesis, the IEEE does not endorse any of [university/educational entity's name goes here]'s products or services. Internal or personal use of this material is permitted. If interested in reprinting/republishing IEEE copyrighted material for advertising or promotional purposes or for creating new collective works for resale or redistribution, please go to http://www.ieee.org/publications_standards/publications/rights/rights_link.html to learn how to obtain a License from RightsLink.

If applicable, University Microfilms and/or ProQuest Library, or the Archives of Canada may supply single copies of the dissertation.

ASME Permission

Dear Mr. Villanueva:

It has been confirmed that your paper was presented at the Conference, therefore, it is our pleasure to grant you permission to use the ASME paper "FLEXLEGS – FLEXIBLE LEGS ACTUATED BY SHAPE MEMORY ALLOY," by Alex Villanueva, Colin Smith, Shashank Priya, Paper Number SMASIS2011-5134, as cited in your letter for inclusion in a Doctoral Thesis entitled Design and Analysis of Biomimetic Medusa Robots to be published by UMI Company.

Permission is granted for the specific use as stated herein and does not permit further use of the materials without proper authorization. As is customary, we request that you ensure full acknowledgment of this material, the author(s), source and ASME as original publisher. Acknowledgment must be retained on all pages printed and distributed.

Many thanks for your interest in ASME publications.

Sincerely,

Beth Darchi

Permissions & Copyrights

ASME, 2 Park Avenue

New York, NY 10016

T: 212-591-7700

F: 212-591-7841

E: darchib@asme.org